Transactions of the ASME

Journal of Heat Transfer (ISSN 0022-1481) is edited and published quarterly at the offices of The American Society of Mechanical Engineers, United Engineering Center, 345 E. 47th St., New York, N. Y. 10017. ASME-TWX No. 710-581-5267, New York. Second-class postage paid at New York, N.Y., and at additional mailing offices.
CHANGES OF ADDRESS must be received at Society headquarters seven weeks before they are to be effective. Please send old label and new address.
PRICES: To members, $36.00, annually; to nonmembers, $72.00. Single copies, $24.00 each. Add $5.00 for postage to countries outside the United States and Canada.

INDEXED by the Engineering Index, Inc.

Journal of Heat Transfer

Published Quarterly by The American Society of Mechanical Engineers

VOLUME 105 • NUMBER 1 • FEBRUARY 1983

ANNOUNCEMENTS

TECHNICAL PAPERS

(Contents Continued on Page 32)

(Contents Continued)

TECHNICAL NOTES

Interaction of the Nucleation Phenomena at Adjacent Sites in Nucleate Boiling

M. Sultan
Technical Specialist,
Westinghouse Canada Limited,
Hamilton, Ontario

R. L. Judd
Professor,
Department of Mechanical Engineering,
McMaster University,
Hamilton, Ontario
Mem. ASME

The present investigation is an original study in nucleate pool boiling heat transfer combining theory and experiment in which water boiling at atmospheric pressure on a single copper surface at two different levels of heat and different levels of subcooling was studied. Cross spectral analysis of the signals generated by the emission of bubbles at adjacent nucleation sites was used to determine the relationship of the time elapsed between the start of bubble growth at the two neighbouring active sites with the distance separating them. The experimental results obtained indicated that for the lower level of heat flux at three different levels of subcooling, the elapsed time and distance were directly related. Theoretical predictions of a temperature disturbance propagating through the heating surface in the radial direction gave good agreement with the experimental findings, suggesting that this is the mechanism responsible for the activation of the surrounding nucleation sites.

Introduction

In recent years, boiling heat transfer has achieved world wide interest since it is a very efficient mode of heat transfer. The boiling phenomenon is associated with the transfer of tremendous quantities of thermal energy relative to the heat-transfer rate attainable in nonboiling systems, and it is for this reason that boiling heat transfer is frequently applied as a cooling mechanism in processes which involve very high density heat generation rates. Because of the extensive experimental and theoretical research conducted by many researchers in the last two decades which has provided better understanding of the nucleate boiling phenomenon, many of the boiling parameters such as bubble growth, waiting time, departure size, bubble emission frequency can be predicted with a reasonable degree of accuracy. However, the interdependence of the nucleation processes at adjacent nucleation sites is not well understood. Henley and Hummel [1] reported a statistical analysis which they had performed upon some high-speed motion picture films of the boiling process that is relevant to this topic. From their analysis, they concluded that nucleation of a bubble inhibited nucleation at all surrounding nucleation sites for a short time interval thereafter whereas there appeared to be a strong tendency for nucleation to occur at one of the surrounding nucleation sites shortly after bubble departure. These observations were explained in terms of a sonic interaction between the growing bubble and its surroundings but no experimental evidence of this effect was presented. The most relevant research has been reported by Chekanov [2] who experimentally studied the interaction between two artificial nucleation sites in water boiling at atmospheric pressure. The time elapsed between the start of bubble growth at two neighbouring artificial nucleation sites was obtained by analysing photoelectric signals corresponding to the formation of bubbles at each of the sites. Water vapour bubbles were formed on a very thin permalloy plate 20 μm in thickness by two heated copper rods of 1.4-mm dia located beneath the permalloy plate which could be moved relative to each other. Chekanov analysed experimental measurements of the time elapsed between the start of bubble growth at two neighbouring nucleation sites as a random variable using statistical methods and found that the results followed a Gamma distribution

$$P(\tau) = \frac{\lambda(\lambda\tau)^{\nu-1}e^{-\lambda\tau}}{\Gamma(\nu)} \tag{1}$$

where $P(\tau)$ is the probability density function, ν is the shape parameter, λ is the scaling parameter, and τ is the time elapsed. Chekanov found the shape parameter, ν, to be a function of the different spacings. For a distance of less than three times the bubble maximum diameter "repulsive" interaction occurred in which ν was found to be greater than unity ($\nu > 1$), and the growth of a bubble on one center inhibited the growth of a bubble on the other. At a distance greater than three times the bubble maximum diameter "attractive" interaction occurred in which ν was found to be less than unity ($\nu < 1$), and the growth of a bubble on one center enhanced the growth of a bubble on the other. Chekanov postulated that the formation of bubbles affected one another by acoustic action and hydrodynamic mixing. At distances between the two nucleation sites much greater than maximum bubble diameter there were no interactions, ostensibly because the acoustic effect is of little importance for these separations.

The bubble flux density distribution on the heating surface is an indirect source of information about the behaviour of the bubble formation process. The fact that very little bubble flux density data exists may be due to the fact that knowledge of the frequency of vapour bubble emission is not very extensive. Recently, Sultan and Judd [3] studied the bubble flux density for water boiling at atmospheric pressure on a single copper surface at different levels of heat flux and subcooling. The bubble flux density was observed to be nonuniformly distributed on the heating surface especially at the lower level of heat flux, suggesting that the formation of bubbles at various locations on the surface were interrelated.

It was deduced from Sultan and Judd's results that the bubble flux density was distributed in cluster form. Irrespective of whether this observaton is indicative of site activation by dryout of the microlayer underlying a bubble and subsequent vapour entrapment as the bubble departed in accordance with Judd and Lavdas [4] or whether it is the result of some other as yet undetermined effect, the results of Sultan and Judd's investigation were inconsistent with Chekanov's results, which indicated that the formation of a bubble at one nucleation site inhibited the formation of a bubble at a neighbouring nucleation site if the nucleation sites

Contributed by the Heat Transfer Division for publication in the JOURNAL OF HEAT TRANSFER. Manuscript received by the Heat Transfer Division October 1, 1982.

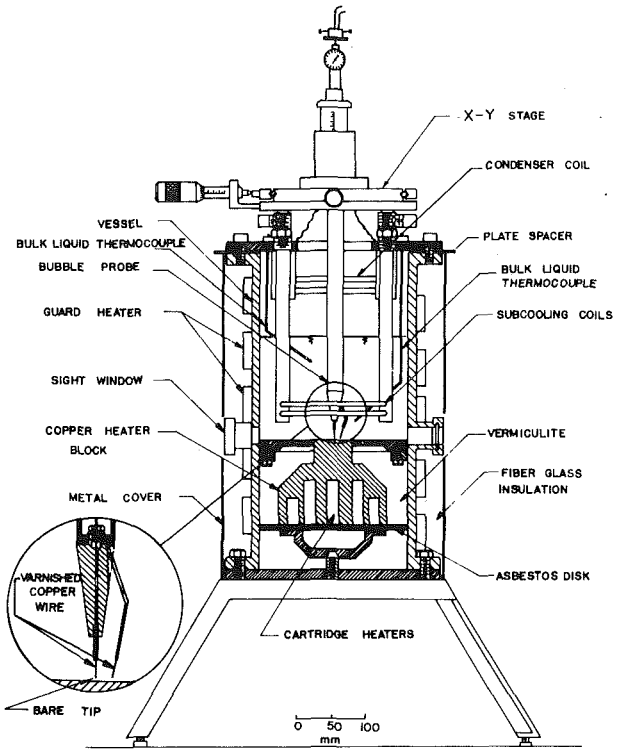

Fig. 1 Section of boiling vessel

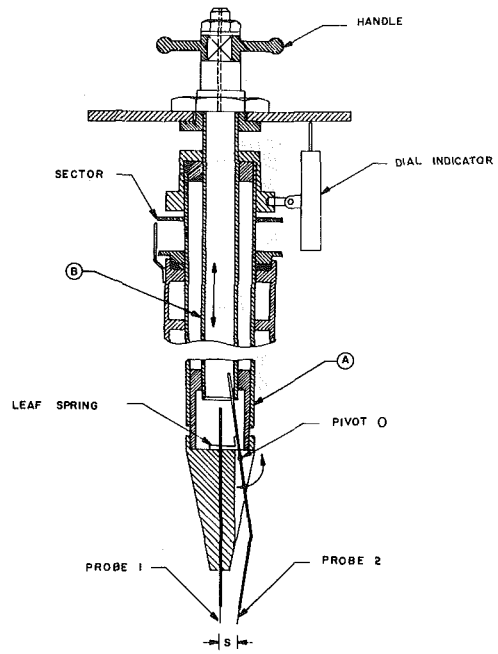

Fig. 2 Bubble detection probe assembly

were close together. The present investigation was undertaken in an attempt to clarify this matter.

Experimental Apparatus and Procedure

The apparatus built by Wiebe [5] in 1970 to measure the liquid temperature distribution perpendicular to the heating surface was later modified by Sultan [6] to examine the active site distribution and bubble flux density over the heating surface. In the present study the apparatus was modified once again, changing the bubble detection probe in order to meet the requirements for studying the interaction of the nucleation phenomena at adjacent sites. The modified apparatus used was capable of:

1 Determining the active site locations with the capability of locating them precisely
2 Measuring the distance between the two neighbouring active sites
3 Enabling the time elapsed between the start of bubble growth at two neighbouring active sites to be determined

The sectional view of the experimental apparatus assembly is presented in Fig. 1 and a more complete description is presented in reference [7].

The single most important component of the apparatus is the bubble probe assembly. Alternating current passing through the 0.007-in dia varnished copper wires of each of the probes comprising the bubble probe assembly enabled the variation in electrical conductance between the probe tips and the grounded heating surface to be detected. The design details of the bubble probe assembly are shown in Fig. 2. Probe #1 was made in a conical shape and a stainless steel tube was soldered at the tip of the cone in order to support the varnished copper wire in such a way as to disturb the flow pattern around the bubble emitted as little as possible. Probe #2 rotated around pivot 0 and a leaf spring was used to keep the stainless steel tube in which the varnished copper wire was inserted in contact with the bottom of tube B. When the handle was rotated, tube B moved with respect to tube A and repositioned the stainless steel tube supporting probe #2 which then rotated around pivot 0 establishing a new separating distance, S, between the probe tips. The relative motion of tube B with respect to tube A was determined with a dial indicator, whose measurements provided the information required to obtain a rough estimate of the probe tip separation.

The surface condition is an important feature of this type of research, and so it is worthwhile noting that the test surface was fine turned on a lathe and finished with 200, 400, and 600 grit emery papers in the summer of 1976, when the first author began his study of active site distrubution and bubble

Nomenclature

A = cross spectrum amplitude
C = heat transfer surface specific heat
f_{xy} = cross spectral frequency
k = heat transfer surface thermal conductivity
Q = ring heat source strength
Q/A = heat flux
r = radial coordinate
r' = ring heat source radius
R_d = bubble departure radius
S = distance separating nucleation sites
t = time
$T(r,z)$ = temperature in the heat transfer surface
T_s = saturation temperature
T_w = surface temperature
$x(t)$ = Probe #1 signal
$y(t)$ = Probe #2 signal
z = axial coordinate
$\theta(r,z)$ = temperature difference
θ_{xy} = cross spectrum phase shift
κ = heat transfer surface thermal diffusivity
ρ = heat transfer surface density
$\rho_{xy}(\tau)$ = cross correlation function coefficient
τ = elapsed time between bubble formations
τ_g = elapsed time to the end of bubble growth period
τ_w = elapsed time to the end of bubble waiting period

flux density. Little attention was given to it from that time until the summer of 1979, when the present investigation was performed, except that just prior to obtaining the data reported in this paper, the test surface was cleaned with a soft cloth moistened with liquid silver polish after which the residue was rinsed away with a stream of methanol from a squeeze bottle.

The boiling vessel was filled to a depth of approximately 15 cm with deionized distilled water containing 0.1 gm of salt/litre. At the beginning of each test, the level of water inside the vessel was checked and the cooling water valves which were used to control the flow rate to the subcooling and vapour condenser coils were opened. The signal generator, the oscilloscope, and the signal conditioning units were turned on, the signal generator was set to 11 kHz and 10 V, and the amplifiers located in the signal conditioning units were set to the appropriate amplification values. The bubble detection probe assembly with zero probe tip separation was lowered until the tips came in contact with the heating surface, after which it was raised a very small distance. The gap between the tips of the bubble detection probes and the heating surface was then adjusted to approximately 0.25 mm and maintained at this value thereafter. The X-Y stage was actuated to move the bubble detection probe assembly in various different directions to check that there was no contact between the probe tips and the heating surface.

A copper block heater setting of approximately 470 kW/m^2 was established to heat up the boiler assembly quickly. A warm up time of approximately 2 hrs was allowed to elapse in order to achieve steady-state conditions and to ensure that the nucleation sites were properly activated at the beginning of each test, after which the heat input was reduced to the desired level. Two hours were required for the system to regain steady state after a change in heat flux or subcooling took place. The attainment of thermal equilibrium was indicated by invariant measurements of the various thermocouples which were located at different places in the boiler assembly. It was found that the water bulk temperature was sensitive to the settings of the vapour condenser and subcooling systems, especially at lower level of heat flux, and consequently care was taken in setting the cooling water flow rates to minimize the interdependence. Once conditions had attained steady state, the individual temperature readings were measured by a manually balanced thermocouple potentiometer. The individual temperatures were measured twice, once at the beginning and again at the end of each test and the average of each set of measurements was recorded. A reading of the barometric pressure was obtained in order to compute the saturation temperature of the water corresponding to the atmospheric pressure.

In order to place the first probe on an active site, the Y micrometer setting was fixed and the X micrometer was moved very slowly until a significant signal appeared on the first channel of the oscilloscope screen. Then X and Y micrometers were moved very small increments in both directions to optimize the strength of the signal. The second bubble detection probe was moved horizontally relative to the first probe, establishing a small separation distance, S, by advancing the mechanism after which the second probe was moved along the periphery of a circle with a radius S until another active site was encountered. The separating distance, S, between the probes was deemed equal to the distance between the two bubble centers when a strong signal appeared on the second channel of the oscilloscope screen. The distance separating the probe tips was measured after each test with an optical comparator to a precision of ± 25 μm in order to obtain an accurate value for the separating distance.

While the signals from the two probes were transmitted to the oscilloscope, the signals were also transmitted to the DECLAB 11/03 digital computer where the signals were digitized at 1000 samples/second. For each signal, a 1000 value data sample was stored in the computer memory for subsequent analysis to calculate the time elapsed between the start of bubble growth at two neighbouring active sites using either cross-spectral density function analysis or cross-correlation function coefficient analysis. Each time that the experiment was repeated for the same test conditions, a new set of 1000 values for each signal was stored in the computer memory for analysis. Consecutive cumulative averages were performed on the power spectra, amplitude and phase of the cross-spectrum and cross-correlation function coefficient until invariant distinct peaks were observed. One hundred one millisecond correlation lag or lead values were investigated in order to cover the complete range of bubble cycle time (growth and waiting periods).

For cross-spectral density function analysis, the time

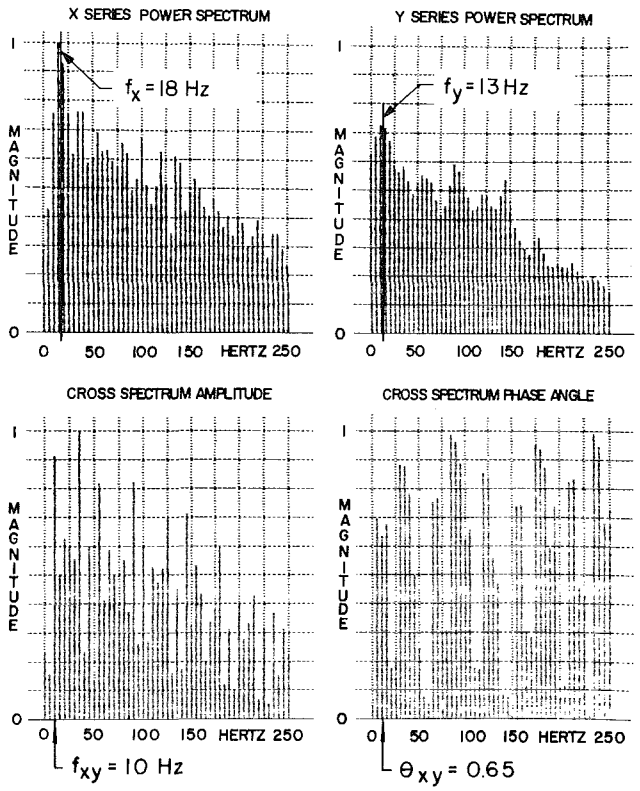

Fig. 3(*a*) Example of cross-spectral density function analysis

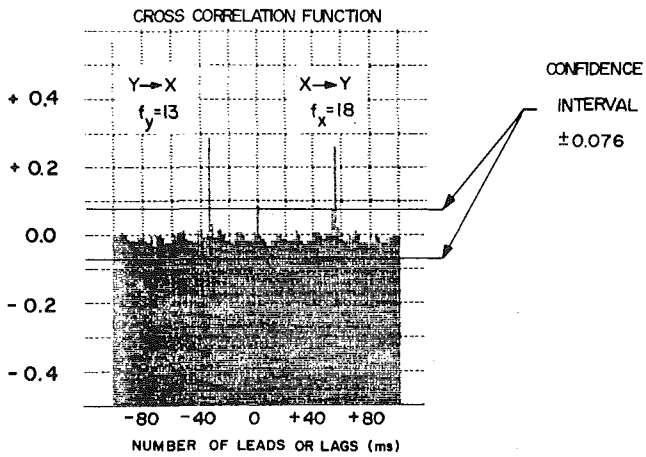

Fig. 3(*b*) Example of cross-correlation function coefficient analysis

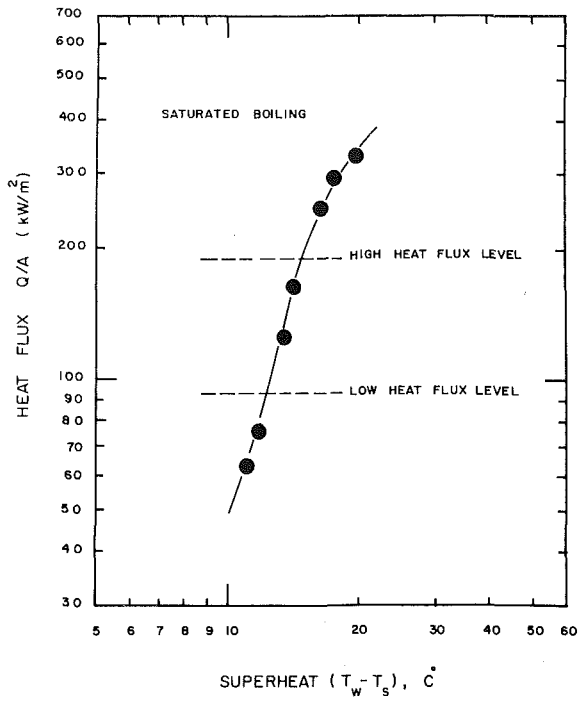

Fig. 4 Characteristic boiling curve for the present investigation

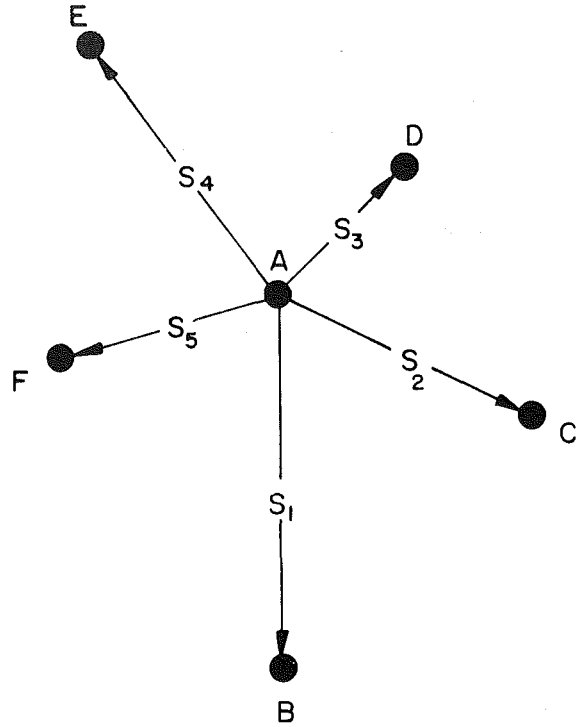

Fig. 5 Arrangement of active nucleation site (A) and its surrounding active nucleation sites (B, C, D, E, F)

difference between the activity in the two time series $x(t)$ and $y(t)$ at any frequency f_{xy} is given by

$$\tau = \theta_{xy}/2\pi f_{xy} \tag{2}$$

In order to measure the time lag between the formation of a bubble at nucleation site X and the subsequent formation of a bubble at nucleation site Y, the first significant peak in the cross spectrum amplitude f_{xy} was determined by inspection of the computer plotted amplitude-frequency diagram. Then the cross spectrum phase lag θ_{xy} was evaluated at the same frequency by inspection of the computer plotted phase-frequency diagram and the time lag was computed in accordance with equation (2).

For cross-correlation function coefficient analysis, the time lag between the formation of a bubble at nucleation site X and the subsequent formation of a bubble at nucleation site Y was determined by inspection of the peaks which appear in the computer plotted cross-correlation function diagram. A crude check was made to ensure that the peak values of the cross-correlation function coefficient $\rho_{xy}(\tau)$ were significant by computing the confidence interval in which $\rho_{xy}(\tau)$ would be 95 percent certain to lie if $\rho_{xy}(\tau)$ were equal to zero meaning that there was no correlation between the two events. All peaks which occurred in the values of $\rho_{xy}(\tau)$ within the confidence interval were ignored and only those which exceeded the confidence interval were considered to be significant.

Figure (3*a*) shows an example of some data which were obtained with Q/A = 92.21 kW/m^2, ΔT_{sub} = 12°C and S = 4.2 mm after a number of cumulative averages had been taken for the results. The autopower spectra of the signals indicate that the predominant frequencies in $x(t)$ and $y(t)$ are approximately 18 Hz and 13 Hz, respectively. Analysis of the cross-spectrum amplitude indicates that the first significant spike which is present in the correlation between the activity in $x(t)$ and $y(t)$ occurs in the vicinity of f_{xy} = 10 Hz while analysis of the cross-spectrum phase shift at f_{xy} = 10 Hz indicates that the phase shift θ_{xy} is approximately 0.65. Since the computed value of the phase shift was expressed in fractions of a circle between 0 and 1, therefore $\theta_{xy} = 0.65 \times 2\pi$ radians so that by substitution in equation (2), the time elapsed between the start of bubble growth at the two neighbouring active sites would appear to be 65 milliseconds.

Analysis of the cross-correlation function corresponding to the same data discussed above as presented in Fig. (3*b*) indicates a strong correlation between the activity in both signals $x(t)$ and $y(t)$ at 55 milliseconds, somewhat different than the value obtained by cross-spectral analysis. However, since the precision of the cross-correlation function analysis is obviously greater than the precision of the cross-spectral density function analysis, it was concluded that site X causes the activation of the site Y after a time lapse of 55 milliseconds. Similarly, a strong correlation exists at −34 ms, in which case site Y causes the activation of site X after a time lapse of 34 milliseconds. So far as the present investigation to study the effect of one active site on its surrounding active sites was concerned, only the peaks corresponding to the cases in which signal $x(t)$ leads signal $y(t)$ were of interest.

Results and Discussion

The characteristic boiling curve for the heating surface used in this study, representing the relationship between the surface superheat $(T_w - T_s)$ and the heat flux Q/A, is shown in Fig. 4. An experimental investigation was performed for water boiling at atmospheric pressure on a single copper surface for various levels of heat flux and subcooling. The purpose of the investigation was to study the nucleation phenomena at the adjacent sites in order to determine whether the time elapsed between the start of bubble growth at two neighbouring active sites, τ, and the separating distance, S, were related.

Different sets of active sites were studied individually at each level of heat flux and subcooling, each set consisting of one active site and its surrounding active sites at various distances (S_1, S_2, . . .) as depicted in Fig. 5. A heat flux level of 192.11 kW/m^2 was tested first at saturation but it was not possible to detect any cross-correlatoin between the two probe signals $x(t)$ and $y(t)$ for this boiling condition. Subcooling changed the situation somewhat since for moderate sub-

cooling at the same level of heat flux it became possible to detect a cross-correlation between the two probe signals although analysis of the results obtained indicated that the correlation between the elapsed time, τ, and the separating distance, S, was weak. However, tests performed at a heat flux level of 92.21 kW/m^2 and the same levels of subcooling yielded results for which it was possible to detect a much stronger cross-correlation between the two probe signals. A definite trend was observed which indicated that time elapsed between the start of bubble growth at the two neighbouring active sites increased with increasing separating distance between them.

In light of this significant finding, a single data set consisting of an active site and its surrounding sites was studied in detail at the lower level of heat flux (92.21 kW/m^2) and three different levels of subcooling (0, 6.5, and 12°C). The combined experimental results are presented in Fig. 6, which shows the existence of a unique relationship for the separating distance and the time elapsed between the start of bubble growth at two neighbouring active sites. The dependence of τ on S disappears for the three different levels of subcooling after approximately 4.5 mm which is about twice the bubble departure diameter in the saturation condition. The distance at which the interaction of nucleation phenomena at adjacent nucleation sites ceases to exist defines a circle whose area is approximately the area of influence identified by Han and Griffith [8].

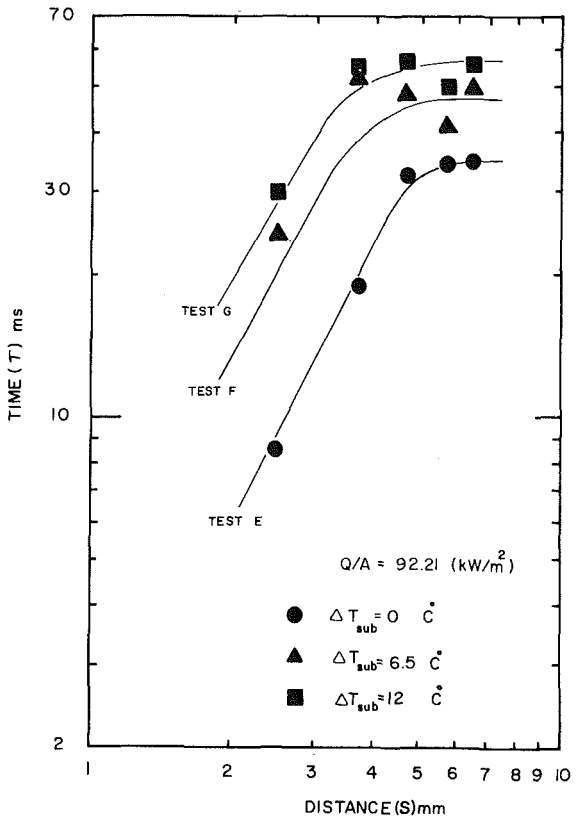

Fig. 6 Relationship between elapsed time (τ) and separating distance (S) for three different levels of subcooling

In the course of the investigation, it was observed that the time elapsed between the start of bubble growth at the surrounding site and the start of bubble growth at the central site was always greater than the time that the bubble at the central site which was supposed to have caused the subsequent emission took to grow to its maximum size and depart. This observation suggested that the interaction of the nucleation phenomena at the two sites might be associated with the departure of the bubble as Henley and Hummel indicated and not with its appearance as had been expected to be the case. Accordingly, the experimental results were analysed in terms of the separating distance-bubble departure size difference ($S-R_d$) and the time elapsed between the start of the bubble growth for the two active sites minus the bubble growth period ($\tau-\tau_g$). Plotting the data in terms of ($S-R_d$) versus ($\tau-\tau_g$) tended to draw the experimental results together into a single curve suggesting that a single relationship might fit all the experimental data.

The approach used in the derivation of a theoretical model to explain the experimental results involved the diffusion of heat through the heating surface. The local instantaneous heat-transfer coefficient on a heat transfer surface has been studied by Barakat and Sims [9] who showed that during the early stages of bubble growth, while there was an outward movement of the flow field around the bubble interface, the local heat-transfer coefficient increased to maximum and then decreased as the bubble interface velocity decreased. The heat-transfer coefficient went through a minimum shortly afterward and then when the bubble left the heating surface the liquid moved inward causing the heat-transfer coefficient at the heating surface in the vicinity of the bubble periphery to attain a maximum once again. After bubble detachment from the heating surface, the heat-transfer coefficient decreased

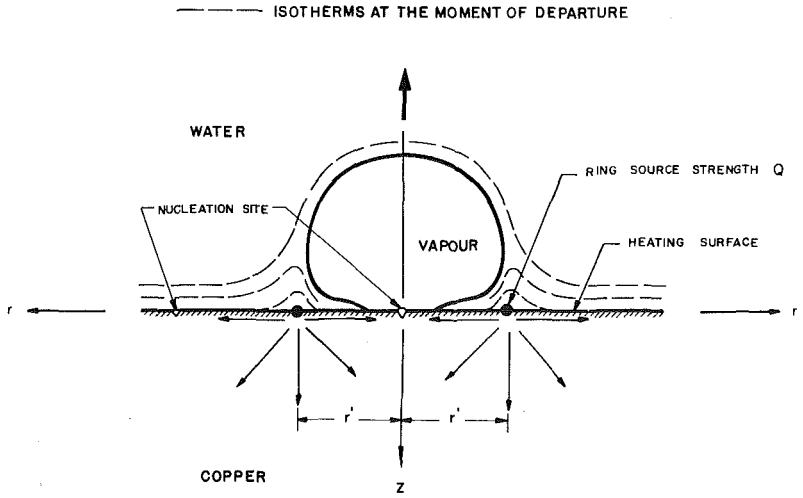

Fig. 7 Idealized model for the transfer of heat from an instantaneous ring source to the heating surface

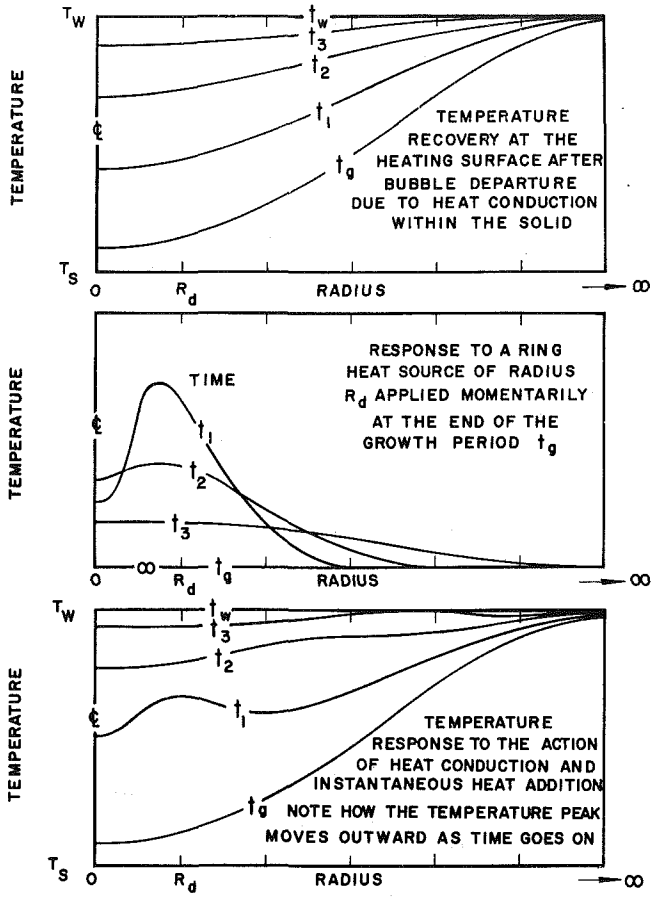

Fig. 8 Schematic representation of the action of heat conduction and instantaneous heat addition on the temperature recovery in the heating surface

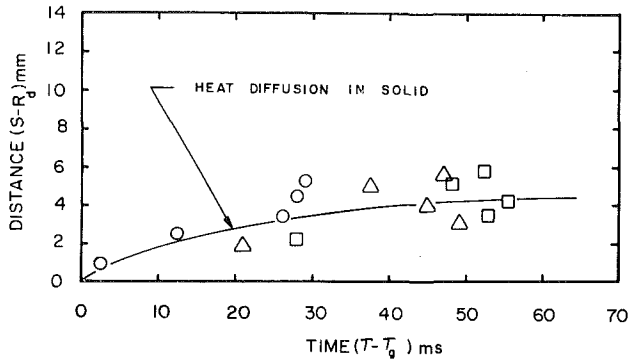

Fig. 9 Comparison between the experimental results and the prediction of heat diffusion in the heating surface

monotonically to its original value. The interesting stage in Barakat and Sims's studies so far as the present investigation is concerned occurs when the bubble leaves the heating surface because then the resistance to heat flow from the liquid at the periphery of the bubble to the surface is at a minimum.

The temperature field around a growing vapour bubble was reported by Beer et al. [10] for Freon 113 boiling under atmospheric pressure conditions. As the bubble started to grow, the superheated liquid layer at the heating surface was pushed away from the nucleation site and high-temperature liquid accumulated at the perhiphery of the growing bubble. The corresponding temperature fields in the surface (copper and steel) around an active site were depressed because much of the heat transferred to the growing bubble was drawn from the heating surface by evaporation of the microlayer underlying the bubble.

On the basis of these observations, the phenomenon responsible for nucleation site interaction was represented by an instantaneous transfer of heat to the surface from a ring source surrounding the bubble base at the moment of departure. The idealized representation of the heat conduction process is depicted in Fig. 7. The temperature disturbance which results propagates outward through the heating surface in the radial direction and establishes the conditions for the nucleii at adjacent nucleation sites to grow after some delay related to the separating distance. Throughout the formulation it was assumed that:

1 Nuclei capable of being activated exist at surrounding nucleation sites at distances $S_1, S_2, \ldots$.

2 Only the pair of active sites being investigated interact with each other.

3 Heat diffuses from an instantaneous ring source through the surface and propagates in the radial direction close to the heating surface.

4 For the purposes of analysis, it is assumed that all of the energy contained by the liquid in the vicinity of the bubble base at the moment of departure passes into the surface and that none of it diffuses into the surrounding liquid.

The axisymmetric conduction equation may be represented as

$$\rho C \frac{\partial \theta}{\partial t} = k\left[\frac{1}{r}\frac{\partial}{\partial r}\left(r\frac{\partial \theta}{\partial r}\right) + \frac{\partial^2 \theta}{\partial z^2}\right] \tag{3}$$

where the initial condition is

$$\theta(r, 0) = 0 \tag{4}$$

and the boundary conditions appropriate to the problem are

$$\frac{\partial \theta(0,z,t)}{\partial r} = 0 \tag{5}$$

$$\theta(\infty, z, t) = 0 \tag{6}$$

$$\frac{\partial \theta(r,0,t)}{\partial z} = 0 \tag{7}$$

$$\theta(r,\infty,t) = 0 \tag{8}$$

The solution of equation (3) for an instantaneous transfer of heat from a ring source of strength Q applied at radius r' was provided by Carslaw and Jaeger [11] as

$$\theta(r,z,t) = \frac{Q/\rho C}{8(\pi\kappa t)^{3/2}} \exp -\left[\frac{r^2 + r'^2 + z^2}{4\kappa t}\right] I_0\left(\frac{r\,r'}{2\kappa t}\right) \tag{9}$$

where I_0 is the modified Bessel function of the first kind order zero. Interpreting this solution to suit the problem by setting $z = 0$, $r = S$, $t = \tau$ and $r' = R_d$, equation (9) becomes

$$\theta(S,\tau) = \frac{Q/\rho\, C}{8(\pi\kappa\,\tau)^{3/2}} \exp -\left[\frac{S^2 + R_d^2}{4\,\kappa\,\tau}\right] I_0\left(\frac{SR_d}{2\kappa\,\tau}\right) \tag{10}$$

Figure 8 depicts the role of the ring source pictorially. The upper diagram shows that the temperature at the surface at time $t = t_g$ has been depressed by the growth of a bubble at the centerline $R = 0$, and as a consequence no active nucleation site in the vicinity will be able to emit a bubble until the temperature has recovered at time $t = t_w$. The middle diagram shows the effect of a ring temperature disturbance which appears at the same time and moves outward with decreasing amplitude. The lower diagram shows the superposition of the two effects and suggests that the ring heat source acts to re-establish the surface temperature and therefore the conditions under which bubble emission at the surrounding sites could occur quicker than would be the case if recovery of the surface temperature were to depend on conduction within the solid alone.

The relationship between the time elapsed from bubble departure ($\tau - \tau_g$) and the distance from the ring source ($S - R_d$) at which the maximum in the temperature distribution

occurs can be obtained from equation (10) as indicated in reference [7]. However, the temperature disturbance propagation outward in the radial direction adjacent to the solid/liquid interface can be approximated by

$$(S-R_d) \cong 2\sqrt{\kappa(\tau-\tau_g)} \tag{11}$$

Equation (11) can be evaluated for copper by substituting the value of the thermal diffusivity $\kappa = 8.15 * 10^{-2}$ mm^2/ms to obtain the relationship

$$(S-R_d) \cong 0.57\sqrt{(\tau-\tau_g)} \tag{12}$$

The prediction of this relationship and the experimental findings are presented in Fig. 9 where it may be seen that the theoretical model for the diffusion of heat through the solid gives good agreement with the experimental findings.

Implications of the Research

The experimental results obtained at the lower level of heat flux (92.21 kW/m^2) and three different levels of subcooling (0, 6.5, and 12°C) showed that the separating distance, S, and the time elapsed, τ, between the start of bubble growth at two neighbouring active sites were uniquely related, such that the time elapsed between the start of bubble growth at the two neighbouring active sites increased with increasing separating distance. For this particular level of heat flux, all the experimental data for the saturated and subcooling boiling conditions plotted as $(S-R_d)$ versus $(\tau-\tau_g)$ tended to draw together into a single curve suggesting that a single relationship would fit the data. A theoretical model involving heat diffusion in the solid close to the heating surface gave good agreement with the experimental findings suggesting that this might be the mechanism responsible for the activation of the surrounding nucleation sites.

As a result of the research performed, it has been demonstrated that the bubble nucleation phenomenon and the distribution of active nucleation sites are related in a manner which is not yet completely understood. One implication of this interdependence is that the emission of a bubble at a nucleation site is governed by the pattern of bubble emissions of all of its neighbours within a certain as yet undetermined distance and that it is not an isolated event as commonly thought. Henceforth, it will be necessary to think in terms of "area-averaged" bubble emission frequencies in the formulation of nucleate boiling heat-transfer models. Obviously more research is required. The investigation reported herein only represents the first step in a series of experimental and theoretical studies which will have to be done for various liquid/surface combinations at different levels of heat flux and subcooling with a number of different applied pressures to investigate more general situations.

It is felt that this sort of investigation will advance our knowledge of the boiling phenomena and help to fill the gaps between the actual behaviour and the predictions of the existing models in nucleate boiling heat transfer. The potentially active nucleation sites are known to be randomly distributed over the surface and if research of the type described above led to the identification of a probability function which would express the likelihood of two adjacent sites being active in terms of frequency of emission of the two sites, it would be a relatively simple matter to determine the bubble flux density for a given surface. Shoukri and Judd [12, 13] have already developed a theory for predicting bubble emission frequency and have shown that nucleate boiling heat flux is uniquely related to bubble flux density, although these theories are both dependent upon a knowledge of the effective cavity size which is related to surface material and finishing technique. Ultimately, it might turn out to be possible to predict nucleate boiling heat flux without recourse to any arbitrary constants.

References

1 Henley, J. J., and Hummel, R. L., "A Third Factor in Boiling Nucleation," *Industrial and Engineering Chemistry, Fundamentals*, Vol. 6, No. 4, 1967, pp. 603-606.

2 Chekanov, V. V., "Interaction of Centers in Nucleate Boiling," translated from *Teplofizika Vysokikh Temperatur*, Vol. 15, No. 1, 1977, pp. 121-128.

3 Sultan, M., and Judd, R. L., "Spatial Distribution of Active Sites and Bubble Flux Density," ASME JOURNAL OF HEAT TRANSFER, Vol. 100, No. 1, 1978, pp. 56-62.

4 Judd, R. L., and Lavdas, C. H., "The Nature of Nucleation Site Interaction," ASME JOURNAL OF HEAT TRANSFER, Vol. 102, No. 3, 1980, pp. 461-464.

5 Weibe, J. R., "Temperature Profiles in Subcooled Nucleate Boiling," Mechanical Engineering Department, McMaster University, Canada, 1970.

6 Sultan, M., "Spatial Distribution of Active Sites and Bubble Flux Density," Mechanical Engineering thesis, Mechanical Engineering Department, McMaster University, Hamilton, Canada, 1977.

7 Sultan, M., "Interaction of the Nucleation Phenomena at Adjacent Sites in Nucleate Boiling," Ph.D. thesis, Mechanical Engineering Department, McMaster University, Hamilton, Canada, 1981.

8 Han, C. Y., and Griffith, P., "The Mechanism of Heat Transfer in Nucleate Pool Boiling," *International Journal of Heat and Mass Transfer*, Vol. 8, 1965, pp. 887-914.

9 Barakat, S. A., and Sims, G. E., "Heat Transfer in Pool Barbotage," *Proceedings of the Sixth International Heat Transfer Conference*, Canada, 1978.

10 Beer, H., Burow, P., and Best, R., "Bubble Growth, Bubble Dynamics and Heat Transfer in Nucleate Boiling Viewed with a Laser Interferometer," Ch. 2 in "Heat Transfer in Boiling," edited by E. Hahne and U. Grigull, Academic Press, 1977.

11 Carslaw, H. S., and Jaeger, J. C., "Conduction of Heat in Solids," Oxford Press, 2nd ed., 1973.

12 Shoukri, M. S. M., and Judd, R. L., "A Theoretical Model for Bubble Frequency in Nucleate Pool Boiling Including Surface Effects," *Proceedings of the Sixth International Heat Transfer Conference*, Canada, 1978.

13 Shoukri, M. S. M., and Judd, R. L., "On the Influence of Surface Conditions in Nucleate Boiling — the Concept of Bubble Flux Density," ASME JOURNAL OF HEAT TRANSFER, Vol. 100, No. 4, 1978, pp. 618-623.

A Solution for Dispersed Flow Heat Transfer Using Equilibrium Fluid Conditions

G. L. Yoder, Jr.[1]

W. M. Rohsenow

Massachusetts Institute of Technology, Cambridge, Mass. 02139

A method for predicting steady state dispersed vertical upflow film boiling heat transfer under constant heat flux conditions is presented. Differential transport equations and accepted heat transfer correlations are used to form a solution dependent upon knowledge of conditions at the dryout point only. Thermal nonequilibrium is included in the analysis and the actual flow quality is determined from local equilibrium conditions. A nondimensional grouping is derived which indicates the extent of nonequilibrium present in the flow. Results of this analysis are compared to data of three fluids in tube geometry: Freon 12, nitrogen, and steam. Predictions compare favorably with data from all three fluids.

Introduction

Film boiling of a flowing liquid occurs when heated surface temperatures are high enough to prevent intimate liquid-surface contact. This heat transfer regime occurs in some cryogenic equipment, in steam generating systems, and may occur during several phases of a nuclear reactor loss of coolant accident. One type of film boiling flow pattern of particular interest is dispersed flow. High heated surface temperatures characterize this flow regime which consists of liquid droplets entrained in a flowing vapor.

Two types of flow patterns may precede formation of dispersed flow. Inverted annular flow occurs at low quality dryout (the point where liquid is no longer in contact with the heated surface) and results from high heat flux conditions or a high heated surface temperature preceding flow initiation. Dispersed flow formation begins when vapor void fractions are greater than ~60 percent [1]. Annular flow occurs at higher dryout qualities and results from lower heat fluxes or low initial heated surface temperatures. After the dryout point, heat transfer is primarily through the vapor, and a sharp rise in the heated surface temperature results. Vapor temperatures may be above the saturation temperature even with liquid remaining in the flow, thus, thermal nonequilibrium may exist. The actual flow quality X at a point will therefore be less than the corresponding local equilibrium quality, X_{eq}.

Two techniques are normally used to develop predictive methods for dispersed flow heat transfer. Several investigators have used various correlation techniques to predict dispersed flow film boiling data. Most have chosen to use a modification of a standard single phase heat transfer coefficient, assuming that heat is transferred primarily to the vapor. A good review of such correlations is given by Groeneveld [2].

The second technique commonly used is numerical. Typically, a mechanistic model is developed which includes several coupled heat transfer mechanisms. Mass, momentum, and energy transport equations are then integrated stepwise along the flow path. Most of these schemes have the ability to predict actual vapor temperature and therefore nonequilibrium within the flow.

Early work using this technique was that of Forslund [3] who modeled heat transfer to both the droplets and the vapor. Other similar models have predicted dispersed flow heat transfer with varying degrees of success [4–7]. Two-dimensional numerical models have also been developed which include the effect of droplet evaporation on the local vapor temperature profile [8–9].

Numerical techniques include phenomena important to dispersed flow; however, they are complicated and require computer solution. This has led to attempts to combine correlational, and phenomenological techniques.

Both Groeneveld [10] and Chen [11] have developed methods of calculating dispersed flow heat transfer using single-phase vapor heat transfer coefficients. Heat transfer is predicted using actual quality. Both developed an empirical correlation for actual quality from post-dryout data assuming that the heat was transferred only to the flowing vapor. These solutions are iterative in nature, but explicitly recognize nonequilibrium within the flow, and do not require stepwise numerical solution.

In this study, a method for predicting actual quality is derived directly from the differential transport equations. Results of a numerical solution similar to those described above are used to simplify the governing equations to allow a nonnumerical solution. The method uses only dryout conditions and local equilibrium fluid conditions to predict heated surface temperatures under constant heat flux conditions.

Heat Transfer Model

Four dispersed flow heat transfer mechanisms can be identified: heat transfer directly from the wall to the vapor, heat transfer from the vapor to the entrained droplets, heat transfer from the wall to the drops, and heat transfer by axial conduction in the wall. These four mechanisms have been included in a numerical model [12] similar to those developed previously [4–7]. Results of this analysis have shown that conduction and wall-to-drop heat transfer play only a minor heat transfer role in most situations. These conclusions have been used to develop a nonnumerical dispersed flow model. The heat transfer model assumes that heat is transferred primarily from the wall to the vapor and then from the vapor to entrained droplets.

It is assumed that the flow is steady state and the heat flux is constant; that equilibrium quality exists at burnout and the liquid is always at the saturation temperature. The drop size distribution is characterized by one average drop size, and liquid and vapor velocities are uniform across the tube. Radiation is neglected and enclosure pressure drop and fluid kinetic energy effects are assumed unimportant.

Droplet Size at Dryout. In order to begin the dispersed flow analysis, droplet size along with liquid and vapor

[1] Currently at Oak Ridge National Laboratory, Oak Ridge, Tenn. 37830

Contributed by the Heat Transfer Division for publication in the JOURNAL OF HEAT TRANSFER. Manuscript received by the Heat Transfer Division, October 26, 1981.

velocities are needed at dryout. Various methods have been used to predict droplet sizes and velocities in dispersed flow film boiling. Most use only information at the dryout point and some type of droplet breakup criterion to determine initial droplet sizes. Typically, a critical Weber number criterion has been used along with some assumption about the slip ratio [7] or droplet acceleration [3, 6] at the dryout point. If dispersed flow forms from annular flow, all droplets are formed previous to the dryout point, and it would be expected that droplet size would be some function of conditions previous to the dryout point.

The calculation method for initial droplet size used in this analysis is presented in [12] and is summarized in the Appendix. It includes both droplet formation from the liquid film (annular flow) or core (inverted annular flow) and droplet breakup subsequent to formation due to a Weber number criterion ($We_c = 6.5$). Droplet sizes at dryout calculated by this method also include the effect of Weber number breakup downstream of the dryout point.

Local Conditions Solution

The differential transport equations used in the local conditions solution are similar to those presented elsewhere [3–7], and details of their derivation are given in those references. A detailed description will only be given where this analysis differs from previous analyses.

Once dryout conditions are known, the governing equations can be used to determine local conditions downstream of dryout. Assuming that drop-wall heat transfer is negligible, the drop diameter gradient can be written as

$$\frac{dd}{dz} = -2\frac{h_d(T_v - T_s)}{V_l \rho_l i_{fg}} \tag{1}$$

where h_d is the vapor-drop heat transfer coefficient presented by Yuen [13] and is defined by equation (12). We have also assumed that an initial drop diameter, d_{do}, can be found that allows us to assume that no droplet breakup occurs downstream of dryout (see Appendix). The mass flow rate of the liquid in terms of the droplet number flow rate is

$$\dot{m}_l = G(1-X) = \rho_l \frac{1}{6}\pi d^3 \dot{\eta} \tag{2}$$

Assuming the number flow rate of droplets, $\dot{\eta}$, remains constant, the liquid mass balance can be written as

$$\frac{dX}{dz} = -\frac{3(1-X)}{d}\frac{dd}{dz} \tag{3}$$

Integrating yields

$$\frac{d}{d_{do}} = \left[\frac{1-X}{1-X_{do}}\right]^{1/3} \tag{4}$$

An overall equilibrium energy balance (assuming constant C_p)

$$X_{eq} - X_{do} = \frac{4Q''}{G i_{fg}}\frac{z}{D^*} \tag{5}$$

along with the nonequilibrium vapor energy equation

$$GX(i_v - i_{vs}) = 4Q''\frac{z}{D^*} - G\, i_{fg}(X - X_{do}) \tag{6}$$

yields an equation for vapor temperature in terms of the actual quality, X, and the equilibrium quality, X_{eq}.

$$C_p(T_v - T_{vs}) \approx (i_v - i_{vs}) = \frac{X_{eq} - X}{X} i_{fg} \tag{7}$$

Defining $\mathrm{Re}'_d = \dfrac{\rho_v V_l d}{\mu_v}$ (8)

and combining equations (1, 3, 4, 5, 7) and (8) yields

$$\frac{2}{3}\frac{d_{do}}{D^*}\frac{1}{(1-X_{do})^{1/3}}\frac{Q''}{G i_{fg}}\mathrm{Pr}_v\frac{\rho_l}{\rho_v}\frac{\mathrm{Re}'_d}{\mathrm{Nu}_d}\frac{X}{(1-X)^{2/3}}\frac{dX}{dX_{eq}} = (X_{eq} - X) \tag{9}$$

The next portion of this paper is devoted to approximating the functional dependence of $\mathrm{Re}'_d/\mathrm{Nu}_d$ on actual quality, X. Assuming small property variations, equation (9) will then become a first order differential equation in terms of X and X_{eq}.

The liquid velocity, V_l can be written in terms of the slip and void fraction

$$V_l = \frac{GX}{\rho_v S \alpha} \tag{10}$$

For dispersed upflow, void fractions are less than one,

Nomenclature

C_p = vapor specific heat at constant pressure
C_D = drag coefficient
d = drop diameter
d_{co} = critical drop diameter at dryout
d_{do} = average drop diameter at dryout
D^* = heated equivalent diameter, 4 × flow area/heated perimeter
D_H = hydraulic diameter, 4 × flow area/wetted perimeter
G = mass flux
g = gravitational constant
g_c = proportionality constant between mass and force
h_d = heat transfer coefficient between the vapor and the drop
h = heat transfer coefficient between the wall and the vapor
i = enthalpy
i_{fg} = heat of vaporization
K = nonequilibrium constant
k = thermal conductivity
L_{do} = distance from dryout
$\dot{m}$ = mass flow rate
Nu = Nusselt number
Nu_0 = zero mass transfer Nusselt number
Pr = Prandtl number
Q'' = heat flux
Re = Reynolds number $\rho_v V_v D_H/\mu_v$
Re'_d = Reynolds number defined by equation (8)
S = slip ratio V_v/V_l
T = temperature
V = velocity
We_c = Critical Weber number, $(V_v - V_l)^2 d\rho_v/\sigma g_c$
X = thermodynamic quality
z = axial coordinate

Greek

α = void fraction, $1/(\rho_v(1-X)S/\rho_l X + 1)$
μ = viscosity
ρ = density
σ = surface tension
$\dot{\eta}$ = droplet number flow rate

Subscripts

a = intercept: preburnout
co = based on d_{co}
do = dryout
d = drop
eq = equilibrium
f = film
l = liquid
lf = liquid film
s = saturation
TA = tangent point
v = actual vapor
vs = saturated vapor
wf = wall (film properties)
wv = wall (actual vapor properties)

while slip ratios are greater than one. As actual quality approaches a value of one, both void fraction and slip also approach one. Therefore, it is assumed that the variation in the product $S\alpha$ will be small. If one then uses equations (4), (8), and (10), ignoring property variations, the dependence of Re_d' on actual flowing quality can be written as

$$\mathrm{Re}_d' \propto X(1-X)^{1/3} \tag{11}$$

The drop Nusselt number is that developed by Yuen [13] which accounts for the effect of droplet evaporation on the heat transfer coefficient.

$$\mathrm{Nu}_d \cdot \left[1 + \frac{C_p(T_v - T_{vs})}{i_{fg}}\right] = \mathrm{Nu}_0 = 2 + 0.6\left[\frac{\rho_v(V_v - V_l)d}{\mu_v}\right]^{1/2} \mathrm{Pr}_v^{1/3} \tag{12}$$

From the numerical solution, it was found that Nu_0 is considerably greater than 2 for the major portion of the quality range. Further developing equation (12), equation (4) can be substituted for d and equation (A9) substituted for $(S-1)$. If the change in the product $S\alpha$ is small, equations (7) and (12) can be combined to yield

$$\mathrm{Nu}_d \propto X^{1/4}(1-X)^{1/4}\frac{X}{X_{eq}} \tag{13}$$

or

$$\frac{\mathrm{Re}_d'}{\mathrm{Nu}_d} \propto \frac{X_{eq}}{X^{1/4}}(1-X)^{1/12} \tag{14}$$

The proportionality given in equation (14) can now be used to neutralize the quality dependence of $\mathrm{Re}_d'/\mathrm{Nu}_d$ in equation (9). Noting that the combination of (12) and (7) gives $\mathrm{Nu}_d/\mathrm{Nu}_0 = X/X_{eq}$, a combination of variables can be defined by equation (15) which results when equation (9) is multiplied and divided by $X_{eq}(1-X)^{1/12}/X^{1/4}$ [from equation (14)].

$$K = \frac{2}{3}\frac{d_{do}}{D^*}\frac{1}{(1-X_b)^{1/3}}\frac{Q''}{Gi_{fg}}\mathrm{Pr}_v\frac{\rho_l}{\rho_v}\frac{\mathrm{Re}_d'}{\mathrm{Nu}_0}\frac{1}{X^{1/4}(1-X)^{1/12}} \tag{15}$$

This quantity, K, should now remain approximately constant with actual quality, X, since the quality dependence of $\mathrm{Re}_d'/\mathrm{Nu}_0$ is neutralized by the quantity $1/[X^{1/4}(1-X)^{1/2}]$ [from the combination of equations (14), (12), and (7)]. Using the definition of K given in (15), equation (9) becomes

$$K\frac{X^{1/4}X_{eq}}{(1-X)^{7/12}}\frac{dX}{dX_{eq}} = (X_{eq} - X) \tag{16}$$

Equation (16) shows that the parameter, K, which we shall call the nonequilibrium constant, contains the group of fluid parameters which dictate the departure from equilibrium (i.e., the behavior of actual quality, X, in relation to the equilibrium quality, X_{eq}).

Figure 1 shows the variation of K with quality as calculated by the numerical soluton scheme. For all of the cases shown, except nitrogen (N_2), no drop breakup occurs, and K remains relatively constant, justifying the previous assumptions. The information shown for N_2(▼) is for an inverted annular dryout where the drops break up after dryout. Therefore, the actual magnitude of K for N_2 shown in Fig. 1 decreases from a high value and becomes essentially constant beyond $X = 60$ percent. In this case, an average value of K would be predicted as 0.59 using the integrated average drop diameter from equation (A5). Even though K varies significantly for this case, the predicted wall temperatures shown later in Fig. 7 agree well with this data. Therefore, K can always be determined from equation (15) using only dryout conditions.

Equation (16) now becomes an initial value problem with $X = X_{eq} = X_{do}$ initially. Unfortunately, an analytic solution to equation (16) is not known. Therefore, it was integrated using a Runga-Kutta scheme for various values of K and dryout quality. Graphs of X versus $(X_{eq} - X_{do})$ as a function of K for dryout qualities from 0.1 to 0.9 are shown in Figs. 2–6. For any dryout quality and value of K, the actual quality can be determined knowing the equilibrium quality at the point of interest.

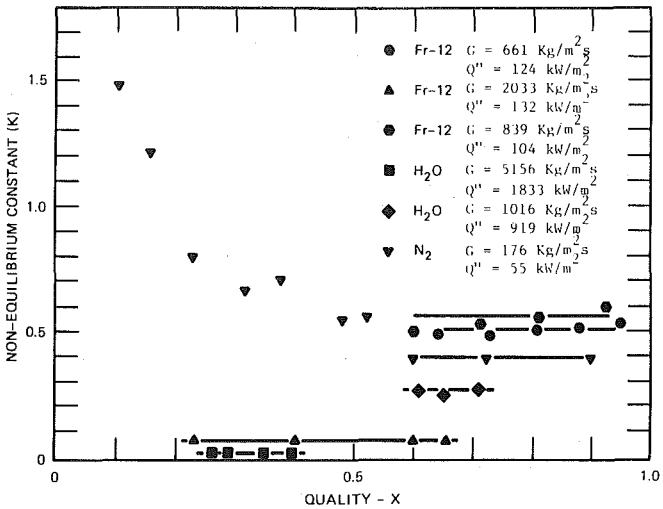

Fig. 1 Variation of the nonequilibrium constant, K, (as predicted by the numerical solution) with actual quality, X

It can be seen from the figures that equation (16) explains the correct physics of the droplet evaporation process. As the value of K increases, the nonequilibrium in the flow increases. A value of $K = 0$ indicates that equilibrium exists in the flow. This corresponds to a drop Nusselt number of ∞ in equation (15), which would mean that all heat goes into evaporating the drops.

The slopes of the K curves must be zero at the dryout point as indicated by equation (16) when $X_{eq} = X_{do} = X$. Since drop wall interactions are ignored and the vapor is saturated at dryout, no drop evaportion can occur initially, and the quality must remain at X_{do} until enough vapor superheat is available to begin to evaporate drops. This effect is most evident in the high dryout quality K curves (Fig. 6), since very little liquid is present at dryout. In the lower burnout quality K curves, this effect is much less pronounced since much more liquid is present in the flow. As K increases, the effect also becomes more prominent as the vapor to liquid heat tansfer mechanism is becoming less effective.

At an actual quality of one, the slopes of the K curves must also be zero as indicated by equation (16). At a quality near one, very little liquid is available to evaporate in the flow, and the slope of the constant K curve must decrease to zero as the amount of liquid in the flow goes to zero.

Once actual quality, X, is determined, a conventional vapor heat transfer coefficient, and the actual vapor temperature calculated from (7) can be used to determine wall temperatures (i.e., $Q''/h + T_v = T_w$). Two wall-to-vapor heat transfer coefficients were used depending on the fluid. For water, the steam correlation of Heineman [14] was used with actual vapor velocity used to evaluate the Reynolds number

$$\mathrm{Nu}_{wf} = 0.0157\,\mathrm{Re}_f^{0.84}\mathrm{Pr}_f^{1/3}\left(\frac{D_H}{L_{do}}\right)^{0.04} \quad \frac{L_{do}}{D_H} < 60$$
$$\mathrm{Nu}_{wf} = 0.0133\,\mathrm{Re}_f^{0.84}\mathrm{Pr}_f^{1/3} \quad \frac{L_{do}}{D_H} > 60 \tag{17}$$

For other fluids, the Dittus-Boelter [15] equation was used,

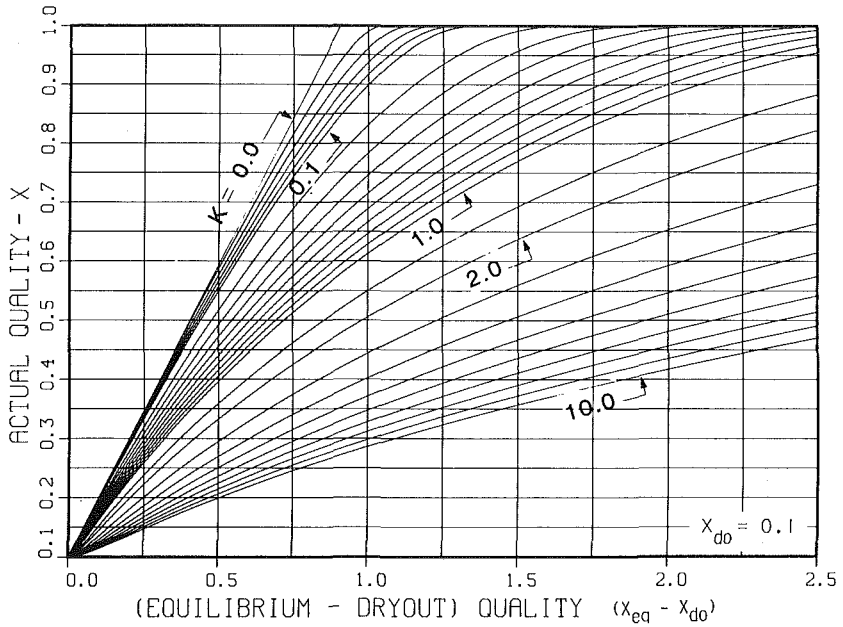

Fig. 2 Actual quality, X, versus equilibrium quality, X_{eq}, for $X_{do} = 0.1$

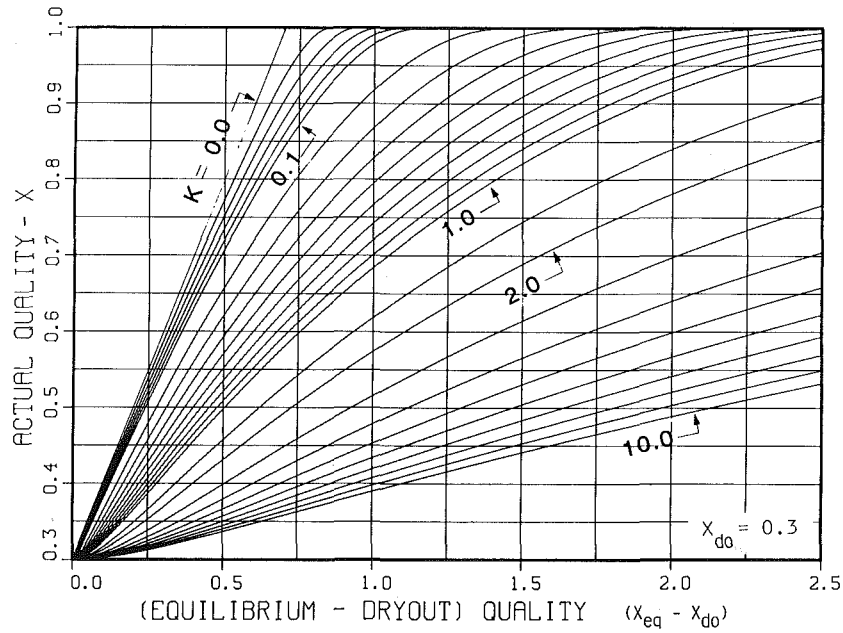

Fig. 3 Actual quality, X, versus equilibrium quality, X_{eq}, for $X_{do} = 0.3$

using actual vapor velocity and a thermal entrance length fit from Kay's [16] numerical solution.

$$\mathrm{Nu}_{wv} = 0.023\ \mathrm{Re}_v^{0.8}\mathrm{Pr}_v^{0.4}\left(1+\frac{0.8D_H}{L_{do}}\right) \tag{18}$$

Summary

Once dryout and flow conditions are known (i.e., X_{do}, G, Q'', property values), the appropriate drop diameter can be determined from equation (A1) for annular dryout and equation (A5) for inverted annular dryout. The value of the constant K can be determined from equation (15) evaluated at dryout using the definitions of Re_d' [equation (8)], Nu_0 [equation (12)], slip [equations (A8) or (A9)], and the definitions of void fraction, vapor velocity, and liquid velocity. This procedure can be simplified for most cases. If Nu_0 is large (i.e., greater than 15), equation (A9) is used for S, and the limiting value of 0.4 is used for C_D, equation (15) can be rearranged and written as

$$K \cong 0.58\left(\frac{d_{do}}{D^*}\right)^{1.25}\frac{1}{(1-X_{do})^{5/12}}\left(\frac{Q''}{Gi_{fg}}\right)^{0.75}\left(\frac{\rho_l}{\rho_v}\right)^{0.75}\left(\frac{GD^*}{\mu_v}\right)^{1/2}\cdot \tag{19}$$

$$\mathrm{Pr}_v^{1/3}\left[\frac{\rho_v}{\rho_l}\frac{(1-X_{do})}{X_{do}}+\frac{1}{1+3.65\sqrt{\dfrac{\rho_l}{\rho_v}\dfrac{Q''}{Gi_{fg}}\dfrac{d_{do}}{D^*}\dfrac{1}{X_{do}}}}\right]^{1/2}$$

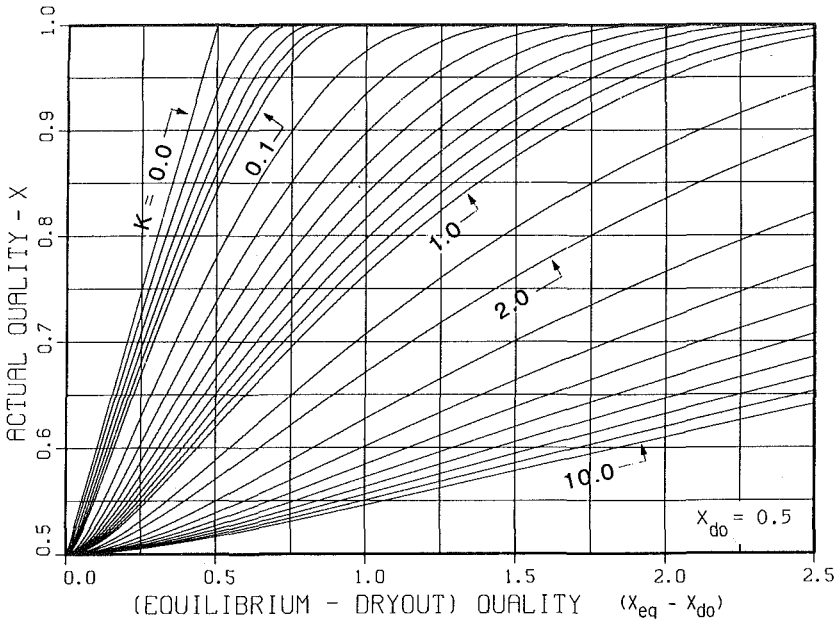

Fig. 4 Actual quality, X, versus equilibrium quality, X_{eq}, for $X_{do} = 0.5$

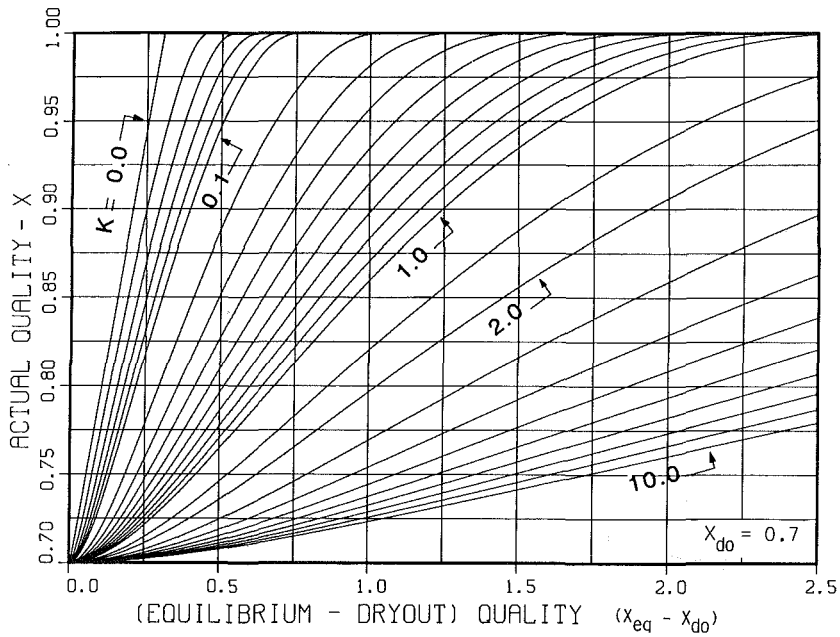

Fig. 5 Actual quality, X, versus equilibrium quality, X_{eq}, for $X_{do} = 0.7$

Values of K calculated using equation (19) differ from values calculated using the definitions of Re_d' and Nu_0 by about 5 percent when the specified conditions hold.

Once a value for K is determined from conditions at dryout, equilibrium quality at any location z is calculated by equation (5). Then Figs. 2–6 are used to determine actual quality from equilibrium quality at any z. Local vapor temperature can then be determined using equation (7) and the vapor heat transfer coefficient determined from equations (17) or (18).

Results

The procedure has been used to evaluate heated wall temperatures from several experiments. Figure 7 shows liquid nitrogen tube data taken by Forslund [3]. The solid curve shows results from a stepwise numerical solution, while the ▲'s are computed from the local conditions solution. Data are shown as ●'s and ■'s. Dryout in this case was inverted annular, and a liquid core existed for a distance beyond the dryout point. Both numerical and local conditions solution schemes assumed dispersed flow existed at the dryout point. It would be expected that they would over predict surface temperatures in this region. At points removed from dryout where dispersed flow would actually exist, both the numerical and local conditions solutions agree well with the nitrogen data. The local conditions solution does not include conduction and drop-wall interactions. These mechanisms have the largest effect near dryout, and tend to decrease wall temperatures.

A comparison of both solution schemes to Bennett's [4] steam data is shown in Fig. 8. Again, agreement between both solution schemes and data is good. Values for the constant K range from a highly nonequilibrium case ($K = 2.3$) to a more

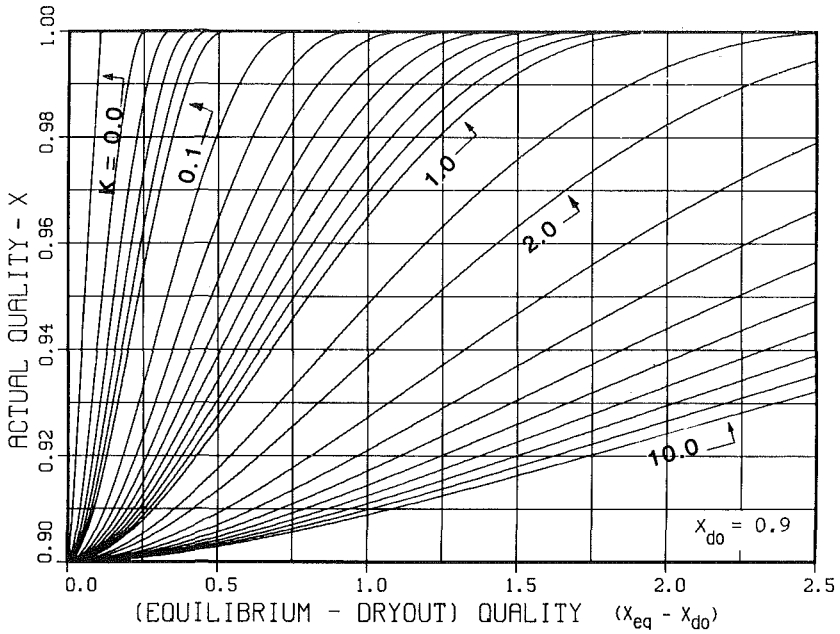

Fig. 6 Actual quality, X, versus equilibrium quality, X_{eq}, for $X_{do} = 0.9$

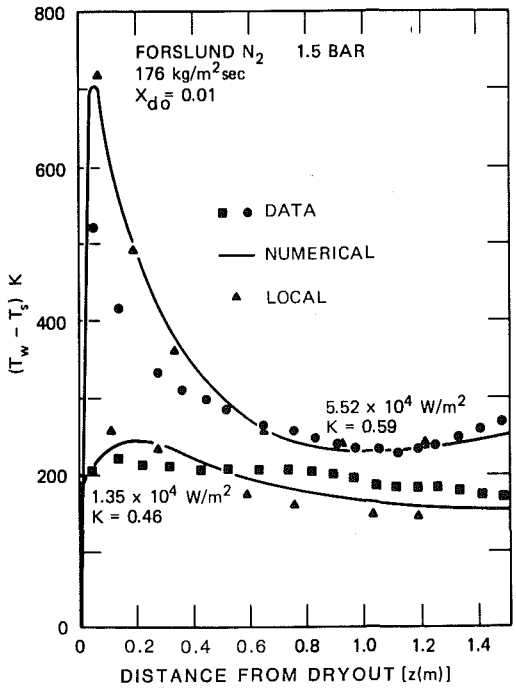

Fig. 7 Comparison of Forslund's nitrogen data to numerical and local conditions prediction

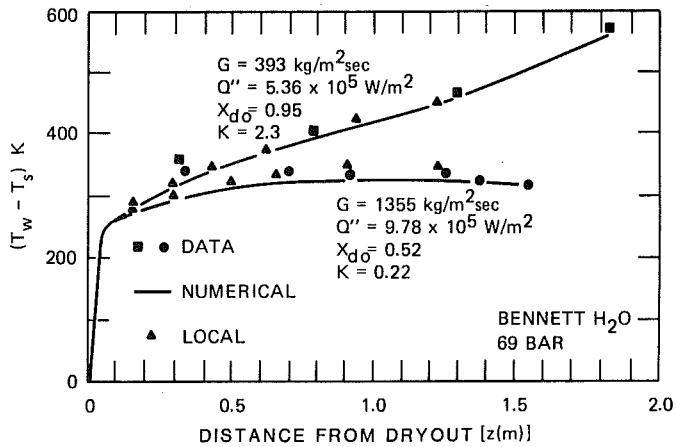

Fig. 8 Comparison of Bennett's water data to numerical and local conditions prediction

closely equilibrium case ($K = 0.22$). Because the local conditions model uses the significant heat transfer mechanisms of the numerical model, it cannot predict wall temperatures better than the computer solution.

Freon 12 data of Groeneveld [7] is presented in Fig. 9. Again, a case of almost complete equilibrium ($K = 0.0714$) is shown along with a case of more nonequilibrium ($K = 0.58$). In both cases, both solutions agree well with the wall temperature data.

Both the numerical and local conditions solutions were compared to Freon 12 data of Cumo [17]. Neither solution scheme does a good job of predicting this data. Because the

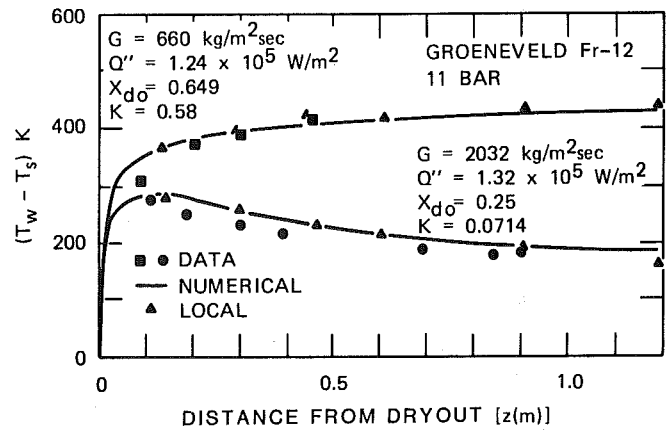

Fig. 9 Comparison of Groeneveld's Fr-12 data to numerical and local conditions prediction

predictions were unsuccessful, the degree of nonequilibrium was varied in the local conditions solution to determine if a good fit was possible. Equilibrium was varied from complete equilibrium to a large degree of nonequilibrium. In general, a variation in equilibrium alters the curve shape while a variation in the form of the heat transfer coefficient raises or lowers the wall temperature curves, retaining a similar shape. The complete equilibrium case lies nearest the data; however, data fit is still poor. It has been found [7] that Freon 12 is susceptible to decomposition, and perhaps this could be the cause of the discrepancy.

The local conditions solution was also compared to experimental Freon data of Koizumi [5] and low-pressure water data of Nijhawan [18, 19]. Unlike the experiments described previously where fluid was subcooled at the inlet to the test section, these experiments used a positive inlet quality. Since droplets would not all be formed in the heated test section, both the standard and an altered drop sizing method based on the Helmholtz instability analysis of Tatterson [20] was used to predict the wall temperature data [12]. The Koizumi surface temperature data was bracketed using the altered (−11 percent error based on the wall superheat) and standard (+8 percent error) droplet sizing methods. However, the Nijhawan surface temperature data was generally overpredicted by both methods (at some points by as much as 35 percent based on wall superheat) even though measured vapor temperatures were higher than predicted vapor temperatures. Nijhawan's experiments were conducted using a hot patch at the entrance to the test section, while Koizumi stripped the liquid film from the wall before entering the test section. Both techniques could alter the liquid distribution over that which might be expected when all boiling takes place within the test section. The experimental methods used in either of these two experiments make it difficult to judge the validity of the nonequilibrium constant concept, although comparisons to these results are reasonable considering the experimental techniques involved.

Conclusions

Dispersed flow heat transfer consists of several individual heat transfer mechanisms. An accurate analysis of dispersed flow must include at least the most important of these. Interactions between the drops, the vapor, and the heated wall influence both the wall heat transfer and the nonequilibrium existing in the flow. These in turn determine the tube wall temperatures. Specifically, this study investigates dispersed flow heat transfer for vertical upflow, constant heat flux conditions.

A local conditions solution based on energy and mass transport equations identifies one nondimensional group, K, [equation (15) or (19)] which alone determines the nonequilibrium present in the flow. Wall temperatures may then be calculated without using complex numerical techniques.

Both numerical and local conditions solutions were compared to world data. Nitrogen, Freon, and water data from four investigators and various flow conditions were compared on the basis of wall superheat. In order to avoid inverted annular flow pattern effects, points less than 0.15 M (6 in.) from dryout in Forslund's inverted annular experiments are excluded from the comparison. The RMS error is 13 percent using all the data presented in this paper.

Acknowledgment

This research was sponsored by the National Science Foundation: Grant 76-82564-CME.

References

1 Baum, A., "A Study of Transition and Film Boiling from Vertical Surfaces," Ph.D. thesis, Carnegie-Mellon University, Apr. 1977.

2 Groeneveld, D. C., and Gardiner, S. R. M., "Post-CHF Heat Transfer Under Forced Convective Conditions," AECL-5883, 1977.

3 Forslund, R. P., "Thermal Nonequilibrium in Dispersed Flow Film Boiling in a Vertical Tube," Ph.D. thesis, Massachusetts Institute of Technology, Dec. 1966.

4 Bennett, A. W., Hewitt, G. F., Kearsey, H. A., and Keeys, R. K. F., "Heat Transfer to Steam-Water Mixtures in Uniformly Heated Tubes in which the Critical Heat Flux has been Exceeded," AERE-R 5373, Oct. 1967.

5 Koizumi, Y., Ueda, T., and Tanaka, H., "Post-dryout Heat Transfer to R-113 Upward Flow in a Vertical Tube," *International Journal of Heat and Mass Transfer*, Vol. 22, 1979, pp. 669–678.

6 Plummer, D. N., Iloeje, O. C., Rohsenow, W. M., Griffith, P., and Ganic, E., "Post-Critical Heat Transfer to Flowing Liquid in a Vertical Tube," MIT Heat Transfer Laboratory Report No. 72718-91, 1974.

7 Groeneveld, D. C., "The Thermal Behavior of a Heated Surface at and Beyond Dryout," AECL-4309, 1972.

8 Rane, A., and Yao, S., "Heat Transfer of Evaporating Droplet Flow in Low Pressure Systems," *Canadian Journal of Chemical Engineering*, Vol. 58, June 1980, pp. 303–308.

9 Webb, S. W., and Chen, J. C., "A Nonequilibrium Model for Post-CHF Heat Transfer," presented at the CSNI Specialist Meeting on Transient Two-Phase Flow, Mar. 23–25, 1981.

10 Groeneveld, D. C., and Delorme, G. G. J., "Prediction of Nonequilibrium in the Post-Dryout Regime," *Nuclear Engineering and Design*, Vol. 36, 1976, pp. 17–26.

11 Chen, J. C., Ozkaynak, F. T., and Sundaram, R. K., "Vapor Heat Transfer in Post-CHF Region Including the Effect of Thermodynamic Nonequilibrium," *Nuclear Engineering and Design*, Vol. 51, 1979, pp. 143–155.

12 Yoder, G. L., and Rohsenow, W. M., "Dispersed Flow Film Boiling," MIT Heat Transfer Laboratory Report No. 85694-103, Mar. 1980.

13 Yuen, M. C., and Chen, L. W., "Heat Transfer Measurements of Evaporating Liquid Droplets," *International Journal of Heat and Mass Transfer*, Vol. 21, 1978, pp. 537–542.

14 Heineman, J. B., "An Experimental Investigation of Heat Transfer to Superheated Steam in Round and Rectangular Tubes," ANL-6213, 1960.

15 Dittus, F. W., and Boelter, L. M. K., "Heat Transfer in Automobile Radiators of the Tubular Type," U. of Cal. Publications, Vol. 2, No. 13, 1930, pp. 443–461.

16 Kays, W. M., *Convective Heat and Mass Transfer*, McGraw-Hill, New York, 1966, p. 190.

17 Cumo, M., Farello, G. E., and Ferrari, G., "The Influence of Curvature in Post-Dryout Heat Transfer," Report of the XXVI National ATI Annual Meeting, L'Aquila, Sept. 1971, *Thermotecnica*, Vol. XXVI, No. 3, 1972, pp. 129–142.

18 Nijhawan, S. M., Chen, J. C., and Sundaram, R. K., "Parametric Effects on Post-Dryout Heat Transfer," ASME Paper 80-WA/HT-50, 1980.

19 Nijhawan, S., Chen, J. C., Sundaram, R. K., and London, E. J., "Measurement of Vapor Superheat in Post-Critical Heat-Flux Boiling," ASME JOURNAL OF HEAT TRANSFER, Vol. 102, 1980, pp. 465–470.

20 Tatterson, D. F., Dallman, J. C., and Hanratty, T. J., "Drop Sizes in Annular Gas-Liquid Flows," *AIChE Journal*, Vol. 23, No. 1, 1977, pp. 68–76.

21 Hewitt, G. F., Kearsey, H. A., Lacey, P. M. C., and Pulling, D. J., "Burnout and Film Flow in the Evaporation of Water in Tubes," AERE-R-4864, 1965.

22 Ahmad, S. Y., "Axial Distribution of Bulk Temperature and Void Fraction in a Heated Channel with Inlet Subcooling," ASME JOURNAL OF HEAT TRANSFER, 1970, pp. 595–609.

APPENDIX

Initial Droplet Size

The local conditions solution assumes that no droplet breakup occurs after dryout. In order for this assumption to be valid, either no drop breakup actually occurs after dryout, or an appropriate initial droplet diameter can be calculated which produces the same nonequilibrium in the flow as that which would occur if droplets present at dryout were allowed to break up as they travel downstream.

For annular type dryout (assumed to exist when $X_{do} > 0.1$), no further droplet breakup is a good assumption. Using entrainment data of Hewitt [21] for heated annular flows, a model was developed which accounts for droplet formation from the liquid film and subsequent droplet breakup due to a critical Weber number criterion ($We_c = 6.5$) [12]. Drop diameters calculated using this method generally fall between diameters calculated using a film instability analysis (i.e., reference [20]) and those using a Weber number criterion at the dryout point [i.e., reference [6]).

Assuming the product $S\alpha$ was near 1 and that $1/S\alpha\, dX/dz >> X\, d(1/S\alpha)/dz$, the average drop diameter for annular dryout was determined.

$$\frac{d_{do}}{D^*} = \frac{1}{X_{do}-0.1}\left\{ \frac{d_{co}}{D^*}(X_a - 0.1) + \left(\frac{\rho_l}{\rho_v}\right)^2 \frac{\mathrm{We}_c}{(S_{lf}-1)^2} \frac{\rho_v \sigma g_c}{G^2 D^*} \frac{1}{\left(\frac{\rho_l}{\rho_v}\frac{1}{S_{lf}} - 1\right)} \left[\frac{1}{1+X_a\left(\frac{\rho_l}{\rho_v}\frac{1}{S_{lf}} - 1\right)} - \frac{1}{1+X_{do}\left(\frac{\rho_l}{\rho_v}\frac{1}{S_{lf}} - 1\right)} \right] \right\} \tag{A1}$$

where X_a is given by

$$\frac{\frac{\rho_v}{\rho_l} + \left(\frac{1}{S_{lf}} - \frac{\rho_v}{\rho_l}\right) X_a}{\frac{\rho_v}{\rho_l} + \left(\frac{1}{S_{co}} - \frac{\rho_v}{\rho_l}\right) X_{do}} = \frac{S_{co}-1}{S_{lf}-1} \tag{A2}$$

and the liquid film slip used is that correlated by Ahmad [22] from void fraction data.

$$S_{lf} = \frac{V_v}{V_{lf}} = \left(\frac{\rho_l}{\rho_v}\right)^{0.205} \left(\frac{GD_H}{\mu_l}\right)^{-0.016} \tag{A3}$$

also,

$$\frac{d_{co}}{D^*} = \left[3 \frac{\rho_v \sigma g_c}{G^2 D^*} \mathrm{We}_c C_D \Big/ \left(16 \frac{Q''}{Gi_{fg}} \frac{\rho_l}{\rho_v} X_{do} + 4 \frac{\rho_v(\rho_l - \rho_v) D^* g}{G^2} \right) \right]^{1/2} \tag{A4}$$

If X_a from equation (A2) is less than 0.1, it is recommended that X_a be set equal to 0.1 for use in equation (A1).

For inverted annular flow (assumed to exist when $X_{do} < 0.1$), similar assumptions were used to arrive at an equation for average droplet diameter including post dryout droplet breakup.

$$\frac{d_{do}}{D^*} = \frac{1}{1-X_{do}} \left\{ \frac{3}{8} \frac{\rho_v}{\rho_l} \sqrt{\frac{\rho_v \sigma g_c}{G^2 D^*} \mathrm{We}_c} \frac{Gi_{fg}}{Q''} C_D \left[\left(\frac{16}{3} \frac{Q''}{Gi_{fg}} \frac{\rho_l}{\rho_v} \frac{X_{TA}}{C_D} + \frac{4}{3} \frac{\rho_v(\rho_l - \rho_v) D^* g}{G^2 C_D} \right)^{1/2} - \left(\frac{16}{3} \frac{Q''}{Gi_{fg}} \frac{\rho_l}{\rho_v} \frac{X_{do}}{C_D} + \frac{4}{3} \frac{\rho_v(\rho_l - \rho_v) D^* g}{G^2 C_D} \right)^{1/2} \right] + (1 - X_{TA}) \frac{d_{TA}}{D^*} \right\} \tag{A5}$$

where

$$X_{TA} = \frac{3}{5} - \frac{1}{10} \frac{\rho_v}{\rho_l} \frac{\rho_v(\rho_l - \rho_v) D^* g\, i_{fg}}{GQ''} \tag{A6}$$

and

$$\frac{d_{TA}}{D^*} = \left[\frac{3 \frac{\rho_v \sigma g_c}{G^2 D^*} \mathrm{We}_c C_D}{16 \frac{Q''}{Gi_{fg}} \frac{\rho_l}{\rho_v} X_{TA} + 4 \frac{\rho_v(\rho_l - \rho_v) D^* g}{G^2}} \right] \tag{A7}$$

Equations for slip at any point in the flow were also developed.

$$(S-1)^2 = \frac{16}{3} \frac{\rho_l}{\rho_v} \frac{1}{X} \frac{Q''}{Gi_{fg} C_D} \frac{d}{D^*} + \frac{4}{3} \frac{\rho_v(\rho_l - \rho_v) D^* g}{G^2} \frac{1}{C_D X^2} \frac{d}{D^*} \tag{A8}$$

in many cases, the second term in equation (A8) is small giving

$$S - 1 = 2.31 \left[\frac{\rho_l}{\rho_v} \frac{1}{X} \frac{Q''}{Gi_{fg} C_D} \frac{d}{D^*} \right]^{1/2} \tag{A9}$$

Thus the slip at dryout, S_{co} in equation (A2) can be determined by evaluating (A8) or (A9) at burnout conditions (i.e., using $X = X_{do}$ and $d/D^* = d_{co}/D^*$).

C_D is the droplet drag coefficient as used by Groeneveld [7] for dispersed flow analysis.

$$C_D = \frac{27}{\mathrm{Re}_d^{0.84}} \quad \mathrm{Re}_d < 150 \qquad C_D = 0.4 \quad \mathrm{Re}_d > 150 \tag{A10}$$

In most situations, $\mathrm{Re}_d > 150$ and a constant value of $C_D = 0.4$ can be assumed. The critical Weber number was assumed to be 6.5 as recommended by Groeneveld [23].

T. Aihara
Professor,
Institute of High Speed Mechanics,
Tôhoku University,
Sendai, Japan

R. Saga
Engineer,
Ryôsan Co., Ltd.,
Tokyo, Japan

Performance of a Compact Cooling Unit Utilizing Air-Water Mist Flow

Performance of a new compact cooling unit for semiconductors, being composed of an atomizer, a fan, and a heat-dissipating surface with no fin, has been measured over a wide range of the mass flow rate of spray water, $\dot{m}$, and the wall heat flux. The heat transfer performance of the present compact, unit with $\dot{m} = 0$ to 1.05 g/s, attains 1.8 to 20 times that of the parallel-plate channel under the same thermal conditions.

Introduction

Air-water mist cooling of heated bodies by suspending water droplets in an air stream has a remarkably improved performance of heat transfer in comparison with the single-phase cooling. Many theoretical and experimental studies of this cooling method have hitherto been made. Maezawa and Tsuchita [1], Heyt and Larsen [2], Simpson and Brolls [3], Bhatti and Savery [4], and Hishida et al. [5] studied the heat transfer for flat plates in air-water mist flows; Abe et al. [6], Hodgson et al. [7], Kosky [8], Nishikawa and Takase [9], Basilico et al. [10], Lu and Heyt [11], for circular cylinders; Aihara et al. [12], Aihara and Fu [13], for wedges; Hishida et al. [14], for an inclined plate.

As for heat exchangers, Simpson et al. [15], and Yang and Clark [16] carried out the heat-transfer experiments on finned tubes and automotive radiator cores, respectively. However, these heat exchangers were for single-phase flow and were not reformed for air-water mist flow. It seems that the form of a heat exchanger suitable for air-water mist flow has never been determined and that there is room for further improvement in the performance.

The authors have developed a new compact unit for air-water mist cooling of semiconductors, composed of an atomizer, a fan, and a heat-dissipating surface with no fin. The present paper describes the construction of the new compact unit having a heat exchanger channel in which one wall is heated with quasi-uniform heat flux and the other is insulated. Finally, the results of an experimental study of the unit's cooling performance are presented.

Experimental Apparatus and Procedure

Test Cooling Unit. Figure 1 illustrates cross-sectional details of the test cooling unit. Air-water mist flow was produced as follows: Pure water was fed to the center of the main disk ⑨ of a fan-atomizer through a 1-mm-i.d. dripping nozzle ① and atomized by the centrifugal effect owing to the rotation of the disk ⑨ driven by a motor shaft ⑩; then the water droplets were mixed with air stream induced by the fan-atomizer. By continuous impingement of these water droplets onto the umbrella-shaped heat transferring surface ⑦, a thin water film was effectively maintained there. The umbrella-shaped surface ⑦ was composed of eight ring-shaped segments of brass. Each segment was separated by 2-mm-width slots so as to minimize a conduction error between the neighboring segments as shown in Fig. 1. The heat transferring surface ⑦ was covered by a glass-wool insulator ④ to prevent heat loss from its back side. An alternating current was supplied to the nichrome heaters ⑫ in eight segments and adjusted to make the wall heat-flux as uniform as possible. The representative temperature of each of the segments was estimated by averaging the values measured with a pair of 0.1-mm-dia. copper-constantan thermocouples ⑪ soft-soldered to axially symmetric locations. The inlet bellmouth ring ⑬, outlet ring ⑤, and bottom disk ⑥ were made of bakelite. The profile of the ABC section of the bottom disk ⑥ was designed to keep an average radial velocity nearly constant throughout the heat exchanger channel ⑥, ⑦. Figure 2 is illustrative of the fan-atomizer with thirteen blades of double suction type, which was developed by the authors. Its volume flow rate of air was 0.075 m^3/s at 2904 rpm, corresponding to the average radial velocity of 4.7 m/s at the inlet of exchanger channel.

The absolute velocity and turbulence intensity of single-phase, isothermal air flow in the exchanger channel were measured by moving the probe of a hot-wire anemometer along the mid-width of the channel.

Experimental Apparatus. Figure 3 is an outline of the experimental apparatus. Air was drawn into the inlet nozzle ⑮ for measuring the flow rate; it was pressurized by an auxiliary fan ⑯; and it was divided into two streams, ② and ⑧, both of which were drawn into the test cooling unit ㉖ through the straighteners ⑳ of honeycomb cores. During that time, the rotating speed of the auxiliary fan ⑯ and the opening angle of damper ⑰ were adjusted so as to make the outlet static pressures ㉒ and ㉙ of the ducts ② and ⑧ nearly equal to the atmospheric pressure. The mixing-cup temperature evaluated from the measured values of thermocouples ㉑ and ㉗ was regarded as the air dry-bulb temperature at the inlet of test cooling unit ㉖; the inlet absolute humidity of the test unit was determined from the air dry- and wet-bulb temperatures measured at the location ⑭.

Pure water was fed from a main tank ⑱ to the fan-atomizer driven by a motor ㉘, through an overflow tank ⑲, an orifice flow meter ㉓, a needle valve ㉔, a measuring section of the water temperature ㉕, and a dripping nozzle ①.

Local Heat Transfer Coefficients and Local Bulk Temperatures. The local heat transfer coefficient, h_x, regardless if single- or two-phase, is defined as

$$h_x = q_x / (T_{wx} - T_i) \tag{1}$$

where T_{wx} is the local temperature of the heat transferring surface, T_i is the air dry-bulb temperature at the channel inlet, and q_x is the local wall heat flux. The value of q_x is determined by subtracting the rear conduction loss and the predicted radiation loss from the electric power input to each heater ⑫, by correcting the radial conduction through the grooved area between segments, and then by dividing by the heat transfer area of each segment. The rear conduction loss for each run was evaluated from a correlation, obtained by a preliminary experiment, with the average temperature difference between the segment surfaces ⑪ and a plastic cover

Contributed by the Heat Transfer Division for publication in the JOURNAL OF HEAT TRANSFER. Manuscript received by the Heat Transfer Division March 15, 1982.

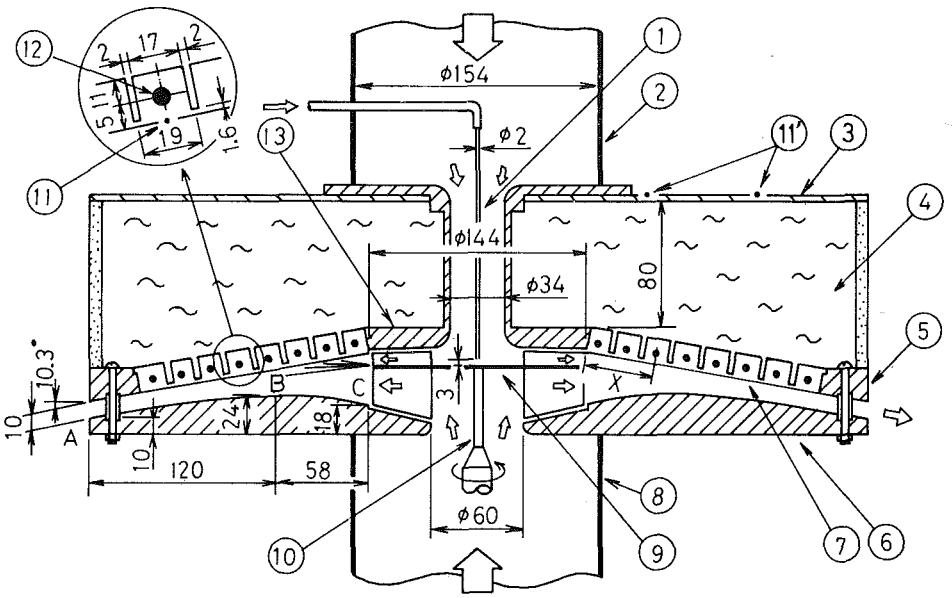

Fig. 1 Sectional details of test cooling unit: ① dripping nozzle; ② and ⑧ air ducts; ③ plastic cover; ④ glass-wool insulator; ⑤ outlet ring of bakelite; ⑥ bottom disk of bakelite; ⑦ umbrella-shaped heat transferring surface; ⑨ main disk of fan-atomizer; ⑩ motor shaft; ⑪ and ⑪′ 0.1-mm-dia thermocouples; ⑫ nichrome heater; ⑬ inlet bellmouth ring of bakelite

③, as shown in Fig. 1. The net rate of radial conduction was estimated with the calculated value of thermal constriction resistance and the measured temperature difference between the neighboring segments.

As for the single-phase experiment, the following local heat transfer coefficient, $h^*_{x(1)}$, and local Nusselt number, Nu^*_x, were also evaluated and compared with the performance of ordinary heat exchangers of parallel-plate type

$$h^*_{x(1)} = q_{x(1)}/(T_{wx} - T_{bx}) \tag{2}$$

$$\mathrm{Nu}^*_x = b_i h^*_{x(1)}/\lambda \tag{3}$$

where T_{bx} is the local bulk temperature, b_i is the inlet width of channel as shown in Fig. 4, and λ is the thermal conductivity of air.

The local bulk temperature, T_{bx}, may be derived as follows: The heat balance with respect to an elementary ring-surface shown in Fig. 4, can be written as shown below

$$(2\pi r dx)\,\bar{q}_{(1)} = (2\pi r dx)\,h^*_{x(1)}(T_{wx} - T_{bx}) = W\rho c_p dT_{bx} \tag{4}$$

where $\bar{q}_{(1)}$ is the average wall heat-flux for single-phase run, and W is the volume flow rate, expressed as

$$W = 2\pi r_i b_i \bar{u}_{ri} = 2\pi r b \bar{u}_r = \text{constant} \tag{5}$$

By combining the first and third expressions of equation (4) and integrating them from $r = r_i$ to $r = r$

$$T_{bx} - T_i = \pi \bar{q}_{(1)}(r^2 - r_i^2)/(W\rho c_p \cos\beta) \tag{6}$$

where β is the inclination angle of the heat transfer surface. By substituting W of equation (5) into equation (6) and by putting $\mathrm{Re}_b = \bar{u}_{ri} b_i/\nu$ and $x\cos\beta = r - r_i$, the local bulk temperature is obtained as

$$T_{bx} - T_i = \left(\frac{b_i \bar{q}_{(1)}}{\lambda}\right)\left(\frac{x}{b_i \mathrm{Pr}\mathrm{Re}_b} \cdot \frac{r + r_i}{2r_i}\right) \tag{7}$$

It should be added that throughout the whole experiment

Nomenclature

b = channel width, m
c_p = specific heat at constant pressure of air, kJ/kg°C
h_x, h^*_x = local heat transfer coefficients defined by equations (1) and (2), respectively, W/m²°C
l = length of heat transferring surface, m
$\dot{m}$ = mass flow rate of spray water, g/s
Nu^*_x = local Nusselt number defined by equation (3)
Pr = Prandtl number of air
q = heat flux at heat transferring surface, W/m²
r = radial distance from the center, m
Re_b = gas Reynolds number defined by $\bar{u}_{ri}\, b_i/\nu$
Re_ξ = local Reynolds number defined by $\bar{u}_a \xi/\nu$
T_i, T_{wx}, T_{bx} = temperatures of inlet air, local wall, and local bulk, respectively, °C
Tu = turbulence intensity, percent
u_a = absolute velocity in heat exchanger channel, m/s
u_r = radial velocity in the channel, m/s
W = volume flow rate of air, m³/s
x = distance from the starting point of heated section, m
β = inclination angle of heat transferring surface, rad
λ = thermal conductivity of air, W/m°C
ν = kinematic viscosity of air, m²/s
ξ = length of streamline in the channel, m
ρ = density of air, kg/m³

Subscript

i = inlet of heat-exchanger channel
para = parallel-plates channel
unit = present cooling unit
(1) = single-phase flow
(2) = air-water mist flow

Superscript

$-$ = average

the deviation in q_x from $\bar{q}$ was normally within 1 percent and was within +18 and −29 percent for the innermost segment of $x/l = 0.054$.

Results and Discussion

The experiment was carried out over the ranges of the inlet air temperature, T_i, from 12 to 20°C with the constant air volume flow-rate of 0.075 m^3/s.

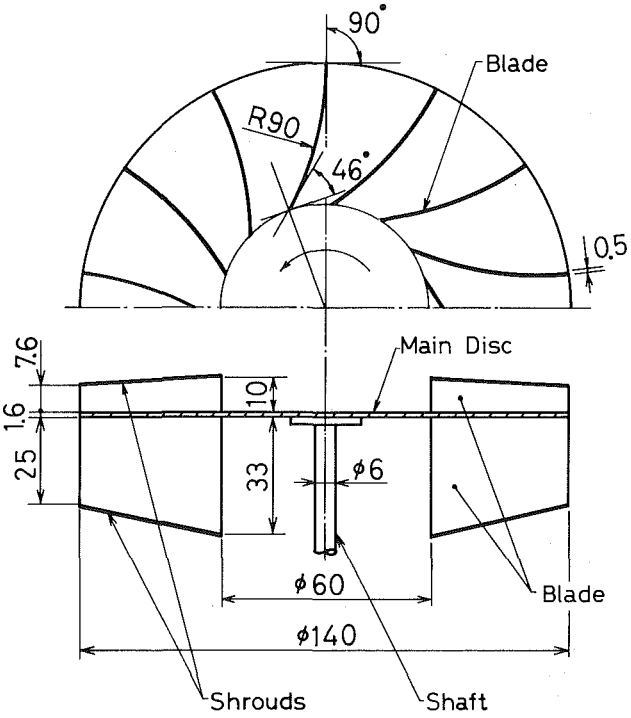

Fig. 2 Impeller of centrifugal fan-atomizer

Single-Phase Heat Transfer. Figure 5 shows the radial distributions of the average radial velocity, $\bar{u}_r$, the absolute velocity, u_a, the turbulence intensity, Tu, and the local Reynolds number, Re_ξ, defined by u_a, and streamline length, ξ, for an isothermal clear air flow in the exchanger channel. The radial velocity, $\bar{u}_r$, is nearly constant throughout the channel; the absolute velocity, u_a, decreases monotonically on proceeding downstream, i.e., with increasing x. The turbulence intensity, Tu, once decreases from 14 percent in the vicinity of the channel inlet to a minimum at $x \simeq 60$ mm, corresponding to $Re_\xi \simeq 7 \times 10^4$, and then increases to 16 percent near the channel outlet.

Figure 6 shows typical oscillograms of the stream turbulence in the exchanger channel. The periods of large velocity fluctuations observed at $x = 25$ mm are nearly equal to the period, 1.6 ms, of the pulsating flow caused by the impeller blades of fan-atomizer; however, on proceeding downstream, those large fluctuations break down and are transformed into the irregular patterns of high frequencies. It may be seen from the abovementioned characteristics that the high turbulence intensity near the channel inlet is not due to conventional irregular turbulence but primarily due to the periodic pulsations in the discharge flow from the fan-atomizer and that by the action of such periodic disturbances as a trigger, the transition to turbulent state occurs at the extremely low Reynolds number of $Re_\xi \simeq 7 \times 10^4$ [17].

The heat transfer data for clear air are plotted in Fig. 7 in the form of $h^*_{x(1)}$ and $h_{x(1)}$ against the location x/l. The possible error in $h^*_{x(1)}$ and $h_{x(1)}$, primarily due to the uncertainty in the radial conduction loss, is within 7 percent in the worst case and normally is ±3 percent; however, the maximum indeterminate error for the innermost segment is predicted to be rather serious as indicated by the limiting line around the data points, because the accurate estimation of heat loss through the inlet bellmouth ring was difficult. The effect of $\bar{q}_{(1)}$ on $h^*_{x(1)}$ and $h_{x(1)}$ was found to be less than ±2 percent in seven runs of $\bar{q}_{(1)}$ ranging from 700 to 5,300 W/m^2. The difference between both the local heat transfer coefficients, $h^*_{x(1)}$ and $h_{x(1)}$, was less than 10 percent because of

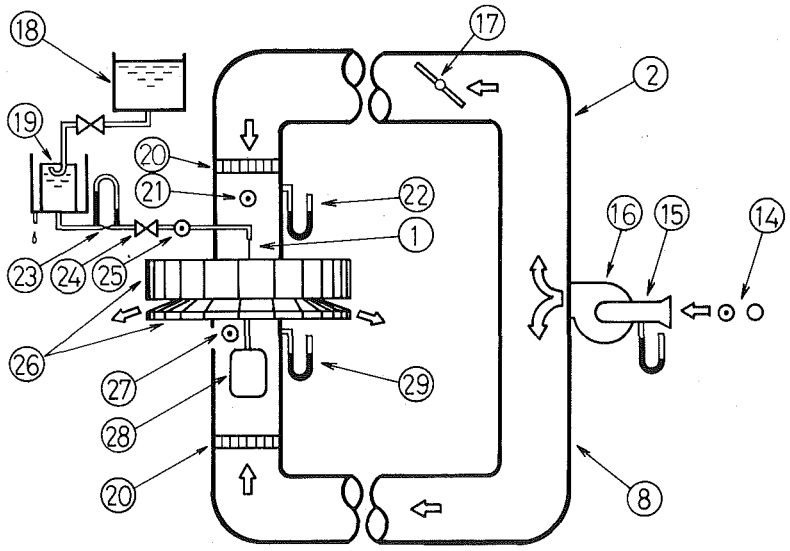

Fig. 3 Outline of experimental apparatus (not to scale): ① dripping nozzle; ② and ⑧ air ducts; ⑭ dry- and wet-bulb thermometers for inlet air; ⑮ inlet nozzle for measuring air flow rate; ⑯ auxiliary fan; ⑰ damper; ⑱ water tank; ⑲ overflow tank; ⑳ straighteners; ㉑ and ㉗ thermocouples for dry-bulb temperature; ㉒ and ㉙ pressure taps; ㉓ orifice flow meter; ㉔ needle valve; ㉕ mercury thermometer for water temperature; ㉖ test cooling unit; ㉘ motor

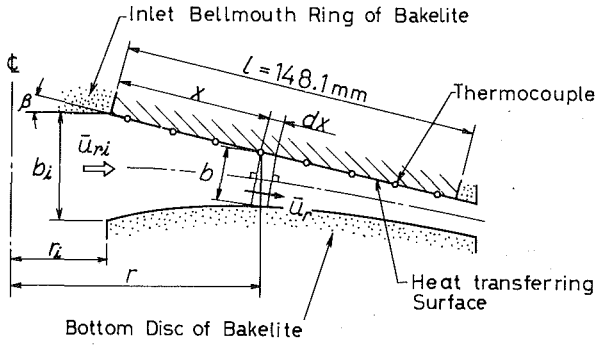

Thermocouple Positions								
No.(L-R)	1	2	3	4	5	6	7	8
x/l	0.054	0.173	0.301	0.431	0.560	0.688	0.817	0.941

Fig. 4 Physical model of the heat balance in heat exchanger channel

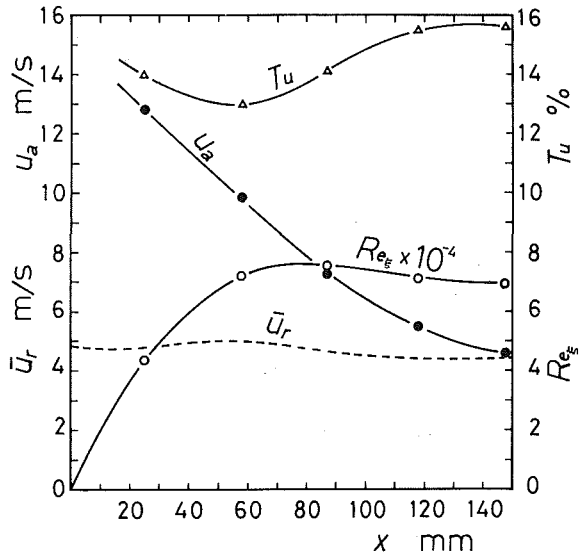

Fig. 5 Radial distributions of average radial velocity, $\bar{u}_r$, absolute velocity, u_a, local Reynolds number, Re_ξ, and turbulence intensity, *Tu*, of isothermal single-phase flows in exchanger channel

$T_{bx} \simeq T_i$ under the condition of Re_b being comparatively large, as is obvious from equation (7).

Figure 8 shows a comparison of the present experimental values for the test cooling unit with the existing theoretical ones for various laminar channel flows in respect of the local Nusselt numbers Nu_x^* defined by equation (3). Although the heat transfer performances for ordinary parallel plates/disks decrease on proceeding downstream, the measured heat transfer coefficients for the present cooling unit are not only considerably higher than the former, but nearly constant throughout the exchanger channel.

It has been already found that the time-averaged heat transfer for laminar channel flow is not appreciably changed by the flow oscillations [21] and that the heat transfer at given turbulence intensity increases as the length-scale of freestream turbulence decreases [22]. Therefore, the result of nearly constant heat transfer coefficients for the present cooling unit may be attributed to the fact that on proceeding downstream the periodic pulsating flow of large length-scale near the channel inlet undergoes transition to the turbulent flow of small length-scale which is effective in the enhancement of heat transfer. A similar uniform distribution of heat transfer was found over an inclined rectangular body with freestream disturbances caused by wake oscillations [23].

Besides, the swirling of flow in the exchanger channel and

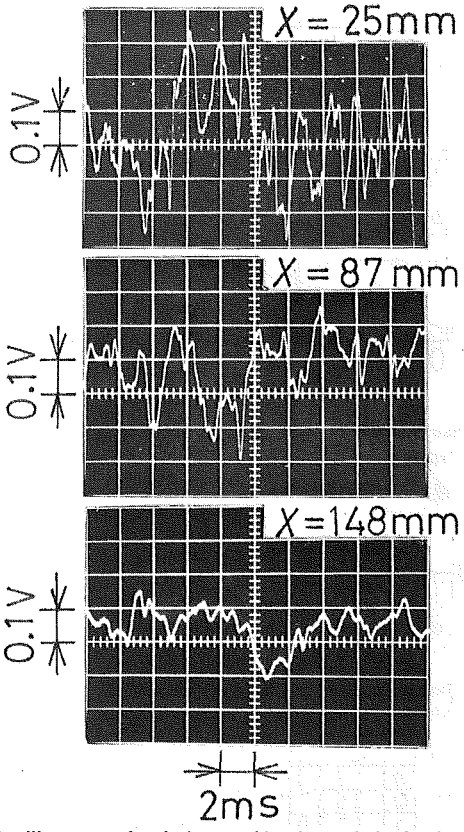

Fig. 6 Oscillograms of turbulence of isothermal single-phase flows in exchanger channel

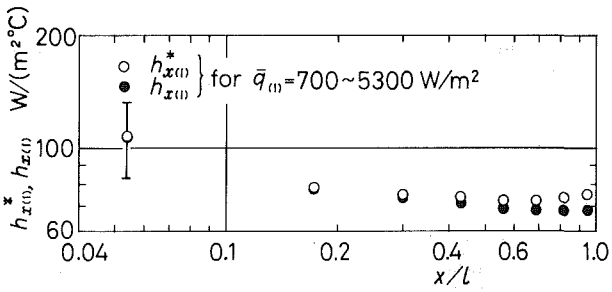

Fig. 7 Local heat transfer coefficients for clear air versus x/l

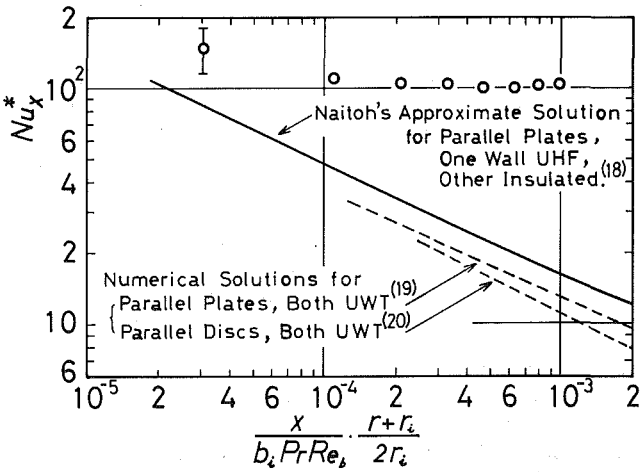

Fig. 8 Comparison of the authors' experimental values for the test cooling unit with the existing theoretical values for various laminar channel-flows of Pr≃0.7 in respect of the single-phase local Nusselt numbers, Nu_x^* (○: Authors' experiments for $\bar{q}_{(1)}$ = 700~5,300 W/m² with Re_b = 11,000)

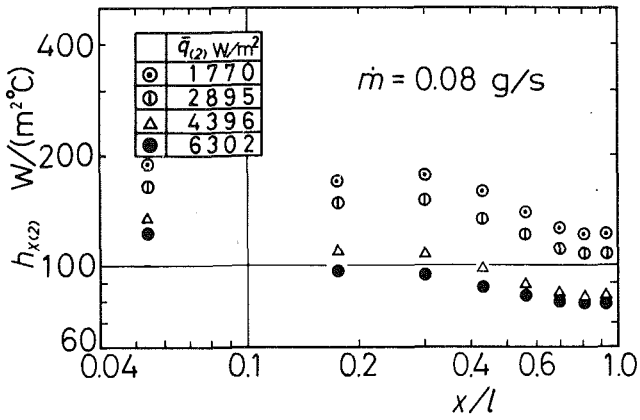

Fig. 9 Distributions of local heat transfer coefficients for air-water mist flow $h_{x(2)}$

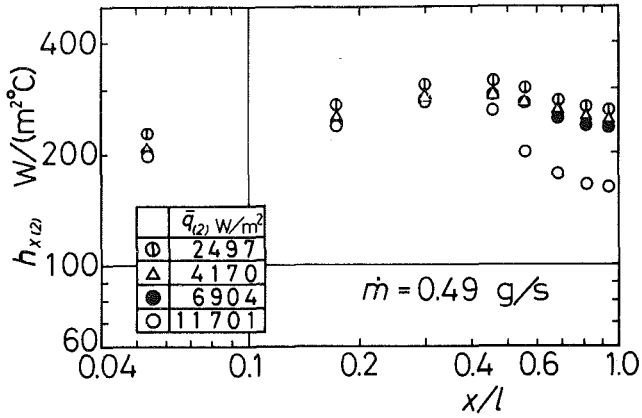

Fig. 11 Distributions of local heat transfer coefficients for air-water mist flow $h_{x(2)}$

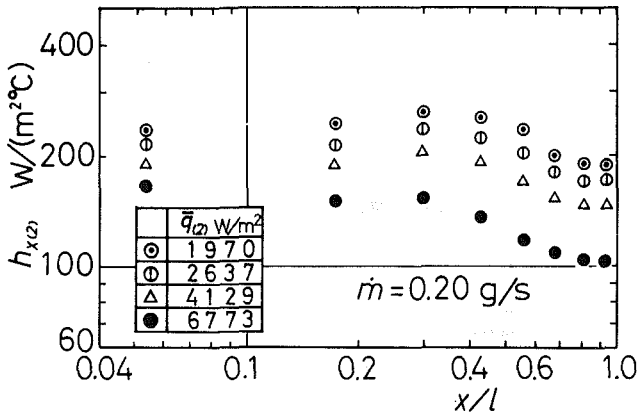

Fig. 10 Distributions of local heat transfer coefficients for air-water mist flow $h_{x(2)}$

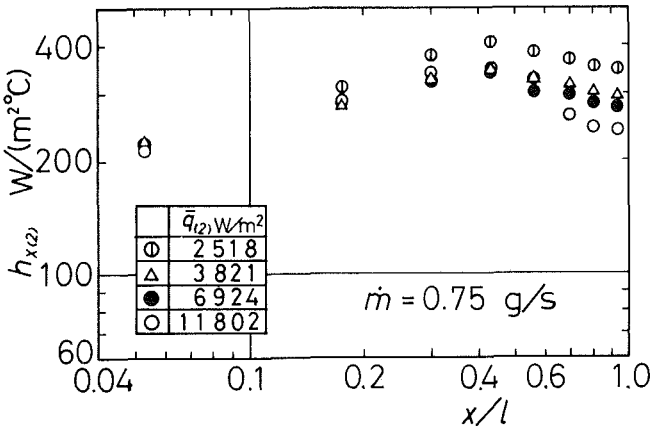

Fig. 12 Distributions of local heat transfer coefficients for air-water mist flow $h_{x(2)}$

the suppressing effect of a converging channel on the boundary-layer development [24] appear to contribute to the high heat transfer performance of the present cooling unit.

Two-Phase Heat Transfer. The experiment on air-water mist flow was carried out over the ranges of the wall heat flux, $\bar{q}_{(2)}$, from 1170 to 11,870 W/m², the relative humidity at channel inlet from 45 to 63 percent, the mass flow rate of spray water, $\dot{m}$, from 0.08 to 1.05 g/s, the temperature difference between feed water and inlet air from 2.9 to 3.8°C.

The measured local heat transfer coefficients, $h_{x(2)}$, are shown in Figs. 9 to 13. Since at low water flow rates, the dryout of water film on the heat transferring surface occurs from the place where the mass evaporation rate of water film exceeds the mass impinging rate of droplets, the value of $h_{x(2)}$ decreases as the wall temperature, T_{wx}, increases with increasing values of $\bar{q}_{(2)}$; however, in the case of high water flow rates where a water film is maintained on most of the heat transferring surface, the value of $h_{x(2)}$ increases with $\bar{q}_{(2)}$, as shown in Fig. 13. This tendency agrees well with the study of Aihara et al. of a wedge surface [12]. Excluding the case of the dryout occurring over the whole surface, as shown in Fig. 9, the distribution of $h_{x(2)}$ has a maximum at $x/l \simeq 0.3$ to 0.5, where active droplet impingement onto the surface was observed on a preliminary experiment using a transparent dummy surface. As the water flow rate, $\dot{m}$, increases, the atomized droplets become greater in size and travel on longer trajectories; accordingly the point of maximum $h_{x(2)}$ moves slightly downstream.

The distributions of the heat transfer enhancement factor, defined by $h_{x(2)}/h_{x(1)}$, were closely similar to those of $h_{x(2)}$,

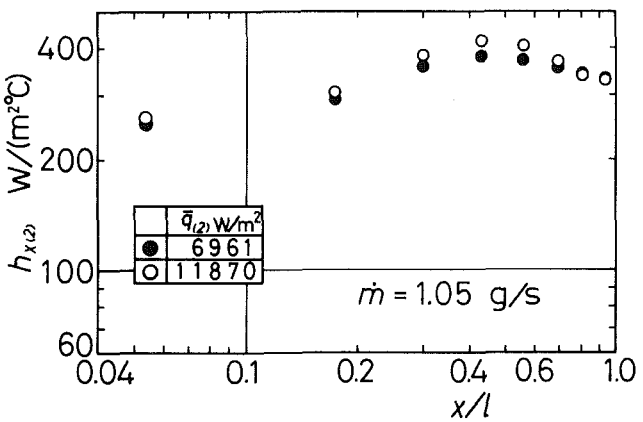

Fig. 13 Distributions of local heat transfer coefficients for air-water mist flow $h_{x(2)}$

because of the value of $h_{x(1)}$ being nearly constant over the range $0.17 < x/l < 0.94$.

Figure 14 shows the effects of the wall heat flux, $\bar{q}_{(2)}$, and mass flow rate of spray water, $\dot{m}$, on the maximum wall temperature $(T_w)_{max}$.

We now compare the present compact unit by air-water mist cooling with an ordinary parallel-plate channel by air cooling in respect of heat transfer performance for various maximum wall temperatures, $(T_w)_{max}$, under the same conditions of the following factors: the whole heat transferring area, the inlet-width, b_i, and length, l, of channel, the

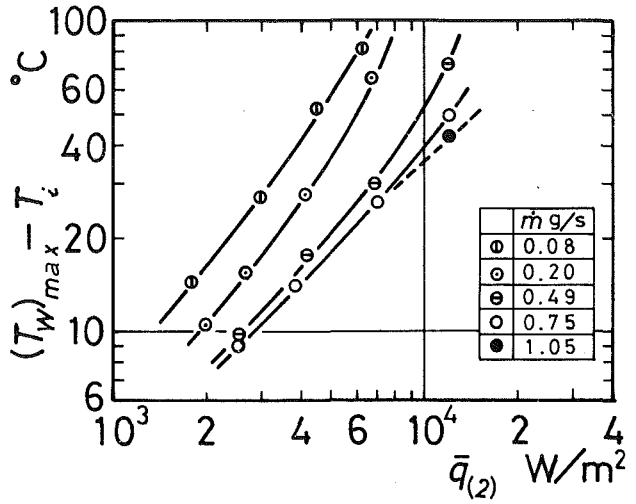

Fig. 14 Effects of average heat flux $\bar{q}_{(2)}$ and water mass flow rate, $\dot{m}$, on maximum wall temperature $(T_w)_{max}$

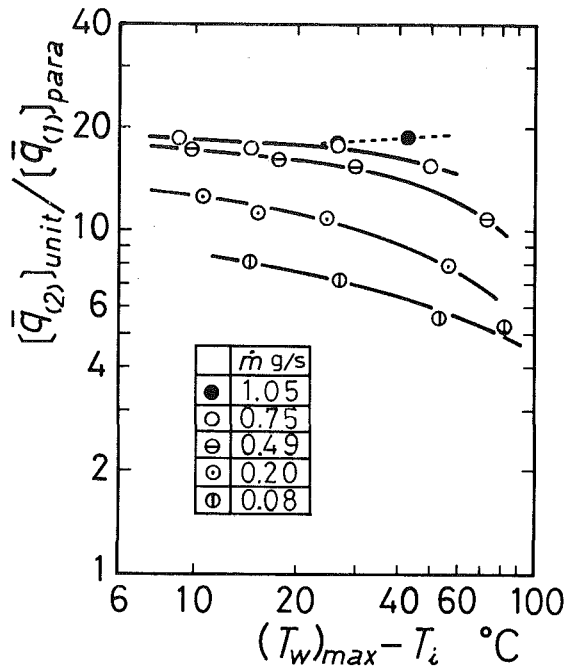

Fig. 15 Performance comparison of heat transfer between the present cooling unit and the corresponding parallel-plate channel: $[\bar{q}_{(2)}]_{unit}$, wall heat flux of the present compact unit by air-water mist cooling; $[\bar{q}_{(1)}]_{para}$, wall heat flux of an ordinary parallel-plate channel by air cooling

inlet dry-bulb temperature, T_i, and the volume flow rate of air, W. The values of heat flux, $[\bar{q}_{(2)}]_{unit}$, for the present compact unit can be obtained from the experimental data of Fig. 14; and the corresponding ones, $[\bar{q}_{(1)}]_{para}$, for the parallel-plate channel may be evaluated from Naitoh's approximate solution [18] for Pr = 0.71, one wall heated with uniform heat flux, and the other insulated. The heat flux ratios, $[\bar{q}_{(2)}]_{unit}/[\bar{q}_{(1)}]_{para}$, obtained as mentioned above, are plotted against $(T_w)_{max} - T_i$ in Fig. 15. It may be seen from the figure that the heat transfer performance of the present unit attains to about 7 times the corresponding one for the parallel-plate channel in the case of $\dot{m}$ = 0.08 g/s, equivalent to the water-to-air mass flow ratio M of 8.9×10^{-4}; and indeed to 20 times in the case of $\dot{m}$ = 0.8 to 1.0 g/s, or M = 8.9×10^{-3} to 1.1×10^{-2}. Thus, the authors' object may be fulfilled by having obtained the result of Fig. 15, since the extension rate of fin area to base area is about seven in ordinary commercial heat sinks for semiconductors.

The authors have designed and made the first trial article for cooling semiconductors, utilizing the principle and construction of the abovementioned compact cooling unit. This trial unit having "no fin" can dissipate heat of 1.4 kW by feeding water of 0.5 g/s at a temperature difference of about 45°C between the inlet air and the metal cases of mounted semiconductors. Figure 16 shows a comparison of compactness between the trial unit and a commercial heat-sink with many forced-air cooling fins having the same performance as the former. As may be seen from the figure, the trial unit is one-third the size of the commercial heat-sink illustrated by the broken lines.

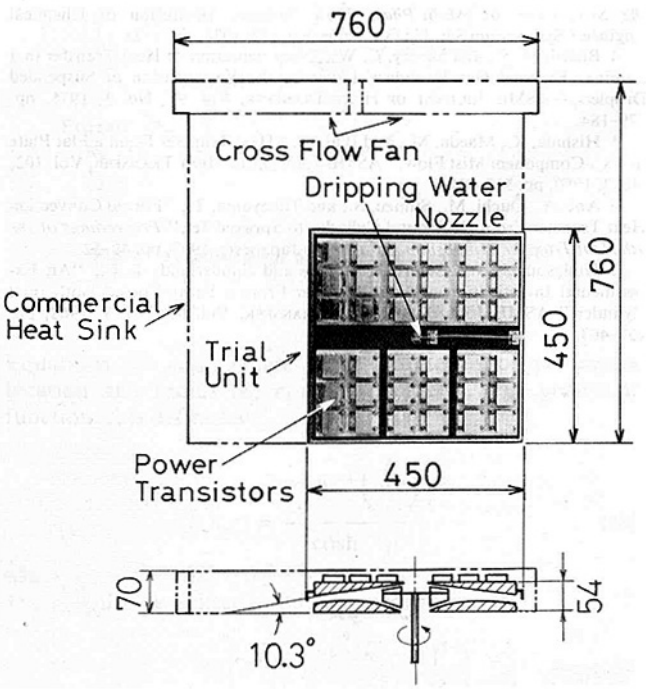

Fig. 16 Comparison of compactness between the present cooling unit without a fin and an ordinary heat sink with forced-air cooling fins

Conclusions

The results obtained are summarized as follows:

1 The single-phase air flow in the exchanger channel of the present compact cooling unit has velocity fluctuations of 14 percent near the channel inlet, similar to the periodic pulsations caused by the fan-atomizer; on proceeding downstream, the large fluctuations break down and are transformed into the irregular patterns of high frequency, peculiar to fully turbulent state; on reaching $Re_\xi \simeq 7\times10^4$, its turbulence intensity increases rapidly and approaches 16 percent near the channel outlet.

Owing to the high turbulence intensity, the swirling flow in channel, and the suppressing effect of a converging channel on boundary-layer development, the single-phase heat transfer coefficients for the present compact unit attain 1.8 to 6.6 times that of the parallel-plate channel in which one wall is heated with uniform heat flux and the other insulated.

2 In the case of low water flow rates where a dryout state occurs, the two-phase heat transfer coefficients for the present compact unit decrease as the wall temperature increases, with increasing values of wall heat flux; however, in the case of high water flow rates where a water film is maintained on most of the heat transferring surface, they increase as the wall heat flux increases.

Excluding the case of the extremely low water flow rate

where dryout occurs over the whole surface, the distribution of the two-phase local heat transfer coefficient has a maximum at $x/l \simeq 0.3$ to 0.5, where the active droplet impingement was observed.

3 The heat transfer performance of the present compact unit with water-feeding of 0.8 to 1.0 g/s attains up to 20 times that of the parallel-plates channel under the same thermal conditions.

4 On the basis of the results already mentioned, the first trial unit has been designed for cooling semiconductors. This trial unit without a fin dissipates 1.4 kW by feeding water of 0.5 g/s; however, it is one-third the size of the ordinary commercial heat-sink with many forced-air cooling fins having the same performance.

Acknowledgments

The authors wish to express their gratitude to Director N. Usami of Fuji Heavy Industries, Ltd. for giving them honeycomb cores, and to Director H. Motomatsu and Chief N. Yasumura of Ryôsan Co., Ltd. for making the test cooling units.

References

1 Maezawa, S., and Tsuchita, A., "Mass and Heat Transfer in Flow of Gas with Liquid-Droplet Suspension (1st report, Laminar Boundary Layer on a Flat Plate)," *Proceedings of the 7th Heat Transfer Symposium of Japan* (in Japanese), 1970, pp. 145–148.

2 Heyt, J. W., and Larsen, P. S., "Heat Transfer to Binary Mist Flow," *International Journal of Heat and Mass Transfer*, Vol. 14, No. 9, 1971, pp. 1395–1405.

3 Simpson, H. C., and Brolls, E. K., "Heat Transfer From a Thick Flat-Plate to an Air-Water Mist in Turbulent Flow Over the Plate," *Proceedings of the Symposium on Multi-Phase Flow Systems*, Institution of Chemical Engineers Symposium Ser. No. 38, Paper No. H2, 1974, pp. 1–23.

4 Bhatti, M. S., and Savery, C. W., "Augmentation of Heat Transfer in a Laminar External Gas Boundary Layer by the Vaporization of Suspended Droplets," ASME JOURNAL OF HEAT TRANSFER, Vol. 97, No. 3, 1975, pp. 179–184.

5 Hishida, K., Maeda, M., and Ikai, S., "Heat Transfer From a Flat Plate in Two-Component Mist Flow," ASME JOURNAL OF HEAT TRANSFER, Vol. 102, No. 3, 1980, pp. 513–518.

6 Abe, A., Ôuchi, M., Simizu, S., and Takeyama, T., "Forced Convection Heat Transfer From Horizontal Cylinder to Sprayed Jet," *Proceedings of the 4th Heat Transfer Symposium of Japan* (in Japanese), 1967, pp. 49–52.

7 Hodgson, J. W., Saterbak, R. T., and Sunderland, J. E., "An Experimental Investigation of Heat Transfer From a Spray-Cooled Isothermal Cylinder," ASME JOURNAL OF HEAT TRANSFER, Vol. 90, No. 3, 1968, pp. 457–463.

8 Kosky, P. G., "Heat Transfer to Saturated Mist Flowing Normally to a Heated Cylinder," *International Journal of Heat and Mass Transfer*, Vol. 19, No. 5, 1976, pp. 539–543.

9 Nishikawa, N., and Takase, H., "Effects of Particle-Size and Temperature Difference on Mist Flow Over a Heated Circular Cylinder," ASME JOURNAL OF HEAT TRANSFER, Vol. 101, No. 4, 1979, pp. 705–711.

10 Basilico, C., Jung, G., and Martin, M., "Convective Transfer Between a Heated Cylinder and an Airstream Charged With Sprayed Water," *International Journal of Heat and Mass Transfer*, Vol. 24, No. 3, 1981, pp. 371–385.

11 Lu, C. C., and Heyt, J. W., "Heat Transfer From Two-Phase Boundary Layers on Isothermal Cylinder: Influence of Drop Trajectory," *AIChE Journal*, Vol. 26, No. 5, 1980, pp. 762–769.

12 Aihara, T., Taga, M., and Haraguchi, T., "Heat Transfer From a Uniform Heat Flux Wedge in Air-Water Mist Flows," *International Journal of Heat and Mass Transfer*, Vol. 22, No. 1, 1979, pp. 51–60.

13 Aihara, T., and Fu, W., "Heat Transfer From a Wedge in Air-Water Mist Flow (Part 2: Theoretical Study of a Vertical Infinite Wedge of Uniform Wall Temperature)," *Transactions of the Japan Society of Mechanical Engineers* (in Japanese), Vol. 48, No. 436, 1982.

14 Hishida, K., Maeda, M., and Ikai, S., "Study on Heat Transfer in Binary Mist Flow," *Transactions of the Japan Society of Mechanical Engineers* (in Japanese), Vol. 48, No. 428, 1982, pp. 1279–1286.

15 Simpson, H. C., Beggs, G. C., and Sen, G. N., "Heat Transfer From Extended Surface Tubes to an Air-Water Mist," *Proceedings of the Symposium on Multi-Phase Flow Systems*, Institution of Chemical Engineers Symposium Ser. No. 38, Paper No. H3, 1974, pp. 1–22.

16 Yang, W. J., and Clark, D. W., "Spray Cooling of Air-Cooled Compact Heat Exchangers," *International Journal of Heat and Mass Transfer*, Vol. 18, No. 2, 1975, pp. 311–317.

17 Eckert, E. R. G., and Drake, R. M., Jr., *Heat and Mass Transfer*, McGraw-Hill, New York, 1959, p. 129.

18 Naitoh, E., "Laminar Heat Transfer in the Entrance Region of Parallel-Plates (The Case of Uniform Heat Flux)," *Kagaku Kogaku, The Society of Chemical Engineers, Japan* (in Japanese), No. 10, Vol. 38, 1974, pp. 739–745.

19 Aihara, T., and Sasago, A., "Study of Total Performance of Heat Exchangers (Report 1)," *Proceedings of the Japan Society of Mechanical Engineers* (in Japanese), No. 800-13, 1980, pp. 117–119.

20 Mochizuki, S., and Numata, K., "Study of Radial Flow and Heat Transfer Between Parallel Disks (Numerical Analysis)," *Proceedings of the Yamanashi Meeting of the Japan Society of Mechanical Engineers* (in Japanese), 1980, pp. 40–42.

21 Siegel, R., and Perlmutter, M., "Heat Transfer for Pulsating Laminar Duct Flow," ASME JOURNAL OF HEAT TRANSFER, Vol. 84, No. 2, 1962, pp. 111–123.

22 Simonich, J. C., and Bradshaw, P., "Effect of Free-Stream Turbulence on Heat Transfer Through a Turbulent Boundary Layer," ASME JOURNAL OF HEAT TRANSFER, Vol. 100, No. 4, 1978, pp. 671–677.

23 Test, F. L., and Lessmann, R. C., "An Experimental Study of Heat Transfer During Forced Convection Over a Rectangular Body," ASME JOURNAL OF HEAT TRANSFER, Vol. 102, No. 1, 1980, pp. 146–151.

24 Yang, J. W., and Price, G. M., "Laminar Flow Development and Heat Transfer in Converging Plane-Walled Channels," *Applied Scientific Research*, Vol. 25, No. 5, 1972, pp. 361–371.

Approximate Phase Change Solutions for Insulated Buried Cylinders

V. J. Lunardini
Mechanical Engineer,
U.S. Army Cold Regions Research and Engineering Laboratory,
Hanover, N.H. 03755
Mem. ASME

The conduction problem for cylinders embedded in a medium with variable thermal properties cannot be solved exactly if phase change occurs. New, approximate solutions have been found using the quasi-steady method. These solutions consider heat flow from the entire pipe surface, rather than from a single point, as has been assumed in the past. The temperature field, phase change location, and pipe surface heat transfer can be evaluated using graphs presented for parametric ranges of temperature, thermal properties, burial depth, and insulation thickness. The theoretical results show good agreement with complete numerical solutions. The accuracy of the method increases as the Stefan number decreases and the results are of particular value for insulated hot pipes or refrigerated gas lines.

Introduction

Freezing or thawing around pipes buried in thawed or frozen material has become an important problem for engineers. The placement of gas and oil pipes in permafrost, the storage of solar energy as latent heat, and buried heat exchangers for heat pumps are significant examples. No exact solution exists for phase change in the cylindrical geometry, however, the problem of a pipe surrounded by an infinite medium, i.e., infinite burial depth, has been evaluated numerically by Lunardini [1], Sparrow et al. [2], Tien and Churchill [3], Carslaw and Jaeger [4], and others, for various temperatures and thermal properties.

The more difficult problem of finite pipe burial has not been evaluated systematically except with approximate techniques such as the quasi-steady method. Porkhaev [5, 6] and Hwang [7] examined the uninsulated pipe while Thornton [8], Seshadri and Krishnayya [9], and Lunardini [13], presented solutions for insulated pipes.

Steady-State Solution

Solutions are available for the steady state, after phase change ceases, using source-sink images or conformal transformations (Carslaw and Jaeger [4] and Lunardini [14]). The results will be given for a thaw problem, as noted in Fig. 1, but freezing is essentially the same. The thermal properties of the medium are constant, but different, for temperatures above and below the phase change value.

The insulation surface temperature is assumed to be a constant $\bar{T}_p$. This is acceptable if the insulation is not extremely thick. The temperature, $\bar{T}_p$, is evaluated by equating the integrated heat flow from the pipe to the heat flow into the medium at the insulation surface. Then

$$\bar{T}_p - T_f = (T_p - T_f)\left(\frac{1-b\alpha\beta}{1+b\alpha}\right) \tag{1}$$

The temperatures in the thawed and frozen regions are

$$\frac{T_1 - T_f}{T_p - T_f} = \frac{1+\beta}{1+b\alpha}\,\frac{\cosh^{-1}\left(\frac{h}{r}\right)}{\cosh^{-1}\mu} - \beta \tag{2}$$

$$\frac{T_2 - T_0}{T_f - T_0} = \frac{1+\beta}{\beta(1+b\alpha)}\,\frac{\cosh^{-1}\left(\frac{h}{r}\right)}{\cosh^{-1}\mu} \tag{3}$$

Contributed by the Heat Transfer Division and presented at the ASME Winter Annual Meeting, Washington, D.C., November 15-20, 1981. Manuscript received by the Heat Transfer Division December 7, 1981. Paper No. 81-WA/HT-50.

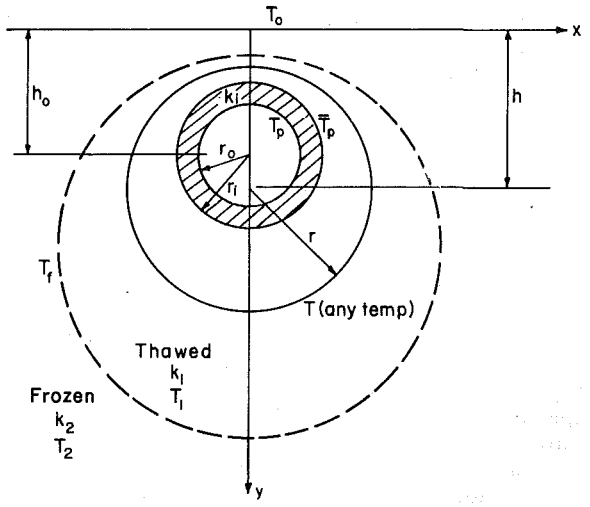

Fig. 1 Phase change around insulated buried pipe

Equations (2) and (3) are written in terms of the center location and radius (h, r) of an isotherm. The geometric function, f, is defined as

$$f(h,r) = \frac{\cosh^{-1}\left(\frac{h}{r}\right)}{\cosh^{-1}\mu} \tag{4a}$$

where $h^2 - r^2 = h_0^2 - r_i^2$

This can also be written in Cartesian coordinates as

$$f(x,y) = \frac{\ln\left\{\dfrac{x^2+[y+\sqrt{h_0^2-r_i^2}]^2}{x^2+[y-\sqrt{h_0^2-r_i^2}]^2}\right\}}{2\ln\left\{\dfrac{h_0}{r_i}+\sqrt{\left(\dfrac{h_0}{r_i}\right)^2-1}\right\}} \tag{4b}$$

In nondimensional form

$$f(H,R) = b\cosh^{-1}(H/R) \tag{5a}$$

$$f(\zeta,\xi) = \frac{b}{2}\ln\left\{\frac{\zeta^2+[\xi+a]^2}{\zeta^2+[\xi-a]^2}\right\} \tag{5b}$$

The value of the function, f, on the phase change interface is

$$f_0 = b\cosh^{-1}(H_0/R_0) = \frac{b}{2}\ln\left\{\frac{\zeta_0^2+(\xi_0+a)^2}{\zeta_0^2+(\xi_0-a)^2}\right\} \tag{6}$$

For the steady state the phase change interface is simply the T_f isotherm. This is given, from equation (2) or (3), by

$$f_{0\infty} = \frac{\beta}{1+\beta}(1+b\alpha) \tag{7}$$

The limiting thaw depth can be evaluated from

$$\xi_{0\infty}/a = \frac{(\mu+a)^K+1}{(\mu+a)^K-1} \tag{8}$$

where

$$K = \frac{\beta}{1+\beta}(1+b\alpha)$$

In this equation, $\xi_{0\infty}$ denotes the depth to the bottom of the thaw interface on the plane of symmetry where $\zeta_0 = 0$.
Also

$$H_{0\infty} = a\left(\frac{e^{2K/b}+1}{e^{2K/b}-1}\right) \tag{9}$$

$$R_{0\infty} = \sqrt{H_{0\infty}^2 - a^2} \tag{10}$$

The insulation thickness needed to keep the soil frozen is given by $\xi_{0\infty} \le \mu + 1$.

Thus, from equation (6) or equation (1), $b\alpha = 1/\beta$ and

$$\left(\frac{\gamma}{\mu}\right)^{k_{1i}} = (\mu+a)^{\frac{1}{\beta}} \tag{11}$$

The heat transfer, from the pipe to the surface, is

$$q = 2\pi k_2 \frac{(1+\beta)b}{\beta(1+b\alpha)}(T_f - T_0) \tag{12}$$

Quasi-Steady Equations

The quasi-steady approximation does not attempt to solve the phase change problem exactly but assumes that the phase change interface moves slowly so that at any instant the temperature profiles satisfy the Laplace Equation. This condition will be approached as the ratio of the sensible to the latent heat—the Stefan number—approaches zero (Lunardini [14]). The motion of the interface then follows by satisfying the energy boundary condition between the two phases. The energy balance may be formulated and solved at various locations on the phase change interface, including the plane of symmetry. The approximate isotherms will be circles, as has been noted for the steady-state solution, although the true isotherms are not circular since they are not constant coordinate surfaces of a bicircular transformation. However, the pipe and ground surface temperatures are always circular isotherms. After an infinite time, when the steady-state is reached, all isotherms become circular. Thus, the intermediate-time, circular, isotherms required by the quasi-steady method should be reasonable approximations to the actual isotherms.

The temperatures, at any instant, satisfy the Laplace equations with the form of the steady-state temperatures, equations (2, 3).

$$\phi_1 = \frac{T_1 - T_f}{T_p - T_f} = \frac{f}{1+b\alpha} + k_{21}\frac{(T_f - T_{0f})}{(T_p - T_f)}\left(\frac{f}{1+b\alpha} - 1\right) \tag{13}$$

$$\phi_2 = \frac{T_2 - T_0}{T_f - T_0} = \left[\frac{T_{pf} - T_f}{T_f - T_0} + k_{21}\right]\frac{f}{k_{21}(1+b\alpha)} \tag{14}$$

The value of the geometric function on the plane of symmetry, $\zeta = 0$, is

$$f(\xi) = b\ln\left(\frac{\xi+a}{\xi-a}\right) \tag{15}$$

T_{0f} and T_{pf} are fictitious, transient, boundary temperatures of the frozen and thawed zones which allow the phase change interface to move from the pipe (or insulation) surface to the final steady-state position. These auxiliary temperatures—a concept developed by Porkhaev [5, 6]—are needed since only one location of the interface, that given by equation (7), is possible with the actual boundary temperatures.

Since the value of f is f_0 on the phase change interface, where the temperature is T_f, then equations (13) and (14) lead to

$$\frac{T_f - T_{0f}}{T_p - T_f} = \frac{f_0}{k_{21}(1+b\alpha-f_0)} \tag{16}$$

$$\frac{T_{pf} - T_f}{T_f - T_0} = \frac{k_{21}(1+b\alpha-f_0)}{(1+b\alpha)} \tag{17}$$

Thus the thawed and frozen zone dimensionless temperatures are

Nomenclature

$a = \sqrt{\mu^2-1}$
$b = 1/\ln(\mu+a)$
C = volumetric specific heat
D = phase change thickness beneath pipe insulation
f, f_0 = functions, defined in text
h = depth to center of arbitrary isotherm
h_0 = depth to center of buried pipe
$H = h/r_i$
H_0 = dimensionless depth to center of phase change isotherm circle
k = thermal conductivity
$k_{12} = k_1/k_2$
k_i = thermal conductivity of insulation
L = volumetric latent heat of fusion
L_e = effective latent heat
q = heat transfer rate per unit length of pipe
r = radius of arbitrary isotherm
r_i = outer radius of insulation
r_0 = radius of pipe
$R = r/r_i$
R_0 = dimensionless radius of phase change isotherm circle
$S_T = C_1(T_p - T_f)/L$
t = time
T = temperature
T_f = freezing temperature
T_0 = ground initial and surface temperature
T_p = pipe temperature
$\bar{T}_p$ = insulation outer surface temperature
x,y = Cartesian coordinate
y_0 = phase change depth on plane of symmetry
z = dummy variable

$\alpha = k_{1i}\ln\left(\frac{r_i}{r_0}\right)$

$\beta = k_{21}\frac{(T_f - T_0)}{(T_p - T_f)}$

$\gamma = h_0/r_0$
$\zeta = x/r_i$
$\mu = h_0/r_i$
$\xi = y/r_i$
$\xi_0 = y_0/r_i$
ρ = dimensionless radial distance from center of phase change isotherm

$\tau = \frac{k_1(T_p - T_f)t}{r_i^2 L_e}$

$\tau^* = 2\sqrt{\tau}$
θ = polar coordinate

$\phi_1 = \frac{T_1 - T_f}{T_p - T_f} = \frac{f - f_0}{1+b\alpha-f_0}$

$\phi_2 = \frac{T_2 - T_0}{T_f - T_0} = \frac{f}{f_0}$

Subscripts

1 = thawed value for thawing, frozen value for freezing
2 = frozen value for thawing, thawed value for freezing

$$\phi_1 = \frac{f - f_0}{1 + b\alpha - f_0} \tag{18}$$

$$\phi_2 = \frac{f}{f_0} \tag{19}$$

Energy Balance on the Symmetry Plane

The latent heat absorbed (melting) is the difference between conduction into and out of the phase change interface. At the lowest point of the symmetry plane this is

$$\left(k_1 \frac{\partial T_1}{\partial y} - k_2 \frac{\partial T_2}{\partial y}\right)_{y_0} = -L \frac{dy_0}{dt} \tag{20}$$

This assumes that the phase change interface grows in exactly the same manner as a plane interface, and introduces a second approximation since it is known that the geometry has a significant effect on the rate of the phase change interface movement (Sparrow et al. [2]).

In nondimensional terms, equation (20) is

$$\left\{\frac{\partial \phi_1}{\partial \xi} - \beta \frac{\partial \phi_2}{\partial \xi}\right\}_{\xi_0} = -\frac{d\xi_0}{d\tau} \tag{21}$$

Substituting equations (15, 18, 19) into equation (21) yields the following relation for the depth to the phase change interface below the pipe.

$$-2ab\tau = \int_{\mu+1}^{\xi_0} \frac{(x^2 - a^2)dx}{\dfrac{1}{f_0 - 1 - b\alpha} + \dfrac{\beta}{f_0}} \tag{22}$$

This equation agrees with the solution of Hwang [7], when $\alpha = 0$, which is the uninsulated case. Equation (22) was used by Lunardini [13] to evaluate the effect of the pipe insulation. Using the functional form of f_0 gives

$$2a\tau = \int_{\mu+1}^{\xi_0} \frac{(x^2 - a^2)\,dx}{\dfrac{1}{\dfrac{1}{b} + \alpha - \ln\left(\dfrac{x+a}{x-a}\right)} - \dfrac{\beta}{\ln\left(\dfrac{x+a}{x-a}\right)}} \tag{23}$$

If a steady-state solution to equation (22) exists, then the denominator must approach zero as time approaches infinity. Thus

$$f_{0\infty} = \frac{\beta}{1+\beta}(1 + b\alpha) \tag{24}$$

or

$$\frac{\beta}{1+\beta}(1 + b\alpha) = b \ln\left(\frac{\xi_{0\infty} + a}{\xi_{0\infty} - a}\right) \tag{25}$$

This is identical to the steady-state solution previously discussed.

Seshadri and Krishnayya [9] used the same concepts but evaluated the insulation temperature by equating the heat flows only at the bottom of the pipe. This led to the following equations

$$-2ab\tau = \int_{\mu+1}^{\xi_0} \frac{(x^2 - a^2)dx}{\dfrac{1}{f_0 - 1 - \dfrac{b(\mu-1)\alpha}{a}} + \dfrac{\beta}{f_0}} \tag{26}$$

$$\frac{\beta}{1+\beta}\left(1 + \frac{b(\mu-1)}{a}\alpha\right) = b \ln\left(\frac{\xi_{0\infty} + a}{\xi_{0\infty} - a}\right) \tag{27}$$

Note that equation (26) also agrees with Hwang [7], when the pipe is uninsulated. For burial depth, $\mu > 2$, equations (25) and (27) are in fairly good agreement and the results tend to converge as β becomes large. For small values of β and μ, equation (27) gives limiting solutions far greater than the known steady-state solution. The use of only the heat flux at the bottom of the pipe not only accelerates the phase change interface growth rate (compared to equation (22)) but also greatly exaggerates its final position.

If only one phase exists, i.e., $T_0 = T_f$ and thus $\beta \equiv 0$, then an exact solution to equation (23) can be found. This is

$$2a\tau = a\frac{\xi_0^3 - (\mu+1)^3}{3} - a^2\{\xi_0 - (\mu+1)\} + \left(-\frac{1}{3}\xi_0^3 + a^2\xi_0\right)\ln\left(\frac{\xi_0 + a}{\xi_0 - a}\right) + \frac{2}{3}a^3\ln(\xi_0^2 - a^2) - \frac{1}{3}a[\xi_0^2 - (\mu+1)^2] + \frac{1}{b}\left[\frac{1}{3}(\xi_0^3 - a^2(\mu+1)\right] - \frac{2}{3}a^3\ln[(\mu+1)^2 - a^2] \tag{28}$$

The heat loss from the pipe and the temperatures at any location can be easily calculated once ξ_0 (and thus f_0) is known. The relations are

$$\frac{T_1 - T_f}{T_p - T_f} = \frac{f_0 - f}{f_0 - 1 - b\alpha} \tag{29}$$

$$\frac{T_2 - T_0}{T_f - T_0} = \frac{f}{f_0} \tag{30}$$

$$q = \frac{2\pi k_1 (T_p - T_f)}{(1 + b\alpha - f_0)\ln(\mu + a)} \tag{31}$$

Energy Balance With Circular Geometry

Thornton [8] integrated the energy balance over the entire phase change interface, rather than directly beneath the pipe. This automatically restricts the phase change to a circular geometry. The general equation for the radius of the region which has changed phase is

$$\int_{-\frac{\pi}{2}}^{\frac{\pi}{2}} \left\{\frac{\partial \phi_1}{\partial \rho} - \rho \frac{\partial \phi_2}{\partial \rho}\right\}_{\rho = R_0} d\theta = -\pi \frac{dR_0}{dt} \tag{32}$$

Again, using equations (18, 19), this is

$$\left(\frac{1}{1 + b\alpha - f_0} - \frac{\beta}{f_0}\right)\int_{-\frac{\pi}{2}}^{\frac{\pi}{2}} \left(\frac{\partial f}{\partial \rho}\right)_{\rho = R_0} d\theta = -\pi \frac{dR_0}{dt} \tag{33}$$

It can be shown that

$$\left(\frac{\partial f}{\partial \rho}\right)_{\rho = R_0} = \frac{-ab}{R_0(H_0 + R_0 \sin\theta)} \tag{34}$$

Thus the general equation is

$$b\tau = \int_1^{R_0} \frac{z\,dz}{\dfrac{1}{1 + b\alpha - f_0} - \dfrac{\beta}{f_0}} \tag{35a}$$

where

$$f_0 = b\ln(p + \sqrt{p^2 - 1})$$

$$p = \sqrt{1 + \frac{a^2}{z^2}}$$

Equation (35*a*) may also be expressed in terms of the depth ξ_0.

$$4\tau = \int_{\mu+1}^{\xi_0} \frac{(x^4 - a^4)dx}{x^3\left\{\dfrac{1}{\dfrac{1}{b} + \alpha - \ln\left(\dfrac{x+a}{x-a}\right)} - \dfrac{\beta}{\ln\left(\dfrac{x+a}{x-a}\right)}\right\}} \tag{35b}$$

The solution to this equation, when $\beta \equiv 0$, is

$$4\tau = \frac{1}{2}(\xi_0^2 + a^4/\xi_0^2)\left(\frac{1}{b} + \alpha - \ln\left[\frac{\xi_0 + a}{\xi_0 - a}\right]\right)$$

$$- \frac{\alpha}{2}[(\mu+1)^2 + a^4/(\mu+1)^2] + a^2 \ln\left[\frac{(\xi_0 + a)}{\xi_0 - a}\frac{(\mu+1-a)}{(\mu+1+a)}\right]$$

$$- a(\xi_0 - \mu - 1) - a^3[1/\xi_0 - 1(\mu+1)] \quad (36)$$

If the heat flux is assumed to be constant around the entire phase change interface,using the value at the bottom of the pipe where $\theta = \pi/2$, equation (34) is,

$$\left(\frac{\partial f}{\partial \rho}\right)_{\rho = R_0} = \frac{-ab}{R_0(H_0 + R_0)}$$

Using equation (33), the phase change radius is governed by

$$ab\tau = \int_1^{R_0} \frac{z^2(p+1)dz}{\frac{1}{1 + b\alpha - f_0} - \frac{\beta}{f_0}} \quad (37a)$$

Once again equation (37*a*) can be written as

$$4a\tau = \int_{\mu+1}^{\xi_0} \frac{(x^4 - a^4)dx}{x^2\left\{\frac{1}{\frac{1}{b} + \alpha - \ln\left(\frac{x+a}{x-a}\right)} - \frac{\beta}{\ln\left(\frac{x+a}{x-a}\right)}\right\}} = 0 \quad (37b)$$

The solution to equation (37*b*), when $\beta = 0$, is

$$4a\tau = \left(\frac{\xi_0^3}{3} + \frac{a^4}{\xi_0}\right)\ln\left[\frac{(\mu+a)(\xi_0 - a)}{\xi_0 + a}\right]$$

$$+ \alpha\left[\frac{1}{3}(\xi_0^3 - g^3) + a^4\left(\frac{1}{\xi_0} - \frac{1}{g}\right)\right]$$

$$- \frac{a}{3}(\xi_0^2 - g^2) + 2a^3 \ln\left(\frac{\xi_0}{g}\right) - \frac{4}{3}a^3 \ln\left(\frac{\xi_0^2 - a^2}{2g}\right) \quad (38)$$

where $g = \mu + 1$

Equations (35) and (37) yield the same steady-state solutions given by equations (9) and (10).

Comparison With Numerical Solutions

The equations can be compared to complete numerical solutions available in the literature and listed in Tables 1-4. These cases are all for hot oil pipes buried in permafrost and the sensible heat is considerably larger than the latent heat. This means that the Stefan number is quite large and in order to account for the sensible heat an effective latent heat is defined as

$$L_e/L = 1 + C_{21}k_{12}\beta S_T + S_T/2 \quad (39)$$

The quasi-steady calculations, given in Tables 1-4, used the effective latent heat.

Discussion

Solutions are presented to the approximate quasi-steady,

Table 1 Comparison of quasi-steady and numerical solutions β = .1396, μ = 4, α = 0, S_T = 1.62

Time Year	τ^*	D/r_i Numerical Gold et al. [10]	equation (23)	Quasi-steady equation (35)	equation (37*b*)
1	12.4	9.0	5.3	9.6	6.4
5	27.6	15.0	9.4	17.9	11.4
10	39.0	19.0	11.8	21.7	14.2

Table 2 Comparison of quasi-steady and numerical solutions, β = .1636, μ = 4, α = 0, S_T = 2.11

Time Year	τ^*	D/r_i Numerical Lachenbruch [12]	equation (23)	Quasi-steady equation (35)	equation (37*b*)
1	13.8	7	5.7	10.3	6.9
5	31.0	11	9.9	17.8	11.9
10	43.8	13	12.2	20.4	14.5
20	61.9	16	14.7	21.6	17.1

Table 3 Comparison of quasi-steady and numerical solutions, β = .0147, μ = 4, α = 0, S_T = 2.11

Time Year	τ^*	D/r_i Numerical Lachenbruch [12]	equation (23)	Quasi-steady equation (35)	equation (37*b*)
1	14.4	8	6.4	13.0	7.9
5	32.1	13	11.8	29.3	14.9
10	45.4	16	15.3	41.0	19.3
20	64.2	20	19.7	57.0	24.9

Table 4 Comparison of quasi-steady and numerical solutions, β = .0191, μ = 1.5, α = 0, S_T = 1.74

Time Year	τ^*	D/r_i Numerical Hwang et al. [11]	equation (23)	Quasi-steady equation (35)	equation (37*b*)
1	13.0	7.8	5.5	17.6	7.1
10	41.2	19.6	12.8	49.6	16.2
12	45.1	21.8	13.6	53.4	17.2

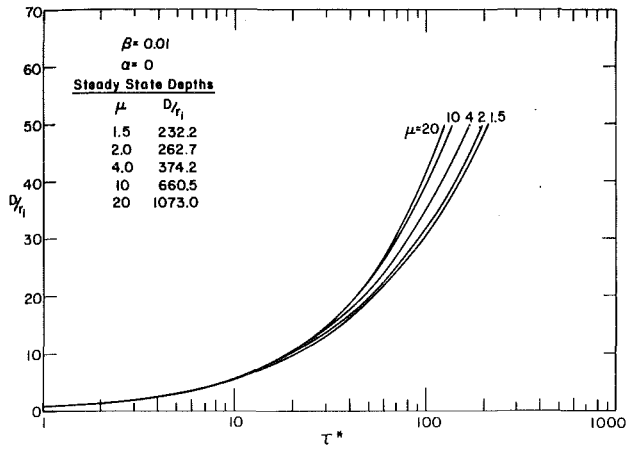

Fig. 2 Phase change beneath a buried pipe, $\beta = .01$, $\alpha = 0$

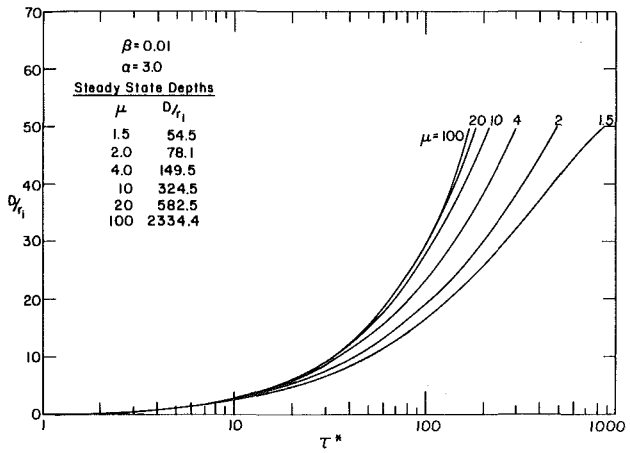

Fig. 3 Phase change beneath a buried pipe, $\beta = .01$, $\alpha = 3$

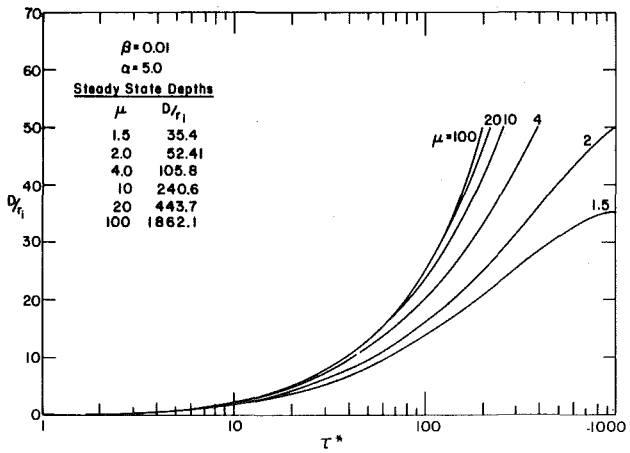

Fig. 4 Phase change beneath a buried pipe, $\beta = .01$, $\alpha = 5$

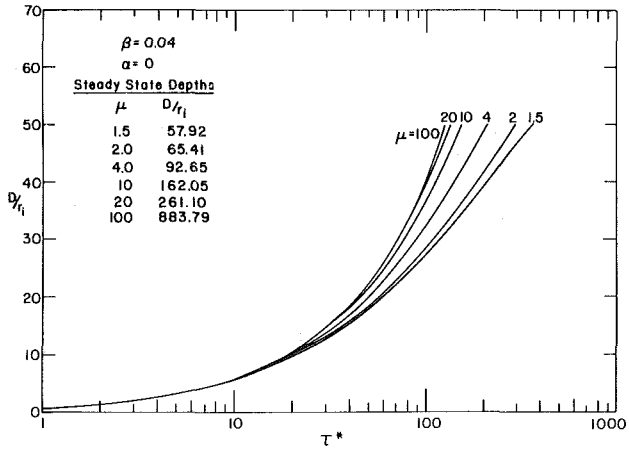

Fig. 5 Phase change beneath a buried pipe, $\beta = .04$, $\alpha = 0$

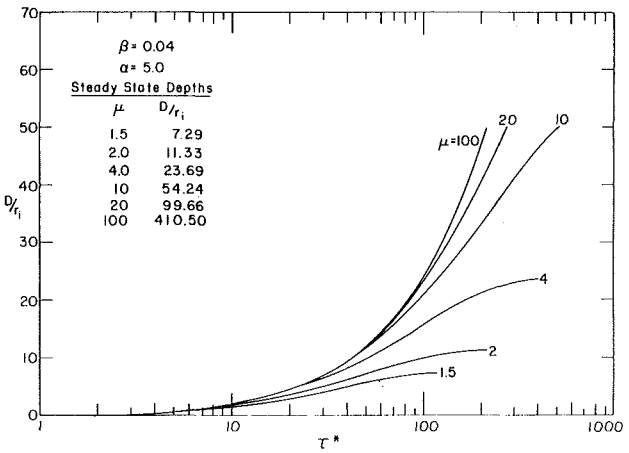

Fig. 6 Phase change beneath a buried pipe, $\beta = .04$, $\alpha = 3$

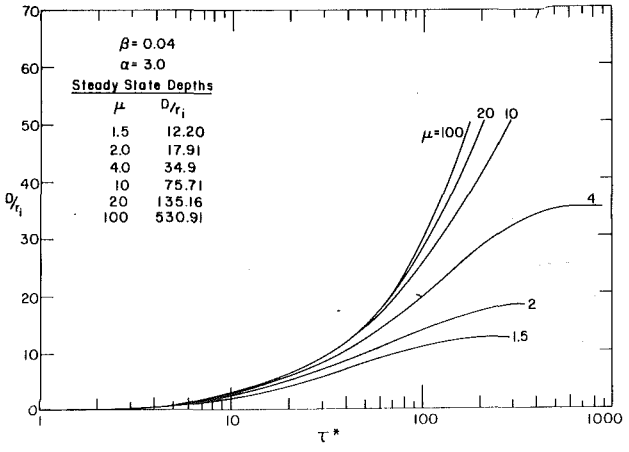

Fig. 7 Phase change beneath a buried pipe, $\beta = .04$, $\alpha = 5$

mathematical model representing the physical system. The validity of such approximate solutions can only be determined by comparison to data or exact solutions. Data available were not extensive or accurate enough to be used for meaningful comparisons. Since no exact solution is available it was necessary to use numerical solutions from the literature. The large Stefan numbers arise since only hot oil pipe solutions have been published to date. As was to be expected, without the correction for sensible heat contained in the effective latent heat, the quasi-steady solution overestimates the rate of thaw. Effective latent heats used with planar quasi-steady solutions, which can be compared to exact solutions, give excellent results when compared to high Stefan number cases. The same is true for circular pipes surrounded by an infinite medium (infinite burial depth) [14]. Thus, comparisons at high Stefan numbers can be used to set upper bounds on the accuracy of the quasi-steady solutions presented.

Tables 1–4 indicate that Thornton's method, equation (35),

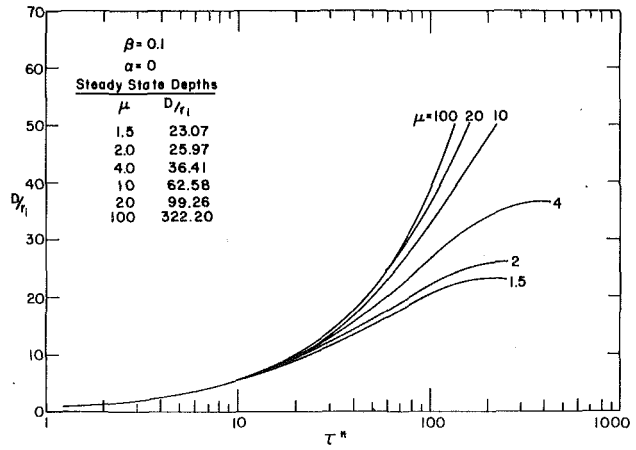

Fig. 8 Phase change beneath a buried pipe, $\beta = .1$, $\alpha = 0$

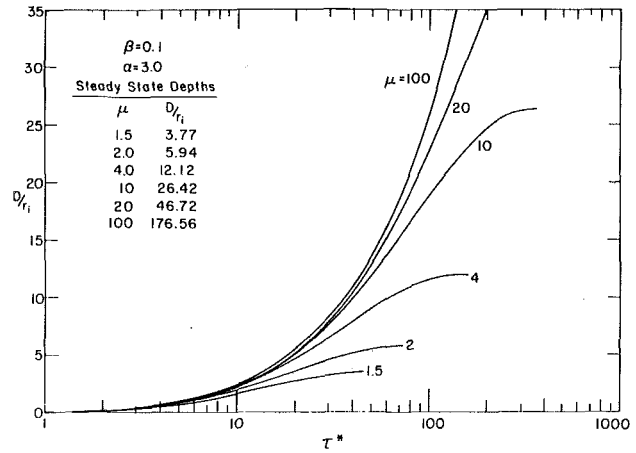

Fig. 9 Phase change beneath a buried pipe, $\beta = .1$, $\alpha = 3.0$

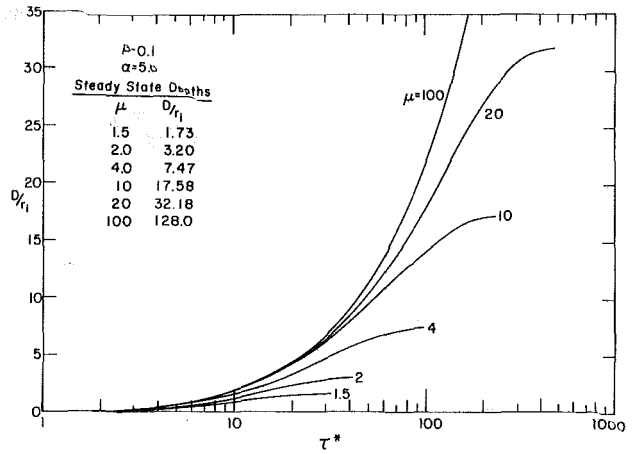

Fig. 10 Phase change beneath a buried pipe, $\beta = .1$, $\alpha = 5.0$

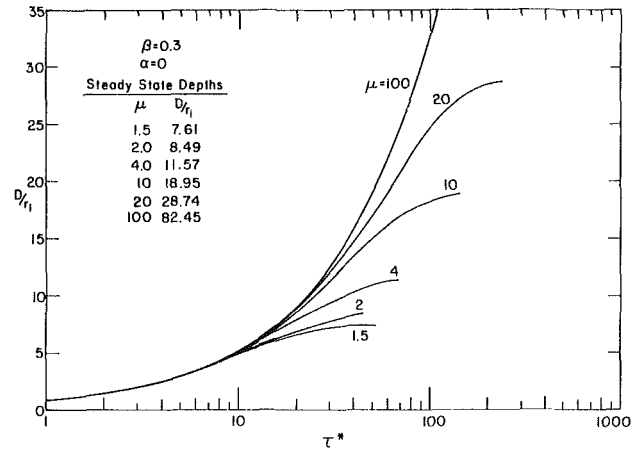

Fig. 11 Phase change beneath a buried pipe, $\beta = .3$, $\alpha = 0$

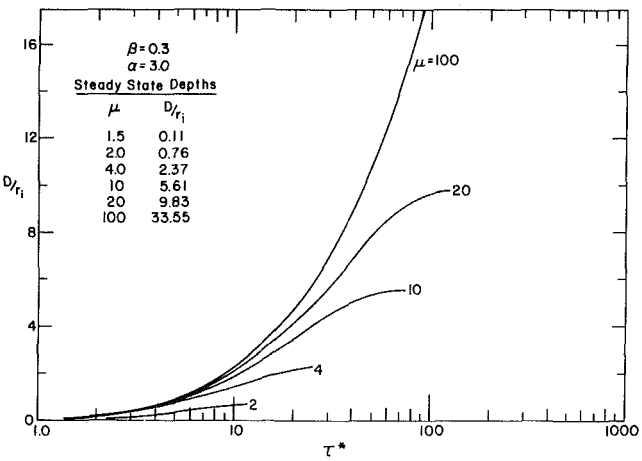

Fig. 12 Phase change beneath a buried pipe, $\beta = .3$, $\alpha = 3$

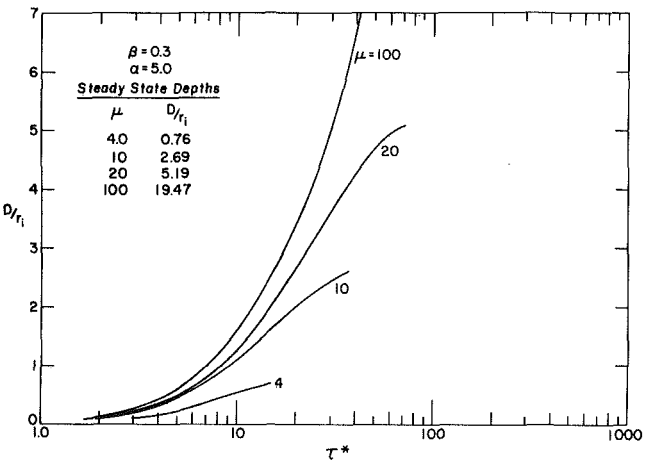

Fig. 13 Phase change beneath a buried pipe, $\beta = .3$, $\alpha = 5$

considerably overestimates the thaw depth for all of the cases considered. The method also leads to a condition where the phase change depth, immediately beneath the pipe, tends to increase as the burial depth decreases, which seems contrary to physical intuition as noted by Hwang [7]. However, a closer examination shows that the total volume of thawed material does increase with increasing burial depth. The peculiarity of a thicker layer of thawed material beneath the pipe for a decreasing burial depth is simply a function of the geometry of the steady solution.

Tables 1 and 4 show that equation (37) is clearly superior to equation (23), while Tables 2 and 3 indicate that the two formulas are essentially the same. The numerical results of Lachenbruch [12] exaggerate the effect of subcooling (β) when compared to Gold et al. [10] and the quasi-steady solutions. The surface heat transfer effect in Lachenbruch's calculation, which is not accounted for in equations (23) and (27), may retard the growth of the thaw bowl. The comparisons of Tables 1–4 indicate that equation (37) gives superior predictions and that the quasi-steady method has a maximum

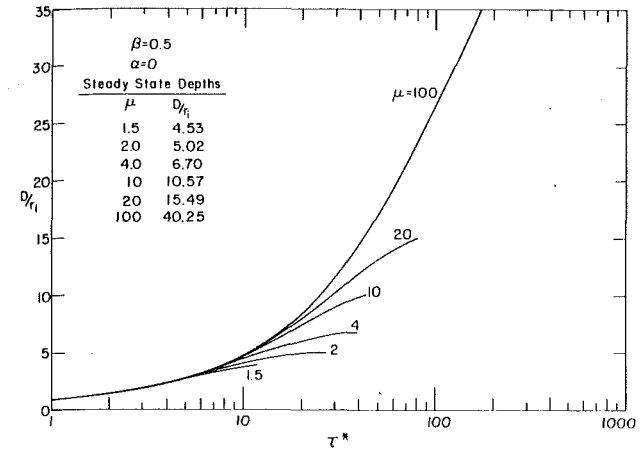

Fig. 14 Phase change beneath a buried pipe, $\beta = .5$, $\alpha = 0$

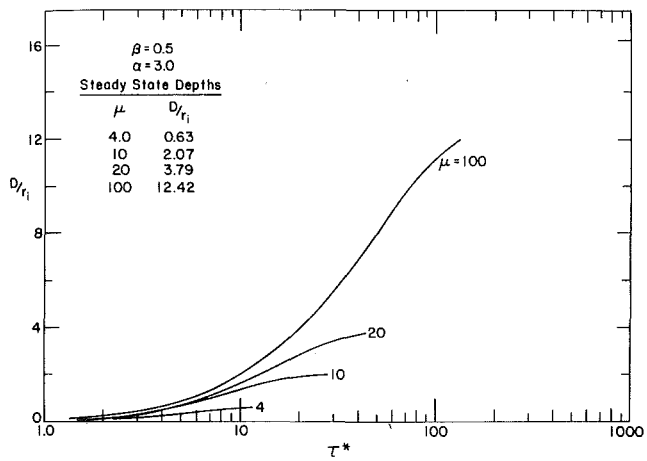

Fig. 15 Phase change beneath a buried pipe, $\beta = .5$, $\alpha = 3$

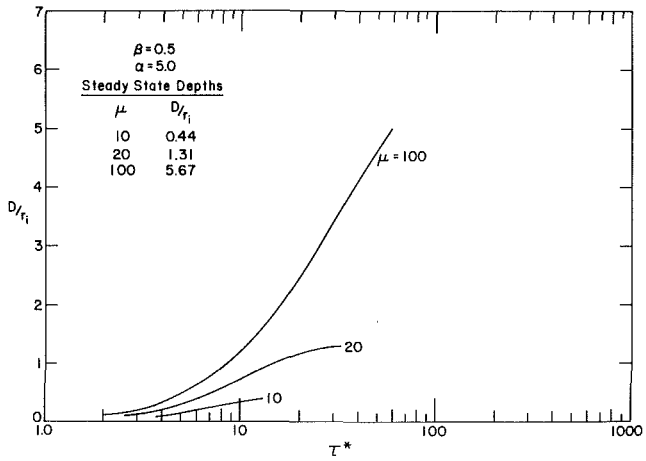

Fig. 16 Phase change beneath a buried pipe, $\beta = .5$, $\alpha = 5$

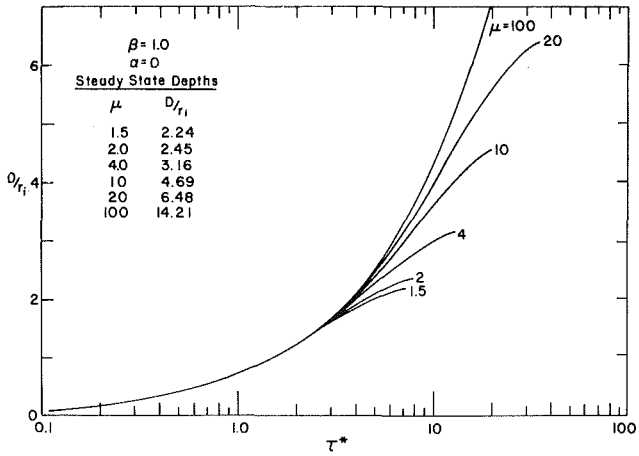

Fig. 17 Phase change beneath a buried pipe, $\beta = 1$, $\alpha = 0$

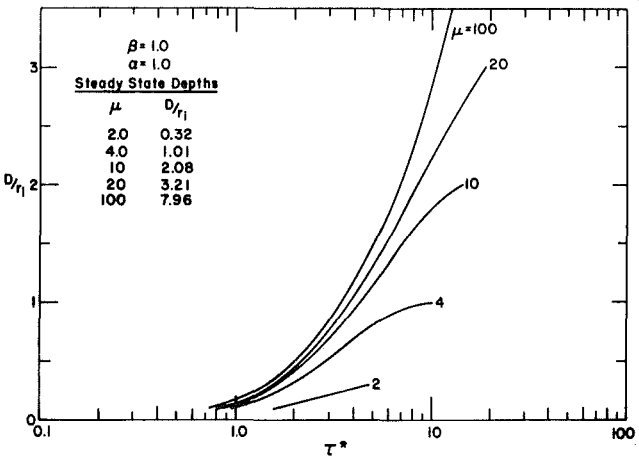

Fig. 18 Phase change beneath a buried pipe, $\beta = 1$, $\alpha = 1$

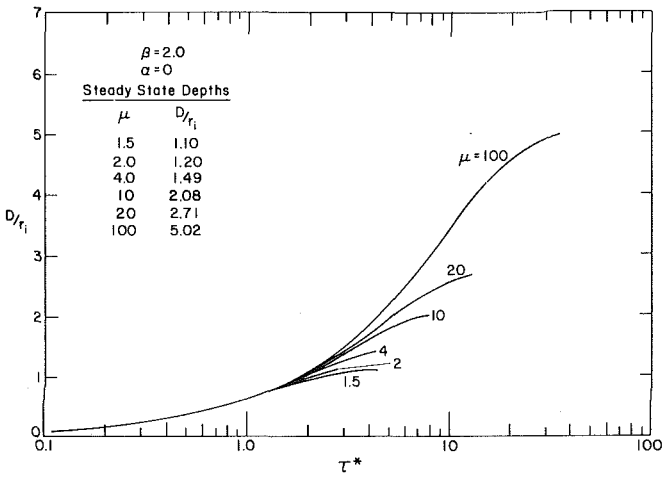

Fig. 19 Phase change beneath a buried pipe, $\beta = 2$, $\alpha = 0$

error of ±20 percent. The accuracy should improve if the Stefan number decreases towards zero, as will be the case for lower pipe surface temperatures or for a chilled pipe. The correction for the phase change depths suggested by Hwang [7] will not always improve the prediction and is not recommended. Numerical quadrature of equation (37) was carried out and values are plotted in Figs. 2–19 for practical ranges of β, α, and μ.

The quasi-steady method is useful since it can be applied to a number of practical cases with no exact solutions, and the results can be presented in a compact form. The graphs are felt to be acceptable for engineering estimates if accuracies on

the order of 20 percent are acceptable. For insulated pipes, where the phase change is expected to be more limited, the graphs should be more accurate.

The equations and graphs presented for the thawing case are all valid for the freezing problem if

$$\tau \equiv \frac{k_1 (T_f - T_p) t}{r_i^2 L_e}$$

and k_1, etc., refer to the frozen values.

References

1 Lunardini, V. J., "Phase Change Around a Circular Pipe," U.S. CRREL Report 80-27, Hanover, N.H., 1980.

2 Sparrow, E. M., Ramadhyani, S., and Patankar, S. V., "Effect of Subcooling on Cylindrical Melting," ASME JOURNAL OF HEAT TRANSFER, Vol. 100, No. 3, 1978, pp. 395–402.

3 Tien, L. C., and Churchill, S. W., "Freezing Front Motion and Heat Transfer Outside an Infinite Cylinder," AIChE *Journal*, Vol. 11, No. 5, 1965, pp. 790–793.

4 Carslaw, H. S., and Jaeger, J. C., *Conduction of Heat in Solids*, 2nd ed., Oxford at the Clarendon Press, 1959.

5 Porkhaev, G. V., "Temperature Fields in Foundations," *Proceedings Permafrost Int. Conference*, National Academy of Science, Washington, D.C., Pub. No. 1287, 1963, pp. 285–291.

6 Porkhaev, G. V., *Thermal Interaction Between Buildings, Structures, and Perennially Frozen Ground*, Nauka Publisher, Moscow, 1970.

7 Hwang, C. T., "On Quasi-Static Solutions for Buried Pipes in Permafrost," *Canadian Geotechnical Journal*, Vol. 14, 1977, pp. 180–192.

8 Thornton, D. E., "Steady State and Quasi-Static Thermal Results for Bare and Insulated Pipes in Permafrost," *Canadian Geotechnical Journal*, Vol. 13, No. 2, 1976, pp. 161–170.

9 Seshadri, R., and Krishnayya, A. V. G., "Quasi-Steady Approach for Thermal Analysis of Insulated Structures," *International Journal of Heat and Mass Transfer*, Vol. 23, 1980, pp. 111–121.

10 Gold, L. W., Johnston, G. H., Slusarchuk, W. A., and Goodrich, L. E., "Thermal Effects in Permafrost," *Proc. Can. Northern Pipeline Res. Conf.*, 1972, pp. 25–45.

11 Hwang, C. T., Murray, D. W., and Brooker, E. W., "A Thermal Analysis for Structures on Permafrost," *Can. Geotechnical Journal*, Vol. 9, No. 2, 1972, pp. 33–46.

12 Lachenbruch, A. H., "Some Estimates of the Thermal Effects of a Heated Pipeline in Permafrost," *U.S. Geol. Surv. Circ.*, 1970, p. 632.

13 Lunardini, V. J., "Phase Change Around Insulated Buried Pipes: Quasi-Steady Method," ASME *Journal of Energy Resources Technology*, Vol. 103, No. 3, 1981, pp. 201–207.

14 Lunardini, V. J., *Heat Transfer in Cold Climates*, Van Nostrand Reinhold, New York, Apr. 1981.

Influence of Free-Stream Turbulence on Turbulent Boundary Layer Heat Transfer and Mean Profile Development, Part I—Experimental Data

M. F. Blair
Senior Research Engineer,
Gas Turbine Technology Group,
United Technologies Research Center,
East Hartford, Conn. 06108
Mem. ASME

An experimental research program was conducted to determine the influence of free-stream turbulence on zero pressure gradient, fully turbulent boundary layer flow. Convective heat transfer coefficients and boundary layer mean velocity and temperature profile data were obtained for a constant free-stream velocity of 30 m/s and free-stream turbulence intensities ranging from approximately 1/4 to 7 percent. Free-stream multicomponent turbulence intensity, longitudinal integral scale, and spectral distributions were obtained for the full range of turbulence levels. The test results with 1/4 percent free-stream turbulence indicate that these data were in excellent agreement with classic two-dimensional, low free-stream turbulence, turbulent boundary layer correlations. For fully turbulent boundary layer flow, both the skin friction and heat transfer were found to be substantially increased (up to ~ 20 percent) for the higher levels of free-stream turbulence. Detailed results of the experimental study are presented in the present paper (Part I). A comprehensive analysis is provided in a companion paper (Part II).

Introduction

The growth of boundary layers beneath highly unsteady and/or turbulent mainstreams is of practical interest in numerous engineering applications. Turbomachinery airfoils and heat exchanger flows are two examples of high turbulence environments where accurate predictions of both boundary layer development and convective heat transfer distributions are critical. In the case of gas turbine airfoil design, the accuracy of these predictions influences the aerodynamic efficiency and, through its impact on the cooling design, both the cycle efficiency and hardware durability. Improvement of analytical techniques for predicting heat transfer distributions with high turbulence is currently restricted by the lack of an adequate supply of appropriate, accurate experimental data.

The impact of free-stream turbulence on fully turbulent boundary layer flow has been examined by others in numerous experimental, analytical, and computational studies. In particular for adiabatic turbulent boundary layer development, previous studies [1-8] have consistently indicated that increases of skin friction and boundary layer growth rate are produced by increased free-stream turbulence levels. Charnay et al. [2], Huffman et al. [3], and Evans [5] have also determined that increased free-stream turbulence results in significant changes to the boundary layer turbulence and shear stress distributions. Bradshaw [10], Hancock [8], and Green [9] have provided comprehensive analytical examinations and interpretations of the phenomena involved. The following is a very brief summary of the results of these previous studies of adiabatic turbulent boundary layer flow.

(*i*) The data of references [2-5] indicate that for a given boundary layer Reynolds number, $U\Theta/\nu$, the skin friction coefficient increases in a roughly linear manner with the local free-stream turbulence intensity (approximately 10 percent increase for $u'/U = 0.05$). (*ii*) The data of Meier and Kreplin [7] and the analysis of Bradshaw [10] indicate that for low turbulence levels ($u'/U < 0.005$) the skin friction coefficient is proportional to u'^2/U. (*iii*) The data and analysis of Hancock [8] and the analysis of Bradshaw [10] indicate that these free-stream turbulence effects depend upon both the free-stream turbulence intensity and length scale with the maximum impact of the free-stream turbulence expected for cases where the boundary layer thickness (δ) and streamwise dissipation length scale (L_e^u) are about equal.

In contrast to these reasonably consistent results measured for adiabatic experiments, previous data for the impact of free-stream turbulence on turbulent boundary layer heat transfer [11-21] are highly contradictory. References [11-16] report negligible influence of free-stream turbulence on turbulent heat transfer while references [17-21] report significant effects. Interpretation of these data has been clouded by the use of coarse boundary layer trips and/or unconventional free-stream turbulence generating devices in a number of the experiments. Additional uncertainty has arisen from the fact that most of the heat transfer data were obtained for transitional and low Re_θ boundary layers. In-depth discussions of these contradictions in the available heat transfer data are given by both Simonich [18] and Simonich and Bradshaw [19]. Clearly, if some form of Reynolds analogy holds for these flows, the increases of skin friction measured for the adiabatic studies [1-8] require that the heat transfer increase as well. Based on this argument, Simonich and Bradshaw [19] and McDonald and Kreskovsky [22] have concluded that enhanced heat transfer rates should be expected for increased free-stream turbulence levels.

The objectives of the present study were to determine accurately the magnitude of the effects of free-stream turbulence on turbulent boundary layer heat transfer and to provide a thoroughly documented set of experimental data for use in improving the analytical modeling of this phenomena. The experimental program was conducted in a zero pressure gradient, two-dimensional channel designed for boundary layer studies. Data were obtained on a densely instrumented heated flat plate model for turbulence intensities ranging from

Contributed by the Heat Transfer Division for publication in the JOURNAL OF HEAT TRANSFER. Manuscript received by the Heat Transfer Division November 30, 1981.

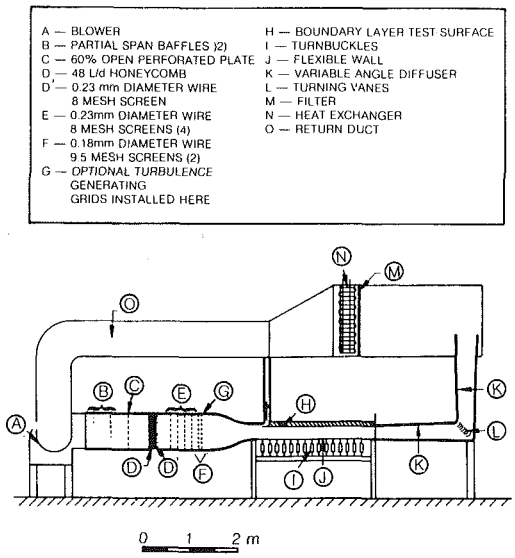

Fig. 1 United Technologies Research Center boundary layer wind tunnel

1/4 to 7 percent. The experiment consisted of the documentation of a comprehensive and accurate set of boundary layer profile, skin friction, and heat transfer data, along with an associated set of multicomponent free-stream turbulence intensity, integral scale, and spectral distribution data.

Results of this study show that for fully turbulent boundary layer flow, both the skin friction and heat transfer were substantially increased for increased levels of free-stream turbulence. Cross checks of the wall heat transfer and boundary layer profile data indicate that these measurements were self-consistent and that the test flows were highly two-dimensional. Data obtained for low free-stream turbulence levels agreed very well with the results of similar earlier studies [23-24], indicating a high level of accuracy for the present experiment. These present results indicate increases of approximately 14 and 18 percent for skin friction and heat transfer respectively for a free-stream turbulence intensity of 6 percent. A detailed analysis of these results is presented in Part II of this paper [25].

Experimental Apparatus

Wind Tunnel and Heat Transfer Test Surfaces. All experimental data for the present investigation were obtained in the United Technologies Research Center (UTRC) Boundary Layer Wind Tunnel (Fig. 1). This tunnel was designed specifically to generate large-scale, two-dimensional, incompressible boundary layers with Reynolds numbers and free-stream turbulence levels typical of turbomachinery airfoils. A complete description of this facility, including measurements documenting the tunnel flow uniformity and two-dimensionality of the test boundary layers, is given in reference [26]. The tunnel test section consisted of a flat upper wall instrumented for heat transfer measurements which served as the boundary layer test surface (H), plexiglass vertical sidewalls and a flexible lower wall (J). The test section was 86-cm wide, 244-cm long and 20-cm high at the entrance. For all test flows in this study, the lower flexible test section wall was adjusted to produce a constant velocity along the test section.

The boundary layer test surface (upper wall of test section) consisted of a uniform heat flux electrically heated plate instrumented for the measurement of local convective coefficients. The heated flat plate was constructed from a block of rigid urethane foam 86-cm wide by 244-cm long by 10-cm thick mounted in a plexiglass frame with 15.3-cm wide strips of 316 stainless steel foil cemented to the test surface. Details of the flat plate model and its instrumentation are presented in references [26] and [27]. Rigid foam was employed for the substrate of the heated flat plate model because of its extremely low thermal conductivity (8×10^{-5} gm-cal/cm-s K). Less than 1/2 percent of the heat generated on the surface of the plate was conducted away from the test surface. Electric current passing through the metal foil strips cemented to the test surface produced the surface heating. The metal foil strips were wired in series and were powered by a single low-ripple, regulated d-c power supply. The foil test surface was instrumented with an array of 203 Cr-Al 0.13-mm-dia bead welded thermocouples. Each thermocouple was welded to the back surface of the foil through a hole in the rigid foam plate. Forty-eight surface static pressure taps were also installed along the test surface.

The d-c power current passing through the surface strips was measured using two precision shunt resistors and a digital voltmeter. The temperature of the test surface thermocouples were measured relative to a single test section free-stream reference junction using a digital voltmeter.

In order to insure a known, constant test surface emissivity, and hence a known radiation loss, the completed foil test surface was coated with 3M C-101 high-emissivity flat black paint ($\epsilon = 0.99$). Test results indicated that this surface was aerodynamically smooth, producing no premature boundary layer transition.

Local convective coefficients were determined by ignoring the negligible conductive losses, subtracting power lost through thermal radiation and dividing by the temperature difference from the wall (T_w) to the freestream (T_e). To

Nomenclature

c_f = skin friction coefficient
c_p = specific heat at constant pressure
h = heat transfer coefficient
k = thermal conductivity
L_e^u = streamwise turbulence dissipation length scale
Pr = molecular Prandtl number
Pr_t = turbulent Prandtl number
Re_x = length Reynolds number
Re_θ = momentum thickness Reynolds number
St = Stanton number
U = velocity
U_τ = friction velocity
u',v',w' = streamwise, normal, and transverse fluctuating velocities
x = distance from plate leading edge
X = distance from contraction entrance
X_Λ = distance from origin of turbulence growth
Λ_f = longitudinal integral scale of turbulence
δ = boundary layer thickness
ϵ = surface emissivity
ϵ_h = coefficient of eddy diffusivity of heat
ϵ_m = coefficient of eddy diffusivity of momentum
μ = molecular viscosity
ν = kinetic viscosity
τ_w = wall shearing stress

Subscripts

e = free-stream value
w = wall value

illustrate the magnitude of the radiation losses from the test surface, for $U_e = 30$ m/s, for turbulent boundary layer flow with $T_w - T_e = 14°C$, the radiation loss was approximately 4 percent of the total surface power.

As shown in Fig. 1 at the test section entrance, a bleed scoop formed the leading edge of the heated boundary layer test surface. The scoop, which was mounted smoothly on the front edge of the heated test wall, provided a very short unheated starting length ($\xi = 4.3$ cm) upstream of the heated test surface. The leading edge of the scoop was a 4 × 1 ellipse in order to prevent a local separation bubble and premature transition of the test surface boundary layer. Details of the scoop including its instrumentation and adjustment are given in references [26] and [27].

Turbulence Generating Grids. As described in [26], this wind tunnel had a relatively low residual test section turbulence level (< 1/4 percent). Higher turbulence levels required for this study were generated by inserting various square array biplane grids constructed from rectangular bars at the entrance to the main tunnel contraction (see Fig. 1). Four turbulence generating grids were designed using the correlations of [28]. The grids will be referred to as Grids 1, 2, 3, and 4, corresponding to mesh widths, M, of 2.24, 6.51, 17.79, and 22.86 cm. The minimum turbulence configuration (no grid) will be referred to as Grid 0. Details of the grid configurations are given in [26]. This present arrangement differs from that used for nearly all the earlier investigations of this subject in which the turbulence grids were located in the test section just upstream of the boundary layer test surface. The benefits derived from locating the grids at the contraction entrance were that the generated turbulence was more homogeneous and had a lower decay rate along the test section. Since grid generated turbulence decays approximately as $u'/U \propto (x/b)^{-5/7}$ [28], the change in turbulence level with distance along the test section was reduced by increasing the distance from the grid to the test section entrance. In addition, the results of [28] indicate that approximately ten grid mesh lengths are required to establish a uniform turbulent flow. These advantages of locating the grid a distance upstream of the test section require, of course, a more coarse grid to achieve a given test section turbulence intensity.

Another effect considered was the expected influence of the contraction on the components of the grid generated turbulence. It was recognized that rearrangement of the relative magnitudes of the turbulence components would occur due to the contraction. However, since the contraction ratio was small (2.8), it was concluded that any effects of induced anisotropy would be small in comparison to the advantages gained in homogeneity and reduced decay rate. To determine the validity of the assumption, all three components of the test section turbulence were documented for all test cases.

Boundary Layer Probes and Traverse Control. Boundary layer mean velocity profile data were measured using United Sensor Model BA-0.020 impact probes with flattened tips. The probes used in the program were inspected for defects using both a Nikon Model II toolmakers microscope and a Jones and Lamson Model PC14 Shadowgraph. Mean temperature data were measured with miniature thermocouple probes designed using the results of [29]. The thermocouple sensing element for these probes was constructed from 0.02-mm dia Chromel-Alumel bead welded wires. The thermocouple bead (≈ 0.08-mm dia) was located at the center of the probe support prongs which were fabricated of heavier Chromel and Alumel wire. The results of [29] indicate that a probe of this design was virtually free of wire conduction errors and was capable of measuring boundary layer mean temperature profile data into the viscous sublayer region.

Movement of the boundary layer probes was achieved using an L. C. Smith ball/screw traverse drive with an optical shaft encoder capable of resolving relative probe location to within 0.01 mm. The traverse mechanism was suspended on a linear ball bearing track beneath the test section. The traverse could be located anywhere in the center 75 percent of the test section width from the leading to trailing edges of the test wall. A

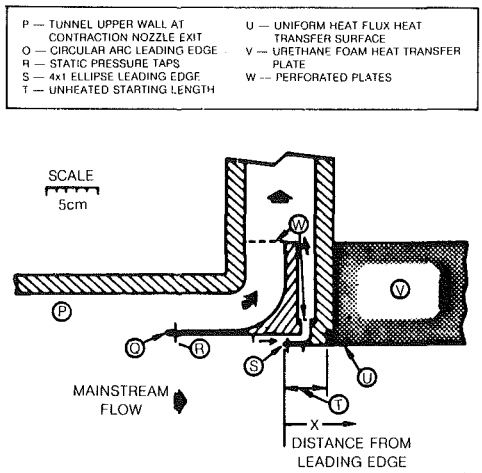

Fig. 2 Test wall leading edge bleed scoop

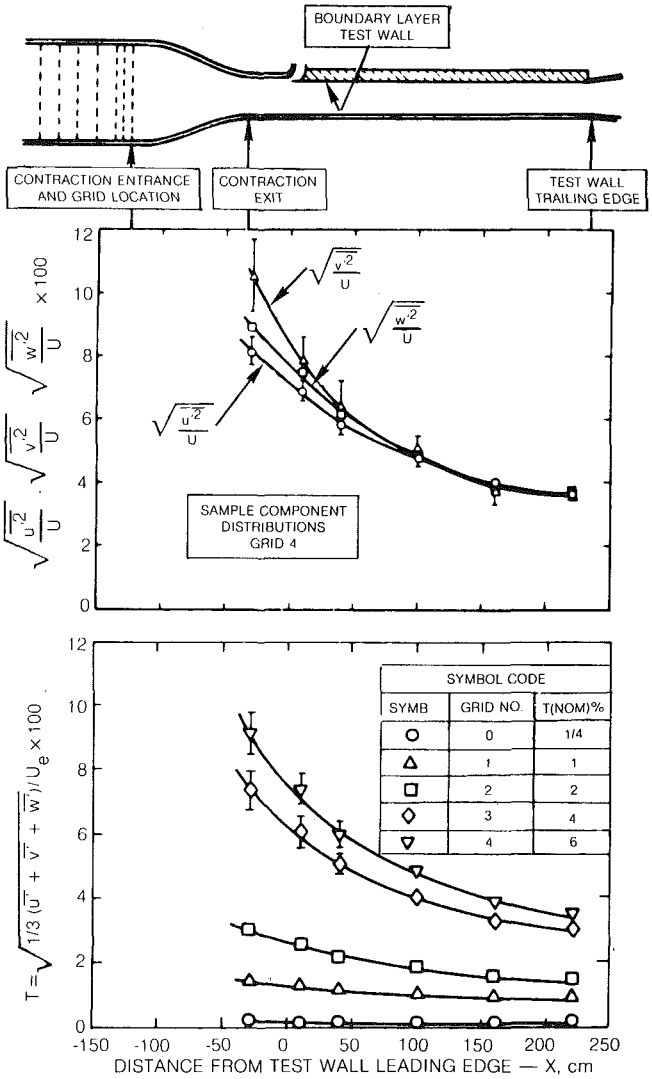

Fig. 3 Distributions of turbulence intensity in the test section

telescope sighted through the tunnel sidewall was used to accurately position probes relative to the test wall. Estimated absolute accuracy of measured probe distance from the test surface was 0.03 mm for any location in the test boundary layers.

Experimental Data

General. Experiments were conducted to determine the influence of free-stream turbulence on heat transfer for zero pressure gradient, fully turbulent boundary layer flow. Convective heat transfer coefficients, boundary layer mean velocity and temperature profile data, and wall static pressure distribution data were obtained for five free-stream turbulence levels ranging from approximately 1/4 to 7 percent. Free-stream multi-component turbulence intensity, longitudinal integral scale and spectral distributions were obtained for the various turbulence levels. For all test cases the tunnel test section was adjusted such that both the streamwise and transverse pressure gradients were negligible along the flat test wall. Conditions common to all test cases were U_e = 30.3 m/s, ambient test section pressure, T_e = 22°C, Max $T_{wall} - T_e$ = 20°C, Max Re_x = 5 × 10^6. Depending upon the free-stream turbulence level, maximum boundary layer thickness reached ranged from 3 to 6 cm. Samples and summaries of these data are presented here. The complete data [27, 28] are available from the author upon request. Included in [28] are tabulations of the individual velocity and temperature profile data, as well as the calculated integral thicknesses (momentum, displacement, enthalpy, and "Clauser delta") and skin friction coefficients.

Free-Stream Turbulence Intensity Distribution. To eliminate any uncertainties related to anisotropy of the free-stream turbulence, the distributions of all three components (u', v', and w') of the free-stream turbulence were documented for all test cases. Measurements of the turbulence intensity distributions for the various generating grids were obtained with TSI Model 1243 X hot film probes and a TSI series 1050 linearized constant temperature, two-channel anemometer system. The system employed a Model 1052 polynomial linearizer, a Model 1063 sum/difference unit, and Model 1076 RMS voltmeters. Descriptions of the anemometer and signal processing equipment used to obtain these data as well as descriptions of the techniques employed to reduce and interpret the measured quantities can be found in [27]. Surveys of the turbulence distributions were obtained over six planes located at the following stream-wise distances from the test plate leading edge: $X = -30$ (the plane of the contraction exit), 10, 40, 100, 163, and 224 cm. For each survey plane, data were obtained at 5 cm vertical intervals for three transverse locations: $Z = C_L$ and ± 15 cm.

The turbulence distributions measured with the various grids installed are presented in Fig. 3. For cases when all the turbulence levels over the data plane did not fall within the plotting symbol, bars indicate the range of the measured results. The upper half of Fig. 3 presents a sample multicomponent turbulence distribution measured with Grid 4 installed. The slight anisotropy shown for these multicomponent measurements for Grid 4 are typical of the results found for all five turbulence levels. These multicomponent measurements demonstrate that for most of the length of the boundary layer development ($x > 0$ in Fig. 3) the turbulence was nearly isotropic. For all grid configurations, the relationship between the magnitudes of the three turbulence components in the test section was $v' > w' > u'$ with the difference between the various components decreasing with increasing distance from the grids. The slight anisotropy of the turbulence in the tunnel test section resulted from combined effects of flow through coarse grids and the influence of the tunnel contraction on the grid turbulence. A discussion of these effects and a qualitative prediction of the relative turbulence component strengths are given in [26].

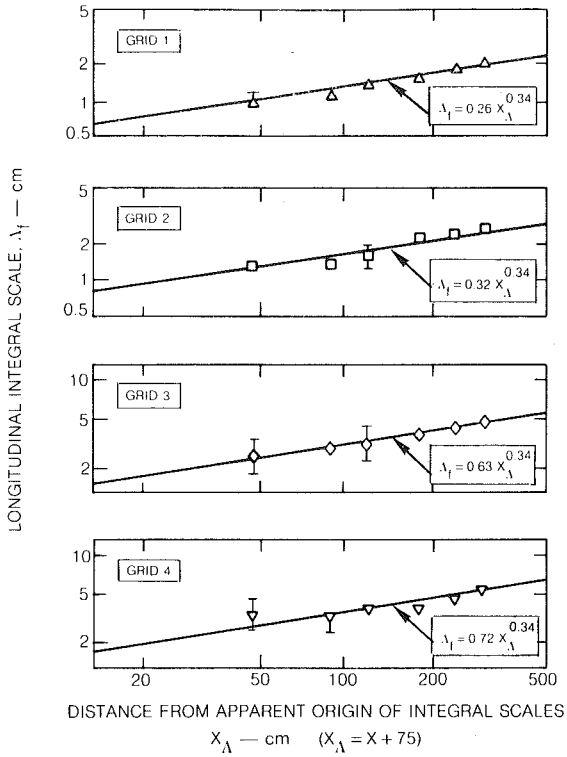

Fig. 4 Growth of the longitudinal integral scale along the test section

A composite plot showing the total turbulence intensity distribution for all five turbulence levels is presented in the lower half of Fig. 3. For all locations with Grids 1 and 2 and for the far downstream locations for Grids 3 and 4, the turbulence data over the various survey planes were extremely uniform with the data falling within the plotting symbols. The largest nonuniformities in measured turbulence resulted for $x < 50$ cm for Grid 3 and $x < 100$ cm for Grid 4. These regions were within ten grid mesh spacings (M) from the grid location. This result was in agreement with [29] which indicated that a distance of approximately five to ten mesh lengths downstream of a grid was required to establish uniform flow. It has been shown in [26] that by accounting for the effects of the contraction, the turbulence decay rates measured for the present configurations agree very well with the decay correlations of [29]. The following expression accurately represented the total turbulence distributions along the test wall for all four turbulence grids.

$$T = 0.78\left(\frac{x+132}{b}\right)^{-5/7} \tag{1}$$

where b (grid bar width) = 0.48, 1.27, 3.81, and 5.08 for Grids 1, 2, 3 and 4, respectively. For ease of discussion, nominal free-stream turbulence levels have been assigned to each of the grids and are given in Fig. 3. As shown in Fig. 3, however, the turbulence decays considerably with distance along the plate and these nominal levels are not an accurate singular representation of the turbulence for the test cases.

For the tunnel configuration with no grid installed, the turbulence level in the tunnel test section was 1/4 percent. For applications related to internal flows and turbomachinery, 1/4 percent turbulence is extremely low. Turbulent boundary layer heat transfer and profile data obtained for this "no grid" configuration can be considered as having negligible effects from the free-stream turbulence. Figure 3 indicates, as would be expected far downstream of a fine screen such as

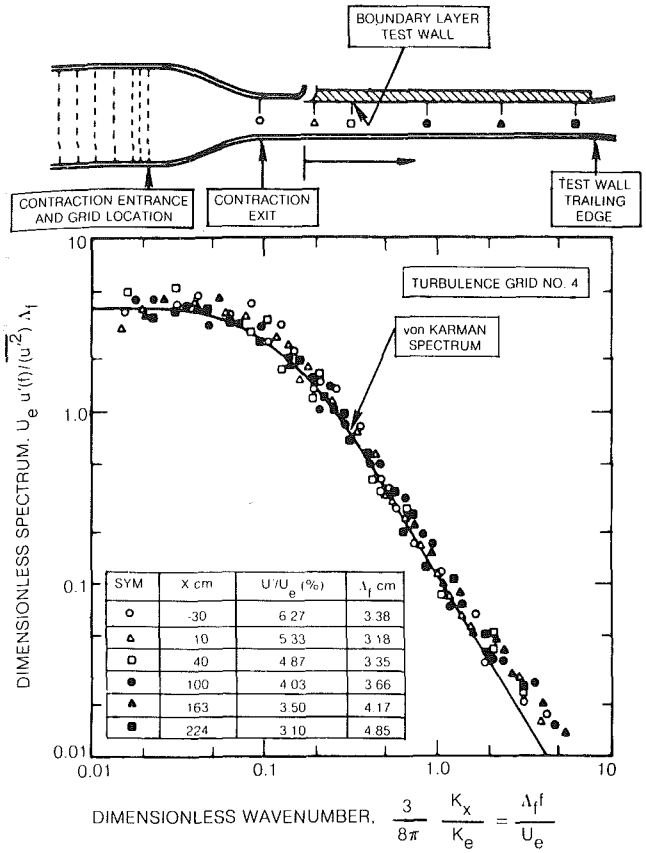

Fig. 5 Free-stream power spectral density distributions measured at various streamwise locations in the test section with grid number 4 installed

this, that the turbulence decayed only slightly over the entire length of the test section.

Free-Stream Turbulence Length Scale Distribution. Assessment of the role of the free-stream turbulence scale in turbulent boundary layer development has been hampered to date by an extreme shortage of pertinent data. To provide one "direct" experimental measurement of scale for these present data, autocorrelations of the fluctuating streamwise velocity component were processed to determine the longitudinal integral length scale. Measurements of the longitudinal integral scale of the free-stream turbulence downstream of the various turbulence grids were obtained using single sensor TSI Model 1220 hot film probes, a TSI 1050 constant temperature anemometer system, and a Saicor Model SAI 42 correlator. Integral scale measurements were obtained for the four grid configurations over the same survey plane locations as described in the previous section. Integral length scale growth can be approximately represented by a power law of the form $\Lambda_f = A_i\ (X_\Lambda)^m$ [31], where X_Λ is the distance from the apparent origin of the growth, and A_i is a constant related to the scale of the turbulence source. A best-fit power law was determined from the present data by constructing logarithmic plots with a series of assumed apparent origins and selecting the one which produced the longest straight line fits. A single apparent origin (75 cm upstream of the test plate leading edge) common to all four turbulence grids was selected. The integral scale measurements plotted as a function of distance from their apparent origin are presented in Fig. 4. For this figure, the symbols are plotted at the average of the integral scale measurements obtained at each survey plane. The vertical bars indicate the range of the individual measured values. The power law exponent ($m = 0.34$) determined from these logarithmic plots is in excellent agreement with the value determined by Compte-Bellot and Corrsin in [31]. The correlations shown in Fig. 4 show that the present measurement techniques were self consistent and that the length scale growth rates measured for these tests were consistent with results from other studies.

Free-Stream Power Spectral Density Distributions. To assure that the free-stream turbulence distributions generated for the present study were free of anomalies, the spectral distributions of the streamwise fluctuating velocity components were documented. Spectral distribution data were obtained along the tunnel centerline at tunnel mid-height for the following streamwise locations: $X = 30$, 10, 40, 100, 163, and 224 cm. These data were obtained using a TSI Model 1220 single sensor hot-film probe, a TSI 1050 constant temperature anemometer, and a spectral dynamics Model SD 340 narrow band spectrum analyzer. Figure 5 presents sample spectral distribution data for Grid 4 ($T_{NOM} = 6$ percent). For Fig. 5 and for all three other grids, the measured data were in excellent agreement with the von Karman one-dimensional spectrum for isotropic turbulence [32]. This result indicates that the test section turbulence has the classic characteristics of grid generated turbulence.

Two-Dimensionality of Test Boundary Layers. Boundary layer mean velocity and temperature profile data for the various test cases were obtained with the previously described miniature pitot and thermocouple probes. For each case, profiles were documented at numerous (typically 10) streamwise locations along the test wall at the tunnel centerline and at $Z = \pm 15$ cm. Momentum (θ) and displacement thicknesses (δ^*) were calculated from the mean velocity and temperature profile data. Variations between profiles measured at the various transverse but fixed streamwise locations were negligible.

For the fully turbulent profiles, wall skin friction coefficients were inferred by fitting the inner region velocity profile data to the "law-of-the-wall"

$$\frac{U}{U_\tau} = \frac{1}{\kappa} ln \frac{yU_\tau}{\nu} + C \tag{2}$$

with $\kappa = 0.41$ and $C = 5.0$. Following the methods outlined by Coles (Ref. 24), these skin friction coefficients were used with the calculated momentum thickness distributions to form a streamwise momentum balance for each test flow. The balance is satisfied for ideal zero pressure gradient two-dimensional flow when

$$\frac{\rho_e U_e^2}{\tau_w}\frac{d\theta}{dx} = 1 \tag{3}$$

Figure 6 presents a sample momentum balance for the profile data obtained with Grid 2 installed. A momentum balance is given along the tunnel centerline and at $Z = \pm 15$ cm. Also shown in Fig. 6 are the results of a streamwise thermal energy balance of the boundary layer profile and wall heat transfer data. The thermal energy balance data of Fig. 6 are a ratio of the total convective heat generated per unit tunnel width upstream of any profile location to the measured thermal energy contained in the boundary layer at the location. The results shown in Fig. 6 reveal that both the momentum and thermal energy balances were within approximately ± 5 percent of unity for all measured profiles. These results, which were typical of all the test cases, indicate that the profile data form an accurate, consistent set and that the test boundary layers were highly two-dimensional.

An error analysis, following the procedures of Kline and McClintock [33], was conducted for a number of the measured or computed quantities. This analysis indicated the following uncertainties: Stanton numbers ± 2.5 percent, integral thicknesses ± 1.5 percent, location Reynolds

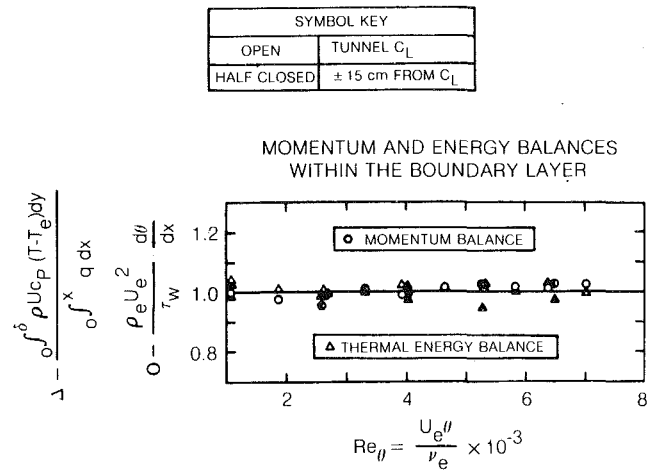

Fig. 6 Momentum and energy balances within the boundary layer for grid 2

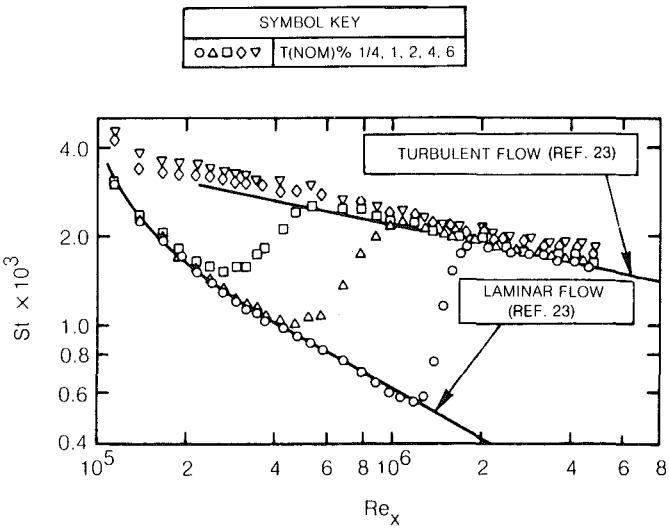

Fig. 7 Heat transfer distributions along the test wall for five free-stream turbulence levels

numbers ± 1 percent. The skin friction coefficients inferred from the "law-of-the-wall" are estimated to be accurate within ± 3 percent.

Heat Transfer Measurements. Stanton number distributions measured for the five free-stream turbulence levels are presented in Fig. 7 as a function of Re_x. Also included in Fig. 7 are (*i*) the laminar boundary layer analytical solution of [23].

$$St\ Pr^{2/3} = 0.453\ Re_x^{-1/2}[1-(\xi/x)^{3/4}]^{-1/3} \quad (4)$$

for zero pressure gradient flow with a uniform convective heat flux wall and unheated starting length (for this plate ξ = 4.3 cm) and (*ii*) a correlation for fully turbulent, zero pressure gradient boundary layer flow with uniform wall heat flux and low free-stream turbulence [23].

$$St\ Pr^{0.4} = 0.0307\ Re_x^{-0.2}\ (Tw/Te)^{-0.4} \quad (5)$$

For the low free-stream turbulence case (Grid 0) and for the cases with Grids 1 and 2, the measured heat transfer rates agreed very well with equation (4) upstream of their respective transition sites. Mean velocity and temperature profile data measured at three transverse locations at $Re_x = 6 \times 10^5$ for the Grid 0 case confirmed that the boundary layer was laminar at this station and that the flow was two-dimensional (see [26]). From $Re_x = 1.8 \times 10^6$ to the downstream end of

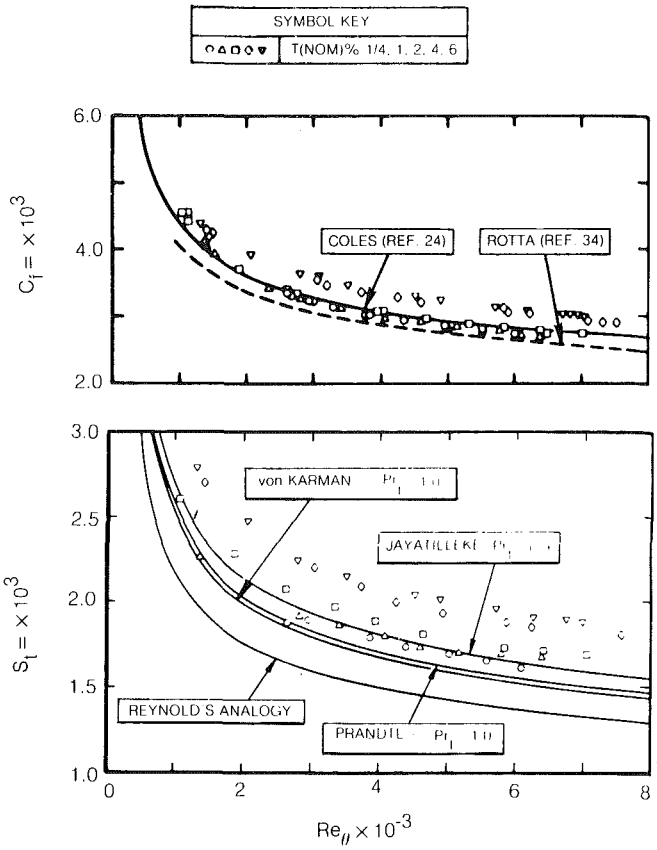

Fig. 8 Skin friction and heat transfer distributions for five turbulence levels as a function of Re_θ

the plate, the heat transfer rates measured for the Grid 0 case agreed within ± 2 percent of equation (5). The agreement between the present low turbulence heat transfer data and classic, well-established predictions and correlations indicates that the experimental techniques employed for this study were accurate and that the flow was well behaved.

Examination of Fig. 7 reveals that, as expected, the location of boundary layer transition moved progressively upstream with increasing free-stream turbulence level until, for Grids 3 and 4, the test boundary layers were apparently turbulent at the upstream row of wall thermocouples.

The heat transfer data of Fig. 7 show that the free-stream turbulence had a negligible effect on zero-pressure gradient flat wall laminar boundary layer heat transfer. For fully turbulent boundary layer flow, however, a progressive and significant increase of the Stanton number was observed with increasing free-stream turbulence level. As an example at $Re_x = 4 \times 10^6$ for Grid 4 (nominal turbulence of 6 percent) the Stanton number was 18 percent greater than would be predicted by equation 5.

Skin Friction and Heat Transfer Dependence on Re_θ. Figure 8 presents composite plots of the local skin friction coefficients and Stanton numbers determined for all five grids. Each skin friction coefficient or Stanton number was plotted as a function of the momentum thickness Reynolds number calculated from the profile data obtained at that location. Comparison of these results at equal boundary layer Reynolds numbers minimized the influence arising from the different transition locations at the various test cases.

For the upper half of Fig. 8, skin friction coefficients determined for the various turbulence levels are compared to the well-known incompressible turbulent boundary layer skin friction law formulations of Coles [24] and Rotta [34]. These correlations, which apply for isothermal incompressible

turbulent boundary layer flow have been corrected for density variations due to wall heating using Coles' "law of corresponding stations" [24]. Figure 8 shows that for the low free-stream turbulence case, the measured skin friction coefficients were bracketed by the two correlations. This result indicates that the present Grid 0 data were in excellent agreement with the measurements of numerous other investigators. A progressive increase of skin friction coefficient was observed with increasing free-stream turbulence level at a fixed momentum thickness Reynolds number. An analysis of these results will be presented in Part II of this paper.

For the lower half of Fig. 8, the Stanton numbers for the 5 test cases were compared with four analytical predictions for low free-stream turbulence, fully turbulent boundary layer heat transfer. These analyses assume various relationships between the turbulent heat and momentum transfer to predict a heat transfer distribution from a prescribed skin friction distribution. The predicted distributions of Fig. 8 were all calculated using the skin friction distribution inferred for the minimum free-stream turbulence configuration (Grid 0). As such, these predictions can only be compared directly with the heat transfer data measured for the minimum turbulence case. The four predictions presented in Fig. 8 are as follows:

(*i*) Reynolds analogy (circa 1890) (Pr = 1, Pr_t = 1)

$$S_1 = C_f/2 \tag{6}$$

(*ii*) Prandtl's (circa 1928) laminar sublayer-fully turbulent region solution (Pr_t = 1)

$$S_1 = \frac{C_f/2}{1+11(C_f/2)(\mathrm{Pr}-1)};\ (\mathrm{Pr}=0.71) \tag{7}$$

(*iii*) von Karman's (circa 1939) laminar sublayer-transition zone – fully turbulent region solution (Pr_t = 1)

$$S_t = \frac{C_f/2}{1+5\sqrt{C_f/2}\left[\mathrm{Pr}-1+ln\left(\frac{5}{6}\mathrm{Pr}+\frac{1}{6}\right)\right]};\ (\mathrm{Pr}=0.71) \tag{8}$$

(*iv*) Jayatelleke's (1969) solution for $Pr_t \neq 1$ [35]

$$S_t = \frac{C_f/2}{\mathrm{Pr}_t\sqrt{2/C_f}+(\mathrm{Pr}_t-P_s)} \qquad \begin{pmatrix}\mathrm{Pr}=0.71\\ \mathrm{Pr}_t=0.9\end{pmatrix} \tag{9}$$

where

$$P_s = \frac{8.23}{Pr_t}\left[\left(\frac{\mathrm{Pr}}{\mathrm{Pr}_t}\right)^{3/4}-1\right]\left[1+0.28\ \exp\left(-0.007\frac{\mathrm{Pr}}{\mathrm{Pr}_t}\right)\right]$$

(P_s is a dimensionless "extra resistance" to heat transfer in the sublayer resulting from the difference between the laminar and turbulent Prandtl numbers in that region.)

The predictions range from the earliest model, the classic Reynolds analogy, to the modern solution of Jayatelleke (which incorporates the results of a very large number of experiments). The best agreement between the various predictions and the "no grid," minimum free-stream turbulence heat transfer data resulted for the Jayatelleke solution. The prediction from this analysis agreed within about 3 percent with the present data for $Re_\theta > 3000$. Because of this excellent agreement between the present results and the solution of Jayatelleke, it has been concluded that the present Grid 0 skin friction and heat transfer data are self consistent and form a sound data base for comparison with data taken for higher levels of free-stream turbulence.

Figure 8 shows that for fixed Re_θ, the Stanton number increased systematically with increasing free-stream turbulence level. For example, at Re_θ = 4500, the Stanton number is approximately 16 percent greater for T_{NOM} = 6 percent than would be expected for low free-stream turbulence. Note that for Fig. 8 both the skin friction and heat transfer data for higher turbulence levels were roughly parallel to their respective low-turbulence correlation curves. This despite the fact that for all grids (in particular Grids 3 and 4) the free-stream turbulence intensity decayed significantly with distance along the test surface (see Fig. 3). This result suggests that the effects of free-stream turbulence on turbulent boundary layers do not scale on turbulence intensity alone. An analysis of these data are presented in Part [25] of this paper. Included in Part II is an examination of the influences of the free-stream turbulence intensity, length scale, and boundary layer Reynolds number on both the skin friction and heat transfer.

Conclusions

1 The measurements of the free-stream turbulence properties for the various test cases indicate that the test section turbulence exhibited classical grid-generated characteristics. The test section turbulence was shown to be nearly homogeneous and only slightly anisotropic. Measurements of longitudinal integral length scale growth with distance along the test section were in good agreement with data from other investigations.

2 Cross checks of the wall heat transfer and mean velocity and temperature profile data indicate that all these measurements were accurate, formed a self-consistent set, and that the test boundary layer flows were highly two-dimensional.

3 Skin friction and heat transfer data obtained with low free-stream turbulence are in excellent agreement with well-established, two-dimensional, incompressible analytical solutions and/or correlations.

4 These data indicate that free-stream turbulence has a significant effect (as much as a 20 percent increase for a nominal turbulence intensity of 6 percent) on both skin friction and heat transfer for fully turbulent boundary layer flow. An analysis of these measurements is presented in Part II of this paper.

Acknowledgment

Research sponsored by the Air Force Office of Scientific Research (AFSC), under Contract F49620-78-C-0064. The United States Government is authorized to reproduce and distribute reprints for governmental purposes notwithstanding any copyright notation hereon. The contract monitors for this project were Col. Robert C. Smith (Ret.), Dr. D. George Samaras, and Dr. James D. Wilson.

References

1 Kline, S. J., Lesin, A. V., and Waitman, B. A., "Preliminary Experimental Investigation of Effects of Free-Stream Turbulence on Turbulent Boundary Layer Growth," NASA TN D-368, 1960.

2 Charnay, G., Compte-Bellot, G., and Mathieu, J., "Development of a Turbulent Boundary Layer on a Flat Plate in an External Turbulent Flow," AGARD CP93, Paper No. 27, 1971.

3 Huffman, G. D., Zimmerman, D. R., and Bennett, W. A., "The Effect of Free-Stream Turbulence Level on Turbulent Boundary Layer Behavior," AGARD AG164, pp. 91-115.

4 Robertson, J. M., and Holt, C. F., "Stream Turbulence Effects on Turbulent Boundary Layers," *J. Hydraulics Divs., Proc. ASCE*, Vol. 93, HY6, 1972, pp. 1095-1099.

5 Evans, R. L., "Free-Stream Turbulence Effects on the Turbulent Boundary Layer," A.R.C. C.P. 1282, 1974.

6 Arnal, D., "Effect of Free-Stream Turbulence on Turbulent Boundary Layers in Incompressible Flow," European Space Agency, TT-411, Sept. 1977.

7 Meier, H. V., and Kreplin, H. P., "Influence of Freestream Turbulence on Boundary Layer Development," *AIAA Journal*, Vol. 18, No. 1, 1980, pp. 11-15.

8 Hancock, P. E., "Effect of Free-Stream Turbulence on Turbulent Boundary Layers," Ph.D. thesis, Imperial College, University of London, 1980.

9 Green, J. E., "On the Influence of Free-Stream Turbulence on a Turbulent Boundary Layer, As it Relates to Wind Tunnel Testing at Subsonic Speeds," *Fluid Motion Problems in Wind Tunnel Design*, AGARD Report No. 602, 1973, also published as RAE TR 72201, 1972.

10 Bradshaw, P., "Effect of Free-Stream Turbulence on Turbulent Shear Layers," A.R.C. 35 648, 1974.

11 Edwards, A., and Furber, B. N., "The Influence of Free-Stream Turbulence on Heat Transfer by Convection From an Isolated Region of a Plane Surface in Parallel Air Flow," *Proceedings of the Institution of Mechanical Engineers*, Vol. 170, 1956, pp. 941–953.

12 Kestin, J., Maeder, P. F., and Wang, H. E., "Influence of Turbulence on the Transfer of Heat from Plates With and Without a Pressure Gradient," *International Journal of Heat and Mass Transfer*, Vol. 3, 1961, pp. 133–154.

13 Buyuktur, A. R., Kestin, J., and Maeder, P. F., "Influence of Combined Pressure Gradient and Turbulence on the Transfer of Heat From a Plate," *International Journal of Heat and Mass Transfer*, Vol. 7, 1964, pp. 1175–1186.

14 Junkhan, G. H., and Serovy, G. K., "Effects of Free-Stream Turbulence and Pressure Gradient on Flat Plate Boundary-Layer Velocity Profiles and on Heat Transfer," ASME JOURNAL OF HEAT TRANSFER, Vol. 169, 1967, pp. 169–176.

15 Brown, A., and Burton, R. C., "The Effects of Free-Stream Turbulence Intensity and Velocity Distribution on Heat Transfer to Curved Surfaces," ASME *Journal of Engineering for Power*, Vol. 100, 1978, pp. 159–168.

16 Consigny, H., Chan, C. K., and Richards, B. E., "The Effect of Pressure Gradient and External Turbulence on Heat Transfer to a Cold Flat Plate," VKI-Technical Note 128, Feb. 1979.

17 Sugawara, S., Sato, T., Hirosyasa, K., and Osaka, H., "The Effect of Free-Stream Turbulence on Heat Transfer From a Flat Plate, NACA Tech. Memo 1441, 1958.

18 Simonich, J. C., "Heat Transfer From a Turbulent Boundary Layer in a Zero Pressure Gradient," M. Sc Project Report, Imperial College, London, 1976.

19 Simonich, J. C., and Bradshaw, P., "Effect of Free-Stream Turbulence on Heat Transfer through a Turbulent Boundary Layer," ASME JOURNAL OF HEAT TRANSFER, Vol. 100, 1978, pp. 671–677.

20 Slanciavskas, A., and Pedisius, A., "Effect of Free-Stream Turbulence on the Heat Transfer in the Turbulent Boundary Layer," *Proceedings of the 6th International Heat Transfer Conference*, Vol. 2., Toronto, Aug. 7–11, 1978.

21 Zysina-Molozhen, L. M., and Roost, E. G., "Influence of Turbulence of the Approach Flow on Local Heat Transfer in Turbine Nozzle Cascades," *Thermal Engineering*, Vol. 26, No. 4, 1979, translated from *Teploenergetika*, Vol. 26, No. 4, 1979, pp. 31–36.

22 McDonald, H., and Kreskovsky, J. P., "Effect of Free-Stream Turbulence on the Turbulent Boundary Layer," *International Journal of Heat and Mass Transfer*, Vol. 17, 1974, pp. 705–716.

23 Kays, W. M., *Convective Heat and Mass Transfer*, McGraw-Hill, New York, 1966, pp. 222 and 244.

24 Coles, D. E., "The Turbulent Boundary Layer in a Compressible Fluid," Rand Report, R-403-PR, 1962.

25 Blair, M. F., "Influence of Free-Stream Turbulence on Turbulent Boundary Layer Heat Transfer and Mean Profile Development, Part II—Analysis of Results," ASME JOURNAL OF HEAT TRANSFER, Vol. 105, Feb. 83, pp. 41–47.

26 Blair, M. F., Bailey, D. A., and Schlinker, R. H., "Development of a Large-Scale Wind Tunnel for the Simulation of Turbomachinery Airfoil Boundary Layers," ASME *Journal of Engineering for Power*, Vol. 103, Oct. 1981, pp. 678–687.

27 Blair, M. F., and Werle, M. J., "The Influence of Freestream Turbulence on the Zero Pressure and Gradient Fully Turbulent Boundary Layer," UTRC Report R80-915388-12, Sept. 1980.

28 Blair, M. F., "Velocity and Temperature Profile Data for Zero Pressure Gradient, Fully Turbulent Boundary Layers," Final Data Report, Vol. I, UTRC Report R81-914388-15 1981 (microfiche).

29 Baines, W. D., and Peterson, E. G., "An Investigation of Flow Through Screens," ASME *Trans.*, Vol. 73, July 1951, pp. 467–480.

30 Blackwell, B. F., and Moffat, R. J., "Design and Conduction of a Low Velocity Boundary-Layer Temperature Probe," AIAA Paper No. 74-709, ASME Paper No. 74-HT-29, July 1974.

31 Compte-Bellot, G., and Corrsin, S., "The Use of a Contraction to Improve Isotropy of Grid Generated Turbulence," *Journal of Fluid Mechanics*, Vol. 25, 1966, pp. 657–682.

32 Hinze, J. O., *Turbulence*, McGraw-Hill, New York, 1959.

33 Kline, S. J., and McClintock, F. A., "Describing Uncertainties in Single Sample Experiments," *Mechanical Engineering*, Jan. 1953, pp. 3–8.

34 Rotta, J. C., "Turbulent Boundary Layers in Incompressible Flow," *Progress in Aeronautical Sciences*, Vol. 2, Pergamon Press, Ltd., London 1962.

35 Jayatilleke, C. L. V., "The Influence of Prandtl Number and Surface Roughness on the Resistance of the Laminar Sublayer to Momentum and Heat Transfer," *Progress in Heat and Mass Transfer*, Vol. 1, Pergamon Press, Ltd., London, 1969.

Influence of Free-Stream Turbulence on Turbulent Boundary Layer Heat Transfer and Mean Profile Development, Part II—Analysis of Results

M. F. Blair
Senior Research Engineer,
Gas Turbine Technology Group,
United Technologies Research Center,
East Hartford, Conn. 06108

An experimental research program was conducted to determine the influence of free-stream turbulence on zero pressure gradient, fully turbulent boundary layer flow. In Part I of this paper, convective heat transfer coefficients, boundary layer mean velocity and temperature profile data, as well as wall skin friction coefficient distribution data were presented for five flow conditions of constant free-stream velocity (30 m/s) and free-stream turbulence intensities ranging from approximately 1/4 to 7 percent. These data indicated that the turbulence had significant effects on both the turbulent boundary layer skin friction and heat transfer. In the current paper, these new data are compared to various independent experimental data and analytical correlations of free-stream turbulence effects. This analysis has shown that the effects documented in Part I were a function of the free-stream turbulence intensity, the turbulence length scale, and the boundary layer momentum thickness Reynolds number. In addition, the Reynolds analogy factor ($2St/c_f$) was shown to increase by just over 1 percent for each 1 percent increase in free-stream turbulence level. New correlations for the influence of free-stream turbulence on skin friction, heat transfer, and the Reynolds analogy factor are presented.

Introduction

The influence of highly turbulent mainstreams on boundary layer development is important in a number of engineering applications. One example is the impact of turbulence on convective heat transfer distributions on airfoil surfaces. In Part I of this paper [1] experimental heat transfer and boundary layer profile data obtained in a study of these effects were presented. These data demonstrated that for fully turbulent flow, both the skin friction and heat transfer were substantially increased for increased levels of free-stream turbulence. An analysis of the data of Part I and comparisons of these data with the results of numerous other studies are presented here.

Analyses by Bradshaw [2] and McDonald and Kreskovsky [3] can be formally combined to give a general expression for the expected effects of free-stream turbulence on turbulent boundary layers with low Reynolds numbers ($Re_\theta < 5000$).

$$\Delta(c_f, \mathrm{St}, U(y), T(y)) = f\left(\frac{u_e'}{U_\tau}, \frac{L_e}{\delta}, \mathrm{Re}_\theta\right) \quad (1)$$

Equation (1) suggests that the effects of the boundary layer will depend not only on the free-stream turbulence intensity but also upon the ratio of dissipation length scale (L_e) to shear layer thickness (δ), and for low Reynolds number upon the boundary layer momentum thickness Reynolds number (Re_θ). Bradshaw [2] has justified the use of the free-stream turbulence intensity (u'/U_e) to replace the more cumbersome parameter u_e'/U_τ of equation (1). This simpler turbulence intensity parameter will be used for the present analysis.

Throughout this paper, comparisons are presented between like quantities measured in the absence or presence of significant free-stream turbulence. These comparisons will be made exclusively for equal Reynolds numbers based upon boundary layer thicknesses (Re_θ and Re_δ), thereby minimizing the effects of transition location on the data. Turbulence effects were interpreted as being solely dependent upon local values of intensity and length scale, ignoring the possible historical influence on the streamwise decay rate of the turbulence. Effects on the boundary layer profiles and/or wall heat transfer measurements are presented as functions of the free-stream turbulence properties measured at corresponding streamwise locations.

Particular attention has been paid during the present program to exploring the importance of the influence of the Reynolds number in equation (1). It should be noted that for all existing aircraft gas turbine engines, turbine airfoil boundary layer momentum thickness Reynolds numbers (Re_θ) are less than 5000, and for nearly all cases, less than 3000. For this study, test boundary layer Re_θ's ranged from 1000 to 6500.

Measurements of the influence of free-stream turbulence on adiabatic turbulent boundary layer skin friction and velocity profile development have been obtained by numerous other investigators. In the present analysis, it is shown that excellent agreement between these earlier results and the present skin friction data are obtained by employing an intensity and length scale dependent correlation developed recently by Hancock [4, 5]. A modification to Hancock's correlation is proposed to include effects associated with low boundary layer Reynolds numbers. The Stanton numbers measured for the present program are shown to increase at a somewhat higher rate with increasing free-stream turbulence intensity than does the skin friction. The Reynolds analogy factor ($2\,St/c_f$) is shown to linearly increase with increasing free-stream turbulence level. The results of this present study are shown to be self-consistent and, when possible, are shown to compare

Contributed by the Heat Transfer Division for publication in the JOURNAL OF HEAT TRANSFER. Manuscript received by the Heat Transfer Division November 30, 1981.

well with the result of other investigators. It is anticipated that these measurements will provide a valuable data set for comparison with analytical predictions of heat transfer with high free-stream turbulence.

Influence of Free-Stream Turbulence on the Velocity and Temperature Profiles

Sample mean velocity and temperature profile data from the present program demonstrating the effect of free-stream turbulence are presented in Fig. 1. Each of these profiles was measured for $Re_\theta \cong 3000$ but at different free-stream turbulence levels. The velocity profiles of Fig. 1 all exhibited shapes compatible with the logarithmic zero pressure gradient law of the wall for $30 < Y^+ < 200$. (At least some of the data points had to fall on the log law, since c_f was determined from a least squares force fit to the curve.) This result is in agreement with the data of references [4] through [9], all of which indicated negligible effects on the velocity profile in the logarithmic region. In contrast to this insensitivity in the logarithmic region, the velocity profiles of Fig. 1 demonstrate the significant capacity of the free-stream turbulence for depression of the boundary layer wake. A strong wake, approximately equal to the value predicted by Coles [10] for this Re_θ is observed for the minimum turbulence case. At the other extreme, with 5.3 percent free-stream turbulence, the wake has nearly vanished.

The temperature profile data of Fig. 1 were obtained with the velocity profiles data, and they are shown in the same order and format. The temperature profile data of Fig. 1 were not force-fitted to the "temperature law of the wall." The values of T^+ plotted in Fig. 1 were calculated from the measured wall, free-stream, and profile temperatures, the inferred wall shear stress, and the measured heat flux. Because so many experimentally determined quantities are incorporated into the dimensionless temperature (each with inherent inaccuracies) some slight discrepancies can be seen in Fig. 1 between the level of the temperature data and the temperature log law (note the data for T = 1 percent). As with the velocity profiles, these temperature profile data indicate that the influence of the free-stream turbulence was felt only in the wake region, the logarithmic region being left unaltered. The depression of the temperature wake component by the free-stream turbulence is clearly shown. While there is a prominent wake for $T = 0.2$ percent, there is no wake remaining for $T = 5.3$ percent.

Velocity boundary layer thicknesses (δ) and wake strengths (Π) for the present profiles were evaluated using two local friction law formulations from Coles [11].

$$\frac{U_e}{U_\tau} = \frac{1}{\kappa} ln \frac{\delta U_\tau}{\nu} + C + \frac{2\Pi}{\kappa} \tag{2}$$

$$\left(\frac{\frac{\delta^* U_e}{\nu} - 65}{\frac{\delta U_\tau}{\nu}} \right) = 1 + \Pi \tag{3}$$

In addition, the location of the shear layer edge ($\delta_{0.995}$) was determined directly from the velocity profile data. A plot of the ratios of these two boundary layer thicknesses as a function of free-stream turbulence intensity is presented in Fig. 2(*a*). The negative slope of the data of Fig. 2(*a*) results from a long outer region of very small normal velocity gradient which was characteristic of the profiles with high free-stream turbulence. References [4–7] all documented this long outer-region "tail" for their velocity profiles. In addition, all three studies reported turbulent shear stress distributions which extended even beyond $\delta_{0.995}$. These outer region characteristics observed for both the present and other high free-stream turbulence flows are in marked contrast to those expected for low free-stream turbulence where δ, $\delta_{0.995}$, and the edge of the turbulent shear are all practically equal. These outer region effects are symptoms of the interactions between the shear layer and the free-stream turbulence and point out the probable importance of careful modeling of the "wake" region for these flows.

Figures 2(*b*) and 2(*c*) demonstrate the influence of the free-stream turbulence on the boundary layer integral parameters. The effect of turbulence intensity on the kinematic shape factor (H_k) at a fixed Re_θ is given in Fig. 2(*b*). In this plot, H_0 is determined from the shape factors measured for the lowest turbulence case tested ($T < 1/4$ percent), here designated Grid 0. It should be noted that the kinematic shape factors measured in the present study for Grid 0 were about 1 percent larger than would have been predicted from Cole's [10] low turbulence correlation. Kinematic shape factor was employed for Fig. 2(*b*) in order to eliminate the influence of the wall heating on the density distribution and focus on changes to the velocity profile. Also shown in Fig. 2(*b*) are the correlations of Robertson and Holt's [12] and Green's [13] analysis of the data of [7]. It can be seen that for the present data, the decrease of the shape factor with free-stream turbulence agrees more closely with Green's analysis than the correlation of [12]. It is unclear if there is any evidence from the present data to support the asymptotic behavior at high turbulence levels suggested by the Robertson and Holt correlation.

Figure 2(*c*) presents a comparison between the present data

Nomenclature

C = constant in the law of the wall
c_f = skin friction
c_p = specific heat at constant pressure
G = Clauser shape parameter
h = heat transfer coefficient
H_k = kinematic shape factor
k = thermal conductivity
L_e^u = streamwise turbulence dissipation length scale, equation (10)
Pr = molecular Prandtl number
Re_θ = momentum thickness Reynolds number
St = Stanton number
T = temperature
U = velocity
U^+ = dimensionless velocity
U_τ = friction velocity
u', v', w' = streamwise, normal, and transverse fluctuating velocities
y = distance from the wall
Y^+ = dimensionless distance from the wall
Λ_f = longitudinal integral scale of turbulence
δ = boundary layer thickness, equation (3, 4)
δ^* = displacement thickness
δ_k^* = kinematic displacement thickness
Δ = Clauser delta
θ = momentum thickness
θ_k = kinematic momentum thickness
κ = von Karmon constant
μ = molecular viscosity
ν = kinematic viscosity
Π = wake strength equation (3, 4)

Subscripts

e = free-stream value
w = wall value
0.995 = where $u = 0.995\ U_e$
0 = value for negligible free-stream turbulence

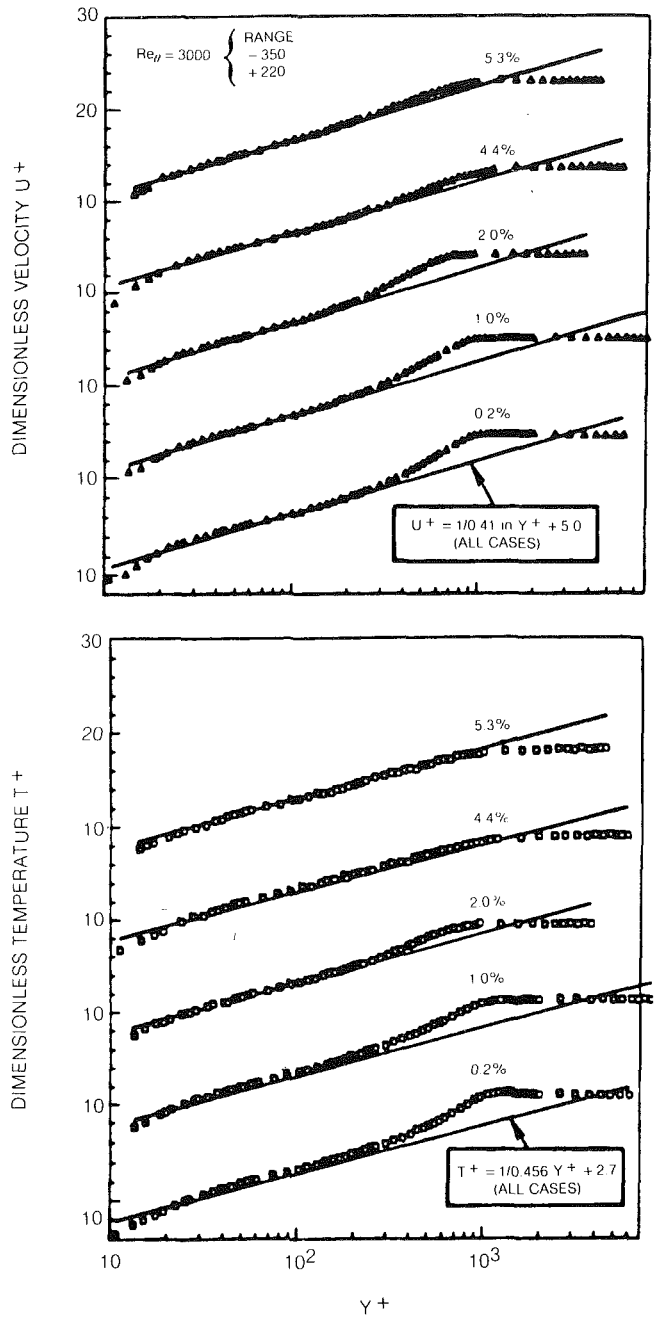

Fig. 1 Effects of free stream turbulence on mean velocity and temperature profiles for Re_θ = 3000

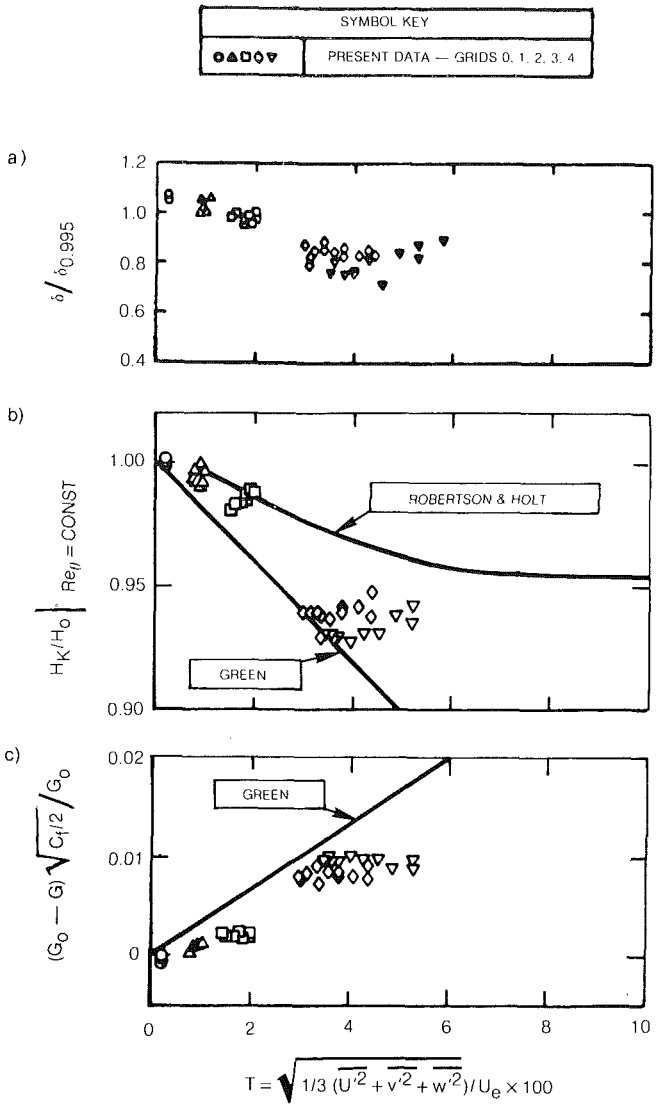

Fig. 2 Effects of free-stream turbulence on profile parameters

and an analysis by Green [13]. Green, using the data of [6] and [7], determined that the influence of the free-stream turbulence on the Clauser shape parameter would be represented by

$$G = G_0\left(1 - \frac{1}{3}\sqrt{2/c_f}\,\frac{u'}{U_e}\right) \tag{4}$$

where G_0 is the low free-stream turbulence equilibrium boundary layer Clauser shape parameter. The value G_0 = 7.0, as determined from the present Grid 0 data, was used for the present results (Clauser [14] suggested a value of 6.8 for G_0). Green's analysis and the present data are substantially in agreement with nearly equal slopes.

Figures 2(*b*) and 2(*c*) demonstrated that the shape of the measured boundary layer velocity profiles, as reflected by the integral parameters H_k and G, were systematically dependent on the free-stream turbulence intensity. The changes in profile shape recorded for the present data were in good agreement with those observed in other investigations. Detailed plots of the integral quantities (δ^*, θ, G) for the various test cases are available in [15].

Influence of Free-Stream Turbulence Intensity on Skin Friction and Heat Transfer

Skin friction coefficient data measured for both the present study and for five previous investigations are shown in Fig. 3(*a*) as a function of free-stream turbulence intensity. These data are presented as ratios of the measured skin friction to values for the corresponding Re_θ with low free-stream turbulence intensity. Comparison of these results from such a large group of studies is complicated by the fact that differing experimental techniques were employed. In addition, all the investigations did not document the same set of test quantities and flow properties. Details of the interpretation techniques employed for these various data sets are given in Appendix A.

The skin friction measurements (c_f inferred from fits to "law-of-the-wall") for the present experiment fell within the range of results found for the other studies. Despite the extreme scatter evident in Fig. 3(*a*), the data clearly demonstrate

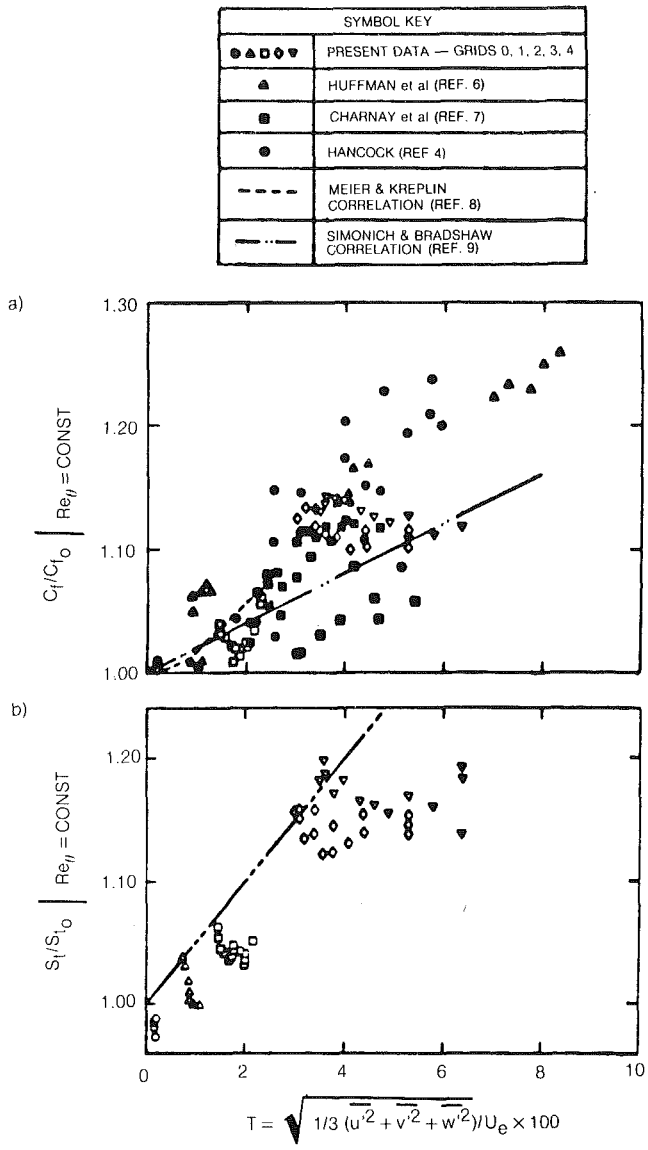

Fig. 3 Influence of free-stream turbulence intensity on the skin friction and heat transfer coefficients

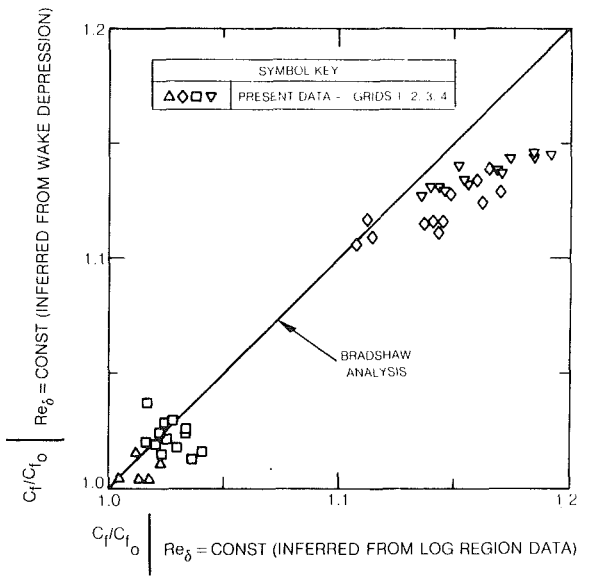

Fig. 4 Changes in skin friction inferred from log-law fits and from depression of the wake strength

that the skin friction coefficient increased with increasing free-stream turbulence intensity. The data and correlations of Fig. 3(*a*) covered wide ranges of L_e/δ and Re_θ. It will be demonstrated in a later section that the scatter of Fig. 3(*a*) can be greatly reduced by accounting for the effects of these secondary parameters.

Stanton numbers measured for the present program are presented in Fig. 3(*b*) as a function of the local free-stream turbulence intensity. This figure presents the ratio of the measured Stanton numbers to the level expected for the same Re_θ for low free-stream turbulence intensity as predicted by Jayatilleke (see Part I – Fig. 7). Also included in Fig. 3(*b*) is the correlation of Simonich and Bradshaw [9]. Both the present data and the correlation of [9] indicated that significantly increased heat transfer coefficients resulted from increased free-stream turbulence intensity. As with the skin friction data of Fig. 3(*a*), the results shown in Fig. 3(*b*) show considerable scatter when plotted as a function of free-stream turbulence intensity. Again, this suggests the influence of secondary variables such as length scale and/or Reynolds number. It should be noted that the data upon which the correlation of [9] is based, show even greater scatter than the present results in these coordinates.

Skin Friction Determined From Wake Data

Bradshaw [2] has shown that for boundary layers with the same $U_e\delta/\nu$ differences in wall skin friction can be inferred from changes in the profile wake strength as follows:

$$c_f/c_{f_0}\Big|_{Re_\delta = \text{CONST}} = 1 - \frac{4}{\kappa}(\Pi - \Pi_0)\left(1 - \frac{1}{\kappa}\sqrt{c_{f_0}/2}\right)\sqrt{c_{f_0}/2} \quad (5)$$

where c_{f_0} and Π_0 are the skin friction and wake strength for a boundary layer with the same Re_δ in a low free-stream turbulence flow. For Fig. 4, skin friction ratios computed from the wake depression using equation (5) were plotted versus skin friction ratios determined from fits of the velocity profile data to the law of the wall. The near agreement of these two separate methods of determining changes to the skin friction coefficient is an indication of the self-consistency of the present velocity profile data.

The Reynolds Analogy Factor

The ratio 2 St/c_f is commonly referred to as the Reynolds analogy factor. Figure 5 presents two separate sets of evidence from the present program that this factor increased with increasing free-stream turbulence intensity. In Fig. 5(*a*), the measured Stanton numbers and skin friction coefficients inferred from the fits of the velocity profile data to the law of the wall are shown as a function of free-stream turbulence intensity. Also given in Fig. 5(*a*) are three values of the Reynolds analogy factor for low free-stream turbulence turbulent boundary layers recommended by other sources as follows: (*a*) 1.21, Spalding [16], (*b*) 1.19, Simonich and Bradshaw [9], and (*c*) 1.16, Chi [17]. The Reynolds analogy factor is seen to increase with increasing free-stream turbulence level with the following expression representing the results within reasonable accuracy.

$$2S_t/c_f = 1.18 + 1.3T \quad (7)$$

Simonich and Bradshaw [9], extending an earlier analysis by Kader and Yaglom [18], have shown that the Reynolds analogy factor can be determined from relative changes

between the wake strengths of the velocity and temperature profiles. Their analysis gives the following relationship:

$$2S_t/c_f = \frac{\kappa/\kappa_\theta}{1+\sqrt{c_f/2}\left(\frac{c_\theta\kappa_\theta - c\kappa + 2(\Pi_\theta - \Pi)}{\kappa}\right)} \tag{8}$$

where C_θ and κ_θ are coefficients in the "temperature law of the wall"

$$T^+ = \frac{1}{\kappa_\theta} ln Y^+ + c_\theta \tag{9}$$

and Π_θ is the wake strength of the temperature profile.

Using the values inferred from the present data of Π, Π_θ, C_f and St and assumed values of $\kappa = 0.41$ and $C = 5.0$, $\kappa_\theta = 0.46$ and $C_\theta = 2.7$, the left- and right-hand sides of equation (8) have been calculated and plotted for Fig. 5(*b*). Agreement between the present results and the analysis of Simonich and Bradshaw is shown to be reasonably good. It can be concluded from Fig. 5(*b*) that the "wall inferred" and "wake inferred" Reynolds analogy factors are self-consistent. This consistency in turn lends credibility to the conclusion that increases of the Reynolds analogy factor resulted from increased free-stream turbulence intensity.

Influence of Turbulence Length Scale and Reynolds Number

Bradshaw reasoned [2] that the effects of free-stream turbulence on boundary layers will depend not only on the intensity but also upon the ratio of the dissipation length scale (L_e) to shear layer thickness (δ). He suggested a particular form of the dissipation length scale to be used for interpretation of differing types of free-stream turbulence data. His streamwise turbulence dissipation length scale was defined as follows:

$$L_e^U = \frac{[\overline{u_e'^2}]^{3/2}}{U\frac{d\overline{u_e'^2}}{dx}} \tag{10}$$

For grid generated turbulence, this dissipation scale and the longitudinal integral scale measured for the present program are related as

$$L_e^U \cong 1.5\Lambda_f \tag{11}$$

The impact of free-stream turbulence is expected [2] to reach a maximum for $L_e^U/\delta = 0$ [1]. For cases in which this ratio is either significantly larger or smaller than unity, the effects would be expected to diminish. In addition, the analysis of McDonald and Kreskovsky [3] indicates that reduced influence of the free-stream turbulence on turbulent boundary layers should also be expected for low Reynolds number boundary layers ($Re_\theta < 5000$). As discussed in detail by Hancock [4, 5], all the experimental data currently available on this subject, including the present work, were conducted downstream of turbulence generating grids with the effective origins of the test turbulent boundary layers located some distance downstream of the grids. With this arrangement, the turbulence intensity decays while the boundary layer Reynolds number and the length scale of the turbulence grow with increasing x. Most of the experiments have used roughly the same experimental scale with about the same free-stream velocity. The resulting experimental data cover only a narrow range of L_e^u/δ (data range $0.2 < L_e^u/\delta < 2$) while most contain potential low Re_θ effects (data range $1000 < Re_\theta < 6000$). Because of this situation, it is difficult to separate the low Re_θ from the length scale effects.

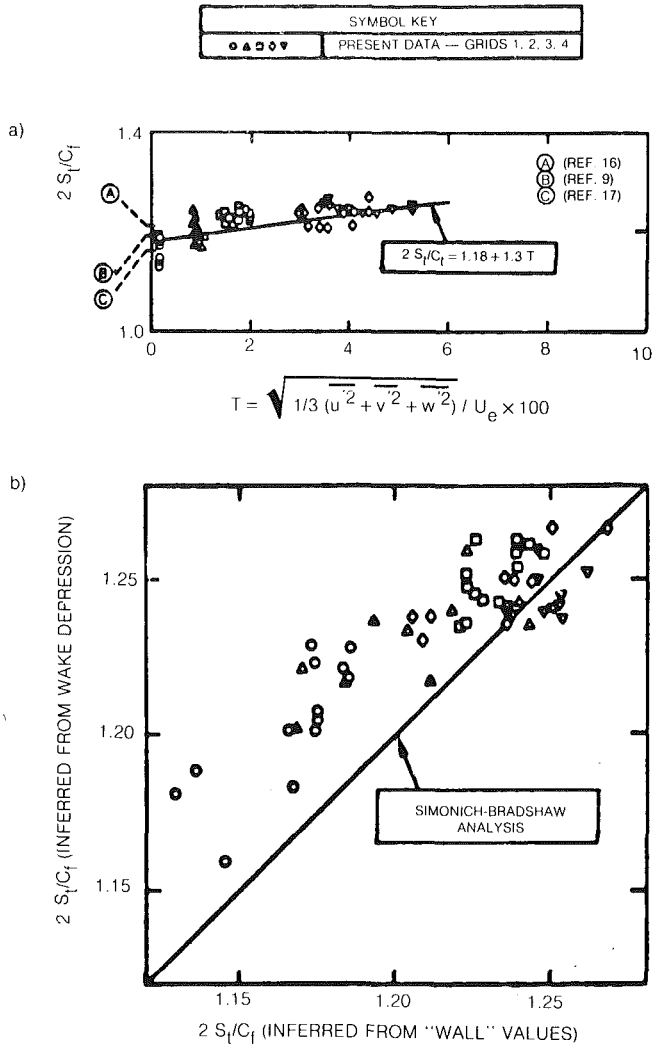

Fig. 5 Influence of free-stream turbulence on the Reynolds analogy factor

Hancock [4, 5] has recently conducted an experiment designed so that the influence of free-stream turbulence on skin friction could be examined for a wide range of dissipation length scale (L_e^u/δ). Using both his own data and data available from numerous other sources (as interpreted by himself and others), he has developed a skin friction correlation dependent upon both the turbulence intensity and dissipation length scale. The data of Fig. 3(*a*) (reduced using the present interpretation techniques which for some cases differ slightly from those used by Hancock) were compared to Hancock's correlation curve. It was observed that for all the high Re_θ cases, Hancock's correlation provided an excellent representation of both the present and other data. For data obtained at low Re_θ (some of the present data and much of the data of Charnay), however, observed changes in skin friction were considerably less than predicted by Hancock. This very sparse evidence, supportive of the analysis of McDonald and Kreskovsky, suggests that it may be necessary to include a "damping" term in Hancock's coordinates to compensate for reduced effects at lower Re_θ. In Fig. 6(*a*), the skin friction data of Fig. 3(*a*) are presented in Hancock's coordinates with the abscissa modified to include the empirical term

$$\beta = [3e^{-Re_\theta/400} + 1] \tag{12}$$

For the lowest Reynolds number data of Figs. 3(*a*) and 6(*a*) (Re_θ = 700) β = 1.5. Beta drops rapidly to 1 with increasing Re_θ (at Re_θ = 2000, β = 1.02), and for most of the data of Fig. 6(*a*), the effect of Re_θ is insignificant. As a comparative measure of the fits of these data by the two correlations the sum of the squares of the normal point-curve distances were computed. Including all data points from all five sources of Fig. 6(*a*), the "squared deviation" of the data points from the modified correlation was 37 percent of the "squared deviation" from the Hancock correlation. If only data points for $Re_\theta < 2000$ are considered, the "squared deviation" was 28 percent of the "squared deviation" from the Hancock curve. Considering the fact that data from such a large number of experiments covering such a wide range of conditions are all included in Fig. 6(*a*), Hancock's correlation (modified) appears to provide a very good prediction of effects of free-stream turbulence on turbulent boundary layer skin friction. In private communication, P. Bradshaw has pointed out the similarity between the "damping" term of equation (12) and the low Re_θ mixing length factor suggested by Baker and Launder [19].

The present heat transfer data are plotted on similar coordinates in Fig. 6(*b*). For this figure, Hancock's correlation curve has been scaled by the slope of the Reynolds analogy correlation of Fig. 5(*a*) ($\Delta St/St_0 = 1.3\ \Delta c_f/c_{f_0}$). Unfortunately, the present data are the only available with sufficient information to be plotted in these coordinates. Limited though these experimental measurements are, the curve of Fig. 6(*b*) is probably as good a prediction of the effects of free-stream turbulence on turbulent boundary layer heat transfer as is currently available.

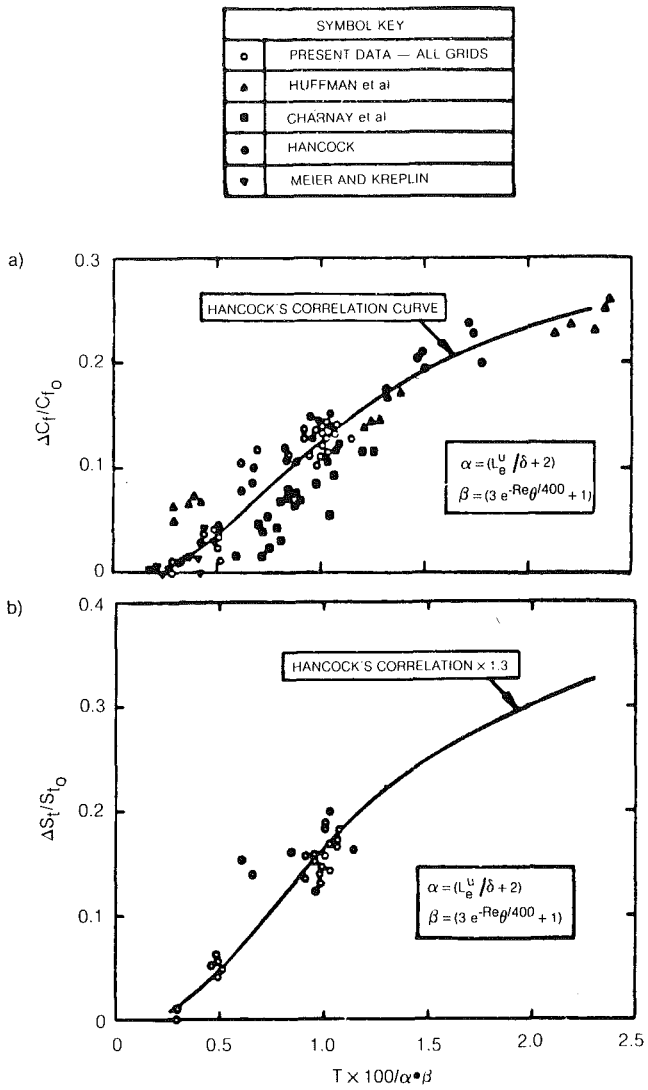

Fig. 6 Skin friction and Stanton number free stream turbulence correlations

Conclusions

Based on the results documented here in [1], it is concluded that:

1 The logarithmic regions of the mean velocity and temperature profiles were seen to be relatively unaffected by changes in the free-stream turbulence level. Progressively greater depression of the wake strengths were observed with increasing free-stream turbulence.

2 Both the kinematic shape factor and Clauser shape parameter decreased with increasing free-stream turbulence. The magnitude of the measured changes agreed well with the results of other analyses and data.

3 The wall shear data inferred from the log-regions of the present velocity profile data indicate that the skin friction coefficient increases with increasing free-stream turbulence intensity.

4 Changes in wall skin friction were inferred from wake depression measurements using an analysis by Bradshaw. These "wake inferred" changes were shown to be consistent with changes inferred from fits of the velocity profile data to the logarithmic law-of-the wall.

5 The measured Stanton numbers increased at a somewhat higher rate with increasing free-stream turbulence intensity than did the skin friction. The Reynolds analogy factor (2 St/c_f) was shown to linearly increase with increasing free-stream turbulence level. Reynolds analogy factors determined from both "wall inferred" measurements and from relative changes to the wake strengths of the mean velocity and temperature profiles were shown to be consistent.

6 A skin friction correlation (from Hancock [4, 5]) dependent upon both the free-stream turbulence intensity and dissipation length scale has been modified to include effects associated with low Reynolds numbers. This modified correlation appears to provide a very good representation of both the present data and a large number of other sets of experimental measurements. A suggested modification of the Hancock correlation curve is given for the effects of free-stream turbulence intensity, length scale, and boundary layer Reynolds number of the Stanton number.

Recommendation

Improvement of techniques for prediction of the effects of free-stream turbulence on turbulent heat transfer will depend upon expansion of the available turbulence structure data for these flows. In particular, it will be necessary to determine the impact of free-stream turbulence of the turbulent heat flux and turbulent Prandtl number distributions in boundary layers.

Acknowledgment

The author wishes to acknowledge the contributions of Professor Peter Bradshaw, Dr. Philip E. Hancock, and Dr. Robert Dring, who all provided numerous helpful suggestions during the course of the work.

Research sponsored by the Air Force Office of Scientific Research (AFSC), under Contract F49620-78-C-0064. The United States Government is authorized to reproduce and distribute reprints for governmental purposes notwithstanding any copyright notation hereon. The contract monitors for this project were Col. Robert C. Smith (Ret.), Dr. D. George Samaras, and Dr. James D. Wilson.

References

1 Blair, M. F., "Influence of Free-Stream Turbulence on Turbulent Boundary Layer Heat Transfer and Mean Profile Development, Part I—Experimental Data," ASME JOURNAL OF HEAT TRANSFER, Vol. 105, Feb. 83, pp. 33-40.

2 Bradshaw, P., "Effect of Free-Stream Turbulence on Turbulent Shear Layers," ARC, Paper 35648, 1974.

3 McDonald, H., and J. P. Kreskovsky, "Effect of Free-Stream Turbulence on the Turbulent Boundary Layer," *International Journal of Heat and Mass Transfer*, Vol. 17, 1974, pp. 705-716.

4 Hancock, P. E., "Effect of Free-Stream Turbulence on Turbulent Boundary Layers," Ph.D. thesis, Imperial College, London University, 1980.

5 Hancock, P. E., and Bradshaw, P., "The Effect of Free-Stream Turbulence Level in Turbulent Boundary Layers," submitted to ASME *Journal of Fluids Engineering*, 1982.

6 Huffman, G. D., Zimmerman, D. R., and Bennet, W. A., "The Effect of Free-Stream Turbulence Level in Turbulent Boundary Layer Behavior," AGARD AG 164, 1972, pp. 91-115.

7 Charnay, G., Compte-Bellot, G., and Mathiew, J., "Development of a Turbulent Boundary Layer on a Flat Plate in an External Turbulent Flow," AGARD, CP 93, Paper No. 27, 1971.

8 Meier, H. V., and Kreplin, H. P., "Influence of Freestream Turbulence on Boundary Layer Development," *AIAA Journal*, Vol. 18, No. 1, Jan. 1980, pp. 11-15.

9 Simonich, J. C., and P., Bradshaw, "Effect of Free-Stream Turbulence on Heat Transfer through a Turbulent Boundary Layer," ASME JOURNAL OF HEAT TRANSFER, Vol. 100, No. 4, Nov. 1978, pp. 671-677.

10 Coles, D. E., "The Turbulent Boundary Layer in a Compressible Fluid," Rand Report R-403-PR, 1962.

11 Coles, D., "Computations of Turbulent Boundary Layers," *Proceedings of the Stanford Conference*, AFOSR-IFP, Vol. II, 1968.

12 Robertson, J. M., and Holt, C. F., "Stream Turbulence Effects on Turbulent-Boundary Layers," *J. Hydraulics Div., Proc. ASCE*, Vol. 98, HY6, 1972, pp. 1095-1099.

13 Green, J. E., "On the Influence of Free-Stream Turbulence on a Turbulent Boundary Layer, as it Relates to Wind Tunnel Testing at Subsonic Speeds," AGARD Report 602, 1973.

14 Clauser, F. H., "The Turbulent Boundary Layer," *Advances in Applied Mechanics*, Vol. IV, 1956.

15 Blair, M. F., and Werle, M. J., "The Influence of Freestream Turbulence on the Zero Pressure Gradient Fully Turbulent Boundary Layer," UTRC Report R80-914388-12, Sept. 1980.

16 Spalding, D. G., "Contribution to the Theory of Heat Transfer Across a Turbulent Boundary Layer," *International Journal of Heat and Mass Transfer*, Vol. 7, 1964, pp. 743-761.

17 Chi, S. W., "Friction and Heat Transfer in a Compressible Turbulent Boundary Layer on a Smooth Flat Plate," Ph.D. thesis, Imperial College, University of London, 1965.

18 Kader, B. A., and Yaglom, A. M., "Heat and Mass Transfer Laws for Fully Turbulent Wall Flows," *International Journal of Heat and Mass Transfer*, Vol. 15, 1972, pp. 2329-2351.

19 Baker, R. J., and Launder, B. E., "The Turbulent Boundary Layer with Foreign Gas Injection," *International Journal of Heat and Mass Transfer*, Vol. 17, 1974, pp. 275-306.

20 Rotta, J. C., "Turbulent Boundary Layers in Incompressible Flow," *Progress in Aeronautical Sciences*, Vol. 2, Pergamon Press, Ltd., London, 1962.

APPENDIX A

Skin Friction Data

The following interpretations were employed so that sets of experimental skin friction test data from both the present and previous studies could be compared on a common basis.

(*i*) The skin friction data of the present study and the studies of [7] and [8] were all presented as ratios to the same low turbulence c_f versus Re_θ correlation. This low turbulence correlation was formed from a simple average of two incompressible skin friction correlations from Coles [10] and Rotta [20]. Both of these correlations contain results from numerous data sources, and their average should be an accurate representation of the dependence of c_f on Re_θ with low mainstream turbulence. Note that the skin friction data obtained from the minimum free-stream turbulence test case for the present study (Part I – Fig. 7) fell between these two skin friction correlations.

(*ii*) For Hancock's data [4, 5], skin friction ratios were plotted directly from results tabulated in his thesis. Hancock compared his measurements to his own low free-stream turbulence skin friction data correlation which agreed within approximately 1 percent of the mean of the Coles-Rotta curves.

(*iii*) Integral boundary layer thickness data were not presented by Charnay et al. [7], for these data boundary layer momentum thicknesses were calculated from the measured $\delta_{0.99}$ values using the data correlation of Robertson and Holt [12] for the influence of T on $\delta_{0.99}/\theta$.

(*iv*) The free-stream turbulence generated for the experiment of Huffman et al. [6] appears to have been highly anisotropic (see [3, 4]). For this reason, their multicomponent turbulence measurements at the boundary layer edge (k in their notation) were used to infer free-stream turbulence.

(*v*) Only the streamwise component of the free-stream turbulence was documented for [4, 7, 8] and [9]. For 4, 7 and 9], the free-stream turbulence appeared to have been nearly isotropic so $T = u'/U \times 100$. Although the grid/contraction arrangement used in [8] probably resulted in highly anisotropic turbulence, no measurements of nonstreamwise components were taken. For want of more information, the correlation of [8] was plotted as if their turbulence was isotropic. (Hancock [4] presented a convincing argument that the results of [8] demonstrate the relatively greater importance of the magnitude of the normal component (v') compared to the streamwise component (u') of the free-stream turbulence.) For other presentations of interpretations of these various skin friction data see [2, 3, 4], and [13].

Heat Transfer Coefficients and Patterns of Fluid Flow for Contacting Spheres at Various Angles of Attack

E. M. Sparrow
Fellow ASME

R. F. Prieto

Department of Mechanical Engineering,
University of Minnesota,
Minneapolis, Minn. 55455

Wind tunnel experiments were performed to determine heat transfer coefficients and fluid flow patterns for two contacting spheres. The experiments were carried out at three different angles of attack and for Reynolds numbers in the range from 4000 to 26,000. Three heat transfer conditions were considered: (a) both spheres thermally active, (b) forwardmost sphere thermally active and rearmost sphere adiabatic, and (c) forwardmost sphere adiabatic and rearmost sphere thermally active. Complementary experiments for a single sphere, encompassing the same parameter ranges, yielded baseline information for comparison with the two-sphere results. It was found that the largest effects of the sphere-to-sphere interaction on the heat transfer occurred when the two spheres were in line. At this orientation and for higher Reynolds numbers in the investigated range, there was substantial enhancement of the heat transfer with respect to that for the single sphere. At the other angles of attack, there was lesser enhancement. The visualization studies revealed such key fluid flow features as the reattachment of the separated flow from the first sphere on the second, the presence of strong recirculations, and the delay of separation due to pressure-driven transverse flows.

Introduction

In many engineering applications, a knowledge of the forced convection heat or mass transfer from solid spherical bodies or particles is required, and this has evoked extensive research, both experimental and analytical. The published research has been concerned almost exclusively either with the case of the single sphere or with highly populous multiparticle systems such as packed and fluidized beds. An extensive account of the transport processes relevant to single spheres is provided in [1], while [2] contains a review of heat transfer information for fluidized beds. In contrast, there is little in the literature on interacting spheres deployed in simple arrays, and the available work [3, 4] is restricted to flows with very low Reynolds numbers (Re $<$ 170).

The present research was undertaken to experimentally investigate the heat (mass) transfer and fluid flow characteristics for an interacting two-sphere system at relatively high Reynolds numbers (up to Re = 26,000). The work had two main foci. One was to determine the heat (mass) transfer coefficients for the individual spheres. The other was to study the patterns of fluid flow adjacent to the surfaces of the spheres. In addition, single sphere experiments were performed to provide baseline information against which to compare the results for the two-sphere system and also to enable comparisons with the literature.

The system that was investigated here consisted of two spheres in contact. During the course of the experiments, a number of parameters were varied including the direction of the fluid flow, the Reynolds number, and the boundary conditions for heat (mass) transfer at the individual spheres. The fluid flow direction was specified in terms of the angle of attack, which was defined as the angle between the airflow vector and a reference line which interconnects the centers of the contacting spheres. Angles of attack of 0, 45, and 90 deg were employed. Among these, the 0 angle of attack corresponds to the case where the flow vector and the reference line are colinear, and the 90 deg angle corresponds to a perpendicular orientation of the vector and the reference line. The range of the Reynolds number, based on the free stream velocity and the sphere diameter, extended from 4000 to 26,000 (velocity range from 2.5 to 16 m/s).

Three different heat (mass) transfer arrangements of the two-sphere system were investigated. In this regard, it may be noted that the actual experiments were performed for mass transfer by means of the naphthalene sublimation technique. The measured mass transfer coefficients can be transformed to heat transfer coefficients by using the well-established analogy between the two processes, as will be demonstrated later. Thus, the terms *heat transfer* and *mass transfer* will be employed interchangeably throughout the paper.

One of the many advantages of the naphthalene technique, in contrast to direct heat transfer measurements, is that it enables easy attainment of certain standard boundary conditions. At the surface of a naphthalene sphere, the boundary condition is that of uniform concentration of naphthalene vapor. According to the heat/mass transfer analogy, the equivalent heat transfer boundary condition is uniform surface temperature. A solid sphere made of any substance which does not react with naphthalene (e.g., nylon) is a surface of zero mass transfer, which corresponds, via the analogy, to an adiabatic surface.

A sphere which participates in the mass transfer process will be termed an *active* sphere and designated by the symbol, A, while a sphere which does not transfer mass will be termed *inactive* and designated by I. In these terms, the three investigated mass transfer arrangements are A/A, A/I, and I/A. The designation A/A means that both spheres are active; A/I signifies that the forwardmost of the two spheres is active, while the rearmost sphere is inactive; and I/A indicates that the forward sphere is inactive and the rear sphere is active.

For each of these three arrangements, experiments were performed for all the aforementioned angles of attack and Reynolds numbers. The single-sphere experiments were also carried out for the same angles and Reynolds numbers (the

Contributed by the Heat Transfer Division for publication in the JOURNAL OF HEAT TRANSFER. Manuscript received by the Heat Transfer Division March 19, 1982.

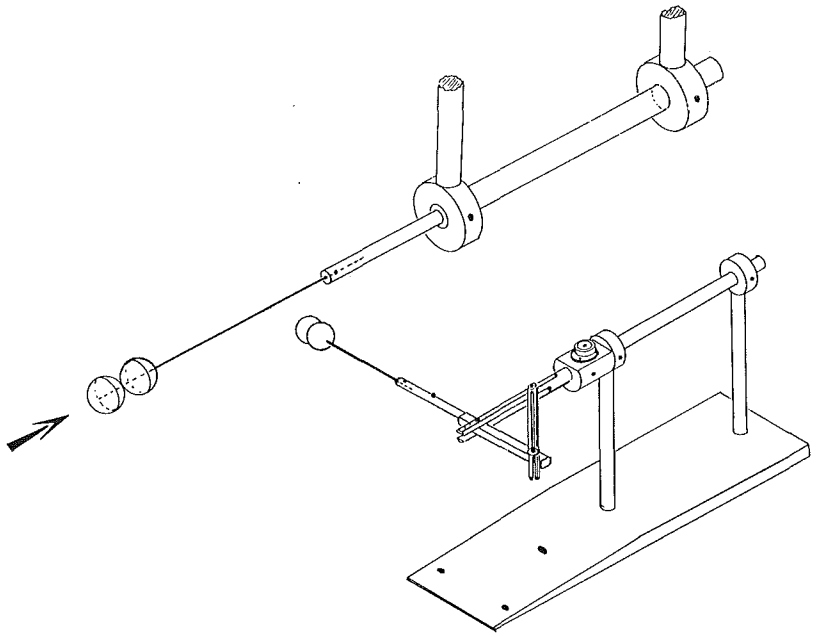

Fig. 1 Support systems for the spheres. Upper diagram: 0 deg angle of attack; lower diagram: arbitrary angle of attack

orientation of the sphere's support with respect to the flow direction changes with the angle of attack).

The heat (mass) transfer results will be presented from two distinct viewpoints. In one, a given angle of attack is selected, and the transfer coefficients for the various mass transfer arrangements are brought together and compared. In the other, a given arrangement is selected, and the results for the various angles of attack are brought together.

Equal emphasis will be placed on the flow visualization results, both for their intrinsic value and for their relationship to the heat (mass) transfer results. The visualization results will be presented via diagrams of the spherical surface on which are marked the zones over which various types of flow patterns prevail.

Another special feature of the present investigation was the development of a compression forming technique for fabricating the naphthalene spheres.

The Experiments

Test Section. The experiments were performed in a low-turbulence (0.2–0.3 percent) subsonic wind tunnel operating in the open-circuit mode, with air being drawn from the interior of the building and discharged out-of-doors. This mode was selected to ensure that the air delivered to the test section was free of naphthalene vapor. The test section had a rectangular cross section, 30.48-cm high by 60.96-cm wide, and an overall length of 243.8 cm. Auxiliary experiments using tufts as an indicator affirmed the parallelism of the flow. The air velocity in the test section was measured just upstream of the cross section at which the spheres were located by a retractable impact probe in conjunction with a wall static tap. Pressure signals from the probe and the tap were sensed by a Baratron solid-state, capacitance-type pressure meter capable of resolving 10^{-3} mm Hg.

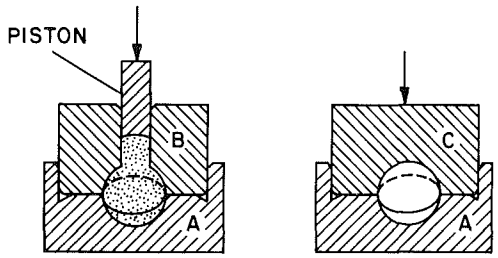

Fig. 2 Molds used in the compression forming of naphthalene spheres

During the course of the experiments, two types of supports were used for the spheres. Both support arrangements were designed to avoid perturbation of the flow (i.e., to approximate a support of zero dimensions). Pictorial views of the support systems have been brought together in Fig. 1.

The support system used in the experiments at zero degree angle of attack is shown in the upper part of the figure. As seen there, the spheres are supported from the rear by a small diameter rod which is, in turn, supported by a structure suspended from the upper wall of the wind tunnel. The support rod was of 0.238-cm dia stainless steel (chosen for strength), with an exposed length of 13.33 cm for the single-sphere case and 10.79 cm for the two-sphere case. Thus, the support rod diameter is only about 9 percent that of the 2.552-

Nomenclature

C = coefficient in Sh,Re relation
D = sphere diameter
$\mathfrak{D}$ = naphthalene-air diffusion coefficient
K = average mass transfer coefficient, $\dot{m}/(\rho_{nw} - \rho_{n\infty})$
$\dot{m}$ = average mass transfer rate per unit area
Nu = average Nusselt number
n = exponent in Sh,Re relation
Re = Reynolds number, $U_\infty D/\nu$
Sc = Schmidt number
Sh = Sherwood number, $KD/\mathfrak{D}$
U_∞ = freestream velocity
ν = kinematic viscosity of air
ρ_{nw} = density of naphthalene vapor at sphere surface
$\rho_{n\infty}$ = density of naphthalene vapor in freestream

cm dia spheres into which it was threaded. At its downstream end, the support rod mated with a 7.62-cm long, 0.637-cm dia brass rod.

The second system, pictured in the lower portion of Fig. 1, was designed to enable the attainment of any angle of attack between 0 and 90 deg. The support structure was mounted on a bevelled aluminum plate bolted to the floor of the wind tunnel. Variation of the angle of attack was acccomplished by the so-called in-line turning-block mechanism, the design details of which are set forth in Fig. 2.16 of [5] and in the related text. Angles were set with the aid of a protractor (not shown).

The support rod used in this system was also 0.238 cm in diameter and of stainless steel. Its exposed length was 6.9 cm for the single-sphere case and 4.4 cm for the two-sphere case. A shorter rod was used with this support system, compared with the first system, because there was no blockage downstream of the spheres for angles of attack of 45 and 90 deg. In addition, it was desired that the sphere(s) be as far from the wind-tunnel side wall as possible, and this suggested a short support. The closest approach of the sphere to the wall was 14.7 cm at an angle of attack of 90 deg.

The support rods for the single-sphere experiments had a 1.90-cm threaded length which was screwed in its entirety into the naphthalene sphere. For the two-sphere case, rods having a threaded length of 4.45 cm were used; the rod passed through the entirety of the rearmost sphere and penetrated part way through the frontmost sphere.

As noted earlier, various mass transfer arrangements were employed using both mass-transfer active and mass-transfer inactive spheres. The latter, made of nylon and with a diameter of 2.54 cm, were commercially available. The fabrication of the mass-transfer active naphthalene spheres will now be described.

Fabrication of the Naphthalene Spheres. Several techniques for fabricating naphthalene spheres were explored before the compression-forming method was selected and developed. The explored techniques included solidification of molten naphthalene in water, and casting in spherical and hemispherical glass-walled molds and in a spherical metal mold. The last of these molds was also employed to investigate the possibilities of compression forming, and on the basis of knowledge gained therefrom, a successful compression-forming method was evolved. A chronicle of the exploratory work is available in [5].

A compression-forming approach for benzoic acid and adipic acid spheres was mentioned in [6], but without any description of the method. Therefore, the present method and related equipment had to be developed without guidance from the literature.

The compression-forming method will be described schematically with the aid of Fig. 2. In the diagram at the left, the first stage of the two-stage fabrication process is illustrated. The equipment employed in this stage includes a two-part mold (parts A and B) and a rod with a contoured end, hereafter referred to as the piston. The hemispherical cavities of parts A and B mate precisely to form a spherical cavity. Part B contains a circular channel which penetrates the apex of the cavity. It is through this channel that naphthalene crystals are introduced into the cavity. Parts A and B are held together by tie rods (not shown). The lower face of the piston is precisely contoured with a radius equal to that of the spherical cavity.

At the beginning of the forming process, the cavity is empty and the piston is withdrawn, leaving the channel open. Naphthalene crystals are then introduced into the cavity, but the initial charge is only part of the total charge. The piston is then implanted in the channel (as shown in the figure), and a force is applied to its exposed end with a hand press. Then, the piston is withdrawn, and the remainder of the charge is introduced.

The piston is then reinserted and force is applied with a hydraulic pressure so that the contoured piston face is brought (approximately) flush with the surface of the spherical cavity. Then, the force is released, the mold parts are separated, and the naphthalene sphere removed from the mold cavity.

The sphere produced by the first-stage forming is not quite perfect in that there is a slight protuberance on the portion of the surface where the piston pressed on the naphthalene. The second stage of the forming procedure was aimed at removing this imperfection and, thereby, at producing perfect spheres. The mold configuration for the second stage is shown at the right of Fig. 2. Mold part C is similar to part B of the first stage, except that it does not have a charging channel. Part A is the same one that was used in the first-stage mold.

Prior to assembly of the mold for the second stage, the naphthalene sphere is placed in the cavity of Part A. Then, part C is placed atop part A, and a hydraulic pressure of 15 kg/cm^2 is applied. This pressure was found to be the proper value to eliminate the raised portion of the sphere and to redistribute the naphthalene to give a perfectly spherical shape. Upon release of the force, part C is removed, with the sphere remaining in either parts C or A. Usually, the sphere could be dislodged with finger pressure. If not, the release was accomplished by a soft blow of a rubber hammer on the rear face of the mold part.

Upon completion of the forming procedure, the sphere was bored with drill no. 43 (2.26-mm dia) and threaded with a 4-40 tap. Depending on whether the sphere was to be employed in a single-sphere setup or as the first or second element in a two-sphere setup, the hole was bored either three-quarters or all the way through, along a diameter. When these operations were completed, the sphere was brushed to remove any loose powder, wrapped in plastic, and placed in an airtight container. In general, the naphthalene spheres, once formed, were never touched directly with the hands.

It was found by experience that a charge of 10.25 g of naphthalene crystals was appropriate for the forming process. The diameters of numerous spheres were measured, yielding an average value of 25.52 mm with a maximum deviation of 0.5 percent.

Foregoing paragraphs convey a detailed account of the compression-forming process but, in the interest of a concise presentation, the fabrication details of the mold (e.g.,

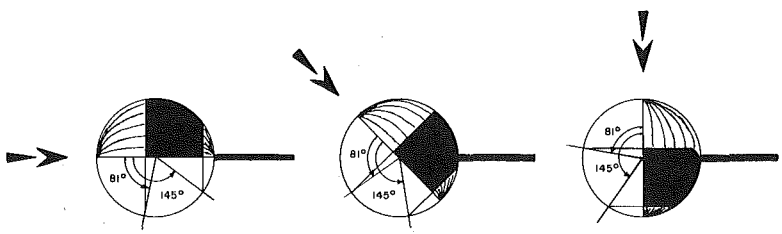

Fig. 3 Flow visualization patterns for the single sphere at various angles of attack

materials, dimensions, tolerances, bevels, reliefs, vents) have been omitted. These features, which are essential to the success of the forming process, are available in [5].

Experimental Procedure. To prepare for a data run, the wind tunnel was allowed to attain steady-steady operation during a suitable warm-up period. During this same time, the sphere(s), sealed in impermeable plastic wrap and positioned at the preselected angle of attack, attained thermal equilibrium with the air stream. The duration of this equilibration period was at least one hour. At the end of the equilibration period, the sphere(s) was weighed (with the wrap removed) and then returned to the wind tunnel (with the wrap once again in place) for an additional 15-min equilibration period.

To initiate the run, the wrap was removed and a stop watch activated. During the run, periodic measurements were made of the air velocity (dynamic and static pressures) and of the air temperature. The duration of the run was selected to limit the change in the sphere diameter due to sublimation to less than 0.0025 cm, which yielded run times in the range from 15 to 60 min, depending on the operating conditions. To conclude the run, the sphere(s) was covered with the plastic wrap and removed from the wind tunnel to be weighed.

There was a slight ambiguity of 5 to 10 s in the duration of a run due to various operations performed at the beginning and end of the run (e.g., removing and installing the plastic wrap, opening and closing the access hatch of the wind tunnel). To remove this ambiguity, a so-called after-run was performed following each data run. In this procedure, all of the steps subsequent to the first weighing were repeated, with the exception of the sublimation period. The change of mass for the after-run, typically 0.3 to 0.4 mg, was used as a correction for the sublimation mass transfer (typically 60 mg) for the data run proper.

The mass measurements were made with a Sartorius ultra-precise electronic balance capable of being read to 10^{-5} g and having a capacity of 160 g. The air temperature in the wind tunnel was read to 0.025°F with an ASTM-certified thermometer.

Flow Visualization. The oil-lampblack technique was used as the visualization tool. Lampblack, a very fine black powder, is mixed with an oil, and the mixture is brushed on the surface whose characteristics are to be studied. Under the action of shear stresses exerted by the flow, an array of streaks is formed on the surface as the oil-lampblack mixture follows the path of the fluid particles that pass adjacent to the surface. In regions of low velocity, the shear stresses are small and the mixture will remain stationary, so that such regions show themselves as black streak-free zones on the surface.

The fluidity of the mixture is critical to the attainment of a sharp streak pattern. Furthermore, a different fluidity is appropriate to various zones on the sphere to accommodate the different flow regimes (and their different shear stresses). Another consideration in the selection of the fluidity is the possibility that a too-fluid mixture will sag under gravity. The optimal fluidities were determined by a trial and error process.

Naphthalene spheres were used exclusively for the visualization runs because the white naphthalene afforded a sharp contrast for the black mixture. Two approaches were used in the coating of the sphere(s) with the oil-lampblack mixture. In one, the mixture was brushed on the entire surface. In the other, the mixture was applied locally at selected positions on the surface in order to reveal the details of the flow pattern at those positions.

The sharpest visualization patterns were obtained at the highest Reynolds number (Re ~ 26,000), and most of the final visualization runs were performed at that Reynolds number. Below about Re = 10,000, definitive visualizations were not obtainable due to the low shear stresses, even when the most-fluid nonsagging mixture was employed.

Photographs were taken through the plexiglass walls of the wind tunnels, with the airflow passing over the sphere(s). Visual observations were also made and recorded.

Flow Visualization Results

As was explained earlier, oil-lampblack mixtures of different fluidities were employed to coat various portions of the sphere surface in order to accommodate sharp differences in shear stress. It was found convenient to use these different mixtures one at a time. Therefore, among the photographs that were taken, there is none in which all the features of the flow field are shown. Because of this, the results of the visualization runs will be presented in sketches prepared using information from all the relevant photographs and from the visual observations.

The visualization patterns for the single-sphere case are presented in Fig. 3 for angles of attack of 0, 45, and 90 deg (left to right). As can be seen in the figure, the flow pattern adjacent to the surface of the sphere is quite similar for all angles of attack. The upstream portion of the surface is washed by a strong forward flow, as witnessed by the clearly etched streak lines. The flow separates at about 81 deg (measured from the forward stagnation point).

Downstream of the separation point and extending back to about 145 deg, there is a zone of relatively low velocities such that no movement of the oil-lampblack mixture could be detected (whence the black band shown in the sketches). In the rear portion of the sphere, for angles between 145 and 180 deg, streak lines are once again in evidence. These lines are traces of a well-ordered backflow; i.e., a flow whose direction is from the rear stagnation point toward the equator. Thus, the separated region, which extends aft of 81 deg, is seen to consist of two subregions distinguished by differences in

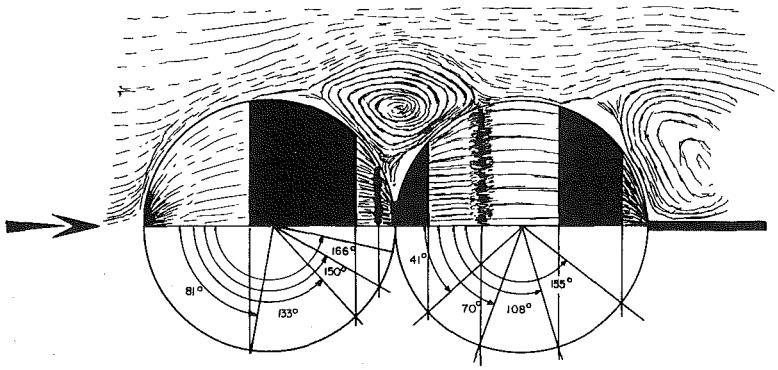

Fig. 4 Flow visualization pattern for the two-sphere system for the 0 deg angle of attack

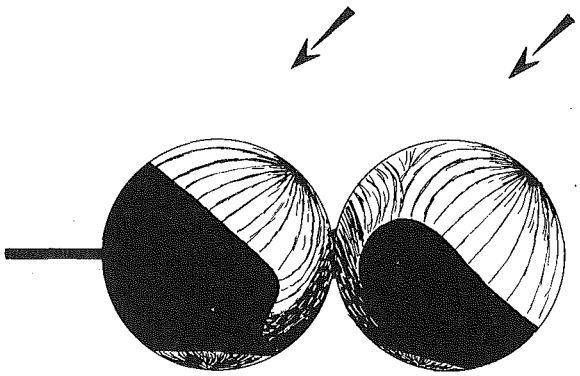

Fig. 5 Flow visualization pattern for the two-sphere system for the 45 deg angle of attack

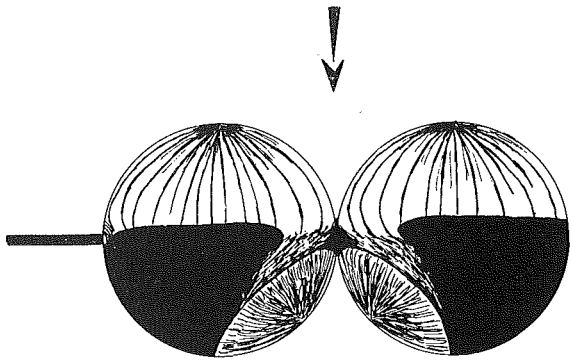

Fig. 6 Flow visualization pattern for the two-sphere system for the 90 deg angle of attack

velocity magnitude and, perhaps, by sharpness of the flow direction.

The differences among the three flow patterns of Fig. 3 occur in the neighborhood of the support rod, with the strongest influence being sustained at the 90 deg angle of attack, where there is a local delay of separation.

Attention is now turned to the two-sphere flow patterns, starting with the results for the 0 deg angle of attack in Fig. 4. An overview of this figure reveals a rich variety of forward flows and backflows whose complexity far exceeds that of the single-sphere case (Fig. 3). To facilitate the forthcoming discussion, the authors' perception of the airflow pattern has been sketched in the figure.

On the first sphere, the fore part of the surface is washed by a forward (boundary-layer-type) flow which persists to an angle of about 81 deg, at which point separation occurs. The separated mainflow bridges between the two spheres and reattaches to the second sphere in a band situated about 70 deg downstream of the nose of the sphere. After reattachment, a boundary layer flow develops which follows the contour of the sphere surface until an angle of approximately 108 deg, where it separates. The ensuing separated region has a two-part structure similar to that encountered in the single-sphere case but with different angular positions for the key landmarks.

The flow patterns on the aft portion of the first sphere and the fore portion of the second sphere are especially interesting, particularly because of the recirculating eddy which occupies the pocket between the spheres. On the first sphere, downstream of the separation point, there is a zone of sluggish flow (the wide black band extending from 81 to 133 deg) which gives way to a stronger, well-ordered backflow which is driven by the aforementioned large recirculating eddy. A smaller, counterrotating eddy presumably occupies the cusp region of the pocket, as suggested by the stagnation band situated at 150 deg and by the zone of forward flow between 150 and 166 deg. Downstream of 166 deg, an accumulation of the oil-lampblack mixture was observed and, in all likelihood, the accumulation interfered with the flow field.

On the forwardmost portion of the second sphere (0 to 41 deg), there were no signs of fluid motion, as witnessed by the quiescence of the oil-lampblack mixture. From 41 to 70 deg, the surface is washed by a vigorous backflow driven by the recirculating eddy which occupies the intersphere pocket. In general, the flow pattern on the second sphere suggests higher heat transfer coefficients then those for the first sphere or for a single sphere.

The visualization for the two-sphere case with a 45-deg angle of attack is shown in Fig. 5. As the fluid passes over the first sphere, it creates a boundary layer flow on the forward portion which subsequently separates. The boundary layer flow is three dimensional and nonaxisymmetric because it is caused to move transversely by a pocket of high pressure generated by the stagnation which occurs at the nose of the second sphere. Furthermore, the thus-driven flow penetrates well into the rearward portions of both spheres in the region where the two spheres face each other, with a consequent delay of separation.

Aside from the aforementioned pocket of delayed separation, the rearward portion of each sphere is dominated by a low-velocity separated region where no movement of the oil-lampblack mixture could be detected. At the very rear of each sphere, as for the single sphere, a cap-like region of higher velocity backflow is in evidence. Owing to the absence of axisymmetry, the cap is not lined up with the freestream velocity vector. It may also be noted that the second-sphere's cap is larger and less circular than that of the first sphere. This is believed due to the fact that the rear of the first sphere is washed only by its own wake, while the rear of the second sphere is washed by the wakes of both spheres.

The last of the flow visualizations to be presented is that for the two-sphere case with a 90 deg angle of attack – Fig. 6. Owing to the stagnation of the flow at the contact of the spheres, an elevated pressure exists in that region. This pressure elevation drives the transverse flow that is in evidence just downstream of the contact. As was the case for the 45-deg angle of attack, the pressure-driven transverse flow is responsible for a localized delay of separation. A strong recirculating flow occupies the cusp-shaped region downstream of the contact and washes both spheres, generating a cap on each sphere which is larger than any of those previously described.

The flow patterns on the two spheres are the same except in the neighborhood of the attachment of the support rod to the second sphere. As noted earlier, the main effect of the support rod in the 90 deg orientation is a localized delay in separation.

Heat (Mass) Transfer Results

The procedure used to evaluate mass transfer coefficients from the measured data will now be briefly described, after which the results will be presented and discussed.

Data Reduction. To begin the data reduction, the measured change of mass due to sublimation is divided by the duration of the data run and by the sphere surface area which participates in the mass transfer process, yielding the average mass flux, $\dot{m}$. If $\dot{m}$ is then divided by the concentration difference which drives the mass transfer, the average mass transfer coefficient, K, and Sherwood number, Sh, follow as

$$K = \dot{m}/(\rho_{nw} - \rho_{n\infty}), \quad \mathrm{Sh} = KD/\mathfrak{D} \tag{1}$$

The quantity ρ_{nw} is the naphthalene vapor density at the surface of the sphere. It was evaluated from the Sogin vapor pressure-temperature relationship [7] in conjunction with the perfect gas law. The freestream naphthalene vapor density

Table 1 Two-sphere mass transfer arrangements

Designation	1st Sphere	2nd Sphere
A/A	active	active
A/I	active	inactive
I/A	inactive	active

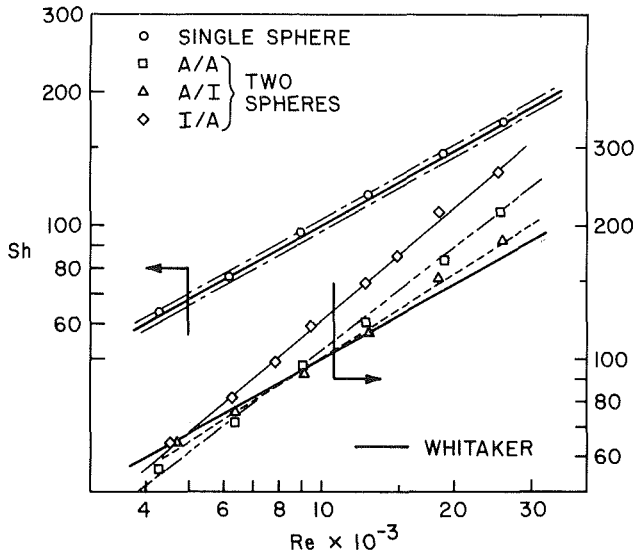

Fig. 7 Mass (heat) transfer coefficients for the 0 deg angle of attack. Upper diagram: single sphere; lower diagram: two-sphere configurations

$\rho_{n\infty}$ is zero in the present experiments. In the Sherwood number, $\mathfrak{D}$, is the mass diffusion coefficient for naphthalene sublimation in air. It was evaluated from the identity $\mathfrak{D} = \nu/\mathrm{Sc}$, where the Schmidt number for naphthalene diffusion in air is 2.5 [7] and ν is the kinematic viscosity of air.

The fluid flow was parameterized by the sphere Reynolds number, Re, given by

$$\mathrm{Re} = U_\infty D/\nu \tag{2}$$

in which U_∞ is the velocity of the approach flow, and D is the sphere diameter.

The Sherwood number is the mass transfer counterpart of the Nusselt number.

According to the analogy between heat and mass transfer

$$\mathrm{Sh} = f(\mathrm{Re},\mathrm{Sc}), \quad \mathrm{Nu} = f(\mathrm{Re},\mathrm{Pr}) \tag{3}$$

where f is the same function for both Sh and Nu. This assertion will be validated shortly by the data from the present experiments.

Presentation of Results. The first set of results to be presented is for the single sphere at a 0 deg angle of attack. These results will be compared with available heat transfer information with a view toward confirming the analogy between heat and mass transfer and establishing the quality standard of the present experiments.

The present Sherwood number data for this case are plotted as a function of the Reynolds number in the upper portion of Fig. 7, and the data show the expected increase of Sh with Re. Along with the data is plotted a heavy black line which represents the widely referenced Whitaker [8] correlation

$$\mathrm{Nu} = 2 + (0.4\mathrm{Re}^{1/2} + 0.06\mathrm{Re}^{2/3})\mathrm{Pr}^{0.4} \tag{4}$$

which has been rephrased for mass transfer as

$$\mathrm{Sh} = 2 + (0.4\mathrm{Re}^{1/2} + 0.06\mathrm{Re}^{2/3})\mathrm{Sc}^{0.4} \tag{5}$$

The Whitaker correlation is based on heat transfer data for air, water, and oil and thereby encompasses a range of Prandtl numbers which extends both below and above the Schmidt number (=2.5) for naphthalene sublimation in air.

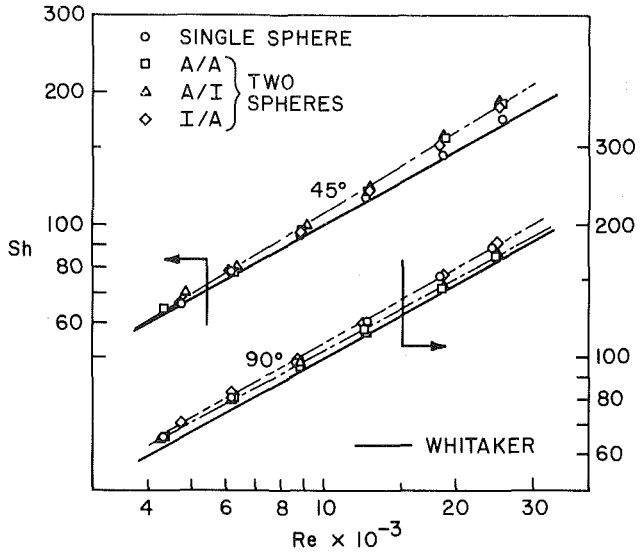

Fig. 8 Mass (heat) transfer coefficients for the 45 and 90 deg angles of attack – upper and lower graphs, respectively

The Whitaker correlation is flanked in the figure by two lighter-weight lines that are displaced from it by ± 3 percent.

Inspection of the figure reveals a remarkable level of agreeement between the present data and the Whitaker correlation. On the average, the data is about 2.4 percent above the correlation, with a maximum deviation of 3.6 percent. The excellent agreement not only confirms the analogy between heat and mass transfer but also establishes the quality standard of the experiments. In view of the confirmation of the analogy, it may be concluded that all of the Sherwood number results obtained here may be regarded as Nusselt number results.

The main body of the experimental results will be presented in two different formats. In the first, a given angle of attack is selected, and the sphere arrangement serves as the curve parameter. For the two-sphere case, the investigated arrangements are identified in Table 1.

The term *active* indicates a naphthalene sphere which participates in the mass transfer process while the term *inactive* indicates a sphere where there is no mass transfer. In addition to the aforementioned three arrangements for the two-sphere case, results for the single sphere will also be presented.

In the second presentation format, a sphere arrangement is selected, and the angle of attack serves as the curve parameter.

Fixed Angle of Attack. The results for each of the three angles of attack are presented in the lower portion of Fig. 7 and in Fig. 8, respectively, for the 0 angle and for the 45 and 90 deg angles. Attention will first be turned to the zero degree results.

As seen in the lower portion of Fig. 7, Sherwood number data for the A/A, A/I, and I/A two-sphere arrangements are plotted as a function of the Reynolds number. To provide continuity, the data are interconnected with least-squares straight lines. The Whitaker single-sphere equation is also plotted in this figure (and in all subsequent figures) as a reference line. The 0 deg, single-sphere data have already been presented in the upper portion of Fig. 7 and discussed in detail, thereby obviating the need for their inclusion in the lower portion of the figure.

Over most of the investigated Reynolds number range, there is a general enhancement of the mass transfer coefficient for all the two-sphere arrangements relative to that for the single sphere. In the range of significant enhancement, there is a definite ordering of the results according to the mass

transfer arrangement of the two spheres. The highest coefficients occur when a mass transfer sphere is situated downstream of a nonparticipating sphere (i.e., the I/A case). The coefficients for the two active spheres[1] (A/A) are the second highest, and those for the first-sphere active (A/I) are the lowest among the two-sphere cases.

The remarkably high second-sphere mass transfer coefficient for the I/A case, which is about 55 percent higher than the single sphere value at a Reynolds number of about 25,000, may be attributed to the presence of the zones of reattached flow situated upstream and downstream of the reattachment of the separated flow from the first sphere (see Fig. 4). For the first sphere, there is no counterpart of these mass transfer enhancing zones, so that the case where the first sphere is active and the second sphere is inactive (i.e., the A/I case) has relatively lower transfer coefficients than the I/A case. These characteristics also explain why the case of two active spheres (A/A) is intermediate to the others. It should be noted that the coefficient for the A/A case is, on the average, 8.7 percent lower than the arithmetic mean of the A/I and I/A coefficients. This deviation is caused by the presence of naphthalene vapor in the recirculatory flow which is situated in the pocket between the two spheres.

As the Reynolds number decreases, the spread between the various cases diminishes and, in fact, it appears that the ordering of the results reverses. This suggests an alternation in the flow pattern with decreasing Reynolds number. This issue was examined with the oil-lampblack technique but, as noted earlier, definitive visualizations could not be obtained below Re ~ 10,000. It was observed, however, that as the Reynolds number decreases, there is a reduction in the size of the highly enhanced region on the second sphere that lies downstream of the reattachment of the separated flow from the first sphere. In addition, the vigor of the recirculation in the pocket between the spheres diminishes at lower Reynolds numbers, thereby reducing the velocity of the backflow which washes the portion of the second sphere that lies upstream of the reattachment. These characteristics are supportive of the trends in the Sherwood number data.

The wind tunnel does not operate stably at Reynolds numbers below those of the figure, so that the newly emerging ordering of the results could not be positively established. The new ordering is, however, confirmed by the available low Reynolds number data (Re < 60) of [4], where the A/I results are higher than those for the I/A arrangement.

The results for an angle of attack of 45 deg are presented in the upper part of Fig. 8. For the two-sphere case, the data for the three mass transfer arrangements cluster within 3 percent or less at a given Reynolds number. With decreasing Reynolds number, there is a tendency for even this small spread to diminish.

The single-sphere data fall, on the average, about 1.8 percent above the Whitaker line, with a maximum deviation of 3.1 percent. There is a general enhancement of the two-sphere coefficients relative to those for the single sphere but to much smaller extent than for the 0 angle of attack. The enhancement is in the 9–12 percent range at the higher Reynolds numbers and diminishes as the Reynolds number decreases. It is believed that the enchancement is due to delayed separation in evidence in Fig. 5.

The results for the third angle of attack, 90 deg, are presented in the lower part of Fig. 8. As seen there, the data tend to cluster, and the spread among the data for the various configurations diminishes as the Reynolds number decreases. In general, all of the data fall within 10 percent of the Whitaker single-sphere correlation.

The coefficients for the single sphere lie, on the average,

[1] The coefficients for the A/A case correspond to an average over the two spheres.

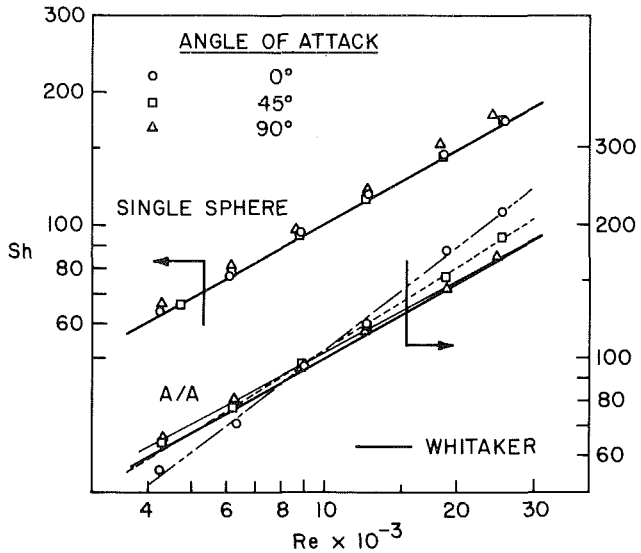

Fig. 9 Mass (heat) transfer coefficients for the single sphere and for the A/A two-sphere configuration – upper and lower graphs, respectively

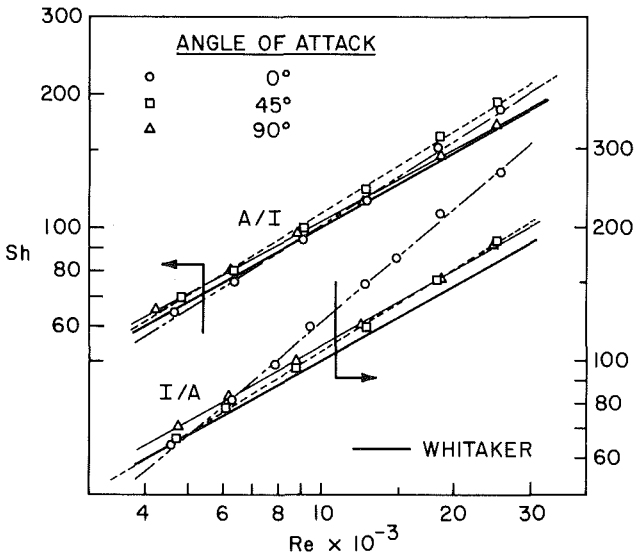

Fig. 10 Mass (heat) transfer coefficients for the A/I and I/A two-sphere configurations – upper and lower graphs, respectively

about 6½ percent above the Whitaker line, reflecting the delay of separation due to the crossflow support (Fig. 3). Furthermore, for the I/A configuration (active sphere attached to the support rod) the coefficients are indistinguishable from those of the single sphere, suggesting that the fluid flow features associated with the interaction of the spheres do not, *on the average*, affect the mass transfer. This same conclusion emerges from the data for the A/I configuration, where the active sphere is outboard (away from the support). These coefficients are lower than those for the I/A configuration and differ little from the Whitaker line. The coefficients for the A/A configuration lie below the average of the I/A and A/I values, reflecting the carryover of naphthalene vapor between the spheres.

Fixed Sphere Arrangement. The results will now be regrouped according to sphere arrangement, with the angle of attack serving as the curve parameter.

The single-sphere Sherwood numbers for all three angles of attack have been brought together in the upper part of Fig. 9, where the Whitaker line is also plotted. The data for both the

0 and the 45 deg angles are virtually coincident and are in close agreement with the Whitaker line. For both of these cases, the support rod is located in the separated region and has a very small effect on the mass transfer. For the 90 deg case, the support rod delays the separation of the flow in its neighborhood, causing an increase in the transfer coefficient.

Results for the case of two active spheres (A/A) are presented in the lower part of Fig. 9. The figure shows that the deviations between the two-sphere and single-sphere transfer coefficients (the latter represented by the Whitaker line) are greatest at the 0 angle of attack, a finding which is consistent with the flow visualization patterns of Figs. 3–6. In addition, the 0 deg results are more responsive to the Reynolds number than are the results for the other angles. Thus, at the higher Reynolds numbers, the 0-degree Sherwood numbers are the highest of all, while in the low Reynolds number range they are the lowest of all. The results for the 90 deg angle tend to follow the Whitaker single-sphere line quite closely.

Attention will now be turned to Fig. 10 and to the results of the A/I two-sphere arrangement that are plotted in the upper part of the figure. Overall, the presence of an inactive sphere located either behind or beside a mass-transfer-active sphere is enhancing – but moderately and then primarily at the higher Reynolds numbers. The 90 deg transfer coefficients are virtually the same as those for the single sphere over the entire investigated range of Reynolds numbers, and the coefficients for the other angles are very close to the single-sphere values for $Re < 10{,}000$.

In the lower part of the figure are the results for the I/A two-sphere arrangement. Here again, enhancement relative to the single-sphere case is in evidence, indicating that the flow field spawned by the forwardmost (inactive) sphere is beneficial for the mass transfer at the active second sphere. The most significant enhancement is seen to occur at the 0 deg angle of attack and at the higher Reynolds numbers. At lower Reynolds numbers, the enhancement for both the 0-and 45-deg angles disappears due to changes in the fluid flow pattern. The enhancement for the 90 deg case is due to the delay of separation brought about by the presence of the support, and this enhancement, albeit moderate, persists over the entire investigated range of Reynolds numbers.

Concluding Remarks

The foregoing presentation of results has identified all of the main trends in the data and has, whenever possible, suggested rationalizations. Consideration will now be given to a quantitative representation of the results.

The data presented in Figs. 7–10 appear either to lie on straight lines or may be well approximated by straight lines. This suggests a Sh, Re power-law relation:

$$Sh = CRe^n \tag{6}$$

Indeed, over the investigated range, the Whitaker equation (5) is very well represented for $Sc = 2.5$

$$Sh = 0.589Re^{0.558} \tag{7}$$

The C and n values specific to each of the twelve investigated configurations were determined via least-squares techniques and are listed in [5]. Here, a somewhat smaller set of C and n values will be presented.

For the 0 deg angle of attack, the single-sphere results are well represented by equation (7). For the A/A, A/I, and I/A two-sphere configurations at this angle of attack, the corresponding n values are 0.773, 0.632, and 0.848, with respective C values of 0.085, 0.296, and 0.050.

At 45 deg, equation (7) again provides a very good representation of the single-sphere results. The data for all three two-sphere cases can be represented by the single equation $Sh = 0.376Re^{0.613}$. A single equation, $Sh = 0.632Re^{0.556}$, suffices for both the single-sphere and two-sphere results at the 90 deg angle of attack.

In view of the analogy between heat and mass transfer, equation (6) can be rephrased in heat transfer terms and then generalized to apply to a wide range of Prandtl numbers by adopting the $Pr^{0.4}$ dependence indicated by the Whitaker equation. If it is noted that $(1/2.5)^{0.4} = 0.693$, the transformed and generalized correlation equation is

$$Nu = (0.693C)Pr^{0.4}Re^n \tag{8}$$

in which the C and n values are those of the preceding two paragraphs.

Acknowledgment

This research was performed under the auspices of the National Science Foundation.

References

1 Clift, R., Grace, J. R., and Weber, M. E., *Bubbles, Drops, and Particles*, Academic Press, New York, 1978.

2 Botterill, J. S. M., *Fluid-Bed Heat Transfer*, Academic Press, London, 1975.

3 Peltzman, A., and Pfeffer, R., "The Effect of a Small Number of Inert Particles on the Local and Overall Mass Transfer Rates from a Single Sphere at Low Reynolds Numbers," *Chemical Engineering Progress Symposium Series*, Vol. 63, No. 77, 1967, pp. 49–65.

4 Chen, W. C., and Pfeffer, R., "Mass Transfer Rates with First Order Homogeneous Chemical Reaction Around Two Spheres," *Chemical Engineering Progress Symposium Series*, Vol. 66, No. 105, 1970, pp. 109–122.

5 Prieto, R. F., "Heat Transfer and Fluid-Flow Patterns for Contacting Spheres Situated at Various Angles of Attack in an Airflow," Master's thesis, Department of Mechanical Engineering, University of Minnesota, Minneapolis, Minn., 1981.

6 Garner, F. H., and Suckling, R. D., "Mass Transfer from a Soluble Solid Sphere," *AIChE Journal*, Vol. 4, 1958, pp. 114–124.

7 Sogin, H. H., "Sublimation from Disks to Air Streams Flowing Normal to Their Surfaces," *Trans.* ASME, Vol. 80, 1958, pp. 61–71.

8 Whitaker, S., "Forced Convection Heat Transfer Correlations for Flow in Pipes, Past Flat Plates, Single Cylinders, Single Spheres, and for Flow in Packed Beds and Tube Bundles," *AIChE Journal*, Vol. 18, 1972, pp. 361–371.

Heat Transfer and Fluid Flow Experiments With a Tube Fed by a Plenum Having Nonaligned Inlet and Exit

E. M. Sparrow
Fellow ASME

L. D. Bosmans

Department of Mechanical Engineering,
University of Minnesota,
Minneapolis, Minn. 55455

Local turbulent heat transfer coefficients for airflow were measured in a tube situated downstream of a cylindrical plenum chamber in which the inflow was radial and the outflow was axial. Pressure drop measurements and flow visualization were performed to supplement the heat transfer experiments. The plenum length and diameter were varied systematically during the experiments, and the Reynolds number ranged from 10,000 to 60,000. Substantially higher Nusselt numbers in the tube were encountered for the present nonaligned plenum inlet/exit configuration than for a plenum with axially aligned inlet and exit or for an upstream hydrodynamic development section. For a given Reynolds number, the Nusselt numbers corresponding to the present plenum configuration were quite insensitive to the investigated geometrical parameters. The thermal development length was found to be substantially elongated due to swirl carried into the tube from the plenum; the presence of the swirl was confirmed by flow visualization. The net pressure loss due to the presence of the plenum was about 1.75 velocity heads and was quite insensitive to the geometrical parameters and to the Reynolds number.

Introduction

Fluid may be delivered to the tubes of a heat exchanger via a wide variety of plenum chamber geometries. Frequently, the fluid inlet to the plenum is not aligned with the fluid exit, so that the flow must turn as it passes through the plenum. The turning of the flow may induce a swirling motion which is carried into the tubes. In general, the nonaligned plenum inlet and exit will cause the flow which is fed to the tubes to be three dimensional, with transverse velocity components superposed on the axial mainflow. Despite the clear relevance to heat exchanger practice, it appears that a systematic study of heat transfer and pressure drop in the presence of a plenum with nonaligned inlet and exit has not yet appeared in the open literature.

In the experimental investigation to be reported here, a cylindrical plenum chamber is supplied with air through an inlet port that is transverse to the cylinder axis, so that the inflow is radial. The plenum exit, through which the air passes into a heated, instrumented tube, is axial. This configuration requires that the air turn as it passes through the plenum, thereby inducing the complex fluid flow phenomena that were discussed in the foregoing paragraph.

The research program encompassed three complementary sets of experiments, and two apparatuses were employed for its execution. In the main set of experiments, local heat transfer coefficients were measured along the length of the aforementioned electrically heated tube which is fed by the plenum discharge. For the most part, the heat transfer data were processed so as to yield circumferential average coefficients as a function of axial position along the tube. However, circumferential variations were also examined to identify the effect of swirl and fluid flow three dimensionality.

The second and third sets of experiments were devoted to fluid flow studies (without heat transfer). For these experiments, the heated test section was replaced with an unheated tube of identical bore diameter along which pressure taps were deployed. Pressure distributions were measured along both the tube which supplies air to the plenum and the just-mentioned tube which receives the plenum discharge. These measurements enabled the determination of the net pressure loss due to the presence of the plenum, and these data will be presented in dimensionless form relative to the velocity head.

In the third set of experiments, the objective was to determine the patterns of fluid flow within the plenum. For this purpose, the oil-lampblack technique was employed. This technique is very well suited for revealing the flow pattern adjacent to a surface, as will be demonstrated via photographs to be presented later.

Geometrical parameters and airflow rate were varied during the course of the investigation. Two cylindrical plenums of different diameter were employed. Each of these plenums was designed to enable its axial length to be varied, and heat transfer data were collected for two plenum lengths for each. In the presentation of results, separate graphs are employed to portray the effects of the plenum length and diameter. For each of the plenum geometries for which heat transfer data were collected, the tube Reynolds number was varied from about 10,000 to 60,000. The pressure drop work was performed for four plenum lengths and spanned the same Reynolds number range as for the heat transfer.

As noted earlier, it does not appear that there is any published information on the effects of nonaligned plenum inlet and exit configurations, thereby eliminating the possibility of direct literature comparisons. To establish the effect of nonalignment, the present data will be compared with data corresponding to cylindrical plenums with aligned axial inlet and axial exit [1]. A further quantitative comparison is made with heat transfer results (also taken from [1]) for turbulent pipe flow without a plenum, where the heated tube is preceded by a hydrodynamic development length. Qualitative comparisons will be made with tube-flow heat transfer data in the presence of intentionally induced swirl [2, 3]. The measured heat transfer coefficients in the far-downstream portion of the test section tube will be compared

Contributed by the Heat Transfer Division for publication in the JOURNAL OF HEAT TRANSFER. Manuscript received by the Heat Transfer Division February 8, 1982.

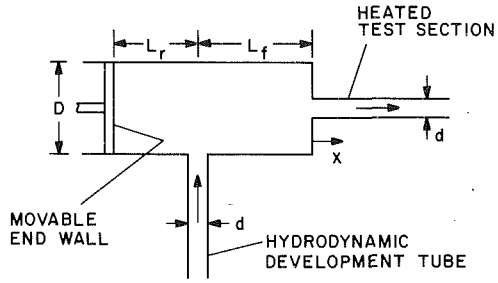

Fig. 1 Plenum chamber configuration used in the experiments

with those of the Petukhov-Popov correlation [4] for fully developed heat transfer.

The Experiments

Plenum Chambers. A schematic diagram of the plenum chamber configuration that was employed in the experiments is presented in Fig. 1. The plenum is a cylinder of diameter, D, and length, $(L_r + L_f)$, both internal dimensions. These dimensions were varied parametrically, as will be described shortly. Air was delivered to the plenum via a hydrodynamic development tube oriented so that the flow is radially inward at the inlet cross section. The plenum exit is a circular aperture centered in one of the end faces. Both the hydrodynamic development tube and the test section tube (which mates with the plenum exit) have the same internal diameter, d, which had a fixed value throughout the experiments.

The axial position of the plenum inlet port is specified by the lengths L_f and L_r, which respectively represent the distances between the centerline of the port and the front and rear faces of the plenum. Variation of L_r was accomplished by axial movement of the rear wall of the plenum.

Two positions of the rear wall were employed during the heat transfer experiments, respectively characterized by $L_r/d = 1$ and 5. The first of these corresponds to a minimal clearance between the inlet port and the rear wall so that, in effect, the entering fluid is denied the option of spreading rearward. The $L_r/d = 5$ rear-wall position was selected to match the $L_f/d = 5$ front-wall position that was built into the plenum. By this positioning, the entering fluid was given the option of spreading rearward (as well as forward), if that were its inclination. Thus, for the heat transfer studies, the employed variations of plenum length enabled evaluation of the effect of the presence or absence of an expansion space in the rear of the plenum, beyond the inlet port.

For the pressure drop studies, the same two values of L_r/D (equal to 1 and 5) were employed along with front-zone lengths L_f/d of 3 and 5. The $L_f/d = 3$ condition was obtained by implanting a disk of diameter, D, and length $= 2d$ into the forwardmost portion of the plenum. A hole of diameter, d, bored along the axis of the disk mated perfectly with the aperture in the front face of the plenum. With the disk in place, the forward-zone length available to the air was reduced from $L_f/d = 5$ to $L_f/d = 3$.

The use of an inserted disk to vary L_f/d in the heat transfer studies was considered and rejected. This is because such a disk would have created a hydrodynamic development length (equal to $2d$) upstream of the heated tube and might also have provided a path for extraneous heat conduction.

Two different plenum chamber diameters were employed, respectively $D/d = 3$ and 6 (actually, 2.96 and 5.91).

Both plenums were made of plexiglass, with the exception of the front face, as will be described shortly. The movable rear wall consisted of a disk fitted with a handle-like rod, as seen in Fig. 1. An air-tight seal between the plenum wall and the contacting edge of the disk was achieved with a pair of O-rings. Once moved to a desired axial position, the disk could be locked in place.

The plenum inlet port consisted of a bored hole which passed radially through the cylindrical wall of the plenum and through a contoured plexiglass boss that had been affixed to the outside of the wall to provide added thickness. The bored hole was recessed in such a way that there was no discontinuity in the flow cross section as the hydrodynamic development tube mated with the plenum inlet port.

For the pressure drop studies, the front wall of the plenum was a plexiglass disk with a centered aperture sized to accommodate the outer diameter of the pressure test section. In the heat transfer experiments, the plenum front wall was part of the defense devised to avoid extraneous heat losses. In the case of the smaller diameter plenum, the entire front wall consisted of an annular disk made of 0.043-cm (0.017-in.) thick fiberglass circuitboard. For the larger diameter plenum, the fiberglass disk was framed by a plexiglass annulus.

The inner diameter of the fiberglass disk was made identical to the outer diameter of the test section tube, so that the disk could just slip over the tube. When assembled, the upstream faces of the disk and tube lay in a continuous plane. The only thermal path between disk and tube was through their 0.043 cm (0.017 in.) interface. This minimal contact, taken together with the low conductivity of the fiberglass, created a strong blockage of extraneous heat conduction. Possible air leaks were sealed with a filet of silicone rubber applied just downstream of the fiberglass disk and by the use of pressure-sensitive tape at strategic locations.

Heated Test Section. The test section was a stainless steel tube with an internal diameter (after honing) of 2.362 cm (0.930 in.), a wall thickness of 0.089 cm (0.035 in.), and a

Nomenclature

c_p = specific heat of air
D = plenum chamber diameter
d = diameter of test section and development tubes
h = local circumferential-average heat transfer coefficient
K = dimensionless pressure loss coefficient, equation (5)
k = thermal conductivity of air
L_f = length of forward part of plenum
L_r = length of rearward part of plenum
$\dot{m}$ = mass flow rate
Nu = local circumferential-average Nusselt number, hd/k
p = local static pressure
p_o = reference pressure
Δp_p = net plenum-related pressure loss, Fig. 2
Q_{cv} = convective heat transfer per control volume
q_x = convective heat flux
Re = Reynolds number, $4\dot{m}/\mu\pi d$
T_{bx} = bulk temperature at x
$\bar{T}_{wx}$ = circumferential-average wall temperature at x
$T_{wx}(\theta)$ = local circumferential temperature at x,θ
$\Delta T_{b,cv}$ = bulk temperature rise per control volume
V^* = velocity at plenum inlet port
x = axial coordinate for test section
x' = axial coordinate for hydrodynamic development tube
θ = angular coordinate
μ = viscosity of air
ρ^* = density of air at plenum inlet port

heated length of about 70 diameters. Heating was accomplished by the passage of voltage-stabilized a.c. electric current through the tube wall. To facilitate the heating, copper rings were soldered to the tube at its upstream and downstream ends. Current was conveyed to (or from) the respective rings by six rod-like copper conductors.

The copper rods situated at the upstream end of the tube were each fitted with a differential thermocouple to detect possible extraneous heat conduction. To null out the extraneous conduction, a guard heating/cooling arrangement was devised which enabled the readings of the differential thermocouples to be reduced to zero. It was not thought necessary to use a similar arrangement at the downstream-end current conductors because data were not collected in that immediate neighborhood.

As a further defense against extraneous losses, the test section tube was suspended by monofilament nylon lines rather than being supported by rigid structural members. In addition, the test section, the plenum, and a mixing box positioned downstream of the test section were situated within an insulation enclosure. The enclosure consisted of a plywood box whose inner walls were lined with polystyrene sheet insulation. Silica aerogel powder with a thermal conductivity 15 percent less than that of air filled the core of the enclosure.

The test section tube was instrumented with 30-gage, specially calibrated copper-constantan thermocouples spot welded to its outer surface. The thermocouples were oriented so that the leads lay along the expected isothermal directions. In the first eight diameters of the tube, thermocouples were installed at twelve axial stations, and each such station was equipped with four thermocouples affixed 90 deg apart. The subsequent fifteen measurement stations were each equipped with two thermocouples.

Other Components and Instrumentation. To identify the other system components, it is convenient to follow the flow path of the air. The system was operated in the open-circuit mode, with air being supplied from a dryer-equipped regulated central compressor. After passing through a valve, regulator, and filter, the air was ducted to a settling chamber whose discharge was fed into the 65-diameters-long hydrodynamic development pipe. The settling chamber served to uncouple the airflow from its previous history, while the hydrodynamic development tube provided a well-defined velocity distribution at the plenum inlet. The air then passed through the plenum and the test section (as noted earlier, different test sections were used for the heat transfer and fluid flow experiments). At the test section exit, in the case of the heat transfer experiments, the air was mixed in a multiple-baffle mixing box. In both sets of experiments, the last component of the flow circuit was a rotameter which measured the volume flow. Two rotameters, both specifically calibrated, were employed to cover the investigated Reynolds number range (10,000 to 60,000).

The test section thermocouples have already been mentioned. In addition, two thermocouples threaded through the wall of the plenum served to measure the inlet bulk temperature of the air. A pair of thermocouples were also positioned in the mixing box at the downstream end of the test section. All thermocouples were read and recorded by a Fluke 2240B scanning, programmable datalogger having a 1 μV resolution.

For the pressure drop studies, the signals from the various taps were conveyed via plastic tubing to a selector switch, the output of which was sensed by a Baratron capacitance type, solid-state pressure meter capable of resolving 10^{-4} Torr.

Flow Visualization. The oil-lampblack technique was employed to facilitate visualization of the pattern of fluid flow adjacent to the walls of the plenum chamber. To enable a permanent record of the visualized flow patterns to be obtained, white, plasticized contact paper was applied to each portion of the plenum wall at which the flow was to be examined. A mixture of oil and lampblack powder, whose fluidity could be varied by using various oils and also by adding different proportions of lampblack to the oils, was applied to the surface of the contact paper. The mixture was either brushed on so that it covered a selected area of the surface or else was applied as a series of dots.

Under the action of the stresses exerted by the airflow, the mixture moved along the surface, and by doing so it revealed the direction of the flow adjacent to the surface. Once the visualization pattern had been established, the contact paper was removed from the plenum wall and placed flat on a cardboard backing. In this way, the visualization pattern was available for careful study and for photography.

Entry to the plenum chamber for installation and removal of the contact paper was via the movable end wall, which could be detached from the rest of the plenum. The installation and removal procedure required that a hand be inserted into the plenum. This was possible only for the larger of the two plenum diameters (i.e., $D/d = 6$), so that the visualization studies were confined to that plenum.

Visualization runs were attemped over the same range of Reynolds numbers as for the heat transfer experiments, but crisply defined flow pattern traces could be obtained only at the higher Reynolds numbers. This is because the shear stresses associated with the lower Reynolds number flows were too weak to move the oil-lampblack mixture (for these Reynolds numbers, the fluidity of the mixture was made as low as possible consistent with the avoidance of sagging).

Data Reduction

Heat Transfer Coefficients. The main focus of the data reduction was the evaluation of local heat transfer coefficients at each of the instrumented cross sections along the heated test section tube. The coefficients to be obtained are circumferential average values; however, as will be demonstrated later, even the largest circumferential variations were modest and were confined to the first few diameters downstream of the tube inlet.

The ingredients needed to evaluate the local coefficients are the convective heat transfer rate per unit surface area, the inside wall temperature, and the bulk temperature – all local quantities. The experimental data available for the determination of these quantities are the measured wall temperatures (on the outside of the tube) and the power input to the test section. It is readily shown by calculation that the temperature difference across the tube wall is negligible (actually, the same order as the resolving power of the instrumentation). Thus, the inside wall temperatures were obtained from the measured outside wall temperatures. At any axial station, x, the wall temperature was taken as the average of the circumferential temperature measurements and will, correspondingly, be denoted as $\bar{T}_{wx}$.

The procedure for determining the local heat flux and local bulk temperature will now be described. For the heat flux determination, the tube wall is subdivided into a succession of axial segments of length Δx_1, Δx_2, ... The axial boundaries of each segment are positioned midway between the neighboring temperature measurement stations. Each of these segments is used as a control volume for a heat balance. For each control volume, the following energy transfers are considered:

1 Internal heat generation, which is determined by prorating the power input to the test section as a whole
2 Axial heat conduction entering the control volume at its downstream face

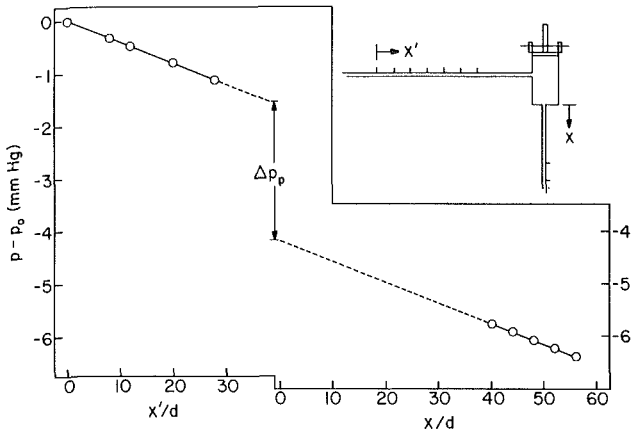

Fig. 2 Illustration of the determination of the net plenum-related pressure loss Δp_p. The data correspond to $D/d = 6$, $L_f/d = L_r/d = 5$, Re = 27,900.

3 Axial heat conduction leaving the control volume at its upstream face
4 Heat loss from the outer cylindrical surface of the control volume through the insulation and into the ambient air
5 Convective heat transfer from the inner cylindrical surface of the control volume to the airflow in the tube

The axial heat conduction terms (items 2 and 3) were evaluated from the measured wall temperatures with the aid of a central-difference form of Fourier's law. Item 4, the calculated heat loss though the insulation, was based on a conduction shape factor for the insulation enclosure that had previously been obtained from a finite difference solution.

From the foregoing, it is seen that all terms of the energy balance except the convective heat transfer (item 5) were evaluable from the experimental data, thereby enabling its determination. The convective heat transfer for each control volume was divided by the corresponding convective surface area, yielding the heat flux, q_x, where x is the coordinate of the temperature measurement station contained within the control volume. Aside from the first two or three measurement stations, where the net axial conduction was not negligible, q_x was essentially uniform along the test section tube.

The determination of the bulk temperature, T_{bx}, at x will now be described. For a fluid control volume which has the same axial boundaries as the tube-wall control volume, the bulk temperature rise of the air is

$$\Delta T_{b,cv} = Q_{cv}/\dot{m}c_p \tag{1}$$

where Q_{cv} is the convective heat transfer for the control volume (already evaluated as described in the preceding paragraph), and $\dot{m}$ and c_p respectively denote the mass flow rate and the specific heat. Repetitive application of equation (1) to the successive control volumes, starting with the measured inlet bulk temperature, T_{bi}, yields the bulk temperature at all of the axial boundaries of the control volumes. Then, for the axial station, x, within any given control volume, T_{bx} was obtained by linear interpolation between the bulk temperatures at the boundaries.

From the computations described in the foregoing, the local (circumferential average) heat transfer coefficient was obtained from

$$h = q_x/(\bar{T}_{wx} - T_{bx}) \tag{2}$$

which was then made dimensionless via the local Nusselt number

$$\mathrm{Nu} = hd/k \tag{3}$$

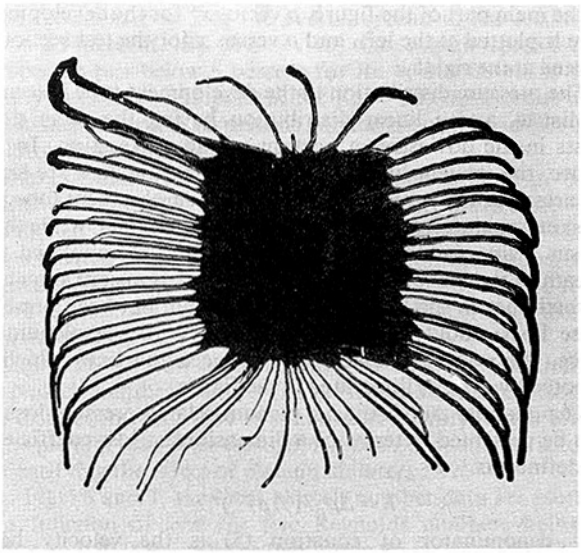

Fig. 3 Fluid flow pattern along the cylindrical wall of the plenum which faces the inlet port

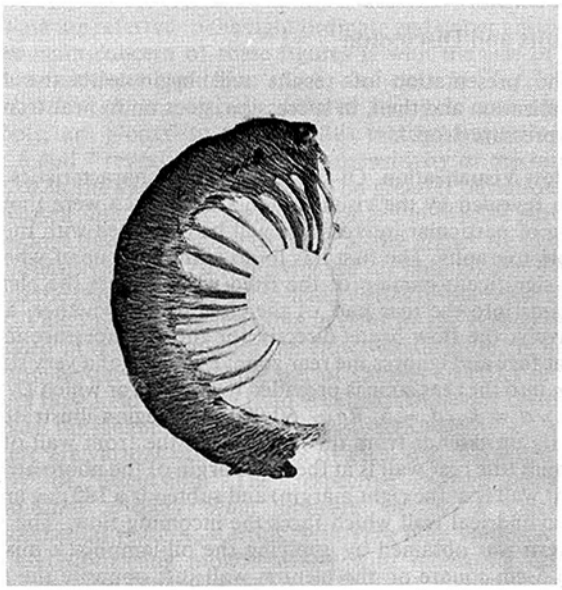

Fig. 4 Fluid flow pattern showing the presence of swirl at the plenum exit

The thermal conductivity appearing in equation (3) was based on the local bulk temperature.

The Nusselt number results are parameterized by the Reynolds number defined in the conventional manner for pipe flows

$$\mathrm{Re} = 4\dot{m}/\mu\pi d \tag{4}$$

where μ is the viscosity corresponding to the mean bulk temperature of the air.

Plenum-Related Pressure Loss. Attention is now turned to the net pressure loss due to the presence of the plenum, which is illustrated in Fig. 2. Although the figure corresponds to a specific case ($D/d = 6$, $L_f/d = L_r/d = 5$, $\mathrm{Re} = 27{,}900$), the character of the pressure distribution shown there pertains to all of the cases for which data were collected. A schematic diagram at the upper right of the figure shows the setup for the pressure measurements and identifies the coordinates x and x' which respectively correspond to axial stations in the test section tube and in the hydrodynamic development tube.

In the main part of the figure, p versus x' for the development tube is plotted at the left, and p versus x for the test section is plotted at the right.

The pressure distribution in the development tube is seen to be linear, and a linear distribution having the same slope exists in the downstream portion of the test section. In the figure, the straight lines that pass through the data are least-squares fits. The p versus x' line for the development tube has been extrapolated downstream to the plenum inlet, while the p versus x line for the test section has been extrapolated upstream to the plenum exit. These extrapolations are shown as dashed lines in the figure. Had the plenum not been present, these lines would have been colinear. With the plenum in place, there is a vertical offset between the lines which is denoted by Δp_p, as illustrated in the figure.

The quantity Δp_p is the net plenum-related pressure loss. It will be presented in terms of a dimensionless loss coefficient, K, defined as

$$K = \Delta p_p / (\tfrac{1}{2}\rho V^2)^* \tag{5}$$

The denominator of equation (5) is the velocity head corresponding to the density ρ^* of the air in the tube at the inlet of the plenum, so that

$$(\rho V^2)^* = \dot{m}^2 / \rho^* (\pi d^2/4)^2 \tag{6}$$

Results and Discussion

The presentation of results will begin with the flow visualization and then, in succession, goes on to heat transfer and pressure drop.

Flow Visualization. Of the various flow characteristics that were revealed by the visualization studies, two were thought to be of particular interest and will be described with the aid of photographs. The first has to do with the issue of whether any significant portion of the fluid which enters the plenum streams into the rear part of the chamber or whether, alternatively, the flow heads directly for the exit aperture in the front face and ignores the rear zone. Evidence of a very strong flow into the rear zone is provided by Fig. 3, for which D/d = 6, L_f/d = L_r/d = 5, Re ~ 60,000. The region illustrated in the figure extends from the rear wall to the front wall of the plenum (the rear wall is at the left margin of the photo and the front wall is at the right margin) and subtends a 180 deg arc on the cylindrical wall which faces the incoming flow. The flow pattern was obtained by applying the oil-lampblack mixture to a 5-cm square on the plenum wall just opposite the fluid inlet port.

It can be seen from the figure that after impinging on the wall, the air moves in all directions, but most of the flow is in the axial direction, either backward toward the rear wall of the plenum or forward toward the front wall. The strong backflow along the wall is quite remarkable. Since this backflowing fluid must eventually exit the plenum through the aperture in its front wall, it must turn (presumably at the very rear of the plenum) and then become a forward flowing axial stream.

The absence of a rear-zone expansion space (small L_r/d) eliminates the strong backflow shown in Fig. 3 and, by this, profoundly affects the pattern of fluid flow in the plenum. It would not be surprising, therefore, if the flow presented to the tube by the plenum were to be quite different for small L_r/d and large L_r/d. This matter will be revisited when the heat transfer results are presented.

The curling of the flow lines adjacent to the left and right margins of the photograph corresponds to the turning of the flow as it responds to the blocking action of the front and rear walls. Aside from the turning, strong circumferential motions are not in evidence.

The presence of circumferential motions near the end walls suggests the possibility that fluid passing from the plenum into the test section may carry with it a swirl. This is confirmed by the photograph presented in Fig. 4, which corresponds to D/d = 6, L_f/d = 5, L_r/d = 1, Re ~ 60,000. The flow pattern was obtained by applying the oil-lampblack mixture in the form of a 180 deg arc on the front face of the plenum. As is evident from the figure, the flow lines emanating from the arc are not radial but curved, indicating the existence of a swirling flow near the exit of the plenum (i.e., at the inlet of the test section). Swirl was also observed for the longer plenum ($L_f/d = L_r/d = 5$), but the flow lines were less sharply etched than those of Fig. 4. It may be expected that the swirl will affect the heat transfer in the test section.

Heat Transfer Results. The first set of heat transfer results to be presented is aimed at identifying the effects of the upstream fluid-flow geometry on the local Nusselt number distribution for turbulent heat transfer in a tube, and Fig. 5 has been prepared for this purpose. The figure consists of two graphs, respectively for Re = 10,700 and Re = 50,000. In each graph, the local Nusselt number is plotted as a function of the dimensionless axial coordinate x/d.

As illustrated schematically in the right-hand graph, the results for three different configurations are compared. The solid line corresponds to the present nonaligned inlet/exit plenum configuration, and the short-dashed lines are for a plenum with axially aligned inlet and exit. The third line (long dashes) depicts the results for a very short plenum so that, in effect, they correspond to the case of heat transfer in a tube preceded by an unheated hydrodynamic development section of the same diameter. Both comparison cases were taken from [1]. Although all of the results of Fig. 5 are experimental, the data points have been omitted to obtain greater clarity (the actual data for the present experiments will be reported in Figs. 6 and 7).

The present results shown in Fig. 5 are for D/d = 3, L_f/d = 5, L_r/d = 1, while those for the aligned inlet-exit configuration are for the same D/d and for a plenum length equal to $5d$ (the closest length-diameter ratio available for the comparison). Although the plotted results pertain to the aforementioned geometrical parameters, it is important to note that graphs which are both qualitatively and quantitatively similar to Fig. 5 would be obtained if the results for the other investigated geometrical parameters had been plotted.

Inspection of Fig. 5 shows that there is a definite ordering of the local Nusselt numbers with upstream fluid-flow geometry. Those for the nonaligned plenum inlet/exit are the highest, followed by those for the aligned plenum inlet/exit. The lowest Nusselt numbers are those for the no-plenum case.

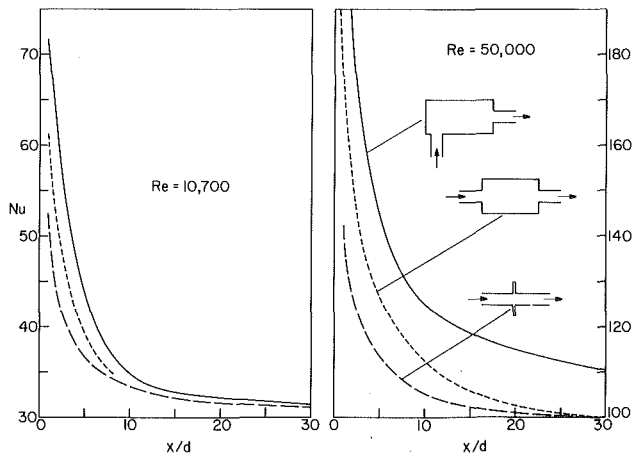

Fig. 5 Comparison of Nusselt number distributions corresponding to various upstream fluid-flow geometries

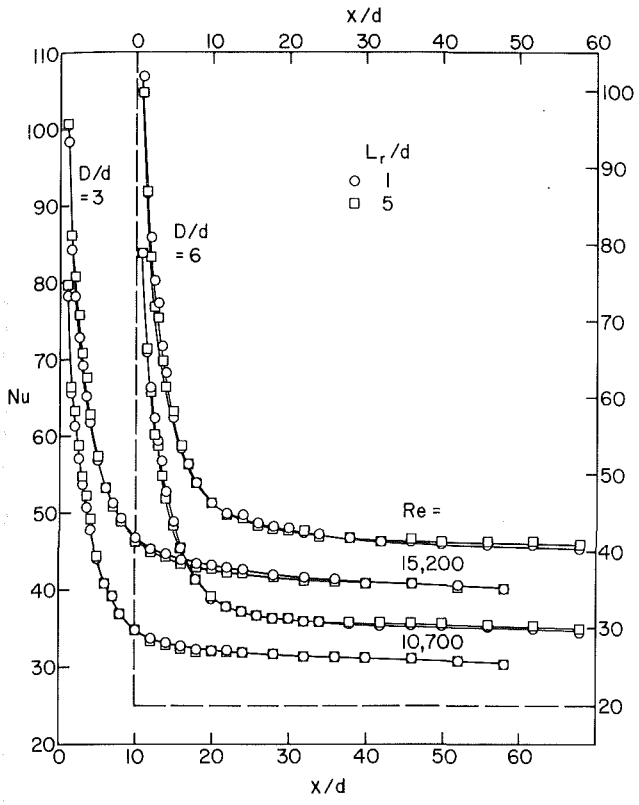

Fig. 6 Nusselt number distributions showing the effect of the size of the plenum rear-zone expansion space L_r/d, Re = 10,700 and 15,200

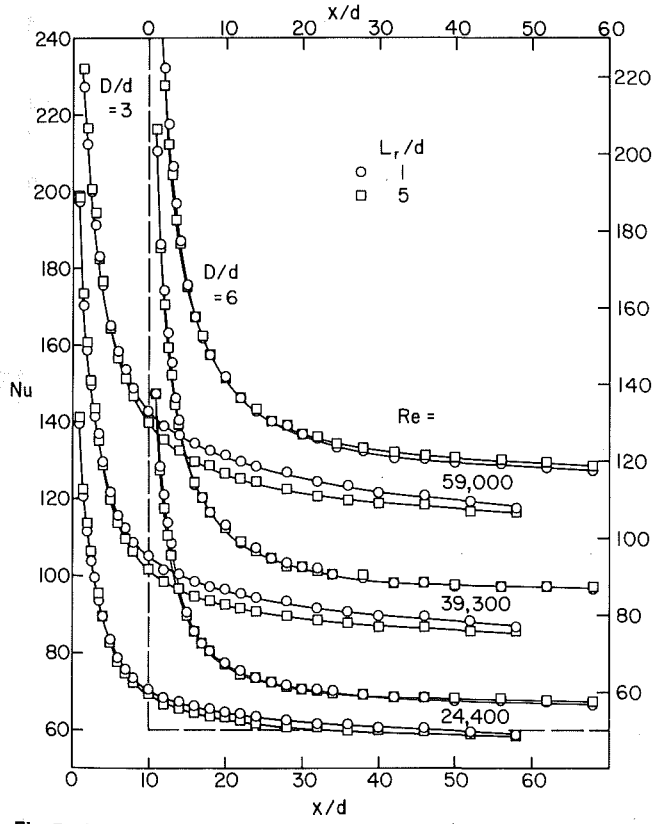

Fig. 7 Nusselt number distributions showing the effect of the size of the plenum rear-zone expansion space L_r/d, Re = 24,400, 39,300, and 59,000

As is to be expected, the greatest spread among the three sets of results occurs in the immediate neighborhood of the inlet, with decreasing deviations with increasing downstream distance. At $x/d = 2.5$, the overall spread in the results is about 35 percent. By $x/d = 10$, the overall spread has dropped to just below 5 percent for Re = 10,700 but is still slightly in excess of 15 percent for Re = 50,000. Even at $x/d = 30$, there is still a 10 percent enhancement in evidence for the latter Reynolds number.

The just-discussed ordering of the curves in Fig. 5 is consistent with physical expectation. In particular, the nonaligned plenum inlet/exit yields a more agitated flow, supplemented by swirl, than do the other configurations. The aligned plenum inlet/exit presents a non-fully-developed flow to the test section, thereby giving rise to higher coefficients than does the already developed flow.

Attention will now be turned to a detailed presentation of the Nusselt number results. The presentation will be made in two distinct formats – the first aimed at identifying the effect of the plenum rear-zone expansion space L_r/d, and the second at identifying the effect of plenum diameter D/d.

In Figs. 6 and 7, the local Nusselt number data are plotted as a function of x/d for five Reynolds numbers between 10,700 and 59,000, with the two lower Re presented in Fig. 6 and the three upper Re in Fig. 7. Each of these figures shows results for $D/d = 3$ and 6 on respective axes that are displaced both vertically and horizontally, so that the $D/d = 3$ data are referred to the left ordinate and lower abscissa while the $D/d = 6$ data are referred to the right ordinate and upper abscissa.

The main concern of these figures is with the size of the plenum rear-zone expansion space, and data for $L_r/d = 1$ and $L_r/d = 5$, respectively denoted by circle and square symbols, are plotted to examine this matter. Inspection of Figs. 6 and 7 reveals a remarkable insensitivity of the results to L_r/d in the range investigated. The greatest deviations in the Nusselt numbers for the two L_r/d are in the 3–4 percent range, and these tend more to occur at the higher Re values. The insensitivity to L_r/d is in evidence for both $D/d = 3$ and 6, with the results for the latter being virtually independent of L_r/d. This finding is remarkable in light of the expectations discussed in connection with the flow visualization. It may, perhaps, be due to a washing out of various specifics of the plenum flow field when the fluid is caused to sharply contract as it exits the plenum and enters the test section.

There are various other aspects of Figs. 6 and 7 which are worthy of discussion. The respective Nusselt number distributions display what appears to be a classical developmental pattern, starting with very high values at the inlet and decreasing monotonically with increasing downstream distance. The absence of evidence of flow separation at the sharp-edged inlet may, at first thought, seem somewhat surprising. However, in other experiments at Minnesota, unrelated to the present work, it was found that the separated flow reattaches upstream of $x/d = 1$. Since $x/d = 1$ is the first measurement station in the present apparatus, the possible flow separation could not be detected.

Another point worthy of mention is the persistence of a slow dropoff of the distributions in the far downstream portion of the tube. Indeed, fully developed conditions appear not to have been attained even at $x/d = 58$, the last measurement station. This behavior is believed due to the swirl which was carried into the test section tube from the plenum.

In this regard, the literature was examined and corroborating information encountered. Blum and Oliver [2] also obtained heat transfer coefficients which continued to drop off beyond the tube length at which fully developed turbulent heat transfer coefficients are normally obtained. In their investigation, swirl was generated by tangential injection of air near the entrance of a heated tube. By extrapolating the measured axial distributions of the heat transfer coefficient beyond the region of measurement, they estimated that about 100 diameters (from the inlet) would be required to obtain

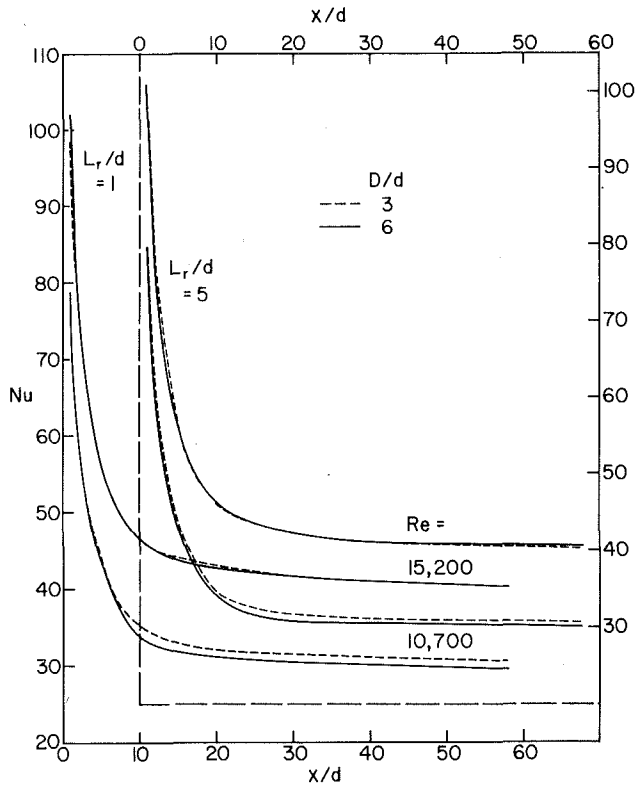

Fig. 8 Nusselt number distributions showing the effect of the plenum diameter *D/d*, Re = 10,700 and 15,200

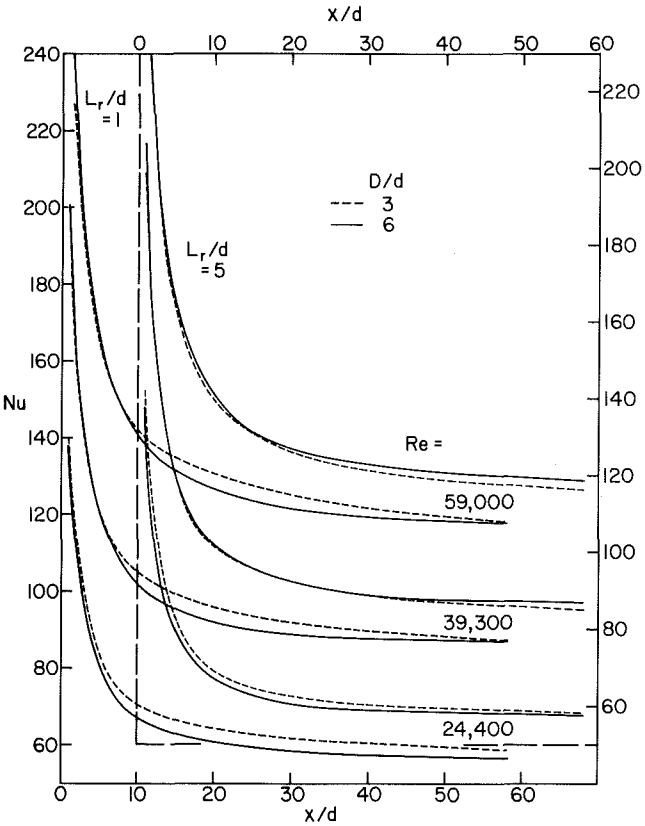

Fig. 9 Nusselt number distributions showing the effect of the plenum diameter *D/d*, Re = 24,400, 39,300 and 59,000

fully developed conditions at Re = 50,000. For a Reynolds number of approximately 7000, a 75-diameter estimate was made. The elongated development length for swirl-flow heat transfer was confirmed by Hay and West [3]. They found that

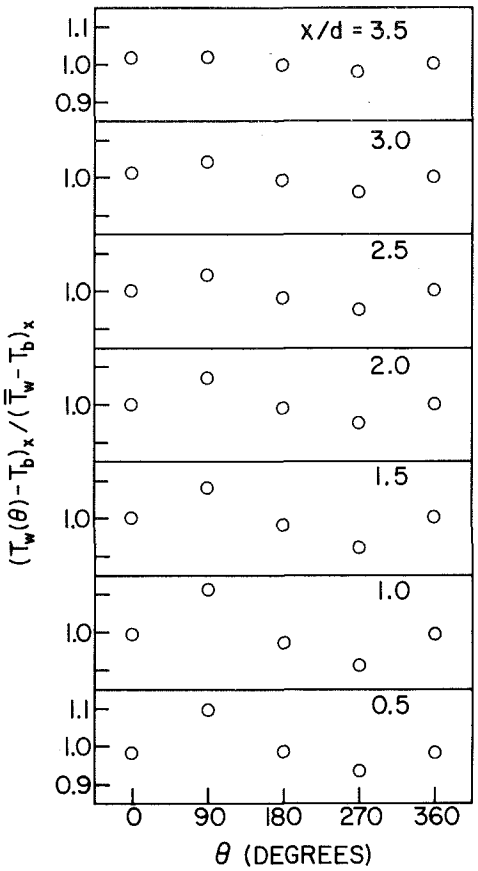

Fig. 10 Circumferential wall temperature distributions showing the largest variations encountered in all of the investigated cases

the heat transfer coefficients at 18 diameters from the pipe inlet (their last measuring station) were continuing the decrease that marks the thermal entrance region.

The data of Figs. 6 and 7 affirm the expected increase of the Nusselt number with Reynolds number at all axial stations. The Nusselt numbers at the downstream end of the tube will shortly be compared to literature correlations for fully developed heat transfer conditions.

Although Figs. 6 and 7 indicate a qualitatively similar behavior of the results for $D/d = 3$ and 6, these figures do not lend themselves to a quantitative comparison of the effect of D/d. To facilitate such a quantitative comparison, Figs. 8 and 9 have been prepared. Figures 8 and 9 are similar in structure to Figs. 6 and 7, but with the difference that results for different D/d are compared for a given L_r/d (Figs. 6 and 7, results for different L_r/d are compared for a given D/d). Figure 8 conveys results for Re = 10,700 and 15,200, while results for Re = 24,400, 39,300, and 59,000 are presented in Fig. 9. In each figure, the results for $L_r/d = 1$ and 5 are plotted on displaced axes to preserve clarity. The data points have been omitted from these figures because the actual data have already been presented in Figs. 6 and 7.

Examination of Figs. 8 and 9 shows that the effect of D/d is modest. For the most part, the spread between the curves for the two D/d values is no more than 4 percent, and there is only one case ($L_r/d = 1$, Re = 24,400) where a 6 percent spread is encountered. It appears that plenums with a smaller rear-zone expansion space (i.e., smaller L_r/d) are slightly more sensitive to D/d than are plenums with a larger expansion space.

When taken together, Figs. 6–9 indicate a general insensitivity of the local Nusselt number results to the plenum geometrical parameters that were investigated. Thus, the results presented here are of a universal character.

Table 1 Pressure loss coefficient K

L_f/d	L_r/d	D/d = 3	D/d = 6
3	1	1.83	1.68
3	5	1.86	1.73
5	1	1.68	1.79
5	5	1.75	1.66

Although thermally developed conditions were not strictly attained in the far downstream portion of the tube, it is evident from the foregoing figures that fully developed Nusselt numbers were being approached. In this regard, it is interesting to compare the measured coefficients at the last axial station (x/d = 58) with the well-established Petukhov-Popov equation [4] for fully developed heat transfer. The comparison shows that the present data deviate by no more than 6 percent from the Petukhov-Popov equation, which is its purported accuracy.

As a final matter in the presentation of the heat transfer results, brief consideration will be given to the circumferential variations induced by the nonaligned plenum inlet and exit. The nonalignment causes circumferential nonuniformities in the velocity entering the test section.

A presentation of the *extreme* circumferential variations encountered in all of the investigated cases is shown in Fig. 10. This figure contains a succession of graphs, each for a given x/d ranging from 0.5 to 3.5. In each graph, the measured circumferential wall-temperature distribution is plotted as a function of the angle, θ. The temperature distribution is presented in dimensionless form, with $(T_{wx}(\theta)\text{-}T_{bx})$ as the numerator and $(\bar{T}_{wx} - T_{bx})$ as the denominator. For purposes of orientation, θ values between 180 and 360 deg are on the side of the tube opposite the plenum inlet port, while angles between 0 and 180 deg are on the same side as the inlet port. The results shown in Fig. 10 are for D/d = 6, L_f/d = 5, L_r/d = 1, and Re = 59,000.

From Fig. 10, it is seen that the circumferential temperature distribution is nearly sinusoidal, with a maximum at θ = 90 deg and a minimum at θ = 270 deg. Since the flow entering the tube is expected to be concentrated on the side opposite the plenum inlet port, the temperature minimum at θ = 270 deg is altogether reasonable, as is the maximum at θ = 90 deg.

The amplitude of the variation (relative to the mean) is about 10 percent at the first two measurement stations, whereafter it decreases such that at x/d = 3.5 temperature uniformity is nearly established. It should be emphasized that these are the largest amplitudes that were encountered. Thus, it can be concluded that circumferential variations are moderate and do not merit special consideration for most applications.

Plenum-Related Pressure Losses. The net plenum-related pressure loss, Δp_p, was illustrated in Fig. 2, and its dimensionless counterpart, K, was defined in equation (5). For a fixed plenum geometry, K was found to be relatively insensitive to the Reynolds number, with typical variations being ± 3 percent about the mean. This behavior indicates that inertial losses dominate over friction losses.

The mean value of K for each of the investigated geometrical configurations is listed in Table 1. The range of K is seen to be markedly narrow – between 1.66 and 1.86 – and there are no consistent trends with the geometrical parameters. An overall average is 1.75, and this value may be suitable for most design purposes. In round numbers, the mean K value for the present nonaligned plenum inlet/exit configuration exceeds that for an axially aligned inlet/exit configuration [1] by about one.

The accuracy of the K values was assessed using a realistic estimate of ± 3 percent as the uncertainty in the fully developed pressure gradient in the test section tube. The corresponding uncertainty in K is ± 1.2 to 2 percent depending on the Reynolds number.

Concluding Remarks

The present investigation appears to be the first systematic experimental study of the effect of a nonaligned plenum inlet/exit configuration on the turbulent heat transfer characteristics of a tube fed by the plenum. Pressure drop measurements and flow visualization were performed to supplement the heat transfer experiments. The plenum used in the experiments was a cylinder with a radial inlet and an axial exit.

The flow visualization showed that when there is an expansion space in the plenum to the rear of the inlet port, the entering fluid tends to stream into that space before turning and heading toward the exit in the front face of the plenum. The presence of swirl in the flow entering the test section tube was also confirmed by the visualization.

The perturbed, nonaxisymmetric flow induced in the plenum by the nonaligned inlet and exit gives rise to enhanced heat transfer in the test section. Enhancement was identified by comparisons with results for a tube fed either by a plenum with axially aligned inlet and exit or by an unheated hydrodynamic development tube having a diameter equal to that of the test section. The extent of the enhancement is greater at higher Reynolds numbers.

The distributions of the local Nusselt number along the length of the test section at a given Reynolds number was found to be quite insensitive to the investigated geometrical parameters – the size of the plenum rear-zone expansion space and the plenum diameter. The distribution curves did not show evidence of flow separation at the inlet, but separation might have occurred upstream of the first measurement station (x/d = 1). A slow dropoff of the curves persisted even in the far downstream portion of the tube. The elongated thermal development length is due to the swirl that was carried into the test section from the plenum. The Nusselt numbers at the last measurement station agreed well with those from the Petukhov-Popov equation.

Circumferential temperature variations induced by the nonaxisymmetric flow entering the test section tube were moderate and were confined to the immediate neighborhood of the inlet.

The net pressure loss induced by the plenum, nondimensionalized by the velocity head, was relatively insensitive to both the Reynolds number and the geometrical parameters. The mean value of the pressure loss is 1.75 velocity heads.

Acknowledgment

This research was performed under the auspices of the Power Program of the Office of Naval Research.

References

1 Lau, S. C., Sparrow, E. M., and Ramsey, J. W., "Effect of Plenum Length and Diameter on Turbulent Heat Transfer in a Downstream Tube and on Plenum-Related Pressures Losses," ASME JOURNAL OF HEAT TRANSFER, Vol. 103, 1981, pp. 415–422.

2 Blum, H. A., and Oliver, L. R., "Heat Transfer in a Decaying Vortex System," ASME Paper No. 66-WA/HT-62, 1966.

3 Hay, N., and West, P. D., "Heat Transfer in Free Swirling Flow in a Pipe," ASME JOURNAL OF HEAT TRANSFER, Vol. 97, 1975, pp. 411–416.

4 Petukhov, B. S., "Heat Transfer and Friction in Turbulent Flow With Variable Physical Properties," in *Advances in Heat Transfer*, Vol. 6, 1970, pp. 503–564.

Heat Transfer From the Heated Convex Wall of a Return Bend With Rectangular Cross Section

N. Seki
Professor.

S. Fukusako
Associate Professor.

M. Yoneta
Graduate Student.

Department of Mechanical Engineering,
Hokkaido University,
Sapporo 060, Japan

An experimental investigation has been performed to clarify the turbulent heat transfer characteristics along the heated convex wall of a return bend which has a rectangular cross section with large aspect ratio for various heights of the duct. The experiments are carried out under the condition that the convex wall is heated at constant heat flux while the concave wall is insulated. Water is used as the working fluid with duct heights of 15, 40, 60 and 80 mm, Reynolds numbers of 8×10^3 to 8×10^4, and Prandtl numbers ranging from 6.5 to 8.5. The mean and the local heat transfer coefficients are always smaller than those for the straight parallel plates and straight ducts. Both the local and the mean heat transfer coefficients decrease as the duct height increases. Near the outlet region of the return bend the local heat transfer coefficient increases in the flow direction as the height decreases. Behavior is just the opposite at the inlet. Correlation equations for the mean and the local Nusselt numbers are determined in the range of parameters covered.

Introduction

A number of investigations on heat transfer in curved ducts with rectangular cross sections have been carried out, because of their wide application. The bulk of the previous work on the turbulent heat transfer in curved ducts with rectangular cross section seems to have been directed toward experimental investigation, though the laminar heat transfer investigations have been mainly analytical [1, 2]. Representative contributions to the heat transfer literature in the turbulent region may be found in the works by Kreith [3], Uchida and Koizumi [4] and Mayle et al. [5]. Kreith [3] investigated analytically the turbulent heat transfer from the convex and concave walls of the rectangular cross-sectional curved duct, when the fluid flow is hydrodynamically and thermally fully developed, for the Reynolds numbers ranging from 10^4 to 10^6 with the Prandtl numbers varied from 10^{-2} to 10^2. He also completed measurements using water and alcohol as test fluid. Uchida and Koizumi [4] treated the same problem finding mean heat transfer coefficients, both numerically and experimentally. Mayle et al. [5] measured local turbulent heat transfer characteristics along the convex and concave walls, respectively, of the $\pi/2$ [rad] curved duct utilizing air as the working fluid. In spite of these studies, however, it appears that the turbulent local heat transfer characteristics in the thermal boundary layer along the heated convex wall of a return bend with rectangular cross section and large aspect ratio, W/c, are not well understood, particularly as concerns the effects of duct height and radius of curvature.

In the present study, the effects of duct height, radius of curvature, velocity of fluid, and Prandtl number on the local heat transfer from the convex wall, in the thermal entrance region, are determined.

Experimental Apparatus and Procedure

Experimental Apparatus. The schematic diagram of the apparatus is presented in Fig. 1. The apparatus consists of a test section, a system of thermometric measuring instruments, an entrance duct with rectangular cross section made of lucite (400 mm in width), a contracted duct, a heat exchanger, a storage tank, a controlling valve, an orifice meter, and a centrifugal pump.

The convex wall forms a hydrodynamically smooth cylindrical surface with a radius of curvature of 121 mm. Thirty copper strips (2 mm in thickness and rolled to 121 mm in radius) are arranged in three columns across the width of the convex wall and in ten rows across the streamwise direction, as shown in Fig. 2. The copper strips are thermally isolated from each other with a low thermal conductivity filler and firmly contact with mica heaters, as shown in Fig. 2. The convex wall is heated using ten main mica heaters. Guard heaters are mounted underneath the main heaters, spaced with a bakelite plate of 2-mm thickness, to prevent heat loss from the main heaters to the environment. In order to insure thermal two-dimensionality along the convex wall, guard heaters are arrayed on both sides of the main heaters, as shown in Fig. 2, using Nichrome belts (0.14 mm in thickness and 0.8 mm in width) as the heating material. The heaters are electrically isolated so that the electrical power input could be related directly to the local heat transfer.

Seventy Chromel-Alumel thermocouples (0.1 mm in diameter) are soldered into small holes drilled in the copper strips from the underside, to measure the surface temperature. Moreover, 140 similar thermocouples are buried on the both sides of the bakelite plate to monitor the guard heater requirements.

The concave wall is covered with insulation and has the structure which can be changed to vary the duct height. A thermocouple probe and Pitot tube with traversing device are installed upstream of 200 mm before the inlet.

Experimental Procedure. The flow of water is provided by the centrifugal pump at a flow rate measured with the orifice meter. The water enters the test section as the fully developed turbulent flow through the contracted duct with an entrance duct 4 m in length. The convex wall is heated at constant heat flux from $\theta = 0$ to π [rad], where θ is angle of advance of convex wall in the flow direction. After heating in the test section, the water is cooled in a heat exchanger to gain the proper inlet temperature. All measurements of heat transfer are carried out after the test section has reached a thermally steady state, which takes 6 to 8 hrs. The flow rate is changed with the controlling valve.

The heat loss from the main heaters to the environment or the excess guard heater input to the main heaters is ascertained to be less than 5 percent, respectively, from the result of the preliminary experiment.

Contributed by the Heat Transfer Division for publication in the JOURNAL OF HEAT TRANSFER. Manuscript received by the Heat Transfer Division September 2, 1981.

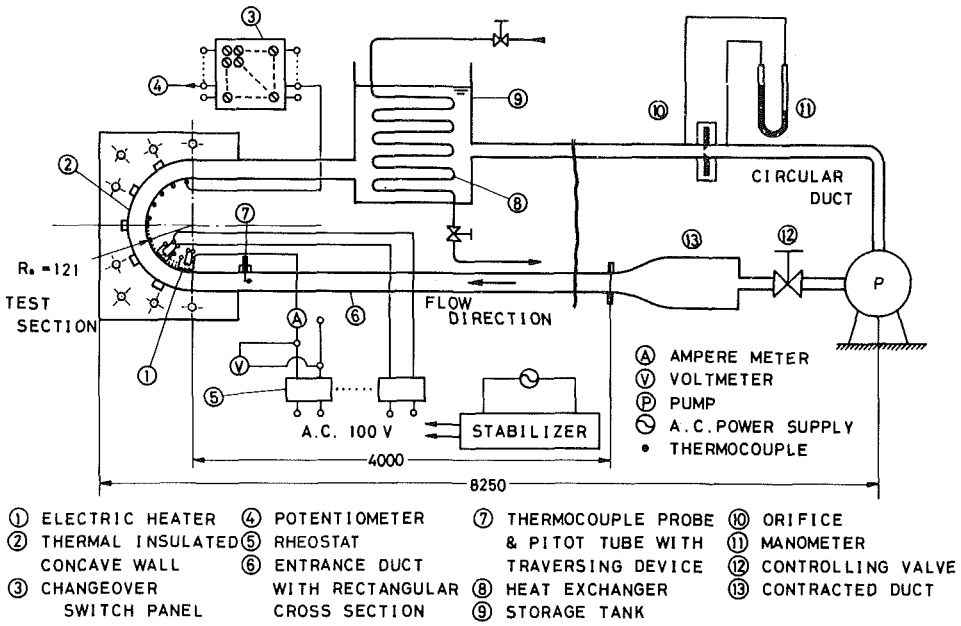

Fig. 1 Schematic drawing of experimental apparatus

Results and Discussion

Velocity Profile of Inflow and Definition of Local Nusselt Number. Since the fluid has passed through a long entrance duct, it is fully developed in the inlet of the return bend. The velocity profile just before the inlet was measured with a Pitot tube. It was observed that at every Reynolds number the velocity profile approximates the $1/n$-power law ($n \simeq 8.5$).

The representative temperature is the inlet temperature of the bend, T_{in}. All the physical properties in the present study are determined based on this temperature. The local Nusselt number, Nu, is also based on T_{in} as follows:

$$\mathrm{Nu} = h \cdot (2c)/\lambda = q \cdot (2c)/\{\lambda (T - T_{in})\} \quad (1)$$

Local Nusselt Number Distribution. The distribution of local Nusselt number is presented in Fig. 3 for four duct heights ($c = 15$, 40, 60, 80 mm) and various Reynolds numbers. At the inlet of the return bend, Nu decreases with increasing x, yielding the typical characteristic of a thermal entrance region.

The local distribution of $(\mathrm{Nu}/\overline{\mathrm{Nu}})$, that is, the ratio of the local Nusselt number to the mean Nusselt number, $\overline{\mathrm{Nu}}$ $(= \bar{h} \cdot (2c)/\lambda)$, where $\bar{h}$ is mean heat transfer coefficient defined in equation (2), is presented in Fig. 4

Nomenclature

c = duct height
c_p = specific heat at constant pressure
De = local Dean number, $(\bar{u} \cdot x/\nu)\sqrt{c/R}$
$\overline{\mathrm{De}}$ = Dean number, $\{\bar{u} \cdot (2c)/\nu\}\sqrt{c/R}$
d_e = hydraulic diameter of duct
F = Richardson number, defined in equation (9)
f_c = centrifugal force per unit volume, $\rho(\bar{u}^2/R)$
$\bar{h}$ = mean heat transfer coefficient, defined in equation (2)
h = local heat transfer coefficient at x
K = rate of increase of $(\mathrm{Nu})_{d_e}/(\mathrm{Nu}_\infty)d_e$ in x-direction, defined in equation (4)
Nu = local Nusselt number, defined in equation (1)
$\overline{\mathrm{Nu}}$ = mean Nusselt number, $\bar{h} \cdot (2c)/\lambda$
Nu_∞ = Nusselt number of hydrodynamically and thermally fully developed straight flow
n = reciprocal of exponent of $1/n$-power law
Pr = Prandtl number, $\mu \cdot c_p/\lambda$
q = constant heat flux from convex wall
R = radius of curvature of center line of passage in return bend, $R_0 + c/2$
Re = local Reynolds number, $\bar{u} \cdot x/\nu$
$\bar{\mathrm{Re}}$ = Reynolds number, $\bar{u} \cdot (2c)/\nu$
Re_d = Reynolds number based on d_e, $\bar{u} \cdot d_e/\nu$
R_0 = radius of curvature of convex wall
T = local temperature on convex wall at x
T_{in} = temperature in inlet of return bend
u = fluid velocity
$\bar{u}$ = mean fluid velocity
u^+ = u/u^*
u^* = friction velocity, $\sqrt{\tau_w/\rho}$
W = width of duct
x = streamwise coordinate along convex wall with origin at beginning of heating
y = coordinate perpendicular to x
y^+ = $u^* \cdot y/\nu$

Greek Symbols

δ^{**} = momentum thickness
θ = angle of advance of convex wall taken from inlet
θ_1, θ_2 = angle of advance to define K $(\theta_1 < \theta_2)$
λ = thermal conductivity of fluid
μ = coefficient of viscosity of fluid
ν = kinematic viscosity of fluid
ρ = density of fluid
τ_w = wall shear stress
Φ = implicit function to determine h
χ = $\bar{\mathrm{Re}}^{1.25} \cdot \bar{\mathrm{De}}^{-0.25} \cdot \mathrm{Pr}^{0.5}$
χ^+ = $\mathrm{Re}^{1.9} \cdot \mathrm{De}^{-2.1} \cdot \mathrm{F}^{0.8} \cdot \mathrm{Pr}^{0.3}$

Subscripts

d_e = condition based on hydraulic diameter
in = bend inlet
L = condition in which equation (7) is realized
∞ = condition of hydrodynamically and thermaly fully developed straight flow

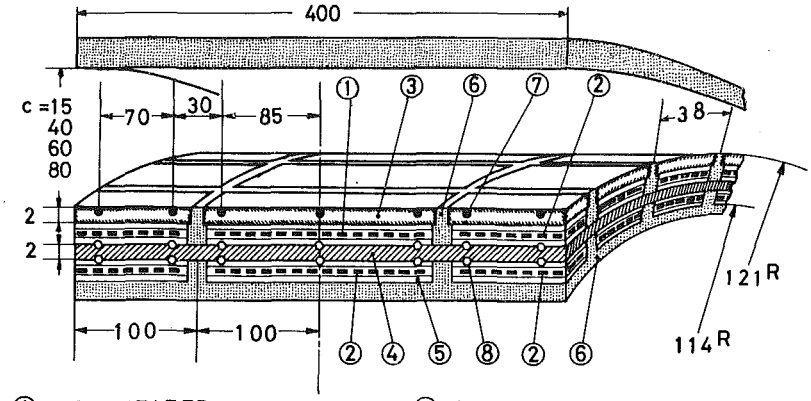

Fig. 2 Detailed sketch of heater

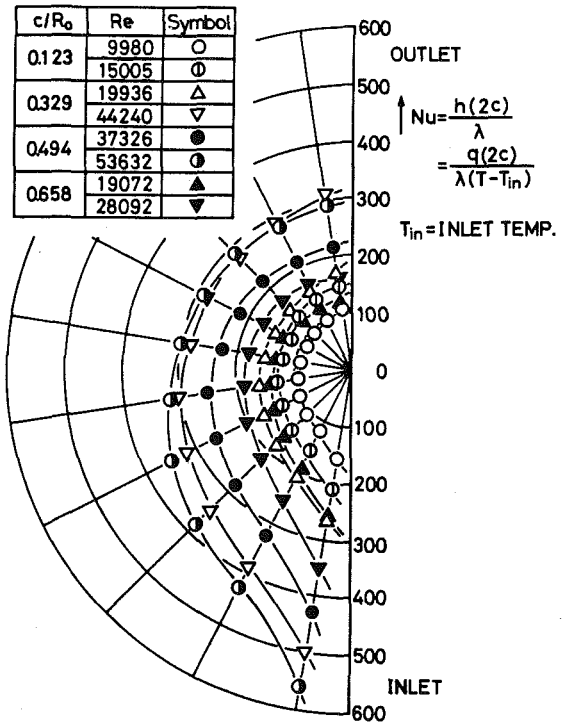

Fig. 3 Local Nusselt number distribution

$$\bar{h} = (1/\pi R_0)\int_0^{\pi R_0} h\, dx \qquad (2)$$

The curves in Fig. 4 show that the distributions of the heat transfer coefficients for various duct heights are weakly influenced by the variation of Reynolds number. This seems to imply that the local heat transfer coefficient is characterized more predominantly by the duct height rather than the Reynolds number.

Comparison of Heat Transfer Characteristics between Flow along Convex Wall and Straight Flow. In Fig. 6, the present measurements are compared with experimental and analytical findings for hydrodynamically fully developed flow through a straight duct or parallel plates in the thermal entrance region. In Fig. 5, the abscissa, the distance, is normalized by the hydraulic diameter of duct and the ordinate is

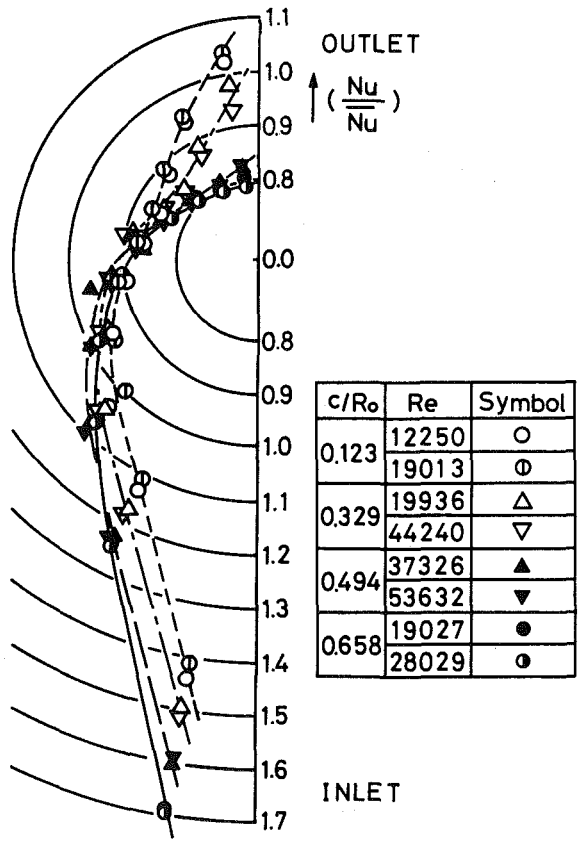

Fig. 4 Nu/Nu distribution

$(\mathrm{Nu})_{d_e}/(\mathrm{Nu}_\infty)_{d_e}$, where $(\mathrm{Nu})_{d_e}$ $(= h \cdot d_e/\lambda)$ is local Nusselt number based on d_e, and $(\mathrm{Nu}_\infty)_{d_e}$ is Nusselt number for thermally and hydrodynamically fully developed flow through a straight duct. $(\mathrm{Nu}_\infty)_{d_e}$ is due to Deissler's equation [6] in the present work. The Deissler equation is

$$(\mathrm{Nu}_\infty)_{d_e} = \frac{0.0396\mathrm{Re}_d^{0.75}\mathrm{Pr}}{1+1.7\mathrm{Pr}^{-1/4}\mathrm{Re}_d^{-0.125}(\mathrm{Pr}-1)} \quad (\mathrm{Pr}>0.5) \qquad (3)$$

The present experimental results show that the local heat transfer rate in the turbulent flow along the heated convex wall of the return bend is greatly influenced by the variation

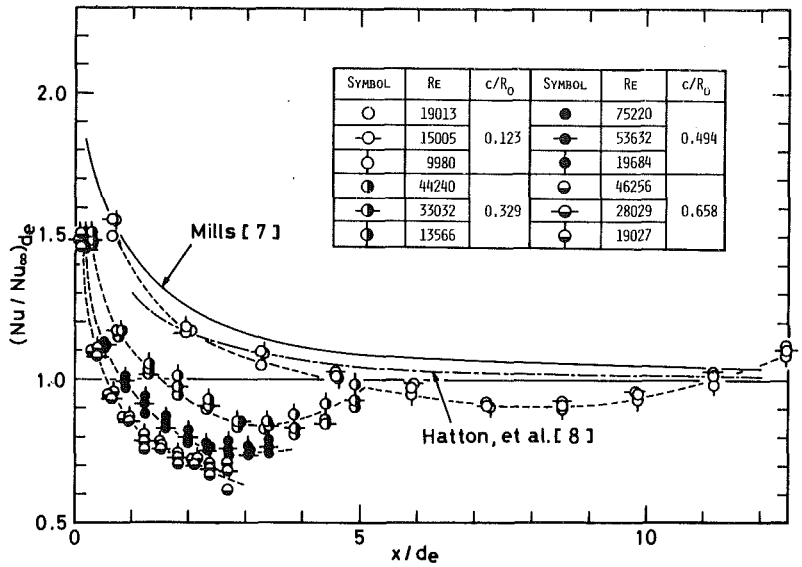

Fig. 5 Comparison of heat transfer characteristic between flow along convex wall and straight flow

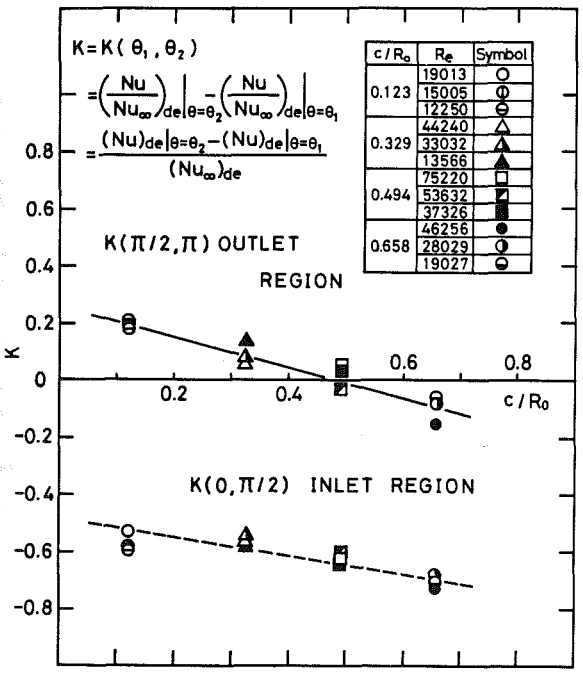

Fig. 6 Rates of increase in local Nusselt number for different duct heights

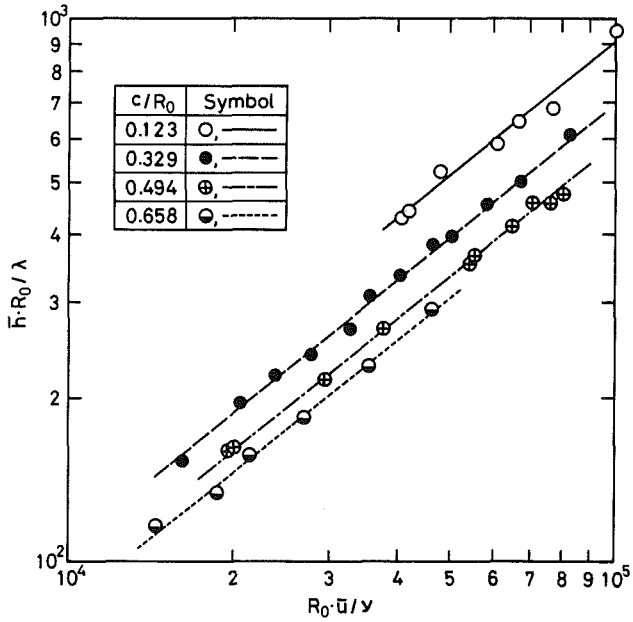

Fig. 7 Relation between mean heat transfer rate and mean velocity

of duct height. As the duct height is reduced, $(Nu/Nu_\infty)_{d_e}$ increases for all values of x/d_e, particularly near the outlet region of the return bend. The values of $(Nu/Nu_\infty)_{d_e}$ from the present study are almost always less than those for a straight duct [7] and parallel plates [8]; the latter involving one surface heated at constant heat flux while the other is adiabatic. An exception is observed near the outlet region of the return bend with the duct height of 15 mm (c/R_0 = 0.123). However, it should be noted that the local heat transfer coefficient along the heated convex wall of a return bend tends to approach to that along the wall of a straight duct or parallel plates as duct height is decreased and can become greater if the duct height is small enough, e.g., the present data for c/R_0 of 0.123 in the range of (x/d_e) from about 11 to 12.5 in Fig. 5.

The analytical result by Kreith [3] and the experimental one by Mayle et al. [5] indicate that the heat transfer coefficient along the convex wall is generally less than that along the flat plate. This agrees with present findings, although the effect of the height-variation is not dealt with in the earlier studies. According to the work by So and Mellor [9], both the wall shear stresses on the convex wall and the Reynolds stresses near the wall are always less than those on and near the flat plate, respectively, in the turbulent boundary layer. Thereby it is quite reasonable that the diffusivity for heat near the convex wall is less than that near the flat plate. Centrifugal force causes the reduction of wall shear stresses on the convex wall and, thereby, the reduction of heat transfer coefficient. In the outlet of the return bend, however, the direction of the passage turns suddenly at an angle of π [rad] with that in the inlet. Therefore, the centrifugal force is alleviated, which contributes to the rise of the heat transfer coefficient in the outlet region of the convex wall observed in Fig. 5. According to the work by Ellis and Joubert [10], flow in a curved duct tends to approach that in the straight duct having the same duct height and aspect ratio as c/R decreases. They also show that the flow developes sooner as c/R is decreased. This suggests that the eddy diffusivity for heat in the outlet region

along the convex wall will be influenced significantly by the variation of duct height.

Heat Transfer Characteristics in Inlet and Outlet Regions. The rate of increase of $(\mathrm{Nu}_x)_{d_e}/(\mathrm{Nu}_\infty)_{d_e}$ in the flow direction, K, which is defined in equation (4),

$$K = K(\theta_1,\theta_2) = (\mathrm{Nu}_x)_{d_e}/(\mathrm{Nu}_\infty)_{d_e}\,|_{\theta=\theta_2} - (\mathrm{Nu}_x)_{d_e}/(\mathrm{Nu}_\infty)_{d_e}\,|_{\theta=\theta_1}$$
$$= \{(\mathrm{Nu}_x)_{d_e}\,|_{\theta=\theta_2} - (\mathrm{Nu}_x)_{d_e}\,|_{\theta=\theta_1}\}/(\mathrm{Nu}_\infty)_{d_e}$$
$$(\theta_1 < \theta_2,\ 0 \leqq \theta_1, \theta_2 \leqq \pi) \qquad (4)$$

is illustrated in Fig. 6. In the inlet region along the convex wall, the value of K is always negative, characteristic of thermal entrance region, and also decreases monotonically with an increase in c/R_0. On the other hand, in the outlet region if $(c/R_0) < 0.5$, K is positive while if $(c/R_0) > 0.5$, K is negative, exhibiting significantly different phenomenon from the inlet region.

Characteristic of Mean Nusselt Number. In Fig. 7, $\bar{h}\cdot R_0/\lambda$ is plotted against $\bar{u}\cdot R_0/\nu$. Since R_0 is constant, Fig. 7 shows that as the duct height is reduced, the mean heat transfer rate is increased for fluid velocity. It can be observed that the mean heat transfer rate for $c/R_0 = 0.123$ is about 1.65 times as large as that for $c/R_0 = 0.658$, for the same flow velocity in Fig. 7.

Cheng et al. [1] solved the laminar heat transfer problem in curved square channels in the thermal entrance region numerically and introduced the relation between the asymptotic Nusselt number and Dean number, adopting Prandtl number as a parameter. However, in the turbulent region the mean Nusselt number of a return bend cannot be expressed by only the Dean number and the Prandtl number. The Dean number is a quotient of the geometrical mean of centrifugal force and inertia force divided by viscous shear force and cannot express the effect of virtual turbulent shear stress owing to eddy viscosity. Therefore, introducing Reynolds number correctively in addition to Dean number and Prandtl number, it appears that the mean Nusselt number, $\overline{\mathrm{Nu}}$, may be described by equation (5), which is also illustrated in Fig. 8.

$$\overline{\mathrm{Nu}} = 0.0318\,\overline{\mathrm{Re}}^{0.971}\cdot\overline{\mathrm{De}}^{-0.194}\cdot\mathrm{Pr}^{0.389}$$

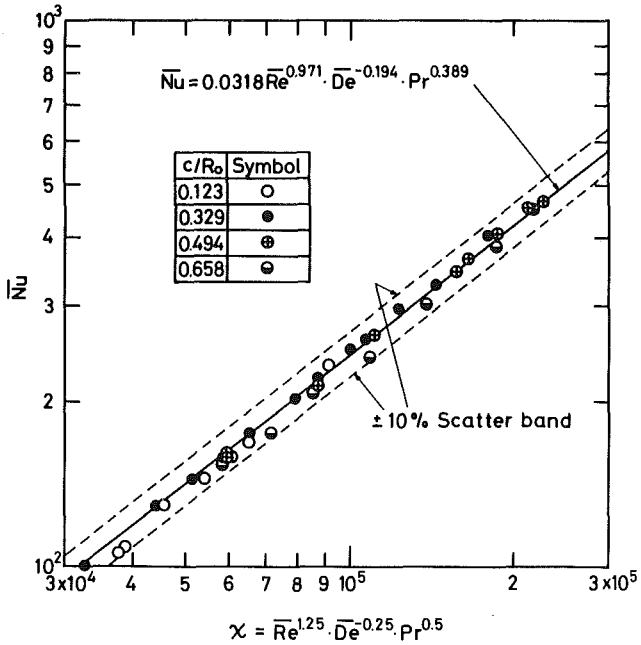

Fig. 8 Correlation of mean Nusselt number

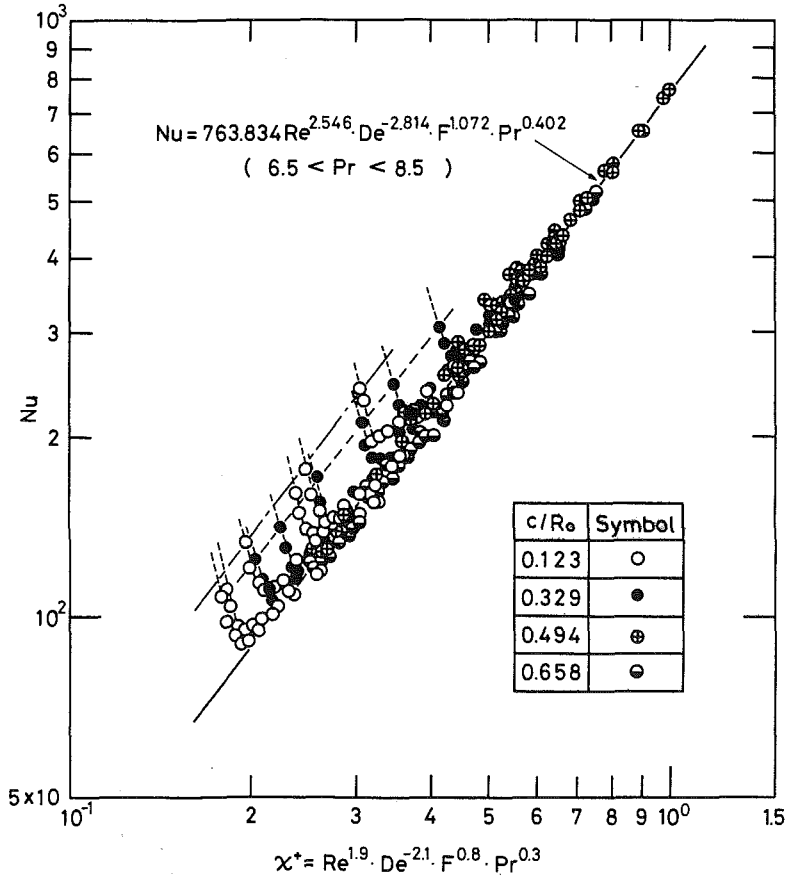

Fig. 9 Correlation of local Nusselt number

$$(8 \times 10^3 < \mathrm{Re} < 8 \times 10^4,\ 6.5 < \mathrm{Pr} < 8.5) \quad (5)$$

Correlation Equation of Local Nusselt Number. The local heat transfer coefficient on the convex wall, h, can be written as the implicit function as follows

$$h = \Phi(x, c, R, f_c, \bar{u}, u^*, \mu, \rho, \lambda, c_p) \quad (6)$$

where f_c is centrifugal force per unit volume; u^*, friction velocity; and μ, viscosity; respectively. In general, the wall shear stress, τ_w, or friction velocity, u^*, on the convex wall must be treated as an unknown. However, So and Mellor [9] measured velocity distributions in the turbulent boundary layers on the convex wall in detail, utilizing air as a testing fluid, and found that there exists a layer corresponding to the buffer-layer in the turbulent boundary layer on the flat plate in which the following logarithmic law holds

$$u^+ = 5.6 \log_{10} y^+ + 4.9 \quad (7)$$

According to the work by Klebanoff [11] the value of shear stress in the buffer-layer when y^+ is small enough, is approximately equal to that in the viscous sublayer. Therefore, the physical meaning of equation (6) can still be maintained sufficiently if $(\partial u/\partial y)_L$ is taken in place of u^* in equation (6). Performing dimensional analysis in terms of equation (6) yields the following correlation equation:

$$\mathrm{Nu} = 763.834\ \mathrm{Re}^{2.546} \cdot \mathrm{De}^{-2.814} \cdot F^{1.072} \cdot \mathrm{Pr}^{0.402}$$

$$(0 \leqq x/\pi R_0 \leqq 1,\ 6.5 < \mathrm{Pr} < 8.5,\ 8 \times 10^3 < \mathrm{Re} < 10^4) \quad (8)$$

which is also illustrated in Fig. 9. F is the Richardson number, defined as follows

$$F = 2(\bar{u}/R)/(\partial u/\partial y)_L \quad (9)$$

Equation (8) is in good agreement with the present data in Fig. 9, except near the outlet region of the return bend having a relatively small duct height. As the duct height decreases, Nu tends to deviate upward from equation (8) with an increase in x (corresponding to decrease in χ^+). Moreover, in Fig. 9 it can be observed that the points which coincide with the values of Nu near the terminus of curvature in the outlet of the return bend for each duct height form a nearly straight line parallel to equation (8).

Concluding Remarks

Experimental results were obtained for heat transfer from the convex wall of a return bend having a rectangular cross section and a large aspect ratio. The following major concluding remarks may be drawn in the range of parameters covered.

1 Both the mean and the local heat transfer coefficients are almost always smaller than those for the straight parallel plates and straight ducts.

2 The mean heat transfer coefficient decreases as the duct height increases.

3 Equation (5) provides a satisfactory correlation for the mean Nusselt number.

4 Near the inlet of the return bend, increasing the duct height causes local heat transfer coefficient to decrease more rapidly in the flow direction.

5 Near the outlet of the return bend, if $c/R_0 < 0.5$, the local heat transfer coefficient increases in the flow direction, while if $c/R_0 < 0.5$, the opposite trend is observed.

6 Equation (8) provides a satisfactory correlation for the local Nusselt number.

$$\mathrm{Nu} = 763.834\ \mathrm{Re}^{2.546} \cdot \mathrm{De}^{-2.814} \cdot F^{1.072} \cdot \mathrm{Pr}^{0.402}$$

Acknowledgment

The authors wish to thank N. Ebina and T. Jyouraku for their technical support in making the experimental and the preliminary experimental apparatus, respectively.

References

1 Cheng, K. C., Lin, R. C., and Ou, J. W., "Graetz Problem in Curved Square Channels," ASME JOURNAL OF HEAT TRANSFER, Vol. 97, 1975, pp. 244–248.

2 Yee, G., Chilukuri, R., and Humphrey, J. A. C., "Developing Flow and Heat Transfer in Strongly Curved Ducts of Rectangular Cross Section," ASME JOURNAL OF HEAT TRANSFER, Vol. 102, 1980, pp. 285–281.

3 Kreith, F., "The Influence of Curvature on Heat Transfer to Incompressible Fluids," *Trans. ASME*, Vol. 77, 1955, pp. 1247–1256.

4 Uchida, Y., and Koizumi, H., "Forced Convective Heat Transfer in a Curved Channel with a Rectangular Cross Section," *Trans. Japan Society of Mechanical Engineers*, Series B, Vol. 45, No. 399, 1979, pp. 1708–1717.

5 Mayle, R. E., Blair, M. F., and Kopper, F. C., "Turbulent Boundary Layer Heat Transfer on Curved Surfaces," ASME JOURNAL OF HEAT TRANSFER, Vol. 101, 1979, pp. 521–525.

6 Katto, Y., "Den-Netsu-Gairon," *Yokendo*, 1976, pp. 100–146.

7 Mills, A. F., "Experimental Investigation of Turbulent Heat Transfer in the Entrance Region of a Circular Conduit," *Journal of Mechanical Engineering Science*, Vol. 4, 1962, pp. 63–77.

8 Hatton, A. P., and Quarmby, A., "The Effect of Axially Varying and Unsymmetrical Boundary Conditions on Heat Transfer With Turbulent Flow Between Parallel Plates," *International Journal of Heat and Mass Transfer*, Vol. 6, 1963, pp. 903–914.

9 So, R. M. C., and Mellor, G. L., "Experiment on Convex Curvature Effects in Turbulent Boundary Layers," *Journal of Fluid Mechanics*, Vol. 60, 1973, pp. 43–62.

10 Ellis, L. B., and Joubert, P. N., "Turbulent Shear Flow in a Curved Duct," *Journal of Fluid Mechanics*, Vol. 62, 1974, pp. 65–84.

11 Klebanoff, P. S., "Characteristics of Turbulence in a Boundary Layer with Zero Pressure Gradient," NACA Rep. 1247, 1955.

Radiative Heat Transfer in Fibrous Insulations—Part I: Analytical Study

T. W. Tong
Assistant Professor,
Department of Mechanical Engineering,
University of Kentucky,
Lexington, Ky. 40506
Assoc. Mem. ASME

C. L. Tien
Professor,
Department of Mechanical Engineering,
University of California,
Berkeley, Calif. 94720
Fellow ASME

The purpose of this work is to develop models for predicting the radiant heat flux in lightweight fibrous insulations (LWFI). The radiative transport process is modeled by the two-flux solution and the linear anisotropic scattering solution of the equation of transfer. The radiative properties of LWFI consistent with these solutions have been determined based on extinction of electromagnetic radiation by the fibers. Their dependence on the physical characteristics of fibrous insulations has been investigated. It has been found that the radiant heat flux can be minimized by making the mean radius of the fibers close to that which yields the maximum extinction coefficient. The results obtained in this study are useful to those concerned with the design and application of LWFI.

Introduction

Heat transfer in lightweight fibrous insulations (LWFI) has been a subject of fundamental importance due to its wide application in many engineering systems. The current U.S. energy situation has caused an unprecedented increased usage of fibrous materials as insulating media. Many new homes are currently built with walls and attics insulated by LWFI and old structures are retrofitted with them. The increase in usage has given further impetus to the research in this area. A better understanding of the heat transfer characteristics of fibrous insulations is essential. Because of its widespread usage, a slight improvement of the insulating effectiveness would amount to substantial savings both in terms of total cost and overall energy consumption.

In a two-dimensional slot filled with fibrous insulations and air, thermal energy could be transferred by thermal radiation, conduction, and natural convection. The relative importance of the different modes of heat transfer depends on the operating conditions as well as the properties of the insulation. For example, it has been found that under moderate temperatures (300–400 K), air conduction and thermal radiation are the two dominant modes of heat transfer in LWFI [1–3]. In situations where the modified Rayleigh number (a measure of the buoyancy force to the resistance to flow) is large enough, natural convection may also become a factor in the overall heat transfer process [4]. Although the mechanisms of heat transfer in fibrous insulations are generally well understood, quantitative computations are often severely limited due to the lack of theories describing certain heat transfer phenomena and/or the unavailability of some of the heat transfer properties of the insulations.

This work is concerned with the prediction of the radiant heat transfer in LWFI. Contrary to many people's belief that thermal radiation is only important at high temperatures, studies have shown that it could account for as much as 30 percent of the total heat transfer in LWFI even at moderate temperatures [1–3]. A number of articles have appeared on radiative heat transfer in fibrous insulations and a brief review of the various transfer models has been given by Tong and Tien [5]. It can be summarized that there are basically two approaches in calculating the radiant heat flux. The first is to employ a radiative conductivity and model radiation as a conductive process. The second is to consider the equation of transfer governing the intensity of radiation in an absorbing and scattering medium. The first method is widely used because it is mathematically simple. The radiative conductivities that have been derived, however, contain a parameter which needs to be determined experimentally [5]. This could be undesirable because the parameter not only depends on the inherent property of the fiber material, such as its chemical composition, but also on the physical structure of the insulation, such as the volume fraction and the fiber size. Whenever the volume fraction and/or the fiber size are changed, the experiment for determining the parameter must be repeated even though the fiber material used has not been altered. The second method requires solutions to the equation of transfer as well as the radiative properties consistent with the solutions. It is the objective of this paper to develop models for predicting the radiant heat transfer in LWFI by constructing approximate solutions to the equation of transfer. The two-flux and linear anisotropic scattering (LAS) models are employed. The radiative properties compatible with these models are determined from consideration of extinction of electromagnetic radiation by the fibers. The effects of chemical compositions and fiber sizes are studied by performing calculations for two different types of fiberglass insulations and various fiber size distributions.

Radiative Transport Theory

For a homogeneous planar system with uniform boundary conditions, the radiative heat transfer is one-dimensional and the intensity of radiation is governed by the equation of transfer which takes the form

$$\mu \frac{\partial i_\lambda(y,\mu,\phi)}{\partial y} = -(\sigma_{a\lambda}+\sigma_{s\lambda}) i_\lambda(y,\mu,\phi) + \sigma_{a\lambda} i_{b\lambda}(T) + \sigma_{s\lambda}\int_{4\pi} f_\lambda(\Omega'\to\Omega) i_\lambda(y,\mu',\phi') d\Omega' \quad (1)$$

with

$$\mu \equiv \cos\theta$$

In equation (1), σ_a and σ_s are the absorption and scattering coefficients, respectively, i is the intensity, y the coordinate, θ the polar angle, ϕ the azimuthal angle, i_b the blackbody intensity, T the temperature, f the scattering phase function, Ω the solid angle, and subscript λ and superscript $'$ denote spectral quantity and in-coming, respectively. It is implicitly assumed in equation (1) that the participating medium is isotropic, otherwise σ_s and σ_a would be a function of direction. In reality, even insulations with randomly oriented

Contributed by the Heat Transfer Division for publication in the JOURNAL OF HEAT TRANSFER. Manuscript received by the Heat Transfer Division February 5, 1982. Paper No. 81-HT-42.

fibers are not truly isotropic; but in view of the great simplication of the problem, the isotropy approximation is assumed to be applicable. The one-dimensional energy equation in the absence of heat generation and convection is

$$k\frac{d^2T(y)}{dy^2} = 4\pi\int_o^\infty \sigma_{a\lambda} i_{b\lambda}(T)\,d\lambda - \int_o^\infty \sigma_{a\lambda}\int_{4\pi} i_\lambda(y,\mu',\phi')\,d\Omega'\,d\lambda \tag{2}$$

where k is the thermal conductivity. Because the purpose of this work is to develop models for predicting radiative heat transfer in LWFI, it is assumed that the conductive mode of heat transfer does not exist. Cases where conduction and radiation are both contributing to the total heat transfer may be treated by superposition as a first-order approximation [6]. Hence, dropping the conduction term in equation (2) yields

$$4\pi\int_o^\infty \sigma_{a\lambda} i_{b\lambda}(T)\,d\lambda = \int_o^\infty \sigma_{a\lambda}\int_{4\pi} i_\lambda(y,\mu',\phi')\,d\Omega'\,d\lambda \tag{3}$$

which is the condition for radiative equilibrium. Assuming the boundaries are diffuse, the boundary conditions can be written as

$$i_\lambda^+(y=0) = B_{\lambda 1}/\pi \tag{4a}$$

$$i_\lambda^-(y=\mathrm{L}) = B_{\lambda 2}/\pi \tag{4b}$$

where B is the surface radiosity, L the insulation thickness, and 1 and 2 denote surfaces 1 and 2, respectively.

Equations (1) and (3) are coupled through $i_{b\lambda}(T)$ and have to be solved simultaneously. Due to the spectral dependency of the radiative properties and the complex mathematical nature of the equation of transfer, analytical solutions are difficult to obtain. Very often, analytically well-based approximate solutions are more desirable from an engineering point of view. In this work, two approximate solutions are considered, namely, the two-flux and LAS models. The radiative properties are assumed gray in both models. As will be shown later, the radiative properties of the two types of fiberglass insulations considered do exhibit some gray characteristics, and since many insulations are made from fiberglass, the gray approximation is adopted.

Two-Flux Model. The two-flux model represents the intensity of radiation in the forward and backward directions by two different but isotropic components. This empirical assumption raises the question of determining the radiative properties which best represent the true properties [7]. The two-flux model employed here is derived on the basis that the radiative properties are kept consistent with those in the equation of transfer. Introducing the two-flux and gray approximations, equations (1) and (3) reduce to

$$\frac{dq^+}{d\tau} = -\beta(q^+ - q^-) \tag{5a}$$

$$-\frac{dq^-}{d\tau} = -\beta(q^- - q^+) \tag{5b}$$

Here, q^+ and q^- are the radiant heat flux in the forward and backward directions, respectively, the optical depth, τ, is defined as

$$d\tau \equiv \sigma_e\,dy \tag{6}$$

The following substitutions have also been used in arriving at equation (5)

$$\sigma_e \equiv \sigma_s + \sigma_a \tag{7}$$

$$\beta \equiv (1 - \omega + 2\omega b) \tag{8}$$

$$\omega \equiv \frac{\sigma_s}{\sigma_e} \tag{9}$$

$$b \equiv \int_\sigma f(\Omega' \to \Omega)\,d\Omega' \tag{10}$$

Equations (7), (9), and (10) define the extinction coefficient, the single scattering albedo, and the back-scattered fraction factor, respectively. In equation (10), σ stands for the backward hemisphere. Notice that subscript λ has been dropped from equation (5) on. The solutions for q^+ and q^- can be obtained by first decoupling equations (5*a*) and (5*b*), then integrating the decoupled equations. The integration constants are determined by applying the boundary conditions (equation (4)). The final result for the net radiant heat flux is

$$q_T = q^+ - q^- = (B_1 - B_2)/(1 + \beta\tau_o) \tag{11}$$

where subscript T is introduced to distinguish that the result is derived from the two-flux model and τ_o is the optical thickness ($\sigma_e L$).

Linear Anisotropic Scattering Model. The LAS model originates from simplification introduced to the scattering phase function for spherical particles. Hence, in a strict sense, the LAS model is only valid for media composed of spherical particles, but because of its ability to simplify the integral term in equation (1) it would be desirable if it could be used for studying radiative heat transfer in media containing cylindrical fibers. This is possible if the scattering charac-

Nomenclature

a = coefficients
a_1 = angular distribution coefficient
A = function as defined in equation (20)
b = coefficients or back-scattered fraction factor
B = surface radiosity
f = scattering phase function
f_v = volume fraction of fibers
$f(r)$ = normalized size distribution
G = function as defined in equation (16)
i = intensity of radiation
k = thermal conductivity
L = insulation thickness
q = radiant heat flux
Q_a, Q_s = absorption and scattering efficiencies, respectively
r = radius of fibers
$\bar{r}$ = mean fiber radius
T = temperature
y = coordinate
α = size parameter
β = function as defined in equation (8)
γ = function as defined in equation (14)
η = angle, as shown in Fig. 1
θ = polar angle
θ_o = scattering angle for a sphere
λ = wavelength
μ = $\cos\theta$
ξ = angle, as shown in Fig. 1
σ = standard deviation
$\sigma_e, \sigma_a \sigma_s$ = extinction, absorption and scattering coefficients, respectively
τ, τ_o = optical depth and optical thickness, respectively
ϕ = azimuthal angle
ω = single scattering albedo
Ω = solid angle

Superscripts

$+, -$ = forward and backward directions, respectively
$'$ = in-coming

Subscripts

1,2 = surfaces 1 and 2, respectively
b = blackbody
L = linear anisotropic scattering model
T = two-flux model

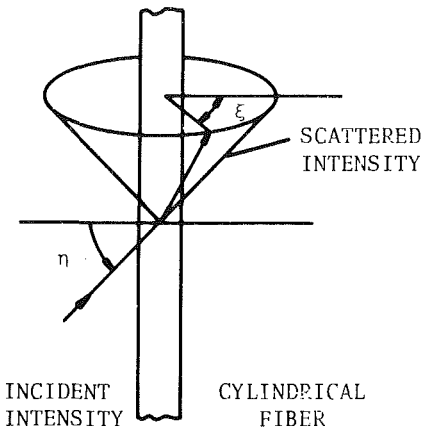

Fig. 1 Scattering by a cylindrical fiber

teristics of the cylindrical fibers can be approximated by some equivalent spheres based on some prescribed criteria. This will be discussed in more detail later.

The LAS phase function for an isotropic, homogeneous and perfectly spherical particle is [8]

$$f(\Omega' \to \Omega) = (1 + a_1 \cos\theta_o)/4\pi \tag{12}$$

where a_1 is the angular distribution coefficient characterizing forward-backward scattering and θ_o is the scattering angle. Combination of equations (1), (3), and (12) will result in two coupled integral equations governing the irradiance and the radiant heat flux. Analytical closed-form solutions for these integral equations have been obtained by Dayan and Tien [8] using the method of kernel substitution. The result for the radiant heat flux is

$$q_L = (B_1 - B_2)/(1 + \gamma\tau_o) \tag{13}$$

where L stands for LAS model and

$$\gamma \equiv (3 - \omega a_1)/4 \tag{14}$$

It is seen that q_T and q_L are very similar in form and they can be computed once the radiative properties are determined.

Radiative Properties

The radiative properties required in the two-flux model are σ_s, σ_a, and b, and the same properties (except b is replaced by a_1) are required in the LAS model. The derivations for the spectral quantities of σ_s, σ_a and, b have been given in a previous paper [5]. They were derived based on the extinction of radiation by a cylindrical fiber, then averaged over the incidence angle and the fiber size distribution. The expression for b_λ was determined as [5][1]

$$b_\lambda = \frac{1}{2} - \frac{2}{\pi}\int_o^\infty \frac{\int_o^{\frac{\pi}{2}} G\,d\eta}{\alpha\int_o^{\frac{\pi}{2}} Q_s\,d\eta} f(r)\,dr \tag{15}$$

where

$$G \equiv \sum_{n=1}^{\infty} (b_{o1}\bar{b}_{n1} + \bar{b}_{o1}b_{n1} + a_{o2}\bar{a}_{n2} + \bar{a}_{o2}a_{n2}) \frac{\sin n\frac{\pi}{2}}{n}$$

$$- \frac{1}{2}\sum_{n=1}^{\infty}\sum_{\substack{m=1 \\ m\neq n}}^{\infty} \left\{ (b_{n1}\bar{b}_{m1} + a_{n2}\bar{a}_{m2}) \left[\frac{\sin(n-m)\xi}{(n-m)} + \frac{\sin(n+m)\xi}{(n+m)} \right]_{\frac{\pi}{2}}^{\frac{3\pi}{2}} + (a_{n1}\bar{a}_{m1} + b_{n2}\bar{b}_{m2}) \left[\frac{\sin(n-m)\xi}{(n-m)} - \frac{\sin(n+m)\xi}{(n+m)} \right]_{\frac{\pi}{2}}^{\frac{3\pi}{2}} \right\} \tag{16}$$

In these equations, η and ξ are the angles shown in Fig. 1, $f(r)$ is the normalized radius distribution, α the size parameter ($\alpha \equiv 2\pi r/\lambda$) and Q_s the scattering efficiency. The bars denote the complex conjugates of the respective coefficients. The coefficients a, b, and Q_s are functions of η, α and the complex refractive index of the fibers. To conserve space, their expressions will not be given here and the readers are referred to the publications by Lind and Greenberg [9] and Kerker [10]. As mentioned before, the application of the LAS model to fibrous media is based on approximating the scattering characteristics of the fibers by some equivalent spheres. This is accomplished by assuming the equivalent spheres to have the same fraction of backward scatter as the fibers. Hence, when equation (12) is integrated with respect to the backward hemisphere, averaged over the fiber size distribution and equated to b_λ, the following expression is obtained

$$a_{1\lambda} = 2(1 - 2b_\lambda) \tag{17}$$

Note that subscript λ is added in equation (17), since it is the spectral value that is being examined at the moment. The scattering and absorption coefficients are [5]

$$\sigma_{s\lambda} = \frac{4f_v}{\pi^2 A}\int_o^{\frac{\pi}{2}}\int_o^\infty Q_s r f(r)\,dr\,d\eta \tag{18}$$

$$\sigma_{a\lambda} = \frac{4f_v}{\pi^2 A}\int_o^{\frac{\pi}{2}}\int_o^\infty Q_a r f(r)\,dr\,d\eta \tag{19}$$

where f_v is the volume fraction of the fibers, Q_a the absorption efficiency which has the same functional variables as Q_s [9,10] and

$$A \equiv \int_o^\infty r^2 f(r)\,dr \tag{20}$$

It should be pointed out that most fibrous insulations contain phenolic resins which act as binders to hold the fibers together. The above radiative properties were, however, derived assuming the fibers existed alone. The resins could have some effects on the radiative properties such as altering the effective complex refractive index and the geometry of the fibers. These effects are uncertain at the present time and they will be investigated in the future.

Results and Discussions[2]

The information required to compute b_λ, $a_{1\lambda}$, $\sigma_{s\lambda}$ and $\sigma_{a\lambda}$ from equations (15), (17), (18), and (19), respectively, are the complex refractive index, the size distribution, and the volume fraction of the fibers. The computations have been carried out for two types of fibrous insulations. Both are assumed to be composed of fibers made from silica based

[1] A brief description of the derivation of b_λ is given in the Appendix.

[2] This paper was presented in a slightly different form as ASME Paper No. 81-HT-42 where an error was discovered in the numerical computation of the integrations over η in equations (15), (18) and (19).

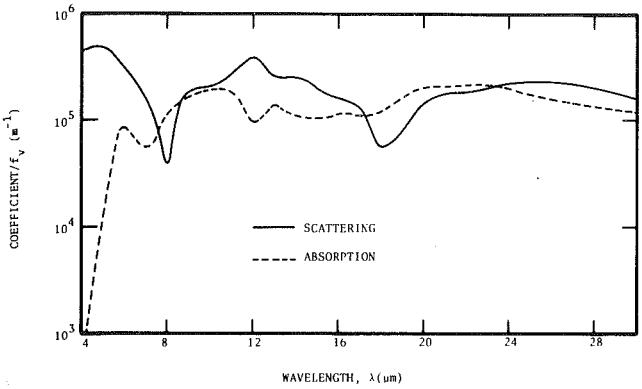

Fig. 2 Scattering and absorption properties of the silicate fibrous insulation with a Gaussian distribution of $\bar{r} = 2.5$ μm, $\sigma = 1$ μm

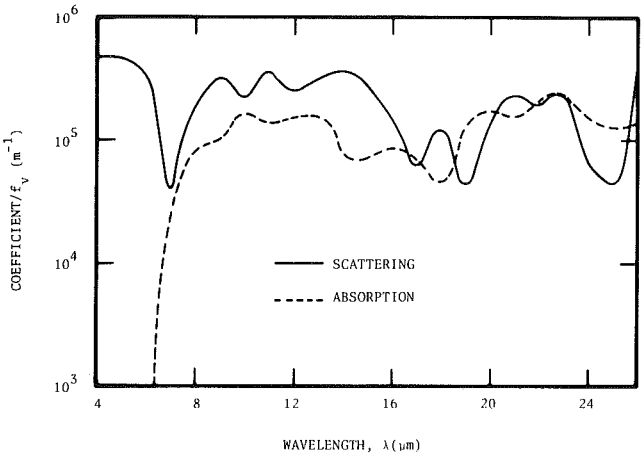

Fig. 3 Scattering and absorption properties of the pure silica fibrous insulation with a Gaussian distribution of $\bar{r} = 2.5$ μm, $\sigma = 1$ μm

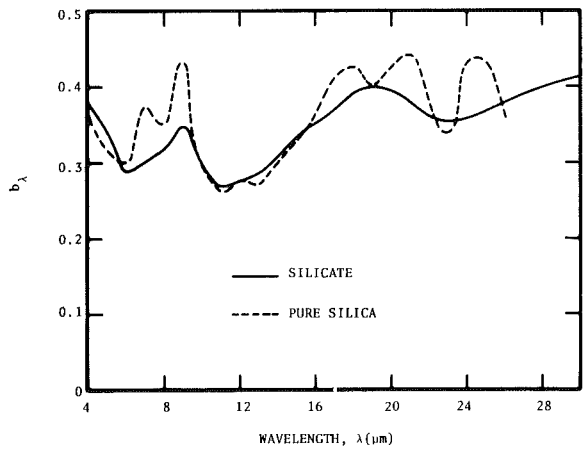

Fig. 4 Back-scattered fraction factor of fiberglass insulation with a Gaussian distribution of $\bar{r} = 2.5$ μm and $\sigma = 1$ μm

glass, but with different chemical compositions so that its effect can be studied. Various size distributions are also assumed in each fiberglass insulation in order to investigate the fiber size dependency.

The two types of glass that have been considered are silicate glass and pure silica glass. Hsieh and Su [11] have reported the complex refractive index for a silicate glass with weight compositions: SiO_2 (73.5 percent), Na_2O (21.3 percent), CaO (5.2 percent). The values given are for a wavelength range of 0.32–206.6 μm. The complex refractive index for the pure silica glass in the 7–26 μm range can be found in a report by

Table 1 Wavelength-averaged radiative properties for silicate fibrous insulations

Size distribution	σ_s/f_v (m^{-1})	σ_a/f_v (m^{-1})	b
$r = \bar{r} = 2.5$ μm	2.378×10^5	1.517×10^5	0.328
$\bar{r} = 2.5$ μm, $\sigma = 1$ μm	2.125×10^5	1.375×10^5	0.351
$\bar{r} = 2.5$ μm, $\sigma = 2$ μm	1.756×10^5	1.104×10^5	0.363
$r = \bar{r} = 5$ μm	1.373×10^5	8.478×10^4	0.272
$\bar{r} = 5$μm, $\sigma = 1$μm	1.337×10^5	8.193×10^4	0.304
$\bar{r} = 5$μm, $\sigma = 2$μm	1.196×10^5	7.629×10^4	0.318

Table 2 Wavelength-averaged radiative properties for pure silica fibrous insulations

Size distribution	σ_s/f_v (m^{-1})	σ_a/f_v (m^{-1})	b
$r = \bar{r} = 2.5$ μm	2.513×10^5	1.205×10^5	0.331
$\bar{r} = 2.5$ μm, $\sigma = 1$ μm	2.281×10^5	1.089×10^5	0.360
$\bar{r} = 2.5$ μm, $\sigma = 2$μm	1.850×10^5	8.691×10^4	0.379
$r = \bar{r} = 5$μm	1.380×10^5	6.257×10^4	0.330
$\bar{r} = 5$μm, $\sigma = 1$μm	1.336×10^5	6.139×10^4	0.347
$\bar{r} = 5$μm, $\sigma = 2$μm	1.223×10^5	5.704×10^4	0.353

Champtier and Friese [12] and those below 7 μm are given by Malitson [13]. They are used, along with some assumed fiber size distribtuions, to calculate the radiative properties. Some representative results are shown in Figs. 2–4. They are for fibers with a Gaussian distribution of mean radius, $\bar{r}$, equals 2.5 μm and standard derivation, σ, equals 1 μm. The results for the silicate fibrous insulation are from 4 to 30 μm. This spectral range covers at least 90 percent of the blackbody emissive power for temperatures between 350 K and 500 K. The results for the pure silica fibrous insulation are, however, only obtained up to 26 μm (the 4–26 μm range covers over 86 percent of the blackbody emissive power for the same temperatures), because the complex refractive index is not available beyond this wavelength [12]. Since $\sigma_{s\lambda}$ and $\sigma_{a\lambda}$ are proportional to f_v, they are presented as $\sigma_{s\lambda}/f_v$ and $\sigma_{a\lambda}/f_v$. In general, $\sigma_{s\lambda}/f_v$ is greater than $\sigma_{a\lambda}/f_v$, except at some small regions where the reverse is true. At the short wavelength region, $\sigma_{a\lambda}/f_v$ is comparatively smaller. This is because the imaginary part of the complex refractive index, which accounts for the absorption of radiation, is smaller. Since $a_{1\lambda}$ is linearly related to b_λ, only results for b_λ are presented. Figure 4 shows the fibers scatter predominantly in the forward direction. It is difficult to compare quantitatively the spectral results as presented in the figures. But since the results oscillate as a function of wavelength, it would be more convenient to assume the radiative properties are gray and compare some averaged values. In this work, the wavelength-averaged (arithmetic mean) values are compared. It should be noted that the arithmetic means are different from those obtained by weighting by another function. Just to demonstrate the difference, consider the silicate fibrous insulation with $\bar{r} = 2.5$ μm, $\sigma = 1$ μm and a temperature of 350 K. The mean values, when the spectral blackbody emissive power is used as the weighting function, are: $\sigma_s/f_v = 1.987 \times 10^5$ m^{-1}, $\sigma_a/f_v = 1.200 \times 10^4$ m^{-1}, $b = 0.299$. They differ by less than 15 percent from those given in Table 1.

Shown in Tables 1 and 2, respectively, are the wavelength-averaged results for the silicate and pure silica fibrous insulations of various size distributions. The size distributions considered are: (*i*) uniform; (*ii*) Gaussian with $\sigma = 1$ μm; (*iii*) Gaussian with $\sigma = 2$ μm. For each size distribution, results have been obtained for $\bar{r}$ equals 2.5 and 5 μm. Most LWFI available commercially have a mean radius somewhere between these two values. It is clear that as far as σ_s/f_v and σ_a/f_v are concerned, doubling the mean radius has a far

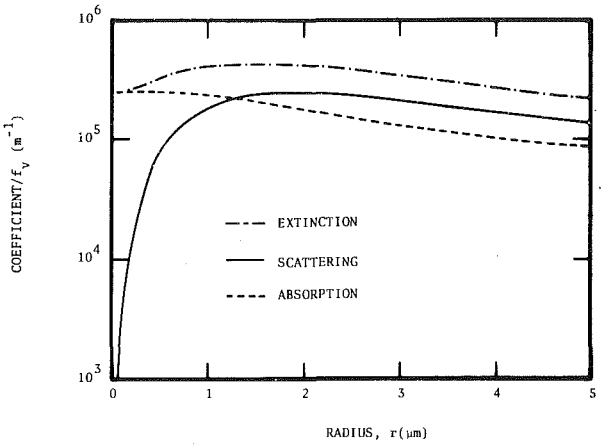

Fig. 5 Wavelength-averaged coefficients of silicate fibrous insulations

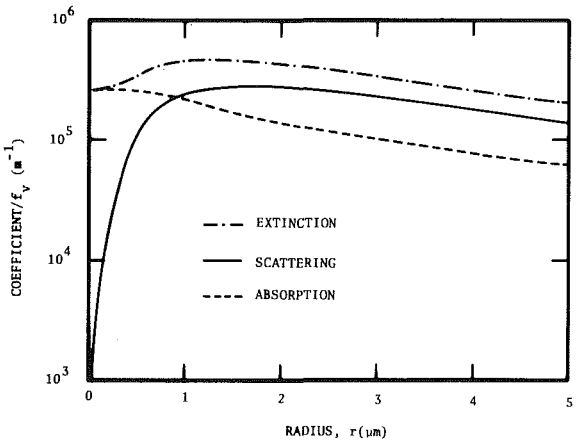

Fig. 6 Wavelength-averaged coefficients of pure silica fibrous insulations

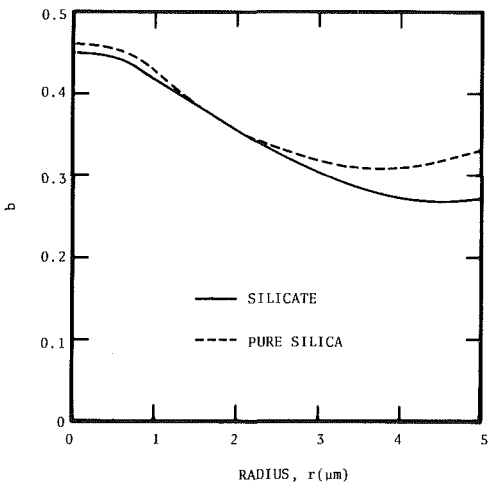

Fig. 7 Wavelength-averaged back-scattered fraction factor

greater influence than keeping the mean radius fixed and varying the standard deviation. Some values decrease almost by half when $\bar{r}$ is changed from 2.5–5 μm. For b, the effects of changing the mean radius and the standard deviation are comparable. It should be noted that the radiative heat flux has a weaker dependence on b than on σ_s and σ_a. Thus, for the kind of magnitude change involved, the variation in b due to a change in $\bar{r}$ or σ is of lesser importance. The effect of different

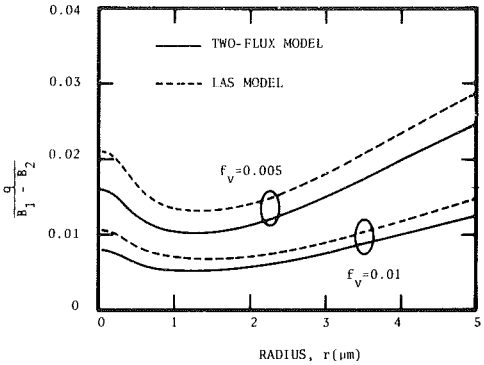

Fig. 8 Radiative heat transfer for silicate fibrous insulations with $L = 0.05$ m

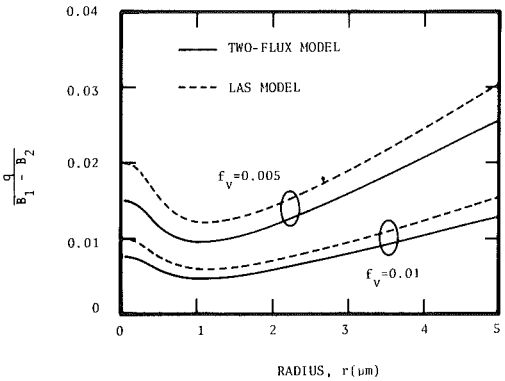

Fig. 9 Radiative heat transfer for pure silica fibrous insulations with $L = 0.05$ m

chemical compositions is also demonstrated in Tables 1 and 2. While the properties for the silicate fibrous insulation and the pure silica fibrous insulation are not the same, the difference is not nearly as large as that caused by doubling the mean radius.

In light of the above discussions, the influence of the mean radius is analyzed in more detail. Because the effect of the type of size distribution is comparatively smaller, only uniform distribution will be considered from this point on (i.e., $r = \bar{r}$). The calculations for the radiative properties have been repeated for different r and the wavelength-averaged results are shown in Figs. 5–7. In Figs. 5 and 6, the scattering coefficients (here it means scattering coefficient/f_v) drops off much faster than the absorption coefficient when $r \to 0$. This is because in the small fiber limit, Q_s, is proportional to the fourth power of r, and Q_a is only proportional to the first power [10]. The scattering coefficient is greater than the absorption coefficient for larger radii, and both decrease as r increases. The extinction coefficients go through a peak at $r = 1.6$ μm and 1.4 μm for the silicate and pure silica fibrous insulations, respectively. The back-scattered fraction factors as shown in Fig. 7 start off at almost equal amounts of forward and backward scattering when r is small. As r gets larger, the scattering becomes forward preferential. The trend is similar to those presented by Larkin and Churchill for scattering of radiation by a single fiber [14].

To demonstrate the usefulness of the results presented so far, the wavelength-averaged radiative properties are used with the two-flux and LAS models to calculate the radiant heat flux. Figures 8 and 9 show how the dimensionless radiant heat flux changes with r and f_v. It is clear that the radiant heat flux goes through a minimum right around where the extinction coefficient is maximum (compare to Figs. 5 and 6). This is important because for a given f_v (or equivalently, for a given insulation density), the insulating value can be

maximized by making the mean fiber radius close to that which gives the maximum extinction coefficient. It should be noted that the mean radius which yields the minimum radiant heat flux does not correspond exactly with the one that has the maximum extinction coefficient. This is because the radiant heat flux depends on b (or a_1) and ω as well and they do not necessarily have the optimum values at the same mean radius. For the conditions considered, the LAS model gives a 15–30 percent higher prediction than the two-flux model. The physical thickness of LWFI under typical operating conditions is of the order of several centimeters. Thus, for $f_v \geq 0.005$, the optical thickness falls in the optically thick region. From equations (11), (13), (18), and (19), it is seen that the radiant heat flux is approximately proportional to the inverse of f_v in the optically thick limit. Indeed, as shown in the figures, the radiant heat flux is roughly decreased by half when f_v is doubled. This means that thermal radiation can be reduced by increasing the insulation density. However, the design of insulations must take into account the economic factor, as a denser insulation would cost more to manufacture, and also fiber-to-fiber conduction heat transfer will become appreciable when f_v reaches approximately 0.03 [2]. Therefore, increasing the insulation density may not always be the most desirable method to reduce radiative heat transfer. Comparison of the results in Figs. 8 and 9 indicates that there is only a few percent difference between the two types of fiberglass insulations. This suggests that the chemical composition will have little affect on the radiative heat transfer result as long as the fibers are made from silica based glass.

Conclusions

The radiative heat transfer in LWFI has been modeled by two gray transfer models. They are the two-flux and LAS models. The radiative properties needed in these transfer models have been determined by considering the extinction of radiation by the fibers. The radiant heat flux and the radiative properties are found to be calculable once the physical characteristics of the fibrous bed such as the complex refractive index, size, and volume fraction of the fibers are known. This allows the influence of each of these properties to be studied independently.

Results obtained for silicate fiberglass insulations and pure silica fiberglass insulations show that the mean radius of the fibers has a more pronounced effect than the type of size distribution and the chemical composition of the fibers. For a given insulation density, the radiant heat flux can be minimized by making the mean radius close to that which yields the maximum extinction coefficient. The radiant heat flux is found to be approximately proportional to the inverse of the volume fraction of the fibers. It is also found that the LAS model gives a higher prediction of the radiant heat flux than the two-flux model.

Acknowledgment

The authors wish to acknowledge the joint support of this work by the National Science Foundation and the U.S. Department of Energy.

References

1 Verschoor, J. D., and Greebler, P., "Heat Transfer by Gas Conduction and Radiation in Fibrous Insulation," ASME Trans., Vol. 74, 1952, pp. 961–968.

2 Bankvall, C. G., "Heat Transfer in Fibrous Materials," *Journal of Testing and Evaluation*, Vol. 1, 1973, pp. 235–243.

3 Pelanne, C. M., "Heat Flow Principles in Thermal Insulations," *Journal of Thermal Insulation*, Vol. 1, 1977, pp. 48–80.

4 Bankvall, C. G., "Natural Convective Heat Transfer in Insulated Structures," Lund Institute of Technology, Report 38, 1972.

5 Tong, T. W., and Tien, C. L., "Analytical Models for Thermal Radiation in Fibrous Insulations," *Journal of Thermal Insulation*, Vol. 4, 1980, pp. 27–44.

6 Tong, T. W., Yang, Q. S., and Tien, C. L., "Radiative Heat Transfer in Fibrous Insulations—Part II: Experimental Study," ASME JOURNAL OF HEAT TRANSFER, Vol. 105, Feb. 1983, pp. 76–81.

7 Chan, C. K., and Tien, C. L., "Radiative Transfer in Packed Spheres," ASME JOURNAL OF HEAT TRANSFER, Vol. 96, 1974, pp. 52–58.

8 Dayan, A., and Tien, C. L., "Heat Transfer in Gray Planar Medium With Linear Anisotropic Scattering," ASME JOURNAL OF HEAT TRANSFER, Vol. 97, 1975, pp. 391–396.

9 Lind, A. C., and Greenberg, J. M., "Electromagnetic Scattering by Obliquely Oriented Cylinder," *Journal of Applied Physics*, Vol. 37, 1966, pp. 3195–3203.

10 Kerker, M., *The Scattering of Light*, Academic Press, New York, 1969.

11 Hsieh, C. K., and Su, K. C., "Thermal Radiative Properties of Glass from 0.32 to 206 μm," *Solar Energy*, Vol. 22, 1979, pp. 37–43.

12 Champetier, R. J., and Friese, G. J., "Use of Polished Fused Silica to Standardize Directional Polarized Emittance and Reflectance Measurements in the Infrared," The Aerospace Corporation Report SAMSO-TR-202, 1974.

13 Malitson, I. H., "Interspecimen Comparison of the Refractive Index of Fused Silica," *Journal of the Optical Society of America*, Vol. 55, 1965, pp. 1205–1209.

14 Larkin, B. K., and Churchill, S. W., "Scattering and Absorption of Electromagnetic Radiation by Infinite Cylinders," *Journal of the Optical Society of America*, Vol. 49, 1959, pp. 188–190.

APPENDIX

Derivation for b_λ

The expression for the scattered intensity from a single filter, $i_s(\xi,\eta)$, has been given in the literature [5,10]. The scattered intensity averaged over all incidence is

$$\bar{i}_s(\xi) = \frac{2}{\pi}\int_o^{\pi/2} i_s(\xi,\eta)\,d\eta \tag{A1}$$

A scattering phase function based on $\bar{i}_s(\xi)$ can be defined as

$$f(\xi) = \frac{\bar{i}_s(\xi)}{\int_{4\pi} \bar{i}_s(\xi)\,d\Omega} \tag{A2}$$

Combining equations (A2) and (10) gives

$$b_\lambda = \frac{\int \bar{i}_s(\xi)\,d\Omega}{\int_{4\pi} \bar{i}_s(\xi)\,d\Omega} \tag{A3}$$

To perform the integrations in equation (A3), we envision the fiber being encompassed by a sufficiently large sphere so that $d\Omega = \sin\nu d\nu d\xi$, where ξ is the angle shown in Fig. 1, and ν is the angle between the fiber axis and the center line of $d\Omega$. Thus, equation (A3) becomes

$$b_\lambda = \frac{\int_{\pi/2}^{3\pi/2}\int_o^{\pi} \bar{i}_s(\xi)\sin\nu d\nu d\xi}{\int_o^{2\pi}\int_o^{\pi} \bar{i}_s(\xi)\sin\nu d\nu d\xi} \tag{A4}$$

When the integrations in equations (A1) and (A4) are performed analytically and the resultant expression for b_λ is averaged over the size distribution, one obtains equation (15).

T. W. Tong
Assistant Professor,
Department of Mechanical Engineering,
University of Kentucky,
Lexington, Ky. 40506
Assoc. Mem. ASME

Q. S. Yang[1]

C. L. Tien
Professor.
Fellow ASME

Department of Mechanical Engineering,
University of California,
Berkeley, Calif. 94720

Radiative Heat Transfer in Fibrous Insulations—Part II: Experimental Study

Two experiments have been conducted to study radiative heat transfer in lightweight fibrous insulations (LWFI). The spectral extinction coefficients for a commercial LWFI have been measured via transmission measurements, and a guarded hot plate apparatus has been used to measure the radiant heat flux as well as the total heat flux in the insulation. The experimental results are compared with the theoretical values calculated according to the analytical models presented in Part I of this paper. The comparisons reveal that the analytical models are useful in giving representative values for the radiative properties of typical LWFI. However, only qualitative agreements have been obtained for the heat transfer results.

Introduction

In Part I of this paper [1], analytical models were developed for predicting the radiant heat flux in lightweight fibrous insulations (LWFI). The radiative heat transfer was modeled by the two-flux and linear anisotropic scattering (LAS) models. The radiative properties consistent with these models were also determined. One important feature of the analytical models was that the radiative properties, and thus the radiant heat flux, could be calculated once the physical characteristics (complex refractive index, size distribution, and volume fraction of fibers) were known. As the second part of paper, two experiments designed to test the validity and accuracy of the analytical models are described and the results are presented. A transmission experiment and a guarded hot plate experiment have been conducted to measure the extinction coefficient and the heat transfer, respectively, in a commercial LWFI. The experimental results are compared to the values obtained from the analytical models.

The transmission experiment has been used by Love and Saboonchi [2] for measuring extinction coefficients of fiberglass insulations. This involves measuring the transmission of a beam of radiation through a sample and deducing the extinction coefficient from Beer's law

$$\frac{i_\lambda(L)}{i_\lambda(0)} = e^{-\sigma_{e\lambda}L} \tag{1}$$

The symbols in equation (1) have the same definitions as in Part I of this paper [1] (also see nomenclature). The quantity on the left-hand side is the ratio of the intensities after and before the beam of radiation has passed through the sample. It physically corresponds to the transmission, and once it is measured for a specified L, $\sigma_{e\lambda}$ can be determined.

Various specifications have evolved in the course of developing standard methods for measuring the heat flow in insulations. Specifications such as the C177 (guarded hot plate method) and the C518 (heat flow meter method) have been established by the American Society for Testing and Materials [3]. These specifications are for steady-state measurement of one-dimensional heat transfer. The guarded hot plate method measures the heat flow through insulations installed between hot and cold plates. Usually, the hot plate is electrically heated and the cold plate is water cooled. Heat transfer is determined via measurement of the electrical power required to maintain the surfaces at certain prescribed temperature. The heat flow meter method is very similar to the guarded hot plate method except the heat flux is directly measured with a heat flow meter. The specification requires the heat flow meter to be calibrated against other standard specimens already tested by the guarded hot plate method. For situations where interest is in testing the thermal performance of built-up sections such as roofs and walls of buildings, the C236 (guarded hot box method) is recommended [3]. The hot and cold sides are composed of two chambers separated by the specimen. Both the temperatures and the air velocities in the chambers can be adjusted to simulate the actual operating conditions. In this study, the guarded hot plate method, being the simplest and the most widely accepted method, is employed to measure the heat transfer in the same fibrous insulation tested in the transmission experiment. In order to separate thermal radiation from the total heat transfer, the measurements were carried out under vacuum (1×10^{-3} torr) as well as at atmospheric pressure.

Description of the Apparatus

Transmission Experiment. As depicted in Fig. 1, radiant energy is emitted by a blackbody source (IR Industries, Inc. 463) which is electrically heated to about 1300 K. The radiant energy is collimated by a guide tube (1.778×10^{-1}m long, 6.4×10^{-3}m dia), then directed through the test section and another guide tube (1.016×10^{-1}m long, 6.4×10^{-3}m dia). This arrangement ensures that only the beam transmitted in the incident direction is measured. The beam is focussed on

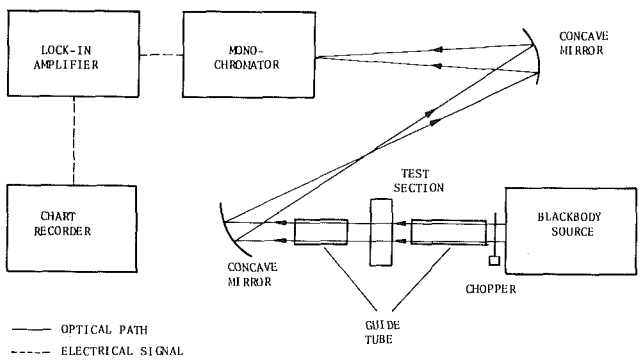

Fig. 1 Experimental system for transmission measurement

[1] Visiting scholar from Shanghai Jiaotong University, People's Republic of China

Contributed by the Heat Transfer Division for publication in the JOURNAL OF HEAT TRANSFER. Manuscript received by the Heat Transfer Division, February 5, 1982. Paper No. 81-HT-43.

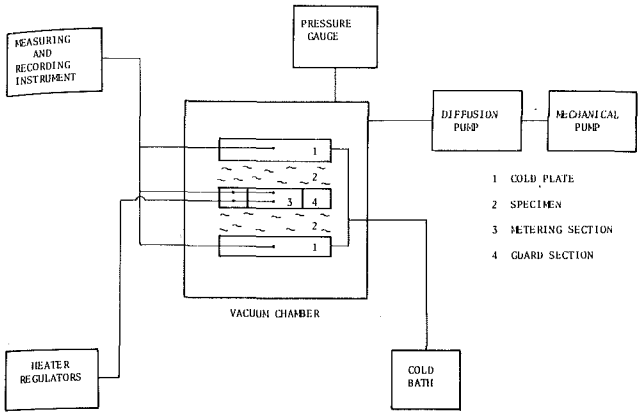

Fig. 2 Schematic diagram of the guarded hot plate experiment

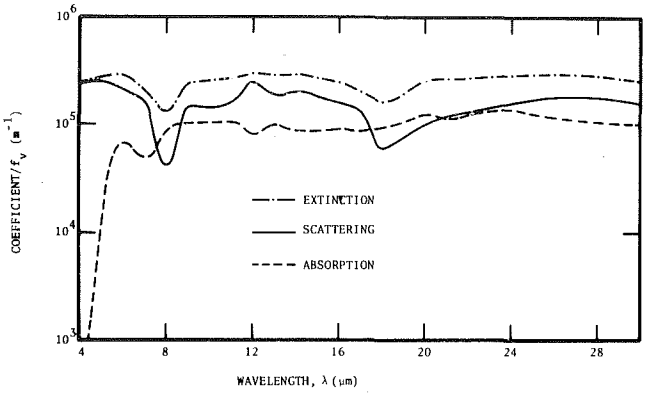

Fig. 3 Scattering and absorption properties of insulation A

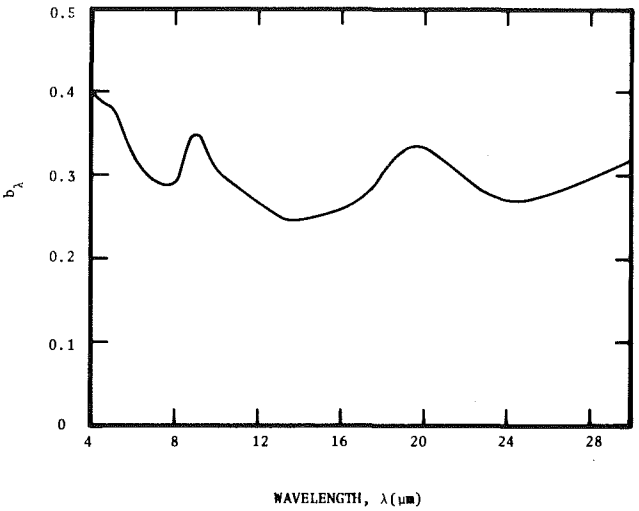

Fig. 4 Back-scattered fraction factor of insulation A

the entrance slit (3×10^{-4}m) of a monochromator (Perking-Elmer 98) which spectrally resolves the beam and converts it to an electrical signal with a thermocouple detector. A low-input impedance preamplifier located inside the monochromator provides a first-stage amplification. A phase sensitive detection system is made by passing the electrical signal to a lock-in amplifier (Princeton Applied Research 122) tuned to the same frequency (12 cps) as the chopper located right in front of the blackbody source. Since the lock-in amplifier only responds to the signal at the chopped frequency, emission by the specimen (unchopped signal) is eliminated in the measurements. After amplification, the signal is recorded on a chart recorder.

The sample tested was a commercially available fiberglass insulation (to be referred as insulation A). It is commonly used in insulating buildings and homes. Three 1.3×10^{-2}m thick specimens were tested. The thickness was determined by measuring the lateral lengths and weight, and assuming that the specimen had the same bulk density. The lateral dimensions of the specimens were 8.9×10^{-2}m by 1.0×10^{-1}m. The test specimen was secured between two metal plates held together by bolts. Each of the plates has a 7.62×10^{-2}m dia hole for the beam to pass through. The space between the plates was adjusted to accommodate the specimen by inserting spacers with the same thickness. The transmission was determined by taking the ratio of the signals with and without the specimen in the test section. The thickness obtained as described above was the mean thickness over the entire specimen. As the thickness at the point of measurement might differ from the mean thickness, measurements were made at no less than four different locations on each specimen and the averaged result was taken to give a representative value.

Guarded Hot Plate Experiment. A schematic diagram of the experimental system is shown in Fig. 2. The guarded hot plate apparatus is located horizontally inside a chamber and is composed of three 3.048×10^{-1}m square plates: one hot plate in the center and two cold plates, one above and one below. Since the plate surfaces should be at uniform temperatures, it is necessary that the plates be made from material with a high thermal conductivity. In this case, the plates are made from copper. The top and bottom of the hot plate are each composed of one metering section (1.524×10^{-1}m square, 6.4×10^{-3}m thick) and one guard section (7.46×10^{-2}m wide, 6.4×10^{-3}m thick) with the heating elements sandwiched between. A 1.6×10^{-3} gap separates the metering and the guard sections in order to minimize heat flow in the lateral direction. The heating elements for the two sections are separate and are insulated from the copper plates with 1×10^{-4}m thick mica. The cold plates are each 1.91×10^{-2}m thick with water passages carved inside. Copper-constantan thermocouples are installed on the grooves

Nomenclature

a_1 = angular distribution coefficient
b = back-scattered fraction factor
B = surface radiosity
i = intensity
k_{rad} = radiative conductivity
L = insulation thickness
q = heat flux
T = temperature
β = function as defined in equation (4)
γ = function as defined in equation (5)
λ = wavelength
σ = Stefan-Boltzmann constant
$\sigma_e, \sigma_a, \sigma_s$ = extinction, absorption and scattering coefficients, respectively
τ_o = optical thickness
ω = single scattering albedo

Subscripts

1,2 = surfaces 1 and 2, respectively
L = linear anisotropic scattering model
m = mean
T = two-flux model

provided on the surfaces facing the specimens. In order to make the surfaces radiate as black boundaries, they are painted with the 3M Nextel velvet black paint which has emittance of 0.955 ± 0.005 from 6 to 12 μm [4]. The plates are mounted on frames which can be moved up and down along four posts. This provision makes it possible to adjust the distances among the plates in order to accommodate specimens of different thicknesses.

The vacuum chamber is 6.60×10^{-1}m high, 6.86×10^{-1}m in diameter and the wall is made from 9.6×10^{-3}m thick steel. The lid on top can be opened and a hoist is employed to transport the guarded hot plate apparatus into the vacuum chamber after the specimens are installed. Pressure as low as 1×10^{-3} torr can be achieved with a pumping unit consisting of a diffusion pump (National Research Corp. 0159) and a mechanical pump (The Welch Scientific Co. 1402). A thermocouple gage (National Research Corp. 531) is used to measure the pressure inside the vacuum chamber. Two separate power regulators control the electrical power supplied to the metering and guard heaters. By careful adjustment of the regulators, a temperature difference of no larger than 0.5 K between the metering and the guard sections can be achieved. The thermocouples are connected to a switchboard so that any particular thermocouple can be selected and the signal is displayed with a digital multimeter (Kiethley 191). The cold bath (Blue M MW1110A1) supplies cooling water for the cold plates and is capable of maintaining the water at a constant temperature anywhere between 5 K above ambient and 373 K.

Specimens (two for each thickness) with thicknesses 2.54×10^{-2}m, 3.30×10^{-2}m and 4.06×10^{-2}m were prepared according to the same method as described earlier. These thicknesses were chosen so that the maximum uncertainty in the measurements was no greater than three percent when the temperature difference between the hot and cold plates was at least 50 K [5]. The specimens were the same type of insulation as tested in the transmission experiment.

Testing was started with the thinnest specimen; first under vacuum, then at atmospheric pressure. At each pressure, the hot plate was run at 363 K, 393 K, and 423 K. Due to the capability of the cold bath (at least 5 K above ambient), the cold plate temperature was set at 308 K and kept at this value for the entire experiment. Each test condition was maintained and the thermocouple readings were recorded every hour. Steady state was deemed to have been achieved when three successive sets of observations gave temperatures differing by not more than 0.5 K. It generally took about 15 hrs to reach steady-state. The electrical power input to the metering heater was also recorded. This procedure was repeated for the other thicknesses. The heat flux was computed by dividing the electrical power input by the total surface area of the metering section.

Analytical Considerations

The expressions developed for the radiant heat flux are [1]

$$q_T = (B_1 - B_2)/(1 + \beta\tau_o) \tag{2}$$

for the two-flux model and

$$q_L = (B_1 - B_2)/(1 + \gamma\tau_o) \tag{3}$$

for the LAS model with

$$\beta \equiv 1 - \omega + 2\omega b \tag{4}$$

$$\gamma \equiv (3 - \omega a_1)/4 \tag{5}$$

$$\omega \equiv \sigma_s/\sigma_e \tag{6}$$

$$\sigma_e \equiv \sigma_s + \sigma_a \tag{7}$$

and b and a_1 are related by

$$a_1 = 2(1 - 2b) \tag{8}$$

Table 1 Chemical composition of fiberglass insulation A

	SiO_2	Fe_2O_3	Al_2O_3	CaO	MgO	Na_2O	K_2O
% weight	64.48	0.31	5.17	8.79	3.40	15.24	2.61

Again, the symbols in the above equations are as previously defined [1]. For simplicity, it is often desirable to have a radiative conductivity so that the radiant heat flux can be calculated according to Fourier's law. In the following, radiative conductivities will be derived from both the two-flux and LAS solutions. The derivation from the two-flux solution will first be presented. If the bounding surfaces are sufficiently black, equation (2) becomes

$$q_T = \sigma(T_1^4 - T_2^4)/(1 + \beta\tau_o) \tag{9}$$

where T_1 and T_2 are the temperatures of surfaces 1 and 2, respectively and σ is the Stefan-Boltzmann constant. As already pointed out [1], the optical thickness lies in the optically thick region under typical operating conditions, and since β is not likely to approach zero (see Figs. 3 and 4 and equation (4)) equation (9) can be approximated as

$$q_T \simeq \frac{\sigma(T_1^4 - T_2^4)}{\beta\,\sigma_e(T_1 - T_2)} \frac{(T_1 - T_2)}{L} \tag{10}$$

For moderate temperature difference (e.g., $(T_1 - T_2) < 200$ K), q_T can be further approximated as

$$q_T \simeq \frac{4\sigma T_m^3}{\beta\sigma_e} \frac{(T_1 - T_2)}{L} \tag{11}$$

without introducing significant error, and T_m is the arithmetic mean of T_1 and T_2. A radiative conductivity can now be defined from equation (11) as

$$k_{\text{rad},T} \equiv \frac{4\sigma T_m^3}{\beta\sigma_e} \tag{12}$$

Starting from equation (3) and following the derivation of equations (10) to (12) yields

$$k_{\text{rad},L} \equiv \frac{4\sigma T_m^3}{\gamma\sigma_e} \tag{13}$$

which is the radiative conductivity from the LAS model. Note that the radiative conductivities derived above are very similar in form to those obtained by other investigators (see Table 1 in [6]). The important differences are: (*i*) the present ones contain information describing the relative amount of scattering and absorption (contained in ω) and the scattering pattern of the fibers (contained in b and a_1); and (*ii*) they are in terms of radiative properties that can be analytically determined.

In addition to equations (2) and (3), the thermal conductivities $k_{\text{rad},T}$ and $k_{\text{rad},L}$ will also be used with Fourier's law to predict the radiant heat flux. They will be referred to as two-flux conduction model and LAS conduction model, respectively.

Results and Discussions

Radiative Properties. The theoretical radiative properties of the tested insulation are presented first. The information needed for calculating the radiative properties are: the complex refractive index, the volume fraction, and the size distribution of the fibers. The complex refractive index is a function of the chemical composition of the fiber material. An industrial chemical laboratory was contracted to determine the chemical composition of the tested insulation, and the results are shown in Table 1. The main components are SiO_2 and Na_2O. The composition is quite close, but not identical, to that of the silicate glass considered in Part I of this paper [1]. A spectrographic analysis also shows the fibers

Table 2 Comparisons of results

	$\sigma_e(m^{-1})$				ω	
$\lambda(\mu m)$	Present theoretical	Present experimental	Experimental [8]	Theoretical [9]	Present theoretical	Theoretical [9]
2	680	497	570		1.00	
2.5	742	512	602		1.00	
3	733	531	650		1.00	
3.5	744	542	685		0.98	
4	758	561	723	988	0.98	1.00
4.5	768	596	740		1.00	
5	807		760		0.96	
6	912		766	1267	0.76	0.92
7	710		600		0.77	
8	411		478	583	0.33	0.42
9	771		750		0.57	
10	806		979	1024	0.53	0.56
15	851		1069	1201	0.66	0.64
20	778		750		0.48	
25	959		750	775	0.57	0.62
30	875		750	912	0.62	0.63

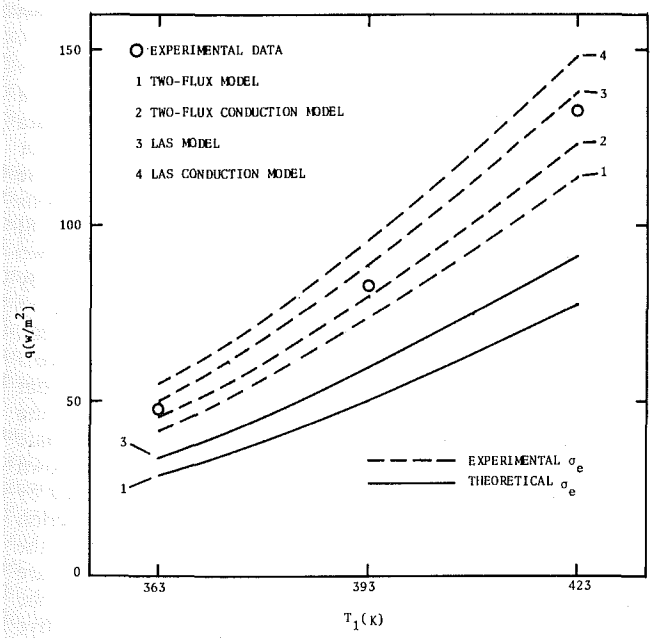

Fig. 5 Radiative heat transfer in insulation A for $L = 2.54 \times 10^{-2}$m and $T_2 = 308$ K

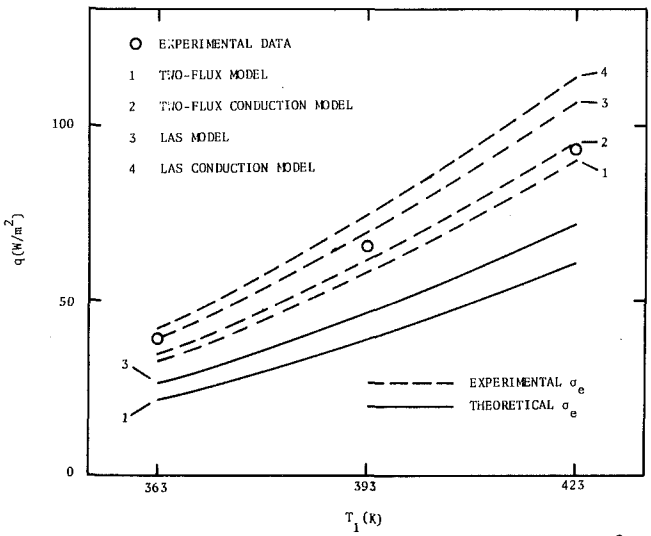

Fig. 6 Radiative heat transfer in insulation A for $L = 3.30 \times 10^{-2}$m and $T_2 = 308$ K

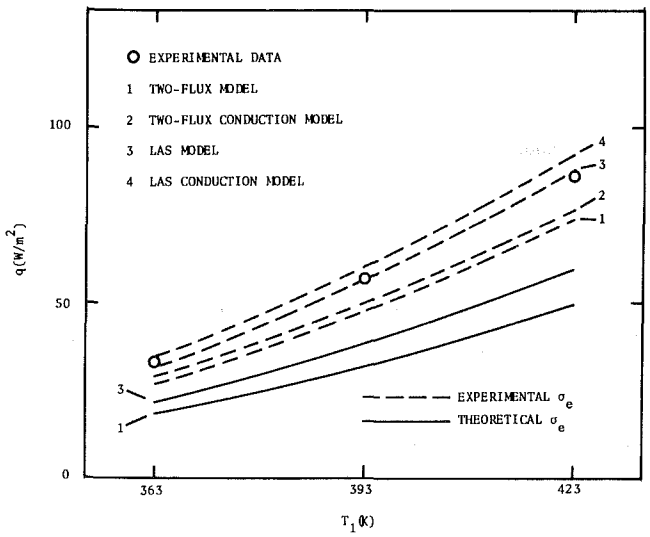

Fig. 7 Radiative heat transfer in insulation A for $L = 4.06 \times 10^{-2}$m and $T_2 = 308$ K

contain trace elements such as Cu, Ni, Cr, Pb, Sn, Sr, Zr, and Ba. The complex refractive index for this specific type of glass is, to the authors' knowledge, not available in the literature. But since earlier results [1] have shown that the dependence on chemical composition is rather minor as long as the fibers are made from silica-based glass and in view of nothing else better available, the complex refractive index of the silicate glass [7] is used for the insulation A.

The density of the solid material with composition as shown in Table 1 is determined to be 2.55×10^3 Kg/m^3 and the density of insulation A is 8.41 Kg/m^3. Hence, the volume fraction, defined as the ratio of the insulation density to that of the solid material, is found to be 3.3×10^{-3}. The size distribution was obtained by microscopic counting of the fibers with an optical microscope. The mean diameter is 6.9 μm and the distribution skews towards the smaller sizes.

Based on the physical properties obtained above, calculations for the radiative properties were carried out according to the analytical expressions obtained earlier [1].[2]

[2] This paper was presented in a slightly different form as ASME Paper No. 81-HT-43 where an error was discovered in the numerical computation of the integrations over η in equations (15), (18), and (19) in Part I of the paper.

The results for 4 to 30 μm are given in Figs. 3 and 4. This spectral range covers at least 90 percent of the blackbody emissive power for temperatures between 320 and 500 K.

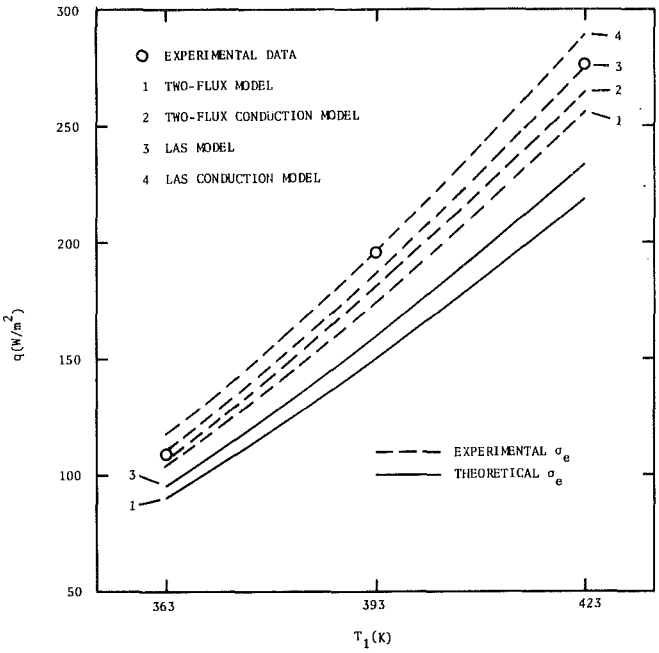

Fig. 8 Combined air conduction and thermal radiation in insulation A for $L = 2.54 \times 10^{-2}$ m and $T_2 = 308$ K

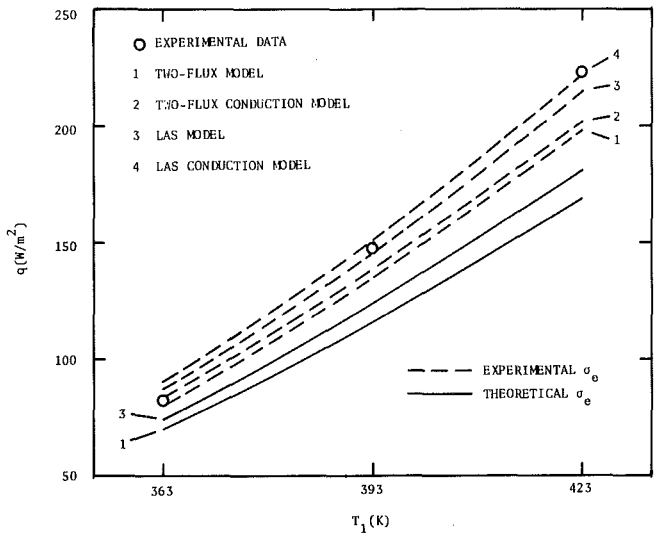

Fig. 9 Combined air conduction and thermal radiation in insulation A for $L = 3.30 \times 10^{-2}$ m and $T_2 = 308$ K

since $a_{1\lambda}$ is linearly related to b_λ, only results on b_λ are presented.

Extinction Coefficient. Transmission measurements could only be made in the wavelength range of 2 to 4.5 μm because the transmitted intensity at longer wavelengths was too low to be detected. It is seen from Table 2 that the theory overpredicts the experimental results by 22 to 31 percent. It should be noted that the experimental results deduced from Beer's law has neglected the effect of in-scattering (or multiple scattering). In a strict sense, in-scattering is negligible only if the sample is optically thin, otherwise it will augment the transmitted intensity and result in smaller measured extinction coefficient. Since the optical thicknesses of the test samples are either in the intermediate or thick range, the measured values are believed to be smaller than the true values. Birkebak et al. [8] have recently reported some measured extinction coefficients for a fiberglass insulation similar to

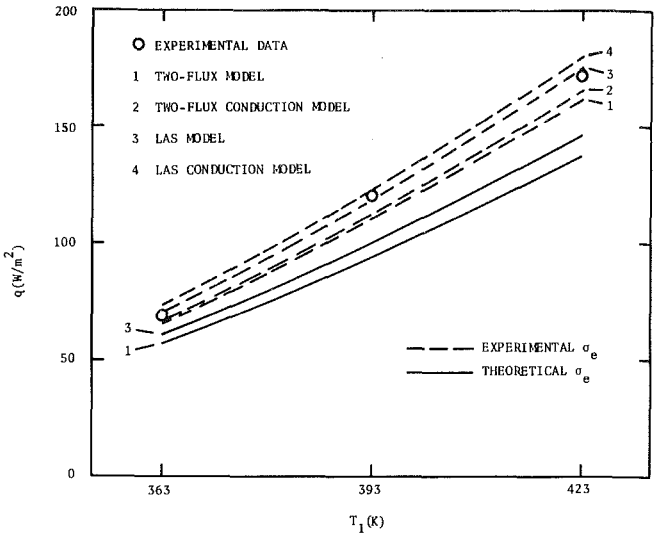

Fig. 10 Combined air conduction and thermal radiation in insulation A for $L = 4.06 \times 10^{-2}$ m and $T_2 = 308$ K

that tested in the present study. They have incorporated a first-order in-scattering correction in the Beer's law data reduction method by linearly extrapolating the results for samples of different thicknesses to that for zero sample thickness. It is seen in Table 2 that the present predictions have closer agreement with the results of Birkebak et al. [8] than with the present measured values, and the former two sets of results certainly follow the same general trend. By comparing the present experimental values and those of Birkebak et al. [8] in the spectrum from 2–4.5 μm, one can infer that in-scattering may cause a 13–23 percent difference if it is not corrected for. It must be cautioned, however, that these numbers are not exact indicators of the in-scattering effect because the linear extrapolation is only an approximate correction and the tested insulations are not identical. Shown in the same table are some radiative properties reported by Houston and Korpela [9]. Their prediction of the extinction coefficients is higher than ours except at $\lambda = 25$ μm where the converse is true. The values for the single scattering albedo are seen to be in general agreement with each other. From the above comparisons, it is clear that the models for the radiative properties [1] are capable of producing predictions that are representative of fiberglass insulations.

Heat Transfer. Shown in Figs. 5–7 are the results for pure radiative heat transfer for the specimens with different thicknesses. The experimental data were obtained under vacuum (1×10^{-3} torr) and the theoretical values were calculated from the models as indicated in the figures. In the calculation, the bounding surfaces were assumed black. The solid lines represent results calculated with the wavelength-average radiative properties obtained from Figs. 3 and 4. They are $\sigma_e = 8.25 \times 10^2 m^{-1}$, $\omega = 0.605$, $b = 0.299$ and $a_1 = 0.804$. The results from the two-flux conduction and the LAS conduction models are not shown because they are very close to those obtained from the two-flux and LAS models, respectively. They differ by at most 3 percent. This is because even the optical thickness of the thinnest specimen is greater than 20. Thus, the radiative conductivities which contain the optically thick approximation do not cause any significant difference. As can be seen, all the theoretical results underpredict the experimental values by 20 to 40 percent. The dash lines in the figures are the theoretical results calculated similarly as before except the experimentally determined wavelength-averaged extinction coefficient ($\sigma_e = 5.40 \times 10^2 m^{-1}$) is used instead. This is a 35 percent decrease in σ_e

and depending on the particular transfer model used, it causes an increase of the radiant heat flux by about 50 percent and yields a much closer agreement between the models and the experimental data. The closer agreement, however, does not necessarily imply that the experimental σ_e is the true value for reasons discussed earlier.

Figures 8–10 present the combined air conduction and thermal radiation results. The measurements were made at atmospheric pressure. The theoretical results were obtained by superimposing the radiant and conductive heat fluxes. The conductive heat flux was determined from Fourier's law with the air thermal conductivity evaluated at the mean of the boundary tempertures. The superposition method for treating combined conduction and radiation problem has been shown to be a reasonable approximation for systems with large emissivities [10]. The solid and dash lines have the same representation as those in Figs. 5–7 and similar interpretations can be made. Again, the results calculated with the theoretical extinction coefficient underpredict the measured values. However, the degree of underprediction is reduced approximately by half. This is believed to be caused by the air conduction which has the effect of suppressing part of the disagreement due to thermal radiation. A comparison of the results in Figs. 5–10 shows that thermal radiation is 42 to 49 percent of the total heat transfer.

In a similar study by Houston and Korpela [9], excellent agreements between the theoretical heat transfer results and experimental data have been reported. The major difference between their radiation model and the present two-flux and LAS models is that their model is nongray whereas the present ones are gray. It is difficult to attribute the overpredictions entirely on the gray approximation since it is not the only dissimilarity among the models. But it does suggest that the nongray behavior could be a possible cause for the discrepancies.

One other point that should be noted is that the insulation has been treated as homogeneous in the analysis [1]. In practice, most LWFI including the test insulation are not homogeneous. Some portions of the insulation contain more fibers and are optically thicker than the others. As the radiant heat flux decays exponentially with optical thickness, the decay in an optically thick region is much smaller than in a thinner region. Therefore, as one portion becomes optically thicker, the decrease in heat flux will not be as large as the increase in another portion which becomes optically thinner. What this amounts to is a net increase of heat flux due to inhomogeneity. This may also account for some of the overprediction of the radiant heat flux.

Summary

The analytical models developed in Part I of this paper for predicting the radiant heat flux and the radiative properties of LWFI have been tested against measured results from a transmission experiment and a guarded hot plate experiment. The insulation tested was a commercial building insulation. Based on the results, it can be concluded that:

(*i*) The analytical models for the radiative properties are capable of predicting representative values for typical commercial LWFI.

(*ii*) The simple data reduction method of employing Beer's law in the transmission experiment may not be adequate, as in-scattering can be appreciable.

(*iii*) Only qualitative agreements have been obtained between the theoretical heat transfer results and the experimental data, and indications are that the nongray and nonuniform characteristics of the properties may need to be incorporated in future improvements of the present models.

Acknowledgment

The authors wish to acknowledge the joint support of this work by the National Science Foundation and the U.S. Department of Energy.

References

1 Tong, T. W., and Tien, C. L., "Radiative Heat Transfer in Fibrous Insulations—Part I: Analytical Study," ASME JOURNAL OF HEAT TRANSFER, Vol. 105, Feb. 1983, pp. 70–75.

2 Love, T. J., and Saboonchi, A., "Determination of the Extinction Coefficient of Glass Fiber Insulation," *AIAA 15th Thermophysics Conference*, AIAA-80-1528, 1980.

3 *Annual Book of ASTM Standards*, Pt. 18, 1979.

4 Birkebak, R. C., "A Technique for Measuring Spectral Emittance," *The Review of Scientific Instruments*, Vol. 43, 1972, pp. 1027–1030.

5 De Ponte, F., and Di Fillippo, P., "Design Criteria for Guarded Hot Plate Apparatus," *Heat Transmission Measurements in Thermal Insulations*, ASTM Special Technical Publication 544, 1973, pp. 97–117.

6 Tong, T. W., and Tien, C. L., "Analytical Models for Thermal Radiation in Fibrous Insulations," *Journal of Thermal Insulation*, Vol. 4, 1980, pp. 27–44.

7 Hsieh, C. K., and Su, K. C., "Thermal Radiative Properties of Glass from 0.32 to 206 dm," *Solar Energy*, Vol. 22, 1979, pp. 37–43.

8 Birkebak, R. C., Enoch, I. E., and Ozil, E., "Experimental Study of Heat Transfer in Fiberglass Material," *AIAA/ASME Joint Fluids, Plasmas, Thermophysics and Heat Transfer Conference*, ASME Paper No. 82-HT-51, 1982.

9 Houston, R. L., and Korpela, S. A., "Heat Transfer Through Fiberglass Insulation," *Proceedings of the 7th International Heat Transfer Conference*, Vol. 2, 1982, pp. 499–504.

10 Yuen, W. W., and Wong, L. W., "Heat Transfer by Conduction and Radiation in a One-Dimensional Absorbing, Emitting and Anisotropically Scattering Medium," ASME JOURNAL OF HEAT TRANSFER, Vol. 102, 1980, pp. 303–307.

Y. S. H. Najjar
Mechanical Engineering Department,
Yarmouk University,
Irbid, Jordan
Mem. ASME

E. M. Goodger
Cranfield Institute of Technology,
School of Mechanical Engineering,
Cranfield, Bedford, England

Radiation and Smoke From the Gas Turbine Combustor Using Heavy Fuels

Broadening of aviation fuel specifications has been simulated using blends of gas oil and residual fuel oil. Radiation, smoke, and temperature measurements in an experimental combustor at various air pressure, inlet temperture, and air/fuel ratios showed a diminishing rate of increase of radiation with soot concentration and reduced sensitivity of smoke to fuel hydrogen content at higher combustor pressures.

1 Introduction

The major price increases and the impending shortage of liquid fuels relative to the rising demand is bringing about a serious examination of the possible changes in fuel properties. The most probable changes are expected to be a decrease in hydrogen content together with increases in aromatic compounds, the percentages of nitrogen and sulphur, and the fuel boiling range.

In a previous paper [1] and experimental investigation was reported on the effect of fuel type on flame radiation and, consequently, on flame tube durability.

In this present work, the experimental facility has been slightly modified, and the fuel specifications broadened, with parametric investigation of the relative effects of the combustor operating conditions to predict soot formation and oxidation with particular emphasis on the effect of fuel type.

2 Experimental Facilities and Procedures

A continuous-combustion rig (Fig. 1) has been developed at Cranfield for the measurement of radiation at different axial stations in a spray-stabilized flame based on the Schmidt method [2]. It has been further developed and modified in this investigation to suit operation at high inlet air temperature. The test facility consists essentially of the following:

(*a*) An air heater
(*b*) Air ducting
(*c*) A combustion section including the flame tube and its casing
(*d*) A fuel inlet and traversing tube which carries an atomizer location section (ALS), a flare (flame stabiliser) and an atomiser
(*e*) A tail pipe

The atomiser is a duple Dart unit with the pilot injector have a spray angle of 100 deg and a flow number (F.N.) of 0.332, corresponding values for the main injector being 120 deg and 1.233. The atomiser is located in a Dart flare welded to an atomiser location section which slides into a truncated Mamba combustion chamber in a duct of 154-mm bore, dilution air being admitted downstream in the conventional manner. Diametrically-opposed calcium fluoride windows are fitted at as fixed plane in the flame zone, and purged with nitrogen gas to prevent contact with hot gases or fuel droplets. This system permits measurement of radiation, and calculation of emissivity, using a Land NRF total-radiation pyrometer and amplifier, and a Spembly 10 kVA black-body furnace with a Land MQO pyrometer, following the modified Schmidt method based on the comparison of radiation from the flame and the black background in the furnace [1]. The air supply facility provided mass flows up to 1.8 kg/s at a pressure of 10 atm and temperature of 460 K, the combustion and dilution air flows being controlled separately and remotely. Air mass flows were measured with conventional orifices, and fuel mass flow from the pressure readings of the calibrated atomiser. Chamber pressure was controlled by means of outlet back-pressure valve.

A major feature of the rig is the ability to move the swirler/injector assembly through an axial distance of 102 mm, effectively providing different observation stations along the flame. One thermocouple is fitted to the flame-tube liner within the observation plane, six others at the combustor exist to measure temperature traverse quality (TTQ) of the flame, and three at the exhaust section in the tailpipe. After cooling within a water-jacketed section of the tailpipe, the gas flow was sampled by means of Bacharach pump at a point 1720 mm downstream from the observation plane, and then passed through a filter paper, the intensity of the resulting strain being measured by a reflectometer.

A range of commercial hydrocarbon fuels were used: kerosine (*K*) represents aviation fuel, gas oil (*G*) as a current industrial gas turbine fuel and possible future aviation fuel R25 (where 25 is the volume percentage of residual fuel oil in the blend with gas oil) as equivalent to crude oil, and R50 and R70 to check the potential of the gas turbine when using heavier fuels. The fuel properties are shown in Table 1.

The combustor operating conditions were chosen as follows: combustor pressures were 3, 7, and 10 atm to cover, idle, half-load, and the full-load settings of an industrial gas turbine.

Inlet air temperatures (TIN) were 313, 390, and 460 K. The lowest temperature was determined by the compressor house arrangement without additional heating. The highest temperatue was restricted by the temperature limit on the combustor pressure control valve at the rig outlet.

Primary air/fuel ratios (AFR_p) were 12, 15, and 25. The change was achieved by maintaining constant the fuel mass flow and adjusting the air mass flow entering the primary zone. The total air/fuel ratios (AFR_T) were 120 and 60 to simulate idle and full power settings.

General Discussion

Radiation. Radiant energy is the result of complicated molecular and atomic disturbances, and occurs at the expense of other kinds of energy, mostly thermal. Since the temperature of the body is the original cause of interatomic

Contributed by the Heat Transfer Division for publication in the JOURNAL OF HEAT TRANSFER. Manuscript received by the Heat Transfer Division October 1, 1981.

Table 1 Fuel properties

Property of fuel	Kerosine	Gas oil	R25	R50	R70	R100	Typical Crude
Composition							
Proximate composition							
Aromatics % Vol	18.4	28.2				50	
Olefins % Vol	0.6	0.6				1.0	
Saturates % Vol	81.0	71.2				49.0	
Ultimate composition							
Carbon % wt	86.19	85.71	85.7	85.7	85.7	85.7	86.0
Hydrogen %	13.3	12.67	12.324	12.0	11.756	11.41	12.1
Suphur % wt	0.1	0.31	0.6858	1.38	1.3243	1.68	1.14
Nitrogen % wt	0.1	0.1				0.1	
ppm		500				900	630
Ash % mass	Negl.	0.005	0.011	0.017	0.023	0.03	0.011
C/H mass ratio	6.48	6.765	6.952	7.134	7.282	7.5	7.11
Contaminants							
Sodium ppm		0.5	6	12	16	23	5
Vanadium ppm		0.5		12		69	7
Water % Vol	Negl.	Negl.				0.05	
Sediment % mass	Negl.	Negl.				0.04	
Volatility							
Boiling range °C	160-285	180-360					
Spon.ign.temp°C	255	245	241	237	234	230	
Flash point, closed °C	56	67	86	96	104	116	
Relative density 15°C/15°C	0.79	0.852	0.88055	0.93194	0.93194	0.9662	0.87
Correction to R.D./°C	0.00072	0.00068	0.00067	0.00067	0.00067	0.00067	
RMM	180.18	220.64	234.6	248.56	259.2	276.7	
Fluidity							
Pour point °C	−60	−45	−28	−11	3	24	−10
Kinematic viscosity cSt							
@ 15°C	2.04	6.0	14.5	65	220	3300	35
@ 37.8°C	1.5	3.3	7.0	22.0	60	862	
Surface tension							
mN/m (dyne/cm)@ 20°C	24	29	30.5	32	33.2	35	
Min. storage temp. °C	amb.	amb.				35	
Combustion							
Specific energy MJ/kg							
Gross	46.287	45.217	44.769	44.4	44.1	43.682	44.739
Net	43.187	42.517	42.106	41.814	41.617	41.282	42.049
Latent heat of Vapor kJ/kg	291.0	267.0					
Mean specific heat							
kJ/kg.K (liquid)	2.008	1.992	1.985	1.9787	1.9739	1.967	
Mean specific heat							
kJ/kg.K (vapour)	1.674	1.674	1.674	1.674	1.674	1.674	
Flamm. range %Vol.fuel	1-6	1-5				1-5	
(A/F) by mass	5-25					1-5	
Dew point of exhaust gas °C	51	50				48	
Stoic.A/F mass ratio	14.554	14.42	14.312	14.212	14.135	14.027	
Enthalpy of formation kJ/kg	−1373	−1348	−1324.4	−1302.3	−1285.6	−1262	
Activation energy of combustion, kJ/mol	113.01	114.67	115.501	116.332			
Formula	$C_{13}H_{24}$	$C_{16}H_{28}S_{0.02}$	$C_{17}H_{29}S_{0.05}$	$C_{18}H_{30}S_{0.08}$	$C_{18.8}H_{30.8}S_{0.11}$	$C_{20}H_{32}S_{0.147}$	
Thermal stability							
Conradson wt%	0.2	0.7	2.84	4.84	6.36	8.5	

Nomenclature

AFR_p = primary zone air/fuel mass ratio
AFR_T = total air/fuel mass ratio
ALS = atomiser location section
$\bar{C}$ = soot concentration
C_{exh} = concentration of exhaust smoke at standard conditions, g/Sm^3
C/H = carbon/hydrogen ratio of fuel
EQT = maximum radiation temperature, K
FN = flow number of fuel atomiser
G = gas oil
K = kerosine
P = pressure, atm
R_1 = total flame radiation with cold background, kW/m^2
R_2 = total flame radiation with hot background, kW/m^2
R_3 = total radiation of background, kW/m^2
RX = blend of X percent by volume of residual fuel oil in gas oil
r_s = reflectance of smoke stain
r_w = reflectance of clean filter paper
SN = smoke number
TAA = maximum gas temperature, K
TDA = adiabatic flame temperature, K
T_f = flame temperature, K
TIN = inlet air temperature, K
TTQ = temperature traverse quality at combustor outlet
α = total flame absorptivity
ϵ = total flame emissivity
ϵ_λ = spectral emissivity
α_λ = spectral absorptivity

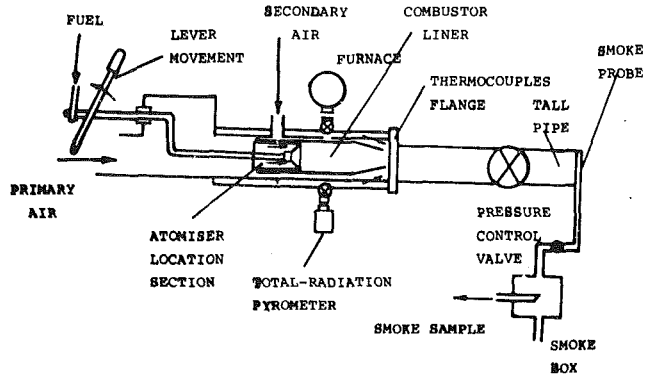

Fig. 1 Schematic of flame radiation rig

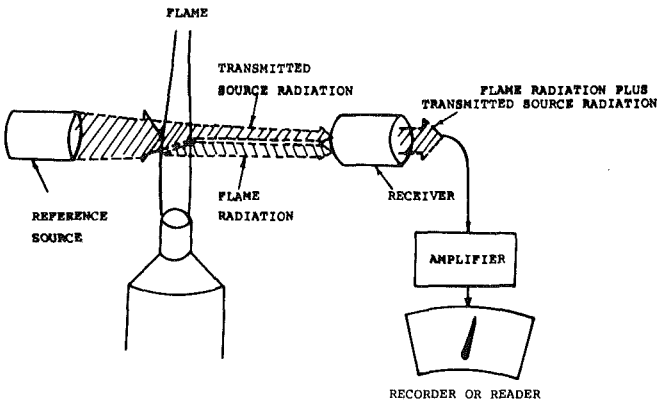

Fig. 2 Schematic of Schmidt method

disturbances, the quantity of radiant energy generated depends essentially on that temperature.

Visible light and infrared rays, which are approximately of wavelengths ranging from 0.4 to 40 μm, can be absorbed by substances, and their kinetic energy turns into heat energy in the course of absorption.

The burning of hydrocarbon fuel in the combustor produces gases, the most radiative of which are such polyatomic gases as H_2O, CO_2, and SO_2. An intermediate stage in the combustion process is often the production of clouds of carbon particles which, at the high temperature of combustion, radiate intensely.

The measuring technique which has been used in this work is optical, and avoids the drawbacks of direct sampling and light scattering techniques. The method was first suggested by Schmidt [2] for determination of flame temperature from simultaneous measurements of spectral radiation and spectral absorptance. This method is claimed to be more precise when used monochromatically because the flame is not assumed to be grey where emissivity (ϵ) is independent of wavelength. However when flames are heavily charged with soot, and where the soot acts primarily to absorb radiation and not to scatter it (small soot particles = 0.06 μm), it is often assumed that sooty gas is a grey body. In this work this assumption is valid because the energy-absorbing molecules will be abundant since the flame is optically not thin, and because high pressures were used. The flame was heavily charged with soot, in the region of measurement, even with distillate fuels. Furthermore, the use of heavy fuels generate more soot particles. Therefore the modified Schmidt method or the total emission-absorption method was used. It is attractive because it is relatively simple to apply, and requires no quantitative previous knowledge of the gas properties. A diagram of this method is shown in Fig. 2, where a blackbody furnace has been used as a reference source, and a total radiation fluxmeter (radiometer) used as detector.

Thus the grey body assumption involves an optically thick flame. Therefore, if it happened within very few experiments of this work that the flame was not thick enough to be considered grey, the effect is less important than the simplified assumption that the flame absorbs entirely between 0–10 μm of the transmitted spectrum of the windows in the experimental rig. Under such a condition of total absorption and emission, T_f, is the true flame temperature only when $T_f = T_B$ and the corresponding value of α is equal to the total emissivity, ϵ, according to Kirchoff's law. Therefore, throughout the experiments the black body temperature (T_B) was changed with each set of tests to approach the expected T_f as much as possible.

Smoke. The control of exhaust smoke has become a significant engine operating requirement. Broadly, smoke can be reduced by controlling the production of soot in the fuel-rich regions of the primary zone, together with its subsequent consumption in the other regions of the primary zone and in the secondary zone.

The fuel composition is believed to affect soot formation under the prevailing conditions of high temperature and low oxygen concentration. It also affects smoke through the influence of viscosity and volatility of fuel on atomization and vaporization. Thermal stability affects cracking tendency. The soot forming tendency of a fuel increases with aromatic content, type of aromatics, final boiling point and C/H ratio.

The relationship between the aromatic content and smoke point of kerosine flame is shown in [3] as follows:

aromatic content, % vol.	10	18	22	28
smoke point, mm	23	19	14	12

Furthermore, hydrocarbons having approximately equal boiling points may form carbon differently. Also carbon formation from hydrocarbons having equal C/H ratios may be different. Bocca et al. [4] showed that particular emission from fuel oil can be directly related to the presence in the fuel of heavy, highly condensed aromatic rings in the range of C_{30} ot C_{80}. They defined these compounds quantitatively as the sum of polar aromatics plus asphaltenes content of the fuel. They showed particulate emissions as follows:

Fuel type	Particulates emitted mg/Sm^3
Paraffinic	4
Aromatic	11.1
Asphaltenic	234

Numerous methods have been suggested and used for smoke reduction, for example:

(*a*) Combustor design modifications, including leaning the primary zone, increased the pressure loss factor, improving the fuel injection technique, axial fuel staging, variable geometry staged combustion and premix/prevaporization systems:
(*b*) Fuel additives
(*c*) Fuel-water emulsions
(*d*) Water injection
(*e*) Electric field

Experimental Results and Discussion

The experimental program has been carried out with the following parameters: fuel type, combustor pressure, inlet temperature, primary zone air/fuel ratio, AFR_p, and total air/fuel ratio, AFR_T. Total radiation was measured, from which flame total emissivity (ϵ) and flame temperature (T_f) have been calculated, at five locations along the primary zone. Maximum T_f has been averaged with the calculated adiabatic

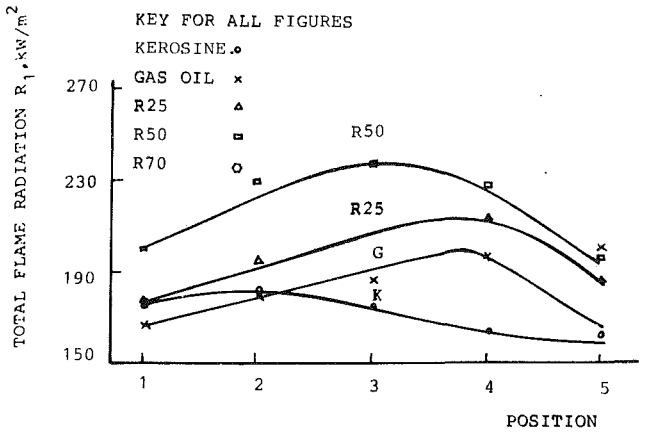

Fig. 3 Flame radiation along the primary zone at $P = 10$ atm and $TIN = 313$ K

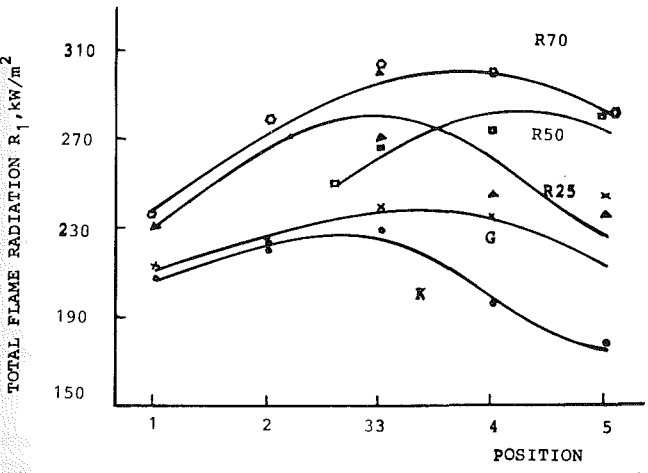

Fig. 4 Flame radiation along the primary zone at $P = 10$ atm and $TIN = 460$ K

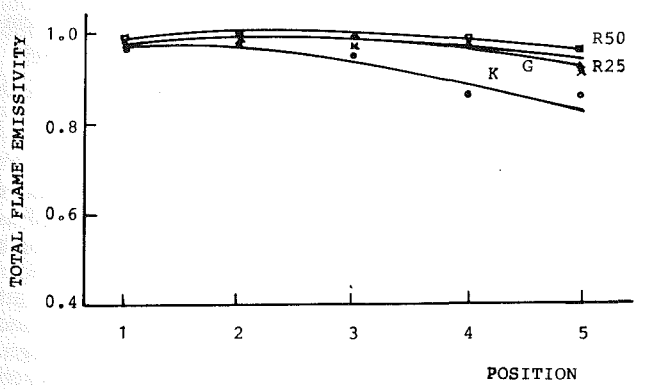

Fig. 5 Flame emissivity along the primary zone at $P = 10$ atm and $TIN = 313$ K

flame temperature. Then the average temperature with the associated ϵ at the particular location have been used to calculate soot concentration ($\bar{C}$).

Flame Radiation. Figures 3 and 4 illustrate the change in flame radiation along the primary zone at five 1-in. (2.5-cm) stations, under different conditions of inlet air temperature (*TIN*) and pressure (*P*) with the different fuels. It is noted that radiation increases to a peak after a certain distance along the

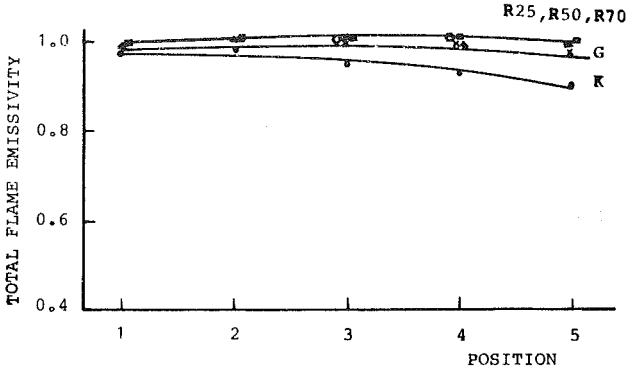

Fig. 6 Flame emissivity along the primary zone at $P = 10$ atm and $TIN = 460$ K

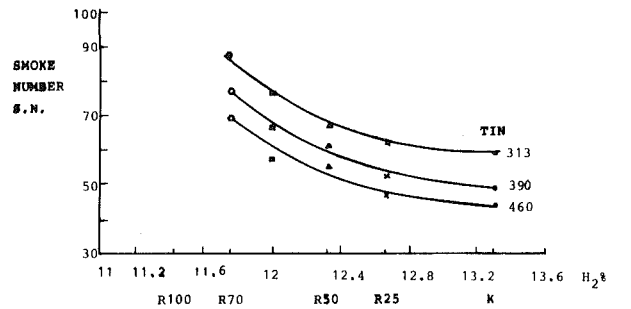

Fig. 7 Influence of fuel hydrogen content on smoke number at 3 atm

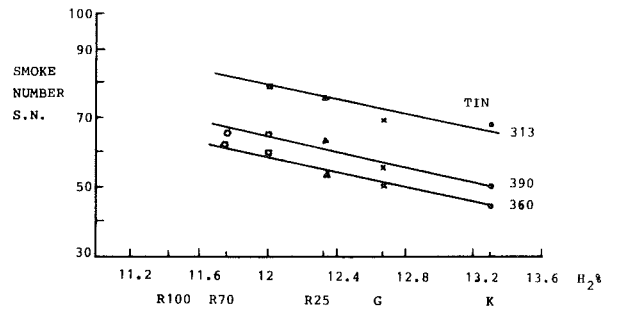

Fig. 8 Influence of fuel hydrogen content on smoke number at 10 atm

primary zone, followed by a reduction. The peak and distance are affected by the running conditions and fuel type. This is attributed to the increase of soot concentration which, after a certain time depending on the running condition, will start to burn. Radiation increases with soot concentration, and with the temperature of the soot particles, through its effect on the incandescence. This effect is noted clearly by comparing Fig. 3 and 4, where the same fuel gives higher radiation levels at higher inlet temperatures. The pressure effect was observed to double flame radiation between 3 and 10 atm.

Total Flame Emissivity (ϵ). This has been calculated from equation

$$\epsilon = 1 - (R_2 - R_1)/R_3 \tag{1}$$

where,

R_1 = total flame radiation with cold background
R_2 = total flame radiation with hot background
R_3 = total radiation of the background

Representative curves are shown in Figs. 5 and 6 for different fuels at different running conditions. Total flame emissivity

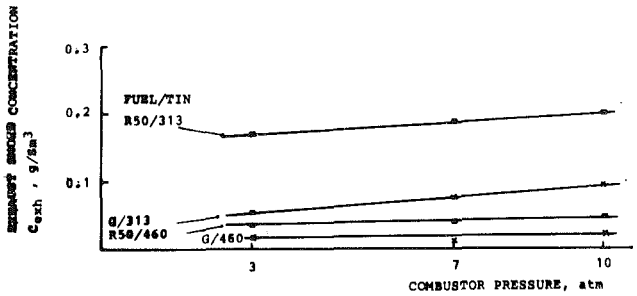

Fig. 9 Influence of combustor pressure on exhaust smoke concentration

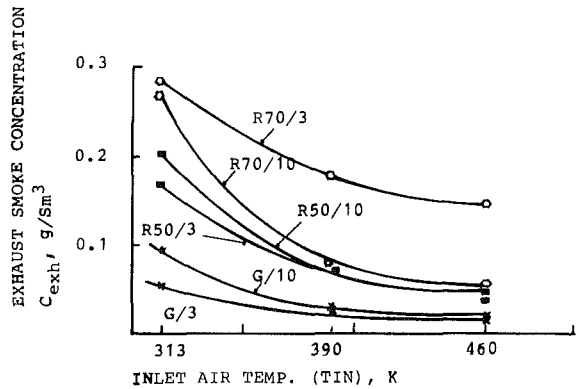

Fig. 10 Influence of inlet air temperature on exhaust smoke concentration

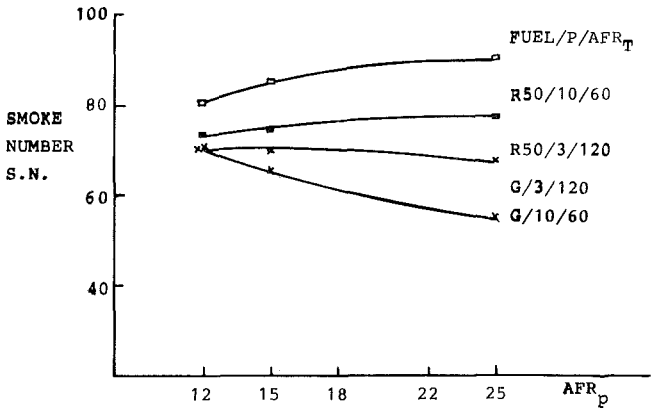

Fig. 11 Influence of primary air/fuel ratio on smoke number at 460 K

(ϵ) is shown to be affected remarkably by combustor pressure increase. While differences can be noted between fuels at 3 atm, all the fuel flames become highly emissive at 10 atm (more than 0.9). However the increase in inlet air temperatures does not seem to have any clear effect.

Flame Temperature. The radiation flame temperature was calculated from equation

$$T_f = (537 \times 10^8 R_1/\epsilon)^{0.25} \quad (2)$$

knowing the flame radiation and total emissivity (ϵ). However when conditions differ from those of grey flame due to the existence of cold air or small fuel droplets, this temperature will fall. To compensate for the underestimation, the adiabatic flame temperature (*TDA*) was calculated theoretically by a computer programme "TEMP." This temperature was then averaged with the maximum radiation temperature (*EQT*). The average of both temperatures is

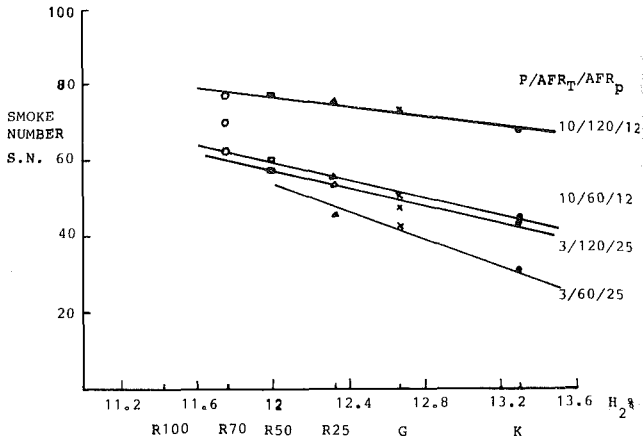

Fig. 12 Influence of total air/fuel ratio on smoke number at 460 K

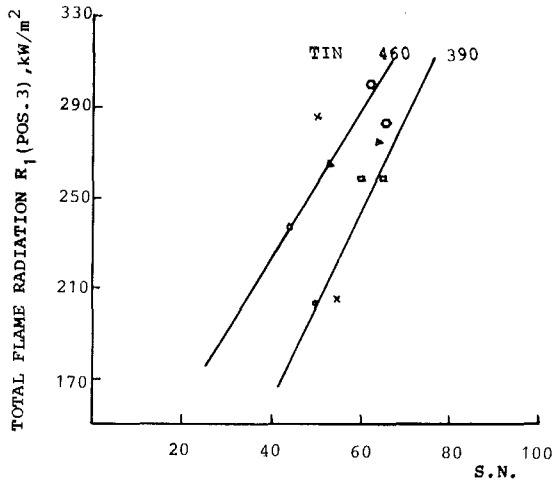

Fig. 13 Correlation of primay zone flame radiation with smoke number at $P = 10$ atm and $TIN = 390$ & 460 K

taken as the maximum gas temperature (*TAA*). The temperature profile along the primary zone was then constructed.

Exhaust Smoke. Exhaust smoke was estimated as smoke number (*SN*) from equation

$$SN = (1 - r_s/r_w)\,100 \quad (3)$$

where r_s and r_w are the reflectometer readings from the smoke stain and white filter paper, respectively, and expressed as concentration at standard conditions C_{exh} g/Sm^3 by using a correlation from (5). Figures 7 and 8 illustrate the correlations between smoke number and the fuel, represented by its hydrogen content (percent mass) at different pressures and inlet temperatures. The effect of decreasing the fuel hydrogen content is manifested in increasing exhaust smoke. However, the sensitivity of smoke to the fuel type falls with increased combustor pressure. This sensitivity is further decreased when higher pressures are associated with higher inlet air temperatures as shown in Fig. 9. If the fuel is heavier than R50 then the sensitivity to pressure rise decreases to the extent of being negative; that is, with R70 smoke would be less at 10 atm than at 3 atm especially at high inlet temperature as shown in Fig. 10. This sheds light on the very remarkable influence of gas temperature during the oxidation process regardless of the soot formed in the primary zone. This is true because the effect of difference in residence time in the secondary zone between the idle and full power conditions was insignificant. Since smoke is a full-power setting

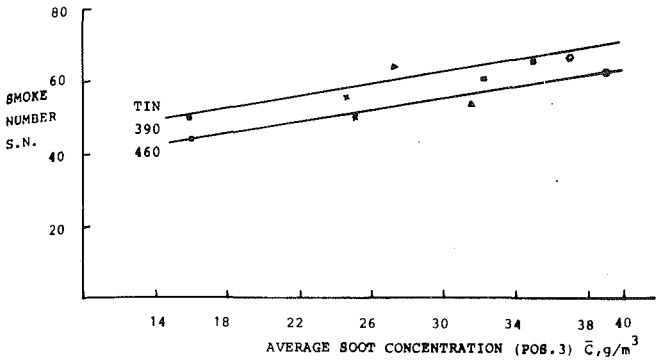

Fig. 14 Correlation of primary zone soot concentration with smoke number at $P = 10$ atm and $TIN = 460$ K

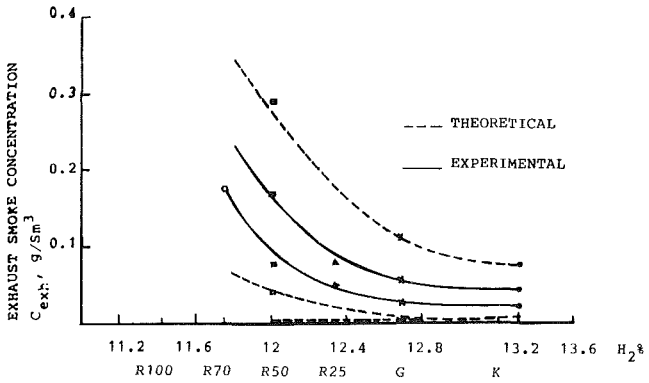

Fig. 15 Comparison of predicted and experimental concentrations of exhaust smoke at 3 atm

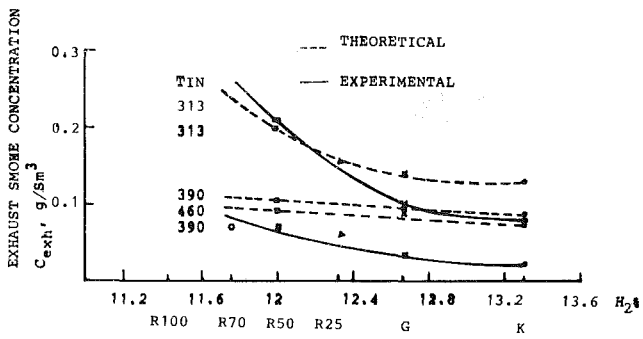

Fig. 16 Comparison of predicted and experimental concentrations of exhaust smoke at 10 atm

emission, this leads to a very important result; that is, for replicated engine conditions, use of heavier fuels is not expected to aggravate seriously the smoke emission at full power setting at which the engine will be operating most of the time.

The effects of the primary zone air-fuel ratio AFR_p and the total air-fuel ratio AFR_T are depicted in Figs. 11 and 12 and discussed below:

(*a*) At idle conditions (3 atm), with kerosine, gas oil and R25, it was found experimentally that at the inlet air temperatures of this work, smoke level decreases slightly by leaning the primary zone towards $AFR_p = 25$. However, smoke level increases with R50 and R70. Both cases are represented by the G/3 and R50/3 curves in Fig. 11.

With regards to the effect of total air-fuel ratio, kerosine, gas oil and R25 give less smoke with $AFR_T = 60$ than $AFR_T = 120$, as shown by the 3/120/25 and 3/60/25 curves in Fig. 12. When R50 or R70 is used, smoke was found to increase at $ARF_T = 60$ especially at low inlet air temperatures.

In this last case, the smoke level at $AFR_p = 15$ was found to be less than with $AFR_p = 25$. Therefore, with heavy fuels, the usual conclusion that leaning of the primary zone reduces smoke, does not apply, especially at low inlet air temperatures. Hence, it can be concluded that, for operation at idle conditions, the optimum distribution of air is appoximately as follows:

(*i*) for kerosine, gas oil, R25: $AFR_p = 15$, $AFR_T = 60$

(*ii*) for R50 and R70: $AFR_p = 15$, $AFR_T = 120$

(*b*) At half-load setting (7 atm) all the fuels produce higher smoke level by leaning the primary zone to $AFR_p = 25$, so the optimum conditions would be $AFR_p = 15$, $AFR_T = 60$, approximately.

(*c*) At full-power setting (10 atm), with kerosine, gas oil, and R25 for all inlet air temperatures, smoke level decreases by leaning the primary zone towards $AFR_p = 25$. However, with R50 and R70 the smoke level increases (Fig. 11). Insofar as the total air-fuel ratio affects smoke level, all the fuels give less smoke with $AFR_T = 60$ than with 120. Hence, the optimum distribution of air would be as follows:

(*i*) For kerosine and gas oil: $AFR_p = 25$, $AFR_T = 60$ approximately

(*ii*) For R25, R50 and R70: $AFR_p = 15$, $AFR_T = 60$ approximately

There is thus no need to emphasize the necessity for varying the air distribution in the combustor to cater for different fuel requirements in order to reduce smoke to a minimum. This is the area where a variable-geometry combustor may help in solving the problem.

Since it is always very much easier to measure smoke than to measure radiation in the primary zone, a correlation such as that shown in Fig. 13 can be beneficial. This correlation shows the strong dependence of smoke level on flame radiation in the primary zone for different fuels. Furthermore, since flame radiation increases with soot concentration, it follows that fuel type affects exhaust smoke only through its effect on soot concentration in the primary zone.

It would also be convenient to draw a correlation between the soot concentration in the primary zone and the smoke number as shown in Fig. 14. It is interesting to note that, although the time of combustion of a carbon particle is an order of magnitude greater than the corresponding fuel particle, the soot level in the primary zone would drop about 1000 times in its travel through the secondary zone before emerging as smoke. Because of this strong effect of temperature on soot oxidation, addition of a relatively large quantity of cool air only reduces the gas temperature and increases the lifetime of the soot particles.

It is noteworthy that during the experimental tests blue and white smoke were seen, especially at idle conditions with gas oil and residual fuel blends. Although black smoke is recognized to be due to lack of air, blue smoke seems to occur at an inefficient condition associated with fuel quenching and excess air. The exhaust at this condition has an objectionable smell and irritates the eyes, probably due to the presence of traces of formaldehyde. The white smoke with heavy fuels at idle conditions is expected to be due to the increased presence of sulphuric acid in the unburnt fuel, thus elevating the dew point of the exhaust gas considerably.

Prediction of Exhaust Smoke and Comparison With Experiment

The model to predict soot oxidation in the secondary zone, and hence the soot concentration available as exhaust smoke, was presented in a programe "OXID." The results have been graphically represented in Figs. 15 and 16. It is interesting to note that the model prediction compares favourably with the

experimental measurements. However, it should be noticed that at 3 atm and high temperature, the model predicts complete combustion of the soot. This is not seriously in error as the corresponding measured values are around 0.003 g/Sm^3 which is considered as the threshold of visibility of the smoke plume for large turbojets.

The increase of smoke level at 3 atm over that at 10 atm with R50 corresponds to that found experimentally. This emphasizes the importance of gas temperature in the oxidation process, especially with heavy fuels. The model calculations show that the surface oxidation rate is maximum near $\phi = 0.7$. Thus, to reduce the smoke emission level, say, from R70 down to that of kerosine, the addition and distribution of the secondary air should be controlled through combustor design to allow the residence of the gas at that equivalence ratio to be as long as possible.

Conclusions

1 Flame radiation to the flame tube increases only slightly with the increase of soot concentration above about 25 g/Sm^3.

2 The sensitivity of smoke to the fall in hydrogen content of the fuel decreases at higher combustor pressures, and decreases further with higher inlet air temperatures. Thus, at replicated engine conditions of nearly full power, the use of heavier fuels might not aggravate seriously the smoke emission.

3 Optimum distribution of air for minimum smoke emission is approximately as follows:

(*a*) Idle conditions

(*i*) for kerosine, gas oil and R25: $AFR_p = 15$, $AFR_T = 60$

(*ii*) for R50 and R70: $AFR_p = 15$, $AFR_T = 120$

(*b*) Half-load conditions (for all fuels): $AFR_p = 15$, $AFR_T = 60$

(*c*) Full power conditions

(*i*) For kerosine and gas oil: $AFR_p = 25$, $AFR_T = 60$

(*ii*) For R25, R50 and R70: $AFR_p = 15$, $AFR_T = 60$

References

1 Goodger, E. M., and Najjar, Y. S. H., "Heavy-Fuel Flame Radiation in Gas Turbine Combustors—Explanatory Results," *Fuel*, Vol. 56, Oct. 1977, pp. 437–440.

2 Schmidt, H., *Ann Physik*, Vol. 29, 1909, p. 971.

3 Kuhbach, C., Ritcheske, W., and Strauss, K., "Jet Engines Have Deposit Problems, Too!," *S. A. E. Journal*, Vol. 63, Aug. 1955, pp. 64–68.

4 Bocca, P., Fontana, M., Belli, R., Billi, B., and Tarli, R., "Chemical Factors Influencing Particulate Emissions From Fuel Oil," *La Rivista Dei Combustibili*, Vol. XXX, Fasc. 8, Aogsto, 1976.

5 Norgren, C. T., and Ingebo, R. D., "Particulate Exhaust Emissions From an Experimental Combustor," NASA TMX-3254, 1975.

6 Toone, B., "A Review of Aeroengine Smoke Emission," *Combustion in Advanced Gas Turbine Systems*, Pergamon Press, 1967, pp. 271–293.

Radiation-Natural Convection Interactions in Two-Dimensional Complex Enclosures

L. C. Chang[1]

K. T. Yang
Fellow ASME

J. R. Lloyd
Mem. ASME

Department of Aerospace and Mechanical Engineering, University of Notre Dame, Notre Dame, Ind. 46556

A numerical finite-difference study has been carried out for the two-dimensional radiation-natural convection interaction phenomena in square enclosures with equal vertical finite-thickness partitions located at the centers of the ceiling and floor. Both participating gases (CO_2 and NH_3) and nonparticipating gas (air) are considered. In the radiation calculations, the nongray exponential wide-band models for CO_2 and NH_3 are used, together with a radial flux method utilizing a more realistic polar description for the radiation exchange in the enclosure. Results on the effects of both surface and gas radiation on the velocity and temperature fields and the overall heat transfer rates as functions of the partition heights at two levels of the Grashof number are presented and discussed in terms of the physical phenomena.

Introduction

In a room fire situation, the spread of fire, smoke and toxic gases is governed by turbulent buoyant flow generated by the fire, the combustion process, the heat transfer processes of conduction through the walls, ceiling and floor, convection due to the hot gases, and radiation exchange between the flame, hot gases and the room surfaces. There is no method of analysis at this time to deal with this complete spread phenomena, and much of its physical understanding is still lacking. One good example is how thermal radiation, known to be important in room fires, affects the energy transfer process, particularly that which leads to flashover. However, before this problem can be studied, it is desirable to treat a simpler process of radiation-convection interaction in an enclosure filled with a participating gas to sort out the conditions under which radiation becomes important. Also, it would be pertinent to consider internal partitions in the enclosure to determine the sensitivity of radiation-convection interaction to such partitions. The partitions could represent the doorway soffits in adjoining rooms or dividers in a single room. The purpose of this numerical study is to address this simpler problem by considering a square enclosure partitioned into two connecting regions by two vertical finite-thickness partitions mounted midway at the enclosure ceiling and floor (Fig. 1).

There are few studies available in the literature on enclosure heat transfer with combined convection and radiation. Larson and Viskanta [1] treated the problem of transient laminar free convection in a rectangular enclosure with thermal radiation, and found that radiation heats up the enclosure surface and the gas body very quickly and thus significantly alters the flow pattern and the corresponding convection process. Modak and Mathews [2] studied the thermal radiation feedback from hot enclosure surfaces and ceiling hot gas layer to arbitrarily oriented targets within a box enclosure and found that radiation plays a very significant role in controlling the growth of fires. Lloyd, Yang and Liu [3] considered one-dimensional surface, gas, and soot radiation for turbulent buoyant flow in a rectangular enclosure induced by a volumetric heat source at the floor. In this study, the nongray exponential wide-band model was used for a mixture of water vapor and carbon dioxide. They found that the radiation effects tend to make the vertical temperature profiles more uniform, and also clarified the relative roles of surface, gas, and soot radiation. In a more recent numerical study, Larson [4] treated turbulent buoyant flow in a rectangular enclosure containing a given flame; however, radiation-convection interaction was not considered external to the flame. The results again showed the significance of the contribution of radiation, especially in heating up the walls in the enclosure.

The enclosure geometry in the present study is shown in Fig. 1. The vertical side walls are maintained isothermal with $T_h > T_c$. Other bounding walls including the surfaces of the partitions are taken to be adiabatic, and all solid surfaces are black. The enclosure is filled with air as the nonparticipating gas, or CO_2 or NH_3 as the participating gases. Scattering of radiation is neglected, and the flow is taken to be laminar. Results of a companion pure natural-convection study dealing with the effects of Grashof numbers and size and location of the partitions are given in [5].

Mathematical Formulation

The Eulerian formulation in the Cartesian coordinate system is adopted with the gravitational acceleration vector g in the direction of $-\bar{y}$. The independent variables are the spatial coordinates, $\bar{x}$ and $\bar{y}$, and time, $\bar{t}$. The flow and

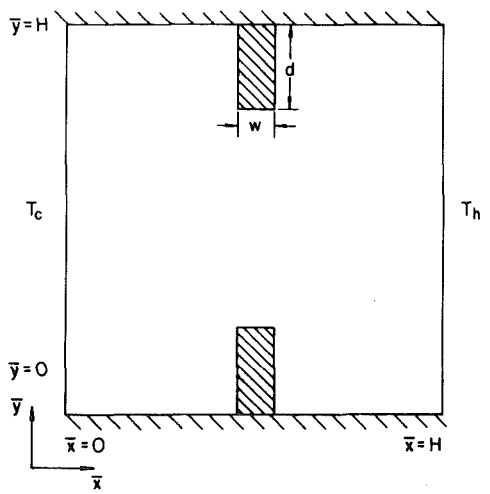

Fig. 1 Geometry of the square enclosure

[1] Present address: Detroit Diesel Division, General Motors Corporation.

Contributed by the Heat Transfer Division and presented at the AIAA/ASME Fluids, Plasma, Thermophysics, and Heat Transfer Conference, St. Louis, Missouri, June 7-11, 1982. Manuscript received by the Heat Transfer Division February 16, 1982. Paper No. 82-HT-49.

temperature fields can be described in terms of the following dependent variables: density, ρ, temperature, T, and pressure, p. The governing equations are from the conservation of mass, momentum and energy, and the equation of state for an ideal gas. The gas is considered to be Newtonian and the flow is laminar, but compressible. For simplicity, transport properties except density are assumed to be constant at the average temperature of $\bar{T}_c$ and $\bar{T}_h$. Pressure work done on the fluids and viscous dissipation are neglected in view of the low velocities involved. The flow is generated by buoyancy only, and the normal stresses due to dilation of the fluid are also neglected. The gas is initially stationary at a uniform temperature of $\bar{T}_a$, taken arbitrarily to be 277.8 K, and the pressure is initially at the static equilibrium atmospheric condition.

The following nondimensional quantities are introduced

$$x = \frac{\bar{x}}{H}, \quad y = \frac{\bar{y}}{H}, \quad t = \frac{\bar{t}u_o}{H}$$

$$u = \frac{\bar{u}}{u_o}, \quad v = \frac{\bar{u}}{u_o}, \quad P = \frac{\bar{P}-\bar{P}_e}{\bar{\rho}_a {u_o}^2}$$

$$\rho = \frac{\bar{\rho}}{\rho_a}, \quad T = \frac{\bar{T}}{\bar{T}_a}, \quad \rho_e = \frac{\bar{\rho}_e}{\rho_a}$$

$$q_c = \frac{\bar{q}_c}{\rho_a C_p u_o \bar{T}_a}, \quad q_r = \frac{\bar{q}_r}{\sigma \bar{T}_a{}^4}, \quad \mathrm{Re} = \frac{u_o H}{\nu}$$

$$Gr = \frac{g\beta(\bar{T}_a - \bar{T}_c)H^3}{\nu^2}, \quad \mathrm{Pr} = \frac{\nu}{\alpha}$$

where the barred quantities are dimensional and u_o is an arbitrary reference velocity. Also ρ_e is the equilibrium density corresponding to the hydrostatic conditions as given by $\rho_e = \rho_a \exp[-g\bar{H}y/R\bar{T}_a]$. The governing equations can then be written as follows

$$\frac{\partial \rho}{\partial t} + \frac{\partial(\rho u)}{\partial x} + \frac{\partial(\rho v)}{\partial y} = 0 \tag{1}$$

$$\frac{\partial(\rho u)}{\partial t} + \frac{\partial(\rho u^2)}{\partial x} + \frac{\partial(\rho uv)}{\partial y} = -\frac{\partial P}{\partial x} + \frac{2}{\mathrm{Re}}\frac{\partial^2 u}{\partial x^2} + \frac{1}{\mathrm{Re}}\left[\frac{\partial^2 v}{\partial x \partial y} + \frac{\partial^2 u}{\partial y^2}\right] \tag{2}$$

$$\frac{\partial(\rho v)}{\partial t} + \frac{\partial(\rho uv)}{\partial x} + \frac{\partial(\rho v^2)}{\partial y} = -\frac{\partial P}{\partial y} - \frac{gH}{{u_o}^2}(\rho - \rho_e) + \frac{2}{\mathrm{Re}}\frac{\partial^2 v}{\partial y^2} + \frac{1}{\mathrm{Re}}\left[\frac{\partial^2 u}{\partial x \partial y} + \frac{\partial^2 v}{\partial x^2}\right] \tag{3}$$

$$\frac{\partial(\rho T)}{\partial t} + \frac{\partial(\rho uT)}{\partial x} + \frac{\partial(\rho vT)}{\partial y} = \frac{1}{\mathrm{RePr}}\left[\frac{\partial^2 T}{\partial x^2} + \frac{\partial^2 \bar{T}}{\partial y^2}\right] + \frac{\sigma \bar{T}_a{}^3}{\rho_a C_p u_o \bar{T}_a} \nabla \cdot q_r \tag{4}$$

$$\rho T = \frac{{u_o}^2}{R\bar{T}_a} P + \rho_e \tag{5}$$

The term, q_r, is the dimensionless net radiation flux, when radiation from all directions is accounted for. The radiation heat flux arrives from a gas layer of thickness $(L - \bar{z})$ at a distance $\bar{z}$ bounded by an infinite black flat plate at an isothermal temperature $\bar{T}_o$ from above can be written [6, 7], in accordance with the scaling technique of Felske and Tien [8], as

$$q_r(\bar{z}) = e_b(\bar{T}_o) - \sum_{i=1}^{N} \bar{\omega}_i \int_{\bar{z}}^{L} A_{si}^*(\bar{\tau}'_{Hi} - \bar{\tau}_{Hi}) \frac{\partial e_{bv}(\bar{T})}{\partial z'} d\bar{z}' \tag{6}$$

Here, $\bar{z}$ is a physical distance, not necessarily related to the coordinate $\bar{z}$ in Fig. 1, and L is the total distance between the bounding black surfaces in the direction of $\bar{z}$. According to the exponential wide-band model, the slab band absorptance A_{si}^* is given by

$$A_{si}^*(\bar{\tau}'_{Hi} - \bar{\tau}_{Hi}) = \int_o^1 \left\{1 - \exp\left[-\frac{3}{2}(\bar{\tau}'_{Hi} - \bar{\tau}_{Hi})\tau_i^*\right]\right\} \frac{d\tau_{\tau_i}^*}{\tau_i^*} \tag{7}$$

where the difference in the optical path length is

Nomenclature

A_{si}^* = dimensionless slab band absorptance
C_p = isobaric specific heat
d = partition height
e = emissive Power
f = constant
Gr = Grashof Number, $g\beta(\bar{T}_a - \bar{T}_c)H^3/\nu^2$
g = gravitational acceleration
H = enclosure height
i, j = arbitrary calculation cell indices
k = gas conductivity
L = radiation path length
M = number of angle spans
N = number of gas absorption bands
$\bar{\mathrm{N}}\mathrm{u}$ = average Nusselt number on either vertical end wall
n = outward normal
P = pressure
Pr = Prandtl number
Q_{rB} = radiative flux evaluated from $\bar{z}_B$ to L
Q_{rT} = radiative flux evaluated from y_T to L
q = heat flux
R = gas constant
Re = Reynolds number, $u_o H/\nu$
s = surface of circular cell
T = temperature
T_c, T_h = cold wall and Hot Wall temperatures, respectively
T_o = temperature of radiating surface
t = time variable
u, v = velocity components, Fig. 1
u_o = reference velocity
w = width of partition
x, y = rectangular coordinates, Fig. 1
$\bar{z}$ = distance used in equation (6)
α_i = integrated band intensity parameter
β = coefficient of volumetric expansion
$\Delta x, \Delta y$ = rectangular cell sizes
θ = angle for evaluating view factors
ν = kinematic viscosity, wave number
ν_i = wave number at band head
ρ = density
σ = Stefan-Boltzmann constant
τ = optical path length
τ_i^* = dimensionless quantity given in equation (9)
ω = band width parameter

Subscripts

a = reference state
b = black body
c = conduction quantity
e = equilibrium state
H = band head
i = ith band
r = radiation quantity
w = either vertical end wall
ν = monochromatic quantities

Superscript

$-$ = dimensional quantities
$-$ = averaged quantities along path length $\bar{z}$ to $\bar{z}'$

$$\bar{\tau}'_{Hi} - \bar{\tau}_{Hi} = \int_{\bar{y}}^{\bar{y}'} \rho \frac{\bar{\alpha}_i}{\bar{\omega}_i} d\bar{z} \tag{8}$$

where ω_i is the band width parameter and α_i the integrated band intensity, and

$$\tau_i^* = \exp\left[- \frac{\nu_i - \nu}{\omega_i} \right] \tag{9}$$

where ν_i is the wave number at the center or head of the band. In equations (6) through (9), the barred quantities, except $\bar{z}$ and $\bar{z}'$, denote averaged quantities with the path length $\bar{z}$ to z' due to scaling for nonisothermal gas conditions [8], and the subscript, H, refers to the band head. Finally, the slab band absorptance can be written by invoking the single continuous correlation of Tien and Lowder [9]

$$A_{si}^*(\bar{\tau}_{Hi} - \bar{\tau}_{Hi}) = ln\left\{ \left[\frac{3}{2} (\bar{\tau}'_{Hi} - \bar{\tau}_{Hi}) \right] \cdot f \cdot \left[\frac{\frac{3}{2} (\bar{\tau}'_{Hi} - \bar{\tau}_{Hi}) + f}{\frac{3}{2} (\bar{\tau}'_{Hi} - \bar{\tau}_{Hi}) + 2f} \right] + 1 \right\} \tag{10}$$

where f is a constant taken to be 2.94.

It is noted that this slab band absorptance is strictly only valid for one-dimensional problems, and it is only used here as an approximation for the two-dimensional problem. However, this approximation is not expected to result in gross errors in view of the polar structure of the radiation calculation grid shown in Fig. 2. When the circles away from the cell under consideration intercept the solid walls, some error would occur if the wall temperatures have large minimum variations. In the present study, equation (6) is utilized to determine the net radiation flux in the energy equation by means of a radial flux method which will be described in the next section. In particular, a differential method is somewhat awkward for this modified method and hence is not used. The band characteristics in terms of ν_i, ω_i, and α_i/ω_i for both CO_2 and NH_3 are given in Table 1 from [10, 11].

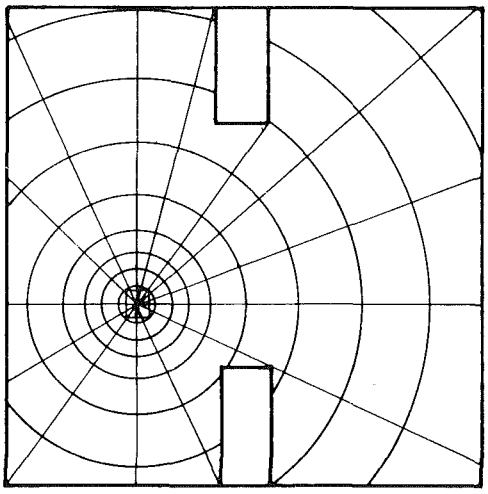

Fig. 2 Polar coordinates for radiation heat flux calculations at (i, j)

Calculation Procedure

The governing differential equations have been solved by a finite-difference algorithm very similar to that of [3, 5], both of which utilize an upwind differencing scheme for the convection terms and difference equations formulated on the basis of the control volume approach. Staggered cells for the velocity components are used. A nonuniform grid [5] is adopted for the pure convection calculations while for the calculations including radiation a 20 × 20 grid was adopted to save computer time and space. The fine grid at the wall for the pure convection results makes the calculation of wall gradients equivalent in accuracy to an 80 × 80 grid in the enclosure. For the cases including radiation, the convection contribution is expected to be small compared to the

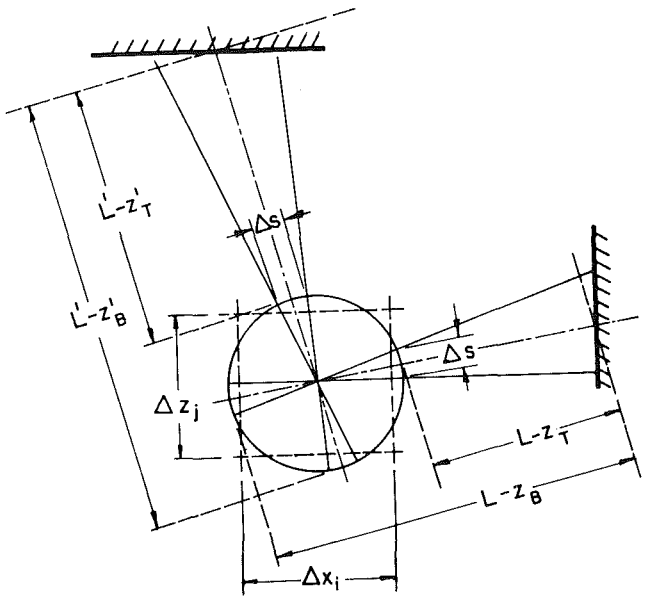

Fig. 3 Net radiation flux gained by cell (i, j) in two sample directions

Table 1 Band properties of major vibration-rotation bands for CO_2 and NH_3 [10, 11]

	CO_2			NH_3	
Band	2.7 μ	4.3 μ	15.0 μ	6.15 μ	10.5 μ
$\nu_i\left(\frac{1}{\text{cm}}\right)$	3715	2350	667	1627	950
$\omega_i\left(\frac{1}{\text{cm}}\right)$	$41.569\left(\frac{T}{300}\right)^{1/2}$	$19.92\left(\frac{T}{300}\right)^{1/2}$	$22.343\left(\frac{T}{300}\right)^{1/2}$	$95.0\left(\frac{T}{300}\right)^{1/2}$	$97.0\left(\frac{T}{300}\right)^{1/2}$
$\frac{\alpha_i}{\omega_i}\left(\frac{\text{cm}^2}{\text{gm}}\right)$	$962.25\phi(T)\left(\frac{300}{T}\right)^{1/2}$	$5.5225\times10^4\left(\frac{300}{T}\right)^{1/2}$	$8.503.61\left(\frac{300}{T}\right)^{1/2}$	$1904\left(\frac{300}{T}\right)^{1/2}$	$1.201\times10^4\left(\frac{300}{T}\right)^{1/2}$

$$\phi(T) = \frac{1 - \exp(-5341.35/T)}{[1 - \exp(-1943.88/T)][1 - \exp(-3447.47/T)]}, \quad T \text{ in K}$$

radiation, and therefore the coarse grid employed is not expected to create significant errors. The readers are referred to [3, 5] for details of the finite-difference calculations. In addition, the two-dimensional radiation flux term based on equation (6) is evaluated with a radial flux method based on a polar description of radiation exchange.

By approximating an interior rectangular cell (i, j) in the enclosure with an equivalent circle of the same surface area, and then by dividing the enclosure space into M angular segments as shown in Fig. 2, the net radiation heat flux gained by the cell can be written as

$$\int_s \underline{q}_r \cdot \underline{n}\, ds = \sum_{m=1}^{M} (Q_{rT} - Q_{rB})\, \Delta s_m \tag{11}$$

where n is the outward normal, and s is the total surface area of the circular cell. As shown in Fig. 3, Q_{rT} is evaluated from z_T to L and Q_{rB} is evaluated from z_B to L in the direction, L. Note that here z_T, z_B and L have all been normalized by H and also that the subscripts T and B denote top and bottom, respectively. Another sample direction with z_T', z_B' and L' is also shown in Fig. 3. Here the following assumptions are made. One is that at each segment, Δs, at z_T of the circle, the element sees the radiation from $z = L$ as in a slab of gas of thickness, $L - z_T$. This is an approximation, but is expected to be adequate in view of the radial structure utilized (Fig. 3). Another one is that only the area, Δs, of the circle responds to the radiation exchange in that L-direction. The concept utilized here is similar to that of the well-known flux method, except that all zones in the radiation field are covered as compared to only two directional zones in the flux method. Consequently, it is expected that the present method should produce more realistic results.

At the surface elements of the enclosure, the center of the approximating circle is set at the center of the element and the semicircle encircling the surface has the same area as the surface. Q_{rT} is evaluated by integrating from the center to the limit of the radius where it meets another surface element. Each angle is spanned by another surface element at the other end of the radius. Q_{rB} is given by σT_o^4, where T_o is the temperature of the surface element itself. Surface areas such as Δx_i or Δy_j are used to replace Δs and a geometrical view factor of $1/2 \int d(\sin\theta)$ is used. It is a method which enables the calculation of view factors between an infinitesimal two-dimensional surface and a finite two-dimensional surface. Due to the very small surface element size ($\Delta x = \Delta y \sim 1/20$), the calculation of view factors is very accurate. If the connecting line between the centers of two surface elements is intercepted by an opaque surface, the radiative interchange is blocked and has a zero value for the geometry view factor. This happens only when partitions are present. When gas radiation is neglected, an exact surface radiation energy balance is maintained. It is noted that the present radial flux method is different from the discrete transfer method recently proposed by Lockwood and Shah [12]. Even though this latter method has some definite computational advantages, it has an inherent weakness in that the radiation source term is invariably overestimated due to beam overlapping, while the present radial flux method is free from this problem.

Calculation of radiative heat fluxes is not needed at every time step to give reliable steady-state results. The radiative heat flux is updated every tenth time step. Before the calculations of temperatures from the energy equation at a new time instant, wall surface temperatures and surface radiative heat fluxes are calculated based on the interior point temperatures at the previous time step. A two-variable interpolation formula is used to transfer T, ρ, and P values from rectangular cells to node points along the path of the radiation ray in each span of angle in the polar coordinates, and the radiation flux at surfaces is calculated by balancing with conduction heat flux at the adiabatic boundaries. By assuming that the radiation flux due to attenuation by the gas does not have a major effect on the energy balance, the Newton-Raphson method is used to iterate on the non-prescribed surface temperatures, and subsequently radiation heat flux. Wall temperatures and radiative fluxes thus obtained are then considered as heat sources to complete the boundary condition for the energy equation in the rectangular cells. Surface temperature and radiation flux are then updated with new interior temperatures. The radiation heat flux values are then used for the next nine time steps. However, surface temperatures are recalculated and changed accordingly with interior point temperatures at each time step. Density and flow field quantities are calculated after temperature field is obtained. Finally, the change of the average Nusselt number at both vertical end walls is checked at successive time steps to determine whether steady state is reached.

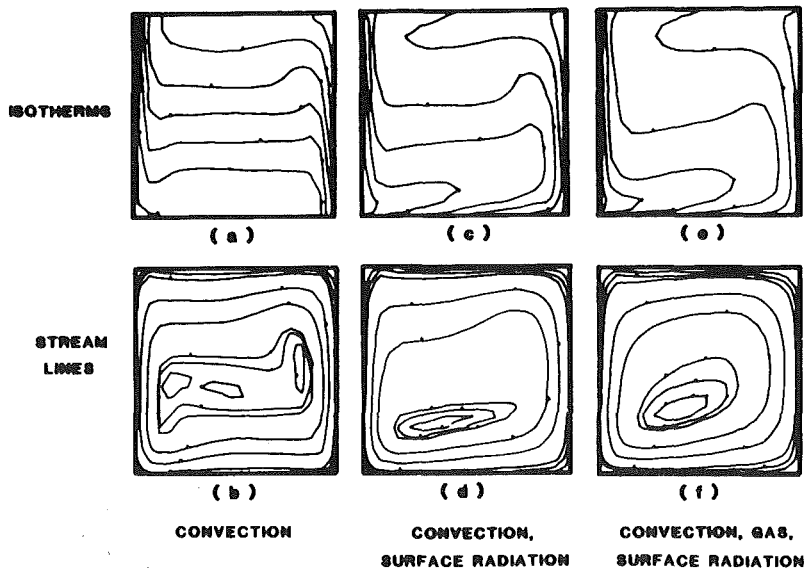

Fig. 4 Isotherm and steamlines for CO_2 enclosure without partitions ($Gr = 6.55 \times 10^6$ and $Pr = 0.686$)

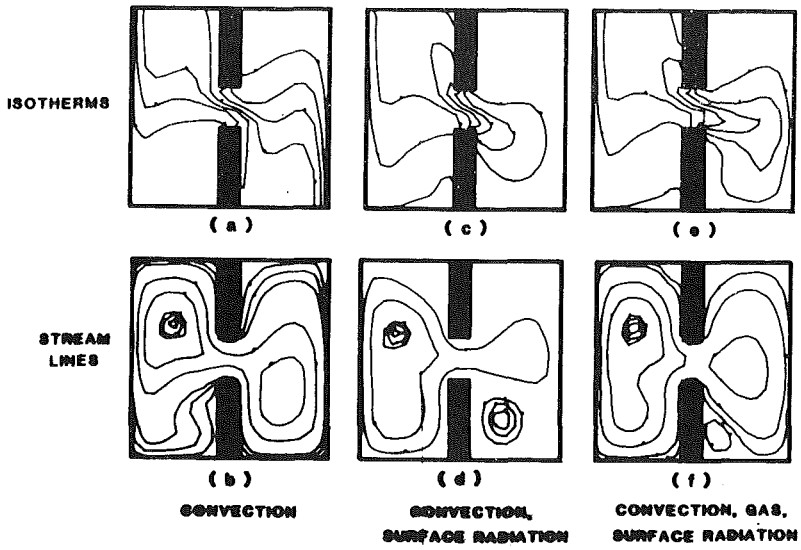

Fig. 5 Isotherm and streamlines for CO_2 enclosure with $0.25H \times 0.1H$ partitions (Gr = 6.55×10^6 and Pr = 0.686)

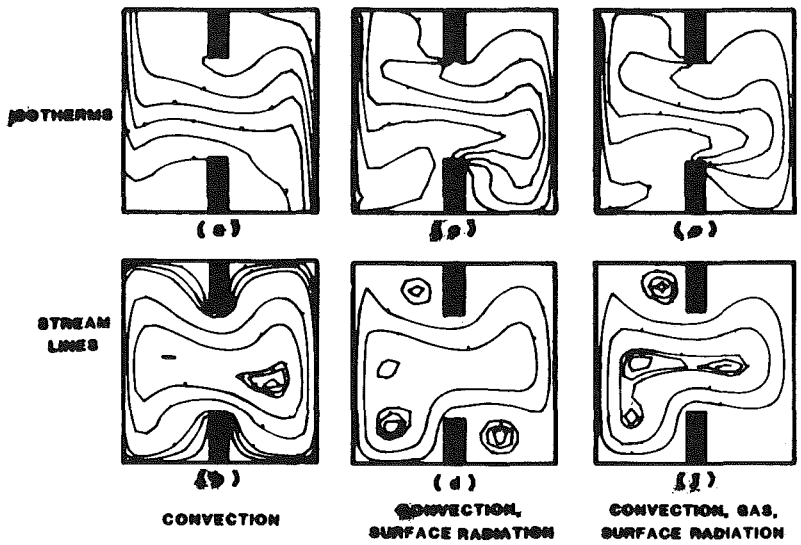

Fig. 6 Isotherms and streamlinies for CO_2 enclosure with $0.4H \times 0.H$ partitions (Gr = 6.55×10^6 and Pr = 0.686)

Results and Discussion

Results of the present calculations for an empty square enclosure filled with CO_2 having a left wall temperature of $T_c = 1$, a right wall temperature of $T_h = 3$, and insulated ceiling and floor, are shown in Fig. 4. The Grashof number Gr is 6.55×10^6 and the Prandtl number Pr = 0.686. For convenience, the Grashof number is based on a value of the coefficient of volumetric expansion of $\beta = 2/(T_h + T_c)$, and all property values are based on the average temperature, i.e., $(T_h + T_c)/2$. The isotherms are shown in (*a*), (*c*), and (*e*), corresponding to the cases of pure natural convection, natural convection with surface radiation, and natural convection with surface and gas radiation, respectively. The corresponding stream lines are shown in (*b*), (*d*) and (*f*). Figures 4(*a*) and 4(*b*) are identical to those shown in [5], which also discusses the effects of Gr and size and location of the partitions in the pure natural convection case. Also, it should be noted that at Gr = 6.55×10^6, and when no partitions are present parts of the flow already exhibit degrees of unsteadiness at long times. The temperature and flow behaviors are shown here in Fig. 4 to provide a reference for the discussion of results with partitions. As shown in [5], steady natural convection behavior does exist at this Gr when partitions are present due to increased internal flow resistance. When only surface radiation is considered, Fig. 4(*c*) shows that the heating from the hot wall effects the floor of the enclosure more than the ceiling and also that the core of the fluid becomes warmer when compared to the pure natural convection case. The cool region is now more restricted to the immediate neighborhood of the cold wall and the lower left corner of the enclosure. It is also seen that the temperature stratification is less pronounced. The corresponding flow field indicated in Fig. 4(*d*) shows that the low velocity region is moved from the core region to the lower part of the enclosure, leaning toward the cold wall. Figures 4(*e*) and 4(*f*) show the corresponding results for the case where both surface and gas radiation takes place. In general, the participation of gas in the absorption and emission of radiation tends to produce more uniform gas temperatures. Radiative communication between the hot and cold walls is lessened due to the attenuation of the gas body. It

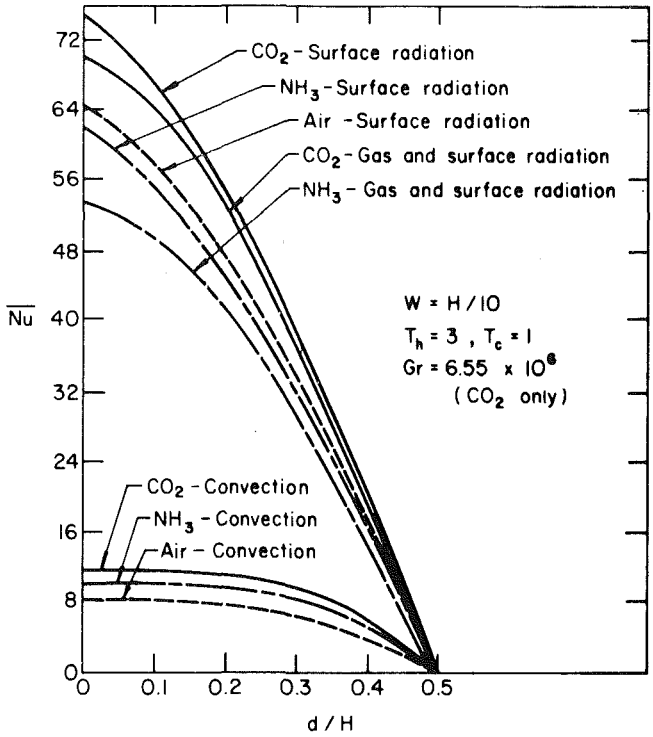

Fig. 7 Average Nusselt numbers Nu for various partition heights

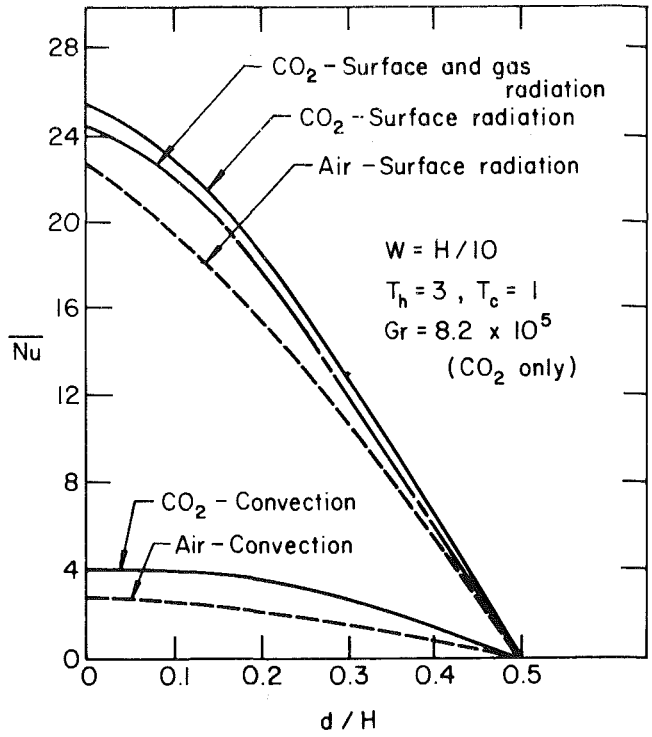

Fig. 8 Average Nusselt numbers $\overline{Nu}$ for various partition heights

is seen here that a further increase of the core region temperature is evident due to the direct interaction between the gas and the nonadiabatic walls. On the other hand, the effect of gas radiation is also to produce a more uniform flow when compared to the case with only surface radiation.

Figures 5 and 6 show the same results for two different partitioned enclosures with partitions of the sizes of 0.25 $H \times 0.1\ H$ and 0.4 $H \times 0.1\ H$, respectively. For the pure natural convection cases, the stream lines are essentially symmetrical, the slight deviation being caused by the nonsymmetrical compressibility effects. Of particular interest is the shear region between the two partitions. As expected, the shear is much more pronounced in Fig. 6(*b*) than that in Fig. 5(*b*) due to the smaller gap size. When the gap is large, Fig. 5(*a*) shows that temperature stratification persists, except for very high (upper right corner) and low (lower left corner) temperature regions, which are essentially isolated by the insulated partitions. For the small gap size as shown in Fig. 6(*a*), the temperature gradient within the gap becomes quite large. In these partitioned cases, the effects of radiation are quite dramatic, and the basic reason is the effect of radiation blockage due to the presence of the insulated partitions. With radiation, the partitions essentially separate the higher temperature region on the right from the lower temperature region on the left. This is obviously more pronounced for the larger partition case as shown in Fig. 6, where it is seen that the isotherms from one side do not in most of the cases penetrate into the other side of the enclosure. Here again the effect of gas radiation is to equalize the temperatures of the gas bodies on either side of the partitions. For the flow fields, the natural convection flow is already reduced by the presence of the partitions [5], and the effects of radiation of equalizing the gas temperatures further slow down the flow inside the enclosure. The relatively strong vortices on the lee side of the lower partition for the surface radiation cases, Figs. 5(*d*) and 6(*d*), further decrease their strengths when gas radiation is included.

To determine the steady-state heat transfer characteristics at either of the two vertical walls, it is necessary to include both the convection and radiation contributions. In the present study, the following average Nusselt number $\overline{Nu}$ is introduced

$$\overline{Nu} = \frac{\bar{q}_c + \bar{q}_r}{k\dfrac{(\bar{T}_h - \bar{T}_c)}{H}} \tag{12}$$

where the denominator represents the pure conduction heat transfer rate for the enclosure. In dimensionless form, the above equation reduces to

$$\overline{Nu} = \frac{\left(\dfrac{\partial T}{-\partial x}\right)_w + \left(\dfrac{\sigma \bar{T}_a{}^3 H}{k}\right) q_r}{T_h - T_c} \tag{13}$$

For Gr = 6.55 $\times$ 10^6, the average Nusselt numbers for CO_2 and NH_3 as the participating gases and air as the nonparticipating gas are shown in Fig. 7 as a function of the partition height. Also shown are the corresponding values for the pure natural convection cases. It is seen here that for the temperature range considered, radiation plays a dominant role in the heat transfer process and the main mechanism is by surface radiation. The effect of the partition height is quite dramatic, especially in the radiation cases where even small partitions exert a sufficient blockage for the radiation transfer. On the other hand, pure natural-convection heat transfer is almost unaffected until the partitions occupy one-half of the enclosure height. As d/H further increases, the average Nusselt numbers drop off at increasing rates until the partitions completely isolate the two subcompartments. At that point, we have uniform temperatures T_h and T_c at the right and left sides of the partition, respectively, and the corresponding heat transfer rates are zero. Also, for the conditions of black surfaces and constant temperatures at the vertical end walls, as imposed in the present problem, surface radiation heat transfer rates are independent of the gases in the enclosure. The fact that the average $\overline{Nu}$ values for the three gas-cases are different is due to the small, but different

convection contributions, which do depend on surface radiation exchange, and the different conductivity values, as shown in equation (13). For the participating gas cases of CO_2 and NH_3, gas radiation essentially produces more uniform temperatures in the enclosure, thus reducing the overall rates of heat transfer. Even though the effect of gas radiation is relatively small, it is still sufficiently important to consider it in the overall radiation-convection interaction phenomena, especially for NH_3 at small d/H values. Calculations have also been made for CO_2 and air at the lower Grashof number of Gr = 8.20×10^5, and the results for the average $\overline{Nu}$ are shown in Fig. 8. The trends follow closely those in Fig. 7, except that the $\overline{Nu}$ levels are much lower.

Conclusions

In the present numerical study, calculations have been made for the radiation-natural convection phenomena in square enclosures with equal vertical finite thickenss partitions mounted at the midpoint of the ceiling and floor. The dimensionless temperatures at the vertical wall ends are taken to be 3.0 and 1.0. The participating gases, CO_2 and NH_3, and one nonparticipating gas, air, are considered, together with five values of the partition heights and two Grashof numbers for CO_2 of 6.55×10^6 and 8.20×10^5, with a constant Prandtl number of 0.686. Also, in all partition cases studied the width of the partitions is taken to be $H/10$. In the radiation calculations, the nongray exponential wide-band models for CO_2 and NH_3 are used, together with a modified radial flux method utilizing a more realistic polar description for the radiation exchange in the enclosure, the following conclusions can be made:

1 For empty square enclosures, the effect of radiation is to increase the bulk temperatures of the gas in the enclosure, except in the immediate neighborhood of the cold wall and in a small region at the lower corner close to the cold wall. The net effect is that the natural convection flow is somewhat reduced, but this is overwhelmingly compensated by the increase in heat transfer by radiation for the temperature levels studied.

2 For the partitioned enclosures, the partitions provide an effective means to block the radiation exchange and also to increase the internal resistance for the convective flow. This effect tends to maintain a higher gas temperature on the hot side of the partitions and a cooler gas temperature on the other side. The radiation effects are much more sensitive to the presence of the partitions then the convective flows. The natural convection contributions to the overall heat transfer remain essentially the same until the partitions occupy one-half of the enclosure height.

3 The predominant mechanism in the present study by which the radiation process will increase the overall heat transfer rates is the surface radiation. This is due to the surface emmissivity being taken as one and the large temperature difference between the hot and cold surfaces. The effect of gas radiation is to provide more uniform gas temperatures in the enclosure, thus leading to lower rates of heat transfer when compared to those with surface radiation alone. However, the net gas-radiation effect is not large, tends to be more significant as the partition height is reduced, and would be expected to increase in importance as the overall temperature levels of the enclosure increase. The effect also depends on the participating gas considered.

It should also be noted that the present calculations, due to the large temperature differences considered, do not invoke the Boussinesq approximation for the density variations. However, properties have still been taken as constant, evaluated at the mean temperature, $(T_h + T_c)/2$. However, in view of the pure natural convection study by Leonardi and Reizes [13], in which it has been demonstrated that variable properties do not affect significantly the overall heat transfer rates, and the fact that natural convection here only contributes a small portion of the overall heat transfer process, the validity of the present results is not expected to be significantly altered by variable property effects.

Acknowledgment

The support of the National Science Foundation under grants ENG-7681904 and CME7918682 and the Computer Center of the University of Notre Dame is gratefully acknowledged.

References

1 Larson, D. W., and Viskanta, R., "Transient Combined Laminar Free Convection and Radiation in a Rectangular Enclosure," *Journal of Fluid Mechanics*, Vol. 78, 1976, pp. 65–85.

2 Modak, A. T., and Mathews, M. K., "Radiation Augumented Fires Within Enclosures," *Technical Report*, 22361-B, RC 77-BT-2, Factory Mutual Research, 1977.

3 Lloyd, J. R., Yang, K. T., and Liu, V. K., "A Numerical Study of One-Dimensional Surface, Gas, and Soot Radiation for Turbulent Buoyant Flows in Enclosures," *Proceedings of the First National Conference on Numerical Methods in Heat Transfer*, Sept. 1979, pp. 142–161.

4 Larson, D. W., "Enclosed Radiation and Turbulent Natural Convection Induced by a Fire," *Numerical Methods in Heat Transfer*, edited by R. W. Lewis, K. Morgan, and O. C. Zienkiewicz, John Wiley and Sons, 1981, pp. 467–487.

5 Chang, L. C., Lloyd, J. R., and Yang, K. T., "A Finite Difference Study of Natural Convection in Complex Enclosures," Paper No. 82-IHTC-59, to be presented at the 7th International Heat Transfer Conference.

6 Novotny, J. L., "Formulation of One-Dimensional Radiation Flux for Non-Homogeneous Nongray Gases and Soot," Technical Report TR-37191-74-1, Department of Aerospace and Mechanical Engineering, University of Notre Dame, 1974.

7 Chang, L. C., "Finite Difference Analysis of Radiation-Convection Interactions in Two-Dimensional Enclosures," Ph.D. thesis, University of Notre Dame, Notre Dame, Ind. 1981.

8 Felske, J. D., and Tien, C. L., "Infrared Radiation from Non-Homogeneous Gas Mixtures Having Overlapping Bands," *Journal of Quantitative and Spectroscopic Radiative Transfer*, Vol. 14, 1974, pp. 35–48.

9 Tien, C. L., and Lowder, J. E., "A Correlation for Total Band Absorption of Radiating Gases, *International Journal of Heat and Mass Transfer*, Vol. 9, 1966, pp. 698–701.

10 Edwards, D. K., and Menard, W. A., "Correlations for Absorption by Methane and Carbon Dioxide Gases," *Applied Optics*, Vol. 3, 1964, pp. 847–852.

11 Tien, C. L., "Band and Total Emissivity of Ammonia," *International Journal of Heat and Mass Transfer*, Vol. 16, 1973, pp. 856–857.

12 Lockwood, F. C., and Shah, N. G., "A New Radiation Solution Method for Incorporation in General Combustion Prediction Procedures," *18th International Symposium on Combustion*,. 1981, pp. 1405–1414.

13 Leonardi, E., and Reizes, J. A., "Convective Flows in Closed Cavities with Variable Fluid Properties, *Numerical Methods in Heat Transfer*, edited by R. W. Lewis, K. Morgan, and O. C. Zienkiewicz, John Wiley and Sons, 1981, pp. 387–412.

Buoyancy Effects on a Boundary Layer Along an Infinite Cylinder With a Step Change of Surface Temperature

L. S. Yao
Department of Mechanical and Aerospace Engineering, Arizona State University, Tempe, Ariz. 85287

The laminar boundary layer induced by a horizontal forced flow along an infinite vertical cylinder with a step change of surface temperature is studied by a finite-difference method. Close to the thermal leading edge, the buoyancy force induces a strong free-convection boundary layer. Slightly above the thermal leading edge, the boundary layer starts to separate at the rear stagnation line ($\phi = 180$ deg). The region of separated flow grows toward the forward stagnation line and becomes stationary at $\phi \simeq 104$ deg as one moves upward. In other words, free convection dominates the heat transfer along the thermal leading edge. The importance of forced convection increases as one moves vertically from the thermal leading edge and eventually becomes the dominant mode. The numerical results show that the free-convection boundary layer is suppressed at the forward stagnation line and is carried toward the rear stagnation line by the forced convection. The phenomenon shares many similarities with a thermal plume affected by forced convection.

1 Introduction

Free-forced convection is a fundamentally important problem in fluid mechanics and heat transfer. Most early studies were limited to two-dimensional flow geometries. Three-dimensional combined free and forced convection has received little detailed study. Young and Yang [1] studied the effect of small crossflow and surface temperature variation on laminar free convection along a vertical plate. By coincidence, Eichhorn and Hasan [2], and Plumb [3] reported their studies of mixed convection about a vertical surface in crossflow at the same time. The asymptotic solutions for a forced-convection dominant flow for both internal flow [4] and external flow [5, 6] have been obtained by perturbation of the forced convection solutions. The numerical solution of the boundary layer along a heated horizontal cylinder shows that the range of validity of the asymptotic solution is limited to a small region close to the leading edge of the cylinder [7] where the free-convection effect is small.

The central receiver of a solar power plant contains a series of vertical pipes and looks like a large vertical cylinder. The receiver is designed as a once-through heat exchanger to boil water by solar heating. The surface temperature of the receiver is much higher than the ambient temperature. A significant free convection is induced by the density stratification of air inside the thermal boundary layer. Simultaneously, a breeze may pass by the receiver and modify the free convection around it. The resulting free and forced convection is three dimensional. The distributions of temperature and flow are needed to design the structure for rigidity and to estimate the free-forced convective heat loss.

Due to the large dimension of the receiver and the likely high ambient turbulence level, the boundary-layer flow around the receiver is expected to be turbulent. In particular, the vertical pipes of small radius, which form the receiver, behave as a roughened surface. In this paper, however, we concentrate on the interaction of free and forced convection around the receiver by studying the laminar flow along an infinitely long vertical cylinder.

The asymptotic solution [8] for free-forced convection along a partially heated, infinitely long vertical cylinder indicates that free convection is dominant in the neighborhood of the thermal leading edge. Since the free-convection boundary layer is rather thin there, no separation has been predicted along the aft part of the cylinder. Intuitively, one can expect that the asymptotic solution is valid only in the neighborhood of the thermal leading edge. On the other hand, Oosthuizen and Leung [9, 10] found that the accuracy of their numerical solution deteriorates near the thermal leading edge. To avoid this difficulty, their computation was started a short distance above the thermal leading edge. Consequently, an error due to mistreating the leading-edge condition is to be expected. In this paper, a finite-difference solution provides information on the size of the thermal leading-edge region in which the asymptotic solution is valid, and the distribution of temperature and flow further upward from the thermal leading edge.

The axial length scale for the region in which free and forced convection are both important is $a \cdot \mathrm{Gr}/\mathrm{Re}^2$; this result is derived from the asymptotic solution. The idealized potential flow is selected as the zeroth-order outer solution. This implies that the Reynolds number is assumed large. Furthermore, the boundary layer is assumed to be laminar. Comparison of the asymptotic solution with the numerical solution shows that the asymptotic solution is valid only for extremely small z. The size of this region depends on the Prandtl number. For Pr = 10, the asymptotic solution is valid for $\bar{z} \leq 10^{-5} \cdot a \cdot \mathrm{Gr}/\mathrm{Re}^2$, while for Pr = 0.733, $\bar{z} \leq 10^{-4} \cdot a \cdot \mathrm{Gr}/\mathrm{Re}^2$ is required. The numerical solution also shows that forced convection becomes dominant farther upward than predicted by the early numerical solution. The location of boundary layer separation starts at the rear stagnation line, moves forward, and stays at about $\phi = 104$ deg, which agrees with the theoretical prediction of a two-dimensional forced flow. Also, the development of the boundary layer separation depends on the Prandtl number.

2 Physical Model and Mathematic Formulations

The physical model considered is an infinite vertical cylinder with a uniform horizontal freestream flowing past it (Fig. 1). The velocity and temperature of the freestream are

Contributed by the Heat Transfer Division for publication in the JOURNAL OF HEAT TRANSFER. Manuscript received by the Heat Transfer Division January 13, 1982.

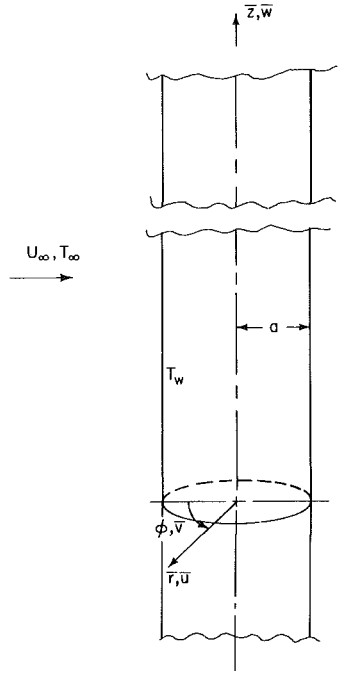

Fig. 1 Physical model and coordinates

denoted by U_∞ and T_∞, respectively. The cylinder for $z \geq 0$ is heated and its surface temperature is held constant at $T_w > T_\infty$. For $z < 0$, the cylinder is unheated. Density variations within the thermal boundary layer ($z \geq 0$) induce a vertical flow and the boundary layer is three-dimensional. Owing to diffusion, the boundary layer for $z < 0$ is also affected; however, the magnitude of the buoyancy effects there is much smaller than that for $z \geq 0$. Therefore, the thermal leading edge provides a convenient location to start the numerical computation of the boundary layer flow. In this paper, we will concentrate on the development of the boundary layer for $z \geq 0$. Weak diffusion in the negative z-direction is ignored in the following formulation; therefore, we assume that the thermal boundary layer starts at $z = 0$. It should be pointed out that the assumption of an inviscid flow outside the boundary layer restricts the model to large Reynolds numbers.

The dimensionless variables suggested by the upsteam asymptotic solution are

$$z = \bar{z}/(a\,\mathrm{Gr}/\mathrm{Re}^2),\ r = \bar{r}/a \quad \text{(coordinates)} \tag{1a}$$

$$W = \bar{w}/[U_\infty(\mathrm{Gr}/\mathrm{Re}^2)^{1/2}],\quad U = \bar{u}/U_\infty,\ V = \bar{v}/U_\infty \quad \text{(velocities)} \tag{1b}$$

$$\mathrm{I} = \bar{p}/(\rho U_\infty^2) \quad \text{(pressure)} \tag{1c}$$

$$\Theta = (T - T_\infty)/(T_w - T_\infty) \quad \text{(temperature)} \tag{1d}$$

$$\mathrm{Re} = U_\infty a/\nu \quad \text{(Reynolds No.)} \tag{1e}$$

$$\mathrm{Gr} = \beta \cdot g \cdot (T_w - T_\infty) \cdot a^3/\nu^2 \quad \text{(Grashof No.)} \tag{1f}$$

$$\epsilon = \mathrm{Re}/\mathrm{Gr}^{1/2} \tag{1g}$$

2.1 Inviscid Flow. Substitution of equation (1) into the Navier-Stokes equations in cylindrical coordinates results in the dimensionless governing equations:

$$\frac{\partial U}{\partial r} + \frac{U}{r} + \frac{1}{r}\cdot\frac{\partial V}{\partial \phi} + \frac{\partial W}{\partial z} = 0\ , \tag{2a}$$

$$U\frac{\partial U}{\partial r} + \frac{V}{r}\frac{\partial U}{\partial \phi} + W\frac{\partial U}{\partial z} - \frac{V^2}{r} = -\frac{\partial P}{\partial r} + 0(\mathrm{Re}^{-1}) \tag{2b}$$

$$U\frac{\partial U}{\partial r} + \frac{V}{r}\frac{\partial U}{\partial \phi} + W\frac{\partial V}{\partial z} + \frac{UV}{r} = -\frac{1}{r}\frac{\partial P}{\partial \phi} + 0(\mathrm{Re}^{-1}) \tag{2c}$$

$$U\frac{\partial W}{\partial r} + \frac{V}{r}\frac{\partial W}{\partial \phi} + W\frac{\partial W}{\partial z} = \Theta - \epsilon^4\cdot\frac{\partial P}{\partial z} + 0(\mathrm{Re}^{-1}) \tag{2d}$$

$$U\frac{\partial \Theta}{\partial r} + \frac{V}{r}\frac{\partial \Theta}{\partial \phi} + W\frac{\partial \Theta}{\partial z} = 0(1/\mathrm{Pr}\cdot\mathrm{Re}) \tag{2e}$$

The solution of equations (2) which satisfies the slip condition on the surface of the cylinder and matches the free stream far away from the cylinder is a simple superposition of the free stream with a doublet at $r = 0$ so that the inviscid velocity components are

$$V = \sin\phi\cdot\left(1 + \frac{1}{r^2}\right) \tag{3a}$$

$$U = -\cos\phi\cdot\left(1 - \frac{1}{r^2}\right) \tag{3b}$$

$$W = 0 \tag{3c}$$

2.2 Boundary Layer. Equations (1) suggest that the appropriate boundary-layer coordinate is

$$y = (r-1)\cdot\mathrm{Re}^{1/2} \tag{4a}$$

$$\tilde{u} = U\cdot\mathrm{Re}^{1/2} \tag{4b}$$

The rest of the independent variables are the same; however, they are denoted by lower case symbols with superscript "˜" to distinguish them from those for the inviscid flow. In terms of equations (4), the governing equations for the boundary layer are

$$\frac{\partial \tilde{u}}{\partial y} + \frac{\partial \tilde{v}}{\partial \phi} + \frac{\partial \tilde{w}}{\partial z} = 0 \tag{5a}$$

$$\tilde{u}\frac{\partial \tilde{v}}{\partial y} + \tilde{v}\frac{\partial \tilde{v}}{\partial \phi} + \tilde{w}\frac{\partial \tilde{v}}{\partial z} = -\frac{\partial \tilde{p}}{\partial \phi} + \frac{\partial^2 \tilde{v}}{\partial y^2} + 0(\mathrm{Re}^{-1/2}) \tag{5b}$$

$$\tilde{u}\frac{\partial \tilde{w}}{\partial y} + \tilde{v}\frac{\partial \tilde{w}}{\partial \phi} + \tilde{w}\frac{\partial \tilde{w}}{\partial z} = \Theta - \epsilon^4\frac{\partial \tilde{p}}{\partial z} + \frac{\partial^2 \tilde{w}}{\partial y^2} + 0(\mathrm{Re}^{-1/2}) \tag{5c}$$

$$\frac{\partial \tilde{p}}{\partial r} = 0(\mathrm{Re}^{-1}) \tag{5d}$$

$$\tilde{u}\frac{\partial \Theta}{\partial y} + \tilde{v}\frac{\partial \Theta}{\partial \phi} + \tilde{w}\frac{\partial \Theta}{\partial z} = \frac{1}{\mathrm{Pr}}\frac{\partial^2 \Theta}{\partial y^2} + 0(\mathrm{Re}^{-1/2}) \tag{5e}$$

Nomenclature

a = radius of cylinder
f = stream function, equation (8)
g = gravitational acceleration
G = temperature function, equation (8)
Gr = Grashof number
Nu = Nusselt number
P = pressure
Pr = Prandtl number
r = radial coordinate
Re = Reynolds number
T = temperature
u,v,w = boundary-layer velocities
U,V,W = inviscid flow velocities
z = axial coordinate
β = thermal expansion coefficient
ϵ = expansion parameter, equation (1)
η = similarity variable
Θ = dimensionless temperature, equation (2)
ν = kinematic viscosity
ϕ = azimuthal coordinate
τ = shear stress

Subscripts

w = surface
∞ = freestream

Superscripts

$-$ = dimensional quantities
$'$ = derivatives with respect to η

Equation (5*d*) implies that the pressure gradient normal to the wall is negligible and that the pressure gradients along the ϕ and z-directions can be estimated from the solution for the inviscid flow (equations (3)). Because the cylinder is very long, the magnitude of $\partial P/\partial z$ is proportional to ϵ^4. This implies that the inviscid flow induced by the displacement effect of the thermal boundary layer, whose order is Re^{-1}, has very little effect on the boundary-layer flow as long as $\mathrm{Re}^3 < \mathrm{Gr}^2$. In other words, its effect is $0(\epsilon^4/\mathrm{Re})$.

For a numerical solution of equations (5), it is convenient to use transformed coordinates. Equations (5) in the coordinates ($\eta = y/(4z)^{1/4}$, ϕ, z) are

$$\frac{\partial u}{\partial \eta} + 2w - \eta \frac{\partial w}{\partial \eta} + (4z)^{1/2} \cdot \frac{\partial v}{\partial \phi} + (4z) \cdot \frac{\partial w}{\partial z} = 0 \qquad (6a)$$

$$(u - \eta w) \frac{\partial v}{\partial \eta} + (4z)^{1/2} \cdot v \frac{\partial v}{\partial \phi} + (4z) \cdot w \frac{\partial v}{\partial z} = -(4z)^{1/2} \cdot \frac{\partial p}{\partial \phi} + \frac{\partial^2 v}{\partial \eta^2} + 0(\mathrm{Re}^{-1/2}) \qquad (6b)$$

$$(u - \eta w) \frac{\partial w}{\partial \eta} + 2w^2 + (4z)^{1/2} \cdot v \frac{\partial w}{\partial \phi} + (4z)\, w \frac{\partial w}{\partial z} = \Theta + \frac{\partial^2 w}{\partial \eta^2} + 0(\epsilon^2, \mathrm{Re}^{-1/2}) \qquad (6c)$$

$$(u - \eta w) \frac{\partial \Theta}{\partial \eta} + (4z)^{1/2} \cdot v \frac{\partial \Theta}{\partial \phi} + (4z)\, w \frac{\partial \Theta}{\partial z} = \frac{1}{\mathrm{Pr}} \cdot \frac{\partial^2 \Theta}{\partial \eta^2} + 0(\mathrm{Re}^{-1/2}) \qquad (6d)$$

where the velocities have been rescaled to reduce their variations along the z-direction according to the upstream asymptotic solution and are now defined by

$$u = (4z)^{1/4} \cdot \tilde{u} \qquad (7a)$$

$$v = \tilde{v} \qquad (7b)$$

$$w = (4z)^{-1/2} \cdot \tilde{w} \qquad (7c)$$

moreover,

$$P = \tilde{P} \qquad (7d)$$

It is interesting to notice that equations (6), in the limit as $z \to \infty$, show that w, v, and Θ are independent of z. In other words, the boundary layer approaches a two-dimensional forced convection flow when z approaches infinity.

The upstream asymptotic solution in the current coordinates can be expressed as

$$w = f_0' + 5(4z)^{1/2} \cdot f_1' (2\ \cos\phi) + (4z)(4\ \cos^2\phi f_{3c}' + 4\ \sin^2\phi f_{3s}') + \ldots \qquad (8a)$$

$$v = f_2' (2\ \sin\phi) + (4z)^{1/2} \cdot f_4' (2\ \sin^2\phi) + \ldots \qquad (8b)$$

$$u = (\eta f_0' - 3f_0') + (4z)^{1/4} \cdot (\eta f_1' - f_1 + f_2)(2\ \cos\phi) + (4z)^{3/4} [\eta f_{3c}' - 7f_{3c} + f_2)(4\ \cos^2\phi) + (\eta f_{3s}' - 7f_{3s} + f_4) \cdot (4\ \sin^2\phi)] + \ldots \qquad (8c)$$

$$\Theta = G_0 + (4z)^{1/2} \cdot G_1 \cdot (2\ \cos\phi) + (4z)[G_{2c} \cdot (4\ \cos^2\phi) + G_{2s} \cdot (4\ \sin^2\phi)] + \ldots \qquad (8d)$$

where f's and G's are defined in [8]. Taking limits of equations (6) as $z \to 0$ results in the governing equations for f_0, f_2, and G_0. This indicates that the upstream asymptotic solution is included in the downstream solution given in this paper. The limiting forms of equations (6) are independent of z and their solution can be used as the initial conditions (conditions at $z = 0$) to start the numerical solution of equations (6). It should be re-emphasized here that the existence of a thermal leading edge allows us to treat the boundary-layer flow for $z > 0$, and for $z < 0$, separately. Since buoyancy effects are mainly important for $z > 0$, we exclude consideration of the boundary layer for $z < 0$. In fact, it can be shown that buoyancy has effects of much smaller order on the boundary layer for $z < 0$. It is also worthwhile to re-emphasize that the flow along the thermal leading edge is pure free convection.

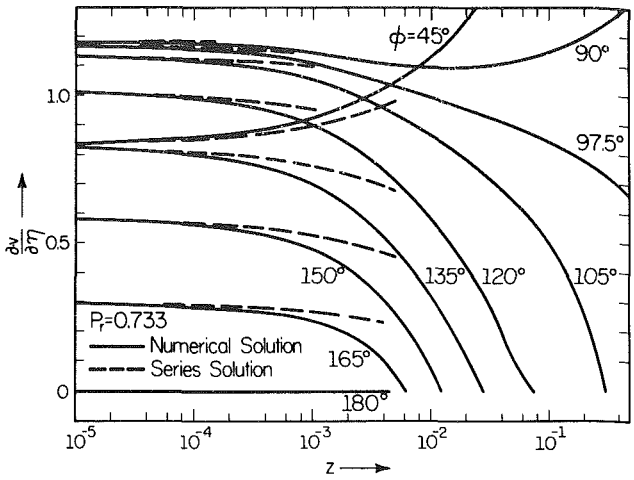

Fig. 2(*a*) Distribution of $\left.\frac{\partial v}{\partial \eta}\right|_{\eta=0}$

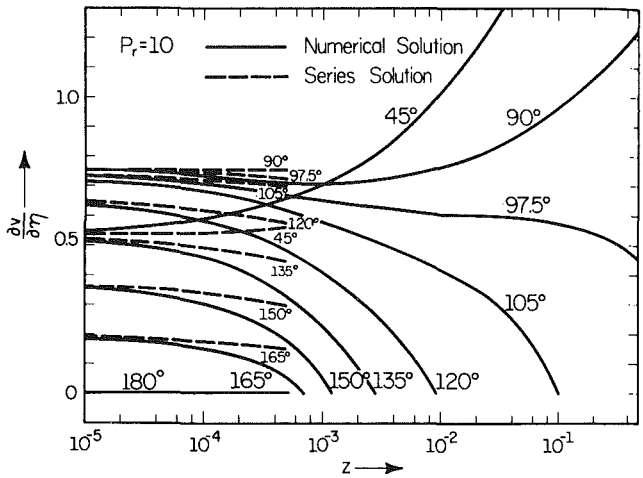

Fig. 2(*b*) Distribution of $\left.\frac{\partial v}{\partial \eta}\right|_{\eta=0}$

The required boundary conditions are

(i) $\eta = 0$, $u = v = w = 0$ (no-slip condition) (9*a*)

$\Theta = 1$ (constant wall temperature) (9*b*)

(ii) $\eta \to \infty, w, \Theta \to 0$, $v \to 2\ \sin\phi$ (matching with the inviscid flow) (9*c*)

Along the symmetry line, $\phi = 0$, the conditions are

$$v = 0, \frac{\partial u}{\partial \phi} = \frac{\partial w}{\partial \phi} = \frac{\partial \Theta}{\partial \phi} = 00\ , \ \frac{\partial p}{\partial \phi} = 0 \qquad (10)$$

Values of the dependent variables are required along $\phi = 0$ to start the numerical computation at each z station. The equations that govern the flow along $\phi = 0$ can be obtained by taking the limit of equations (6), according to equation (10). This gives

$$\frac{\partial u}{\partial \eta} + 2w - \eta \frac{\partial w}{\partial \eta} + (4z)^{1/2} \cdot \left(\frac{\partial v}{\partial \phi}\right) + (4z)\left(\frac{\partial w}{\partial z}\right) = 0 \qquad (11a)$$

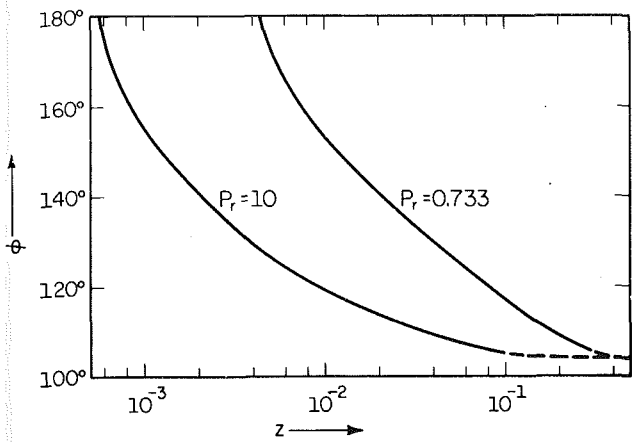

Fig. 3 Location of boundary layer separation

$$(u-\eta w)\frac{\partial}{\partial \eta}\left(\frac{\partial v}{\partial \phi}\right)+(4z)^{1/2}\cdot\left(\frac{\partial v}{\partial \phi}\right)^2$$

$$+(4z)\cdot w\frac{\partial}{\partial z}\left(\frac{\partial v}{\partial \phi}\right)=-4(4z)^{1/2}+\frac{\partial^2}{\partial \eta^2}\left(\frac{\partial v}{\partial \phi}\right) \quad (11b)$$

$$(u-\eta w)\frac{\partial w}{\partial \eta}+2w^2+(4z)\cdot w\frac{\partial w}{\partial z}=\Theta+\frac{\partial^2 w}{\partial \eta^2} \quad (11c)$$

$$(u-\eta w)\frac{\partial \Theta}{\partial \eta}+(4z)\cdot w\frac{\partial \Theta}{\partial z}=\frac{1}{\mathrm{Pr}}\frac{\partial^2 \Theta}{\partial \eta^2} \quad (11d)$$

Equations (11) can be solved for w, u, Θ and $\partial v/\partial \eta$ along $\phi = 0$. These values can be used to start the solution of equations (6) at each z station.

The pressure gradients in equations (6) can be evaluated from the solution of the inviscid flow (3) on the surface of the cylinder. They are

$$\frac{\partial P}{\partial \phi}=-2\ \sin\ 2\phi \quad (12a)$$

and

$$\frac{\partial P}{\partial z}=0 \quad (12b)$$

3 Numerical Method and Results

The numerical method used to solve equations (6) and (11) is similar to that used in [11]. However, it is found that an extremely small Δz is needed in order to obtain convergent results. Therefore variable Δz steps are used. For $z \le 2 \times 10^{-3}$, $\Delta z = 10^{-6}$ is used. The value of Δz is gradually increased to 10^{-4} for $z \le 10^{-2}$ and is further increased gradually to 5×10^{-2} for $z \le 0.75$. Normal to the wall $\Delta \eta = 0.05$ is used. $\Delta \phi = 7.5$ deg is used for $0 < \phi \le 97.5$ deg, and a finer $\Delta \phi$ is used for $\phi \ge 97.5$ deg in order to locate the boundary-layer separation line more precisely. After comparing the numerical results with different Δz, $\Delta \eta$, and $\Delta \phi$, we believe that the accuracy of the numerical results is better than 1 percent.

The location of the boundary-layer separation line is determined ($\partial v/\partial \eta = 0$) by interpolation. The numerical results remain regular and convergent about two to three z-stations after the point where $\partial v/\partial \eta = 0$. They actually show a reverse flow along the ϕ-direction, and qualitatively describe a picture of a three-dimensional base flow. Further upward, convergent results can not be achieved. We do not believe that the boundary-layer computation can provide an accurate prediction after separation. The data associated with the points inside the wake are indicated by dashed lines in the Figures.

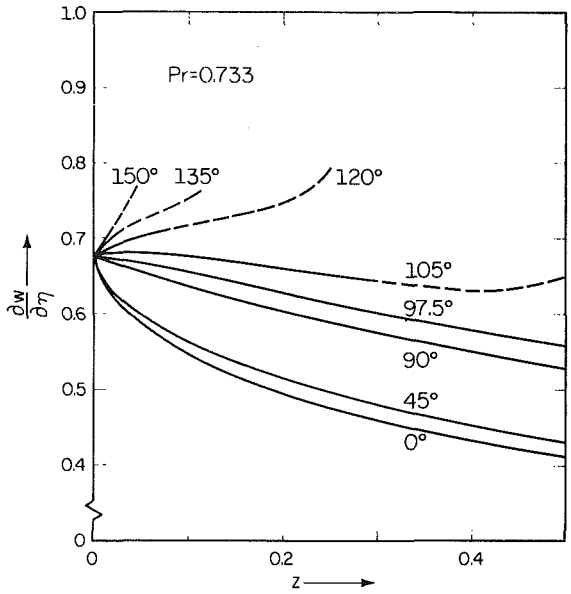

Fig. 4(a) Distribution of $\left.\frac{\partial w}{\partial \eta}\right|_{\eta=0}$

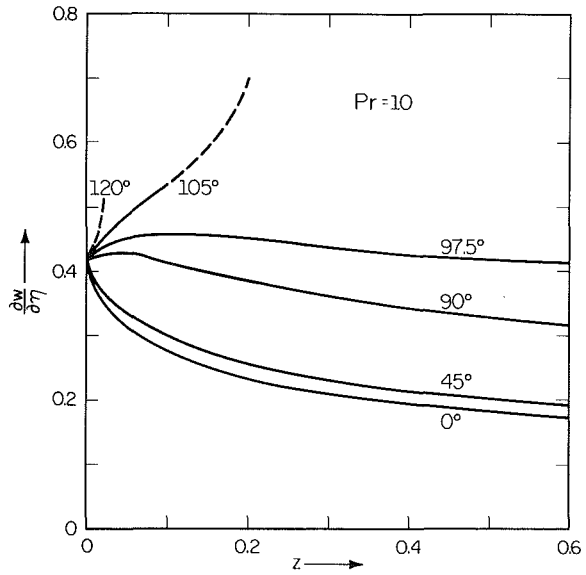

Fig. 4(b) Distribution of $\left.\frac{\partial w}{\partial \eta}\right|_{\eta=0}$

The values of $\partial v/\partial \eta$ at $\eta = 0$ are given in Fig. 2. for Pr = 0.733 and 10, respectively. They clearly demonstrate the characteristics of the interction of free/forced convection. The values of $\partial v/\partial \eta$ increase when one moves upward from the thermal leading edge for $\phi < 90$ deg and decrease for $\phi > 90$ deg due to the unfavorable pressure gradient in the ϕ direction. The interpolated locations of zero $\partial v/\partial \eta$ are plotted in Fig. 3. It shows that the boundary layer separates earlier for Pr = 10 than that for Pr = 0.733. For Pr = 10, separation starts at $z \simeq 5.6 \times 10^{-3}$ along the rear stagnation line ($\phi = 180$ deg), propagates forward as z increases until it reaches $\phi \simeq 104$ deg at $z \simeq 0.5$. The final separation angle, $\phi = 104$ deg, agrees with early numerical computations of the two-dimensional boundary layer along an unheated cylinder [12].

That the boundary layer does not separate close to the thermal leading edge is not a surprise. It has been well recognized that a buoyancy force concurrent with the free stream (two-dimensional flow) can suppress boundary-layer separation [13]. This is because the buoyancy force acts as a

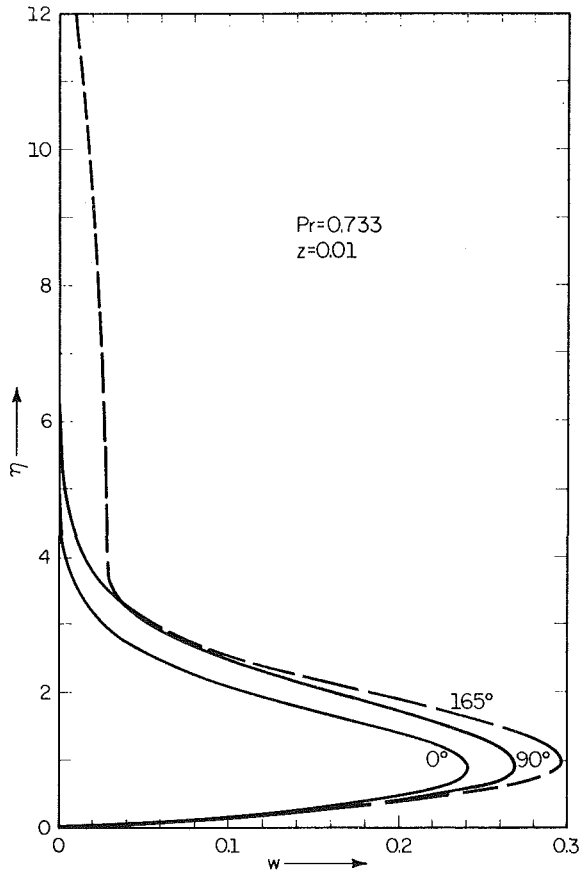

Fig. 5 Axial velocity profile

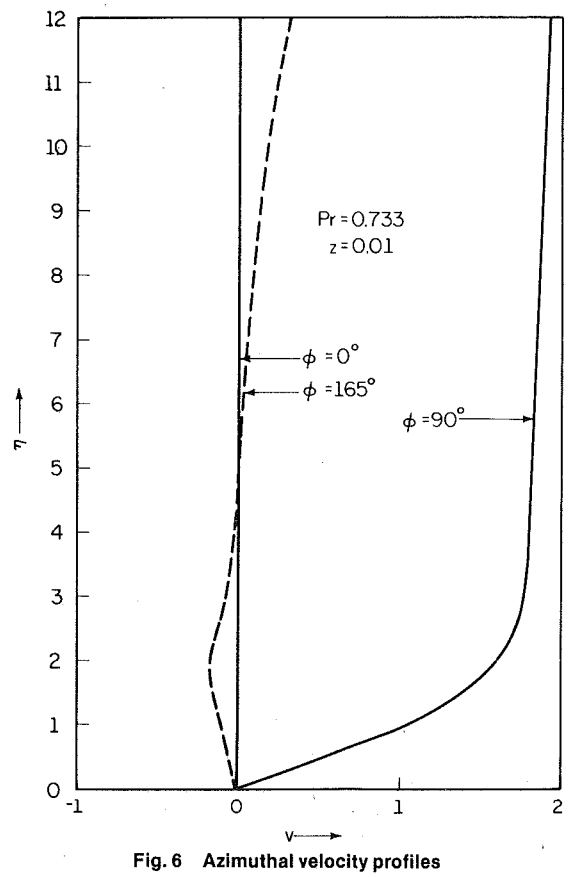

Fig. 6 Azimuthal velocity profiles

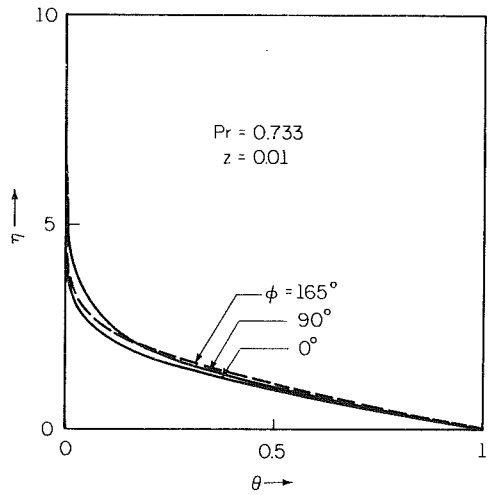

Fig. 7 Temperature distribution

favorable body force and counterbalances the unfavorable azimuthal pressure gradient. When the buoyancy force is perpendicular to the free stream, the reason why separation is delayed is different. The buoyancy force drives a thin vertical boundary layer close to the thermal leading edge. The thinner the boundary layer, the less likely it is to be separated. The thickness of the boundary layer increases as one moves upward and the effect of the unfavorable azimuthal pressure gradient gradually overcomes the density produced boundary layer. This eventually causes boundary-layer separation. For Pr = 10, the thermal boundary layer is much thinner than the momentum boundary layer; therefore, it has a smaller effect on delaying the separation of the momentum boundary layer than that for Pr = 0.733. This is the reason why the boundary layer separates earlier for Pr = 10 than it does for Pr = 0.733.

The upstream asymptotic solutions are also plotted in Fig. 2 in order to compare with the numerical results. The comparison shows that the upstream asymptotic solution is only valid in a small neighborhood of the thermal leading edge. For Pr = 0.733, the upstream asymptotic solution can be applied with confidence for $z \leq 10^{-4}$; for Pr = 10, it is valid for $z \leq 10^{-5}$. On the other hand, it should be remembered that the dimensionless axial coordinate, z, is stretched by a factor $\mathrm{Gr}/\mathrm{Re}^2$. Under the circumstance that the intensity of free convection is much larger than that of the free stream, i.e. $\mathrm{Gr}/\mathrm{Re}^2 >> 1$, the upstream asymptotic solution can provide accurate data over the region bounded upward from the thermal leading edge by several diameters.

The azimuthal shear stress can be evaluated in terms of $\partial y/\partial \eta$ and is

$$\tau_{r\phi}/(\rho U_\infty^2) = \mathrm{Re}^{-0.5} \cdot (4z)^{-0.25} \cdot \left.\frac{\partial v}{\partial \eta}\right|_{\eta=0} \qquad (12a)$$

while the axial shear stress is

$$\tau_{rz}/(\rho U_\infty^2) = \mathrm{Gr} \cdot \mathrm{Re}^{-2.5} \cdot (4z)^{-0.25} \cdot \left.\frac{\partial v}{\partial \eta}\right|_{\eta=0} \qquad (12b)$$

In Figs. 2 and 4, one can see that the buoyancy force smooths out the azimuthal dependence of $\tau_{r\phi}$ and τ_{rz}. As z increases, the effect of forced convection gradually overcomes the buoyancy effect, and the azimuthal dependence of $\tau_{r\phi}$ and τ_{rz} increases. $\tau_{r\phi}$ eventually approaches the distribution for forced convection when z becomes large.

Close to the forward stagnation line ($\phi = 0$), the free stream suppresses the axial flow, w, and decreases $\partial w/\partial \eta$. Typical axial velocity profiles are given in Fig. 5 for Pr = 0.733 at $z = 0.01$. The dashed line, $\phi = 165$ deg, is inside the trailing wake so that its value is not reliable. However, the

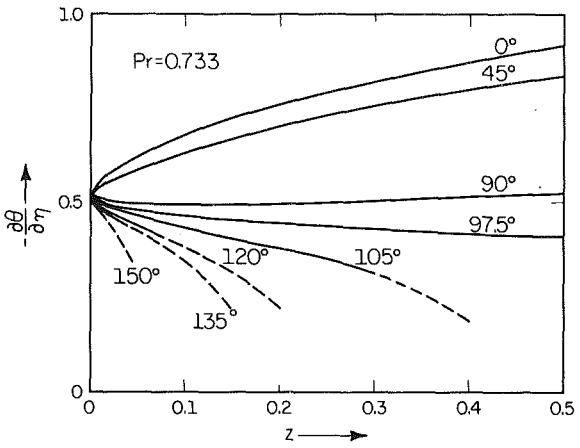

Fig. 8(a) Normal temperature gradient on the wall

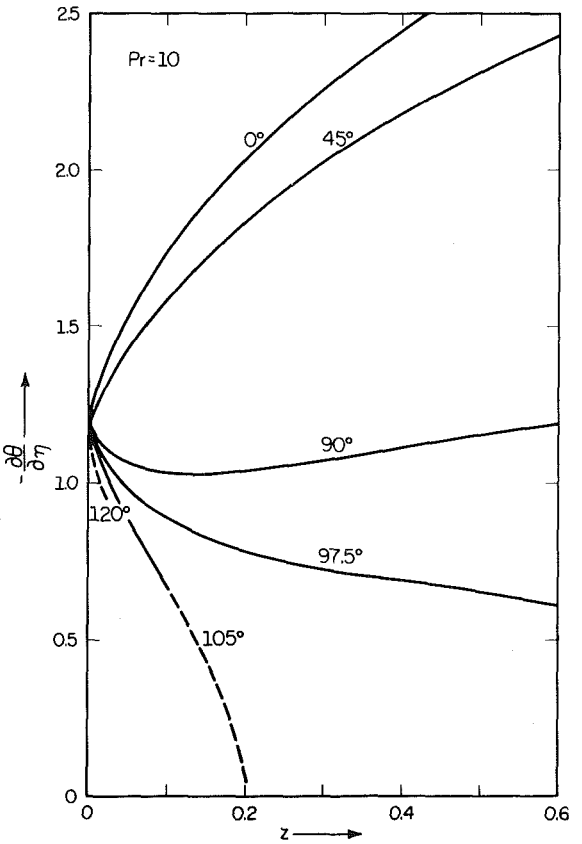

Fig. 8(b) Normal temperature gradient on the wall

profile at $\phi = 165$ deg does show some interesting information. Close to the wall, the profile is regular, yet it fails to match with the inviscid flow as $\eta \to \infty$. This is an indication that the numerical results have not converged.

In general, forced convection suppresses w in the forward part of the cylinder ($\phi \leq 90$ deg). The magnitude of w increases with ϕ. The phenomenon is very similar to the interaction of a free stream with a rising plume, in that the smoke rises faster where it is farther away from the air nozzle. Consequently $\partial w/\partial\eta$ increases with ϕ as shown in Fig. 4.

Typical azimuthal velocity profiles are shown in Fig. 6 for $Pr = 0.733$ at $z = 0.01$. Its value increases from zero at $\phi = 0$ deg to its maximum at $\phi = 90$ deg and decreases to zero at $\phi = 180$ deg. The dashed line ($\phi = 165$ deg) indeed shows a reversed flow and qualitatively matches with the distribution of a base flow. Since the numerical results diverge a few z stations after $z = 0.01$ along $\phi = 165$ deg, we do not trust its value.

Figure 7 shows a typical temperature distributon. The dimensionless temperature gradient normal to the wall on the surface of the cylinder is given in Fig. 8. It attains its maximum value at $\phi = 0$ and its value monotonically decreases toward the real stagnation line. The Nusselt number can be expressed in terms of $\partial\Theta/\partial\eta$ as

$$\mathrm{Nu} = \frac{q \cdot a}{k(T_w - T\infty)} = -\mathrm{Re}^{0.5} \cdot (4z)^{-0.25} \cdot \frac{\partial\Theta}{\partial\eta}\bigg|_{\eta=0} \tag{13}$$

This clearly shows that the heat transfer rate is higher on the forward part of the cylinder. Intuitively, one may imagine that the heat transfer rate will approach the value for two-dimensional forced convection. For two-dimensional forced convection the value of $(4z)^{-0.5} \cdot \partial\Theta/\partial\eta\,|_{\eta=0}$ equals 2.68 for $Pr = 10$ and approximately equals one for $Pr = 0.733$ along $\phi = 0$. A careful comparison indicates that the influence of free convection on the heat transfer rate is still noticeable for $z \leq 0.75$.

4 Conclusion

The analysis shows that buoyancy has a substantial effect on the boundary-layer development and heat transfer in the neighborhood of the thermal leading edge when $Gr \cdot Re^{-2}$ is large. The separation of the boundary layer is delayed in the buoyancy dominant region, but is quickly developed upward away from this region. The disturbance of the separated boundary layer could have a significant effect on the inviscid flow which can alter the boundary-layer solution presented in this paper. However, we believe that the boundary-layer solution is realistic in the region $0 \leq \phi \leq 90$ deg based on experience with the two-dimensional cylinder forced flow. The validity of the attached boundary layer for $\phi > 90$ deg in the neighborhood of the thermal leading edge requires experimental verification.

References

1 Young, R. J., and Yang, K. T., "Effect of Small Crossflow and Surface Temperature Variation on Laminar Free Convection Along a Vertical Plate," ASME *Journal of Applied Mechanics*, Vol. 30, 1963, pp. 252-256.

2 Eichhorn, R., and Hasan, M. M., "Mixed Convection About a Vertical Surface in Crossflow: A Similarity Solution," ASME Paper No. 80-HT-129, 1980.

3 Plumb, O. A., "The Effect of Crossflow on Natural Convection From Vertical Heated Surfaces," ASME Paper No. 80-HT-71, 1980.

4 Yao, L. S., "Free-Forced Convection in the Entry Region of a Heated Straight Pipe," ASME JOURNAL OF HEAT TRANSFER, Vol. 100, 1978, pp. 212-219.

5 Yao, L. S., "Variable Viscosity Effect on the Laminar Water Boundary Layer on Heated Cones," ASME *Journal of Applied Mechanics*, Vol. 45, 1978, pp. 481-486.

6 Yao, L. S., and Catton, I., "Buoyancy Crossflow Effects in the Boundary Layer on a Heated Longitudinal Horizontal Cylinder," ASME JOURNAL OF HEAT TRANSFER, Vol. 99, 1977, pp. 122-124.

7 Yao, L. S., Catton, I., and McDonough, J. M., "Free-Forced Convection Along a Horizontal Cylinder," *Numerical Heat Transfer*, Vol. 1, 1978, pp. 255-266.

8 Yao, L. S., and Chen, F. F., "A Horizontal Flow Past a Partially Heated, Infinite Vertical Cylinder," ASME JOURNAL OF HEAT TRANSFER, Vol. 103, 1981, pp. 546-551.

9 Oosthuizen, P. H., and Leung, R. K., "Combined Convective Heat Transfer From Vertical Cylinders in a Horizontal Flow," Paper No. 78-WA/HT-45, ASME Winter Annual Meeting, San Francisco, Calif., 1978.

10 Oosthuizen, P. H., "Numerical Study of Combined Convective Heat Transfer From a Vertical Cylinder in a Horizontal Flow," *Proceedings of the 6th International Heat Transfer Conference*, Toronto, Canada, Mc-4, 1978.

11 Yao, L. S., Catton, I., and McDonough, J. M., "Buoyancy-Driven Asymmetric Water Boundary Layer Along a Heated Cylinder," *Journal of Fluid Mechanics*, Vol. 98, Part 2, 1980, pp. 417-433.

12 Schlichting, H., *Boundary-Layer Theory*, McGraw-Hill Book Company, 1968, pp. 201-204.

13 Sparrow, E. M., Eichhorn, R., and Gregg, J. L., "Combined Forced Convection in a Boundary Layer Flow," *Physics of Fluids*, Vol. 2, 1959, p. 319.

Ikuo Tokura
Research Assistant.

Hakaru Saito
Professor.

Koki Kishinami
Associate Professor.

Kazuo Muramoto
Research Assistant.

Department of Industrial Mechanical Engineering,
Muroran Institute of Technology,
27-1 Mizumoto-cho, Muroran 050,
Japan

An Experimental Study of Free Convection Heat Transfer From a Horizontal Cylinder in a Vertical Array Set in Free Space Between Parallel Walls

Empirical formulas are proposed from experiments on free convective heat transfer from a cylinder array arranged in a vertical line. Subsequently, experiments were carried out to examine the effect of two parallel plates enclosing the array as a heat transfer promoter. Finally, through a discussion of the heat transfer from the entire cylinder systems, both in open and in restricted spaces, a recommendation is made for designing a heat exchanger of a single-line type of cylinder bank.

1 Introduction

Cylinders set in an array have been used as a free convection heat exchanger and will be employed more in the future because no power is required to drive air through it. The heat transfer from a cylinder in an array is quite different from a single cylinder due to interaction of the temperature and flow fields around neighboring cylinders—even when the array is in free space. In many practical applications, however, the cylinder array is installed in a restricted space. Therefore, it is very important to know the heat transfer characteristics of a cylinder array both in confined and free space.

Studies on free convection heat transfer from horizontal tube arrays in free space have been conducted mainly by an experimental approach because of difficulties in analytical treatment of the subject. The only analytical study has been reported by Katsuta and Ishihara [1] for an array with two lines of tubes having relatively narrow pitch. They used Levy's integral method [2] to analyze the problem and found good agreement between analysis and experiment when the spacing of the cylinders was small ($b/d<0.2$, $d=50.8$ mm). Experimental studies have been carried out by Lieberman and Gebhart [3] who used an array with ten cylinders of 0.127-mm dia, and Marsters [4] who used three, five, and nine cylinders of 6.35-mm dia under conditions of uniform heat flux. Eckert and Soehngen [5] performed experiments for a uniform surface temperature, using three cylinders of 22.3-mm dia with vertical and stagger arrangements. From these experiments, the heat transfer rate from a cylinder in an array was found to decrease with decreasing cylinder spacing because of interference by the hot buoyant flow from the preceding cylinders when the cylinder spacing was small. For larger spacings, the heat transfer increased with spacing because the buoyant flow acts as a forced flow on the succeeding cylinders. Recently, Sparrow and Niethammer [6] carried out experiments on the heat transfer from a pair of heated horizontal cylinders ($d=37.87$ mm) in a vertical line and reported the effect of the vertical separation distance and the cylinder-to-cylinder temperature imbalance on the upper-cylinder Nusselt number. They found that the upper-cylinder Nusselt number takes on a maximum value as a function of separation distance and that the cylinder-to-cylinder temperature difference has a great effect on the Nusselt number at small separations. However, few data have been published on the local Nusselt number of cylinders in an array, especially for arrays with three cylinders or more. Furthermore, the heat transfer correlations have not been proposed for individual cylinders arranged in an array or for a whole array of cylinders.

The so-called chimney effect will cause an increase in the heat transfer rate when an array is placed between parallel plates. In this connection, Marsters [7] carried out experiments on the heat transfer around a single horizontal cylinder between two parallel plates and proposed an empirical formula for predicting the average heat transfer coefficient of the cylinder as a function of distance and height of the plates and the cylinder diameter. The effect of parallel plates on the heat transfer characteristics of cylinder banks has not been clarified up to now.

In this report, experiments on free convection heat transfer from vertical arrays of two, three, and five lines have been carried out to find the local and average heat transfer coefficients of each cylinder and the average for an entire array. We also clarify the dependence of those values on both the flow fields around the arrays and geometric factors such as diameter, spacing, and number of cylinders. In addition, the effect of bounding parallel plates was examined by measuring heat transfer coefficients promoted by plates between which an array was set. From the experimental results, recommended conditions for practical arrangements of cylinder arrays are given. The discussion describes how to select the optimum dimensions of cylinder spacing, plate separation distance, and the number of cylinders.

2 Experimental Apparatus and Procedure

The experiments were carried out in a room of dimensions $4.8\times7.2\times2.8$ m with shrouded windows, using two different arrangements. One is the apparatus in which average heat transfer rates of the cylinder can be measured, which consists of a main heating cylinder and some auxiliary heating cylinders. The schematic view of the heating cylinders is shown in Fig. 1. Both types of heating cylinder are constructed of copper tubes having a 600-mm length, 1-mm thickness and 28.5-mm outer diameter—supported at the ends by V-notched, vinyl-chloride rods attached to vertical supporting columns. Inserted in the tubes are vinyl-chloride bobbins, as heaters, with sheathed nickel-chrome wires wound in spiral grooves on the surface having a pitch of 7

Contributed by the Heat Transfer Division for publication in the JOURNAL OF HEAT TRANSFER. Manuscript received by the Heat Transfer Division January 13, 1982.

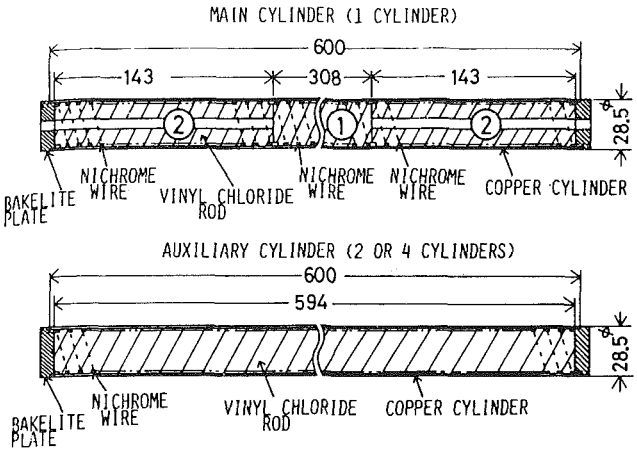

Fig. 1 Construction of heating cylinders: 1, main heater; 2, guard heater

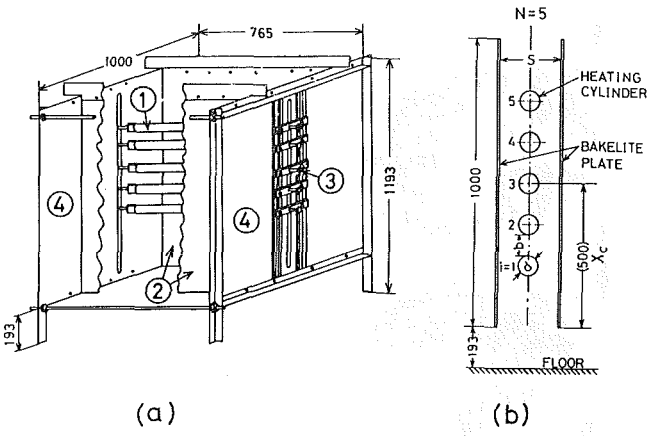

Fig. 2 Schematic view of cylinder array between parallel plates: 1, heating cylinder; 2, parallel plates; 3, fixing bolt; 4, side wall

mm. The surface temperatures of the cylinders were measured by thermocouples (type T) of 0.1-mm dia positioned along the top of the cylinders at every 100 mm of axial distance from one end of each cylinder. The main heating cylinder is a cylinder by which the average heat transfer rates are measured, with three heaters in it, one main heater at the center and two guard heaters at both ends. The heaters were controlled independently so that the temperature distribution along the cylinder was uniform within 0.5°C. The circumferential temperature variations were less than 0.3°C which were measured by rotating the cylinders for the same electric power input and ambient temperature conditions. The auxiliary heating cylinders only maintain prescribed temperatures; therefore, they have no guard heaters. In the multicylinder arrays, the electric power input to each cylinder was controlled until uniformity within 1.0°C was achieved in the cylinder-to-cylinder temperature. It can be estimated to cause the variation in 0.8 percent in the upper-cylinder Nusselt number in a two-cylinder system of $b/d = 1$ [6]. This variation in the cylinder Nusselt number can be ignored. Thus, the average heat transfer coefficient for the cylinder can be estimated from the electric power input to the main heater of 308-mm length set at the center of the main heating cylinder. After this, the main heating cylinder is replaced by one of the auxiliary ones. This procedure is continued until the average heat transfer coefficients for all the cylinders in array are obtained.

Another apparatus was mainly used to obtain the local Nusselt numbers for cylinders in an array. The heating cylinders of 22.2 mm or 38.0 mm in diameter and 220 mm in length are constructed in the same way as the auxiliary heating cylinders. To compensate for heat loss from the ends of the cylinder, the turn of winding nickel-chrome wire on the bobbins is increased near the ends. The axial uniformity of the surface temperature of each cylinder achieved in this method was within 0.8°C which was measured by three thermocouples positioned along an angular position of 90 deg measured from the bottom of the cylinder at axial distances of 20 mm, 110 mm, and 200 mm from one end of the cylinder. This corresponds to an error of less than 2 percent in the wall-to-ambient temperature difference. The local heat transfer coefficients at the surface of the cylinder can be obtained by analyzing interferometric fringes obtained using a Mach-Zehnder interferometer. This method is useful when center-to-center cylinder separation distance is relatively narrow, for example, less than twice the cylinder diameter; however, it is very difficult to take sharp photographs, when the spacing is wide, because of unstable waving motion of flow around the cylinders.

The experiment was carried out for vertical arrays with two,

Nomenclature

b = diameter-to-diameter cylinder separation distance (spacing)
d = cylinder diameter
Gr = Grashof number based on cylinder diameter, $g\beta d^3 \Delta T/\nu^2$
h = average heat transfer coefficient for a cylinder ($h \equiv q/\Delta T$)
k = thermal conductivity of air
L = height of parallel plates
N = number of cylinders in an array (2, 3, or 5)
Nu_i = Nusselt number of ith cylinder between parallel plates, hd/k
$\mathrm{Nu}_{i\infty}$ = Nusselt number of ith cylinder in free space, hd/k
Nu_N = average Nusselt number for an array between parallel plates, $\sum_{i=1}^{N} \mathrm{Nu}_i/N$
$\mathrm{Nu}_{N\infty}$ = average Nusselt number for an array in free space, $\sum_{i=1}^{N} \mathrm{Nu}_{i\infty}/N$
$\mathrm{Nu}_{s\infty}$ = Nusselt number for a single horizontal cylinder in free space
Pr = Prandtl number
q = heat flux of a heated cylinder
Ra = Rayleigh number, Gr•Pr
S = distance between parallel plates
ΔT = temperature difference between the surface of cylinder and the ambient air (outside of the parallel plates)
x = center-to-center cylinder separation distance measured from the bottom cylinder
x_c = distance from the bottom of parallel plates to the center of a cylinder array
$x_{\max}$ = center-to-center cylinder separation distance between the bottom and the top cylinder
β = thermal expansion coefficient
ν = kinematic viscosity
ϕ = circumferential (angle) coordinate

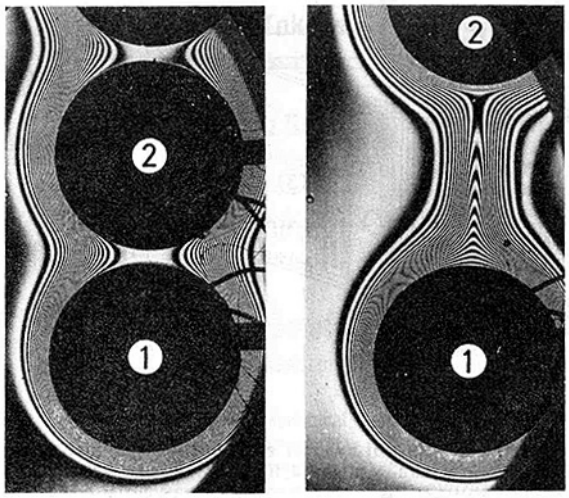

Fig. 3 Interferometric photograph for a three-cylinder array (each fringe represents an isothermal line, $\Delta T = 62°C$, $d = 38$ mm): 1, bottom cylinder; 2, middle cylinder

three, and five cylinders having equal spacing under the condition of constant surface temperature. The maximum spacing of the cylinders was nineteen times the cylinder diameter for two- and three-cylinder arrays and nine times for the five-cylinder array. Figure 2(*a*) shows the schematic view of the experimental apparatus used for testing the effect of the parallel walls on the heat transfer from cylinders in an array. The heating cylinders were fixed to the side walls by bolts which were allowed to slide along the walls. The parallel walls were constructed of bakelite plates (5-mm thickness, 1000-mm height and 765-mm width). Aluminum foil was attached to the inside surfaces in order to minimize the effect of radiation heat transfer between the walls and the cylinders. Therefore, the boundary condition at the parallel plates can be considered to be adiabatic. The distance from the floor to the bottom ends of the parallel plates was 193 mm. The heating cylinders set between the plates were the same as mentioned in the foregoing paragraph. Since the main concern was the increase in heat transfer rates of cylinders by setting them between the parallel plates, the main variables in this experiment were the distance between the parallel plates (40–829 mm) and the spacing of the cylinders (one, two, and six times their diameter) for the arrays with three and five lines. The method for measuring the average heat transfer coefficient of each cylinder is the same as used in the experiment mentioned above. Cylinder arrangement and main dimensions of the apparatus are shown in Fig. 2(*b*) for a five-line array. Throughout the experiments, the temperature difference between the surfaces of the cylinders and the ambient air was maintained at about 50°C, corresponding to a Grashof number based on the cylinder diameter in the range 4×10^4 to 4×10^5. The Prandtl number was 0.71.

3 Experimental Results and Discussion

3.1 Heat Transfer Characteristics of a Cylinder Array in Free Space.

3.1.1 Local Heat Transfer Behavior of Cylinders. The heat transfer behavior of cylinders in array is quite different from a single horizontal cylinder due to mutual interaction between the cylinders. In the following the variation of the local heat transfer coefficients for the cylinders will be described as a function of angular position, ϕ, measured from the stagnation point at the bottom of a cylinder, taking a

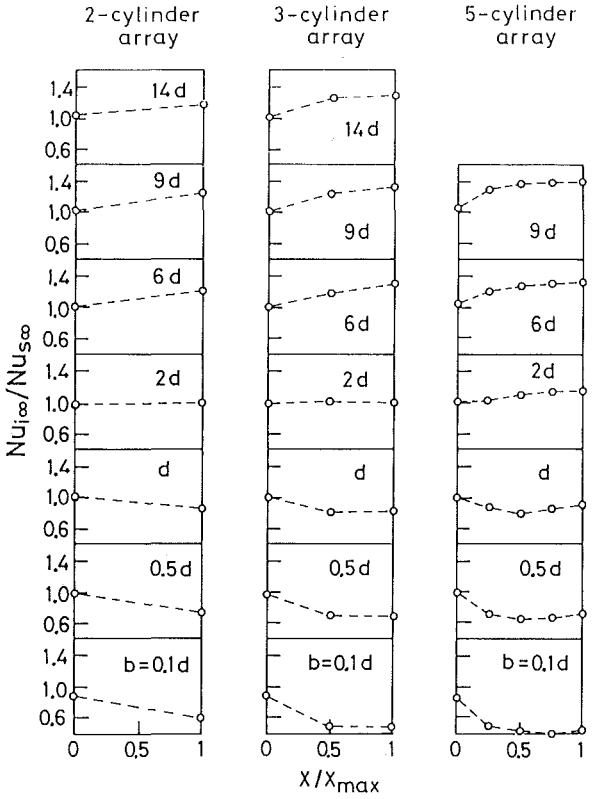

Fig. 4 Average Nusselt numbers for cylinders in an array ($d = 28.5$ mm, $Gr = 1.2 \times 10^5$, $Nu_{s\infty} = 7.91$)

three-cylinder system as an example. The local heat transfer coefficient for the first cylinder, which is at the bottom in an array, is almost the same as that of a single horizontal cylinder except for the region near $\phi = 180$ deg, when the spacing of the cylinders is small. In contrast, the local value of the second cylinder, which is in the middle of the array, shows obvious interference effects since its lower surface faces the wake flow from the first cylinder and its upper surface faces the third cylinder. The heat transfer coefficient of the second cylinder was observed to significantly decrease near $\phi = 0$ deg and $\phi = 180$ deg, when the spacing is very small. This may be explained from the formation of so-called hot spots around the stagnation points. In the case where the spacing is very small, the buoyant flow around a cylinder cannot penetrate the narrow space between cylinders and "dead water regions" form at the top and the bottom of the cylinder (see Fig. 3(*a*)). In contrast, for larger spacing the heat transfer coefficient near $\phi = 0$ deg increases with increasing spacing and exceeds the value for a single horizontal cylinder. This effect can be explained from Fig. 3(*b*) which shows that the buoyant flow from the first cylinder impinges on the bottom of the second one—exerting the same action as a forced convection flow. The same circumstances mentioned above hold for the heat tranfser coefficient at $\phi = 0$ deg of the third cylinder.

3.1.2 Average Heat Transfer Rates of Cylinders in Array. First of all, the average heat transfer coefficient for a single horizontal cylinder was measured since this provides the basis of estimation of the heat transfer rates of cylinders in an array. The measured values are correlated by the following formula in the range $Ra = 2.8 \times 10^4$ to 2.8×10^5.

$$Nu_{s\infty} = 0.463\ Ra^{1/4} \tag{1}$$

This equation predicts Nusselt numbers 3.5 percent smaller than those proposed by Morgan [8] but can be considered to be good enough to use in practice.

In the case of a cylinder array in open space, the radiation

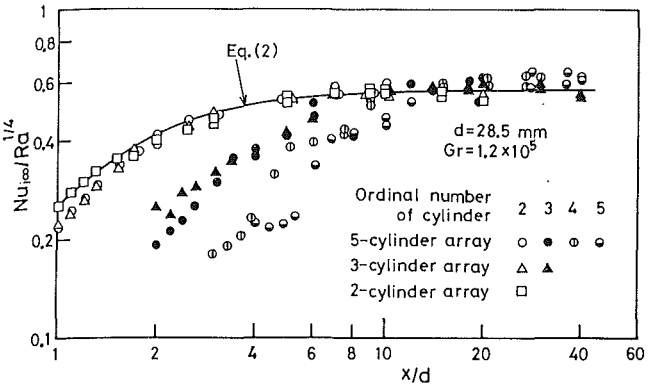

Fig. 5 Average Nusselt numbers for downstream cylinders

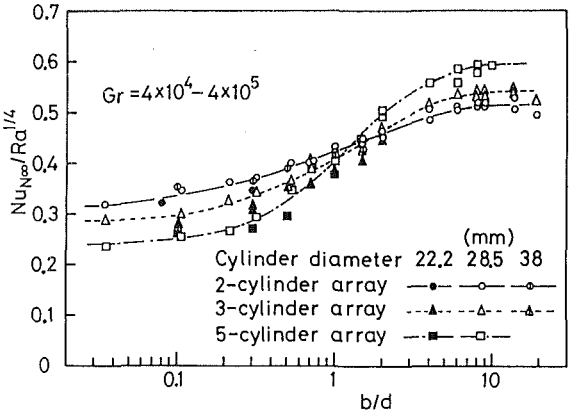

Fig. 6 Average Nusselt numbers for whole arrays—effect of b/d

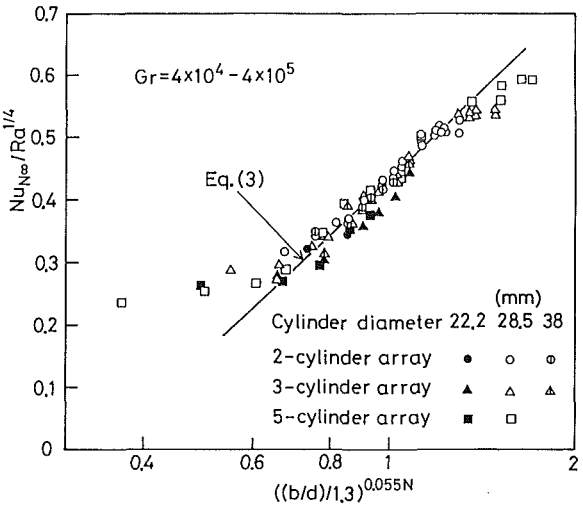

Fig. 7 Average Nusselt numbers for whole arrays—effect of $[(b/d)/1.3]^{0.055N}$

heat transfer between the surface of cylinders and the ambient walls can be calculated using the same method as Marsters [4] by assuming that the emissivity of the cylinder surface is already known. An emissivity of 0.072 was employed for the polished surface of copper tubes in the following. The calculated contribution of the radiative heat transfer to the total proved to be less than nine percent. Figure 4 shows the ratio of average Nusselt number for each cylinder in arrays with two, three, and five lines to that of a single tube. It can be seen that the average Nusselt numbers of the cylinders after the second line of an array are very small when the spacing is extremely narrow. However, Nusselt numbers increase with increasing spacing and approach to almost the same value when the spacing exceeds six times the cylinder diameter. On the other hand, the Nusselt number of the first cylinder has nearly the same value as a single cylinder. This is not the case when the spacing is very small, however, as described before.

The variation of average Nusselt numbers for downstream cylinders in arrays with two, three, and five lines with the distance between the axes of the cylinders (measured from the bottom cylinder) is illustrated in Fig. 5. As mentioned above, these values increase gradually with increasing spacing until they reach a maximum when the spacing is greater than about five times the cylinder diameter. From these results, the authors tried to deduce an empirical formula to predict the average Nusselt number for upper cylinder in two-cylinder array. To begin with, the functional relation $Nu_{2\infty}/Ra^{1/4} = f(x/d)$ was assumed by referring to Fig. 5. The function is required to satisfy the following two conditions:

(*i*) $f(x/d) = C_1$ at $x/d = 1$. ($C_1 = 0.261$, see Fig. 5)
(*ii*) $f(x/d) = C_2$ when x/d is large

Assuming the simplest equation that satisfies these conditions and determining the constants, the following equation can be obtained.

$$Nu_{2\infty}/Ra^{1/4} = 0.261(x/d)^{3/4}[1 - \exp\{-2.22/((x/d)^{3/4} - 1)\}] \quad (2)$$

This gives, when x goes to infinity, $Nu_{2\infty}/Ra^{1/4} = 0.58$, which is slightly larger than the value for a single horizontal cylinder, i.e., equation (1). However, as indicated by the solid line in Fig. 5, it represents the measured values within the accuracy of ±9 percent in the range of $x/d = 1$ to 15 at $Gr = 1.2 \times 10^5$. The variations of the average Nusselt numbers for the downstream cylinders in arrays with lines more than two are also shown in the same figure. According to our visual observation, a flow field around a cylinder is always influenced, more or less, by a preceding line (or lines) and also the buoyant flow induced by lines which follow. This effect can obviously be seen in the behavior of heat transfer coefficients shown in this figure. For instance, the average Nusselt numbers of second cylinders in arrays with more than two lines are lower than two lines alone, especially for very small spacings. This lowering effect becomes, as seen in the figure, insensible as the spacing increases. Also one can see in Fig. 5 that the maximum value of the average Nusselt numbers for downstream cylinders in three- and five-line arrays are approximately the same as the value of the upper cylinder in the two-cylinder system. Therefore, from the heat transfer point of view, it can be said from this result that when the spacing is large enough the downstream cylinders in arrays with more than two lines can be regarded as the same as the upper one in two-cylinder array. The reason may be that the heat transfer rate of a downstream cylinder in array with large spacing is determined more by the interference with the nearest upstream cylinder rather than the entire array. In other words, when the spacing is large, heat transfer rates of the downstream cylinders can be estimated to some extent from equation (2) which is appropriate for the upper cylinder of a two-cylinder array.

3.1.3 Average Nusselt Number for a Whole Cylinder Array. By taking the arithmetic mean value of the Nusselt numbers for an array, the heat transfer from a whole cylinder array can be represented in the same functional form as is used for a conventional single cylinder and indicated in Fig. 6 as a function of the spacing. It can be shown from this figure that the average Nusselt number for a whole cylinder array decreases considerably when the spacing is less than three times the cylinder diameter. On the other hand, when the spacing is larger than ten times the diameter, the heat transfer rate for an array cannot be promoted any more by increasing the spacing but also requires a larger space for installation.

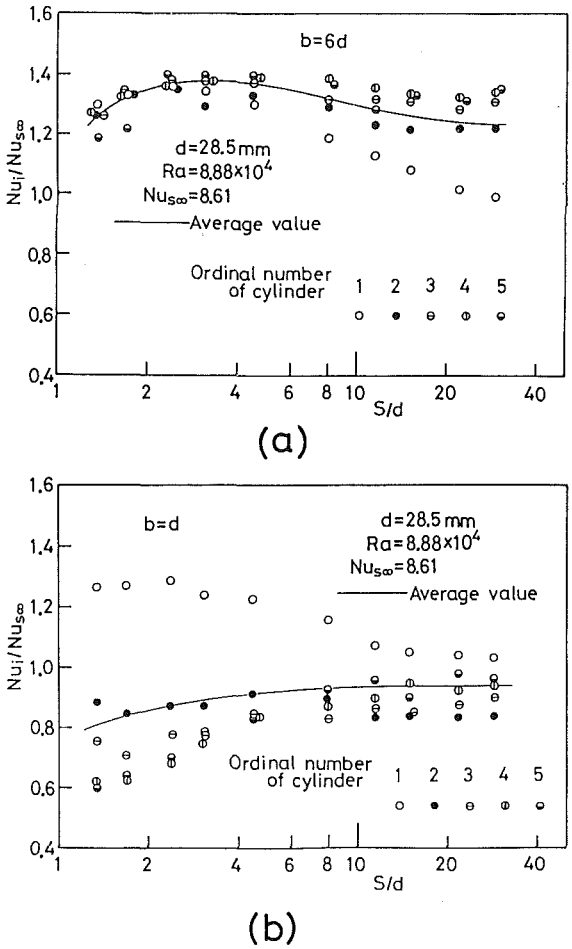

Fig. 8 Average Nusselt numbers for cylinders in a five-cylinder system between parallel plates: (*a*) $b = 6d$, (*b*) $b = d$

For this reason, the suitable spacing ratio (b/d) for a heat exchanger having good heat transfer performance and compact in size was found to be about 6 for the cylinder diameters employed in this study. Figure 7 presents the data used in Fig. 6 but with the new variable $[(b/d)/1.3]^{0.055N}$ as the abscissa. It shows that all the values for arrays with different lines can be represented by an S-shaped curve. As indicated in the figure, the solid line having a slope of 0.410 can represent the measured values for the new variable in the range 0.7 to 1.2. Therefore, the following formula is available for predicting the average Nusselt number of an array in the linear part of the figure. That is,

$$\mathrm{Nu}_{N\infty} = \sum_{i=1}^{N} \mathrm{Nu}_{i\infty}/N = 0.410\,\mathrm{Ra}^{1/4} \ln([(b/d)/1.3]^{0.055N}) + 0.434. \tag{3}$$

This equation represents the experimental data within ± 10 percent in the ranges of $[(b/d)/1.3]^{0.055N} = 0.7$ to 1.2 and $\mathrm{Gr} = 4 \times 10^4$ to 4×10^5.

3.2 Heat Transfer Characteristics of Cylinder Arrays between Parallel Plates. A cylinder array was set between parallel plates with the center of the array located 500 mm above the bottom ends of the plates. The heat transfer coefficients of the cylinders in the array were defined using temperature difference between the surface of cylinder and the ambient room air. The coefficient defined here is an apparent one since its definition is not based on the conventional temperature difference. The radiation heat transfer between the cylinders and the surrounding wall surfaces can

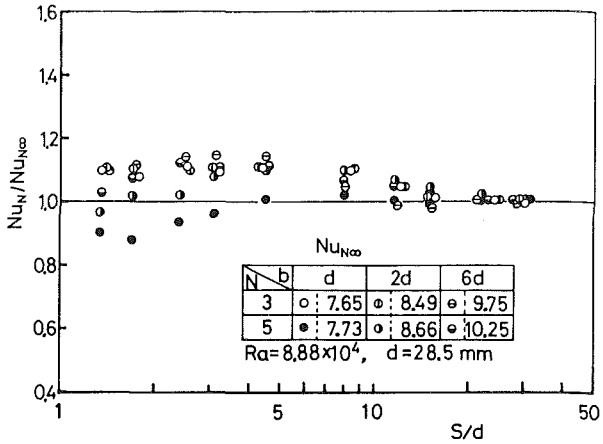

Fig. 9 Effect of parallel plates on Nusselt numbers

be considered to be small in comparison with the total heat transfer rate and can be ignored. The variation of average Nusselt numbers of the cylinders—normalized by the value for a single horizontal cylinder in open space—with the distance between the parallel plates is presented in Fig. 8 for a cylinder array with five lines. The average Nusselt numbers for a whole cylinder array are also shown by the solid lines in the figures. From the figures, there is no effect of the plates for heat transfer promotion when the distance between the plates is larger than thirty times the cylinder diameter. It can also be seen in Fig. 8(*a*) that the average Nusselt number for the whole cylinder array with five lines has a maximum when the distance between the parallel plates is about three times the cylinder diameter. This indicates that at that distance between the plates the cylinder array attains the maximum chimney effect. The average Nusselt number of every cylinder set between the parallel plates with moderate distance is nearly the same when $b = 6d$ (Fig. 8(*a*)). When $b = d$, however, the average Nusselt numbers for the downstream cylinders between the parallel plates are considerably smaller than that of the first one (Fig. 8(*b*)). This may be understood from the fact that the average Nusselt number for the first cylinder in array set between the parallel plates is considerably larger than that set in open space, while the heat transfer coefficients of the following cylinders after the bottom one remain almost in the same values as those set in open space. While the first cylinder in an array between the plates is always exposed to the induced air flow of ambient room temperature, the downstream cylinders are compelled to transfer energy to the hot air flow from upstream portions of the array. Therefore, the more downstream the cylinder is located, the smaller the average Nusselt number of the cylinder becomes when both the distance between the plates and the spacing of cylinders are small (see Fig. 8(*b*)). Consequently, if one intends the increase the heat transfer rate of the downstream cylinder, attaching various fins to the surfaces of cylinders seems to be very effective for the improvement on the heat transfer performance of a cylinder array between parallel plates when the spacing of cylinders is small. One can see from the figures that the spacing of cyinders is the most important parameter that affects heat transfer from a cylinder array between parallel plates, because the variation of the average Nusselt number with the spacing is greater than with the distance between parallel plates and with the number of cylinders in an array.

In order to examine the benefit of promoting heat transfer by setting an array between the parallel plates, the ratio of the average Nusselt number for a whole cylinder array between the plates and that in free space is illustrated (Fig. 9) as a function of the distance between the plates. It can be seen

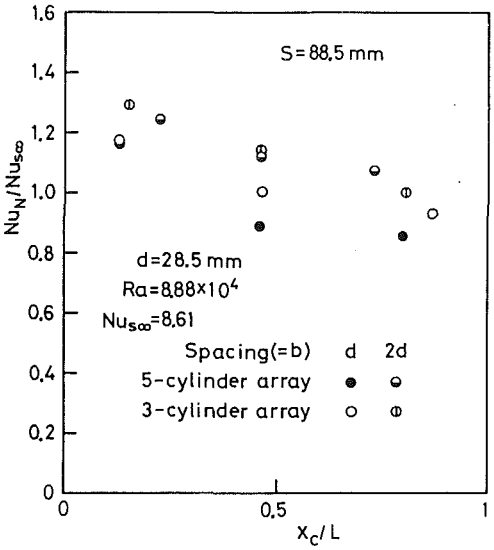

Fig. 10 Change in Nusselt numbers versus elevation of an array between parallel plates

from this figure that the heat transfer from a cylinder array set between the parallel plates increases by 10 to 15 percent from an array in open space when the spacing of cylinders is large and the distance between the plates is about two to six times the cylinder diameter.

Figure 10 shows the effect of the location of the cylinder array between the parallel plates on the heat transfer rate. The heat transfer from the whole cylinder array increases when the array is placed in the lower portion of the plates. The reason may be that the chimney effect is promoted by setting the array in the bottom between the plates because of the increase in length of the path in which the hot air flows. The distance between the bottom of the plates and the surface of floor seems to have little effect on the heat transfer from a cylinder array except when the distance is extremely small; less than 10 mm in these experiments.

4 Conclusions

Experiments were conducted on free convection heat transfer from horizontal cylinder arrays in a vertical line in open space and between parallel plates under a constant surface temperature condition. The following conclusions were drawn in this study.

(*i*) The mutual interaction between heating cylinders in free space is most obvious at locations near the narrow regions between the cylinders. The heat transfer rates at $\phi = 0$ deg of downstream cylinders exhibit low values when the spacing of cylinders is small. But heat transfer rates increase as spacing increases, eventually exceeding values for a single horizontal cylinder.

(*ii*) The average heat transfer coefficient of the first cylinder in an array in open space is almost the same as a single horizontal cylinder, regardless of the number of cylinders in the array, except when the spacing is less than the diameter of the cylinder. The average heat transfer coefficients of the downstream cylinders in an array in free space approach maximum values when the spacing is larger than five times the cylinder diameter. The empirical formula to predict the average Nusselt number for upper cylinder in a two-cylinder system was obtained in the form of equation (2). The average Nusselt numbers for the downstream cylinders in an array with more than two lines can be estimated to some extent by the same equation when spacing of cylinder is large.

(*iii*) The average Nusselt number for a whole cylinder array with two, three, and five lines in open space was expressed by experimental formula, equation (3). A recommendable spacing ratio (b/d) for a heat exchanger with good performance in heat transfer and compact in size was found to be about 6.

(*iv*) When an array of cylinders was set between parallel plates, the spacing of the cylinders was the most important parameter that affected heat transfer from the array. The average Nusselt number for the first cylinder in an array between the plates greatly increases in comparison with that in free space. This results in an increase of the average Nusselt number for an entire array of cylinders by 10 to 15 percent in comparison with the case in open space. The overall heat transfer rate of an array considerably increases when the array is placed in the lower parts of the plates.

Acknowledgment

The authors wish to express their appreciation to Professor N. Seki, Hokkaido University, Japan, for his valuable suggestions, and also to Mr. Tatsuyuki Suzuki and Mr. Koichi Okada for their help in the experiments.

References

1 Katsuta, K., and Ishihara, I., "Natural Convection Heat Transfer from a Vertical Array of Cylinders," *Proceedings of the 15th National Heat Transfer Symposium of Japan*, 1978, pp. 208–210.

2 Levy, S., "Integral Methods in Natural-Convection Flow," ASME *Journal of Applied Mechanics*, Vol. 22, 1955, pp. 515–522.

3 Lieberman, J., and Gebhart, B., "Interactions in Natural Convection from an Array of Heated Elements, Experimental," *International Journal of Heat and Mass Transfer*, Vol. 12, 1969, pp. 1385–1396.

4 Marsters, G. F., "Arrays of Heated Horizontal Cylinders in Natural Convection," *International Journal of Heat and Mass Transfer*, Vol. 15, 1972, pp. 921–933.

5 Eckert, E. R. G., and Soehngen, E. E., "Studies on Heat Transfer in Laminar Free Convection with Zehnder-Mach Interferometer," AF Technical Report 5747, United States Air Force, Air Material Command, Wright-Paterson Air Force Base, Ohio, 1948.

6 Sparrow, E. M., and Niethammer, J. E., "Effect of Vertical Separation Distance and Cylinder-to-Cylinder Temperature Imbalance on Natural Convection for a Pair of Horizontal Cylinder," ASME JOURNAL OF HEAT TRANSFER, Vol. 103, 1981, pp. 638–644.

7 Marsters, G. F., "Natural Convective Heat Transfer from a Horizontal Cylinder in the Presence of Nearby Walls," *Canadian Journal of Chemical Engineering*, Vol. 53, 1975, pp. 144–149.

8 Morgan, V. T., "The Overall Convection Heat Transfer from Smooth Circular Cylinders," in *Advances in Heat Transfer*, Vol. 11, Academic Press, New York, 1975, pp. 199–264.

Natural Convection Heat Transfer Between Eccentric Horizontal Cylinders

J. Prusa
Department of Mechanical and Industrial Engineering, University of Illinois, Urbana, Ill. 61801

L. S. Yao
Department of Mechanical and Aerospace Engineering, Arizona State University, Tempe, Ariz. 85287
Assoc. Mem. ASME

Laminar natural convection flow between vertically eccentric horizontal cylinders is studied numerically. The inner and outer cylinders are heated and cooled, respectively, to maintain constant surface temperatures. A physical model is introduced which accounts for the effects of fluid buoyancy as well as the eccentricity of the outer cylinder. A radial transformation is used to map the eccentric outer boundary into a concentric circle. Both eccentricity and buoyancy have a significant influence on the heat transfer and flow field of a fluid between horizontal cylinders. The effect of buoyancy, which enhances average heat transfer, increases with the Grashof number. Eccentricity influences the flow in two ways. First, by decreasing the distance between the two cylinders over part of their surfaces, it increases the local heat transfer due to conduction. Second, the eccentricity influences the convective mode of heat transfer. Results show that moderate positive values of eccentricity, enhance convective heat transfer. Results for a range of Grashof number are given, for varying eccentricity, for a radius ratio of 2.6 and a Prandtl number of 0.706. Detailed predictions of the temperature and flow fields, and local heat transfer rates are given for representative cases. Also presented is the variation of average heat transfer rate and average shear stress with Grashof number and eccentricity. Comparisons with earlier numerical, experimental and analytic results are made.

Introduction

The prediction of heat transfer due to natural convection (and conduction) between eccentric cylinders is a problem which currently receives considerable attention from researchers in many diverse fields of applications. Examples range from determining the requirements for aircraft cabin insulation [1] to nuclear reactor design [2]. Still other applications are found in computations for thermal storage systems utilizing phase change materials. The problem also arises in energy transmission applications, such as in the use of pressurized gas for insulation in high-voltage electric transmission cables. More recently, it has been acknowledged that in water-cooled underground cables, "snaking" (due to the thermal expansion of the cable) causes the position of the cable to vary with respect to the outer pipe wall. As a result, heat transfer is modified by the eccentricity of the outer pipe relative to the cable [3].

Considerable experimental and theoretical work has been done on the flow and heat transfer due to natural convection between concentric cylinders. It appears that the basic effect of buoyancy on the fluid between concentric cylinders is to set it into a motion whereby two crescent-shaped convective cells, symmetric with respect to the vertical, are developed. Fluid immediately adjacent to the warm inner cylinder rises. Near the top of the inner cylinder, the fluid separates, forming a thermal plume. This plume rises to the top of the outer cylinder at $\psi = 180$ deg, where it is cooled. The fluid immediately adjacent to the outer cylinder, being cooler, falls towards the bottom of the outer cylinder. As the falling fluid nears the bottom at $\psi = 0$ deg, it encounters an adverse pressure gradient which forces it to separate away from the outer cylinder, and move towards the bottom of the inner cylinder. A cyclic motion is produced. This has a marked effect on the heat transfer, since the mode of transfer develops from one of pure conduction to one of mixed convection and conduction. The net result is an increase in overall heat transfer, with maximum local heat transfer rates occurring at the bottom ($\psi = 0$ deg) of the inner cylinder, and top ($\psi = 180$ deg) of the outer cylinder. A measure of the relative strength of the convective cells, and subsequently of average heat transfer, is the Grashof number, Gr. As Gr increases, the convective mode dominates the conductive mode, with large increases in average heat transfer resulting.

While experimental work in the sixties (Liu, Mueller, and Landis [4], among others) and earlier tends to agree with this picture of fluid motion for low to moderate values of Gr, disagreement occurs for high values of Gr, particularly in regard to the transition from laminar to turbulent flow. Powe, Carley, and Bishop [5] attempted to draw together these disparate results. They noted that there appeared to be a transition Grashof number, above which the laminar convective motion abruptly changed its character. The nature of the change varied from oscillations of the convective cells, to the formation of two-dimensional separated vortices at the top of the annular region between the cylinders, to the formation of three-dimensional spiral vortices along the walls of the outer cylinder. At even higher values of Gr, each of these unsteady laminar flows developed into turbulent flow. By designing an experiment to clearly distinguish these three types of unsteady flow, they were able to develop a flow regime map which predicts the particular type of unsteadiness to appear at the transition Gr.

Theoretical results in the form of analytical and numerical solutions are also available in the literature. Mack and Bishop [6] determined the first three terms of a perturbation solution in terms of the Rayleigh number. They found the effect of Prandtl number, Pr, on the flow to be of fourth-order globally. For very low Pr (liquid metals), secondary convective cells were predicted. However, these have only a minor effect on the heat transfer rates, since for liquid metals heat transfer occurs primarily by conduction. The perturbation solution also predicts the formation of two-dimensional separated vortices at the top of the annular region, although it

Contributed by the Heat Transfer Division for publication in the JOURNAL OF HEAT TRANSFER. Manuscript received by the Heat Transfer Division, February 5, 1982. Paper No. 82-HT-43.

does not generally agree quantitatively with the experimentally observed transition Gr. This higher order influence of Pr on global heat transfer rates is also predicted by a perturbation solution for natural convection between concentric spheres [7]. All of the results so far considered use isothermal boundary conditions. Rotem [8] generated a perturbation solution for the concentric case using conjugate boundary conditions. In this model, *a priori* boundary conditions (e.g., isothermal, or constant heat flux) are not used; the values of temperature on the boundary are coupled with the fluid motion.

Abbott [1] computed a numerical solution valid for concentric cylinders with large aspect ratio, L, using a matrix inversion method. Other numerical solutions are those of Kuehn and Goldstein [9] and Powe, Carley, and Carruth [10]. Kuehn and Goldstein's numerical results were verified experimentally, using a Mach-Zehnder interferometer. This allowed visualization of the temperature field.

Further experimental studies have considered the effects of density inversion [11] and constant heat flux boundary conditions [3].

More recently, investigations for the eccentric case have begun. Kuehn and Goldstein [12] developed a correlation for the average equivalent conductivity, k_{eq}, for a large range of Pr, radius ratio, and Rayleigh number. Based on boundary-layer analysis, it approaches the correlation for heat transfer from a free horizontal cylinder as the radius ratio $F \to \infty$ (a remains finite) and the correlation for quasisteady heat transfer to the fluid within a horizontal cylinder as $F \to \infty$ (b remains finite). Kuehn and Goldstein [13] measured the effects of eccentricity on local and average equivalent conductivities. The equivalent conductivity is the ratio of heat transfer from convection and conduction (eccentric case) to that of heat transfer from pure conduction (concentric case). Yao [14] developed a perturbation solution for slightly eccentric cylinders, using a two-parameter expansion in terms of eccentricity and Rayleigh number.

Apparently, the average heat transfer is enhanced for positive values of eccentricity (*center of outer cylinder lies above center of inner cylinder*) and is decreased for moderate negative values of eccentricity. This can be understood when one considers:

(*i*) that the size and strength of the convective cells increase with eccentricity; and

(*ii*) that the relative importance of convection and conduction varies with eccentricity.

The average heat transfer does not decrease monotonically with eccentricity, ϵ, for all values of $\epsilon < 0$. As ϵ decreases towards its minimum value of $-1/L$ (cylinders touch at $\psi = 180$ deg), conduction contributes more and more to the average heat transfer. Ultimately, its contribution will increase enough to completely offset the loss in strength of the convective cells, and the average heat transfer will begin to increase wtih decreasing ϵ. Thus, one observes that a critical eccentricity ϵ_{crit} exists whereby the average heat transfer is at a minimum for given values of F, Pr, and Gr. Heat conduction also becomes important as ϵ increases towards its maximum value of $1/L$ (cylinders touch at $\psi = 0$ deg). For positive eccentricity, we see a small gradual increase in average heat transfer as ϵ increases from zero. Convection dominates the heat transfer, so the result is little different from the concentric case. As ϵ approaches its maximum value, however, conduction plays a more important role. Eventually it dominates the convective mode, and forces the average heat transfer to increase rapidly with ϵ.

The present paper is motivated by interest in demonstrating the effects of eccentricity as well as buoyancy in the flow between two cylinders. The formulation of the problem follows the method proposed by Yao [14] with a slight modification necessary for the numerical procedure. The details of the method are described in the next section. We wish to point out that our formulation is very general and is suitable for various natural convection problems involving two-dimensional bodies of arbitrary shapes. The formulation can handle moving boundaries as well. Extension of the method to include the capability of adopting a variable-mesh system according to local gradients of some predetermined physical quantities are discussed in [15]. The generalized method has the same capability as the "Solution-Adaptive-Grids" (SAG) method originally proposed by Thompson et

Nomenclature

a = inner cylinder radius
b = outer cylinder radius
B = dimensionless gap function, $(R-a)/a$
f = dimensionless stream function, $\bar{f}/\nu$
F = radius ratio, b/a
g = acceleration of gravity
Gr = Grashof number, $\beta g a^3 (T_i - T_o)/\nu^2$
$\bar{k}_{eq}$ = average equivalent conductivity, $\overline{\mathrm{Nu}}/\mathrm{Nu}_{\mathrm{cond}}$
$k_{eq,i}$ = local equivalent conductivity along inner cylinder, $\mathrm{Nu}_i/\mathrm{Nu}_{\mathrm{cond}}$
$k_{eq,o}$ = local equivalent conductivity along outer cylinder, $\mathrm{Nu}_o/\mathrm{Nu}_{\mathrm{cond}}$
L = aspect ratio, $a/(b-a)$
$\underline{M}$ = differential operator
$\overline{\mathrm{Nu}}$ = average Nusselt number (length scale = a)
$\mathrm{Nu}_{\mathrm{cond}}$ = Nusselt number for concentric cylinder, Gr = 0
Nu_i = local Nusselt number along inner cylinder
Nu_o = local Nusselt number along outer cylinder
Pr = Prandtl number, ν/α
P,Q = dummy variables
r = dimensionless radial coordinate
R = outer boundary radius as measured from pole
T = dimensionless temperature, $(\bar{T} - T_o)/(T_i - T_o)$
T_i = inner cylinder temperature
T_o = outer cylinder temperature
u = dimensionless radial velocity, $\bar{u}/(\nu/a)$
v = dimensionless azimuthal velocity, $\bar{v}/(\nu/a)$
x,y = dummy variables
α = thermal diffusivity
β = coefficient of expansion
$\bar{\gamma}_i$ = average dimensionless shear stress along inner cylinder
$\bar{\gamma}_o$ = average dimensionless shear stress along outer cylinder
ϵ = dimensionless eccentricity (see Fig. 1), $\bar{\epsilon}/a$
ϵ_{crit} = critical eccentricity (value of ϵ for which k_{eq} is a minimum)
ν = kinematic viscosity
ϕ = arbitrary dependent variable
ψ = dimensionless angular coordinate
ω = dimensionless vorticity, $\bar{\omega}/(\nu/a^2)$
∇_1^2 = differential operator

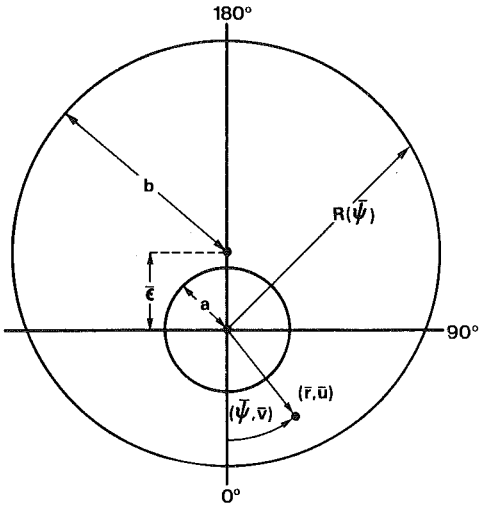

Fig. 1 Physical plane

al. [16], but requires much less effort, computer time, and storage. At the end of the next section, the formulation is applied to the specific problem at hand, natural convection between two eccentric cylinders. Extension of the method to phase change problems around a heated horizontal cylinder whose outer boundary is not known *a priori* will be reported separately [17].

A numerical method is applied to study the flow and temperature fields. The numerical solution covers a wide range of ϵ and Gr. The upper limit of Gr is selected to insure that the natural convection is laminar and to exclude the cases of transitional natural convections. The numerical solution compliments the earlier perturbation solution [14], as well as the experimental data [13].

Two recent publications came to our attention after this study was completed. Projahn, Rieger and Beer [18] applied the SAG method to study this problem. This required that two additional elliptic partial differential equations, besides those describing the physical problem, be solved to generate the body-fitted coordinates. The complication of the numerical procedure used by Projahn et al. is rather obvious. Cho, Chang and Park [19] have solved this problem concurrently using bipolar coordinates. Unfortunately, in bipolar coordinates, the equations are singular for concentric cylinders. Nevertheless, their solutions promote understanding of the phenomenon of natural convection between two eccentric cylinders. Our results are the first to detect the point of minimum heat transfer which exists at the critical eccentricity. Furthermore, the excellent agreement with pre-existing experimental, numerical, and analytical work serves to convincingly verify the radial transformation method.

Analysis

The analysis begins by considering the basic equations for steady laminar flow in polar coordinates. The dimensional variables are vorticity $\bar{\omega}$, streamfunction, $\bar{f}$, and temperature, $\bar{T}$.

The radius of the inner cylinder is denoted by a. The radius of the outer boundary, as measured from the pole (see Fig. 1), is denoted by R. As a result, boundary conditions for the dimensional equations can be written as

$$\bar{T}=T_i,\ \bar{f}=0,\bar{\omega}=-\frac{\partial^2\bar{f}}{\partial\bar{r}^2}\quad\text{at } \bar{r}=a \tag{1a}$$

$$\bar{T}=T_o,\ \bar{f}=0,\bar{\omega}=-\frac{\partial^2\bar{f}}{\partial\bar{r}^2}-\frac{1}{R^2}\frac{\partial^2\bar{f}}{\partial\bar{\psi}^2}\quad\text{at } \bar{r}=R \tag{1b}$$

The vorticity boundary condition at $\bar{r}=R$ differs from the traditional condition which occurs at $\bar{r}=a$. Since R varies with $\bar{\psi}$, the coordinate system is not aligned with the outer boundary. As a result, $\partial^2\bar{f}/\partial\bar{\psi}^2$ is nonzero there and must be retained in the boundary condition.

The essence of the method lies in the use of dimensionless coordinates which transform the irregularly shaped annulus into the interior of the unit circle. The outer boundary $\bar{r}=R$ is transformed into the unit circle $r=1$, while the inner boundary $\bar{r}=\bar{a}$ is transformed into the pole $r=0$ (see [14]). This transformation uses a variable radial length scale, which in dimensionless form is called the gap function $B=(R-a)/a$.

$$r=\frac{\bar{r}-a}{aB},\psi=\bar{\psi}\quad\text{(transformation)} \tag{2}$$

This transformation has been successfully used in calculating the short time solution for phase-change problems around a hot horizontal cylinder [20, 21].

Equations (2) are substituted into the dimensional governing equations. After reorganizing like terms, the following dimensionless governing equations result

$$\frac{1}{r+1/B}\frac{\partial(f,\omega)}{\partial(r,\psi)}=(\nabla_1^2-M)\,\omega-B\cdot\mathrm{Gr}\left[\frac{\cos\psi}{r+1/B}\frac{\partial T}{\partial r}+\left(\sin\psi-\frac{rB'\cos\psi}{rB+1}\right)\frac{\partial T}{\partial\psi}\right] \tag{3a}$$

$$\frac{1}{r+1/B}\frac{\partial(f,T)}{\partial(r,\psi)}=\frac{1}{\mathrm{Pr}}(\nabla_1^2-M\,T) \tag{3b}$$

$$(\nabla_1^2-M)\,f=-B^2\omega \tag{3c}$$

where

$$u=\frac{-1}{B(r+1/B)}\left(\frac{\partial f}{\partial\psi}-\frac{rB'}{B}\frac{\partial f}{\partial r}\right)\text{and } v=\frac{1}{B}\frac{\partial f}{\partial r},$$

$$\nabla_1^2=\frac{\partial^2}{\partial r^2}+\frac{1}{r+1/B}+\frac{1}{(r+1/B)^2}\frac{\partial^2}{\partial\psi^2},$$

$$M=\frac{1}{(r+1/B)^2}\left[\frac{2rB'}{B}\frac{\partial^2}{\partial\psi\partial r}+r\left(\frac{B''}{B}-\frac{2B'^2}{B^2}\right)\frac{\partial}{\partial r}-\frac{r^2B'^2}{B^2}\frac{\partial^2}{\partial r^2}\right],$$

$$\frac{\partial(P,Q)}{\partial(x,y)}=\frac{\partial P}{\partial x}\frac{\partial Q}{\partial y}-\frac{\partial Q}{\partial y}\frac{\partial P}{\partial x}\text{ and }B'=\frac{dB}{d\psi},B''=\frac{d^2B}{d\psi^2}$$

Note the appearance of the differential operator, M. It represents the effects of irregularities in the shape of the outer boundary. M vanishes when $\epsilon=0$. Consequently the governing equations reduce to those for concentric cylinders when $\epsilon=0$ ($B'=B''=0$).

The dimensionless boundary conditions are

$$T=1,\ f=0,\ \omega=-\frac{1}{B^2}\frac{\partial^2 f}{\partial r^2}\text{at } r=0, \tag{4a}$$

$$T=0,\ f=0,\ \omega=-\frac{1}{B^2}\left[1+\frac{B'^2}{(1+B)^2}\right]\frac{\partial^2 f}{\partial r^2}\ \text{ at } r=1 \tag{4b}$$

Note that a $\partial^2 f/\partial\psi^2$ term does not appear in the vorticity boundary condition at $r=1$. This is indeed consistent with the dimensional version, equation (1*b*). What happens is that the nonzero $\partial^2\bar{f}/\partial\bar{\psi}^2$ term in (1*b*) contributes a $\partial^2 f/\partial r^2$ term to equation (4*b*). This is seen to be the second term inside the brackets. Additional $\partial^2 f/\partial\psi^2$ and $\partial^2 f/\partial r\partial\psi$ terms vanish in the transformed plane, because the boundary is aligned with the coordinate system in the transformed plane.

Note that if the outer boundary has a known elementary

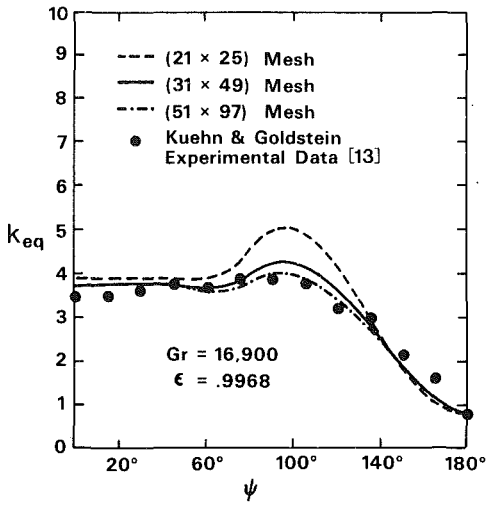

Fig. 2 The effect of mesh refinement on local equivalent conductivity

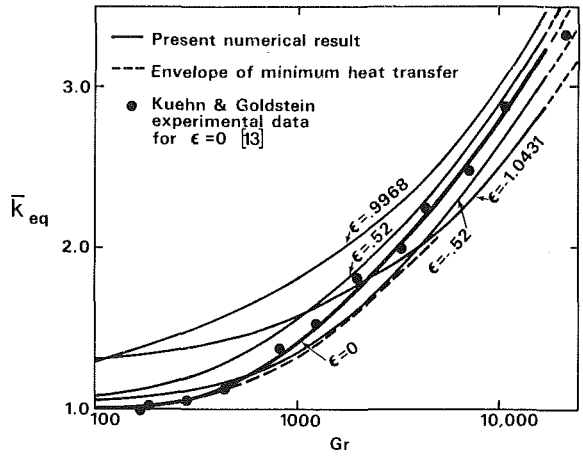

Fig. 3 The effect of Gr on average equivalent conductivity

geometric form, that R may then be determined *a priori*. For the present case, the outer boundary is a cylinder which is vertically offset with respect to the pole. The radius of this cylinder is denoted by b. The distance by which the outer cylinder center is offset from the pole is denoted by the eccentricity $\bar{\epsilon}$. R can then be defined in terms of $\bar{\psi}$, a, b, and $\bar{\epsilon}$ as

$$R(\bar{\psi};\, a,b,\bar{\epsilon}) = (b^2 - \bar{\epsilon}^2 \sin^2\bar{\psi})^{1/2} - \bar{\epsilon}\cos\bar{\psi} \qquad (5a)$$

Because only vertically eccentric cylinders are being considered, the flow and temperature fields are symmetric with respect to the vertical. Consequently

$$\frac{\partial \bar{T}}{\partial \bar{\psi}} = 0,\ \bar{f} = \bar{\omega} = 0 \text{ at } \bar{\psi} = 0,\ 180 \text{ deg} \qquad (5b)$$

If horizontally eccentric cylinders were to be considered, R would have to be appropriately modified, and the boundary conditions along $\bar{\psi} = 0$ and 180 deg would be replaced with appropriate boundary conditions along $\bar{\psi} = 0$ and 360 deg.

Details of the numerical method and computational procedure can be found in [17]. The range of computation covers the values $-1.0431 \le \epsilon \le 0.9968$ and $0 \le \text{Gr} \le 16{,}900$ for $F = 2.6$ and $\text{Pr} = 0.706$. The choices for F, Pr, and extrema of ϵ and Gr match specific experimental results by Kuehn and Goldstein [13], allowing direct quantitative comparisons to be made.

A measure of the accuracy of the method is given by the energy balance between the inner and outer cylinders. This indicated that for a given computational mesh, errors increased with Gr and positive values of ϵ. In the results that follow a (21×25) computational mesh (21 radial and 25 angular nodes) was used for all low Gr computations. For large values of Gr or intermediate Gr with large positive ϵ, a (31×49) mesh was used. Finally, for the cases of large Gr and large positive eccentricity, a (51×97) mesh was employed. The need for increased mesh resolution is clearly seen in Fig. 2.

Results and Discussion

Buoyancy and eccentricity effects may be divided into two categories: global and local effects. The average heat transfer, in the form of an equivalent conductivity and the average shear stresses on the inner and outer cylinders (denoted by $\bar{\gamma}_i$ and $\bar{\gamma}_o$, respectively) are global parameters characteristic of the flow.

Average Equivalent Conductivity. In order to compare our data with earlier results, we present the average heat transfer rate in the form of an equivalent conductivity

$$\bar{k}_{eq} = \overline{\text{Nu}}/\text{Nu}_{\text{cond}}, \text{ and } \text{Nu}_{\text{cond}} = 1/\cosh^{-1}[(1+K^2)/(2K)] \qquad (6)$$

where $\overline{\text{Nu}}$ is the average Nusselt number and Nu_{cond} is the Nusselt number for the concentric annuli case with $\text{Gr} = 0$.

By integrating the local heat flux along the inner cylinder in the physical plane, and then nondimensionalizing, we find

$$\overline{\text{Nu}} = \frac{-1}{\pi}\int_0^{\pi} \frac{1}{B}\frac{\partial T}{\partial r}\bigg|_{r=0} d\psi \qquad (7a)$$

On the other hand, an energy balance requires that the average Nusselt number based upon the outer cylinder have the same value. So one may alternately integrate around the outer cylinder, nondimensionalize, and find

$$\overline{\text{Nu}} = \frac{-1}{\pi}\int_0^{\pi}\left[1 + \frac{B'^2}{(1+B)^2}\right]\frac{(1+B)}{B}\frac{\partial T}{\partial r}\bigg|_{r=1} d\psi \qquad (7b)$$

The variation of average equivalent conductivity with Gr and ϵ is shown in Fig. 3. The curve corresponding to $\epsilon = 0$ represents the concentric cylinder case. Experimental data (using pressurized nitrogen) from Table 1 of [13] for concentric cylinders is plotted for comparison. We observe that the experimental data and our numerical results agree fairly well.

The strength of the convective cells increases with the magnitude of the buoyant force. Thus, the convective heat transfer, and hence the average equivalent conductivity, increase with Gr. From Fig. 3, we observe that this is true for all values of eccentricity considered.

Just as an increase in Gr means an increase in convective heat transfer, an increase in the absolute magnitude of ϵ means an increase in conduction heat transfer. However, positive values of ϵ will enhance the buoyant effect while negative values will decrease it. This is simply a geometrical effect.

For positive values of ϵ, this means that k_{eq} will always be greater than for the concentric case. This is clearly observed for the $\epsilon = 0.52$ and $\epsilon = 0.9968$ curves in Fig. 3. Note also that these curves tend to approach the concentric case, $\epsilon = 0$, as Gr increases. Convection becomes more important than conduction, for a given ϵ, as Gr increases. Ultimately, convection dominates the heat transfer mechanism, and the average heat transfer rate is determined only by the strength of the convective cells.

Negative values of ϵ initially cause a decrease in k_{eq}. This occurs because the geometrical configuration of the cylinders becomes less favorable for convection as ϵ decreases from zero. Heat transfer by conduction, on the other hand, increases as ϵ decreases from zero because the cylinders approach each other along $\psi = 180$ deg. At first, this increase in conduction as ϵ decreases from zero is not enough to counter

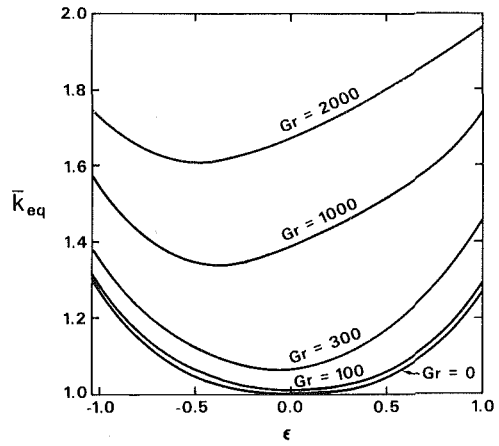

Fig. 4 The effect of ϵ on the average equivalent conductivity

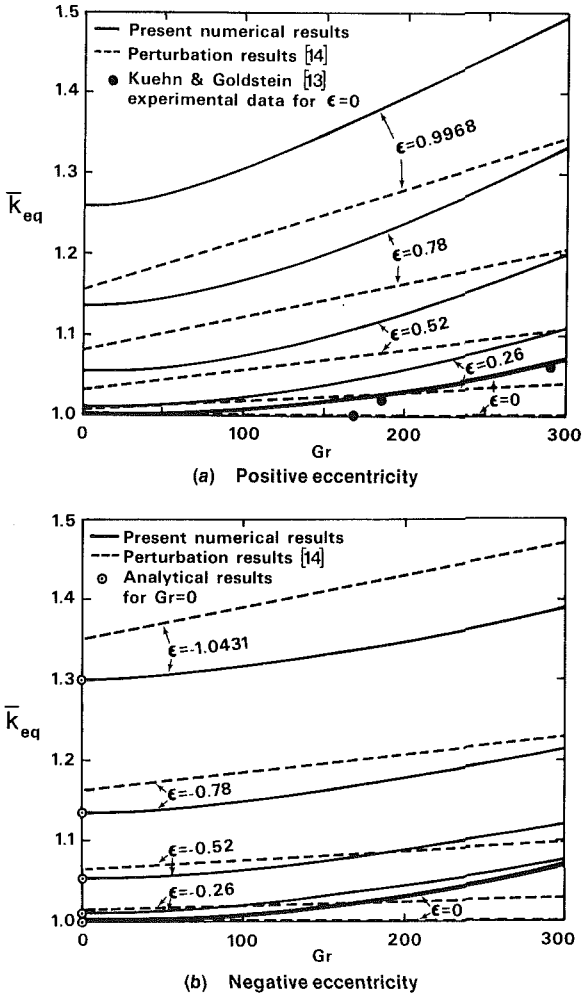

Fig. 5 The variation of average equivalent conductivity with ϵ and small values of Gr

the loss in convective heat transfer. As a result, k_{eq} decreases. As ϵ continues to decrease, however, conduction continues to increase. At a critical value of eccentricity ϵ_{crit}, the increase in conduction is enough to offset the decrease in convection. At this point, k_{eq} has reached a minimum value. The set of ϵ_{crit} for all Gr produces an envelope of minimum heat transfer, which is shown in Fig. 3. For values of $\epsilon < \epsilon_{crit}$, conduction heat transfer increases rapidly enough, with decreasing ϵ, to actually cause k_{eq} to increase. For example, our numerical results indicate that $\epsilon_{crit} = -0.40$ for Gr = 1000. The envelope is terminated at Gr = 5000 since at this point ϵ_{crit} goes beyond the range of the computations.

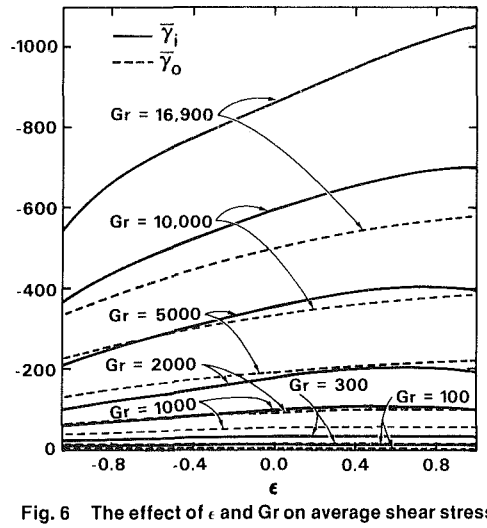

Fig. 6 The effect of ϵ and Gr on average shear stress

The variation of k_{eq} with ϵ for constant values of Gr is explicitly shown in Fig. 4. One can observe directly the minimum value of k_{eq} which occurs at $\epsilon = \epsilon_{crit}$. For very small Gr, heat transfer is dominated by conduction. The lines of constant Gr appear symmetrical about $\epsilon = 0$. As Gr increases, the effects of convection increase k_{eq} overall. As a result, the cylinders must approach each other (i.e., become eccentric) in order for conduction effects to become significant. This is why ϵ_{crit} recedes from $\epsilon = 0$ as Gr increases.

Figure 5 is a small Gr extension of Fig. 3. It compares the present numerical results with the perturbation solution (a two parameter expansion in terms of Rayleigh number and eccentricity) by Yao [14]. Yao's solution correctly predicts the qualitative variation of k_{eq} with Gr and ϵ throughout the region of Fig. 5. The perturbation solution clearly shows the existence of ϵ_{crit}, a value of eccentricity (given Gr and K) for which k_{eq} is minimum. However, good quantitative predictions of k_{eq} (say within 5 percent of the numerical results) appear only for Gr $\tilde{<}$ 200 and $\epsilon \tilde{<} 0.2$.

The analytical values for k_{eq}, as given by

$$k_{eq} = \cosh^{-1}[(1+K^2-\epsilon^2)/(2K)]/\mathrm{Nu}_{cond} \tag{8}$$

for Gr = 0 are also plotted in Fig. 5. Equation (8) is deduced by using a conformal transformation to solve the pure conduction problem between eccentric cylinders. Finally, the experimental results of Kuehn and Goldstein [13] for $\epsilon = 0$ in the region of small Gr are shown.

Average Shear Stress. $\bar{\gamma}_i$ denotes the average shear stress exerted by the fluid on the inner cylinder, and $\bar{\gamma}_o$ denotes the average shear stress exerted on the outer cylinder. By integrating the local shear stress along the inner cylinder in the physical plane, and then nondimensionalizing, it is found that

$$\bar{\gamma}_i = -\frac{1}{\pi}\int_0^{\pi} \frac{1}{B^2}\frac{\partial^2 f}{\partial r^2}\bigg|_{r=0} d\psi \tag{9a}$$

The calculation of the average shear stress, $\bar{\gamma}_o$, along the outer cylinder is found in similar fashion. One now integrates the local shear stress along the outer cylinder in the physical plane, and nondimensionalizes to find

$$\bar{\gamma}_o = \frac{-1}{K\pi}\int_0^{\pi}\left[1+\frac{B'^2}{(1+B)^2}\right]^{-1/2}\left[1+\frac{2B'^2}{(1+B)^2} + \frac{B'^4}{(1+B)^4}\right]\frac{(1+B)}{B^2}\frac{\partial^2 f}{\partial r^2}\bigg|_{r=1}\psi d\psi \tag{9b}$$

The variation of average shear stresses is shown in Fig. 6. Both $\bar{\gamma}_i$ and $\bar{\gamma}_o$ increase with Gr for given values of ϵ. This is to be expected, since the magnitude of the buoyant force and hence the strength of the convective cells increases with Gr. Both average shear stresses also generally increase with ϵ for given values of Gr because the geometric configuration of the two cylinders becomes more favorable for convection as ϵ increases. Curiously, however, this trend does not continue in all cases. For moderate values of Gr, $\bar{\gamma}_i$ actually begins to decrease slightly as ϵ approaches a value of 1. Apparently, the annulus at its bottom (ψ = 0 deg) has become narrow enough to inhibit the motion of fluid there. The higher Gr cases do not show this type of behavior because the buoyant force is strong enough in these cases to still push the fluid through this narrowed region.

Flow Field. The motion of the fluid provides one way to observe the local effects of eccentricity and buoyancy.

In Fig. 7, these effects are vividly portrayed in plots of lines of constant stream function. The increment between the streamlines is held constant for all three cases of eccentricity. Consequently, the shape, magnitude, and location of the convective cells for varying values of ϵ for Gr = 16,900 are easily compared.

Figure 7(*b*) shows the ϵ = 0 case. Here, one observes that the convective cell, shaped like a crescent, lies above the centered ψ = 90 deg position (creeping flow solution).

Figure 7(*a*) depicts the lines of constant stream function for the case of positive ϵ. The convective cell is both larger and stronger than in Fig. 7(*b*). The effect of the more favorable geometry is clearly evident. Note also that the center of the cell has moved closer towards ψ = 180 deg relative to Fig. 7(*b*). This is also characteristic of a stronger convective motion.

The effect of negative ϵ is shown in Fig. 7(*c*). Here the convective cell center has moved towards ψ = 0 deg, relative to Fig. 7(*b*). The cell is also less powerful than in the concentric case. Clearly, this geometric configuration of the two cylinders inhibits convective motion in the fluid.

In each case, the motion of the fluid is clockwise. Stagnation points occur on the outer cylinder at ψ = 180 deg and on the inner cylinder at ψ = 0 deg. Consequently, the local heat transfer rates for the inner and outer cylinders are at their maximum values near these two points. Flow separation occurs on the bottom of the outer cylinder near ψ = 0 deg and on the top of the inner cylinder near ψ = 180 deg. As a result, the local heat transfer rates are at their minimum values at these two points.

Temperature Field. Plots of the temperature field provide another way to observe the local effects of eccentricity and buoyancy. Figure 8 shows the variation of position of isotherms with eccentricity for Gr = 16,900.

The ϵ = 0 case is shown in Fig. 8(*b*). The presence of convection is seen in this figure as a temperature inversion. For example, the isotherm leaving the inner cylinder boundary layer near ψ = 90 deg first rises, then falls, and finally rises again as r increases. This is a viscous effect. As fluid near the bottom of the inner cylinder (ψ = 90 deg) is heated and rises along the inner cylinder, it carries along, in part, cooler adjacent fluid because of viscous drag. On the other hand, as fluid near the top of the outer cylinder (ψ = 180 deg) is cooled and descends along the outer cylinder, it drags along warmer adjacent fluid. The net effect is a region of relatively cooler fluid just outside the warm boundary-layer along the outer cylinder.

The boundary-layer around the inner cylinder separates away from it in the topmost region of the annulus, and forms a thermal plume there. This can be seen as isotherms which move away rapidly from the inner cylinder near ψ = 180 deg.

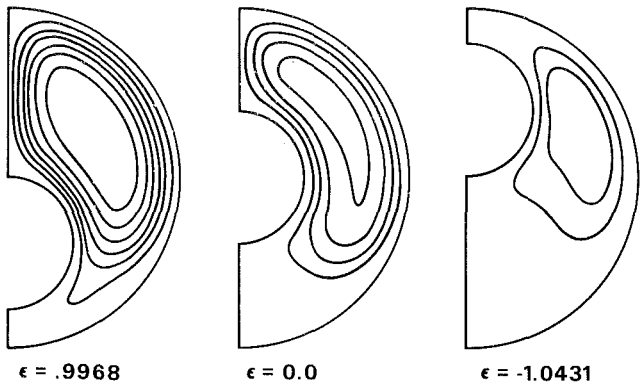

Fig. 7 Lines of constant stream function for Gr = 16,900

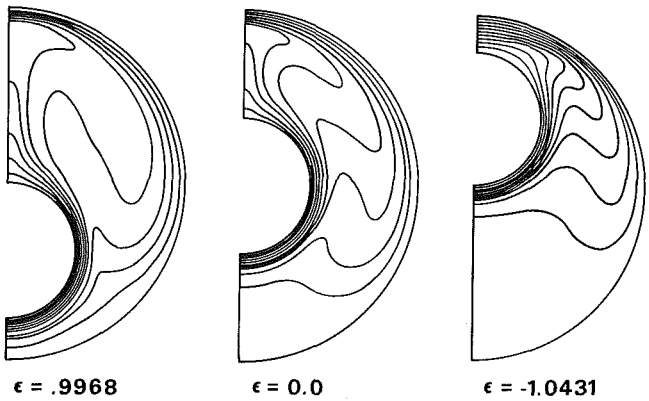

Fig. 8 Lines of constant temperature for Gr = 16,900

In the bottom of the annulus (near ψ = 0 deg), a stagnant region exists. This region of small convection corresponds to the thermally stable fluid between two flat plates, of which the top one is the warmer.

Figure 8(*a*) shows the effects of positive eccentricity. The temperature inversion and thermal plume are more pronounced than in 8(*b*). The two cylinders are very close to each other along ψ = 0 deg. In this region, the effects of convection are diminished, and the shape of the isotherms are largely determined by the conductive mode of heat transfer.

The effect of negative eccentricity is shown in Fig. 8(*c*). The less favorable geometry between the two cylinders inhibits convection. Thus the isotherms show smaller temperature inversions when compared to the concentric case, Fig. 8(*b*). The thermal plume is absent and conduction is the dominant heat transfer mechanism at the top (near ψ = 180 deg). The bottom of the annulus (near ψ = 0 deg) exhibits an enlarged stagnant region of fluid. Although convection is weak in this region, conduction heat transfer is not dominant due to the large separation between the cylinders here. Consequently, the isotherms are not as uniformly spaced as they would be if conduction were the dominant heat transfer mechanism in this region.

Our experiences indicate that the shape of the isotherms provide a sensitive test on the resolving power of the mesh used to obtain the numerical solution. The overall features of the isotherm plot are generally correct even using the coarsest mesh (21×25 nodes). This is in direct contrast to the multicellular results shown in Fig. 14 of Projahn et al. [18]. However, minor departures from the interferograms of Kuehn and Goldstein (Fig. 2 of [13]) occur in the region of the thermal plume for the non-negative eccentricity cases. The isotherms do not separate from the inner cylinder rapidly enough in the numerical computation, using the coarsest

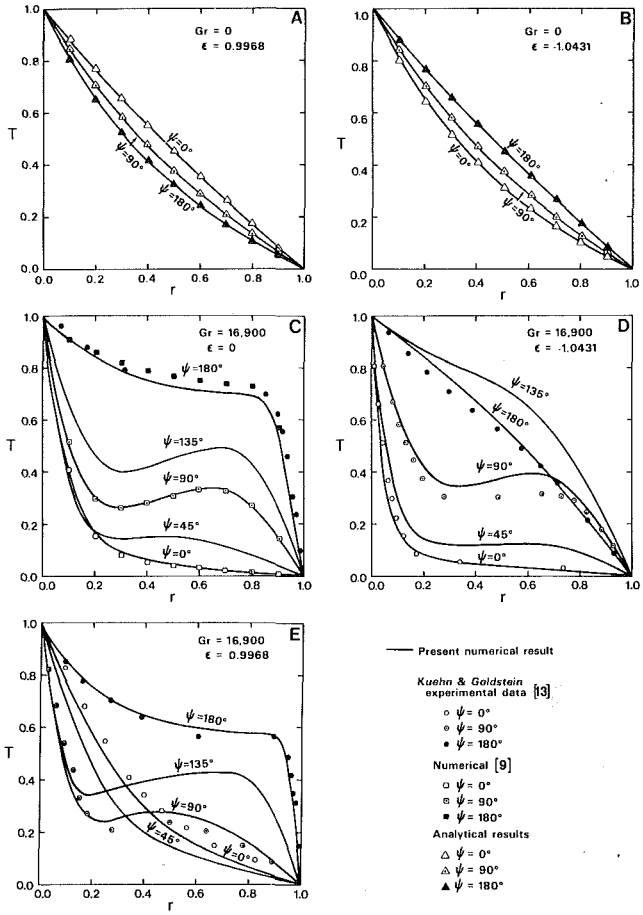

Fig. 9 Variation of temperature with r along lines of constant ψ

mesh. The comparison becomes better as finer meshes are used. But even Figs. 8(*a*) and 8(*b*), which are based on the numerical solution using the finest mesh, fail to precisely match the isotherms in the thermal plume region, as revealed in the interferograms. Apparently, the resolution of this mesh is still insufficient in this region. The thermal plume requires very high resolution in the direction perpendicular to its axis. A high enough resolution may not be practicable with the present generation of computers, in view of the extreme computation time required for the finest mesh (51×96 nodes) used.

Figure 9 shows the temperature along rays of constant ψ, as r varies from 0 to 1. For comparison, the effects of eccentricity alone are shown in Figs. 9(*a*) and 9(*b*). In both figures, the temperature profile for the concentric case lies midway between the $\psi = 0$ deg and $\psi = 180$ deg curves, and slightly above the $\psi = 90$ deg curves. Figure 9(*a*) demonstrates the effect of positive eccentricity. Physically, the two cylinders lie closer together along $\psi = 0$ deg than they would in the concentric case. As a result, along $\psi = 0$ deg, the region locally appears flatter than in the concentric case. The temperature profile along $\psi = 0$ deg approaches the straightline result for a plane wall. Along $\psi = 180$ deg, curvature effects become enhanced, and the profile curves more than the logarithmic solution for the concentric case. The effect of negative eccentricity is precisely the same, except that the "sense" of the solution is changed. In this case, the two cylinders are closer together along $\psi = 180$ deg than they would be in the concentric case. Consequently, Fig. 9(*b*) looks like an inverse of Fig. 9(*a*). Note that both figures compare extremely well with the analytical (conformal transformation) results.

Figure 9(*c*) demonstrates the effect of buoyancy. Steep gradients along the walls have appeared, indicating an increase in heat transfer. The temperature inversion (due to convection [9]) is clearly shown for intermediate values of ψ. Comparison is made with the numerical reuslts of [9]. Agreement is very good except at $\psi = 180$ deg. This may be due to their use of a variable stepsize for ψ near $\psi = 180$ deg, since variable stepsizes increase the formal truncation error [22, 23, 24]. The experimental results of [13] for $\psi = 180$ deg are also included in Fig. 9(*c*) for comparison. Although the experimental data does not unambiguously support one numerical solution over the other, the present results seem to predict the gradient near $r = 0$ more correctly.

Figure 9(*e*) shows the combined effects of positive eccentricity and buoyancy. The resulting more powerful convective cells keep the fluid hot closer to the outer cylinder. This results in increased temperature gradients and heat transfer for larger values of ψ. For smaller values of ψ, convection is suppressed. The temperature inversion at $\psi = 45$ deg disappears, while conduction contributes appreciably to the profile at $\psi = 0$ deg and makes it everywhere hotter than the $\psi = 45$ deg profile.

The influence of negative eccentricity combined with buoyancy is shown in Fig. 9(*d*). The temperature gradients and thus heat transfer now generally appear smaller. Convection is greatly suppressed for high values of ψ. There simply is not much room for fluid to flow here. Note that the temperature profile along $\psi = 180$ deg is closer to a conduction profile than one due to convection. Clearly, conduction has become dominant in this region. The profile at $\psi = 135$ deg is strongly influenced by conduction and exhibits a peculiar bulge because of this. The remaining profiles are all quite similar to the concentric case, except that they are more subdued, for convection is not quite so strong in the negative eccentricity case.

The temperature profiles in Fig. 9(*d*) and 9(*e*) are compared with the experimental data of [13]. Agreement between the experimental results and our numerical results appear satisfactory.

Local Equivalent Conductivity. Figure 10 shows plots of the local heat transfer rates, in the form of equivalent conductivities, along the inner and outer cylinders, denoted here by $k_{eq,i}$ and $k_{eq,o}$. For comparison, the effects of eccentricity alone are shown in Figs. 10(*a*) and 10(*b*). The local equivalent conductivity for the concentric case would be the straightline $k_{eq,i}/k_{eq,o} = 1$. Figure 10(*a*) shows the effect of positive eccentricity. Both $k_{eq,i}$ and $k_{eq,o}$ display maxima at $\psi = 0$ deg, and minima at $\psi = 180$ deg. This is simply because the cylinders are closest together along $\psi = 0$ deg and furthest along $\psi = 180$ deg. Figure 10(*b*) shows the effect of negative eccentricity. It is precisely the same as that of positive eccentricity, except that the "sense" of the solution is changed. Note that both figures compare extremely well with the analytical (conformal transformation) results.

Figure 10(*c*) demonstrates the effect of buoyancy. The data suggest that three regions exist, each with a different influence on the boundary-layer along the walls, and consequently, on the equivalent conductivity. Along the inner cylinder, $k_{eq,i}$ is maximum near the stagnation point ($\psi = 0$ deg), and minimum near the separation point ($\psi = 180$ deg). Note that $k_{eq,i}$ does not immediately start to drop as ψ increases from zero. This is the result of a favorable pressure gradient along the boundary-layer, as it moves away from the region of stagnant fluid (and relatively higher pressure). The favorable pressure gradient keeps the boundary-layer from thickening and, in fact, even causes it to narrow slightly around $\psi = 50$ deg. The result is that the local heat transfer rate, hence $k_{eq,i}$, remains nearly constant in the region from 0 deg $< \psi <$ 50 deg, with a slight maximum at $\psi = 50$ deg. For 50 deg $< \psi <$

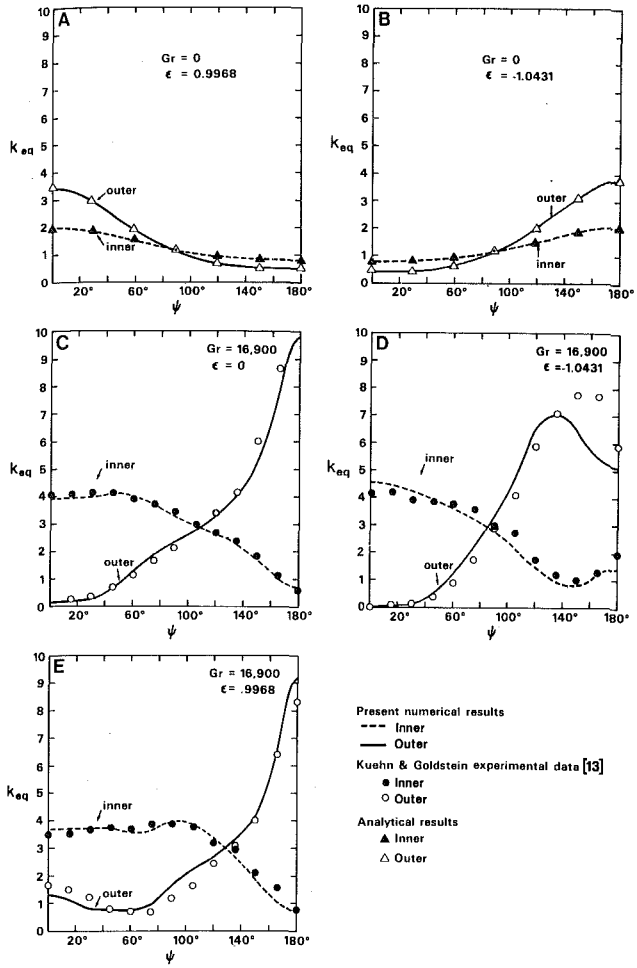

Fig. 10 Variation of local equivalent conductivity with ψ

130 deg, the boundary-layer enters a second region where it encounters a zero pressure gradient. The boundary-layer begins to thicken, and the local heat transfer rate begins to drop. This appears in Fig. 10(*c*) as a more or less uniform drop in $k_{eq,i}$ for 50 deg $< \psi <$ 130 deg. The boundary-layer in this second region behaves like the natural convection boundary-layer in buoyancy-induced flow past a vertical wall. As the boundary-layer along the inner cylinder moves beyond ψ = 130 deg, it enters a third region where it encounters a region of adverse pressure gradient. The boundary-layer thickens more rapidly, and eventually separates from the inner cylinder near ψ = 180 deg, forming a thermal plume. This appears in Fig. 10(*c*) as a more rapid drop in $k_{eq,i}$.

Along the outer cylinder, $k_{eq,o}$ is maximum near the stagnation point (ψ = 180 deg) and minimum near the point of separation (ψ = 0 deg). Note that $k_{eq,o}$ is quite large at ψ = 180 deg. Fluid in the boundary-layer near the stagnation point cools off very rapidly. Because of this, $k_{eq,o}$ does not stay roughly constant even though the boundary-layer is in the region of favorable pressure gradient as ψ decreases from 180 deg. Not enough thermal energy is left in the boundary-layer fluid to allow the high rate of heat transfer to continue very long as ψ decreases from 180 deg. The boundary-layer enters the natural convection region of zero pressure gradient near ψ = 140 deg. This is reflected in Fig. 10(*c*) as a change in slope of the $k_{eq,o}$ curve. Finally, the boundary-layer approaches the region of stagnant fluid and its associated adverse pressure gradient. This appears in Fig. 10(*c*) as a leveling off of $k_{eq,o}$ at ψ = 40 deg.

Figure 10(*e*) shows the effects of positive eccentricity. The local equivalent conductivity along the inner cylinder is quite similar to the concentric case. The difference is that the more powerful convective cell is able to maintain the favorable pressure gradient for a greater distance along the inner cylinder. This results in $k_{eq,i}$ being roughly constant in the interval 0 deg $< \psi <$ 100 deg, with the maximum occurring at ψ = 100 deg.

Again, $k_{eq,o}$ along the outer cylinder is very similar to the concentric case; the difference occurs near ψ = 0 deg. As the boundary-layer encounters the adverse pressure gradient in the region of stagnant fluid, $k_{eq,o}$ can be seen to level off in Fig. 10(*e*) at ψ = 70 deg. The value of $k_{eq,o}$ which the curve levels off at is greater than the corresponding value in the concentric case. This is because convection affects this region more strongly than it does in the concentric case. However, as ψ decreases below 30 deg, $k_{eq,o}$ begins to increase toward a local maximum at ψ = 0 deg. This is inconsistent with a flow separating from the outer cylinder at ψ = 0 deg. It is the result of conduction; since the two cylinders are so close in this region, conduction becomes an important heat transfer mechanism.

The effects of negative eccentricity are shown in Fig. 10(*d*). In this case, $k_{eq,i}$ along the inner cylinder immediately begins to decrease as ψ increases from 0 deg. The convective cells are now too weak to produce a pronounced region of favorable pressure gradient. The boundary-layer begins to thicken immediately, and so the local heat transfer rates decrease as soon as ψ increases from 0 deg. $k_{eq,i}$ continues to decrease as ψ increases until it reaches a minimum at ψ = 150 deg. At this point, $k_{eq,i}$ increases toward a local maximum at ψ = 180 deg. This effect is again due to conduction, which becomes important as the cylinders approach each other near ψ = 180 deg.

The leveling off of $k_{eq,o}$ along the outer cylinder (due to adverse pressure gradient) again occurs in Fig. 10(*d*) for $\psi <$ 30 deg. Note that the value of $k_{eq,o}$ at which the curve levels off is the lowest of Figs. 10(*c*), 10(*d*), 10(*e*). This is a clear indication that convection has the least influence in the region of stagnant fluid (near ψ = 0 deg) when the eccentricity is negative. Near the top of the annular region (ψ = 180 deg), $k_{eq,o}$ exhibits a peculiar behavior. The maximum occurs not at ψ = 180 deg but at ψ = 130 deg. $k_{eq,o}$ is a local minimum at ψ = 180 deg. This can be explained by considering that the region between the cylinders becomes quite narrow as ψ approaches 180 deg. This inhibits the motion of the fluid. The result is a premature maximum in convection heat transfer. As ψ increases beyond this value, the contribution of convection heat transfer to $k_{eq,o}$ decreases. However, conduction heat transfer becomes more important and helps to keep $k_{eq,o}$ from dropping considerably.

The predictions for $k_{eq,i}$ and $k_{eq,o}$ in Figs. 10(*c*), 10(*d*), 10(*e*) are compared with the experimental data of [13]. Agreement between experimental results and the numerical results generally appear satisfactory.

References

1 Abbott, M.R., "A Numerical Method for Solving the Equations of Natural Convection in a Narrow Concentric Cylindrical Annulus With a Horizontal Axis," *Quarterly Journal of Mechanics and Applied Mathematics*, Vol. 17, 1964, pp. 471-481.

2 Peddicord, K.L., Ganapol, B.D., and Henninger, R., "A Consistent Algorithm for the Study of Heat Transfer in Eccentric Annuli," *American Nuclear Society Transactions*, Vol. 22, 1975, pp. 572-573.

3 Van De Sande, E., and Hamer, B.J.G., "Steady and Transient Natural Convection in Enclosures Between Horizontal Circular Cylinders (Constant Heat Flux)," *International Journal of Heat and Mass Transfer*, Vol. 22, 1979, pp. 361-370.

4 Liu, C., Mueller, W.K., and Landis, F., "Natural Convection Heat Transfer in Long Horizontal Cylindrical Annuli," *ASME International Developments in Heat Transfer*, Proceedings of the 1961-62 International Heat Transfer Conference.

5 Powe, R.E., Carley, C.T., and Bishop, E.H., "Free Convective Flow Patterns in Cylindrical Annuli," ASME JOURNAL OF HEAT TRANSFER, Vol. 91, 1969, pp. 310-314.

6 Mack, L.R., and Bishop, E.H., "Natural Convection Between Horizontal Concentric Cylinders for Low Rayleigh Numbers," *Quarterly Journal of Mechanics and Applied Mathematics*, Vol. 21, 1968, pp. 223-241.

7 Mack, L.R., and Hardee, H.C., "Natural Convection Between Concentric Spheres at Low Rayleigh Numbers," *International Journal of Heat and Mass Transfer*, Vol. 11, 1968, pp. 387-396.

8 Rotem, Z., "Conjugate Free Convection from Horizontal Conducting Circular Cylinders," *International Journal of Heat and Mass Transfer*, Vol. 15, 1972, pp. 1679-1693.

9 Kuehn, T.H., and Goldstein, R.J., "An Experimental and Theoretical Study of Natural Convection in the Annulus Between Horizontal Concentric Cylinders," *Journal of Fluid Mechanics*, Vol. 74, 1976, pp. 695-719.

10 Powe, R.E., Carley, C.T., and Carruth, S.L., "A Numerical Solution for Natural Convection in Cylindrical Annuli," ASME JOURNAL OF HEAT TRANSFER, Vol. 93, 1971, pp. 210-220.

11 Seki, N., Fukusako, S., and Nakaoka, N., "Experimental Study of Natural Convection Heat Transfer with Density Inversion of Water Between Two Horizontal Concentric Cylinders," ASME JOURNAL OF HEAT TRANSFER, Vol. 97, 1975, pp. 556-561.

12 Kuehn, T.H., and Goldstein, R.J., "Correlating Equations for Natural Convection Heat Transfer Between Horizontal Circular Cylinders," *International Journal of Heat and Mass Transfer*, Vol. 19, 1976, pp. 1127-1134.

13 Kuehn, T.H., and Goldstein, R.J., "An Experimental Study of Natural Convection Heat Transfer in Concentric and Eccentric Horizontal Cylindrical Annuli," ASME JOURNAL OF HEAT TRANSFER, Vol. 100, 1978, pp. 635-640.

14 Yao, L.S., "Analysis of Heat Transfer in Slightly Eccentric Annuli," ASME JOURNAL OF HEAT TRANSFER, Vol. 102, 1980, pp. 279-284.

15 Yao, L.S., "Direct Determination of Body-Fitted Coordinates for Two-Dimensional Closed Bodies of Arbitrary Shapes," Report No. CR-R-82015, College of Engineering and Applied Science, Arizona State University, 1982.

16 Thompson, J.F., Thomas, F.C., and Mastin, C.W., "Automatic Numerical Generation of Body-Fitted Curvilinear Coordinate System for Field Containing Any Number of Arbitrary Two-Dimensional Bodies," *Journal of Computational Physics*, Vol. 15, 1974, pp. 299-319.

17 Prusa, J., "Numerical Solution of the Two Dimensional Stefan Problem with Natural Convection," Ph.D. dissertation, University of Illinois, 1982 (in preparation).

18 Projahn, U., Rieger, H., and Beer, H., "Numerical Analysis of Laminar Natural Convection Between Concentric and Eccentric Cylinders," *Numerical Heat Transfer*, Vol. 4, 1981, pp. 131-146.

19 Cho, C.H., Chang, K.S., and Park, K.H., "Numerical Simulation of Natural Convection in Concentric and Eccentric Horizontal Cylindrical Annuli," communication with Technical Editor of JOURNAL OF HEAT TRANSFER.

20 Yao, L.S., and Chen, F.F., "Effects of Natural Convection in the Melted Region Around a Heated Horizontal Cylinder," ASME JOURNAL OF HEAT TRANSFER, Vol. 102, 1980, pp. 667-672.

21 Yao, L.S., and Cherney, W., "Transient Phase-Change Around a Horizontal Cylinder," to appear in *International Journal of Heat and Mass Transfer*, ASME Paper No. 80-HT-78, 1980.

22 Roache, P.J., *Computational Fluid Dynamics*, Hermosa Publishers, Albuquerque, New Mexico, 1976, pp. 288-303.

23 Crowder, H.J., and Dalton, C., "Errors in the Use of Nonuniform Mesh Systems," *Journal of Computational Physics*, Vol. 7, 1971, pp. 32-45.

24 Blottner, F.G., and Roache, P.J., "Note on Nonuniform Mesh Systems," *Journal of Computational Physics*, Vol. 8, 1971, pp. 498-499.

Natural Convection Heat Transfer of Water Within a Horizontal Cylindrical Annulus With Density Inversion Effects

P. Vasseur
Assoc. Mem. ASME

L. Robillard

B. Chandra Shekar

Department of Civil Engineering,
Ecole Polytechnique, Université de Montréal,
C.P. 6079, Succursale "A", Montreal,
Canada H3C 3A7

The effect of density inversion on steady natural convection heat transfer of cold water, between two horizontal concentric cylinders of gap width, L, is studied numerically. Water near its freezing point is characterized by a density maximum at 4°C. Numerical solutions are obtained for cylinders with nonlinear Rayleigh numbers RA ranging from 2×10^3 to 7.6×10^4, a radius ratio $1.75 \leq ra \leq 2.6$ and an inversion parameter γ, relating the temperature for maximum density with the cavity wall temperatures, between -2 and 2. The results obtained are presented graphically in the form of streamline and isotherm contour plots. The heat transfer characteristics, velocity profiles, and local and overall Nusselt numbers are studied. The results of the present study were found qualitatively valid when compared with an experimental investigation carried out in the past.

1 Introduction

The steady laminar natural convection in a horizontal concentric cylindrical annulus has been studied in the past both analytically and experimentally [1-3]. In all those investigations, a linear relation between fluid density and its temperature has been assumed, such an assumption being acceptable for most fluids. However, in the case of water near its freezing point a linear relationship is not justified. In fact, the density of water reaches a maximum value at 3.98°C, thereafter decreasing with decreasing temperature. It results from this nonlinearity that convective motion in water behaves in a rather peculiar manner when the temperature domain encompasses the 3.98°C point, for the density of water is maximum at this temperature [4]. Since the pioneering works of Ede [5] and Merk [6], the problem of buoyancy induced flows in cold water has been studied by many investigators, not only because of their intriguing features but also due to the fact that they are a very common occurrence in our environment and in many processes in technology.

The behavior of convective motion of enclosed water, in the region of maximum density, has been studied in the past for several different geometries, boundary conditions, and temperature gradients. For instance Desai and Forbes [7] and Watson [8] have investigated numerically the heat transfer and flow patterns in cold water in a rectangular enclosure with vertical boundaries maintained at different temperatures and insulated horizontal boundaries. Similarly, the effect of density inversion on natural convection heat transfer of a melted water contained in two horizontal concentric cylinders whose surface temperatures are kept isothermal has been studied experimentally by Seki et al. [9]. It was found that, under certain conditions the flow was bicellular, in contrast to the single cell flow obtained for a fluid without maximum density effect, and as a result the heat transfer occurred primarily by conduction.

The transient behaviour of water, contained in a rigid rectangular insulator and cooled from above to near freezing has been considered by Forbes and Cooper [10]. Vasseur and Robillard [11] have studied the transient cooling of water, enclosed in a rectangular cavity with wall temperatures maintained at 0°C. Supercooling of water contained in an enclosure subjected to convective boundary condition has been investigated by Cheng and Takeuchi [12] and Robillard and Vasseur [13] for the case of a circular pipe and a rectangular cavity, respectively. All these studies indicate that the resulting flow motion is greatly influenced by the presence of a maximum density effect, which drives the initial circulation inside the cavity and subsequently reverses it. The resulting heat transfer is thus reduced in comparison to a standard situation without maximum density effect.

The purpose of this investigation is to study theoretically the effect of density inversion on the free convective heat transfer of a mass of water contained in a horizontal cylindrical annulus whose surface temperatures are kept isothermal. The present study is an extension of the experimental work of Seki et al. [9]. Numerical studies of natural convection inside two horizontal concentric cylinders, in the absence of maximum density effect, have been carried out in the past by many investigators; that of Kuehn and Goldstein [3] contains a comprehensive bibliography.

2 Problem Formulation

The problem under consideration is that of two-dimensional laminar convection of a mass of cold water enclosed between two horizontal concentric cylinders. It is assumed that each cylinder is maintained at a different uniform temperature. Using cylindrical coordinates, let the angular coordinate, Φ, be measured from the upward vertical line, $\Phi = 0$. The flow is symmetrical about a vertical plane through the axis of the cylinder. Accordingly, attention is confined to the range $0 \leq \Phi \leq \pi$. All fluid properties, except the water density, are taken to be constant and evaluated at the arithmetic mean temperature of the two cylinders.

The governing equations for the present problem, using the Oberbeck-Boussinesq approximation [14-15] and neglecting viscous dissipation and compressibility effects, are then given in nondimensional form [16] as

$$\frac{\partial \Omega}{\partial \tau} + \frac{1}{R}\left[\frac{\partial (UR\Omega)}{\partial R} + \frac{\partial (\Omega V)}{\partial \Phi}\right] = \mathrm{Pr}\ \nabla^2 \Omega + A\left[\sin\Phi \frac{\partial \bar{\Delta}\rho}{\partial R} + \frac{\cos\Phi}{R} \cdot \frac{\partial \bar{\Delta}\rho}{\partial \Phi}\right] \quad (1)$$

Contributed by the Heat Transfer Division and presented at the 20th ASME/AIChE National Heat Transfer Conference, Milwaukee, Wisconsin, August 2-5, 1981. Manuscript received by the Heat Transfer Division September 15, 1981.

$$\frac{\partial \theta}{\partial \tau} + \frac{1}{R}\left[\frac{\partial URe}{\partial R} + \frac{\partial V\theta}{\partial \Phi}\right] = \nabla^2 \theta \quad (2)$$

$$\Omega = -\nabla^2 \Psi \quad (3)$$

$$U = \frac{1}{R}\frac{\partial \Psi}{\partial \Phi} \qquad V = -\frac{\partial \Psi}{\partial R} \quad (4)$$

The initial and boundary conditions are

$$U = V = \Psi = \Omega = 0; \quad \theta = 0 \text{ at } \tau = 0$$

$$U = V = \Psi = 0 \quad ; \quad \theta = 0 \quad 0 < \Phi < \pi, R = 1/(ra-1)$$

$$U = V = \Psi = 0 \quad ; \quad \theta = 1 \quad 0 < \Phi < \pi, R = ra/(ra-1)$$

$$\frac{\partial U}{\partial \Phi} = V = \Psi = \Omega = 0; \quad \frac{\partial \theta}{\partial \Phi} = 0 \text{ at } \Phi = 0, \pi \text{ (symmetry lines)} \quad (5)$$

It is observed in the boundary conditions that use has been made of the symmetry of the problem with respect to a vertical plane passing through the axis of the cylinder. In fact, even if secondary flows exist they must appear as counterrotating eddies symmetrically located.

When considering the temperature range $0 \sim 20°C$ [17], the density-temperature relationship of water can be approximated by the following equation with an error of less than one unit at the last digit of the tabulated data of Landolt Börnstein [18]:

$$\frac{\rho_o}{\rho} = 1 + \beta_1 T + \beta_2 T^2 + \beta_3 T^3 + \beta_4 T^4 \quad (6)$$

where

ρ_o = 0.9998396 ($g\ cm^{-3}$);

β_1 = $-0.678964520 \times 10^{-4}$ ($1/°C$);
β_2 = $0.907294338 \times 10^{-5}$ ($1/°C^2$);
β_3 = $-0.964568125 \times 10^{-7}$ ($1/°C^3$);
β_4 = $0.873702983 \times 10^{-9}$ ($1/°C^4$);

An examination of the governing equations and boundary conditions, equations (1-6), shows that the present problem is governed by four independent parameters, namely A, ra, T_i and T_o (besides the Prandtl number, Pr, which will be considered as a characteristic constant of the fluid). However, Hung et al. [19] have demonstrated that, in the case of water near its maximum density, it is appropriate to define a nonlinear Rayleigh number RA as

$$RA = \frac{A}{(ra-1)^3}\frac{\beta_2}{\mathrm{Pr}}\Delta T^2 \quad (7)$$

where the value of β_2 is given in equation (6) together with a second parameter

$$\gamma = 2\frac{(T_m - T_o)}{\Delta T} \quad (8)$$

This parameter γ, hereafter called the inversion parameter, relates the temperature for maximum density, $T_m = 4°C$ to the wall temperatures T_i and T_o. A similar parameter γ has been used in the past by Carey et al. [20] to study the effects of inversion on the boundary layer of cold pure and saline water at a vertical isothermal surface. It must be mentioned at this stage that the parameters RA and γ were introduced by Hung et al. [19] on the basis that the equation of state, for water near 4°C, can be approximated by a parabola, resulting in a complete description of the problem in terms of three nondimensional parameters, RA, ra, and γ. In the present study a more precise fourth-order polynominal equation of state, equation (6), is used in the numerical calculations. However, as demonstrated by Robillard and Vasseur [21], it is nevertheless possible, when considering water in the temperature

Nomenclature

A = size parameter, gL^3/α^2
L = gap width, $(r_o - r_i)$
Nu = local Nusselt number, defined as equations (9) and (10)
$\bar{\mathrm{Nu}}$ = overall Nusselt number, defined as equation (11)
Pr = Prandtl number, ν/α
q = local radial heat flow rate per unit area
Q = overall heat flow rate per unit length
r = radial coordinate
ra = radius ratio, r_o/r_i
ΔR_L = dimensionless radial spacing between gridlines
R = dimensionless radial coordinate r/L
R_L = dimensionless radius, $(r - r_i)/(r_o - r_i)$
RA_L = Rayleigh number for an ordinary fluid, $\frac{g\beta\Delta T L^3}{\nu\alpha}$
RA = nonlinear Rayleigh number for cold water, $\frac{gr_i^3}{\alpha\nu}\beta_2\Delta T^2$
T = water temperature
T_m = temperature for maximum density, $T_m = 3.98°C$
ΔT = temperature difference, $T_o - T_i$
T_o = temperature of outer cylinder
T_i = temperature of inner cylinder
t = time
u,v = radial and angular velocities
U,V = dimensionless radial and angular velocities, uL/α, vL/α

Greek Symbols

Φ = angular coordinate
$\Delta\Phi$ = angular spacing between gridlines
ω = vorticity
Ω = dimensionless vorticity, $\omega L^2/\alpha$
ψ = stream function
Ψ = dimensionless stream function, ψ/α
α = thermal diffusivity
β = thermal coefficient of volumetric expansion
γ = inversion parameter, $2(T_m - T_o)/\Delta T$
ν = kinematic viscosity
μ = dynamic viscosity
$\beta_1 \ldots \beta_4$ = constants, defined in equation (6)
ρ = water density
$\Delta\rho$ = $(\bar{\rho} - \rho(\theta))/\bar{\rho}$
θ = dimensionless temperature, $(T - T_i)/\Delta T$
τ = dimensionless time, $\alpha t/L^2$

Superscripts

$-$ = refers to average value

Subscripts

i = refers to inside cylinder
o = refers to outside cylinder
max = refers to maximum value
min = refers to minimum value

range between approximately 0 ~ 10°C, to correlate the results predicted by equation (6) in terms of the parameters R_A and γ without noticeable discrepancies. In fact this temperature range covers essentially all the features associated with the effects of the inversion of density and it was thus found advantageous to follow this approach in the present problem to analyse the results concerning the effects of density inversion.

It may be deduced from equation (8) that when $-2<\gamma<0$, T_m lies in the range of the fluid temperature and the maximum density occurs somewhere between the two walls within the confined fluid. The special value $\gamma = -1$ corresponds to the case where T_m is half way between T_o and T_i, the fluid density on the inner and outer cylinders being the same. This particular case was named "complete inversion" by Hung et al. [19]. When $\gamma \leq -2$ or $\gamma \geq 0$, no inversion is observed. Finally the flow behaviour tends to that of a common fluid with a linear equation of state, when $|\gamma| >> 1$.

The local radial heat-flow per unit area q_i and q_o, at the inner and outer cylinders respectively are related to the local Nusselt numbers Nu_i and Nu_o as $q_i = k\ (T_i - T_o)\ \mathrm{Nu}_i/(r_i\ 1n\ ra)$ and $q_o = k\ (T_i - T_o)\ \mathrm{Nu}_o/(r_o\ 1n\ ra)$. Similarly, one can express the overall heat flow rate, Q, from inner to outer cylinder by means of the overall Nusselt number $\bar{\mathrm{Nu}}$ as $Q = 2\pi k\ (T_i - T_o)\ \bar{\mathrm{Nu}}/1n\ ra$. Furthermore, by the use of Fourier's law of conduction, we have that

$$\mathrm{Nu}_i = -1n\ ra \left[R\frac{\partial\theta}{\partial R}\right]_{R=1/(ra-1)} \tag{9}$$

$$\mathrm{Nu}_o = -1n\ ra \left[R\frac{\partial\theta}{\partial R}\right]_{R=ra/(ra-1)} \tag{10}$$

$$\bar{\mathrm{Nu}} = -\frac{1n\ ra}{\pi}\int_o^{\pi}\left[R\frac{\partial\theta}{\partial R}\right]_{R=1/(ra-1)} d\Phi$$

$$= -\frac{1n\ ra}{\pi}\int_o^{\pi}\left[R\frac{\partial\theta}{\partial R}\right]_{R=ra/(ra-1)} d\Phi \tag{11}$$

An energy balance for the inner and outer cylinders shows that the value of the overall Nusselt number, $\bar{\mathrm{Nu}}$, is the same on those two boundaries. In practice, numerical values obtained for each cylinder using Simpson's rule differed by about 1 percent, and the assigned value of $\bar{\mathrm{Nu}}$ was chosen as the arithmetic means of the two computed results.

3 Numerical Solution of the Governing Equations

Numerical methods such as standard explicit, alternate direction implicit, Dufort-Frankel and other methods may be applied to solve the coupled vorticity and energy equations (1) and (2) which are quasilinear, second-order, partial differential equations spatially elliptic but parabolic in time.

In this study a two-dimensional alternating direction (ADI) procedure is employed and the computational method involved differs slightly from that used by Mallison and de Vahl Davis [22]. The first and second spatial derivatives were approximated by central differences and the time derivatives by a first-order forward difference. The finite difference transformation of the equations were written in conservative form for the advective terms in order to preserve the transportive property [23]. The ADI technique has the advantage over explicit methods that it is numerically more stable and hence allows the use of a larger time step, $\Delta\tau$. However, it has the disadvantage that each iteration requires more computations than does an iteration with the explicit techniques.

The elliptic equation for the stream function, equation (3), was solved by the method of successive over-relaxation (SOR) to have new stream function field which is then used to obtain the velocities from equation (4) and the wall vorticity (which requires the velocity boundary conditions). The major disadvantages of the SOR method is the task of choosing the optimum relaxation coefficient for a given situation. For the present problem it was found that a relaxation factor of 1.8 was an optimum value and the iterative procedure was repeated until the following condition was satisfied

$$\mathrm{Max}\left|\frac{\Psi_{i,i}^{n+1} - \Psi_{i,i}^{n}}{\Psi_{i,i}^{n+1}}\right| \leq 0.5\times 10^{-3}$$

where the superscripts, n, and $n+1$, indicate the values of the nth and $n+1$th interations, respectively. A useful method for checking the convergence of the steady-state solution was to compare the average Nusselt number for the inner and outer cylinder.

Several different mesh sizes have been used, the choice depending largely on the size of the cavity. The mesh size in the r-direction ranged from $\Delta R_L = 1/18$ to $1/30$. In the Φ direction a mesh size of $\Delta\Phi = \pi/18$ to $\pi/30$ was chosen. Typical values of the time step were 0.0001 and 0.0005. The total time steps ranged from 1600 to 2500 and the corresponding computing time was from 530 to 680 s. on the IBM 360/70 computer.

To expedite plotting of the results, an auxiliary computer program was developed to locate points laying on specified isotherms and streamlines by linear interpolation of the computed values at the grid points. All graphs were performed using CALCOMP 563 automatic plotter.

In the following section typical results will be presented in terms of the governing dimensionless parameters, namely RA, γ, ra, and Pr. It must be mentioned at this stage that the value of Pr was evaluated at the mean fluid temperature.

4 Results and Discussion

In order to verify the consistency of the present numerical study, the first cases considered were those corresponding to existing results for fluids with linear temperature-density relationship. Results for some of the cases studied by Crawford and Lemlich [24] and Kuehn and Goldstein [3] for various radius ratios, ra, Prandtl numbers, Pr, and Rayleigh numbers RA_L, were obtained. The current analysis predicted identical results for the flow patterns, temperature profiles, and overall Nusselt numbers, $\bar{\mathrm{Nu}}$. For instance, for $RA_L = 8.925 \times 10^3$, Pr = 0.714 and $ra = 2$, an overall Nusselt number of 1.749 was obtained in the present investigation as compared with the values of 1.765 and 1.792 reported respectively by the two previous studies. An analytical result with $RA_L = 1.842 \times 10^3$, Pr = 0.7 and ra = 1.85 presented by Mack and Bishop [2] was also verified. Again very close agreement was found between their results and those of the present analysis. However, the values of local Nusselt numbers were not in good agreement near $\Phi = 0$ and π positions, where deviations of about 12 percent occurred. This point has also been observed by Powe et al. [1] and may be due to the slow convergence of the power series used by Mack and Bishop. Having thus gained confidence in the present numerical analysis, attempts were made to predict the effects of density inversion on steady natural convection heat transfer of water between two horizontal concentric cylinders. The results obtained will be now discussed in the following sections.

Flow and Isotherm Patterns. Figures 1 to 3 show typical results obtained for annuli with Rayleigh number $RA = 6350$, radius ratio $ra = 2.6$ and for different values of the inversion parameter γ between 0 and -1.33. As mentioned earlier, the problem under consideration is symmetrical with respect to a vertical axis, and it was found advantageous to reproduce

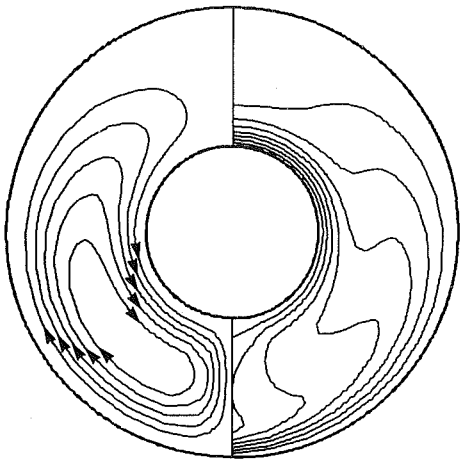

Fig. 1 Isotherms and streamlines for $RA = 6350$, $ra = 2.6$, and $\gamma = 0$; $\psi_{max} = 3.50$, $\Delta\psi = 0.583$

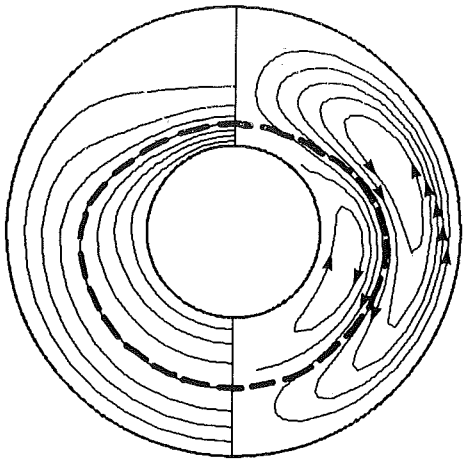

Fig. 2 Isotherms and streamlines for $RA = 6350$, $ra = 2.6$, and $\gamma = -1$; $\psi_{max} = 1.80$, $\psi_{min} = -.0012$ and $\Delta\psi = 0.225$

computer results on a single graph with the flow pattern on the right half of the cavity and isotherms on the left half.

Figure 1 shows the flow and isotherm patterns obtained for $\gamma = 0$, i.e., $T_o = 4°C$. The fluid near the outer cylinder being at 4°C is heavier and is moving downward while the relatively lighter fluid near the inner cylinder is moving upward. As a consequence of the symmetry and the continuity, the resulting fluid motion inside the whole cavity consists of two counterrotating vortices. Figure 1 shows only the right clockwise vortex. The distortion of isotherms in Fig. 1 reveals a strong convective motion inside the cavity. It is also noticed that the maximum heat transfer, indicated by closely spaced isotherms, is located at the top of the cavity for the outer cylinder and at the bottom for the inner one. Since in the present case the outer wall temperature corresponds exactly to the maximum water density, no inversion effects are present. In fact, the flow pattern depicted in Fig. 1 is similar in form to the two usual thermoconvective cells, symmetrical with respect to the vertical axis, that have been described extensively in literature [3, 24, 15] for the case of an ordinary fluid.

Figure 2 shows the flow pattern obtained for $\gamma = -1.0$, and it is seen that the flow field is now characterized by the presence of two counterrotating circulations inside the half cavity as indicated by the dividing streamline. This particular streamline corresponds to the value $\Psi = 0$ of the boundary and is left unconnected with it by the auxiliary computer program used to plot the graphs. The present flow pattern is a direct consequence of the maximum density of water at 4°C. The heavy dashed line represents the 4°C isotherm and thus defines the region of maximum density. The fluid in the neighbourhood of this line is heavier and, as a result, moves downward. On the boundaries, the fluid is lighter and moves upwards. It is also noticed that the eddy near the outer cylinder is larger than the one near the inner cylinder. Further, it is seen from the isotherm field that the convective motion inside the cavity is now considerably reduced as compared with the case $\gamma = 0$. For $\gamma = -2$, Fig. 3 shows that the inner cell has completely disappeared and the circulation is now counterclockwise. Furthermore, the local heat transfer in the present case is seen to be maximum at the bottom of the outer cylinder and at the top of the inner one. This situation is completely opposite to the case described in Fig. 1.

An experimental study on natural convection heat transfer with density inversion of water between two horizontal concentric cylinders has been conducted in the past by Seki et al. [9]. The experimental model consisted of concentric cylinders with radius ratio ranging from 1.18 to 6.39. Temperature of the inner cylinder was maintained at 0°C,

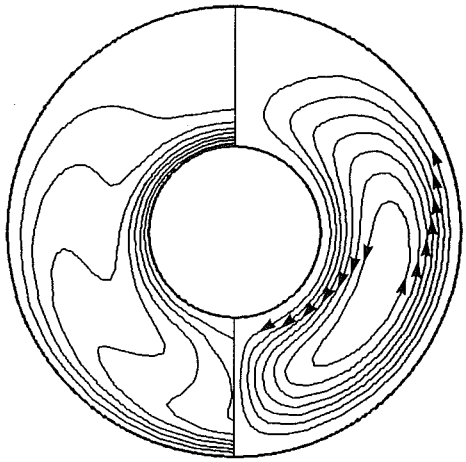

Fig. 3 Isotherms and streamlines for $RA = 6350$, $ra = 2.6$, and $\gamma = -2.0$; $\psi_{max} = 1.90$, $\Delta\psi = 0.238$

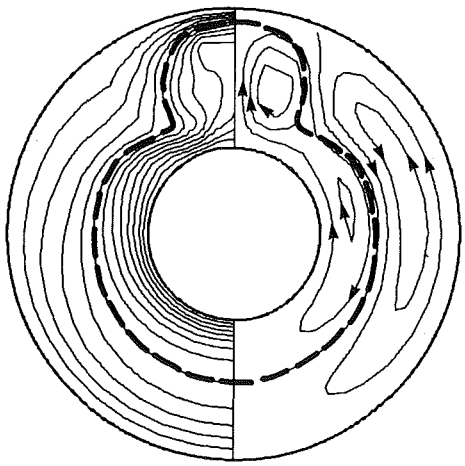

Fig. 4 Isotherms and streamlines for $RA = 17250$, $ra = 2.6$, and $\gamma = -0.77$; $\psi_{max} = 6.70$, $\psi_{min} = -0.75$ and $\Delta\psi = 1.242$

while temperature of the outer cylinder was varied from 1–15°C. Photographs of the flow patterns and quantitative description of the temperature profiles, local and average Nusselt number were presented. The present numerical method could not simulate adequately the high convective motion involved in most of Seki's experimental results. Nevertheless, a similar trend was observed in many aspects. For instance, the sequence of events appearing in Figs. 1 to 3, i.e., formation of unicellular clockwise and counterclockwise

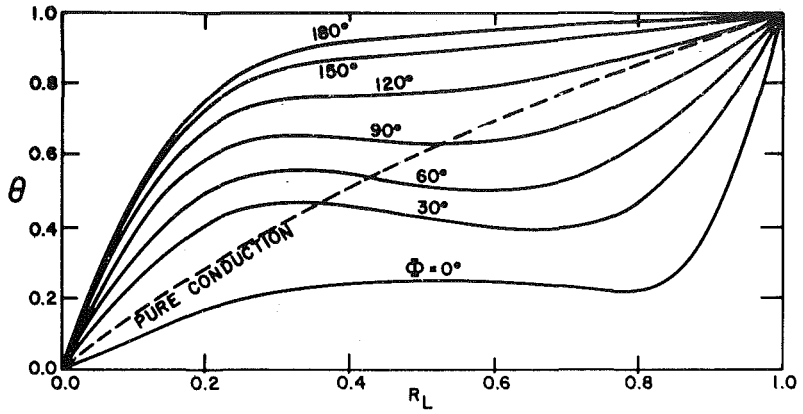

Fig. 5(*a*) Temperature profile for $RA = 6350$, $ra = 2.6$, and $\gamma = 0$

vortices or bicellular flow depending on the parameter γ, were comparable qualitatively. It is worthwhile to mention that it has been possible to simulate numerically one of the experimental cases presented by Seki ($RA = 7.6 \times 10^5$, $ra = 1.22$, and $\gamma = 0$), this latter involving a relatively low convection. A similar flow pattern, not presented here, was obtained numerically. However, Seki et al. have observed the formation of a very small counterclockwise eddy at the top of their cavity. This secondary eddy, that was attributed to the effects of the gap width and cylinder curvature, could not be reproduced by the numerical solution of the present study. It is believed that an initial disturbance should be introduced in the flow field in order to generate this secondary eddy by a numerical method [25].

Another interesting result of the present study is the tendency for the clockwise circulation pattern to form two cells. This phenomenon, illustrated in Fig. 4, for the situation RA = 17250, $ra = 2.6$, and $\gamma = 0.77$, was observed to occur only for a limited range of γ between approximately -0.75 and -0.90. The distortion of the isotherm pattern in the upper part of the cavity is a result of the intense convection generated by the clockwise vortex located in this region. A similar vortex formation has been reported in the past by Saitoh and Hirose [26] in their study of the convection flow surrounding a horizontal ice cylinder. Their experimental observations have revealed the existence of an additional vortex pair over the ice cylinder. Such a phenomenon was observed only for a water temperature range between 5.5 and 6.5°C.

Temperature Distributions and Local Nusselt Numbers. Figure 5(*a*) shows θ versus R_L for the case with $\gamma = 0$. As already mentioned, this case corresponds to the presence of a single clockwise circulation in the right half cavity. In the thermal boundary layer adjacent to the outer cylinder it is seen that the temperature gradient increases considerably as the angular position decreases from $\Phi = 180$ deg towards $\Phi = 0$ deg. However, the trend is opposite near the inner cylinder. A temperature reversal in the central portion of the gap, for Φ ranging from 0 to 90 deg, may also be observed. This is probably due to higher heat transport by angular convection flow rather than radial one. The corresponding local Nusselt number for this case is shown in Fig. 5(*b*). In agreement with the aforementioned behaviour of the temperature profile, the Nusselt number reaches the minimum value at 180 deg on the outer cylinder and 0 deg on the inner one. Naturally the results obtained for $\gamma = -1.33$ were found to have opposite tendency.

The results obtained for $\gamma = -0.77$ have revealed that, with the exception of the angular position $\Phi = 0$ deg, the temperature profiles inside the cavity followed approximately the trend given by the pure conduction curve. This is due to

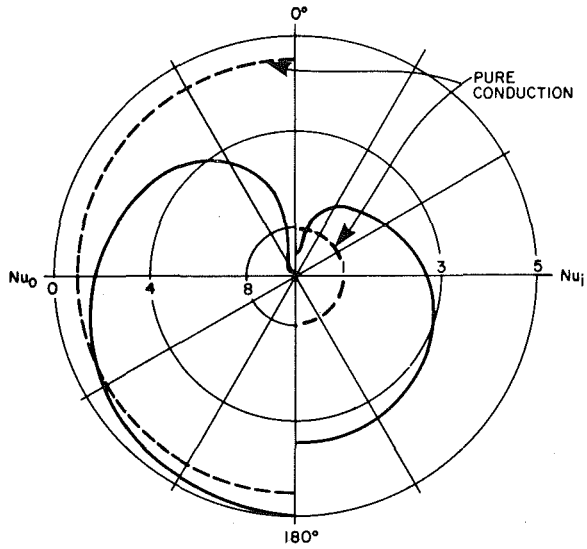

Fig. 5(*b*) Distribution of local Nusselt number for $RA = 6350$, $ra = 2.6$, and $\gamma = 0$

the fact that inside the cavity two eddies of almost equal size coexist. It was also found that at the top of the cavity the Nusselt number is maximum on the outer cylinder and minimum on the inner one. Due to the influence of the flow circulation in the upper region of the annulus on the inner cylinder, the Nusselt number was observed to pass through a peak value at $\Phi = 20$ deg and a minimum, close to the pure conduction value, at $\Phi = 50$ deg, thereafter increasing with increasing angular position.

Overall Nusselt Number. Figure 6(*a*) shows the relationship between the overall Nusselt number, $\bar{Nu}$, and the inversion parameter, γ, for a cavity with a radius ratio $ra = 2.6$ for various values of the nonlinear Rayleigh number, RA, ranging from 2×10^3 to 7×10^4. It is observed from Fig. 6(*a*) that, for a given Rayleigh number, each curve passes through a minimum at about $\gamma \simeq -0.75$, this value corresponding to a situation for which two vortices of approximately equal strength exist in the cavity. For such a situation the fluid velocities are small and the convective heat transfer mechanism attains its minimum efficiency. This phenomenon results essentially from the inversion of the fluid density at 4°C and is one of its most significant effects on the mechanism of heat transfer by convection within an enclosure.

The influence of the radius ratio, *ra*, on the average Nusselt number, $\bar{Nu}$, is illustrated in Fig. 6(*b*) for the case $RA = 10^4$. It is seen that, for a given Rayleigh number, an increase of the

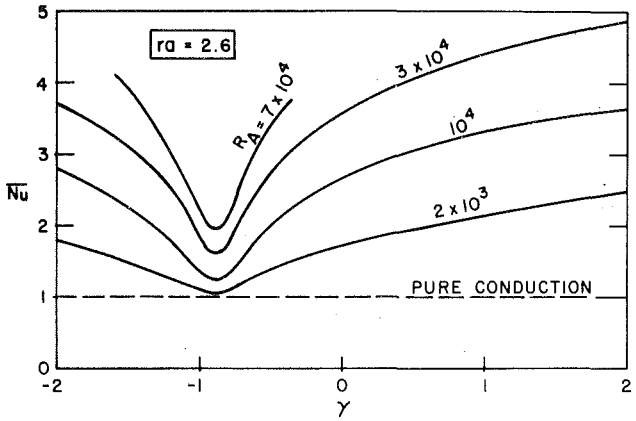

Fig. 6(*a*) Overall Nusselt number $\bar{Nu}$ as a function of γ for various values of *RA*

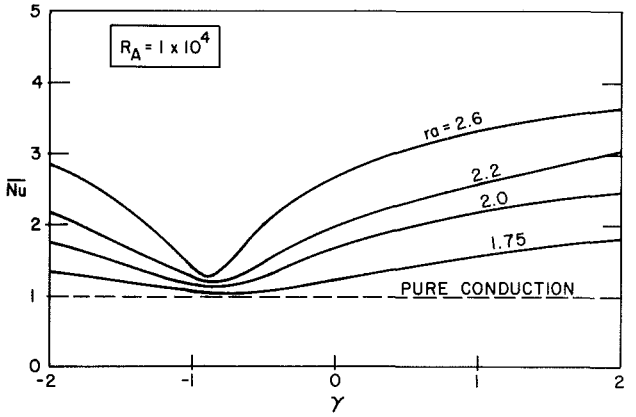

Fig. 6(*b*) Overall Nusselt number $\bar{Nu}$ as a function of γ for various values of *ra*

radius ratio, *ra*, corresponds to an increase of the convection inside the cavity and consequently an increase of $\bar{Nu}$. Furthermore, the minimum Nusselt number, $\bar{Nu}$, occurs at values of γ closer to -1 as the radius ratio, *ra*, decreases. A minimum overall Nusselt number has also been observed in the past for the case of natural convection heat transfer under the influence of density inversion in a rectangular cavity. Analytical studies reported by Watson [8] and Robillard and Vasseur [27] have shown that, for this type of geometrical configuration a minimum value of the average Nusselt number occurs at $\gamma = -1$. The value of γ at which the minimum $\bar{Nu}$ occurs is thus less for the case of cylindrical annuli than for rectangular cavities. The fact that Nu minimum does not correspond to $\gamma = -1$ in the present case may be attributed to the difference in surface area between the inner and outer cylinder.

Correlation between overall Nusselt number $\bar{Nu}$ as a function of ΔT, the temperature difference between the two cylinders, has been established experimentally [9] and numerically [28] in the past by Seki et al. Although, their experimental results were correlated in terms of the parameter ΔT, they were limited to cases for which $T_i = 0°C$, i.e., $\Delta T = T_o$. Seki et al. have observed that their numerical study, although in good agreement qualitatively with their experimental data, underpredicted these latter by about 10 percent. They attributed those discrepancies to the inadequacy of the boundary conditions used in their analytical model. Comparisons was also done between the present numerical approach and one of Seki's experimental results involving a relatively low convection. Accurate values of $\bar{Nu}$ were difficult to obtain from Seki's article, the scale of the graph being rather small. Nevertheless, the analytical results of the present study shows also an underprediction of about 10–15 percent.

5 Conclusions

The natural convection of a mass of water contained between two horizontal concentric cylinders has been investigated numerically at temperatures in the neighbourhood of the maximum density. The problem was shown to depend on three dimensionless parameters, ra, RA, and γ, representing the radius ratio, the nonlinear Rayleigh number, and the inversion parameter, respectively. The results obtained in the present study may be summarized as follows:

1 The density inversion has an important effect on natural convection heat transfer in the cavity. This is particularly true in cases where two counterrotating eddies of approximately equal size coexist in the gap. For such situations the heat transfer rate is considerably reduced.

2 The presence of a secondary vortex pair, at the top of the inner cylinder, has been found numerically to appear for a very limited range of the inversion parameter, γ. A similar phenomenon has already been observed by Saitoh and Hirose in the case of natural convection around a horizontal ice cylinder.

3 A comparison with the existing numerical and experimental results shows that the present theory predicts all the essential features associated with the inversion of density.

Acknowledgment

This work was supported by the National Research Council of Canada through grants NRC A-9201 and NRC A-4197. The authors wish to gratefully thank Ecole Polytechnique for providing necessary time on IBM 360/70.

References

1 Powe, R. E., Carley, C. T., and Bishop, E. H., "Free Convective Flow Patterns in Cylindrical Annuli," ASME JOURNAL OF HEAT TRANSFER, Vol. 91, 1969, pp. 210–220.

2 Mack, L. R., and Bishop, E. H., "Natural Convection Between Horizontal Concentric Cylinders for Low Rayleigh Numbers," *Quarterly Journal of Mechanics and Applied Mathematics*, Vol. 21, 1968, pp. 223–241.

3 Kuehn, T. H., and Goldstein, R. J., "Experimental and Theoretical Study on Natural Convection in the Annulus Between Horizontal Concentric Cylinders," *Journal of Fluid Mechanics*, Vol. 74, 1976, pp. 695–719.

4 Gebhart, B., and Mollendorf, J. C., "Bouyancy-Induced Flows in Water Under Conditions in Which Density Extrema May Arise," *Journal of Fluid Mechanics*, Vol. 89, 1978, pp. 673–707.

5 Ede, A. J., "Heat Transfer by Natural Convection in Refrigerated Liquid," *Proceedings of the 8th International Congress of Refrigeration*, London, 1951, p. 260.

6 Merk, H. J., "The Influence of Melting and Anomalous Expansion on the Thermal Convection in Laminar Boundary Layers," *Applied Science Research*, Vol. 4, 1954, pp. 435–452.

7 Desai, V. S., and Forbes, R. E., "Free Convection in Water in the Vicinity of Maximum Density," *Environmental And Geophysical Heat Transfer*, ASME *Trans.*, 1971, pp. 41–47.

8 Watson, A., "The Effect of the Inversion Temperature on the Convection of Water in an Enclosed Rectangular Cavity," *Quarterly Journal of Mechanics and Applied Mathematics*, Vol. 25, 1972, pp. 423–446.

9 Seki, N., Fukusako, S., and Nakoaka, M., "Experimental Study on Natural Convection Heat Transfer With Density Inversion of Water Between Two Horizontal Concentric Cylinders," ASME JOURNAL OF HEAT TRANSFER, Vol. 97, 1975, pp. 556–561.

10 Forbes, R. E., and Cooper, J. W., "Natural Convection in a Horizontal Layer of Water Cooled From Above to Near Freezing," ASME JOURNAL OF HEAT TRANSFER, Vol. 97, 1975, pp. 47–53.

11 Vasseur, P., and Robillard, L., "Transient Natural Convection Heat Transfer in a Mass of Water Cooled Through 4 °C," *International Journal of Heat and Mass Transfer*, Vol. 23, 1980, pp. 1195–1205.

12 Cheng, K. C., and Takeuchi, M., "Transient Natural Convection of Water in a Horizontal Pipe With Constant Cooling Rate through 4 °C," ASME JOURNAL OF HEAT TRANSFER, Vol. 98, 1976, pp. 581–587.

13 Robillard, L., and Vasseur, P., "Transient Natural Convection Heat Transfer of Water With Maximum Density Effect and Supercooling," ASME JOURNAL OF HEAT TRANSFER, Vol. 103, 1981, pp. 528–534.

14 Gray, D. D., and Giorgini, A., "The Validity of the Boussinesq Approximation for Liquids and Gases," *International Journal of Heat and Mass Transfer*, Vol. 19, 1976, pp. 545–551.

15 Chandrasekhar, S., *Hydrodynamic and Hydromagnetic Stability*, Oxford University Press, 1961.

16 Chandra Shekar, B., "Numerical Study on Natural Convection Heat Transfer With Density Inversion of Water Between two Horizontal Concentric Cylinders," M.Sc.A. thesis, Ecole Polytechnique, Montreal, Quebec, Canada, 1980.

17 Fujii, T., "Fundamentals of Free Convection Heat Transfer," *Progress in Heat Transfer Engineering*, Vol. 3, 1974, pp. 66–67.

18 Landolt-Bornstein, *Zahlewerte Und Funktionen*, Springer-Verlag II (1), 1971, pp. 36–37.

19 Hung Nguyen, T., Vasseur, P., and Robillard, L., "Natural Convection between Horizontal Concentric Cylinders With Density Inversion of Water for Low Rayleigh Numbers," *International Journal of Heat and Mass Transfer*, accepted for publication.

20 Carey, V. P., and Gebhart, B., and Mollendorf, J. C., "Buoyancy Force Reversals in Vertical Natural Convection Flows in Cold Water," *Journal of Fluid Mechanics*, 97, 2, 1980, pp. 279–298.

21 Robillard, L., and Vasseur, P., "Convective Response of a Mass of Water Near 4°C to a Constant Cooling Rate Applied on its Boundaries," *Journal of Fluid Mechanics*, Vol. 118, 1982, pp. 123–141.

22 Mallison, G. D., and de Vahl Davis, D., "The Method of the False Transient for the Solution of Coupled Elliptic Equations," *Journal of Computational Physics*, Vol. 12, 1973, pp. 435–461.

23 Roache, P., *Computational Fluid Dynamics*, Hermosa Publishers, 1976.

24 Crawford, L., and Lemlich, R., "Natural Convection in Horizontal Concentric Cylindrical Annuli," IEC Fundamentals, Vol. 1, 1962, pp. 260–264.

25 Charrier-Mojtabi, M.C., Mojtabi, A., and Caltagirone, J. P., "Numerical Solution of a Flow Due to a Natural Convection in Horizontal Cylindrical Annulus," ASME JOURNAL OF HEAT TRANSFER, Vol. 101, 1979, pp. 171–173.

26 Saitoh, T., and Hirose, K., "Thermal Instability of Natural Convection Flow Over a Horizontal Ice Cylinder Encompassing a Maximum Density Point," ASME JOURNAL OF HEAT TRANSFER, Vol. 102, 1980, pp. 261–267.

27 Robillard, L., and Vasseur, P., "Effet du maximum de densité sur la convection libre de l'eau dans une cavité fermée," *Canadian Journal of Civil Engineering*, Vol. 6, 1979, pp. 481–493.

28 Seki, N., Fukusako, S., and Nakaoka, M., "An Analysis of Free Convective Heat Transfer With Density Inversion of Water Between Two Horizontal Concentric Cylinders," JOURNAL OF HEAT TRANSFER, Vol. 98, 1976, pp. 670–672.

Natural Convection at the Interface Between a Vertical Porous Layer and an Open Space

A. Bejan
Assoc. Mem. ASME

R. Anderson
Student Mem. ASME

Department of Mechanical Engineering,
University of Colorado,
Boulder, Colo. 80309

This paper examines the interaction by natural convection between a fluid-saturated porous medium and a fluid reservoir separated by a vertical impermeable partition. The two fluid systems are maintained at different temperatures. The analysis is simplified by assuming $Pr >> 1$ in the fluid reservoir. It is shown analytically that the flow and temperature fields in the boundary layer regime consist of two fluid layers in counterflow. The interface temperature is shown to increase monotonically with altitude. The important dimensionless group which governs the fluid mechanics is $B = (kRa_K^{1/2})/(k'Ra^{1/4})$, where k, k', Ra_K and Ra are, respectively, the porous medium conductivity, reservoir fluid conductivity, Darcy-modified Rayleigh number based on partition height, and the reservoir Rayleigh number based on partition height. The effect of parameter, B, on the flow, temperature, and heat transfer is documented in the range $0 < B < \infty$.

1 Introduction

Important energy-engineering problems have stimulated the present interest in the fundamentals of buoyancy-driven flows through porous media. The majority of the existing studies have been devoted to the behavior of geothermal systems. The major accomplishments in this area were reviewed recently in a comprehensive monograph by Cheng [1]. The phenomenon of natural convection through a porous medium is known also to play a major role in the performance of double walls filled with fibrous or granular insulations for use in energy-efficient buildings. The most studied configuration consists of a vertical porous layer sandwiched by two isothermal surfaces maintained at different temperatures. Analyses and graphic displays of the flow and temperature field have been reported by Chan et. al. [2], Bankvall [3], Bejan and Tien [4], Walker and Homsy [5] and Hickox and Gartling [6].

Vertical porous layers of the type encountered in architectural applications are not sandwiched between isothermal surfaces, as assumed by the papers listed above, rather, they are surrounded by ambient air. The wall temperature is the result of the complex interaction between two buoyancy-driven flows, one on the inside surface (through the porous medium), and the other on the outside surface of the wall. The same convective interaction may take place between magma chambers (fluid reservoirs) and geothermal systems (porous media).

2 Physical Model and Problem Formulation

Consider the interaction of a vertical porous layer with an adjacent fluid reservoir, as shown schematically in Fig. 1. The two fluid media communicate thermally across a vertical impermeable wall of height, H. Far away from this wall, the two media are at uniform but different temperatures; for the sake of clarity in presentation, we assume from the outset that the left side of the arrangement (the porous space, Fig. 1) is warmer than the right side (the open space), hence $T^*_H > T^*_L$. For *both* sides of the partition, symbols x^*, y^*, u^*, v^*, and T^* denote the actual horizontal position, vertical position, horizontal velocity, vertical velocity, and temperature, respectively.

Porous Space. The dimensionless equations governing the steady-state conservation of mass, energy, and momentum in the isotropic porous medium are

$$\frac{\partial u}{\partial x} + \frac{\partial v}{\partial y} = 0, \tag{1}$$

$$u\frac{\partial T}{\partial x} + v\frac{\partial T}{\partial y} = \frac{\partial^2 T}{\partial x^2} + \frac{1}{\mathrm{Ra}_K}\frac{\partial^2 T}{\partial y^2}, \tag{2}$$

$$\frac{1}{\mathrm{Ra}_K}\frac{\partial u}{\partial y} - \frac{\partial v}{\partial x} = -\frac{\partial T}{\partial x} \tag{3}$$

The nondimensionalization is based on the boundary layer scaling outlined in Weber [7]. The dimensionless variable are defined as

$$x = x^*/\delta \ , \ y = y^*/H,$$
$$u = u^*/(\alpha/\delta) \ , \ v = v^*/(\alpha H/\delta^2), \tag{4}$$

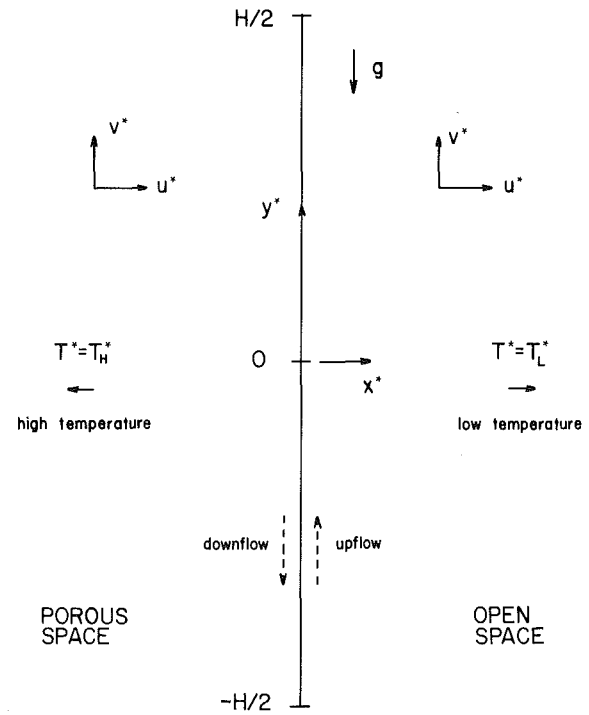

Fig. 1 Schematic of natural convection at the interface between a fluid-saturated porous medium (left) and an open space (right)

Contributed by the Heat Transfer Division for publication in the JOURNAL OF HEAT TRANSFER. Manuscript received by the Heat Transfer Division January 21, 1981.

$$T=\frac{T^*-\frac{1}{2}(T_H^*+T_L^*)}{T_H^*-T_L^*}$$

where Ra_K is the Darcy-modified Rayleigh number based on vertical dimension (H) and medium permeability (K),

$$\mathrm{Ra}_K=\frac{g\beta KH(T_H^*-T_L^*)}{\alpha\nu} \tag{5}$$

and δ is the scale of the boundary layer thickness

$$\delta=H\mathrm{Ra}_K^{-1/2} \tag{6}$$

The governing equations (1-3) are therefore based on the Darcy flow model and on the homogenous porous medium model whereby the fluid is considered in local thermal equilibrium with the solid matrix. It is further assumed that the pressure and temperature variations through the medium are small enough so that the Boussinesq approximation applies

$$\rho=\rho_0[1-\beta(T^*-T_0^*)] \tag{7}$$

where β is the coefficient of thermal expansion. Parameters K, μ, g, ρ, c_p, and k represent the permeability, viscosity, gravitational acceleration, fluid density, and specific heat at constant pressure, and the thermal conductivity of the porous matrix saturated with fluid, respectively.

In the study of the boundary layer regime ($\delta << H$), the terms multiplied by $1/\mathrm{Ra}_K$ in equations (2, 3) will be neglected, since, according to equation (6), $\mathrm{Ra}_K^{-1} << 1$. The appropriate boundary conditions suggested by the schematic of Fig. 1 are

$$u=0, \tag{8}$$

$$T=T_0(y) \tag{9}$$

at $x=0$

$$v=0, \tag{10}$$

$$T=\frac{1}{2} \tag{11}$$

as $x\to-\infty$

It should be remembered that the wall temperature variation with altitude, $T_0(y)$, is unknown at this point. As argued in the introduction, $T_0(y)$ will be determined by the interaction between the two fluid media across the impermeable wall. In the boundary layer regime ($H > \delta$) the wall functions like an extremely long counterflow heat exchanger, hence, $T_0(y)$ will take on values between the two temperature extremes of the semi-infinite spaces, $1/2$ and $-1/2$.

Open space. The nondimensional conservation statements and boundary conditions for the boundary layer flow formed on the cold side of the vertical partition are

$$\frac{\partial\hat{u}}{\partial\hat{x}}+\frac{\partial\hat{v}}{\partial y}=0 \tag{12}$$

$$\frac{\partial^3\hat{v}}{\partial\hat{x}^3}=-\frac{\partial T}{\partial\hat{x}} \tag{13}$$

$$\hat{u}\frac{\partial T}{\partial\hat{x}}+\hat{v}\frac{\partial T}{\partial y}=\frac{\partial^2 T}{\partial\hat{x}^2} \tag{14}$$

where the new dimensionless variables, marked by the sign "$\hat{}$", are defined as

$$\hat{x}=x^*/l,$$

$$\hat{u}=u^*/(\alpha'/l)\ ,\ \hat{v}=v^*/(\alpha' H/l^2) \tag{15}$$

The remaining variables, y and T, are defined the same way as on the porous side [see equations (4)]. Using the scaling arguments presented by Gill [8], one can show that the boundary layer thickness is of order

$$l=H\mathrm{Ra}^{-1/4} \tag{16}$$

where Ra is the Rayleigh number based on wall height

$$\mathrm{Ra}=\frac{g\beta' H^3(T_H^*-T_L^*)}{\alpha'\nu'} \tag{17}$$

In writing the conservation statements as equations (12-14), we treated the fluid filling the open space as Boussinesq - incompressible, with physical properties α', β', ν'. The simplified momentum equation (13) is a balance between the body force and the viscous shear force, which means that inertial effects are small relative to the preceding two: this scaling is valid for Prandtl numbers $\mathrm{Pr} >> 1$; however, it is known to be *approximately* valid for air ($\mathrm{Pr} = 0.72$) as well. The momentum and energy equations (13, 14) contain also the classical boundary layer approximation $l < H$.

The boundary conditions for the fluid occupying the open space are

$$\hat{u}=0, \tag{18}$$

$$\hat{v}=0, \tag{19}$$

$$T=T_0(y) \tag{20}$$

at $\hat{x}=0$

$$\hat{v}=0, \tag{21}$$

$$T=-1/2 \tag{22}$$

as $\hat{x}\to+\infty$

Note here the no-slip condition valid along the impermeable wall, equation (19); a similar condition could not be imposed on the porous side of the impermeable partition due to the limitations inherent in the Darcy flow model. The slip condition on the porous side of the wall is the result of the homogeneous porous medium model employed in writing equations (1-3). As shown recently by Dagan [9], these equations are not valid in a thin layer right next to the wall (the thickness of this thin layer is of the order of the pore diameter). Therefore, our analysis is valid in the "small pore limit" discussed by Dagan.

Nomenclature

B = new dimensionless group
C = constant of integration
c_p = specific heat at constant pressure
g = gravitational acceleration
H = wall height
k = thermal conductivity of fluid-saturated porous medium
K = permeability of porous medium
l = scale of boundary layer thickness on the open (fluid) side
Nu = Nusselt number
Pr = Prandtl number
Ra = Rayleigh number
Ra_K = Darcy-modified Rayleigh number
T = dimensionless temperature
T_0 = interface temperature
T_H^* = high temperature
T_L^* = low temperature
u, v = dimensionless velocity components for the porous side
$\hat{u}, \hat{v}$ = dimensionless velocity components for the open side
x, y = dimensional spatial coordinates for the porous side
$\hat{x}$ = dimensional horizontal coordinate for the open side
α = thermal diffusivity
β = coefficient of thermal expansion
σ, γ, λ = Oseen functions
δ = scale of boundary layer thickness on the porous side
μ = viscosity
ν = kinematic viscosity
ρ = fluid density
σ = Oseen function for the porous side
$(\ )'$ = physical property of the fluid in the open space
$(\ )^*$ = dimensional quantity

Finally, the condition accounting for the thermal contact of the two fluid media across the impermeable wall is the local heat flux conservation statement

$$k\left(\frac{\partial T^*}{\partial x^*}\right)_{x^*=0^-} = k'\left(\frac{\partial T^*}{\partial x^*}\right)_{x^*=0^+} \tag{23}$$

where k' is the thermal conductivity of the open space fluid. In nondimensional form, equation (23) may be written as

$$B\left(\frac{\partial T}{\partial x}\right)_{x=0} = \left(\frac{\partial T}{\partial \hat{x}}\right)_{\hat{x}=0} \tag{24}$$

where B is a new dimensionless group (number) characteristic to the two-fluid free convection problem

$$B = \frac{k/\delta}{k'/l} = \frac{k\mathrm{Ra}_K^{1/2}}{k'\mathrm{Ra}^{1/4}} \tag{25}$$

The B number is known as soon as the physical properties of the two media are known, and the overall temperature difference $\Delta T^* = T_H^* - T_L^*$ is specified. We note that the B number increases with the increasing temperature difference, $B \sim (\Delta T^*)^{1/4}$. We also note that if the temperature difference is held constant, the B number decreases as the height of the interface increases, $B \sim H^{1/4}$. Finally, it is important to keep in mind that the two limits we shall consider for B ($B \to 0$ and $B \to \infty$) do not invalidate the thin boundary layer approximations ($\mathrm{Ra}_K > 1$, $\mathrm{Ra} > 1$) adopted in the beginning of this study. This is due to the fact that the conductivity ratio k/k', which appears in definition (25), is independent of either Ra_K or Ra.

3 Analytical Solution

An analytical solution to equations (1-3) and (12-14) is made difficult by the presence of nonlinear terms in the two energy equations, (2) and (14). In this section we develop an analytical solution in which the energy equations are linearized according to the Oseen technique employed, among others, by Gill [8], Weber [7], and Bergholz [10]. Weber relied on this technique in the study of free convection in a rectangular enclosure containing porous material in the boundary layer regime. Bergholz used the same approach in the study of a porous layer with internal heat sources.

Porous Side. Integrating the momentum equation (3) in x, and applying the $x \to -\infty$ boundary conditions (10, 11) yields a relationship between v and T,

$$v = T - \frac{1}{2} \tag{26}$$

Eliminating T between this result and the energy equation (2), we obtain

$$(u)\frac{\partial v}{\partial x} + \left(\frac{\partial T}{\partial y}\right)v = \frac{\partial^2 v}{\partial x^2} \tag{27}$$

According to the Oseen linearization technique, at this point we regard (u) and $(\partial T/\partial y)$ as two unknown functions of altitude. Consequently, equation (27) can now be integrated in x yielding a solution of the form

$$v = \sum_{i=1}^{2} C_i e^{\sigma_i x} \tag{28}$$

where $\sigma_1(y)$, $\sigma_2(y)$ are the roots of the characteristic equation

$$\sigma^2 - (u)\sigma - \left(\frac{\partial T}{\partial y}\right) = 0 \tag{29}$$

namely

$$\sigma_{1,2} = \frac{1}{2}\left[(u) \pm \sqrt{(u)^2 + 4\left(\frac{\partial T}{\partial y}\right)}\right] \tag{30}$$

Examining equation (30), and recognizing the fact that physically $(\partial T/\partial y)$ must be positive, we conclude that σ_1 and σ_2 are of opposite sign *regardless of the sign of* (u). Therefore, since $v \to 0$ as $x \to -\infty$, in solution (28) we retain only the term containing the positive of the two σ_i's. Let σ be the positive σ_i. Using the remaining boundary condition, equation (9), the complete solution for vertical velocity and temperature in the porous space becomes

$$v = \left(T_0 - \frac{1}{2}\right)e^{\sigma x} \tag{31}$$

$$T = \left(T_0 - \frac{1}{2}\right)e^{\sigma x} + \frac{1}{2} \tag{32}$$

Solution (31, 32) depends on two unknown functions of altitude, $T_0(y)$ and $\sigma(y)$. Function $\sigma(y)$ is the result of having linearized the exact energy equation (2); hence, we can determine σ from the condition that solution (31, 32) satisfies the energy equation (2) integrated over the entire porous space

$$|uT|_0^{-\infty} + \frac{d}{dy}\int_0^{-\infty} vT\,dx = \left|\frac{\partial T}{\partial x}\right|_0^{-\infty} \tag{33}$$

Combining the energy integral (33) with equations (31, 32) and the mass conservation statement (1), we can express $\sigma(y)$ in terms of only $T_0(y)$

$$\frac{d}{dy}\left[\frac{\left(T_0 - \frac{1}{2}\right)^2}{2\sigma}\right] = \left(T_0 - \frac{1}{2}\right)\sigma \tag{34}$$

Open Space. The corresponding analytical expressions for $\hat{v}(\hat{x})$ and $T(\hat{x})$ on the right side of the wall (Fig. 1) can be derived following the steps emphasized in the preceeding subsection. The Oseen-linearization of the energy equation (14) for the semi-infinite fluid side is as justified as in the enclosure flows studied previously [7, 8, 10]: in an enclosure, the boundary layer thickness, l, is considerably smaller than the enclosure length. The resulting expressions for $\hat{v}$ and T are

$$\hat{v} = \frac{T_0 + \frac{1}{2}}{2\lambda\gamma}e^{-\lambda\hat{x}}\sin(\gamma\hat{x}) \tag{35}$$

$$T = -\frac{T_0 + \frac{1}{2}}{2\lambda\gamma}e^{-\lambda\hat{x}}[(\lambda^2 - \gamma^2)\sin(\gamma\hat{x}) - 2\lambda\gamma\cos(\gamma\hat{x})] - \frac{1}{2} \tag{36}$$

where $\lambda(y)$ and $\gamma(y)$ are two additional unknown functions. We determine the two unknowns by forcing solution (35, 36) to satisfy the energy equation (14) in two places, at the wall

$$0 = \frac{\partial^2 T}{\partial \hat{x}^2} \tag{37}$$

and integrated over the entire open space

$$|uT|_0^{\infty} + \frac{d}{dy}\int_0^{\infty} vT\,dy = \left|\frac{\partial T}{\partial \hat{x}}\right|_0^{\infty} \tag{38}$$

Conditions (37) and (38) yield, respectively,

$$\lambda = \gamma \tag{39}$$

$$\frac{d}{dy}\left[\frac{\gamma^2}{4\lambda}\left(\frac{T_0 + \frac{1}{2}}{2\lambda\gamma}\right)^2\right] = (3\lambda^2 - \gamma^2)\frac{T_0 + \frac{1}{2}}{2\lambda} \tag{40}$$

Eliminating γ between equations (39) and (40) leads to a

Table 1 Summary of numerical results

B	C	$T_0(0)$	$\mathrm{Nu/Ra}^{1/4}$
0.03	0.4346	−0.436	0.0272
0.1	1.2183	−0.342	0.0761
0.3	2.6727	−0.180	0.167
1	4.9317	0.055	0.3083
3	6.879	0.240	0.4299
10	8.3125	0.371	0.5195
30	8.9922	0.435	0.5619

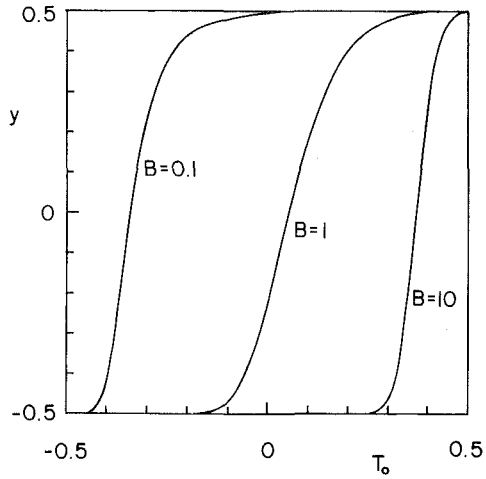

Fig. 2 The interface temperature as a function of altitude and the B number

differential expression for λ in terms of the unknown wall temperature distribution T_0,

$$\frac{d}{dy}\left[\frac{\left(T_0+\frac{1}{2}\right)^2}{(16)\lambda^3}\right]=\left(T_0+\frac{1}{2}\right)\lambda \tag{41}$$

In conclusion, the velocity and temperature distributions on both sides of the impermeable wall, equations (31, 32) and (35, 36), depend on a single unknown: the wall temperature $T_0(y)$. Function $T_0(y)$ can finally be determined by invoking the local heat flux conservation condition, equation (24), which becomes

$$B\frac{\sigma}{\lambda}=\frac{\frac{1}{2}+T_0}{\frac{1}{2}-T_0} \tag{42}$$

Equations (42), (41), and (34) constitute a sufficient set for determining $T_0(y)$, $\lambda(y)$ and $\sigma(y)$. Dividing equations (34) and (41) side by side, using equation (42), and integrating once yields

$$8B\frac{\left(T_0-\frac{1}{2}\right)^2}{\sigma}+\frac{\left(T_0+\frac{1}{2}\right)^2}{\lambda^3}=C \tag{43}$$

where C is the constant of integration. Eliminating σ between this expression and equation (42) we obtain

$$8B^2\frac{\left(\frac{1}{2}-T_0\right)^3}{\lambda\left(\frac{1}{2}+T_0\right)}+\frac{\left(T_0+\frac{1}{2}\right)^2}{\lambda^3}=C \tag{44}$$

From this point on we carried out the solution numerically, on a digital computer, by combining equations (41) and (44) to determine $T_0(y)$ and $\lambda(y)$. In order to circumvent the singularities of λ at $y=\pm 1/2$ we marched from $y=-1/2$ in finite steps of T_0. We then used equation (44) to calculate λ. Finally, we used equation (41) to calculate the resulting step in y. During each march, we found that y starts increasing very slowly, while at the end of the march ($T_0=+1/2$) the value of y reaches a plateau. Our adjustment of constant C was such that the plateau reached by y was eventually $+1/2$. We used a small enough step ΔT_0 so that the final results were no longer susceptible to the step size. We repeated this entire procedure for a series of dicrete values of the B number. The key results of this numerical work are condensed in Table 1.

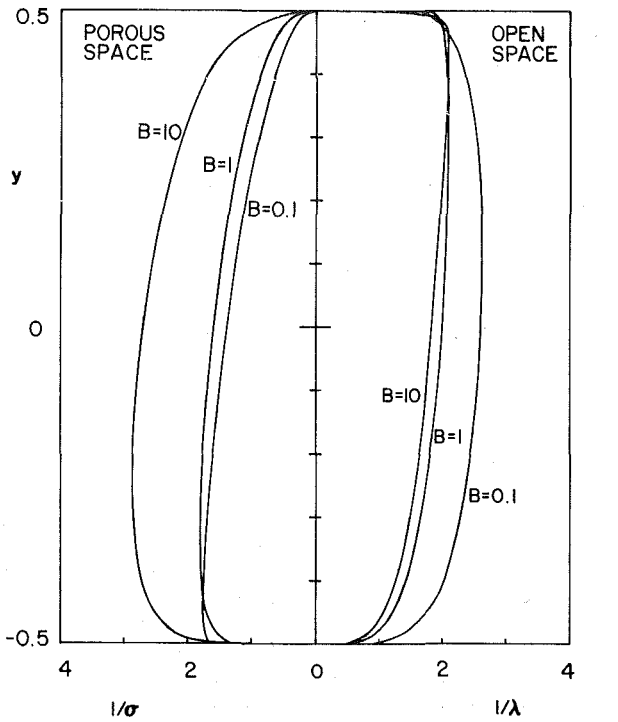

Fig. 3 The two boundary layer thicknesses as functions of altitude and the B number

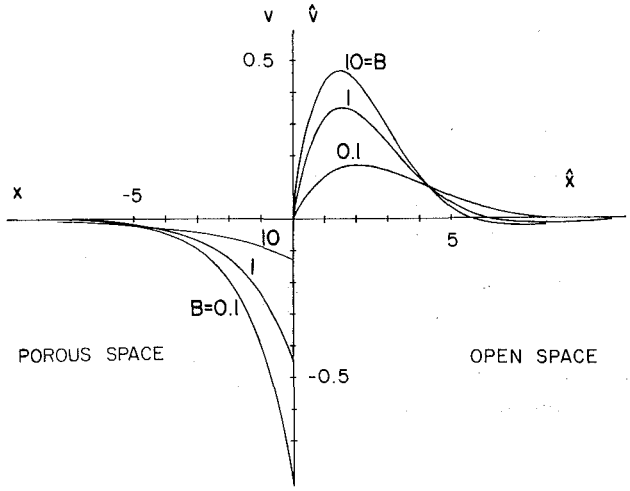

Fig. 4 Vertical velocity profiles at midheight ($y=0$)

4 Results

Figures 2–7 show graphically the main features of the convective interaction at the vertical interface. In Fig. 2, we plotted the wall temperature distribution $T_0(y)$, showing the

changes associated with increasing the B number. The wall temperature increases monotonically with altitude; over roughly 80 percent of the wall height, T_0, is approximately linear in y. At the top and bottom ends of the wall, where the present boundary layer solution breaks down, the wall temperature converges abruptly to the temperature extremes maintained by the two fluid media.

As B increases, the wall temperature gradually approaches the temperature of the porous space ($T = 1/2$). This effect is to be expected since, as suggested by equation (25), in this limit the flow is stronger on the porous side; hence, the thermal contact between the porous space and the interface is superior relative to the contact between the interface and the fluid occupying the open space.

We pointed out in the preceding section that the numerical procedure leading to finding $T_0(y)$ requires also the calculation of $\sigma(y)$ and $\lambda(y)$. These auxiliary results are plotted in Fig. 3 as $1/\sigma$ and $1/\lambda$ versus y. As shown by the closed-form expressions for velocity and temperature, equations (31, 32) and (35, 36), functions $1/\sigma$ and $1/\lambda$ play the role of dimensionless boundary layer thicknesses. Examining Fig. 3, we conclude that both thicknesses increase in the flow direction, except over a small distance in the exit-end of each boundary layer where both thicknesses drop abruptly to zero. We conclude also that as B increases, the porous-side dimensionless boundary layer thickness increases while the open-side thickness decreases. These trends are reversed if the B number decreases.

The vertical velocity and temperature profiles at midheight ($y = 0$) are shown in Figs. 4 and 5. The vertical velocity profile shows two boundary layers in counterflow, the warm stream descending along the porous side of the interface. Parameter B appears to have a strong effect on velocity as well as on temperature. As B increases above one, the temperature drop across the right (open space) boundary layer exceeds the temperature drop across the porous-side layer; consequently, the dimensionless vertical velocity increases on the open side and decreases on the porous side.

The velocity profile on the fluid side (open space) is correct only near the wall, in the layer of thermal boundary thickness, l. The outer zone of the velocity profile should scale as $\mathrm{Pr}^{1/2} l$ [11]; however, the fluid in the outer zone is isothermal and is thus irrelevant as far as heat transfer results are concerned. This is why the present study and Oseen solutions published previously for enclosures correctly describe the heat transfer part of the problem, while failing to discuss the motion of

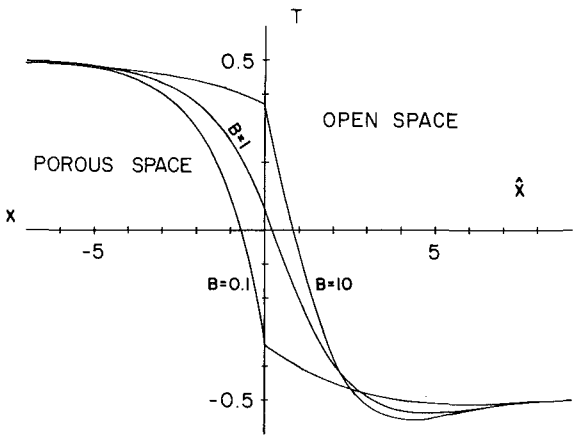

Fig. 5 Temperature profiles at midheight ($y = 0$)

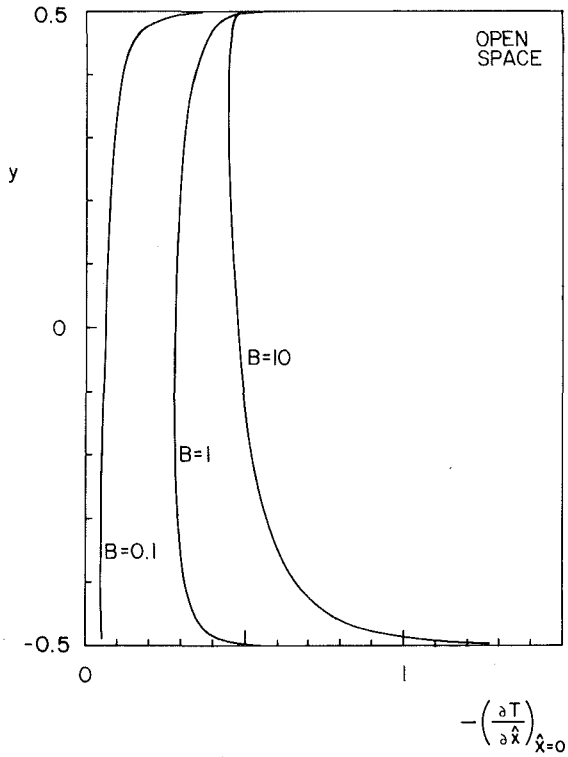

Fig. 6 The distribution of heat flux over the vertical interface

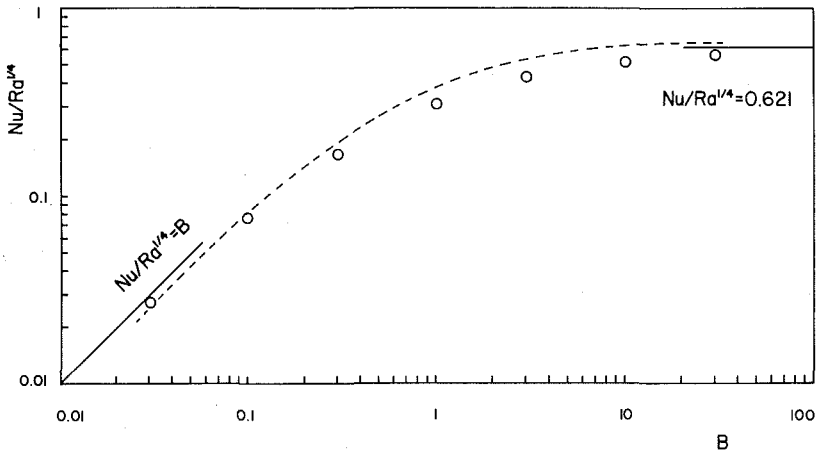

Fig. 7 The Nusselt number, Nu, for overall heat transfer as a function of the open-side Rayleigh number Ra and the B number. The dashed line represents equation (51), while the circles represent the results listed in Table 1.

unheated fluid induced outside the thermal boundary layer.

Of engineering importance is the heat exchange between the two fluid media across the vertical impermeable wall. In Fig. 6 we present the distribution of heat flux along the wall, by plotting the dimensionless temperature gradient on the open side. The gradient $(\partial T/\partial \hat{x})_{\hat{x}=0}$ increases in absolute value as the B number increases, in accordance with the temperature profile behavior illustrated in Fig. 5. As a good approximation, the local heat flux is practically uniform (independent of y) over a large fraction of wall height, especially when the B number is of order one. The heat flux blows up at the two ends $y = \pm 1/2$.

Finally, in Fig. 7 we report the heat flux integrated over the entire heat of the wall, as $\mathrm{Nu}/\mathrm{Ra}^{1/4}$ versus B. Note that the heat flux integral is finite, despite the singularities in heat flux at $y = \pm 1/2$. Finite heat flux integrals based on similar (Oseen) analyses were obtained earlier by Weber [7] for porous media and by Bejan [12] for newtonian fluids. The overall Nusselt number is defined in the usual manner, as for natural convection over an isothermal vertical wall immersed in an isothermal fluid (see, for example, Rohsenow and Choi [13]),

$$\mathrm{Nu} = \frac{Q}{k'(T_H^* - T_L^*)} \tag{45}$$

In this definition, Q $[W/m]$ represents the net heat-transfer rate from $T^*{}_H$ to T_L^* per unit width measured in the direction perpendicular to the plane of Fig. 1. The Nusselt number increases monotonically as the B number increases.

In the limit $B \to \infty$ the wall assumes the temperature of the porous space ($T_0 = 1/2$, Fig. 2), hence, the two-fluid problem collapses into the classical problem of natural convection of Boussinesq-incompressible fluid over a vertical isothermal plate. In this limit, our Nusselt number result approaches the asymptote

$$\mathrm{Nu} = 0.621\ \mathrm{Ra}^{1/4} \tag{46}$$

which can be obtained by solving the "open space" part of the analytical solution (section 3) setting $T_0 = 1/2$. It is important to note that our asymptotic result (46) agrees within 2.6 percent with the "exact" result based on a similarity boundary layer solution in the $\mathrm{Pr} \to \infty$ limit (see, for example, Rohsenow and Choi [13])

$$\mathrm{Nu} = \frac{0.902}{4^{1/4}}\mathrm{Ra}^{1/4} = 0.638\ \mathrm{Ra}^{1/4} \tag{47}$$

In the opposite limit, $B \to 0$, the natural convection effect is extremely effective on the right side; hence, the wall temperature becomes equal to the temperature of the open space ($T_0 = -1/2$, Fig. 2). The value of Nu in this limit can be obtained by reworking the porous half of the analytical solution (section 3), assuming from the outset $T_0 = -1/2$ for wall temperature. The final result is

$$\mathrm{Nu} = \mathrm{Ra}^{1/4} B = \frac{k}{k'}\mathrm{Ra}_K^{1/2} \tag{48}$$

or

$$\frac{Q}{k(T_H^* - T_L^*)} = \mathrm{Ra}_K^{1/2} \tag{49}$$

In the $B \to 0$ limit the two-fluid problem reduces to the classical problem of natural convection over an isothermal surface imbedded vertically in a fluid-saturated porous medium. The similarity solution to this problem was recently reported by Cheng & Minkowycz [14]

$$\frac{Q}{k(T_H^* - T_L^*)} = 0.888\ \mathrm{Ra}_K^{1/2} \tag{50}$$

which falls within 12.6 percent of our Oseen-linearized result (49).

The $\mathrm{Nu}/\mathrm{Ra}^{1/4}$ results obtained for several intermediate values of B are listed in Table 1 and on Fig. 7: these values agree within 21 percent with the engineering estimate based on adding the two thermal resistances for the limiting cases in series (equations (47) and (50)),

$$\mathrm{Nu}/\mathrm{Ra}^{1/4} = [(0.638)^{-1} + (0.888\mathrm{B})^{-1}]^{-1} \tag{51}$$

5 Concluding Remarks

In order to shed new light on the thermofluid interaction of a vertical porous layer with an adjacent fluid reservoir, we focused on the natural convection mechanism working at the impermeable interface between two such systems at different tempertures (Fig. 1). We found that the flow pattern consists of a vertical counterflow in which the warm branch descends along the warm side of the interface (Fig. 4 and 5). The wall temperature increases monotonically with altitude (Fig. 2).

On the basis of scaling arguments, we demonstrated that the complexion of this two-fluid problem is governed by a new dimensionless group, $B = (k\ \mathrm{Ra}_K^{1/2})/(k'\ \mathrm{Ra}^{1/4})$, which *rates the heat transfer effectiveness of the two buoyant* boundary layers, relative to one another. We showed that the limit $B \to \infty$ corresponds to the classical problem of convection about a vertical isothermal plate immersed in an isothermal fluid, whereas the $B \to 0$ limit corresponds to the porous medium – equivalent of the same classical problem.

For the energy engineer, we developed overall heat transfer results valid in the entire domain covered by the B number, $0 < B < \infty$. We showed that our analytical predictions, Table 1 and Fig. 7, agree well with theoretical heat transfer results known in the two extremes, $B \to 0$ and $B \to \infty$. As pointed out in the introduction, the present heat transfer results have a number of important applications, such as the design of energy-efficient building insulation and the interaction between magma chambers and geothermal systems.

Acknowledgment

This study was supported in part by NSF Grant No. ENG 78-20957.

References

1 Cheng, P., "Heat Transfer in Geothermal Systems," *Adv. in Heat Transfer*, Vol. 15, 1979, pp. 1-105.

2 Chan, B. K. C., Ivey, C. M., and Barry, J. M., "Natural Convection in Enclosed Porous Media with Rectangular Boundaries," ASME JOURNAL OF HEAT TRANSFER, Vol. 92, 1970, pp. 21-27.

3 Bankvall, C. G., "Natural Convection in Vertical Permeable Space," *Wärme und Stoffübertragung*, Vol. 7, 1974, pp. 22-30.

4 Bejan, A., and Tien, C. L., "Natural Convection in a Horizontal Porous Medium Subjected to an End-to-End Temperature Difference," ASME JOURNAL OF HEAT TRANSFER, Vol. 100, 1978, pp. 191-198.

5 Walker, K. L., and Homsy, G. M., "Convection in a Porous Cavity," *Journal of Fluid Mechanics*, Vol. 87, 1978, pp. 449-474.

6 Hickox, C. E., and Gartling, D. K., "A Numerical Study of Natural Convection in a Horizontal Porous Layer Subjected to an End-to-End Temperature Difference," ASME JOURNAL OF HEAT TRANSFER, Vol. 103, 1981, pp. 797-802.

7 Weber, J. E., "The Boundary Layer Regime for Convection in a Vertical Porous Layer," *International Journal of Heat and Mass Transfer*, Vol. 18, 1975, pp. 569-573.

8 Gill, A. E., "The Boundary Layer Regime for Convection in a Rectangular Cavity," *Journal of Fluid Mechanics*, Vol. 26, 1966, pp. 515-536.

9 Dagan, G., "The Generalization of Darcy's Law for Nonuniform Flows," *Water Resources Research*, Vol. 15, 1979, pp. 1-7.

10 Bergholz, R. F., "Natural Convection of Heat Generated Fluid in a Closed Cavity," ASME JOURNAL OF HEAT TRANSFER, Vol. 102, 1980, pp. 242-247.

11 Patterson, J., and Imberger, J., "Unsteady Natural Convection in a Rectangular Cavity," *Journal of Fluid Mechanics*, Vol. 100, 1980, pp. 65-86.

12 Bejan, A., "Note on Gill's Solution for Free Convection in a Vertical Enclosure," *Journal of Fluid Mechanics*, Vol. 90, 1979, pp. 561-568.

13 Rohsenow, W. M., and Choi, H. Y., *Heat, Mass and Momentum Transfer*, Prentice Hall, Englewood Cliffs, New Jersey, 1961.

14 Cheng, P., and Minkowycz, W. J., "Free Convection about a Vertical Flat Plate Embedded in a Porous Medium with Applications to Heat Transfer from a Dike," *J. Geophys. Res.*, Vol. 82(14), 1977, pp. 2040-2044.

The Effect of Nonlinear Density Stratification on the Stability of a Vertical Water Layer in the Conduction Regime

A. H. Shaaban

M. N. Özişik
Mem. ASME

Department of Mechanical and Aerospace Engineering,
North Carolina State University,
Raleigh, N. C. 27650

The thermal stability of a layer of water between two vertical parallel plates maintained at different temperatures, T_1 and T_2, is investigated for the conduction regime. Three cases are considered include where: (a) the maximum density layer is within the water region; (b) is at the boundary; and (c) is outside the water region. Cubic polynomials are used to represent the density-temperature relation in the temperature range 0–55°C. The numerical results show that the critical states of stability do not depend on Prandtl number but instead depends on the combinations of T_1 and T_2. Of the three cases considered, the first case is the most unstable. In all three cases, the instabilities set in as a traveling wave, moving against gravity, for most T_1 and T_2 combinations. Stationary waves were also found for case (c).

Introduction

The thermal instability of a layer of fluid contained between two vertical, parallel plates, one of which is heated and the other cooled, has been widely investigated. The works of Eckert and Carlson [1], Elder [2], Hart [3], Korpela, et al. [4], and Vest and Arpaci [5] for the case of large aspect ratio with fluids having a linear density-temperature relationship (i.e., density decreases monotonically with the increase of temperature) produce the well-known trends. That is, for a small Rayleigh number, Ra, heat is transferred across the gap by conduction (this is called the conduction regime), and the fluid circulation is set up with the part of the fluid closer to the hot side rising and the part closer to the cold side falling, forming a velocity profile of odd symmetry. The increase of Ra above a critical value forces the parallel flow of the conduction regime to changes into multicellular flow pattern; this is called tansition regime. As Ra becomes sufficiently large, the flow pattern changes into a boundary layer type of flow over the surface plates, and the heat is transferred mainly by convection (convection regime).

Korpela et al, [4] reported that the instability of the conduction regime, when Gr reaches a critical value, sets in two types of disturbances which is determined by the magnitude of the Prandtl number. For $Pr < 12.7$, the mode of instability is stationary, while for $Pr \geq 12.7$ the instability sets in as two waves traveling in opposite directions. In all of the references quoted above, the variation of the thermal expansion coefficient, γ, of the fluid over the temperature range of interest was neglected by using an average value for γ. For most fluids, which possess a linear temperature density relationship, this is a reasonable approach. But there are few liquids, such as water, which exhibit a maximum value in their density-temperature profile. The presence of maximum density implies that the thermal expansion coefficient changes sign over the temperature range of interest, hence the use of an average value for γ becomes physically unreasonable.

More important, if the liquid possesses a maximum density over a given temperature range, a somewhat more complicated situation arises in the analysis of thermal stability over such temperature range. In the case of water, for example, there is a maximum density at temperature 3.98°C and the density-temperature relation over a temperature range including 3.98°C is no longer linear. The effects of nonlinear density-temperature relationship on thermal instability for the well-known Bénard Problem, has been studied theoretically by Veronis [6] and Sun, Tien and Yen [7] by using the linear theory of stability, and by Legros, Londree and Thomaes [8], and Yen [9], experimentally. The free convection for water at 4°C about a vertical finite flat plate was solved by Vanier and Tien [10] by using a cubic form of density-temperature relationship and by Goren [11] by using a quadratic form. The thermal instability for a semi-infinite horizontal water layer near freezing point cooled or heated from below was studied by Merker and Grigull [12] by using a quadratic polynomial for density-temperature relationship.

No work appears to be reported in the published literature

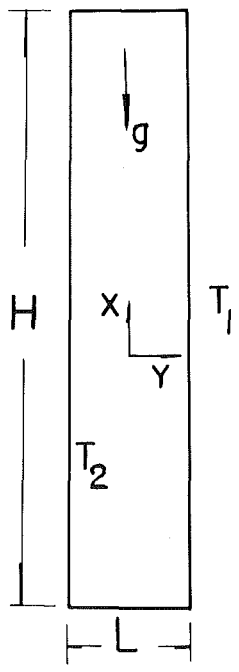

Fig. 1 Geometry and coordinates

Contributed by the Heat Transfer Division for publication in the JOURNAL OF HEAT TRANSFER. Manuscript received by the Heat Transfer Division March 1, 1982.

on thermal instability of a layer of water contained between two vertical parallel plates over a temperature range including the maximum density temperature, 3.98°C. In the present work, we study the thermal instability in a layer of water between two vertical parallel plates, with a temperature range from 0 to 55°C.

Analysis

The schematic diagram of the system considered for this problem is shown in Fig. 1. The model consists of a layer of water contained in a vertical narrow gap of height, H, and width, L, such that $H/L >> 1$. The gap is bounded by two rigid vertical planes, kept at constant but different temperatures, T_1 and T_2, in the range 0–55°C. The Boussinesq approximation is invoked; i.e., the fluid properties are assumed to be constant except for the density which appears in the body force term of the momentum equations, those properties are assumed to be measured at the bulk temperature of the vertical water layer, and the analysis is restricted to the conduction regime.

The nondimensionalized governing equations for the thermal stability problem considered here, using the vector notation, are

Continuity

$$\nabla \cdot V = 0 \tag{1}$$

Momentum

$$\frac{\partial V}{\partial \tau} + \mathrm{Gr}\, V \cdot \nabla V = -\nabla p + \hat{e}_x f + \nabla^2 V \tag{2}$$

Energy

$$\frac{\partial \Theta}{\partial \tau} + \mathrm{Gr}\, V \cdot \nabla \Theta = \mathrm{Pr}^{-1} \nabla^2 \Theta \tag{3}$$

where

$$f = -\frac{1}{\gamma \Delta T}\left(\frac{\rho}{\rho_0}\right), \nabla = \hat{i}\frac{\partial}{\partial x} + \hat{j}\frac{\partial}{\partial y} + \hat{k}\frac{\partial}{\partial z}, V = \hat{i}u + \hat{j}v + \hat{k}w,$$

and Θ is the temperature. Here, the density of water, ρ, over a temperature range 0–55 °C is expressed as a polynomial in the form

$$\frac{\rho}{\rho_{\max}} = 1 - \sum_{k=1}^{3} \beta_k (T - 3.98)^k \tag{4}$$

The coefficients β_k are obtained by a least squares fitting of the data given in Perry [13]. To preserve accuracy, three sets of coefficients are assumed applicable for the temperature ranges 0–20°C, $\beta_1 = -0.25145 \times 10^{-6}\,°\mathrm{C}^{-1}$, $\beta_2 = 0.793953 \times 10^{-5}\,°\mathrm{C}^{-2}$, $\beta_3 = -0.655908 \times 10^{-7}\,°\mathrm{C}^{-3}$; and for 0–35 °C, $\beta_1 = -0.20773 \times 10^{-6}\,°\mathrm{C}^{-1}$, $\beta_2 = 0.742998 \times 10^{-5}\,°\mathrm{C}^{-2}$, $\beta_3 = -0.430608 \times 10^{-7}\,°\mathrm{C}^{-3}$; and for 0–55°C, $\beta_1 = 0.1303279 \times 10^{-4}\,°\mathrm{C}^{-1}$, $\beta_2 = 0.662447 \times 10^{-5}\,°\mathrm{C}^{-2}$, $\beta_3 = -0.273526 \times 10^{-7}\,°\mathrm{C}^{-3}$. The standard errors, which of the same order of the experimental uncertainty are 0.51×10^{-6}, 0.5×10^{-5} and 0.9×10^{-5} for the three ranges respectively. The first two sets of coefficients are the same as those used by Vanier and Tien [10].

The Base Flow Analysis. The equations governing the initial steady motion of water in the vertical channel are obtained from equations (1–4), as

$$\frac{d^2 \bar{U}}{dy^2} + \frac{1}{\gamma \Delta T}[\gamma_1 \Delta T \bar{\Theta} + \gamma_2 (\Delta T \bar{\Theta})^2 + \gamma_3 (\Delta T \bar{\Theta})^3] = \Lambda \tag{5a}$$

$$\frac{d^2 \bar{\Theta}}{dy^2} = 0 \tag{5b}$$

subject to the boundary conditions

$$\bar{U} = 0 \quad \text{at} \quad y = \pm \tfrac{1}{2} \tag{6a}$$

$$\bar{\Theta} = 1 \quad \text{at} \quad y = +\tfrac{1}{2} \tag{6b}$$

$$\bar{\Theta} = 0 \quad \text{at} \quad y = -\tfrac{1}{2} \tag{6c}$$

The constant, Λ, appearing on equation (5*a*) is determined by using the gross mass balance for the closed system given by

$$\int_{-1/2}^{1/2} \bar{U}(y)\, dy = 0 \tag{6d}$$

Nomenclature

a = wave number in x-direction, dimensionless
c_p = constant-pressure specific heat of water
D = operator, $\frac{d}{dy}$
$\hat{e}_x$ = unit vector along x-axis
g = acceleration of gravity
Gr = Grashof number, $\gamma g \Delta T L^3/\nu^2$
H = height of the slot
k = thermal conductivity of water
L = width of the slot
p' = dimensionless perturbed pressure; $\hat{p}/\left(\frac{\mu u_0}{L}\right)$
$\bar{p}$ = dimensionless base flow pressure: $\bar{P}/\left(\frac{\mu u_0}{L}\right)$
Pr = Prandtl number; $c_p \mu/k$
Ra = Rayleigh number Gr•Pr
S = wave speed in x-direction
t = time
T = temperature, °C
$\hat{T}$ = perturbed temperature
$T_{\max}$ = temperature of water at maximum density (= 3.98 °C)
$\bar{T}$ = base flow temperature
T_i = temperature of the wall, i = 1,2
T_0 = mean temperature $(T_1 + T_2)/2$
u', v', w' = dimensionless perturbed velocity components $(\hat{u}, \hat{v}, \hat{w})/u_0$
u_0 = characteristic velocity; $\gamma g \Delta T L^2/\nu$
$\bar{u}$ = base flow velocity
$\bar{U}$ = dimensionless base flow velocity; $\bar{u}/u_0$
X, Y, Z = Cartesian coordinates with Z measured normal to the plane of paper
x, y, z = $(X, Y, Z)/L$

Greek Symbols

α = thermal diffusivity
β_i = coefficients in equation (4), $(i = 1, 2, 3)$
γ = coefficient of thermal expansion of water; equation (7*a*)
Θ' = dimensionless perturbed temperature $T'/(T_1 - T_2)$
$\bar{\Theta}$ = dimensionless base flow temperature $(\bar{T} - T_2)/(T_1 - T_2)$
ν = kinematic viscosity
ρ = density of water
ρ_0 = density of water at the mean temperature
$\rho_{\max}$ = maximum density of water
τ = dimensionless time; $\tau = \nu t/L^2$

Subscript

c = refers to critical state

Superscript

$-$ = base flow quantity
$'$ = perturbed quantity

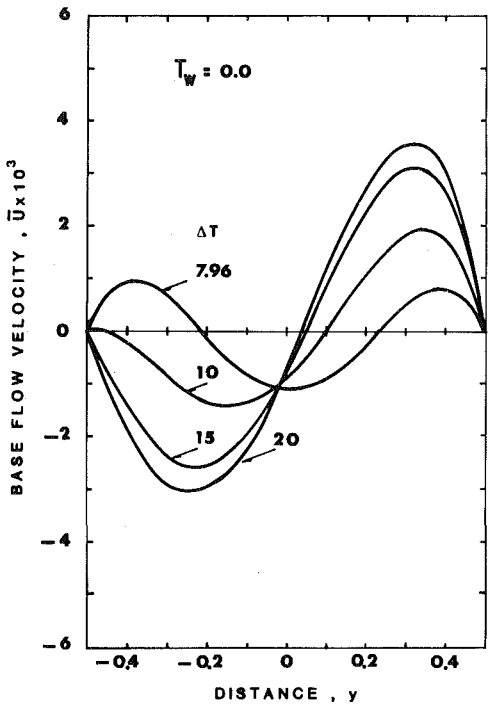

Fig. 2(*a*) The base flow velocity for T_w = 0.0°C

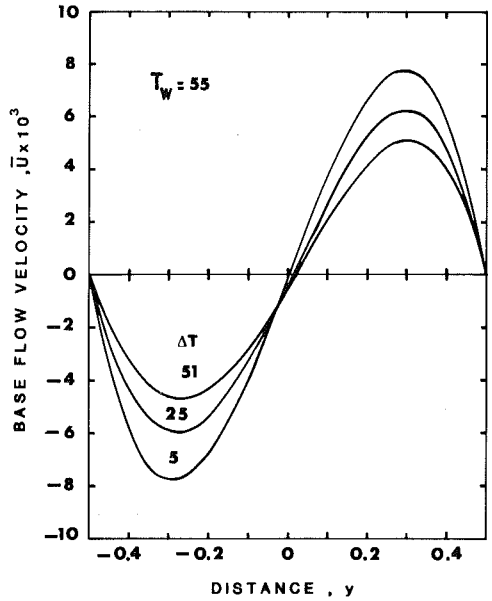

Fig. 2(*b*) The base flow velocity for T_w = 55°C

Here, $\bar{U}$ and $\bar{\Theta}$ are the dimensionless base flow velocity in the x-direction and temperature, respectively. The coefficient of thermal expansion, γ, for water is derived from equation (4) as

$$\gamma = -\frac{d(\rho/\rho_0)}{dT}\bigg|_p = 2\gamma_2\Delta T\left(1+\frac{\gamma_1}{2\gamma_2\Delta T}+\frac{3}{2}\frac{\gamma_3}{\gamma_2}\Delta T\right) \quad (7a)$$

where

$$\left.\begin{aligned}\gamma_1 &= \frac{\rho_{\max}}{\rho_0}[\beta_1+2\beta_2\Delta T_m+3\beta_3\Delta T_m^2]\\ \gamma_2 &= \frac{\rho_{\max}}{\rho_0}[\beta_2+3\beta_3\Delta T_m],\ \gamma_3 = \frac{\rho_{\max}}{\rho_0}\beta_3\end{aligned}\right\} \quad (7b)$$

and $\Delta T_m = T_2 - 3.98$, $\Delta T = T_1 - T_2$

The solution of the above coupled equations (5) and (6) is straightforward and the base flow temperature and velocity are determined as

$$\bar{\Theta}_{(y)} = y + \tfrac{1}{2} \quad (8)$$

$$\bar{U}_{(y)} = \lambda_{15}y^5+\lambda_{14}y^4+\lambda_{13}y^3+\lambda_{12}y^2+\lambda_{11}y+\lambda_{10} \quad (9)$$

where

$$\begin{aligned}\lambda_1 &= -(1+3\frac{\gamma_3}{\gamma_2}\Delta T)/(1+\frac{\gamma_1}{2\gamma_2\Delta T}+\frac{3}{2}\frac{\gamma_3}{\gamma_2}\Delta T),\\ \lambda_2 &= \left(\frac{3}{2}\frac{\gamma_3}{\gamma_2}\Delta T\right)/\left(1+\frac{\gamma_1}{2\gamma_2\Delta T}+\frac{3}{2}\frac{\gamma_3}{\gamma_2}\Delta T\right)\\ \lambda_{10} &= (\lambda_1+\lambda_2)/1920, \lambda_{11} = (\tfrac{1}{2}\lambda_1+\frac{11}{40}\lambda_2+1)/24\\ \lambda_{12} &= -(\lambda_1+\lambda_2)/80, \lambda_{13} = -(0.5\lambda_1+0.25\lambda_2+1.0)/6\\ \lambda_{14} &= (\lambda_1+\lambda_2)/24, \lambda_{15} = -\lambda_2/60\end{aligned} \quad (10)$$

The dimensionless base flow velocity profile, $\bar{U}(y)$, is shown in Figs. 2 for selective wall temperature combinations used in this study.

The Stability Analysis. We consider the total quantities slightly perturbed as

$$F(\tau,x,y,z) = \bar{F}(y) + F'(\tau,x,y,z) \quad (11)$$

where $\bar{F} = \bar{U}$, $\bar{\Theta}$, etc. denote the base flow quantities and $F' \equiv u'$, v', w', Θ', etc., the dimensionless perturbed quantities. The linearized equations governing the initial decay or growth of the disturbances are obtained with the conventional approach by introducing equation (11) into the system of equations (1–4), subtracting the base flow equations, and neglecting the perturbation terms of second and higher orders. A two-dimensional system of disturbances in x-y plane is considered, the dependence of the perturbation quantities on x, y, and τ is taken as a superposition of the Fourier modes of the form

$$F'(\tau,x,y) = F^*(y)\exp(iax+\sigma\tau) \quad (12)$$

where, $F = p,u,v,w$ or Θ, "a" is the wavenumber in the x-direction, and the complex wave frequency, σ, is given by

$$\sigma = \sigma_r + i\sigma_i \quad (13)$$

and the wavespeed is defined as

$$S = -\sigma_i/a\mathrm{Gr} \quad (14)$$

The solution (12) is introduced into the linearized equations and the variables p^*, u^*, w^* are eliminated among the resulting expressions and the stream function ψ^* replaced v^* through the relation $v^* = -ia\psi^*$. The following perturbation equations are obtained.

$$\sigma(D^2-a^2)\psi^* = [(D^2-a^2)^2 - ia\mathrm{Gr}\{\bar{U}(D^2-a^2) - D^2\bar{U}\}]\psi^* + D[\lambda(y)\theta^*] \quad (15a)$$

$$\sigma\Theta^* = ia\mathrm{Gr}D\bar{\Theta}\psi^* + [\mathrm{Pr}^{-1}(D^2-a^2) - ia\mathrm{Gr}\bar{U}]\Theta^* \quad (15b)$$

with the boundary conditions

$$\Theta^* = \psi^* = D\psi^* = 0 \quad \text{at} \quad y = \pm\tfrac{1}{2} \quad (15c)$$

Here, the function $\lambda(y)$ results from the nonlinearity of the density-temperature relation of water and is defined as

$$\lambda(y) = (1+0.5\lambda_1+0.25\lambda_2) - (\lambda_1+\lambda_2)y + \lambda_2 y^2 \quad (15d)$$

The parameters which control the stability problem in the above system of equations (15) are the Grashof number, Gr, Prandtl number, Pr, wavenumber, a, and the coefficients, λ_1 and λ_2, which result from the nonlinearity of the density-temperature relation. For certain combinations of these parameters, the real part of σ becomes zero, and the neutral

state of stability occurs; marking the change over from the conduction regime to the transition regime. It is to be noted that the limiting case for $\lambda_1 = \lambda_2 = 0$ corresponds to the linear density problem.

Disturbances Energy Balance. To study the driving forces and mechanisms of disturbances at the critical points, we applied a power integral method used by Stuart [14] to study the nonlinear mechanics of hydrodynamic stability and later adapted by Bergholz [15] to calculate the relative magnitudes of the energy sources and sinks of the disturbances. Since we are interested only in the driving forces, the method is applied on the momentum equation. In this method, equation (15*a*) is multiplied by $\hat{\psi}$, the complex conjugate of ψ^*, integrated over the region $(-\frac{1}{2}, \frac{1}{2})$ and the physically meaningful result is obtained by considering only the real part of the resulting expression. That is (see the appendix for the details)

$$\sigma_r E = \mathrm{Gr} R_1 + R_2 + R_3 \tag{16}$$

where

$\sigma_r E$ is time rate of growth of the disturbance kinetic energy, E

$\mathrm{Gr} R_1$ represents the rate of transfer of kinetic energy from the mean flow to the disturbances due to Reynolds stress (shear forces)

R_2 represents the rate of transfer of kinetic energy to the disturbance due to buoyancy forces

R_3 represents the rate of viscous dissipation of energy of the disturbance and is always negative

The eigenvalue problem defined by equations (15) can be solved by the Galerkin Method as now described. Following Chandrasekhar and Reid [16], the solutions for $\psi^*(y)$, and $\Theta^*(y)$, that satisfy the boundary conditions (15*c*) are taken in the form

$$\psi^*(y) = \sum_{m=1}^{\infty} a_m C_m(y) + b_m S_m(y) \tag{17a}$$

$$\Theta^*(y) = \sum_{m=1}^{\infty} d_m \sin(2m\pi y) + e_m \cos[(2m-1)\pi y] \tag{17b}$$

where the even functions $C_m(y)$ and the odd functions $S_m(y)$ are those discussed by Harris and Reid [17] and the coefficients a_m, b_m, d_m and e_m are in general complex. Equations (17*a*) and (17*b*) are introduced into equations (15*a*) and (15*b*). The expression resulting from equation (15*a*) is multiplied first by C_n and then by S_n, and for each case integrated over the region. Similarly, the expression resulting from equation (15*b*) is multiplied first by $\sin(2n\pi y)$ and then by $\cos[(2n-1)\pi y]$, and for each case integrated over the region. This procedure leads to an eigenvalue problem for the determination of Gr, and the resulting equations are written in the matrix form as

$$\sigma A X = B X \tag{18}$$

In this equation $X \equiv [a_m, b_m, d_m, e_m]^T$ is the transpose of the coefficient vector; A and B are $4N \times 4N$ matrices, with A real and symmetric, and B complex, arising from the orthogonalization, and N is the number of terms considered in approximating the eigenfunctions given by equations (17). The elements of A and B are given in the Appendix. The matrix equation (18) was solved by using International Mathematical and Statistical Libraries, IMSL [18], and the neutral stability curves were constructed for each given value of T_1 and T_2. Each point on such curves was obtained by applying a secant method of iteration to Gr with "a" fixed by satisfying the requirement that the real part of the highest eigenvalue of the matrix equation (18) equals zero within a specified error of $\pm$ 0.25 for the Grashof number. In solving equation (18), functions (17) were approximated by four to eight terms, and a convergence criteria less than 0.5 percent is satisfied in the determination of the actual neutral Grashof number.

To carry out the computations, the Prandtl number appearing in equation (15*b*) was evaluated at the mean temperature in the slot determined from

$$T_0 = (T_1 + T_2)/2 \tag{19}$$

The specific heat, $c_p(T)$, and the thermal conductivity, $k(T)$, of water were obtained from the data given by Perry [13] and curve fitted by a least squares method to form cubic polynomials as

$$c_p(T) = C_0 + C_1 T + C_2 T^2 + C_3 T^3 \tag{20}$$

$$k(T) = K_0 + K_1 T + K_2 T^2 + K_3 T^3 \tag{21}$$

and the coefficients in equations (20) and (21), for the temperature range 0–55°C, are, $C_0 = 0.10078549$, $C_1 = -0.80088538 \times 10^{-3}$, $C_2 = 0.234867 \times 10^{-4}$, and $C_3 = -0.23198415 \times 10^{-6}$ with standard error of 0.91×10^{-4}; and $K_0 = 0.56584878$, $K_1 = 0.19374081 \times 10^{-2}$, $K_2 = -0.27256 \times 10^{-5}$ and $K_3 = -0.9279525 \times 10^{-7}$, and the standard error 0.41×10^{-3}. The temperature dependence of viscosity, $\mu(T)$, of water is taken as [13]

$$\mu(T) = [2.1482\{(T-8.435) + \sqrt{8078.4 + (T-8.435)^2}\} - 120]^{-1} \tag{22}$$

In equations (20), (21), and (22), T is in degree centigrade, c_p in Kcal/kg.°C, k in w/m.°C and μ in gm/cm.s.

Results and Discussion

The effect of nonlinear density stratification on the critical Grashof number, critical wave number and wavespeed are investigated. The study was directed to uncover the behavior of the natural convection with the maximum density layer appearing: (*a*) within the water region, (*b*) at the boundary, and (*c*) outside the water region. Case (*a*) was studied by maintaining T_2 at 0°C and changing T_1 up to 20°C; case (*b*) was achieved by maintaining T_2 at 3.98°C and changing T_1 up to 55°C. Finally, case (*c*) was investigated by maintaining T_1 at 55°C, 35°C, or 25°C and varying T_2 down to 3.98°C. Since Pr and γ depend on T_1 and T_2, the neutral states of stability for this study are no longer dependent on the Prandtl number, but, unlike the linear density problem [4], depend on the combination of T_1 and T_2.

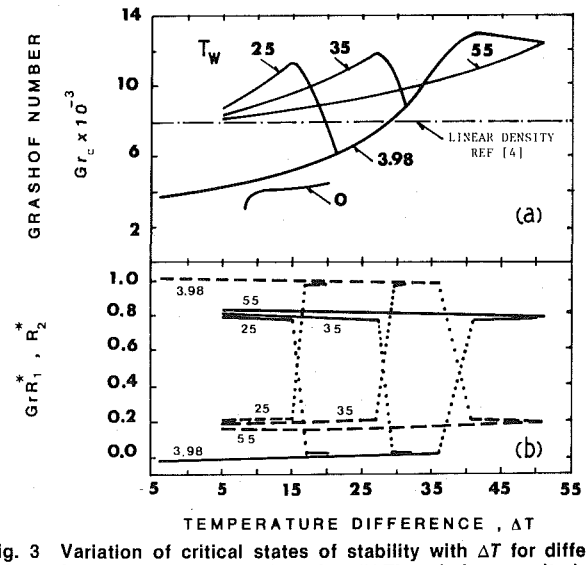

Fig. 3 Variation of critical states of stability with ΔT for different values of T_W: (*a*) critical Grashof number; (*b*) The relative magnitudes of buoyancy; _ _ _, and Shear forces; ___, contributions to the kinetic energy of disturbances

Table 1 Values of critical parameters

ΔT	a_c	$S_c \times 10^3$	Gr_c	Pr	GrR_1^*	R_2^*
			$T_w = 0°C$ (case (*a*))			
7.96	2.35	1.676	3129.0	11.51	0.00085	0.99915
10.0	2.2	2.233	4125.0	11.10	−0.00864	1.00864
15.0	2.0	3.243	4195.0	10.18	−0.01099	1.01099
20	1.8	3.715	4508.0	9.38	−0.00678	1.00678
			$T_w = 3.98°C$ (case (*b*))			
51.02	2.80	0.344	12378.0	5.48	0.78666	0.21334
41.02	2.82	0.344	12926.0	6.20	0.77814	0.22296
36.02	0.85	4.484	11494.0	6.61	0.03177	0.96823
30.0	1.1	4.525	8422.0	7.18	0.01948	0.98052
20	1.4	4.402	5994.0	8.3	0.00520	0.99480
15	1.5	4.458	5318.0	8.95	0.00052	0.99948
10	1.65	4.354	4745.0	9.70	−0.00579	1.00579
5	1.80	4.257	4295.0	10.54	−0.01159	1.01159
− 3.98	2.0	4.155	3659.0	12.38	−0.01686	1.01686
			$T_w = 25°C$ (case (*c*))			
5	2.75	≃ 0	8731.0	6.52	0.80064	0.19940
10	2.76	0.159	9828.0	6.98	0.79621	0.20379
15	2.78	0.251	11283.0	7.48	0.78764	0.21065
17	0.85	4.958	10104.0	7.70	0.02661	0.97339
20	0.95	4.646	7619.0	8.04	0.02322	0.97678
			$T_w = 35°C$ (case (*c*))			
5	2.76	≃ 0	8317.0	5.10	0.81176	0.18653
10	2.76	0.089	8861.0	5.41	0.80814	0.18990
15	2.76	0.144	9529.0	5.75	0.80310	0.19479
20	2.78	0.205	10358.0	6.12	0.79778	0.20223
25	2.78	0.274	11392.0	6.52	0.78695	0.21225
27	2.78	0.303	11881.0	6.70	0.78017	0.21098
30	0.9	4.646	10173.0	6.98	0.02859	0.97141
31.02	1.0	4.566	8863.0	7.07	0.02507	0.97495
			$T_w = 55°C$ (case (*c*))			
5	2.78	0.00	8072.0	3.4	0.83228	0.16729
10	2.78	0.043	8320.0	3.6	0.82973	0.16976
25	2.78	0.131	9296.0	4.12	0.82011	0.17989
35	2.8	0.204	10213.0	4.57	0.81614	0.18370
40	2.8	0.245	10779.0	4.82	0.80922	0.18868
45	2.8	0.289	11436.0	5.10	0.80050	0.19850
47	2.8	0.307	11729.0	5.22	0.79638	0.20262

The variation of the critical Grashof number, Gr_c, with the temperature difference, ΔT, and T_w (T_w is either T_1 or T_2) is illustrated in Fig. 3(*a*). For $T_w = 0°C$, which corresponds to case (*a*), the larger is the ΔT the more stable is the flow. In this curve, the point at $\Delta T = 7.96$ corresponds to the situation in which the maximum density occurs at the midlayer in the water; clearly, the flow is most unstable at this particular condition. Case (*b*) is characterized with the curve for $T_w = 3.98°C$. Decreasing ΔT stabilizes the flow until $\Delta T = 41°C$ is reached; but, further reduction in ΔT destabilizes the flow. The curves marked $T_w = 25$, 35, and 55°C corresponds to case (*c*). With T_w equal to 25°C, increasing ΔT stabilizes the flow until $\Delta T = 15°C$ is reached, and further increase in ΔT destabilizes it. The same behavior is observed for the curve marked $T_w = 35$ until $\Delta T = 27°C$ is reached. In the case of $T_w = 55°C$, increasing ΔT continues to stabilize the flow. A comparison of the results for the above three cases reveals that case (*a*) is the most unstable situation. The behavior of the critical Grashof number shown in Fig. 3(*a*) will be explained later on with a comparison of the corresponding results in Fig. 3(*b*).

The variation of the critical wavespeed, S_c, with ΔT for the three different cases discussed previously is illustrated in Fig. 4. The curve for $T_w = 0$ (i.e., case (*a*)) the instability sets in as traveling wave moving upwards (i.e., against the gravity) with a wavespeed higher than the maximum velocity of the corresponding base flow. As ΔT increases, the wavespeed approaches the corresponding maximum base flow velocity. The curve for $T_w = 3.98°C$ (i.e., case (*b*)) shows that the instability sets in as traveling wave drifting in the upward direction with a speed equal to the corresponding maximum base flow velocity, until the wavespeed exhibits a sudden drop to about one tenth of its value at $\Delta T \doteq 41°C$. Beyond $\Delta T = 41°C$, the wavespeed remains constant at a value much less than the corresponding maximum base flow velocity. The

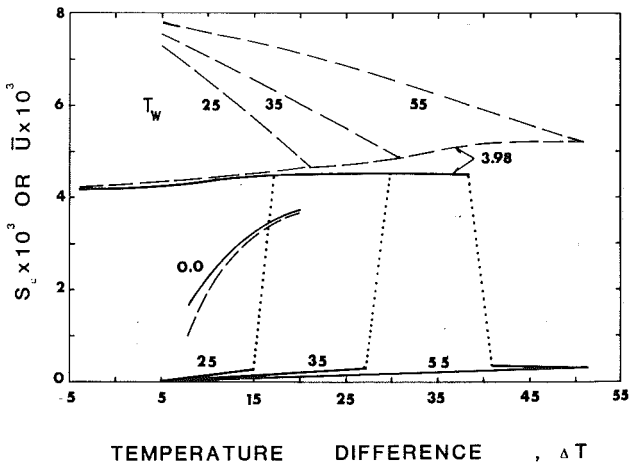

Fig. 4 The critical wavespeed for different values of T_W: --- maximum base flow velocity, $\bar{U}$; ___ wavespeed, S

curves $T_w = 25$, 35, and 55°C corresponds to the condition of case (*c*). For all three cases, the instability sets in as stationary wave for $\Delta T \leq 5°C$. The increase in ΔT will cause the stationary wave to move upwards in the direction opposite to gravity with a wavespeed much less than the corresponding maximum base flow velocity. As ΔT increases the curves for $T_w = 25°C$ and 35°C exhibit sudden jumps at $\Delta T = 15°C$ and 27°C, respectively, reaching to about ten times its magnitude before the sudden jump. It is well known that the critical wavespeed is less than the maximum velocity of the base flow for homogeneous, inviscid, parallel shear flows; then if the traveling wave exercises a speed equal or greater than the maximum base flow velocity, this should be due to the work of buoyancy forces which arise from the base flow temperature field.

A sampling of the values for the critical parameters for three cases considered above are listed in Table 1. The results in this table reveal that, for the case $T_w = 0°C$, the critical wave number, a_c, decreases as ΔT increases. In the case of $T_w = 3.98°C$, there is a sudden drop in a_c at $\Delta T = 41°C$; and as ΔT decreases below 41°C, a_c increases gradually. Finally the cases for $T_w = 25$ and 35°C exhibit a sudden drop for a_c to a one third of its value at $\Delta T = 15°C$ and 27°C, respectively; but for the case $T_w = 55°C$ there appears to be no significant change in the value of a_c with ΔT.

The computation of the kinetic energy balance was conducted to provide enough information to explain the behavior of the critical states of stability. In calculating the relative magnitudes of the energy terms, equation (16) was normalized by setting the rate of viscous dissipation term, R_3, equal to -1, thereafter, the sum $GrR_1^* + R_2^* - 1$ is zero, or very near zero, since $\sigma_r = 0$ at the critical points, where R_1^* and R_2^* are the relative magnitudes of R_1 and R_2 in relation to R_3, respectively. A sampling of GrR_1^* and R_2^* magnitudes at the critical points is also listed in Table 1. Since the nonlinear terms in density-temperature relationship appear only in the base flow velocity and the buoyancy term in equations (15), changing the values of the terms λ_1 and λ_2 resulting from the nonlinearity of temperature-density relation will affect the magnitudes of GrR_1^* and R_2^*. The effects of nonlinearity of density is very strong when the fluid region contains the maximum-density layer or its neighboring layers. As apparent from Figs. 2, the effect of the existence of the maximum density layer, whether it is within the fluid at the boundary or outside the fluid region, is to destroy the odd-symmetry of the base flow velocity encountered in linear-density problem [4]. Furthermore, the symmetry is restored if the effects of the maximum density layer is forced to vanish, by decreasing ΔT as is shown in Fig. 2(*b*).

In Fig. 3(*b*), the magnitudes of GrR_1^* and R_2^* are shown for different values of T_w. For $T_w = 3.98°C$, decreasing ΔT means that the fluid region will contain more layers closer to the maximum density layer, giving rise to the buoyancy forces term, R_2^* over the shear forces term GrR_1^*. As apparent from this figure, the disturbances for $\Delta T < 41°C$ derive most of their kinetic energy from the work of the buoyancy forces, while for $\Delta T > 41°C$, the main contributor to the disturbances kinetic energy is the act of the shear forces. For the cases of $T_w = 25°C$, 35°C, and 55°C, increasing ΔT will allow the fluid region to contain more layers closer to or to include the maximum-density layer, which will increase the role of R_2^* and decrease that of GrR_1^* as contributors to the kinetic energy of the disturbances. Other works like Bergholz [15] and Hart [3] found that, in the conduction regime, increasing the kinetic energy contributed by the buoyancy forces destablized the flow. This situation occurs at $\Delta T = 15$ for $T_w = 25$ and at $\Delta T = 27$ for $T_w = 35$, which corresponds to the other wall being kept at 10°C and 8°C, respectively. If T_w is increased above 35°C, then we expect that the disturbances will derive most of their energy through the work of the buoyancy forces if the other wall temperature is kept at a

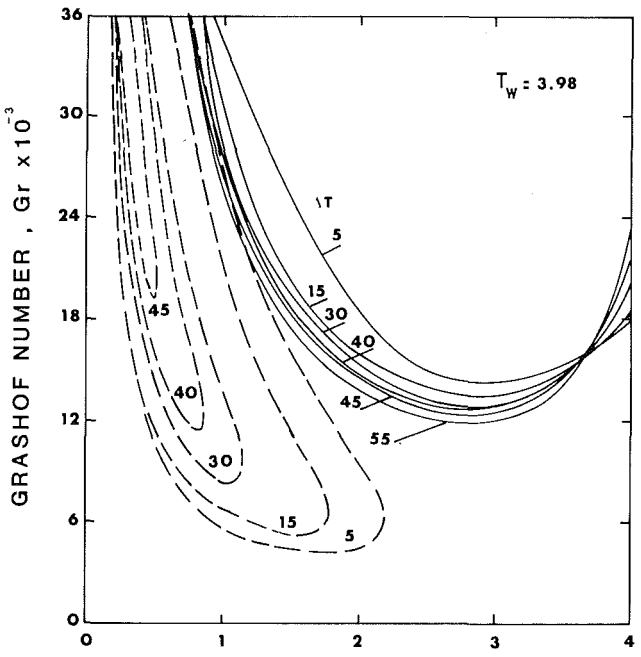

Fig. 5(*b*) Neutral state of stability for $T_w = 3.98°C$

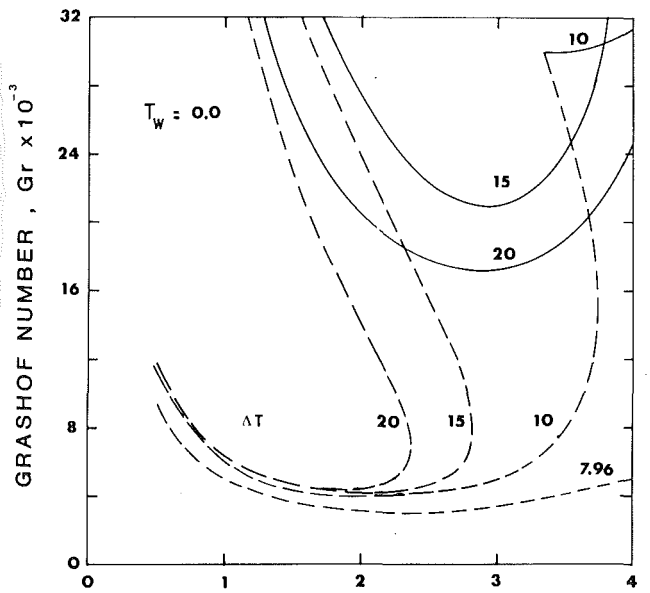

Fig. 5(*a*) Neutral state of stability for $T_w = 0°C$

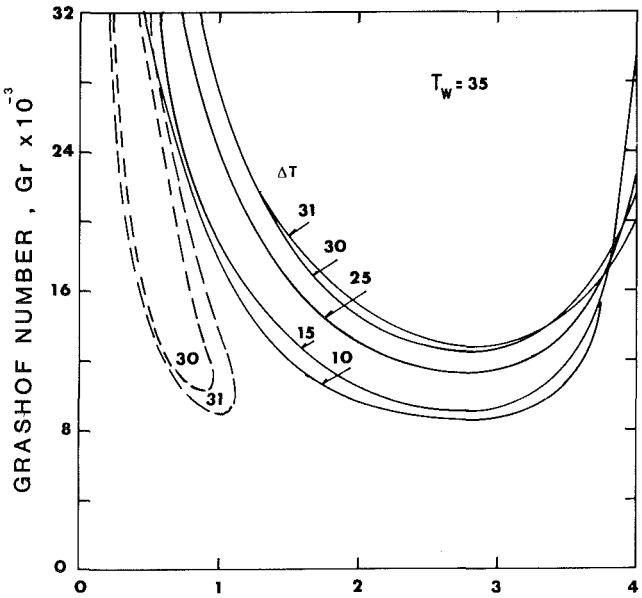

Fig. 5(*c*) Neutral state of stability for $T_w = 35°C$

temperature closer to T_{max}, until T_w reaches a value such that ρ_{max} has little effect. At $T_w = 55°C$, for all ΔT, the disturbances gain most of their kinetic energy from the shear forces. For $T_w = 0°C$, we found that the buoyancy forces are the only contributors to the disturbances kinetic energy. In their study of the buoyancy driven instabilities, Gill and Davey [19] found two minima neutral stability curves at low Prandtl number. They showed that the low-wave number minimum is relevant to the thermal disturbances and disappeared when the buoyancy effects were neglected. Therefore, high-wave number minimum corresponds to hydrodynamic stability arising from the velocity filled of the base flow (i.e., shear forces).

The above conclusion of Gill and Davey [19] can be utilized to analyze the relative contributions of the buoyancy and shear forces from the behavior of the neutral stability curves in addition to that obtained from the energy balance calculations. In Figs. 5(*a*)-5(*c*), the neutral stability curves resulting from the buoyancy (low-wave number minimum) are shown with dashed lines and those resulting from Reynolds stress (high-wave number minimum) are shown with solid lines. Figure 5(*a*), which is for $T_w = 0°C$, shows that the low-wave number minimum is lower than the high-wave number minimum for all ΔT, thus the instabilities are buoyancy derived. In the case of Fig. 5(*b*), which is for $T_w = 3.98°C$, there is a shift in the relative position of the two minima such that the low-wave number minimum is lower than the high-wave number minimum for $\Delta T < 40°C$, but it is higher for $\Delta T > 40°C$; eventually the low-wave number minimum disappears for $\Delta T = 51°C$. Therefore, we conclude that for $\Delta T < 40°C$ the disturbances are due to the work of the buoyancy forces and for $\Delta T > 40°C$ thus are shear deriven disturbances. In Fig. 5(*c*), the neutral curves are shown for $T_w = 35°C$; as ΔT decreases the low-wave number minimum shifts its position upwards while the high-wave number minimum moves downwards. The transition from low-wave number minimum to high-wave number minimum occurs at $\Delta T = 27°C$, as shown previously in Table 1, i.e., for $\Delta T \leq 27°C$ the instabilities are due to the shear forces, while $\Delta T > 27°C$ the instabilities result from the buoyancy forces.

No experimental data appears to be available for the nonlinear density problem considered in this study in order to compare the results of the analytical solution. Therefore, only the limiting cases in which the nonlinearities are weak, that is λ_1 and λ_2 tend to zero, are compared with some of the available linear density problems. Those limiting cases all belong to the category (*c*), for which the maximum density layer is outside the water region. For example, in Table 1, the cases (*c*) for $T_w = 25$, 35, and 55°C when $\Delta T = 5°C$, correspond to, respectively, $\lambda_1 = -0.18483, -0.10173, -0.05128$, and $\lambda_2 = -0.01266, -0.00959, -0.004315$. A comparison of these results with those of Korpela et al. [4] and Vest and Arpaci [5] for $Gr_c \cong 7989$, $a_c = 2.65$ and $Pr < 12.7$ shows that the present results yield a little higher values for the critical Grashof and wave numbers; this is expected since λ_1 and λ_2 are not zero.

Another effect of the nonlinear density stratification is that the single neutral stability curve is no longer applicable for all Prandtl numbers less than 12.7, in contrast to the linear density problem results presented in references [4,5]. As shown in Figs. (5*a*), (5*b*), and (5*c*), there are several neutral stability curves in the range of Prandtl number from 3.4 to 12.38.

Acknowledgment

This work was supported, in part, by the Scientific Affairs Division of NATO, through NATO Research Grant No. 043.82.

References

1 Eckert, E. R. G., and Carlson, W. O., "Natural Convection in an Air Layer Enclosed Between Two Vertical Plates With Different Temperatures," *International Journal of Heat and Mass Transfer*, Vol. 2, 1961, pp. 106-120.

2 Elder, J. W., "Laminar Free Convection in a Vertical Slot," *Journal of Fluid Mechanics*, Vol. 23, 1965, pp. 77-98.

3 Hart, J. E., "Stability of the Flow in a Differentially Heated Inclined Box," *Journal of Fluid Mechanics*, Vol. 47, 1971, pp. 547-576.

4 Korpela, S. A., Gözüm, D., and Baxi, C. B., "On the Stability of the Conduction Regime of Natural Convection in a Vertical Slot," *International Journal of Heat and Mass Transfer*, Vol. 16, 1973, pp. 1683-1690.

5 Vest, C. M., and Arpaci, V. S., "Stability of Natural Convection in a Vertical Slot," *Journal of Fluid Mechanics*, Vol. 36, 1969, pp. 1-15.

6 Veronis, G., "Penetrative Convection," *Astrophysical Journal*, Vol. 137, 1963, pp. 641-663.

7 Sun, Zu-Shung, Tien, C., and Yen, Yin-Chao, "Thermal Instability of a Horizontal Layer of Liquid With Maximum Density," *AICHE Journal*, Vol. 6, 1969, pp. 910-915.

8 Legros, J. C., Londree, D., and Thomaes, G., "Bénard Problem in Water Near 4 °C," *Physica*, Vol. 72, 1974, pp. 410-414.

9 Yen, Yin-Chao, "Free Convection Heat Transfer Characteristics in a Melt Water Layer," ASME *Journal of Heat Transfer*, Vol. 102, 1980, pp. 550-556.

10 Vanier, C. R., and Tien, C., "Further Work on Free Convection in Water at 4 °C," *Chem. Engng. Sci.*, Vol. 22, 1968, pp. 1747-1751.

11 Goren, S. L., "On Free Convection in Water at 4 °C," *Chem. Engng. Sci.*, Vol. 21, 1966, pp. 515-518.

12 Merker, G. P., and Grigull, U., "Onset of Convection in a Semi-Infinite Layer With Nonlinear Density-Temperature Relation," *The 6th International Heat Transfer Conference*, Toronto, Canada, 7-11, Aug. 1978.

13 Perry, J. H., "*Chemical Engineers Handbook*," 4th ed., McGraw-Hill, 1963.

14 Stuart, J. T., "On the Nonlinear Mechanics of Hydrodynamic Stability," *Journal of Fluid Mechanics*, Vol. 4, 1958, pp. 1-21.

15 Bergholz, R. F., "Instability of Steady Neutral Convection in a Vertical Fluid Layer," *Journal of Fluid Mechanics*, Vol. 84, 1978, pp. 743-768.

16 Chandrasekhar, S., Reid, W. H., "On the Expansion of Functions Which Satisfy Four Boundary Conditions," *Proc. U.S. Nat. Acad. Sci.*, Vol. 43, No. 5, May 15, 1957.

17 Harris, D. L., and Reid, W. H., "On Orthogonal Functions Which Satisfy Four Boundary Conditions," *Astrophysical Journal*, Suppl. Serv., Vol. 33, 1958, pp. 429-458.

18 IMSL, ed. 7, 1979, GNB Bldg., Houston, Texas.

19 Gill, A. E., and Davey, A., "Instabilities of a Buoyancy-Driven System," *Journal of Fluid Mechanics*, Vol. 35, 1969, pp. 775-798.

APPENDIX

The matrices A and B of the matrix equation (18) are written in the form

$$A = \begin{bmatrix} C & 0 & 0 & 0 \\ 0 & D & 0 & 0 \\ 0 & 0 & E & 0 \\ 0 & 0 & 0 & F \end{bmatrix}$$

$$B = \begin{bmatrix} GR & 0 & KR & LR \\ 0 & QR & SR & TR \\ 0 & 0 & WR & 0 \\ 0 & 0 & 0 & ZR \end{bmatrix}$$

$$+ ia\mathrm{Gr} \begin{bmatrix} GI & HI & 0 & 0 \\ PI & QI & 0 & 0 \\ 0 & VI & WI & XI \\ MI & 0 & YI & ZI \end{bmatrix}$$

where the elements of the submatrices are given by

$$
\begin{aligned}
C &= \langle \mathcal{L}C_m, C_n \rangle, D = \langle \mathcal{L}S_m, S_n \rangle, E = \langle \sin 2m\pi y, \sin 2n\pi y \rangle \\
F &= \langle \cos[(2M-1)\pi y], \cos[(2n-1)\pi y] \rangle \\
GR &= \langle \mathcal{L}^2 C_m, C_n \rangle, GI = -\langle \mathcal{L}_{\cdot} C_m, C_n \rangle \\
HI &= -\langle \mathcal{L}_{\cdot} S_m, C_n \rangle \\
KR &= \langle D[\lambda(y)\sin(2m\pi y)], C_m \rangle, LR = \langle D[\lambda(y)\cos((2m-1)\pi y)], Cn \rangle \\
PI &= -\langle \mathcal{L}_{\cdot} C_m, S_n \rangle \\
QR &= \langle \mathcal{L}^2 S_m, S_n \rangle, QI = -\langle \mathcal{L}_{\cdot} S_m, S_n \rangle \\
SR &= \langle D[\lambda(y)\sin 2m\pi y], S_n \rangle \\
TR &= \langle D[\lambda(y)\cos((2m-1)\pi y)], S_n \rangle \\
VI &= \langle D\bar{\Theta}S_m, \sin(2n\pi y) \rangle \\
WR &= \mathrm{Pr}^{-1}\langle \mathcal{L}\sin(2m\pi y), \mathrm{Sin}(2n\pi y) \rangle \\
WI &= -\langle \bar{U}\sin(2m\pi y), \sin(2n\pi y) \rangle \\
XI &= -\langle \bar{U}\cos((2m-1)\pi y), \sin(2n\pi y) \rangle \\
MI &= \langle D\bar{\Theta}\cos((2m-1)\pi y), \cos((2n-1)\pi y) \rangle \\
YI &= -\langle \bar{U}\sin(2m\pi y), \cos((2n-1)\pi y) \rangle \\
ZR &= \mathrm{Pr}^{-1}\langle \mathcal{L}\cos((2m-1)\pi y), \cos((2n-1)\pi y) \rangle \\
ZI &= -\langle \bar{U}\cos((2m-1)\pi y), \cos((2n-1)\pi y) \rangle
\end{aligned}
$$

The quantities in equation (16) are given as

$$R_1 = \Re \tfrac{1}{2} ia[\hat{a}_n \hat{b}_n] \begin{bmatrix} GI & HI \\ PI & QI \end{bmatrix} \begin{bmatrix} a_m \\ b_m \end{bmatrix}$$

$$R_2 = \Re \tfrac{1}{2}[\hat{a}_n \hat{b}_n] \begin{bmatrix} KR & LR \\ SR & TR \end{bmatrix} \begin{bmatrix} d_m \\ e_m \end{bmatrix}$$

$$R_3 = \Re \tfrac{1}{2}[\hat{a}_n \hat{b}_n] \begin{bmatrix} GR & 0 \\ 0 & QR \end{bmatrix} \begin{bmatrix} a_m \\ b_m \end{bmatrix}$$

where $\Re$ stands for real part of the expression, $\mathcal{L} = (D^2 - a^2)$, $\mathcal{L}_{\cdot} = [\bar{U}(D^2 - a^2) - D^2\bar{U}]$ and $\hat{a}_r$, $\hat{b}_r$ are the complex conjugate of a_r and b_r.

Natural Convection Correlations for Vertical Surfaces Including Influences of Variable Properties

A. M. Clausing
Associate Professor,
Department of Mechanical and Industrial Engineering,
University of Illinois at Urbana-Champaign,
Urbana, Ill. 61801
Mem. ASME

New correlations are presented for natural convective heat transfer from vertical isothermal surfaces in gases. The influences of variable properties are accounted for by using empirical equations which are of the general form $Nu = g(Ra) \cdot f(Ra, T_w/T_\infty)$. *The influence of the reference temperature at which the thermal properties are evaluated is also established. Comparisons with available data are made over a Rayleigh number range* $10^4 < Ra < 10^{12}$ *and a range in the surface-to-ambient temperature ratio of* $1 < T_w/T_\infty < 2.6$. *Five data sets, which represent over 200 test points, are examined.*

Introduction

A variety of theoretical expressions and correlations of experimental data have been derived for the prediction of heat transfer rates from vertical surfaces by natural convection to a surrounding fluid. Discrepancies exist between these correlations, however, which have not been fully resolved, especially in the turbulent regime. For example, Eckert and Jackson [1] proposed the following correlation for the average Nusselt number, Nu

$$\mathrm{Nu} = 0.021(\mathrm{Ra})^{0.4},\ 10^{10} < \mathrm{Ra} < 10^{12} \tag{1}$$

where Ra is the Rayleigh number—the product of the Grashof and Prandtl numbers, GrPr. Equation (1) is based on Eckert and Jackson's theoretical results and the experimental data of Saunders [2] and Griffiths and Davis [3]. Kutateladze [4] and McAdams [5] proposed the correlation

$$\mathrm{Nu} = 0.13\ \mathrm{Ra}^{1/3},\quad \begin{matrix}\mathrm{Ra} > 2\cdot 10^7\ [4] \\ 10^9 < \mathrm{Ra} < 10^{12}\ [5]\end{matrix} \tag{2}$$

whereas Bayley [6] found that both theory and experiment gave the empirical equation

$$\mathrm{Nu} = 0.10\ \mathrm{Ra}^{1/3},\ 2\cdot 10^9 < \mathrm{Ra} < 10^{12} \tag{3}$$

Warner and Arpaci [7, 8] found good agreement between their data and equation (3). At $Ra = 10^{10}$, correlations (1) and (3) give essentially the same result, which lies 30 percent below that given by equation (2). At $Ra = 10^{12}$, correlations (1) and (2) give essentially the same result, which lies 30 percent above the respective value from equation (3). The questions to be answered are: How can these differences over this relatively narrow range of Ra be explained? Are there undefined quantities which need to be taken into account?

Clausing and Kempka [9] recently showed that one significant source of discrepancy is the influences of property variations, i.e., those other than the essential density difference which gives rise to the free-convective flow. New correlations are given in this paper, which include the effects of property variations for the laminar, transitional, and turbulent regimes. The influence of the reference temperature, which is used in the evaluation of thermophysical properties, is also shown for the turbulent regime. Only gases and isothermal surfaces are considered.

Another source of significant discrepancy is the thermophysical properties which are used in reducing the dimensional experimental data to the dimensionless variables, Nu and Ra. For example, the thermal conductivity, k, of air at a temperature of 316 K and a pressure of 0.1013 MPa, which is used by Saunders [2], 0.0239 W/m-K, lies 13 percent below the value commonly accepted today, 0.0274 W/m-K (see Clausing [10] for a discussion of thermophysical properties of gases and the properties used in this study at standard pressure). Saunders's natural convection data were taken at pressures between 0.043 and 67.7 atm. The elevated pressure property data, which were published in 1932 and are reported in Table 2 of [2], also differ significantly from those used in this study [11]. Even data given in heat transfer textbooks published in the 1980s contain thermal conductivity data for air at standard pressure which differ at high temperatures by as much as 27 percent (see Clausing [10]). Such differences, interpolation errors, etc., give rise to significant discrepancies in the results when reported in dimensionless form. On the other hand, if the dimensional experimental data are reported, appreciably more meaningful comparisons can be made. For example, Saunders's raw data are tabulated [2] and appear to be of exceptional quality. Thus, these data after reduction with consistent thermophysical properties provide excellent tests of proposed correlations. However, this is a difficult task since most of Saunders's data are at pressures significantly different than one atmosphere. Consequently, all of the published comparisons with the Saunders's data (see, e.g. [1, 5, 6, 7, 8]) appear to have utilized the dimensionless parameters.

Other significant sources of discrepancies between the various data sets, and even within a given data set, are:

1 Radiative heat transfer. For example, the estimate of the radiative heat transfer which is provided by Griffiths and Davis [3] exceeds the convective heat transfer for most of their data. Eighteen and 20 percent corrections are reported by Vliet and Ross [12]. Warner [7] states: "Since insulation and radiation losses were difficult to calculate or measure precisely. . .these were accounted for by obtaining a regression fit of the laminar range heat flow data to the laminar theory." Quantitative values were not supplied.

2 Drafts or currents due to extraneous sources. For example, Warner [7] states: "It was found that the ambient turbulence caused by workaday laboratory operations had a large effect upon the air in the test space. To eliminate this, the entire apparatus was isolated from the rest of the laboratory by a special partition, and readings were taken when disturbances were at a minimum." Vliet and Ross [12] state: ". . .standard window screen was installed to minimize the effects of ambient room disturbances. . .and tests were conducted after, or prior to, normal working hours while the air in the room was thermally unstratified and when convective disturbances in the room were minimal."

3 A stratified environment. For example, Cheesewright [13] states (regarding comparisons of his laminar data with

Contributed by the Heat Transfer Division for publication in the JOURNAL OF HEAT TRANSFER. Manuscript received by the Heat Transfer Division April 26, 1982.

theoretical results and other experimental results): "the discrepancy is due to the existence of small vertical temperature gradients in the laboratory during the experiments" (Cheesewright [3, 10]).

4 Three-dimensional effects or surface curvature if vertical cylinders are used.

5 Conductive heat transfer.

New correlations are proposed which are not biased by these influences. Comparisons between these correlations and available data are given in the section entitled, Further Comparisons.

Correlations

The dimensionless groups which govern the heat transfer by natural convection from an isothermal vertical plate of infinite width are deduced from a dimensional analysis of the general, compressible form of the governing equations. The simplifying assumptions are: a laminar flow of a Newtonian fluid, a perfect gas, negligible gas absorption, negligible viscous dissipation, and negligible work done by compression. The dependent variables, c_p/c_{pr}, μ/μ_r and k/k_r, are general functions of only the dimensionless temperature, T/T_r. The average Nusselt number with these assumptions is a function of

$$\mathrm{Nu} = f(\mathrm{Gr}, \mathrm{Pr}, T_w/T_\infty) \tag{4}$$

Including the additional group, T_w/T_∞, enables one to arrive at equation (4) without making the Boussinesq approximation.

The influence of variable properties is taken into account in equation (4) with the parameter, T_w/T_∞. This is contrasted with commonly used procedures—the reference temperature method and the property ratio method. The correlations which are derived are of the form

$$\mathrm{Nu} = g(\mathrm{Ra}) \cdot f(\mathrm{Ra}, T_w/T_\infty) \tag{5}$$

where $g(\mathrm{Ra})$ is defined as the constant property correlation, i.e., $f(\mathrm{Ra},1) = 1$. Although equation (5) is similar to the property ratio method, the stringent constraint of having to account for variable property influences with a function of a single property ratio is removed. The function, f, is, of course, dependent on the reference temperature which is used in the evaluation of Nu and Ra. All properties in this paper, including β, are based on the film temperature, $T_f \equiv (T_w + T_\infty)/2$, unless indicated otherwise with the appropriate subscript.

The data which are used in this study are for free convection in air or gaseous nitrogen. Hence, the influence of the Prandtl number and the ability to consider the single parameter, Ra, in place of the two parameters, Gr and Pr, is not resolved. Since the variations of the thermophysical properties of liquids with temperature are drastically different than those for gases, the derived functions, f, are not applicable to liquids.

The correlations which follow are based on data obtained in a sealed, cryogenic test facility at the University of Illinois at Urbana-Champaign (UIUC). It is a variable ambient temperature facility which can operate with test section temperatures between 80 and 350 K. The cryogenic tunnel provides a means of obtaining large Grashof numbers. The variable, T_∞, feature enables one to cover large ranges of the relevant dimensionless groups, T_w/T_∞ and Gr, with a single model without the results being masked by the radiative mode. The influences of T_∞ and ΔT on Ra and the advantages of the use of a cryogenic environment are described in detail in [14]. The UIUC facility, the model, and experimental procedure are described in [9].

All of the sources of discrepancy, which are discussed in the previous section, are virtually negligible quantities in the UIUC cryogenic facility except, of course, the influence of variable properties—the focus of the investigation. Specifically:

1 The properties of gaseous nitrogen and air (the working fluids) are accurately known (see [10]).

2 Drafts are eliminated in the sealed, cryogenic chamber.

3 Radiative heat transfer is drastically reduced, especially in the turbulent regime where $T_w < 228$ K (the model is polished aluminum).

4 The transient technique which is used in the determination of h reduces both conduction heat transfer and the influences of stratification to negligible quantities.

5 The cylindrical geometry eliminates edge effects. Since $D/(k\ h^{-1})$ is sufficiently small, curvature influences are negligible.

Consider next the specific functions, g and f, for the regimes of interest. Clausing and Kempka [9] found that if the properties were evaluated at the film temperature, all data in the laminar regime lie within 2 percent of the Schmidt-Beckmann correlation [5],

$$\mathrm{Nu} = 0.52\ \mathrm{Ra}^{1/4},\ \mathrm{Ra} < 3.8 \cdot 10^8 \tag{6}$$

that is, the function, f, is unity in the laminar regime if $T_r = T_f$.

In the turbulent regime, Clausing and Kempka [9] used the Bayley correlation, equation (3), for the constant property correlation, $g(\mathrm{Ra})$, and then proceeded to deduce the variable property influence, f. A closer examination of the four data points at the minimum T_w/T_∞, 1.12, shows that they lie slightly below the Bayley correlation. These data would lie even further below this correlation if an adjustment could be made for T_w/T_∞ being greater than unity. Although the 1/3 exponent of the Rayleigh number fits the data well (see Fig. 6 of [9]), it was concluded that the Bayley correlation does not accurately represent the limit—the constant property correlation, $g(\mathrm{Ra})$. Thus, a new constant property correlation was generated solely from the UIUC data.

The 1/3 exponent was accepted, and the conclusion that the variable property influence could be accurately represented by a second-degree polynomial in T_w/T_∞ was adapted. A least

Nomenclature

c_p = specific heat, kJ/kg − K
f = defined by equation (5)
g = defined by equation (5) or gravitational constant, m/s^2
h = convective heat transfer coefficient, W/m^2 − K
k = thermal conductivity, W/m − K
L = characteristic vertical length, m
T = temperature, K
β = coefficient of thermal expansion, 1/K
ΔT = $(T_w - T_\infty)$, K
μ = dynamic viscosity, Kg/m − s
ρ = density, kg/m^3

Subscripts

f = properties based on film temperature, $T_f = (T_w + T_\infty)/2$
l = laminar/transitional boundary
r = reference temperature, T_f, T_w, or T_∞
t = transitional/turbulent boundary
tr = transitional regime
w = wall
∞ = ambient fluid

Dimensionless Groups

Gr = Grashof number, $\rho^2 g\beta(T_w - T_\infty)L^3/\mu^2$
Nu = Nusselt number, hL/k
Pr = Prandtl number, $\mu c_p/k$
Ra = Rayleigh number, GrPr

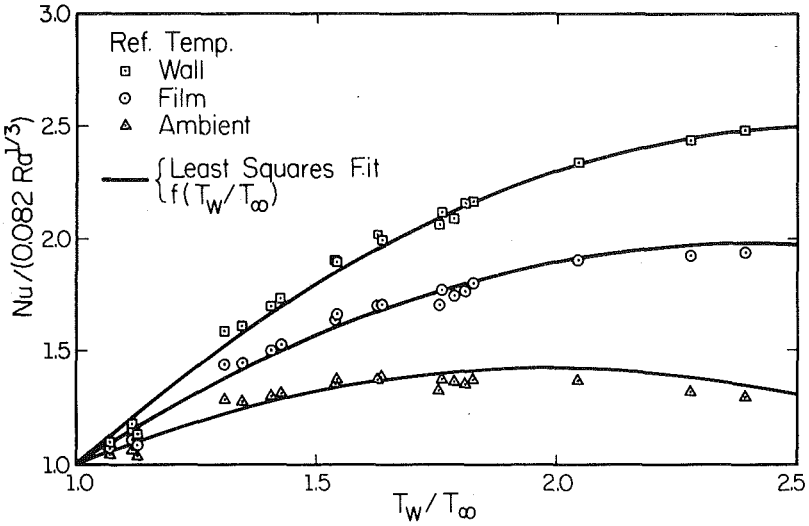

Fig. 1 Variable property correlation—turbulent regime

Table 1 Constants in variable property correlation, f (see equation (8))

Ref. temp.	b_0	b_1	b_2	Mean dif. (%)	Max. dif. (%)
T_w	−1.5	3.1	−0.6	2.5	7.8
T_f	−0.9	2.4	−0.5	2.5	7.2
T_∞	−0.32	1.77	−0.45	2.8	6.2

squares, second-degree fit of the experimental data is used to determine the value of b_i', $i = 1, 2$, or 3 where

$$\mathrm{Nu}_r/\mathrm{Ra}_r^{1/3} = b_0' + b_1'(T_w/T_\infty) + b_2'/T_w/T_\infty)^2 \quad (7)$$

Utilizing the constraint $f(1) = 1$, gives

$$\mathrm{Nu}_r = 0.082\ \mathrm{Ra}_r^{1/3} \cdot \{b_0 + b_1(T_w/T_\infty) + b_2(T_w/T_\infty)^2\} \quad (8)$$

where the constants, b_i are given in Table 1 for three different reference temperatures—T_w, T_f, and T_∞. The average absolute difference and the maximum absolute difference between the data and the respective correlation are also indicated in Table 1. The three variable property correlations and the corresponding experimental data are shown graphically in Fig. 1.

The use of the film temperature as the reference temperature in the turbulent regime might seem more logical since this reference temperature accounts remarkably well for the influence of variable properties in the laminar regime. Thus, it adds conformity and simplifies the presentation of results when both regimes are simultaneously considered. On the other hand, the results in Fig. 1 show that using the ambient temperature as the reference temperature results in a weaker influence of T_w/T_∞ in the turbulent regime. The use of the wall temperature for the reference temperature has little merit and is included only for completeness.

It is expected that the structure of turbulent boundary layers should be more strongly dependent on the ambient properties since most of the temperature drop occurs across the laminar sublayer. Thus, $T_r = T_w$ results in the strongest dependence on T_w/T_∞, and $T_r = T_\infty$ results in the weakest dependence. Hence, if the variable property influence, f, were not available, it is recommended that the ambient temperature be used as the reference temperature. The film temperature and the correlation

$$\mathrm{Nu} = 0.082\ \mathrm{Ra}^{1/3} \cdot f,\ \mathrm{Ra} > 1.6 \cdot 10^9 \quad (9)$$

where

$$f = -0.9 + 2.4(T_w/T_\infty) - 0.5(T_w/T_\infty)^2,\ 1 \le T_0/T_\infty < 2.6 \quad (10)$$

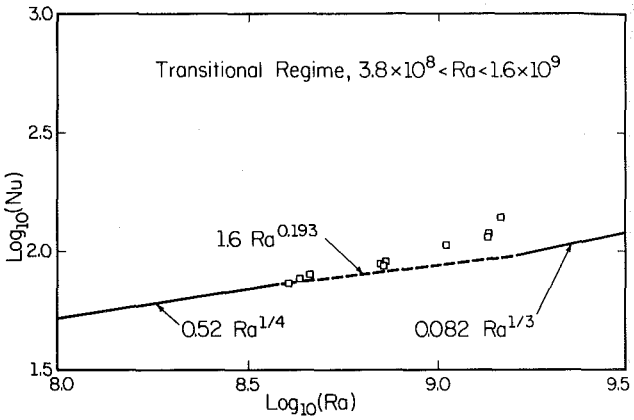

Fig. 2 Data in transitional regime

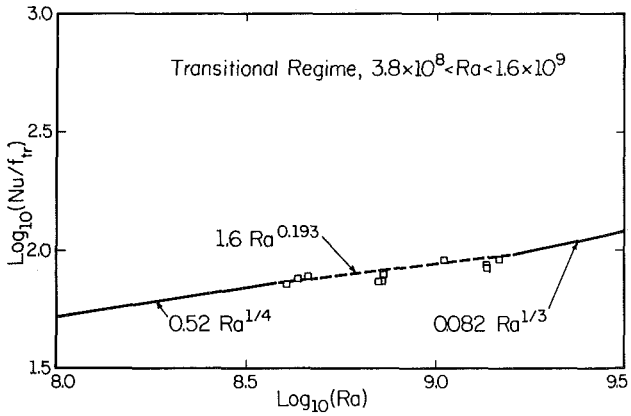

Fig. 3 Transitional data normalized for influences of variable properties

is used throughout the remainder of the paper for the turbulent regime.

The transition regime was determined from the data to be $3.8 \cdot 10^8 < \mathrm{Ra} < 1.6 \cdot 10^9$. Specifically, the influence of T_w/T_∞ was negligible for $\mathrm{Ra} < 3.8 \cdot 10^8$ which will be denoted as Ra_l and could be correlated with equation (10) if $\mathrm{Ra} > 1.6 \cdot 10^9$ which will be denoted as Ra_t. Thus, this is the definition of the "transitional" regime. Although the limits of the so-called transitional regime, Ra_l and Ra_t, appear to be

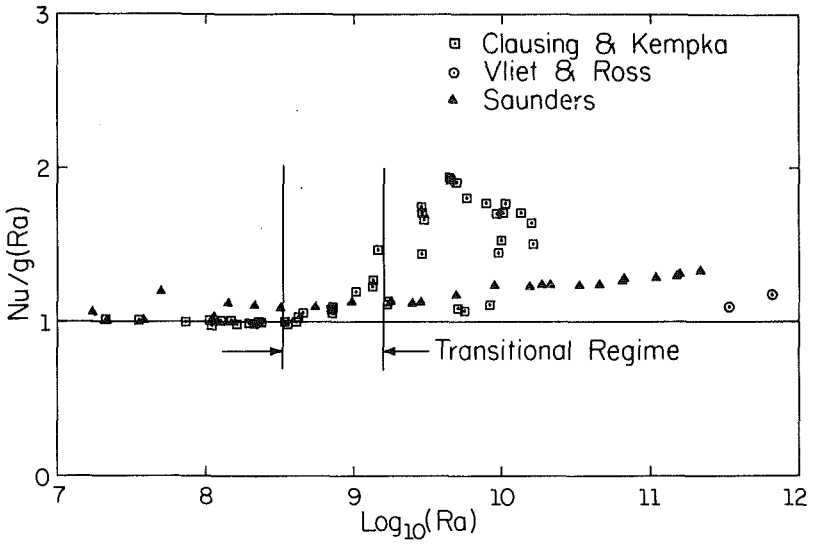

Fig. 4 Comparison of data with constant property correlation

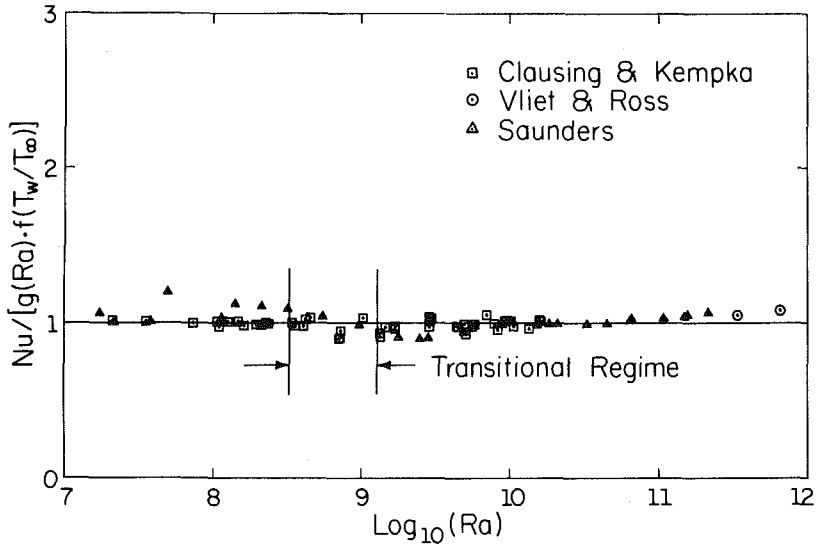

Fig. 5 Comparison of data with variable property correlation

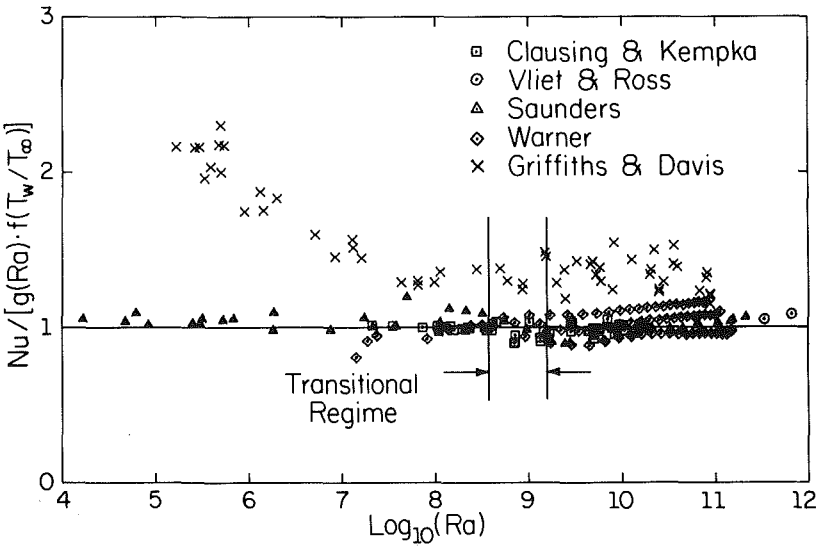

Fig. 6 Comparison between all data and correlations

relatively independent of T_w/T_∞ when T_f is used as the reference temperature, sufficient data have not been obtained to clearly establish such independence. The data in the transitional regime with no variable property correction are shown in Fig. 2.

Since f is unity over the laminar portion of the surface, $L < L_l$ where $L_l \propto \mathrm{Ra}_l^{1/3}$ and since f is given by equation (10) for $L > L_l$ where $L_t \propto \mathrm{Ra}_t^{1/3}$, the variable property influence in the transition regime, f_{tr}, is hypothesized to be

$$f_{tr} = (f-1)\left\{\frac{\mathrm{Ra}^{1/3} - \mathrm{Ra}_l^{1/3}}{\mathrm{Ra}_t^{1/3} - \mathrm{Ra}_l^{1/3}}\right\} + 1 \qquad (11)$$

That is, the difference between the turbulent and laminar variable property influences, $(f - 1)$, is weighted by the fraction of the plate with a turbulent boundary layer. The constant property correlation for the transitional regime was determined by assuming $g(\mathrm{Ra}) = c_1\,\mathrm{Ra}^{c_2}$ and determining the constants c_1 and c_2 from the constraints: $c_1\,\mathrm{Ra}_l^{c_2} = 0.52\,\mathrm{Ra}_l^{1/4}$ and $c_1\,\mathrm{Ra}_t^{c_2} = 0.082\,\mathrm{Ra}_t^{1/3}$. This procedure gives $c_1 = 1.6$ and $c_2 = 0.193$; hence

$$\mathrm{Nu} = 1.6\,\mathrm{Ra}^{0.193} \cdot f_{tr},\ 3.8 \cdot 10^8 \le \mathrm{Ra} \le 1.6 \cdot 10^9 \qquad (12)$$

Unlike the turbulent regime, f is dependent on both Ra and T_w/T_∞ in the transitional regime. The agreement between the data and correlation (12) is shown in Fig. 3.

On a graph of the log Nu versus log Ra, a family of parallel straight lines is obtained in the turbulent regime—one line for each value of the parameter T_w/T_∞. As Ra is decreased, this family of straight lines becomes, at $\mathrm{Ra} = \mathrm{Ra}_t$, a family of curves which converge to a point (Nu = 72.6) at $\mathrm{Ra} = \mathrm{Ra}_l = 3.8 \cdot 10^8$. No discontinuities exist between regimes regardless of the value of T_w/T_∞.

Further Comparisons

Tabulated results are used in all comparisons which follow in order to eliminate translation errors. Except for the data of Warner [7], whose dimensional data were unavailable, the dimensional tabulations are used. Hence, the resulting dimensionless groups are referenced to the same thermophysical property base. A prerequisite to meaningful comparisons with the proposed variable property correlations is knowledge of two of the three quantities, T_w, T_∞, and ΔT, for each point. If the data are unavailable in dimensional form, the reference temperature must also be specified. Not all data in the literature could be considered for these reasons (see, e.g., the data of [13]).

A remarkable set of experimental data for natural convection from vertical isothermal surfaces is the data of Saunders [3]. It was published in 1936 and has already played a major role in testing and generating other empirical correlations. Saunders investigated the effect of pressure upon natural convection in air at pressures ranging from 0.043 atm to 67.7 atm. He used platinum and copper plates which ranged from 3.25 mm to 229 mm in height. The low pressure ($p < 0.5$ atm), low Rayleigh number ($\mathrm{Ra} < 10^4$) data were not considered in order to eliminate the need for accurate thermophysical properties at low pressures and enlarge the dimensionless plots which follow. Saunders's dimensional data appear to contain none of the sources of discrepancy discussed in the Introduction. Specifically: (*i*) drafts and stratification were eliminated by using a steel pressure vessel which was immersed in a tank of water; (*ii*) since the radiative loss is independent of pressure and h increases drastically with increasing pressure, the radiative heat loss ranged from 6 percent to a small fraction of 1 percent; and (*iii*) three-dimensional influences were experimentally shown to be negligible. (Note also that at high pressures, large Rayleigh numbers can be generated with relatively thin boundary layers.) Saunders's data are extensive. A total of 52 tests were reported, of which 39 fell into the regimes being considered.

Two data points were reported by Vliet and Ross [12] for a 7.32-m vertical plate with a constant heat flux over its surface. Average dimensional data were reported for the upper 40 percent of the plate. At the Rayleigh numbers of the data, $\mathrm{Ra} > 3 \cdot 10^{11}$, the plate is nearly isothermal over the upper 90 percent; hence, the data should agree with average data for isothermal surfaces. Stratification was reported to be ±5 percent of ΔT or less; the conduction correction was less than 1 percent, and the radiation corrections were 22 and 18 percent. Side panels and screening ". . .produced an essentially two-dimensional boundary layer flow in the central one-third to one-half of the plate over its length, with no noticeable effect of ambient disturbances on the flow."

The data sets are compared in Figs. 4–6 with the proposed correlations using graphs of $\mathrm{Nu}/(0.082\,\mathrm{Ra}^{1/3} \cdot f)$ or $\mathrm{Nu}/(0.082\,\mathrm{Ra}^{1/3})$ versus log (Ra). In contrast, a more conventional comparison, log (Nu/f) versus log (Ra) is given in Fig. 7. In a log (Nu) versus log (Ra) presentation, the scatter is reduced by the logarithmic scale and the apparent scatter is further reduced by the large range of Ra often used. The ranges of T_w/T_∞, the number of data points, n, in each regime, the means, $\{\Sigma\,\mathrm{Nu}/(g \cdot f)\}/n$, and the mean percentage differences $100\{\Sigma|1 - \mathrm{Nu}/g f)|\}/n$ are given in Table 2.

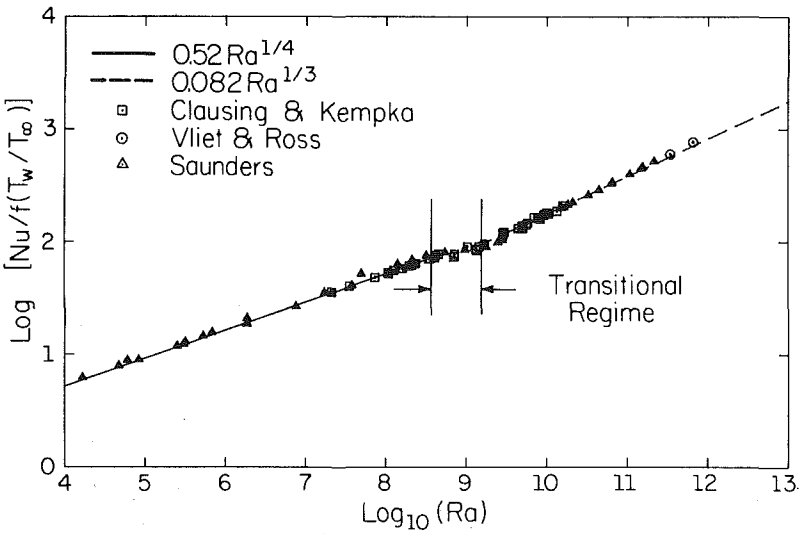

Fig. 7 Comparison between normalized data and correlations

Table 2 Comparisons between data and correlations

Regime	Laminar			Transitional			Turbulent		
Investigator(s) (range of T_w/T_∞)	No. of pts.	Mean	Mean dif. (%)	No. of pts.	Mean	Mean dif. (%)	No. of pts.	Mean	Mean dif. (%)
Clausing & Kempka [9] ($1.04 \le T_w/T_\infty \le 2.53$)	14	.998	1.0	10	.964	5.4	23	.994	2.5
Vliet & Ross [12] ($1.03 \le T_w/T_\infty \le 1.06$)	--	----	---	--	----	---	2	1.065	6.5
Warner & Arpaci [7, 8] ($1.09 \le T_w/T_\infty \le 1.20$)	10[a]	.953	5.3	8[a]	1.010	4.0	78[a]	1.014	2.8
Saunders [2] ($T_w/T_\infty = 1.19$)	21	1.058	6.1	2	1.014	2.8	16	.989	3.9
Griffiths & Davis [3] ($1 < T_w/T_\infty \le 1.51$)	24	1.74	74.1	6	1.357	35.7	28	1.330	33.0
All investigators except [3]	45	1.016	----	20	0.987	----	119	1.008	----

[a]Four tests

The data, without accounting for variable property influences, are given in Fig. 4. The reduction in the scatter which is made with the variable property correlation, f, can be seen by comparing Fig. 4 with Figs. 5 and 7. The agreement is indeed remarkable, especially considering the ranges of the parameters—3.25 mm $\le L \le$ 7,320 mm; $1.03 \le T_w/T_\infty \le 2.53$; 0.97 atm $\le p \le$ 67.7 atm; 9 K $\le \Delta T \le$ 140 K; and 82 K $\le T_\infty \le$ 305 K. More scatter is present in the Warner data [7] (see Fig. 6), although the means agree equally well. Regarding the scatter in these data, it is noted that: (*i*) the data are probably based on a different source of thermophysical properties; (*ii*) the radiation and conduction correction is inferred from laminar theory, and there is appreciable scatter in the laminar data; (*iii*) the thermal stratification in the test apparatus ranged from 0.09 ΔT to 0.16 ΔT. This variation is approximated by a linear function, and h is based on the approximate, local ΔT; and (*iv*) the data represent four different tests with essentially three different values of T_w. T_w simultaneously effects the radiative loss, the influences of stratification, and variable property influences. The latter influence was weak since $1.09 \le T_w/T_\infty \le 1.20$.

The Griffiths and Davis data [3] which were first published in 1922 are also given in Fig. 6. These data are from aluminum and steel plates, 1.27 m in height, and from a series of vertical cylinders with lamp-blacked surfaces, 174 mm in diameter, and with active lengths ranging from 46.5 mm to 2635 mm. The radiative heat transfer was an obvious source of error in these data due to its large contribution. It exceeded the convective heat transfer in most cases. The divergence exhibited in Fig. 6 at low Rayleigh numbers is undoubtedly due to errors in correcting for the conductive loss to the inactive ends of the cylinder. The mean values of $\mathrm{Nu}/\{g(\mathrm{Ra}) \cdot f(T_w/T_\infty)\}$ are 1.30, 1.51, 1.95, and 2.11 for cylinder lengths of 288, 152, 80, and 46.5 mm, respectively.

Conclusions

The following conclusions are drawn from the study.

(*i*) Good agreement exists in all three regimes between the correlations and the data with the exception of the Griffiths and Davis's data. Since the influences of T_w, T_∞ and T_w/T_∞ on errors due to radiation, stratification, thermophysical properties, etc., are not clearly negligible, no conclusions can be drawn regarding the small differences which generally arise.

(*ii*) The film temperature is the most convenient reference temperature unless only the turbulent regime is of interest. In the latter case, the ambient temperature reduces the influence of T_w/T_∞. The value of data, which are reported in dimensionless form, is greatly compromised if T_r or T_w/T_∞ is unspecified.

(*iii*) An accurate thermophysical property base is a prerequisite to correlating the influences of parameters such as ambient temperature, ambient pressure, and wall temperature. Inaccurate thermophysical properties, interpolation errors, incorrect reference temperatures, and other inconsistencies are equally defeating in both the generation and the use of dimensionless correlations.

References

1 Eckert, E. R. G., and Jackson, T. W., "Analysis of Turbulent Free-Convection Boundary Layer on Flat Plate," NACA Technical Report 1015, 1951.

2 Saunders, O. A., "The Effect of Pressure upon Natural Convection in Air," *Proceedings, Royal Society*, Series A, Vol. 157, 1936, pp. 278–291.

3 Griffiths, E., and Davis, A. H., "The Transmission of Heat by Radiation and Convection," Food Investigation Special Report No. 9, London, D.S.I.R., 1922, 1931.

4 Kutateladze, S. S., *Fundamentals of Heat Transfer*, Academic Press, New York, 1963, p. 293.

5 McAdams, W. H., *Heat Transmission*, 3d ed., McGraw-Hill, New York, 1954, pp. 171–172.

6 Bayley, F. J., "An Analysis of Turbulent Free Convection Heat Transfer," *Proceedings, Institute of Mechanical Engineers*, Vol. 169, No. 20, 1955, pp. 361–370.

7 Warner, C. Y., "Turbulent Natural Convection in Air along a Vertical Flat Plate," Ph.D. thesis, Unviersity of Michigan, Ann Arbor, Mich., 1966.

8 Warner, C. Y., and Arpaci, V. S., "An Experimental Investigation of Turbulent Natural Convection in Air at Low Pressure Along a Vertical Flat Plate," *International Journal of Heat and Mass Transfer*, Vol. 11, pp. 397–406.

9 Clausing, A. M., and Kempka, S. N., "The Influences of Property Variations on Natural Convection from Vertical Surfaces," ASME JOURNAL OF HEAT TRANSFER, Vol. 103, 1981, pp. 609–612.

10 Clausing, A. M., "Simple Functional Representations for the Thermophysical Properties of Gases at Standard Pressure" ASHRAE *Transactions*, Vol. 88, pt. 2, 1982.

11 Vargaftik, N. B., *Tables on the Thermophysical Properties of Liquids and Gases*, 2d ed., John Wiley and Sons, New York, 1975.

12 Vliet, G. C., and Ross, D. C., "Turbulent Natural Convection on Upward and Downward Facing Inclined Constant Heat Flux Surfaces," ASME JOURNAL OF HEAT TRANSFER, Vol. 97, 1975, pp. 549–554.

13 Cheesewright, R., "Turbulent Natural Convection from a Vertical Plane Surface," ASME JOURNAL OF HEAT TRANSFER, Vol. 90, 1968, pp. 1–8.

14 Clausing, A. M., "Advantages of a Cryogenic Environment for Experimental Investigations of Convective Heat Transfer," accepted for publication by the *International Journal of Heat and Mass Transfer*, Vol. 25, No. 8, 1982, pp. 1255–1257.

A Correlation Theory for Steady Natural Convective Heat Transport in Horizontal Annuli[1]

R. D. Boyd
Sandia National Laboratories,
Albuquerque, N. M. 87185

A correlation theory for two-dimensional natural convective heat transport data for horizontal annuli of arbitrary cross section has been developed and applied to two configurations: (i) concentric circular cylinders and (ii) annuli formed by an inner hexagonal cylinder and an outer circular cylinder. Also embodied in the theory is the capability to predict local as well as mean heat transfer. Thermal boundary conditions of the form $T'x^m$ can be accommodated. Data for the Rayleigh number (Ra_R) varied from 10 to 10^7, Prandtl number (Pr) varied from 0.7 to 3100, and the aspect ratio (Δ'/r', maximum annulus gap/minimum radius of inner annulus) varied from 0.5 to 2.0. Even with these large variations, the present correlation theory collapses all the experimental data for the annular geometries to a signle line. The physical problem appears to be completely specified by a single equation when the following is known: thermal boundary condition (i.e., m), the fluid (i.e., Pr), the aspect ratio, the Rayleigh number, and the geometry. This work demonstrates that the present theory is applicable to annuli of arbitrary cross section, and therefore the theory will be extended to include curvature effects and axisymmetric geometry.

Introduction

Experimental and theoretical research has been devoted to the study of natural convective heat transfer in horizontal annuli for at least the last half century [1–9]. Many different techniques for correlating the mean heat transfer have been proposed [e. g., 1, 2, 6, 8, and 9]. Flow visualizations (of isotherms and streamlines) have been extremely helpful, both quantitatively and conceptually (e.g., [7, 10, 11]).

The need for accurate correlations for natural convective heat transfer in annuli with regular (e.g., concentric circular cylinders) and irregular (e.g., hexagonal cylinder inside a circular cylinder) boundaries is becoming increasingly important in many technological areas. For example, much research is being conducted in the development of shipping casks which are used to passively cool nuclear reactor spent-fuel subassemblies [12, 13]. Other examples include passive solar systems, photovoltaic systems, thermal storage, cooling electronic equipment, aircraft cabin insulation, and underground electrical power transmission. The existence of such correlations can reduce or eliminate the need for experimentation for a particular application. It can also provide the designer or researcher with needed data for accurate specification or quantitative evaluation.

Previous investigators [1, 2, 4–9, 14] have shown, via dimensional analysis of the governing equations, that the mean Nusselt number ($\overline{Nu}$) or heat transfer can be correlated as a function of the Rayleigh number, Prandtl number, and a geometry or aspect ratio. Most of the fundamental considerations stopped at this point. As a result, the characteristic length and temperature for both the Nusselt and Rayleigh numbers were arbitrarily chosen. Itoh et al. [1] and Raithby and Hollands [9], who correlated circular concentric data with a single line, realized that the characteristic lengths of the Nusselt and Rayleigh number must be different. However, Itoh et al. determined such lengths for $\overline{Nu}$ and Ra by assuming that the thermal energy transport was related to $r_o'\ ln\ (r_o'/r_i')$ and $(r_i'r_o')^{1/2}\ ln(r_o'/r_i')$, respectively. The former length results from a simple analytical treatment of the thermal conduction equation for two concentric circular cylinders. Raithby and Hollands, and Itoh et al. used, for convenience, the concept of effective thermal conductivity.

The present theory is based on fundamental concepts and a detailed formulation of the various flow regions which exist in the annulus. This theory clearly specifies the characteristic quantities and their relation to the aspect ratio and the temperature difference across the annulus. In addition, all correlation constants have physical definitions so that numerical verification is possible. The results presented cover two different two-dimensional annuli: (*i*) concentric circular cylinders and (*ii*) a hexagonal cylinder[2] inside a concentric circular cylinder. There appears to be the capability to extend the technique to other annuli with irregular boundaries and to axisymmetric annuli. For the present cases the boundaries are assumed to be isothermal; however, thermal boundary conditions of the form, $T'x^m$, can also be included where m = constant.[3]

Theory

Consider a horizontal annulus of arbitrary cross section with wall temperature distributions for the inner and outer boundaries of the form $T_i'x_i^{m_i}$ and $T_0'x_0^{m_0}$, respectively (see Fig. 1). For the sake of brevity and clarity, it is assumed that $T_i > T_o$.

The steady two-dimensional annulus flow is divided into six distinct flow regions: (*i*) inner boundary layers (thermal and momentum), (*ii*) outer boundary layers, (*iii*) inner intermediate, (*iv*) outer intermediate, (*v*) plume, and (*vi*) stably stratified. The existence of these flow regions has been confirmed by experimental observations [12] and a matching analysis. The boundary layer regions are perhaps the most important for data correlation and the easiest to understand in the classical sense. These boundary layer regions are

[1] This work performed at Sandia National Laboratories supported by the U.S. Department of Energy under contract number DE-AC04-76-DP00789.
Contributed by the Heat Transfer Division for publication in the JOURNAL OF HEAT TRANSFER. Manuscript received by the Heat Transfer Division January 22, 1981.

[2] Two sides of the hex are horizontal.
[3] More specifically, the local temperature is defined by $T'\,Gr_x^{m/3}$.

characterized by strong lateral diffusion and comparable convection. The boundary layers are formed near the annulus boundaries and are driven by the destabilizing local temperature gradients in the gravity field. The plume region is located adjacent to the axis of symmetry and above the inner boundary where flow separation occurs. In this region, mass flows from the inner boundary layer to the outer boundary layer. By definition, the boundary layer and plume regions are regions where the Rayleigh or Grashof number is large (i.e., $>>1$).

The intermediate region has several important characteristics. It is characterized by a flow reversal which is caused by recirculation of fluid in the annulus. The locus of points at which this reversal occurs identifies the boundary between the inner and outer intermediate regions (i.e., $u_{I_i} = 0 = u_{I_o}$). In addition, there is a significant thermal stratification in the x_I-direction. However, the local temperature gradient is small in the y_I-direction, and therefore thermal diffusion is negligible in this direction. Finally, since the intermediate region flow occurs outside the boundary layers, that flow is inviscid.

In addition to the observations noted above, some additional simplifications are possible. Conditions of local similarity are assumed. Because of the mass source terms which enter the matching conditions at the interfaces between the stably stratified (or plume) and inner (or outer) boundary layer regions, the corresponding boundary layer thicknesses are nonzero at $\phi_i = 0 = \phi_0$. Further, the usual Boussinesq approximation is made. Finally, the annulus boundary radii may vary with ϕ, but the variations are such that flow separation does not occur until the fluid reaches the plume region.

Boundary Layer Region. The governing equations for the laminar boundary layer regime are

$$\frac{\partial u}{\partial x} + \frac{\partial v}{\partial y} = 0$$

$$u\frac{\partial T}{\partial x} + v\frac{\partial T}{\partial y} = \alpha\frac{\partial^2 T}{\partial y^2}$$

$$u\frac{\partial u}{\partial x} + v\frac{\partial u}{\partial y} = -\rho^{-1}\frac{\partial P}{\partial x} + \nu\frac{\partial^2 u}{\partial y^2} \mp g\beta(T - T_I(y_I = 0))\sin\phi$$

$$-\frac{u^2}{r} = -\rho^{-1}\frac{\partial P}{\partial y} + g\beta(T - T_I(y_I = 0))\cos\phi \qquad (1)$$

The minus and plus signs in the third equation apply to the outer and inner boundary layers, respectively. It should be noted that curvature effects have been neglected; this implies that the boundary layer thicknesses must be much less than the radius of curvature of the annulus boundaries. Therefore, the present correlaton will not apply without the inclusion of curvature effects when Δ'/r_i becomes large. It should also be noted that unsubscripted variables apply to both the inner and outer regions. The effect of the boundary shape is included in the body force terms, which can be expanded in terms of ϕ. Terms involving (x/r) are also expanded in terms of ϕ with the coefficients of like powers of ϕ being equated.

The following local similarity transformations, using coordinate stretching variables, were obtained[4]

$$\chi = Q^{a/2} y x^{(n-1)/2}$$

$$T - T_I' \,\mathrm{Gr}_x^{m/3} = T^* Q^{(2a-1)} x^{2(n-1/2)} \theta(\chi)$$

$$\psi = \nu Q^{a/2} x^{(n+1)/2} F(\chi),$$

[4] Differentiation of dimensionless functions such as θ, F, and G with respect to χ is denoted by a prime, e.g., θ', F', and G'. All other dimensional quantities with a prime are constant quantities, e.g., T_i', r_i' or Δ'. Also note that Q has units of reciprocal length cube.

Nomenclature

a = $(n+1)/3$
C^* = annulus geometry factor (see equation (11))
F = a dimensionless local similarity function which is related to the stream function, ψ
f = a dimensionless function which describes the angular variation in the radius ratio, r/r', of the annulus boundaries
f_Δ = a dimensionless function which describes the angular variation in the annulus gap width ratio, Δ/Δ'
G = a dimensionless function which is associated with the local pressure
Gr_x = Grashof number, $\beta g T^* x^3/\nu^2$
k_{eff}/k = ratio of the effective thermal conductivity due to convective transport to thermal conductivity of the fluid; see references [1] or [9]
m = $2(n-1/2)$
Nu = Nusselt number,

$$\left.\frac{\partial T}{\partial y_n}\right|_{y=0} \Delta'/(T_i - T_0')$$

n = a dimensionless constant which describes the thermal boundary conditions, according to $T' x^m$, for the boundaries of the annulus
P = local dynamic pressure
Pr = Prandtl number, $\nu\alpha^{-1}$
R = characteristic radius for two-dimensional laminar natural convective heat transfer in a horizontal annulus
Ra_R = $\mathrm{Gr}_R \mathrm{Pr}$
Ra_Δ = $\beta g(T_i' - T_0')\Delta^3 \alpha^{-1} \nu^{-1}$
r = radius of the boundaries of the annulus, $r = r' f(\phi)$
T = local temperature
T^* = reference temperature
u = local velocity in the principal flow direction
v = local velocity transverse to the principal flow direction
x = coordinate in the principal flow direction
y = coordinate perpendicular to the principal flow direction
$(\ )$ = denotes the integrated mean value
$(\ )'$ = a constant dimensional quantity (see the footnote associated with equation (2) for the exception to this notation)
α = thermal diffusivity
β = thermal coefficient of volumetric expansivity
Δ = local annulus gap width, $\Delta = \Delta' f(\phi)$
θ = a dimensionless local similarity function which is related to the local temperature, T
ϕ = angular coordinate
ν = kinematic viscosity
ξ = annulus shape factor (see equation (11))
χ = local similarity variable
ψ = stream function (see equation (2))

Subscripts

I = intermediate region
i = inner region
o = outer region
n = normal to surface

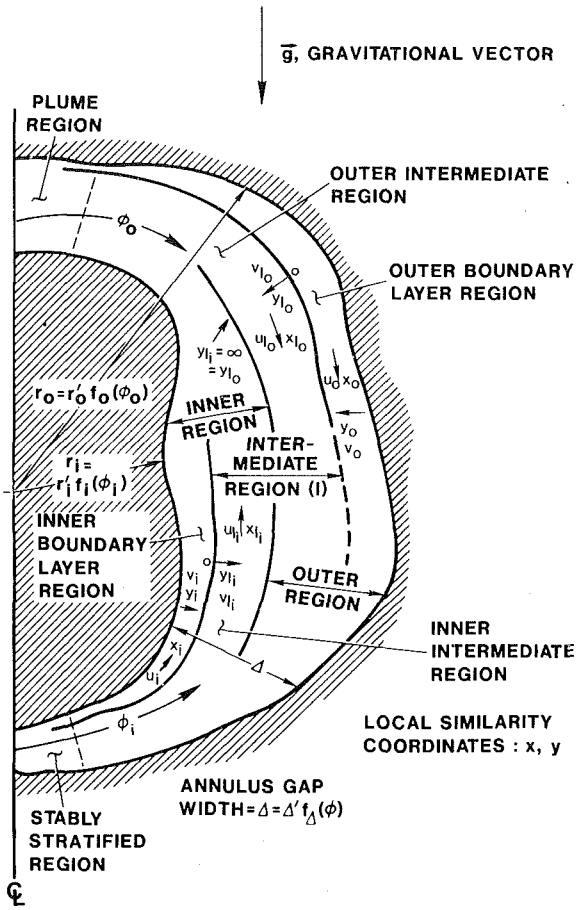

Fig. 1 A schematic of the steady two-dimensional laminar natural convective flow regions existing in a horizontal annulus

and

$$P = \rho\nu^2 Q^{2a} x^{2n} G(\chi), \tag{2}$$

where

$$u = \frac{\partial\psi}{\partial y}, \quad v = -\frac{\partial\psi}{\partial x}, \quad a = (n+1)/3, \quad m = 2(n-1/2),$$

$$Q = \beta g T^* \nu^{-2}, \quad T_i^* = T_i' - T_I', \quad T_o^* = T_I' - T_o',$$

and

$$Q = \mathrm{Gr}_x x^{-3}$$

In the above equations, unsubscripted quantities such as Q, n (or a), and T^* apply to both the inner and outer boundary layer regions. Further, T_I' is a constant characteristic temperature in the intermediate regions. Using these transformations, the governing equations can be transformed to the following form

$$\theta'' + \mathrm{Pr}\{(n+1)/2\, F\theta' - 2(n-1/2)F'(\theta + T_I'/T^*)\}$$

$$F''' - n(F')^2 + (n+1)/2FF'' - [2n\,G - (n-1)\chi G'/2]$$

$$\mp (\theta - \mathrm{Gr}_x^{a/2}\theta_I(0))\sin\phi = 0 \tag{3}$$

$$G' = (\theta - \mathrm{Gr}_x^{a/2}\theta_I(0))\cos\phi$$

$$-(\mathrm{Gr}_x\,\mathrm{Gr}_r^{-1})^{1/3}(F')^2$$

The boundary conditions are

$$(i)\quad y\to 0,\ T\to T'x^m \qquad \text{or}\quad \theta(0) = \pm 1.0$$

$$(ii)\quad y\to\infty,\ T\to T_I \qquad \text{or}\quad \theta(\infty) = \mathrm{Gr}_x^{a/2}\theta_I(0)$$

$$(iii)\quad y\to 0,\ u\to 0 \qquad \text{or}\quad F'(0) = 0$$

$$(iv)\quad y\to 0,\ v\to 0 \qquad \text{or}\quad F(0) = 0$$

$$(v)\begin{cases} y\to\infty \\ y_I\to 0 \end{cases}, u\to u_I \qquad \text{or}\quad F'(\infty) = \mathrm{Gr}_x^{a/4}F_I'(0)$$

$$(vi)\begin{cases} y\to\infty \\ y_I\to 0 \end{cases} P\to P_I \qquad \text{or}\quad G(\infty) = \mathrm{Gr}_x^{a/2}G_I(0) \tag{4}$$

In the first boundary condition, the plus and minus signs apply to the inner and outer boundary layer regions, respectively. The variable, $\theta_I(0)$, is similar to $\theta(0)$, but it applies to the intermediate region. The above equations can be further simplified by way of coordinate and parameter expansions of the dependent variables in terms of Gr_x, and ϕ. The resultant sets of ordinary differential equations must be solved simultaneously with the governing equation for the intermediate region.

Intermediate Region. The governing equations for the intermediate region (laminar regime) are

$$\frac{\partial u_I}{\partial x} + \frac{\partial v_I}{\partial y_I} = 0$$

$$u_I\frac{\partial v_I}{\partial x} + v_I\frac{\partial v_I}{\partial y_I} - \frac{u_I^2}{r} = -\rho^{-1}\frac{\partial P_I}{\partial y_I}$$

$$+ g\beta(T_I - T_I(y_I = \infty))\cos\phi$$

$$u_I\frac{\partial u_I}{\partial x} + v_I\frac{\partial u_I}{\partial y_I} = -\rho^{-1}\frac{\partial P_I}{\partial x} \mp g\beta(T_I - T_I(y_I = \infty))\sin\phi$$

$$u_I\frac{\partial T_I}{\partial x} + v\frac{\partial T_I}{\partial y_I} = \alpha\left(\frac{\partial^2 T_I}{\partial y_I^2} + \frac{\partial^2 T_I}{\partial x^2}\right) \tag{5}$$

Again, the minus and plus signs in the third equation apply to the outer and inner regions, respectively. As noted earlier, viscous effects are negligible and curvature effects have been neglected.

The intermediate region local similarity transformations, which are consistent with equations (1-5), are

$$\begin{aligned} \chi_I &= x^{-1}y_I \\ \psi_I &= \nu\,\mathrm{Gr}_x^{5a/4}F_I(\chi_I) \\ T_I - T_I' &= \mathrm{Gr}_x^{m/3} = T^*\,\mathrm{Gr}_x^{5a/2-1}\theta_I(\chi_I) \\ P_I &= \rho\nu^2\,\mathrm{Gr}_x^{5a/2}x^{-2}G_I(\chi_I) \\ u_I &= \nu\,\mathrm{Gr}_x^{5a/4}x^{-1}F_I' \\ v_I &= -\nu\,\mathrm{Gr}_x^{5a/4}x^{-1}[(15a/4)F_I - \chi_I F_I'] \end{aligned} \tag{6}$$

Using these transformations, equation (5) is transformed to the following

$$\left(\frac{15a}{2} - 1\right)\theta_I F_I' - \frac{15a}{4}\theta_I' F_I + 3(2a-1)\frac{T_I'}{T^*}F_I'\mathrm{Gr}_x^{-a/2}$$

$$= \mathrm{Pr}^{-1}\mathrm{Gr}_x^{5a/4}[(1+\chi_I^2)\theta_I'' + 9\left(\frac{5a}{2} - 1\right)^2\theta_I - 3\left(\frac{5a}{2} - 1\right)\theta_I$$

$$-6\left(\frac{5a}{2} - 1\right)\chi_I\theta_I' + 2\chi_I\theta_I' + 3(2a-1)(6a-4)\frac{T_I'}{T^*}\mathrm{Gr}_x^{-a/2}\Big],$$

$$\left(\frac{15a}{4} - 1\right)(F_I')^2 - \frac{15a}{4}F_I F_I'' + \mathrm{Gr}_x^{1-5a/2}[(5a/2-2)G_I - \chi_I G_I'] \tag{7}$$

$$\mp(\theta_I - \theta_I(\infty))\sin\phi = 0,$$

and

$$G_I' = (\theta_I - \theta_I(\infty))\cos\phi + (x/r)(F_I')^2 + \chi_I(F_I')^2$$

$$+ (15a/4)(\chi_I F_I F_I'' - \chi_I(F_I')^2)$$

The boundary conditions for the inner and outer intermediate regions are

$$
\begin{aligned}
&(i)\ y_I \to \infty,\ T_{I_i} = T_{I_o} && \text{or } {T_i}^{*5a_i/2}{T_o}^{*-5a_o/2}\theta_{I_i}(\infty) = \theta_{I_o}(\infty)\\
&(ii)\ y_I \to \infty,\ \frac{\partial T_{I_i}}{\partial y_{I_i}} = \frac{\partial T_{I_o}}{\partial y_{I_o}} && \text{or } {T_i}^{*5a_i/2}{T_o}^{*-5a_o/2}\theta'_{I_i}(\infty) = \theta'_{I_o}(\infty)\\
&(iii)\ \begin{matrix} y_I \to 0, \\ y \to \infty, \end{matrix}\ \frac{\partial T_I}{\partial y_I} = \frac{\partial T}{\partial y} && \text{or } \theta'(\infty) = \theta'_I(0)\\
&(iv)\ y_I \to \infty,\ u_I = 0 && \text{or } F_I'(\infty) = 0\\
&(v)\ \begin{matrix} y_I \to 0, \\ y \to \infty, \end{matrix}\ v_I = v && \text{or } (3a/2)F(\infty) + (3a/2-1)\chi_\infty F'(\infty) = (15a/4)\mathrm{Gr}_x^{3a/4}F_I(0)\\
&(vi)\ y_I \to \infty, P_{I_i} = P_{I_o} && \text{or } {T_i}^{*5a_i/2}{T_o}^{*-5a_o/2}G_{I_i}(\infty) = G_{I_o}(\infty)
\end{aligned}
\tag{8}
$$

The quantity, χ_∞, corresponds to the limit of χ at the interface between the boundary layer and intermediate regions.

Perturbation Equations. Equations (2), (3), (4), (6), (7), and (8) form a system of regular perturbation equations in terms of the small parameter Gr_x^{-1}, where Gr_x is large (i.e., $>> 1.0$). The perturbation expansions, which satisfy these equations (and the boundary conditions) with the leading terms for θ and F of order one, are

$$
\begin{aligned}
\theta &= \theta_1 + \mathrm{Gr}_x^{-a/2}\theta_2 + \mathrm{Gr}_x^{-a}\theta_3 + \mathrm{Gr}^{-3a/2}\theta_4 + \ldots\\
F &= F_1 + \mathrm{Gr}_x^{-a/2}\mathrm{F}_3 + \mathrm{Gr}_x^{-a}F_5 + \mathrm{Gr}_x^{-3a/2}F_7 + \ldots\\
G &= G_1 + \mathrm{Gr}_x^{-a/2}G_3 + \mathrm{Gr}_x^{-a}G_5 + \mathrm{Gr}_x^{-3a/2}G_7 + \ldots\\
\theta_I &= \mathrm{Gr}_x^{-a/2}\theta_{1I} + \mathrm{Gr}_x^{-a}\theta_{2I} + \mathrm{Gr}_x^{-3a/2}\theta_{3I} + \ldots\\
F_I &= \mathrm{Gr}_x^{-a/4}F_{1I} + \mathrm{Gr}_x^{-3a/4}F_{3I} + \mathrm{Gr}_x^{-5a/4}F_{5I} + \ldots\\
G_I &= \mathrm{Gr}_x^{-a/2}G_{1I} + \mathrm{Gr}_x^{-a}G_{3I} + \mathrm{Gr}_x^{-3a/2}G_{5I} + \ldots
\end{aligned}
\tag{9}
$$

where θ_j, F_j, G_j, θ_{jI}, F_{jI} and G_{jI} (with $j = 1, 2, 3, \ldots$) are all of order of unity (i.e., 1.0). This implies that the coefficients of these dependent variables represents the order of magnitude of each of the higher order terms for a given dependent variable.

The perturbation expansions in equation (9) are substituted into the governing equations and after coefficients of like powers of Gr_x are equated the system of governing perturbation differential equations are obtained. Although the numerical solution of these equations is beyond the scope of this paper, the expansion for θ in equation (9) will be used below to obtain an expansion for the mean Nusselt number.

Specification of Correlation Theory. Before the correlation theory can be completely specified the characteristic temperautre, T_I', must be determined. Recall from equation (2) that T_I' is related to the characteristic temperatures for the inner (T_i^*) and outer (T_o^*) boundary layers. The characteristic temperature T_I' will be determined from the global conservation of energy equation which states that, in the steady state, the total energy transferred (with $T_i' > T_o'$) from the inner boundary is equal to the total energy transferred to the outer boundary, i.e.,

$$
\left.\frac{\overline{\partial T_i}}{\partial y_i}\right|_{y_i=0} = -\left.\frac{\overline{\partial T_0}}{\partial y_o}\right|_{y_o=0}
$$

or

$$
(x_{i_{\max}} - x_i^*)^{-1}\int_{x_i^*}^{x_{i\max}} \left.\frac{\partial T_i}{\partial y_i}\right|_{y_i=0} dx_i =
$$

$$
-(x_{o_{\max}} - x_o^*)^{-1}\int_{x_o^*}^{x_{o\max}} \left.\frac{\partial T_o}{\partial y_o}\right|_{y_o=0} dx_o \tag{10}
$$

where x^* (corresponding to $\phi = 0$) is determined by matching, e.g., the inner boundary layer region to the stably stratified region.[5] The quantity $x_{i_{\max}}$ corresponds to $\phi = \pi$. If the spatial extent of the plume and stably stratified regions is sufficiently small then the above integrals are approximated adequately using the formulation results from the first order terms for the boundary layer region. After the boundary layer transformation is substituted and the results simplified, it is found that

$$
T_i' - T_I' = (T_I' - T_o')^{a_o/a_i}\xi(\beta g \nu^{-2})^{a_o/a_i - 1}, \tag{11a}
$$

where

$$
\xi^{5a_i/2} = C^{*-5a_i/2}\frac{(r_o')^{5n_o/2-3/2}}{(r_i)^{5/2n_i-3/2'}},\ C^{*-5a_i/2} = C_1C_2, \tag{11b}
$$

$$
C_1 = \int_o^\pi f_i(\phi_i)\,d\phi_i\left[\int_o^\pi f_o(\phi_o)\,d\phi_o\right]^{-1}, \tag{11c}
$$

and

$$
C_2 = -\left[\int_o^\pi \theta'_{1_o}(0) f_o(\phi_o)\left(\int_o^{\phi_o} f_o(\phi_o)\,d\phi_o\right)^{5n_o/2-3/2} d\phi_o\right]
$$

$$
\left[\int_o^\pi \theta'_{1_i}(0) f_i(\phi_i)\left(\int_o^{\phi_i} f_i(\phi_i)\,d\phi_i\right)^{5n_i/2-3/2} d\phi_i\right]^{-1}
$$

The quantities $\theta_{1_i}'(0)$ and $\theta_{1_o}'(0)$ are the first order terms in the expansions for $\theta_i'(0)$ and $\theta_o'(0)$, respectively. The quantity, C^*, is an annulus geometry factor which is dependent on the annulus geometry and the thermal boundary conditions at the annulus boundaries. When the inner and outer thermal boundary conditions are of the same form, $a_i = a_o = a$, then

$$
T_I' = (1+\xi)^{-1}(T_i' + \xi T_o'),\ T_i^* = (1+\xi^{-1})^{-1}(T_i' - T_o'), \tag{12}
$$

and

$$
T_o^* = (1+\xi)^{-1}(T_i' - T_o')
$$

In identifying the appropriate correlation relationship, the mean Nusselt number is defined as

$$
\overline{\mathrm{Nu}}_{\Delta_i} \equiv \left.\frac{\overline{\partial T}}{\partial y_n}\right|_{y_i=0}\frac{\Delta'}{(T_i' - T_o')} \tag{13}
$$

where Δ' is the maximum gap width (and r_i' is the minimum radius of the inner boundary) of the annulus. With this definition for $\overline{\mathrm{Nu}}_\Delta$, no additional arbitrary choices will be made for a reference temperature or length for the Grashof (Gr) or Rayleigh (Ra) number. Using the similarity transformation for T_i, we find that the correlation for the laminar natural convective mean heat transfer in a horizontal annulus, in terms of $\overline{\mathrm{Nu}}_{\Delta i}$, is

$$
\overline{\mathrm{Nu}}_\Delta = \lambda_1 \mathrm{Ra}_{R_i}^{5a/2-1} + \sum_{j=2}^{\infty}\lambda_j\gamma^{1-[(6-j)a/2-1][5a/2-1]^{-1}}\mathrm{Ra}_{R_i}^{(6-j)a/2-1} \tag{14}
$$

where

$$
\begin{aligned}
\mathrm{Ra}_{R_i} &= \mathrm{PrGr}_{R_i} = \beta g T_i^* {R_i}^3 \alpha^{-1}\nu^{-1},\\
{R_i}^3 &= (\mathrm{r_i}')^3[(\Delta'/r_i')(1+\xi^{-1})^{-1}]^{(5a/2-1)^{-1}},\\
\gamma &= [(\Delta'/r_i')(1+\xi^{-1})^{-1}],\\
\xi &= C^{*-1}\xi^*,
\end{aligned}
$$

and

[5] Equation (10) is valid only for small values of Δ.

$$\lambda_j = \mathrm{Pr}^{-[(6-j)a/2-1]}\left[\int_o^{\pi} f_i d\phi_i\right]^{-1}\int_o^{\pi} \theta_{j_i}'(o)\left[\left(\int_o^{\theta_i} f_i d\phi_i\right)^3\right]^{(6-j)a/2-4/3} f_i d\phi_i$$

The configuration factor (C^*), which is defined in equation (11), will have different values for different annulus cross sections. However, since all variables have been nondimensionalized, C^* is of the order of one. For example, for concentric circular cylinders, C^* is assumed to be 1.0. Therefore, the correlation for other annular cross-sections will be related to that for concentric circular cylinders via C^*. Notice that λ_j is a function of Prandtl number (Pr) through its dependence on $\theta_j(0)$. As will be shown below, it was found after correlating data from the literature that λ_1 is very nearly constant (deviation $< \pm 2$ percent) and is independent of Pr for isothermal surfaces.

Equation (14) describes the mean Nusselt number[6] for an annulus of arbitrary cross section whose boundaries have the same thermal boundary conditions of the form, $T'\mathrm{Gr}_x^{m/3}$ where Gr_x is large. It should be recalled that curvature effects were neglected and therefore equation (14) will not be applicable for large values of (Δ'/r_i).

Results and Discussion

From Equation (14), the correlation for the mean Nusselt number for an annulus with isothermal boundaries ($n_i = n_o = 1/2$) is

$$\overline{\mathrm{Nu}}_\Delta \equiv \left.\frac{\overline{\partial T_i}}{\partial y_n}\right|_{y=0} \frac{\Delta'}{(T_i' - T_o')} = \sum_{j=1}^{\infty} \lambda_j \gamma^{(i-1)} \mathrm{Ra}_{R_i}^{(2-j)/4}, \quad (15)$$

where

$$\mathrm{Ra}_{R_i} = \beta g T_i^* R_i^3 \alpha^{-1}\nu^{-1}, T_i^* = (T_i' - T_o')(1+\xi^{-1})^{-1}$$

$$R_i^3 = (1+\xi^{-1})^{-4}(r_i')^{-1}(\Delta')^4, \xi = C^{*-1}\left(\frac{r_o'}{r_i'}\right)^{1/5} = C^{*-1}\xi^*$$

$$\lambda_j = \mathrm{Pr}^{-(2-j)/4}\left[\int_o^{\pi} f_i d\phi\right]^{-1}\left[\int_o^{\pi} \theta_{j_i}'(o)\left(\int_o^{\phi} i f_i d\phi_i\right)^{3(2-j)/4-1} d\phi_i\right]$$

$$\gamma = (1+\xi^{-1})^{-1}\Delta'/r_i'$$

The versatility of the correlation technique was demonstrated using the steady two-dimensional laminar mean heat transfer measurements made by: (*i*) Kraussold [8], Kuehn and Goldstein [4, 5] and Grigull and Hauf [7] for concentric circular cylinders, and (*ii*) Boyd [12] for the hex inside a concentric circular cylinder.[7] The ranges of parameter variation are: $10^1 < \mathrm{Ra}_R < 10^7$, $0.706 \le \mathrm{Pr} < 3100$, and $0.50 \le \Delta'/r_i \le 2.16$, where Δ'/r_i is the aspect ratio for the annulus. The correlation constants shown in equation (15) were determined by correlating the laminar flow data due to Kraussold and Kuehn & Goldstein.

The results for the concentric circular cylinder correlation were applied directly to the second annulus, formed by the hex inside the concentric circular cylinder, so that the configuration factor for the latter annulus could be determined. The result of the least squares fit for the first and first two terms, respectively, of equation (15) are

$$\overline{\mathrm{Nu}}_\Delta = 0.794\ \mathrm{Ra}_{R_i}^{1/4} \quad (16a)$$

and

$$\overline{\mathrm{Nu}}_\Delta = 0.784\ \mathrm{Ra}_{R_i}^{1/4} + 0.182\gamma \quad (16b)$$

where $C^* = 1.0$, for concentric circular cylinders ($0.6 \le \mathrm{Pr} < 3100$) and $C^* = 1.05$, for the hex inside the concentric circular cylinder ($0.6 < \mathrm{Pr} \le 0.72$). The standard deviation of the data by Kraussold, and Kuehn and Goldstein relative to the resulting correlation is less than 7 percent. The above formulae for hex inside the concentric circular cylinder is probably valid for $0.6 \le \mathrm{Pr} < 3100$. However, these formulae are not valid for very small values of Pr, found for example in liquid metals.

As pointed out in the previous analysis, the correlation form given in equations (15) and (16) should apply also to two-dimensional annuli of different cross-sections with the geometry factor, C^*, being different for annuli with different geometry or thermal boundary conditions. The correlation for the isothermal concentric circular cylinders is shown in Figs. 2, 3, and 4, and the correlation for the isothermal hex inside the isothermal concentric circular cylinder is shown in Fig. 5. The interesting point is that the same correlation (allowing for C^*) applies to both annuli.

Also included in Figs. 2 and 3 are comparisons of the present correlation with those of Itoh et al., and Raithby and Hollands. The reference number adjacent to an aspect ratio indicates that two correlations almost overlay one another. In Figs. 2 and 3 the correlations agree well with the data of Kuehn and Goldstein [4, 5], Kraussold [8] and Grigull and Hauf [7]. Although agreement appears to be good in most cases it is not possible to determine, using the log-log plots of Figs. 2 and 3, how well the correlations agree with each other and the data for given aspect ratios. At some values of the aspect ratio (Δ'/r_i') good agreement is fortuitous. In order to observe this, each correlation along with selected data are plotted in Fig. 4 on linear scales, where $(\mathrm{Ra}_\Delta^{-1/4}\, k_{\mathrm{eff}}/k)$ is the ordinate and (r_o'/r_i') is the abcissa. Here (k_{eff}/k) is the dimensionless effective thermal conductivity (= $\overline{\mathrm{Nu}}_\Delta\ (\Delta'/\mathrm{r_i}')^{-1}\ ln\ (r_o'/r_i')$ and Ra_Δ is the Rayleigh number based on Δ' and $(T_i' - T_o')$. The arrows on the error bar indicate that the error bar will broaden slightly in the indicated direction due to data not included in this figure. This plot indicates that the present correlation (equation (16)) agrees best with the data at low aspect ratios ($\Delta'/r_i \lesssim 1.4$) and the correlation of Raithby and Hollands agrees best with the data at higher aspect ratios ($\gtrsim 1.4$). As noted earlier, the present theory should not be accurate at high aspect ratios since curvature effects were neglected. However, it is encouraging to note that if curvature effects are included in the present theory, the resulting agreement with the data should improve.

The three correlational techniques, in Fig. 4, were compared with the experimental data [12] for the second configuration, i.e., the annulus formed by a hexagonal cylinder (hex) placed concentrically inside a horizontal circular cylinder. The correlations for concentric circular cylinders were applied to the hex by replacing it with an equivalent circular cylinder with the same surface area. The results of the comparison are shown in Fig. 5. For the data shown, the aspect ratio for the equivalent circular cylinder inside the horizontal concentric circular cylinder is 2.36 ($r_o'/r_i' = 1.36$). The rather substantial differences in the correlations can be explained by reference to Fig. 4, which shows significant differences in the correlations at $r_o'/r_i' = 1.36$.

Further, if the plot in Fig. 5 and those in Figs. 2 and 3 are

[6] The local Nusselt number can be obtained by substituting the expansion for T_i from equations (2) and (9), into the definition Nu, with x replacing Δ'.

[7] The three-dimensional data by Klima [16] was correlated along with that of Boyd in references [12 and 15]; however, it is felt that due to the three-dimensional effects as well as the sparse local measurements, Klima's data should not be included here.

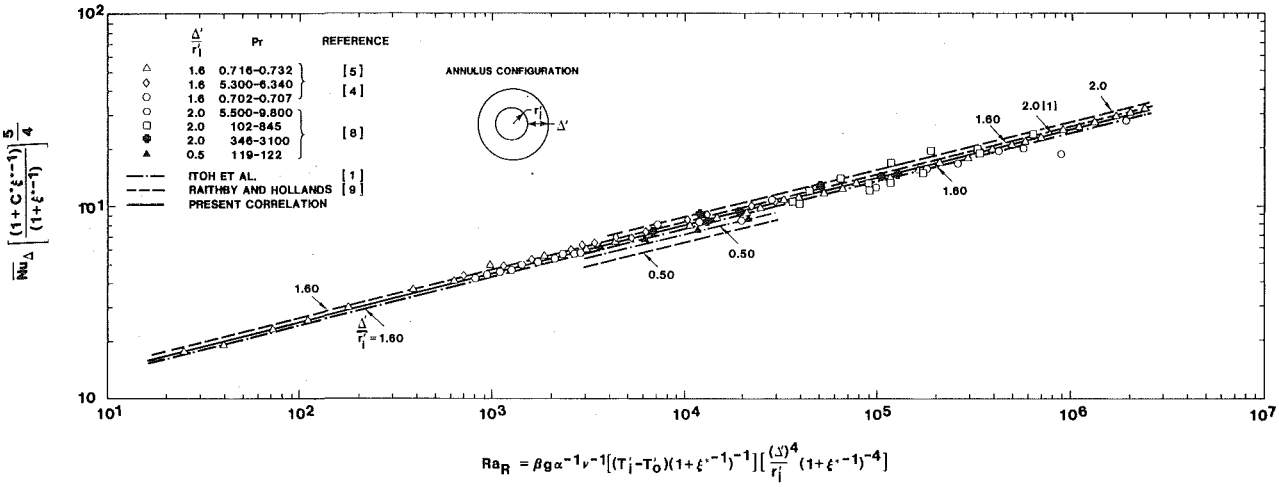

$$Ra_R = \beta g \alpha^{-1} \nu^{-1} [(T_i' - T_o')(1+\xi^{*-1})^{-1}][\frac{(\Delta')^4}{r_i'}(1+\xi^{*-1})^{-4}]$$

Fig. 2 The mean natural convective heat transfer ($\overline{Nu}_\Delta$) for isothermal concentric circular cylinders in terms of the new correlation variables. The data is from Kuehn & Goldstein [4, 5], and Kraussold [8], and is compared with the present correlation and that due to Raithby and Hollands [9] and Itoh et al. [1].

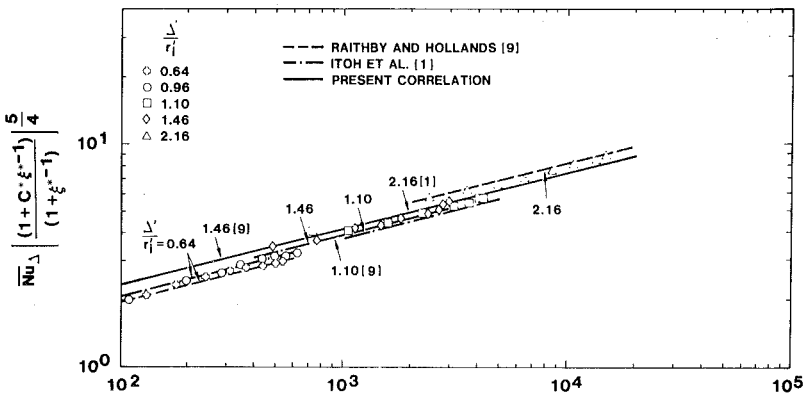

$$\overline{Gr}_R = \beta g \nu^{-2} [(T_i' - T_o')(1+\xi^{*-1})^{-1}][\frac{(\Delta')^4}{r_i'}(1+\xi^{*-1})^{-4}]$$

Fig. 3 The mean natural convective heat transfer ($\overline{Nu}_\Delta$) for horizontal isothermal concentric circular cylinders ($C^* = 1.00$) in terms of the new correlation variables. The data is from Grigull and Hauf [7] and is compared with the present correlation and that due to Raithby and Hollands [9] and Itoh et al. [1].

superimposed, the data for the two different annular configurations would overlay one another (similar to Fig. 6 of reference [15]).

Finally, it is important to describe how the present theory would be used by an engineer for annular configurations other than horizontal concentric circular cylinders or the hex inside the concentric circular cylinder. There are three approaches possible when using the correlation for a new annular geometry with isothermal surfaces (equation 15) and nonisothermal surfaces (equation (14)). All approaches involve determining C^* and λ_j: (*i*) an experimental model could be built to determine C^* and λ_j; (*ii*) one could compute these constants numerically by solving equations (3), (4), (7), and (8) along with equations (9), (11), (14), and (15); or (*iii*) one could use conformal mapping to map an annulus of interest onto one of the two covered here. Future work is planned to numerically compute C^* and λ_j which include curvature effects as well as the axisymmetric geometry.

Conclusions

The results in Figs. 2–5, which display the ability of the present correlation technique to correlate experimental data over a large parameter range and different annulus cross sections, are very encouraging. In the present work, the Rayleigh number varied over a factor of 10^6, the Prandtl number a factor > 4000, and the aspect ratio a factor of 4.0. Even with these large variations, the present correlation technique collapses all the experimental data to a *single line*, which is given by equation (16) for two different two-dimensional annular geometries: (*i*) concentric circular cylinders, and (*ii*) a hex inside a concentric circular cylinder. Due to the arbitrary selection of a characteristic length, previous correlations have resulted in a family of curves with aspect ratio as a parameter. Based on the work completed to date, the physical problem appears to be completely specified by an equation similar to equation (14) when the following is known: boundary conditions (i.e., n), the fluid (i.e., Pr), the aspect ratio, the Grashof or Rayleigh number, and geometry. As demonstrated above, equation (16) applies to both isothermal concentric cylinders and an annulus formed by a hex inside a concentric circular cylinder.

The results of the present methodology can be summarized as follows: (*i*) the theory is applicable to two different two-dimensional configurations; (*ii*) the theory demonstrates that both the characteristic temperatures and lengths in natural

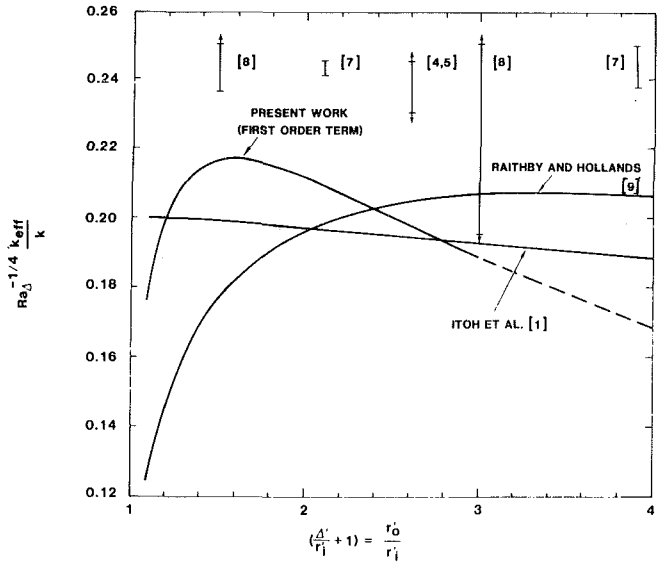

Fig. 4 The present correlation in linear (as opposed to log-log) scales, compared with those of Raithby and Hollands [9] and Itoh et. al. [1] for the case of horizontal isothermal concentric cylinders ($C^* = 1.00$) with coordinates ($Ra^{-1/4}\ k_{eff}\ k^{-1}$) and ($r_0'/r_i'$). Selected data from Kraussold [8], Kuehn and Goldstein [2, 4] and Grigull and Hauf [7] are also included.

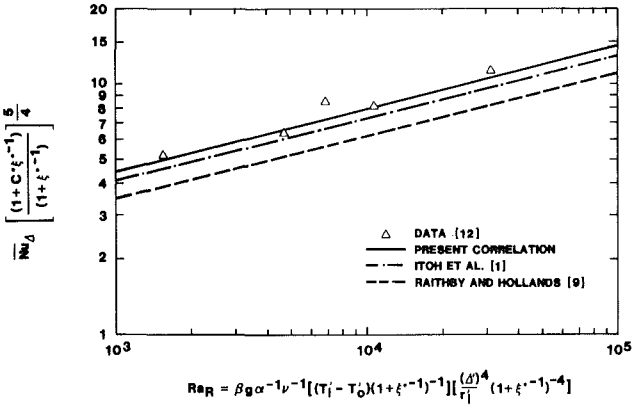

Fig. 5 The present correlation compared with those of Raithby and Hollands [9] and Itoh et al. [1] for the case of natural convective heat transfer inside a horizontal annulus formed by an isothermal hexagonal cylinder inside an isothermal concentric circular cylinder ($C^* = 1.05$). The latter two correlations were used by replacing the hex with an equivalent circular cylinder with equal surface area. The data are from Boyd [12].

convective enclosure flows are interrelated and cannot be arbitrarily chosen without violating the First Law; (*iii*) all correlational constants have physical definitions (equations 11(*c*) and 14); and (*iv*) the present correlation is more accurate than those of Itoh et al. [1] and Raithby and Hollands [9] when used to predict the mean heat transfer in an annulus formed by an inner hexagonal cylinder and an outer circular cylinder.[8]

The applicability of the various equations of the model is summarized below. Equations 15 and 16 are valid for laminar flows with Rayleigh numbers greater than that for the pseudo-conduction regime as displayed by the data of Grigull and Hauf [7]. The two-term correlation (equation (16*b*)) results in negligible improvement over the one-term correlation (equation (16*a*)), and therefore the latter is recommended due to its simplicity relative to the former. Equation (14) is applicable to nonisothermal annulus boundaries with identical thermal boundary conditions. Finally, equation (11) applies to annuli whose boundaries have different thermal boundary conditions.

Finally, it should be emphasized that if a similar analysis was performed for the natural convective flow over a vertical plate or a horizontal circular cylinder the characteristic lengths and temperatures would be the same for both the Nusselt and Rayleigh numbers. Apparently, investigators have assumed that the latter results apply equally to annulus enclosure flows; however, the present analysis clearly demonstrates that no a priori assumptions can be made about the choice of the reference temperature and the characteristic lengths for *both* the Nusselt and Rayleigh numbers used for correlating data for natural convective flows in annuli. One can select the reference length and temperature of either the Nusselt or Rayleigh number but after doing so the other is uniquely determined.

[8] This annulus (with prototypic cross sectional dimensions and low aspect ratio) models in two dimensions a spent nuclear reactor subassembly inside a shipping canister.

References

1 Itoh, M., Nishiwaki, N., and Hirata, M., "A New Method for Correlating Heat-Transfer Coefficients for Natural Convection In Horizontal Cylindrical Annuli," *International Journal of Heat and Mass Transfer*, Vol. 13, 1970, pp. 1364–1368.

2 Kuehn, T. H., and Goldstein, R. J., "Correlating Equations for Natural Convection, Heat Transfer Between Horizontal Circular Cylinders," *International Journal of Heat and Mass Transfer*, Vol. 19, 1976, pp. 1127–1134.

3 Jischke, M. C., and Farshchi, M., "Boundary Layer Regime for Laminar Free Convection Between Horizontal Circular Cylinders," ASME JOURNAL OF HEAT TRANSFER, Vol. 102, 1980, pp. 228–235.

4 Kuehn, T. H., and Goldstein, R. J., "An Experimental and Theoretical Study of Natural Convection in the Annulus Between Horizontal Concentric Cylinders," *Journal of Fluid Mechanics*, Vol. 74, pt. 4, 1976, pp. 695–719.

5 Kuehn, T. H., and Goldstein, R. J., "An Experimental Study of Natural Convection Heat Transfer in Concentric and Eccentric Horizontal Cylindrical Annuli," ASME JOURNAL OF HEAT TRANSFER, Vol. 100, 1978, pp. 635–640.

6 Lis, J., "Experimental Investigation of Natural Convection Heat Transfer in Simple and Obstructed Horizontal Annuli," Third International Heat Transfer Conference, Chicago, 1966, pp. 196–204.

7 Grigull, V., and Hauf, W., "Natural Convection in Horizontal Cylindrical Annuli," Third International Heat Transfer Conference, Chicago, 1966, pp. 182–195.

8 Kraussold, H., "Heat Transfer in Cylindrical Layers of Fluids Involving Natural Convection," *Forschung auf dem Gebiete des Ingenieurswesen*, Vol. 5, 1934, pp. 186–191.

9 Raithby, G. D., and Hollands, K. G. T., "A General Method of Obtaining Approximate Solutions to Laminar and Turbulent Free Convection Problems," *Advances in Heat Transfer*, Vol. 11, Academic Press, New York, 1975, pp. 265–315.

10 Powe, R. E., Carley, C. T., and Bishop, E. H., "Free Convective Flow Patterns in Cylindrical Annuli," ASME JOURNAL OF HEAT TRANSFER, Vol. 91, 1969, pp. 310–314.

11 Powe, R. E., Warrington, R. O., and Scanlan, J. A., "Natural Convective Flow Between a Body and its Spherical Enclosure," *International Journal of Heat and Mass Transfer*, Vol. 23, 1980, pp. 1337–1350.

12 Boyd, R. D., "Steady Natural Convective Heat Transfer Experiments In a Horizontal Annulus bfor the United States Spent Fuel Shipping Cask Technology Program," SAND80-1057, Apr. 1981, Sandia National Laboratories, Albuquerque, N. M.

13 Pope, R. B., "Evaluation of Heat Transfer in Conceptual Designs of Spent Fuel Shipping Casks for the United States Breeder Technology Program," SAND77-1781, May 1978, Sandia National Laboratories, Albuquerque, N. M.

14 Kuehn, T. H., and Goldstein, R. J., "A Parametric Study of Prandtl Number and Diameter Ratio Effects on Natural Convection Heat Transfer in Horizontal Cylindrical Annuli," ASME JOURNAL OF HEAT TRANSFER, Vol. 102, Nov. 1980, pp. 768–770.

15 Boyd, R. D., "A New Correlation Theory for Steady Natural Convective Heat Transport Data for Horizontal Annuli," *Natural Convection*, Vol. 16, edited by I. Catton and R. N. Smith, The 20th ASME/AICHE National Heat Transfer Conference, Milwaukee, Wi., Aug. 2-5, 1981, pp. 135–142.

16 Klima, B. B., "LMFBR Spent Fuel Transport: Single Assembly Heat Transport Test," ORNL-TM-4936, Oak Ridge National Laboratory, Oct. 1975.

The Calculation of a Fire in a Large Building

H. W. Emmons
Gordon McKay Professor of Mechanical Engineering, Abbott and James Lawrence Professor of Engineering, Division of Applied Sciences, Harvard University, Cambridge, Mass. 02138
Hon. Mem. ASME

The complex picture presented by a fire growing in a large building can be understood by considering the process as made up of a large number of space, time, and phenomena zones each one of which is to some degree independent of all others. This approach is explained in detail, the appropriate equations now in use in the Computer Fire Code V are listed and some results compared with full-scale experimental results.

Introduction

Present techniques for attaining fire safety have proven inadequate. Codes specify permitted flammabilities measured by a specified fire test of a material as though it were a property. A given material burns in a way and at a rate that depends upon its entire environment. No small-scale test can be a rigorous model for a large-scale room. In fact, any single full-scale test only reproduces the single case tested. It does not show how the same construction would behave under different circumstances (different ignition points, moisture content, ambient temperatures, etc.).

Thus, fire safety of occupants of a building requires a prediction of the reasonably probable most serious fire from ignition until after everyone is out. Fire safety of fire fighters requires a prediction of first collapse in addition to the temperature and toxic gas history. Fire safety of the property values also requires a prediction of heat and smoke spread rate as well as direct fire destruction.

In a building with many rooms in each of which are various pieces of furnishings, many different fires are possible depending upon where and when a fire starts. Only by some practical method of computation can the worst of these fires be discovered. To test them all is financially prohibitive.

To compute a fire, it is viewed as a large number of parallel and series phenomena. The fire starts by ignition of some item. It grows as energy is fed back from the active combustion regions, smoldering or flaming. Above the object is a column of rising hot gas and usually flames. The gaseous fuel in the plume partly burns in the entrained air and collects at the ceiling in a hot layer. This layer loses heat by convection and radiation to its surroundings. The walls and ceiling as well as other objects get hot and eventually themselves pyrolyze, ignite, and burn.

As the fire grows, the layer deepens until hot smoky gases flow out of the vents. When sufficient fuel collects in the hot layer, it may ignite and burn. Thus, flames move out the top of the vent. These flames, together with direct radiative heat transfer through the vent, causes ignition in the next room.

In the meantime, smoke and soot have been flowing throughout the building spreading destruction and fire danger. When some other items in the room of fire origin get hot enough, they too start to burn. Soon, all combustibles in the room are burning. Shortly thereafter the available oxygen becomes limited by the limited fresh air flow in through the bottom of the vents, and the fire becomes ventilation limited. Fuel can only pyrolyze and burn as fast as the available oxygen becomes available. Thus, after the fire becomes ventilation limited, the computer can calculate the fire in the first room without concern for where the solid fuel is. The major computation effort can shift to other rooms not yet ventilation limited.

Thus, the time history of the temperature, toxicity, and fire destruction can be predicted for a large building. In this paper the equations used to make this calculation for one room are given. In every case relatively crude approximations are used, either because we don't now know any better or because a better calculation of one well-understood effect is not justified in view of the much lower accuracy of other parts. To do otherwise is to waste time with excessive accuracy of one part without any resultant improvement in the final answer. All the zones now recognized for one room in Computer Fire Code V are described (for an earlier version CFC III) in reference [1].

The method of computing a building described in this paper is by use of a zone model. An alternate approach possible in any heat transfer-fluid dynamics problem is to solve the three-dimensional time-dependent integro-differential equations for multicomponent reacting fluids. The motion of gases is, of course, turbulent and much of the heat transfer is by radiation. This very basic approach is to some degree appropriate to research studies of individual zones – the burning solid and its flames, the plume against a wall, the spontaneous ignition process, etc. In the author's opinion, the zone model provides all the accuracy required for engineering decision making. Just as the design of a building structure will forever be accomplished by use of column and beam formulas (and not three-dimensional elasticity), so fire safety will someday be accomplished by use of a zone model (not a three-dimensional fluid mechanics model which gives far finer detail than needed and requires orders of magnitude greater computing time).

The Zones

Rooms. A building is made up of spaces separated from one another by walls (floors and ceilings). (We may have to consider the space in a hollow wall or above a false ceiling as a separate room.) Each room is specified by its size, location within the building, and its connections by walls, and vents, including ventilation ducts with other rooms. A room will have one of a series of states during a fire. It may not be involved at all. It may act as a passageway for air and fire gases to flow through. It may be heating. It may be burning. It may be ventilation limited. It may be cooling. It may be burned out and again be serving only as a passageway.

Objects. Each room will contain various objects. Including walls, floor, ceiling, each object must be specified as to location, size, shape, and material of construction. Each object will have one of many possible states at every instant; thus; the object might not be involved, or it might be heating, pyrolyzing, smoldering, flaming, burning as char, or all burned up. Each of these states must be quantitatively

Contributed by the Heat Transfer Division of THE AMERICAN SOCIETY OF MECHANICAL ENGINEERS and presented at the 20th ASME/AIChE National Heat Transfer Conference, Milwaukee, Wisconsin, August 2-5, 1981. Manuscript received at ASME Headquarters April 14, 1981. Paper No. 81-HT-2.

described by one or more subroutines (or as at present skipped entirely for want of adequate knowledge).

The Fuel. Except for charcoal, solids and liquids generally found in buildings don't burn; they must first gasify. Thus the object must first be heated up to a pyrolyzation temperature. (See zones 9–12). The theory of fire spread for an arbitrary piece of furniture is not yet reliable (generally nonexistent). In the present Computer Fire Code, the initially ignited fuel is a horizontal surface. There are three types of fires that may be chosen by the user:

A Burner. The fuel rate ($-\dot{m}_f$) and fuel area are specified.

A Pool Fire. Liquid or solid fuel is of specified area. The fuel rate is given by energy feedback, $\bar{q}''$

$$-\dot{m}_f = A_f \dot{q}'' / Q_{\text{vap}} \tag{1}$$

A Spreading Fire. Both fuel rate and area must be calculated. The fuel rate is given approximately (see equation (6)) by

$$-\dot{m}_\beta = A_f \dot{q}'' / Q_{\text{vap}} \tag{2}$$

where the area $A_f = \pi R_f^2$ with

$$R_f = R_0 + \int_0^{t_0} \dot{R}_f dt \,(\text{empirically } R_0 \simeq .042\text{m}) \tag{3}$$

Finally, $\dot{R}_f$ is assumed to depend upon the local heat flux

$$\dot{R}_f = .011 \frac{\dot{q}''}{\sigma T_F^4} \left(1 + \frac{\dot{q}''}{2\sigma T_F^4} + \frac{1}{3}\left(\frac{\dot{q}''}{\sigma T_F^4}\right)^2\right) \tag{4}$$

until $M = .95\, M_{\max}$ after which

$$\dot{R}_f = \frac{R_m - R}{10} \tag{5}$$

A more accurate fire decay can be derived for any specific fuel and geometry but this arbitrary decay equation is adequate for the present.

It would be more accurate but computationally more complex to express the spread rate in terms of the fuel surface temperature. This is left for the future.

As the original fuel burns out, many small complex events occur. Instead of trying to follow and predict all of these events in detail an arbitrary fire shutdown is used to give the fuel rate as:

$$-\dot{m}_f = m_f \tanh\left(\frac{-10}{m_f}\dot{m}_\beta\right)/10 \tag{6}$$

The mass of fuel remaining at any time is given by:

$$m_f = m_0 + \int_0^t \dot{m}_f dt \tag{7}$$

where m_0 is the initial fuel mass.

Future work must provide analytical or empirical information adequate to produce subroutines for the burning of walls, ceilings, floors, chairs, tables, drapes, etc.

The Plume. Immediately above the burning fuel, the rising hot gases are reacting – there is a flame. The gaseous fuel, $-\dot{m}_f$, enters the base of the plume but not all of it burns. In fact, the composition of the products are expressed well enough at present as O_2, CO_2, H_2O, CO, unburned hydrocarbons (CH), soot (C). These are computed by use of empirical coefficients

$$\chi_s = \text{mass of } s / -\dot{m}_f \tag{8}$$

Since not all the fuel is burned, not all the available heat is released. Empirically, only a fraction χ of the fuel combustion heat is released. If the flame enters the vitiated layer at the ceiling, the combustion may be limited by the amount of oxygen entrained below. Thus, the burning rate, $\dot{m}_b$, is less than the pyrolysis rate, $-\dot{m}_f$, as given by

$$\dot{m}_b = \min\left(-\chi \dot{m}_f, \frac{\dot{m}_p + \dot{m}_f}{\gamma}\right) \tag{9}$$

where γ is an empirical fuel air ratio (at present $\gamma = 14.5$). The resultant heat release is

$$\dot{E}_b = \dot{m}_b Q_{\text{comb}} \tag{10}$$

Although some progress has been made, [2–4], there is no good theory of a plume with flames. We note that the buoyancy produced by the heat release even if high in a plume, contributes to the entire plume fluid motion through continuity and momentum. Therefore, it is at present assumed that all the heat is released at the fuel surface.

Nomenclature

A = area of item indicated by subscript
A_i = area of one of four rectangular sections of A_R with corner of an object (equation (44))
b = width of plume at hot-cold layer interface, parameter equation (40)
B = width of vent
C_0 = constant equations (15), (16), defined equation (17)
c_p = specific heat of gas
C_D = flow coefficient (= .68)
E = energy of item indicated by subscript
$\dot{E}$ = energy rate to item indicated by subscript, or from first subscript to the second
g = gravity force per unit mass
h = heat transfer coefficient
h = height of item indicated by subscript
H = height of layer interface above virtual source (equation (13))
H = height of layer interface above center of volume of conical flame (equation (41))
L = length of room
m = mass of item indicated by subscript
$\dot{m}$ = mass increase of or flow through item indicated
x_a = distance of radiated surface above flame base (equation (40))
x_b = distance of interface surface above flame base (equation (40))
δx = conduction space increment (equation (56))
Y = mass fraction of specie indicated by subscript
z = vertical coordinate
$z_{i+1} - z_i$ = thickness of ith flow layer in vent (equation (36))
z_{0i}, z_{1i} = parameters (equation (44))
α = entrainment coefficient (equation (12)), thermal diffusivity (equation (54))
γ = fuel air ratio (equation (9))
ϵ = emissivity of item indicated by subscript
K = absorption constant
$\lambda = \frac{1}{\text{K}}$ = optical depth
ρ = density
σ = $(5.67 \times 10^{-8}$ W/m^{2}K$^4)$ Stefan-Boltzman Constant
τ = parameter (equation (40)), thickness (equation (55))
ϕ = parameter (equations (39), (40))
χ = fraction of pyrolysis mass actually burned

A virtual point source plume is used [5]. The plume height is

$$h_p = h_R - h_f - h_L \tag{11}$$

The virtual source is at x below the fuel surface

$$x = \frac{R}{1.2\alpha} \tag{12}$$

The effective plume height is

$$H = h_p + x \tag{13}$$

The plume radius at the bottom of the hot layer (interface) is

$$b = 1.2\alpha H \tag{14}$$

The mean plume velocity at the interface is

$$u = \left(\frac{C_0}{H_p}\right)^{1/3} \tag{15}$$

while that at the fuel surface is

$$u_F = \left(\frac{C_0}{x}\right)^{1/3} \tag{16}$$

where

$$C_0 = \frac{25 g \dot{E}_b}{48\pi\alpha^2 c_p T_a \rho_a} \tag{17}$$

The plume mass flow into the hot layer is

$$\dot{m}_p = \pi\rho_a (b^2 u - R^2 u_F) - \dot{m}_f \tag{18}$$

The plume energy flow into the hot layer (datum at 0°K) is

$$\dot{E}_p = \dot{E}_b + \sum_p \dot{m}_p c_p T_c - \dot{E}_{pR} - \sum_f \dot{m}_f c_p (T_p - T_c) \tag{19}$$

If the interface falls below the surface of the fuel, the plume mass flow into the hot layer reduces to

$$\dot{m}_p = -\dot{m}_f \tag{20}$$

and the energy flow becomes

$$\bar{E}_p = -m_f c_p T_c \tag{21}$$

At present, it is not known how the flame behaves in the vitiated, hot gas layer at the ceiling. This must be fixed in the future.

Various methods have been used to determine the flame temperature. The Computer Fire Code now uses the empirical value of 1260°K, [15].

There are some experimental studies of buoyant plumes against a wall or in a corner, [6]. These have not yet been used in a fire code. To date, no one has examined the nature of the interaction between plume and vent flow in case a fire is burning under a window or in a doorway.

The Hot Layer. The rising gases of a plume very early in a fire are not hot enough to remain at the ceiling but produce global room circulation. These are ignored because this early period is not very important nor does it last very long. The plume gases are assumed to rise to produce a uniform temperature and composition layer at the ceiling. Conservation of mass and energy serve to define the layer.

Mass

$$m_L = \int_0^t \dot{m}_L dt \tag{22}$$

$$\dot{m}_L = \sum_p \dot{m}_p - \sum_v \dot{m}_u - \dot{m}_{Lc} \tag{23}$$

Energy

$$E_L = \int_0^t \dot{E}_L dt \tag{24}$$

$$\dot{E}_L = \sum_p \dot{E}_p - c_p T_L \sum_v \dot{m}_u - \dot{E}_{LD} - \bar{E}_{LR} - c_p T_L \dot{m}_{LC} \tag{25}$$

Once the hot layer energy is known, its depth is known

$$h_L = \frac{E_L}{A_R c_p \rho_a T_a} \tag{26}$$

since by the gas law $p/R = \rho_L T_L = \rho_a T_a =$ constant (nearly).

The temperature

$$T_L = \frac{E_L}{c_p m_L} \tag{27}$$

The composition in species

$$m_s = \sum_p \dot{m}_{sp} - Y_s \sum_v \dot{m}_s + \dot{m}_{sw} \tag{28}$$

Nomenclature (cont.)

χ_S = fraction of pyrolysis mass converted to specie S
ψ = flame cone half apex angle

Subscripts and Superscripts

a = ambient outdoors air
b = burned
c = cold layer
d = property of the inflow through a vent
D = conduction heat transfer
f = fuel
F = flame
i = inside, index
L = hot layer
o = outside, object
p = plume
R = room
s = chemical specie
u = property of outflow through a vent
V = vent
W = wall
$\dot{m}_\beta$ = initial estimate of pyrolysis rate (equation (2))
N = number of conduction computation points (equation (55))
p = pressure
Δp = pressure drop in meters of ambient fluid
Δp_i = pressure drop at bottom of ith flow layer in vent (equation (36))
Δp_{i+1} = pressure drop at top of ith flow layer in vent (equation (36))
$\dot{q}''$ = heat flux – from first subscript to second
Q_{vap} = heat of pyrolysis
Q_{0_2} = heat of combustion per unit mass of oxygen
Q_{comb} = heat of combustion per unit mass of fuel
r = radius of flame at the level of the radiated surface
R = gas constant, flow resistance (equation (61))
R_i = equivalent radius for area A_i (equation (44))
R_1, R_2 = flow resistances of passages in series or parallel (equations (62), (63))
s_a, s_b = parameters (equation (40))
s_i = parameter (equation (44))
t = time
δt = time increment
T = absolute temperature of item indicated by subscript
u = vertical plume gas velocity
W = width of room
x = position of virtual plume source below fuel surface (equation (12))

There are minor corrections for CO_2 and H_2O from atmospheric air.

The most serious unknown for all of fire prediction is the burning of the gases in the hot layer. Current research is aimed at this problem since a way must be found to predict ignition and burning without requiring a knowledge of the actual internal structure of the layer. Without this burning, flames never come out of a vent.

The Cold Layer. This layer is included in the present Computer Fire Code only by the assumption that its temperature is T_a and its depth is that required to fill the room below the interface. This is a fair assumption for a single room, but is completely inadequate for a multiroom structure. In the next version of the Computer Fire Code this will be done correctly.

Again, conservation of mass and energy suffice to define its properties.

Mass

$$m_c = m_{c_0} + \int_0^t \dot{m}_c dt \tag{29}$$

$$\dot{m}_c = \sum_p (\dot{m}_p + \dot{m}_f) + \dot{m}_{LC} + \sum_v \dot{m}_d \tag{30}$$

Energy

$$E_c = c_p T_a m_{c_0} + \int_0^t \dot{E}_c dt \tag{31}$$

$$\dot{E}_c = -c_p T_c \sum_p (\dot{m}_p + \dot{m}_f) + \dot{E}_{cD} + c_p T_L \dot{m}_{LC} + c_p \sum_v T_d \dot{m}_d \tag{32}$$

As soon as the lower layer energy is known its depth is also known

$$h_c = \frac{E_c}{A_c c_p \rho_a T_a} \tag{33}$$

where A_c is less than the room area by that of the plumes.

What looks like a difficulty now arises since the sum of the lower and upper layer depths must equal the room height

$$h_R = h_c + h_L \tag{34}$$

This relation must, of course, be satisfied. However, this relation is automatically satisfied by satisfying the conservation of mass relation for each room during the flow calculation (see subheading "Flow Throughout the Building").

The composition in the lower layer would be found from the inflow and outflow of each specie.

The Vertical Vent Flow. Any opening in a wall between two rooms (one of which may be the atmosphere) will have flow through it, if the pressure is different on the two sides at any level. During a fire, there may be a variation of pressure with height which depends upon the density stratification.

At present, only rectangular openings with vertical sides are considered. Other shapes involve a trivial extension. The flow at each level is calculated by a hydraulic approximation modified by an empirical flow coefficient.

$$d\dot{m} = C_D B (2g\rho\rho_a \Delta p)^{1/2} dz \tag{35}$$

where Δp is measured in height of ambient air. Thus the atmospheric pressure (without wind) equals the height (e.g., above 1st floor level), and $C_D = .68$ [7]. If $\rho(z)$ is known on both sides of the vent above floor level, the mass flow rate, $\dot{m}$, can be found by integration.

For simplicity, a two layer model is at present assumed. Thus the vent is filled by layers in which the pressure drop varies linearly. The flow in each layer is given by

$$\dot{m} = sgn(\Delta p_{i+1} - \Delta p_i) \frac{\sqrt{8}}{3} C_D B (z_{i+1} - z_i) (g\rho\rho_a)^{1/2} \times (\Delta p_{i+1} + \Delta p_i + (\Delta p_{i+1} \Delta p_i)^{1/2}) \tag{36}$$

where ρ is the fluid density in the flowing fluid i.e., of the fluid at that z in the room of flow origin. The number and location of the layers depend upon: the pressure drop at the floor level, the location of the bottom and top of the vent, the location of the layer interfaces on each side of the vent, and the two densities in each room. Special note must be taken of the fact that the linear pressure drop from bottom to top of any layer may pass through zero at which place the direction and hence the density of the flowing fluid changes.

A computer program has been devised which automatically locates all the layers, computes the total inflow and outflow and the net flow through the vent.

At present, with one room (plus the atmosphere) there is only an upper flow out and a lower flow into the room. When there are many flow layers, it becomes less clear where the jet from any given layer goes (up or down) when it enters a room. Our first try, if no further experimental information becomes available, will be to split the flow from any layer in proportion to the location of its temperature relative to those of the layers in the room into which it flows.

As gas flows through a vent into the next room, the vent jet mixes with the gas already in the room. Thus the upper and lower layers in a room are partially mixed by the vent jets. These effects have not yet been incorporated into the Computer Fire Code.

The Horizontal Vent Flow. The simplest approach is to use an orifice formula for a hole in the floor or ceiling.

$$\dot{m} = C_D A (2g\rho\rho_a \Delta p)^{1/2} \tag{37}$$

This has already been done in some codes but not yet in the Computer Fire Codes.

A more careful consideration is required when there are no (or too small) openings in the rooms above or below the horizontal vent. We know that for zero flow a horizontal interface with hot fluid below is unstable. If that instability grows, there will be simultaneous finite flow rate out and in through the same horizontal vent. This in-/ outflow has not, to date, been studied either experimentally or analytically.

Heat Transfer by Radiation. The knowledge of radiation production, transmission, absorption, scattering, etc. is extensive indeed [8]. View factors for specific geometries can be computed to high precision. This knowledge will be of great value when other aspects of the fire can be computed with comparable accuracy. At present however, the use of little of this sophistication can be justified.

The Computer Fire Code contains one program available to the user to compute the emissivity of the hot layer from its composition. It roughly increases the computation time for a one room fire by about 20 percent without a comparable increase in accuracy of prediction. A simpler low-accuracy approximation based upon measurements by Markstein [15], is good enough as currently used

$$K = \frac{1}{\lambda} = 265\ Y_{\text{smoke}} \tag{38}$$

The formulas currently in use find the radiant heat transfer between: the flame (a perhaps truncated cone), the hot layer, the walls (including ceiling), and the objects.

Flame to Fuel (Base of Flame Cone).

$$\dot{q}'' = \sigma T_F^4 (1 - e^{-.776\phi KR}) \tag{39}$$

where

$$\phi = 2\cos\psi\left\{\sin\psi + \cos\psi + \sin\psi\cos\psi\, ln\left[\frac{\sin\psi(1-\sin\psi)}{\cos\psi(1+\cos\psi)}\right]\right\}$$

Flame to Object (Horizontal Surface).

$$\dot{q}'' = \phi\left(\frac{1-e^{-\tau}}{\tau}\right) \tag{40}$$

where

$$\phi = 2K\sigma T_F^4\left\{(L^2+x_b^2)^{1/2} - (L^2+x_a^2)^{1/2} - (s_b - s_a)\cos^2\psi + b\,\sin\psi\,\cos^2\psi\, ln\left[\frac{s_a + x_a\,\cos\psi - r\,\sin\psi}{s_b + h_p\,\sin\psi - b\,\sin\psi}\right]\right\}$$

$$\tau = \frac{4}{\pi}Kr\left(1+.84\left(\frac{r}{L}\right)^2\right)$$

$$b = H_f\tan\psi - r$$

$$s_a = (L^2+x_a^2+r^2)^{1/2}$$

$$s_b = (L^2+h_p^2+[r-(h_p-x_a)\tan\psi]^2)^{1/2}$$

Flame to Hot Layer.

$$\dot{E}_{FL} = \frac{A_f\sigma T_F^4}{2}\left(1-e^{-3.6\frac{KV}{A_F}}\right)\left[1+\frac{R}{(H^2+R^2)^{1/2}}\left\{1-E_2\left(\frac{Kh_L(H^2+R^2)^{1/2}}{R}\right)\right\} - E_2(Kh_L)\right] \tag{41}$$

where

$$E_2(x) = \int_1^\infty e^{-xt}\frac{dt}{t^2} \approx \frac{e^{-x}}{x+1}$$

Flame to Ceiling (Mean).

$$\overline{\dot{q}''} = \frac{A_F\sigma T_F^4\left(1-e^{-3.6\frac{KV}{A_F}}\right)\left(1-\frac{H}{(H^2+r^2)^{1/2}}\right)}{WL+2(W+L)h_L} \tag{42}$$

Total Flame Radiative Loss.

$$\dot{E}_R \approx A_F\sigma T_F^4\left(1-e^{-3.6\frac{KV}{A_F}}\right) \tag{43}$$

Layer to Object.

$$\dot{q}''_{L0} \approx \frac{\sigma T_L^4}{4}\sum_{i=1}^{4}\frac{1-e^{-Ks_i}}{1+\frac{H}{4A_i}} \tag{44}$$

where the sum is over the four rectangular areas into which the layer is divided by two perpendicular planes through the center of the object area parallel to the room walls.

$$s_i = \frac{2z_{0i}^2}{R_i^2}(h_L + z_{0i} - z_{1i})$$

$$z_{0i}^2 = R_i^2 + H^2$$

$$z_{1i}^2 = R_i^2 + (H+h_L)^2$$

$$R_i = \left(\frac{A_i}{\pi}\right)^{1/2}$$

Layer to Fire.

$$\dot{q}''_{LF} = \dot{q}''_{L0}\frac{e^{-KR}+\sin\psi}{1+\sin\psi} \tag{45}$$

Layer Radiative Energy Gain.

$$\dot{E}_{LR} = -\epsilon_w\sigma[A_L T_L^4 - (A_R+A_V)T_a^4 (A_L - A_R - A_v)T_w^4] + \dot{E}_a \tag{46}$$

Layer to Walls (Including Ceiling).

$$\dot{q}'' = \sigma T_L^4\left(1-e^{-\frac{4KV}{A_L\left(1+.18\frac{4KV}{A_L}\right)}}\right) \tag{47}$$

Walls to Layer.

$$\dot{E}_{WL} = (A_L - A_R - A_V)\epsilon_w\sigma T_w^4 \tag{48}$$

Walls to Object.

$$\dot{q}''_{W0} = \epsilon_w\sigma T_w^4\frac{(\dot{E}_F - \dot{E}_{FL})}{A_f\sigma T_F^4\left(1-e^{-3.6\frac{KV}{A_F}}\right)} \tag{49}$$

Walls to Fire.

$$\dot{q}''_{WF} = \dot{q}_{W0}\frac{e^{-KR}+\sin\psi}{1+\sin\psi} \tag{50}$$

The next version of the Computer Fire Code will have all radiation heat transfers expressed in the standard form using $\Delta(T)^4$ and an attempt will be made to find much simplified semiempirical expressions for the view factors applicable to conditions found in rooms.

Heat Transfer by Convection. There is direct convective heat transfer between a fire plume and the room boundaries. For a plume against a wall or in a corner, there is convective heat transfer to the walls. There is limited data on convective heat transfer by a ceiling jet to the ceiling [9, 14].

In the present Computer Fire Code, we use the simple formula for the convective heat transfer between the hot layer and the inside of the wall.

$$\dot{q}''_{LW} = h_i(T_L - T_{Wi}) \tag{51}$$

where

$$h_i = 5 + .45(T_L - T_a)$$

is expressed in SI units w/m^{2}K, while outside we use

$$\dot{q}''_{aW} = 5(T_{W0} - T_a) \tag{52}$$

A special problem arises if one insists that there are only two wall types, one hot and one cold. As the hot layer deepens, wall is transferred from the cold to the hot type. The required energy in our program is imagined to be transferred as a lump from the hot layer to the wall. The required energy is

$$\dot{E} = 2(W+L)h_L\int_0^t(\dot{q}''_{LW} + \dot{q}''_{0W})\,dt \tag{53}$$

At present, this energy is ignored when the layer becomes less deep as the room fire wanes. In the future, this energy will be dumped into the lower layer.

For a multiroom building, each side of the wall will have to be somehow connected with its own room.

Clearly, these formulas can be improved. The magnitude of plume velocities should be included in the evaluation of the

heat transfer coefficients. For a single room the convective heat loss is not of major importance. It will be more important for predicting sprinkler link operation and will be necessary for a large building where the buoyant gas from the fire room cools off a great deal while moving throughout the building.

Heat Transfer by Conduction. The walls and objects in the room absorb heat, pyrolyze and eventually ignite. The interior temperature must be computed. To do this we solve the one-dimensional conduction equation by finite differences [10]. The solution first requires the conduction thickness, τ, to be divided into finite layers. To do this the computer proceeds as follows:

$$\delta x_{\min} = (2\alpha \delta t_{\max})^{1/2} \tag{54}$$

This requires N points

$$N-1 = \frac{\tau}{\delta x_{\min}} \text{ [integer part of]} \tag{55}$$

So that there will not be more than 20 points, we use

$$\delta x = \max \frac{\tau}{N-1}, \frac{\tau}{19} \tag{56}$$

Then

$$T(x,t+\delta t) = 1 - \frac{2\alpha}{\delta x^2} T(x,t) + \frac{\alpha \delta t}{\delta x^2} (T(x+\delta x,t) + T(x-\delta x,t)) \tag{57}$$

and for the boundary points

$$T(0,t+\delta t) = 1 - \frac{2\alpha}{\delta x^2} T(0,t) + \frac{\alpha \delta t}{\delta x^2} \left(T(\delta x,t) + \frac{\delta x}{k} \dot{q}'' \right) \tag{58}$$

Pyrolysis. As various objects are heated, they begin to pyrolyze adding gaseous fuel to the air in the room. Because of the extremely complex chemistry, only empirical information is available and that on only a few materials under limited circumstances [11]. At present, no pyrolysis gases are calculated.

In the future, empirical data for both the amount and rate of gaseous products will probably be used. The blanketing effect of the char greatly complicates the pyrolysis process for many materials. A simple Arrhenious relation between pyrolysis rate and temperature, even if adequate for the chemistry, would be masked by the effects of the char. Much further work of a basic scientific nature is required to put practical applications of this phenomena on a fundamental basis.

Flameover, Flashover and Ventilation Limited Fire. When the fire has progressed to the point that some object is about to ignite, most combustibles in the room are ready to ignite and do so in a short time (perhaps seconds). This is "Flameover." At about the same time the unburned fuel, smoke, and soot concentration in the hot layer reach the lower flammability limit and either burn out or use up the oxygen in the hot layer as the flames come out the vent. This latter we will define as "Flashover." When the Computer Fire Code has been developed to this level, we will be in a position to predict when the rate of heat release inside the room is limited by the amount of oxygen entering the vents and is independent of how the fuel is distributed inside. This condition is called "Ventilation Limited."

Since the heat of combustion of oxygen is about

$$Q_{0_2} = 1.5 \times 10^7 \text{ J/kg}$$

for most organic fuels, the heat released in the room during a ventilation limited fire is

$$Q_{0_2} Y_{0_2} \dot{m}_d = -Q_{\text{vap}} \dot{m}_f + \rho_c c_p (T_R - T_d)(\dot{m}_d - \dot{m}_f) \tag{59}$$

where the heat released is used to vaporize more fuel and heat all the gases up to temperature, T_R.

This temperature must be such that the fuel is indeed evaporated. Thus,

$$A(\sigma(T_R^4 - T_{\text{vap}}^4) + h(T_R - T_{\text{vap}})) = -Q_{\text{vap}} \dot{m}_f'' \tag{60}$$

where A is the fuel area – approximately equal to the area of the room. These two equations determine both the gas temperature, T_R, and the rate of fuel emission, $-\dot{m}_f$.

When the inlet vent flow becomes restricted and the gas temperature is high enough to rapidly vaporize fuel, $-\dot{m}_f$ becomes far more than enough to burn all the oxygen entering the room and hence much flammable and burning gases are supplied outside.

Late in the fire when all the fuel has been reduced to charcoal, T_{vap} and Q_{vap} no longer exist, and a different ventilation limited analysis will be necessary.

Finally, as the last of the charcoal burns up, the room returns to a passive state – merely a gas passage – if the walls are noncombustible. Otherwise, the walls collapse and a whole new building geometry exists. At present, the nature of collapse looks too random to be predicted. The future will tell.

Ignition of the Next Room. Heat transfer by radiation through a vent and convective heat transfer from hot gases and flames are responsible for igniting objects in the next room as well as those in the initial fire room. All the fire development programs used in the first room must be used over again in the next. Thus the fire, for a while, will lead to more and more fire variables and calculations. However, as rooms become ventilation limited and eventually burn out, the variables and computational complexity will reduce. This is very important and will help keep fire computations within practical economic bounds.

The Corridor. Sometimes the "next room" is a long corridor. The fire, the heat transfers, the plumes, etc., will be the same regardless of the size and shape of the "room." However, it is clearly not correct to assume a hot and cold layer to be of uniform properties. Plume gases may heat and ignite the ceiling before the flowing hot gases have reached the distant end of the corridor. Present theories of ceiling jets are of a more complex nature then could, at present, be justified for use in computing a fire in a large building. Somewhat less accurate but less complex computations are probably possible for use in fire growth calculations.

Flow Throughout the Building. Even though the fire has just started in one room, there are gas flows throughout the whole accessible portion of the building no matter how large. This is because the energy released by the fire greatly expands the heated gas (by a factor of 4 or more). If the fire room doors were sealed the resultant rise of pressure (to as high as 4 atmospheres) would burst the walls even if of reinforced concrete. In fact, rooms are never that tight so that leaks and heat losses slow the pressure rise.

By "accessible portions of the building" is meant those parts through which gas can be pushed by the fire gas expansion. Open doors and windows, badly fitted doors, various construction holes, ventilation ducts, etc. can all serve to control the direction and amount of gas flow.

After a short time, the flow will also be driven by buoyancy which takes hot gases to the highest accessible spot.

In any case, the flow through a large building is a flow through a resistance network.

For nonbuoyant flow, a resistance is definable as

$$R = \frac{\Delta p}{\dot{m}^2} \tag{61}$$

Notice that this relation is nonlinear in the flow rate. Thus while series and parallel formulas can be derived, they are not as simple as for thermal or electrical circuits.

Series circuit $$R = R_1 + R_2 + \ldots \tag{62}$$

Parallel circuit $$R = \left(\frac{1}{R_1^{1/2}} + \frac{1}{R_2^{1/2}} + \ldots \right)^{-2} \tag{63}$$

For a large building there are often so many interconnections that these formulas are inadequate. Thus we must use the fact that the net flow at every node (room with more than one exit) must be zero, except where a fire is creating new volume (by gas expansion or burned fuel).

When buoyancy effects are added, several new complications arise. It is no longer possible to assign a unique resistance to a vent. Any change of elevation, as from the first to second floor, acts as a pump driving hot gas up and cold gas down. The method of solution is again to adjust node pressures (say at the floor) to produce zero net mass flow except for fire produced volume.

The best way to handle these problems is still a matter for research.

Detectors and Sprinklers. When the fire growth can be successfully calculated, the known characteristics of various types of detectors and designs of sprinklers can be used to predict their operation. The predicted "smoke" concentration can be used to predict the time of a gas detector alarm. The heat transfer to sprinkler links could predict when sprinkler water will be released. Furthermore, the flow of sprinkler water and its effect in fire extinguishment can some day be added to the fire prediction program.

The Input and Output of the Computer Program

The real fire has as its input the existing building, while the output data of fire development can only be obtained by elaborate instrumentation throughout the structure. The Computer Fire Code knows only the building which the user inputs and will output only that information which it is instructed how to provide.

Material properties can be input from resident data in the computer code. New methods must be devised for rapid input of building data. Just to input the size and location of every room, every vent, every object in a large building would be very tedious. This may be necessary until the whole building design process is carried out in a computer aided manner. In the latter case, the fire program would be an add-on which could be consulted relative to fire safety during the design process. The question of how to most conveniently input the required information is currently under study.

As output, there are a number of obvious fire safety needs:

1 The time dependence of the temperature on all escape routes

2 The time dependence of the concentration of toxic gases, especially CO, on all escape routes

3 The time of sounding of the fire detectors, if any

4 The time of operation of the sprinklers, if any

We know that as soon as we acquire a long-sought capability, we immediately think of many more ambitious needs. As soon as a working computer fire code becomes available, someone will want to examine alternate designs, alternative materials. It will be possible to compute a building and if it is found safe except for a fire which starts in some particular location, that location can be redesigned or an expensive fire suppression system could be supplied in that local area for fire control.

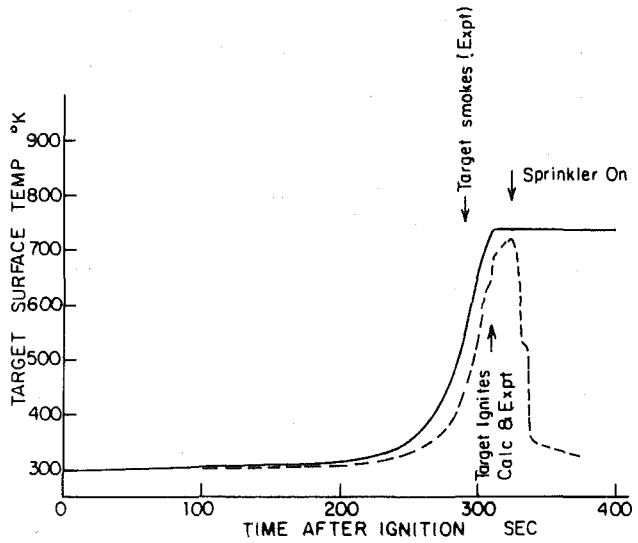

Fig. 1 The time-variation of surface temperature of a cellular plastics target by computation (solid curve) and full-scale experiment

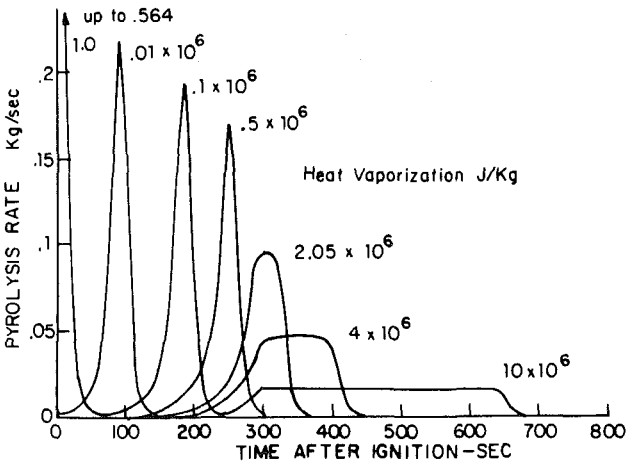

Fig. 2 The rate of pyrolysis of fuels of different heats of vaporization in a fire

In closing, I supply a few figures showing the present capability of Computer Fire Code V to predict the results of a full-scale room fire compared to fire test results.

Results

How well does the computer calculate a real fire? This, of course, is the ultimate use of all the work in mathematical modeling of fire. A series of full-scale tests run for the Home Fire Project by the Factory Mutual Research Corporation were made about five years ago and have all been computed for validation purposes. Many of the computed results have already been published [12, 13] and will not be repeated here.

Figure 1 shows the typical agreement between experimental and computed results. The time-temperature history of the surface of a target slab of polyurethane shows agreement good enough for many fire decisions. Figure 2 shows a result not previously published and shows another use for the computer program.

How does a fire behave as the heat of vaporization (pyrolysis) varies? A decrease of Q_{vap} increases the rate, decreases the time, and increases the temperature of the response of the fire. This figure also shows the erratic nature of the stability properties of the numerical solution techniques. By error, a heat of vaporization of 1 J/Kg was

introduced instead of 1×10^6. As the figure shows, the computer proceeded dutifully to calculate this extreme case. In fact, most of the curve for $Q_{vap} = 1$ was produced by the specified maximum fire decay rate.

Conclusions

The ultimate objective of computing a fire in a high-rise building is still some years away. However, the success of predicting with the required practical accuracy the fire in a single enclosure has disclosed no insurmountable problems. The ultimate objective is attainable.

Acknowledgments

The author is indebted to Dr. Henri Mitler for major parts of the developments described in this paper, and to a large number of Harvard undergraduates who have done much of the computer coding.

This work was supported by the National Bureau of Standards Grant No. G7-9011 and by the Division of Applied Sciences, Harvard University.

References

1 Mitler, H. E., "The Physical Basis for the Harvard Computer Fire Code," Home Fire Project Technical Report No. 34, 1978, Harvard University.

2 Steward, F. R., "Prediction of the Height of Turbulent Buoyant Flames," *Comb. Sci. and Tech.*, No. 2, 1970, pp. 203–249.

3 Fang, J. B., "Analysis of the Behavior of a Freely Burning Fire in a Quiescent Atmosphere," National Bureau of Standards Report No. 73115, 1973.

4 Tamanini, F., "An Integral Model of Turbulent Fire Plumes," Factory Mutual Research Corporation Report No. J. I. OFOJ3.BU RC80-BT-12, 1980.

5 Morton, B., Taylor, G. I., and Turner, J., "Turbulent Gravitational Convection From Maintained and Instantaneous Sources," *Proceedings of the Royal Society*, London, No. A234, 1956, pp. 1–23.

6 Grella, J. J., and Faeth, G. M., "Measurements of a Two-Dimensional Thermal Plume Along a Vertical Adiabatic Wall," *Journal of Fluid Mechanics*, Vol. 7, 1975, pp. 701–710.

7 Prahl, J., and Emmons, H. W., "Fire Induced Flow Through an Opening," *Combustion and Flame*, No. 25, 1975, pp. 369–385.

8 Siegel, R., and Howell, J., *Thermal Radiation Heat Transfer*, 2nd ed., McGraw-Hill, 1980.

9 You, H. Z., and Faeth, G. M., "Ceiling Heat Transfer during Fire Plume and Fire Impingement," *Fire and Materials*, Vol. 3, No. 3, 1979, pp. 140–147.

10 Emmons, H. W., "Heat Conduction Calculations for Zone Fire Modeling," Home Fire Project Technical Report No. 44, 1980, Harvard University.

11 Zinn, B., et al, "Investigation of the Properties of the Combustion Products Generated by Building Fires," Final Report to Products Research Committee, 1978, National Bureau of Standards.

12 Emmons, H. W., "The Prediction of Fires in Buildings," *Proceedings of the Seventeenth Symposium (International) on Combustion*, 1978, pp. 1101–1112.

13 Emmons, H. W., Mitler, H. E., and Trefethen, L. N., "Computer Fire Code III," Home Fire Project Technical Report No. 25, 1978, Harvard University.

14 Zukoski, E., and Kubota, T., "Two-Layer Modeling of Smoke Movement in Building Fires," *Fire and Materials*, Vol. 4, 1980, pp. 17–27.

15 Markstein, G., "Radiative Properties of Plastics Fires," *Seventeenth Symposium (International) on Combustion*, The Combustion Institute, Pittsburgh, 1978, pp. 1053–1062.

Soot Volume Fraction Profiles in Forced-Combusting Boundary Layers

R. A. Beier[1]

P. J. Pagni
Mem. ASME

Department of Mechanical Engineering,
University of California,
Berkeley, Calif. 94720

A multiwavelength laser transmission technique is used to determine soot volume fraction fields and aproximate particle size distributions in a forced flow combusting boundary layer. Measurements are made in diffusion flames of polymethylmethacrylate (PMMA) and five liquid hydrocarbon fuels (n-heptane, iso-octane, cyclohexane, cyclohexene, and toluene) with ambient oxygen mass fractions in the range of $0.23 \lesssim Y_{0\infty} \lesssim 0.50$. *Soot is observed in a region between the pyrolyzing fuel surface and the flame zone. Soot volume fraction increases monotonically with* $Y_{0\infty}$, *e.g., n-heptane and PMMA are similar with soot volume fractions,* f_v, *ranging from* $f_v \sim 5 \times 10^{-7}$ *at* $Y_{0\infty} = 0.23$ *to* $f_v \sim 5 \times 10^{-6}$ *at* $Y_{0\infty} = 0.50$. *For an oxygen mass fraction the same as air,* $Y_{0\infty} = 0.23$, *soot volume fractions are approximately the same as values previously reported in pool fires and a free combusting boundary layer. However, the shape of the* f_v *profile changes with more soot near the flame in forced flow than in free flow due to the different y-velocity fields in these two systems. For all fuels tested, a most probable particle radius is between 20 nm and 80 nm, and does not appear to change substantially with location, fuel, or oxygen mass fraction.*

Introduction

Thermal radiation is the dominant mode of heat transfer in full scale fires [1]. This radiation is primarily soot emission with a small contribution from gas species emission. The soot emission depends on the flame temperature and the volume of solid particles per unit volume of flame, i.e., the soot volume fraction, f_v. Local volume fractions of soot and approximate size distributions are determined here by a multiwavelength laser transmission technique previously described [2-8]. The forced flow, two dimensional, laminar combusting boundary layer used is attractive for the study of soot, because the flame can be easily probed by optical techniques and predicted by mathematical models [9, 10]. Measurements have been reported for soot volume fractions in pool fires [2-6] and a free flow combusting boundary layer [7]. The combustion tunnel used in this study provides a very different streamline pattern from the free flow case and permits control of the oxygen mass fraction so that a wide range of flame temperatures and soot volume fractions are obtained for each fuel.

A schematic diagram of a laminar combusting boundary layer over a pyrolyzing fuel surface is shown in Fig. 1. A pyrolysis zone separates a flame zone from the fuel surface. Part of the carbon in the fuel is converted to carbon particles, which are observed in a soot layer on the fuel side of the flame zone. It is this layer which is probed here. Experimental studies of soot in these well-controlled flames also provide insight into complex soot formation and oxidation processes.

Minchin [11], and Clarke, Hunter and Garner [12] did early studies of the effect of fuel type on soot formation in laminar diffusion flames. They increased the height of a flame on a small circular burner by increasing the fuel flow rate until the flame emitted soot at its tip. This height is called the smoke height or sooting height. When the sooting height is used as a relative measure of sooting tendency, a lower sooting height indicates a greater tendency to form soot. Jagoda, Prado, and

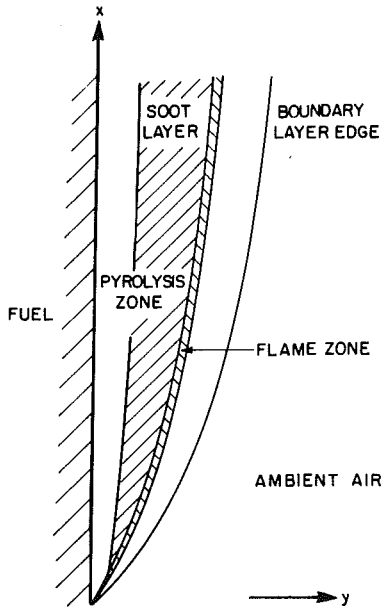

Fig. 1 Schematic diagram of a steady, two-dimensional, laminar, combusting, boundary layer on a pyrolyzing fuel slab

Lahaye [13] measured local soot concentrations by probe and light scattering and absorption techniques in a candle-like diffusion flame. Related experiments for gaseous fuels have been reported by Kent, Jander and Wagner [14], Haynes, Jander and Wagner [15, 16], and Chang and Penner [17].

Recently, Glassman and Yaccarino [18] measured sooting points to determine the effects of oxygen concentration on the sooting tendency of fuels. Santo and Taminini [19] used a modified Schmidt technique to measure the flame radiance of a pool fire against a variable background of black body radiation. These measurements allowed them to determine absorption-emission coefficients and trends in soot volume fraction for different ambient oxygen concentrations. While these previous studies give qualitative trends, the present study reports quantitative data for soot volume fractions at different oxygen concentrations.

[1] Current address: Basic Research Department, Factory Mutual Research, Norwood, Mass. 02062.

Contributed by the Heat Transfer Division for publication in the JOURNAL OF HEAT TRANSFER. Manuscript received by the Heat Transfer Division, January 12, 1982.

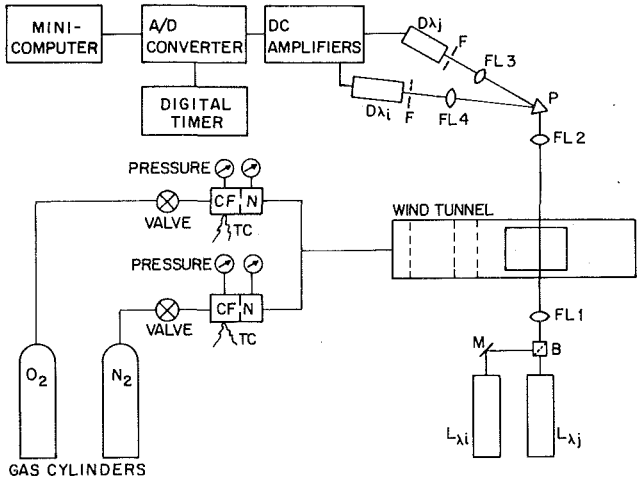

Fig. 2 Schematic diagram of wind tunnel and optical equipment for simultaneous multiwavelength laser transmission measurements:

$L\lambda_i$, $L\lambda_j$	– Laser at λ_i or λ_j
M	– Mirror
B	– Beamsplitter
P	– Prism
FL1	– Focusing lens #1 (f = 550 mm)
FL2	– Focusing lens #2 (f = 250 mm)
FL3	– Focusing lens #3 (f = 200 mm)
FL4	– Focusing lens #4 (f = 78 mm)
F	– Bandpass filter (bandwidth = 30 A)
$D\lambda_i$, $D\lambda_j$	– Detector for transmitted intensity at λ_i or λ_j
CFN	– Critical flow nozzle
TC	– Thermocouple

Kinoshita, Pagni, and Beier [8, 20, 21], Sibulkin, Kulkarni and Annamalai [22], and Liu and Shih [23] recently included radiation in models of a laminar combusting boundary layer. These models require a knowledge of soot volume fraction within the layer, which is provided by the present study.

Extinction Analysis

The multiwavelength laser transmission technique is described elsewhere [2–8], so only a brief outline of the assumptions and data analyses is given here. The transmitted intensity, I, of a monochromatic beam through a polydisperse aerosol is related to the initial intensity, I_o, by

$$I(\lambda)/I_o(\lambda) = \exp(-\tau(\lambda)L) \tag{1}$$

where L is the beam pathlength. The aerosol spectral extinction coefficient, τ, is given by

$$\tau(\lambda,m,r) = \int_0^\infty N(r)\,Q(\lambda,m,r)\,\pi r^2\,dr \tag{2}$$

where Q is the particle extinction efficiency from the Mie scattering theory [24] for spherical particles. Calculation of a spectral extinction coefficient requires knowledge of the size distribution, $N(r)$, and the optical properties of the particles $m(\lambda) = n(\lambda)\,(1 - ik(\lambda))$. Size measurements in premixed flames [25] suggest a gamma size distribution [26] with

$$\sigma/r_m = 1/2 \tag{3a}$$

$$N(r)/N_o = (27\,r^3/2\,r_{\max}^4)\exp(-3\,r/r_{\max}) \tag{3b}$$

is appropriate where $r_{\max}$ is the most probable radius, and N_o is the total particle concentration. While some dependence of $r_{\max}$ on the constant in equation (3*a*) has been reported [27], the soot volume fraction has been shown to be insensitive to the details of the functional form assumed for the size distribution.

The optical properties used here [5] are based on a dispersion relation developed by Lee and Tien [28–31] which has been shown to well represent the soot of many fuels in a variety of flame geometries. The soot is assumed to be sufficiently well aged that C/H ratio effects on $m(\lambda)$ are negligible, while sufficiently young that little agglomeration has taken place so that the spherical assumption is valid. Our transmission method is much less ensitive to particle nonsphericity effects [30] than are other reported light scattering techniques [13–17].

The soot volume fraction is defined by

$$f_v \equiv \frac{4}{3}\,\pi\int_0^\infty N(r)\,r^3\,dr \tag{4}$$

In terms of the two unknowns in equation (3*b*), f_v is

$$f_v = \frac{54\pi}{3^8}\,\Gamma(7)\,N_o r_{\max}^3 = 18.62\,N_o r_{\max}^3 \tag{5}$$

It remains to find N_o and $r_{\max}$ from measurements of I and I_o at two wavelengths over a measured pathlength, L. Substituting these measured values into equation (1) gives two independent values of τ, one at each wavelength. These two τ values give two independent equations (2) to determine the two unknowns in the size distribution, N_o and $r_{\max}$. The volume fraction of soot is obtained from equation (5). In some cases $r_{\max}$ is double valued, so more than one wavelength pair is required to isolate the correct $r_{\max}$. Agreement among several wavelength pairs also substantiates the assumed size distribution and optical properties.

Experimental Method

Multiwavelength laser transmission experiments are performed with the apparatus shown schematically in Fig. 2. The flames are in a combustion tunnel designed to produce a uniform flow of an oxidizing mixture of nitrogen and oxygen above the fuel surface. The tunnel consists of a mixing chamber, contraction section, and test section. The mixing

Nomenclature

f_v = particulate carbon volume/flame volume
I = radiant intensity
L = beam pathlength through fire
m = complex index of refraction
$\dot{m}_p$ = local pyrolsis rate
$\dot{M}_p$ = total pyrolysis rate, $\dot{M}_p = \int_0^l m_p(x)\,dx$
n = real index of refraction
nk = imaginary index of refraction
N_o = total particle concentration
$N(r)\,dr$ = particle concentration in the size range dr about r
Q = extinction efficiency
r = particle radius
x = streamwise direction coordinate
y = transverse direction coordinate

Greek

λ = wavelength
σ = standard deviation
τ = extinction coefficient

Subscripts

i = first wavelength
j = second wavelength
m = mean
max = most probable, i.e., at maximum in $N(r)$
o = oxygen or incident
∞ = ambient

chamber is divided into sections by screens with one section packed with steel wool. A rapid contraction of two walls accelerates the flow and minimizes the thickness of the boundary layers on the walls at the entrance of the test section. With an area contraction ratio of 6, the shape of the contraction is similar to the one used by Brown and Roshko [33]. The horizontal test section has a rectangular cross section, 18-cm wide and 5-cm high. The sides of the tunnel and the ceiling directly over the fuel surface are made of pyrex glass to provide visibility and access for optical measurements. The fuel wicks and solid fuel are placed flush in an inert floor, Marinite-XL (Johns-Manville Co.), 5 cm behind the exit of the contraction, as shown in Fig. 3. The oxidizer flow is measured by a set of four critical flow nozzles for each of the component gases, oxygen and nitrogen. The nozzles are calibrated individually at operating conditions by a wet test meter. For each gas, the stagnant chamber pressure upstream of the critical flow nozzles is measured by a Bourdon tube gauge. A copper-constantan thermocouple upstream of the nozzles is used to measure the stagnant chamber temperature. The static pressure downstream of the nozzles is also monitored to insure choked operation of the nozzles.

The optical equipment for the laser transmission measurements is similar to that described by Pagni and Bard [2-6]. Two lasers are used: a Spectra-Physics Argon Ion tunable laser model 165, operating at either $\lambda = 0.4579$ μm, 0.4880 μm, or 0.5145 μm, and a Spectra-Physics Helium Neon laser model 125, emitting at $\lambda = 0.6328$ μm. After a cube beam splitter superimposes the two beams from the lasers, the beams pass through the same physical space in the flame. Great care was taken before each experiment to align the centers of the Gaussian intensity profiles of each beam. The first simple lens improves spatial resolution by causing a slight convergence of both beams to a minimum beam width of ~ 0.15 mm at the middle of the sample path through the two-dimensional flame. After a second lens collects the transmitted light, an equilateral prism separates the two beams. Each beam passes through another focussing lens and a narrow band pass filter, before it strikes a laser power meter

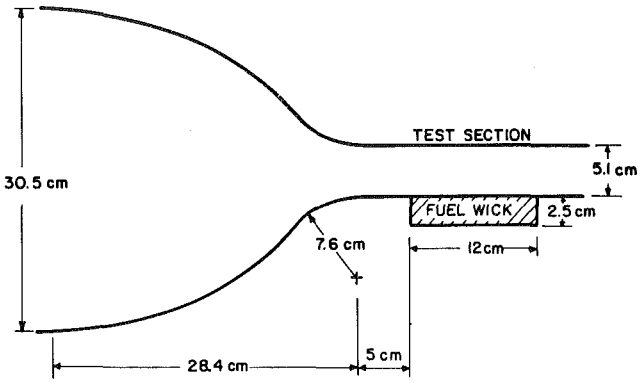

Fig. 3 Contraction and test sections of combustion tunnel

(Newport Research Corp., model 820). The diameter of the laser beam limits the spatial resolution of the transmission measurements. For all pathlengths used, the maximum beam width between points of $1/e^2$ intensity is less than 0.3 mm. Since variations in temperature and species change the index of refraction in the direction normal to the fuel surface, the flame deflects the laser beam. However, this deflection does not decrease the spatial resolution with the lens system shown in Fig. 2.

Since the transmitted intensity of the laser beams varies greatly for different fuels and oxygen mass fractions, wicks of different widths are used as listed in Table 1. The wick is a ceramic fiber board, Fiberfrax Hot Board, Carborundum Company. With aluminum foil around the hidden surfaces of the wick, the inert wall does not absorb liquid fuel. The length of the wick is 12 cm, except for toluene where the length is 8.4 cm. The samples of polymethylmethacrylate (PMMA) are usually 12-cm long, 12-cm wide, and 1.27-cm thick.

The entire combustion tunnel is placed on a milling table, so that the distance between the fuel surface and the superimposed laser beams can be changed by moving the tunnel vertically. A complete scan of the flame is obtained by moving the tunnel horizontally between traverses. After the

Table 1 Summary of the maximum soot volume fractions observed at $x = 4$ cm along with size distributins and sample geometries. Here $u_\infty = 1.5$ m/s and $T_\infty = 298$°K.

Fuel	$Y_{0x,\infty}$	Sample width (cm)	Wave-length pair, i−j	Path-length L (cm)	Distance from fuel surface (mm)	$(I/I_o)_i$	$(I/I_o)_j$	$f_v \times 10^{-6}$	r_{max} (nm)	$N_o \times 10^{-9}$ (cm^{-3})
Toluene (C_7H_8)	0.25	1.7	2-4	2.6	2.7	0.0005	0.0011	22	79	2.4
Cyclohexene (C_6H_{10})	0.23	7.0	2-4	8.3	3.8	0.088	0.20	1.7	40	1.5
	0.25	3.5	1-4	4.7	3.6	0.075	0.25	3.1	31	5.4
	0.25	3.5	1-4	4.7	3.1	0.084	0.27	3.0	30	5.9
	0.25	3.5	2-4	4.5	2.8	0.16	0.27	2.4	48	1.2
	0.25	1.7	2-4	3.1	2.8	0.28	0.43	2.5	39	2.2
	0.35	3.5	1-4	4.7	3.0	0.0016	0.017	7.5	44	4.8
	0.35	3.5	2-4	4.5	3.2	0.010	0.038	6.1	48	2.9
Iso-octane (C_8H_{18})	0.25	7.0	2-4	8.3	3.2	0.20	0.32	1.1	49	0.52
Cyclohexane (C_6H_{12})	0.25	7.0	2-4	8.3	3.8	0.38	0.45	0.78	64	0.16
n-Heptane (C_7H_{16})	0.23	12.0	2-4	13.8	4.0	0.62	0.74	0.21	36	0.24
	0.25	7.0	2-4	8.4	3.7	0.61	0.68	0.37	56	0.11
	0.25	7.0	2-4	8.4	3.8	0.59	0.68	0.38	49	0.17
	0.35	7.0	1-4	8.7	3.5	0.053	0.20	1.9	32	3.2
	0.35	7.0	2-4	8.6	3.2	0.069	0.17	1.9	41	1.4
	0.50	7.0	2-4	8.1	2.9	0.015	0.048	3.1	50	1.3
	0.50	7.0	2-4	8.3	3.1	0.015	0.051	3.0	47	1.6
Polymethyl-methacryl-ate ($C_5H_8O_2)_n$	0.25	12.0	2-4	12.0	2.6	0.48	0.58	0.37	49	0.17
	0.35	12.0	2-4	12.0	2.1	0.0096	0.043	3.0	42	1.6
	0.50	6.0	2-4	6.0	1.9	0.019	0.060	4.0	48	2.0

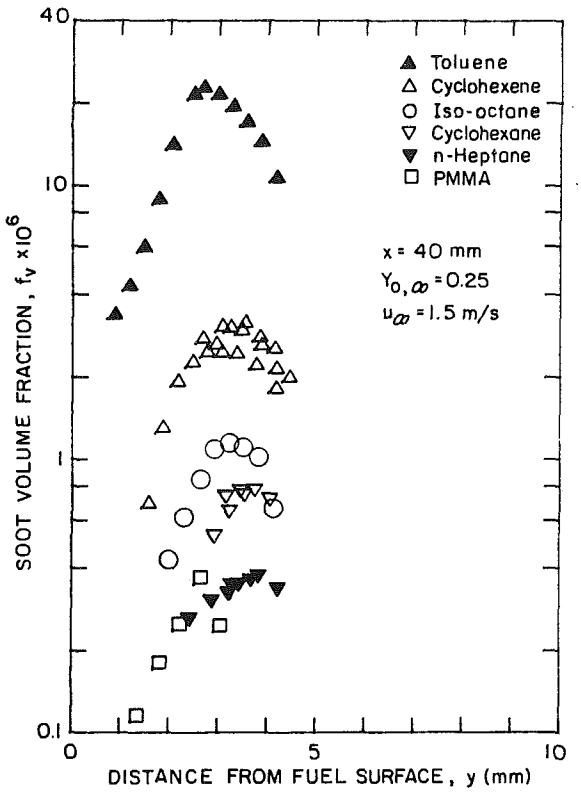

Fig. 4 Soot volume fraction, f_v, as a function of distance from fuel surface at x = 4 cm for five liquid, hydrocarbon fuels and PMMA. T_∞ = 298°K for Figs. 4–10.

mass flow rates of oxygen and nitrogen are set, the fuel is ignited. For the liquid fuels, the supply of fuel in the wick gives a steady fire for a time period between 3 to 5 min, depending on the oxygen mass fraction. This time period allows one vertical scan, with increments of 0.3 mm, through the boundary layer. A PDP-11/34 minicomputer stores the intensity data after the output signals from the detectors pass through a d-c amplifier and a (Digital Equipment Corp.) AR11 16-channel, 10-bit, A/D converter. A digital timer triggers the A/D converter to read the detector outputs 300 times within a 6-s interval. After each vertical scan the flame is extinguished, the horizontal position of the fuel is changed, and the wick is soaked with fuel, before the flame is reignited.

It is observed that the flame zone is in contact with the inert floor beyond the side edges of the wick. Soot is deposited on the inert floor between the fuel surface and this line of flame contact. The width of the soot region and hence the pathlength, L, of the laser beams is well approximated by the distance between the lines of flame contact on each side of the fuel surface. The pathlength is found to be ~ 1 cm longer than the width of the wick and nearly independent of x and y as shown in Table 1. The value determined for the most probable radius is independent of the pathlength measurement. An uncertainty of 5 percent in L results in approximately a 5 percent uncertainty in the soot volume fraction.

For PMMA the fuel regression rate affects the beam distance from the fuel surface. The regression rate is measured before and after each vertical scan through the boundary layer by blocking the laser beams partially with the fuel surface. If the floor of the tunnel remains stationary, the surface of the pyrolyzing fuel slab moves and blocks a smaller part of the laser beams. The regression rate is the rate the tunnel floor must be moved to maintain a constant reading of transmitted intensity for the partially blocked beam. A new sample of PMMA is burned for the transmission and regression rate measurements at each streamwise position.

Table 2 Total pyrolysis rates for liquid fuels from wicks 6 cm wide and 12 cm in length with u_∞ = 150 cm/s (*u_∞ = 225 cm/s). Rates are per unit width.

Fuel	$Y_{0\infty}$	Total pyrolysis rate $\dot{M}_p$(g/m•s)
n-heptane	0.23	2.3
	0.25	2.5
	0.35	3.4
	0.35*	4.1*
	0.50	4.7
cyclohexene	0.23	2.9
	0.25	3.2
	0.35	4.3
cyclohexane	0.25	3.3
iso-octane	0.25	2.9
toluene	0.25	3.5

Results and Discussion

Profiles of volume fracton of soot are shown in Fig. 4 for five liquid fuels and PMMA at 4 cm downstream of the fuel leading edge with u_∞ = 1.5 m/s, T_∞ = 298°K and $Y_{0\infty}$ = 0.25. The standard deviations in the data are within the size of the symbols in the graph. When the data are compared with previous measurements [2–8], the rank and magnitude of the soot volume fraction is preserved among small pool fires, and free and forced boundary layers. Smaller error bars exist for the more stable forced flames.

The most striking difference between free and forced flow systems is the change in the shape of the f_v profile. The tail of the profile shown near the fuel surface in Fig. 4 is near the flame in free flow (see, e.g., Fig. 3 of [7]). This is due to the difference in the y-velocity field between free flow, with a negative y-velocity throughout the soot and flame region and forced flow with a positive y-velocity everywhere. The fact that the free flow soot lies between a converging streamline and the flame means that any soot near the flame must have been generated there. While in forced flow soot can be convected toward the flame as well as generated there. Therefore, higher soot concentrations exist closer to the flame in forced flow than in free flow for the same fuel at the same $Y_{0\infty}$ and T_∞.

Table 1 lists values of soot volume fractions, the most probable radius, and total particle concentrations at the maxima in the f_v profiles. The five liquid hydrocarbon fuels have approximately the same thermal and physical properties, and adiabatic flame temperature. The large variation in soot volume fraction indicates the chemical structure of the fuel has a strong influence on soot formation. Since no significant changes occur for wicks of different widths, errors due to edge effects are negligible. With wicks of 12 cm length, measurements of burning time and mass of the wicks, before and after the burning, show the total pyrolysis rate at the fuel surface for toluene is 40 percent greater than that of n-heptane at $Y_{0\infty}$ = 0.25. As listed in Table 2, the pyrolysis rates of the other liquid fuels are between these two extremes. For toluene, the large soot volume fraction provides some significant radiative heat flux into the fuel surface.

The soot volume fraction increases with downstream distance, x, for all fuels tested, but for fuels with a high soot volume fraction the variation with x is smaller. In Fig. 5, the profiles for cyclohexene indicate a larger variation in soot volume fraction with x than determined in the free flow case for $Y_{0\infty}$ = 0.23. The outer edge of the soot layer follows the flame zone away from the fuel surface with increasing downstream position, the width of the layer increases, the

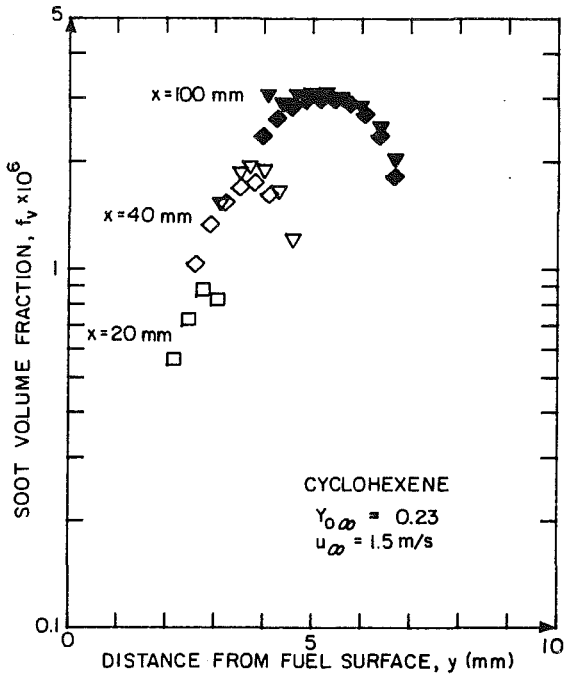

Fig. 5 Soot volume fraction, f_v, as a function of distance from fuel surface at different downstream positions for cyclohexene. Wavelength pair numbers refer to λ_i (λ_1 = 0.4579 μm, λ_2 = 0.4880 μm, λ_3 = 0.5145 μm, λ_4 = 0.6328 μm).

Symbol	x (mm)	Wavelength pair
△	20	1-4
□	20	2-4
▽	40	1-4
◇	40	2-4
▼	100	1-4
◆	100	2-4
▲	100	3-4

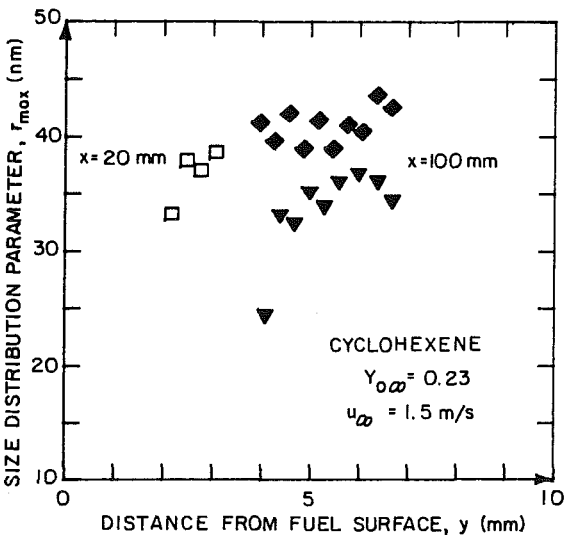

Fig. 6 Most probable particle radius, r_{max}, as a function of distance from the fuel surface and downstream position for cyclohexene at $Y_{O\infty}$ = 0.23. The symbol definitions are those given in the caption to Fig. 5.

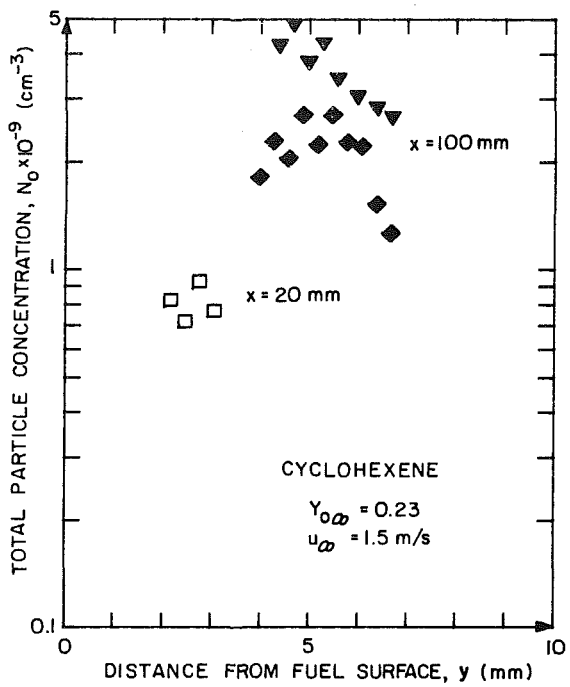

Fig. 7 Total particle concentration, N_0, as a function of distance from the fuel surface and downstream position for cylohexene in forced flow at $Y_{O\infty}$ = 0.23. The symbol definitions are those given in the caption to Fig. 5.

profile flattens and the tail moves from the fuel side to the flame side. It is planned to use such data to develop a model for soot formation, growth and destruction.

The particle radii do not appear to change significantly across the soot layer as shown in Fig. 6. The most probable radius is between 20 nm and 80 nm for all the fuels at $Y_{O\infty}$ = 0.25. Since the particle sizes do not vary with downstream position, the particles apparently do not have sufficient time to agglomerate into larger clusters. The peaks in the particle concentration profiles correspond to peak soot volume fractions as seen by comparing Figs. 5 and 7. So it appears that more particles rather than larger particles are responsible for the downstream increase in f_v.

The soot volume fraction increases with increasing oxygen mass fraction for all the fuels. Measurements were limited to values of $Y_{O\infty}$ greater than 0.23, since below this value a steady flame over the entire fuel surface could not be obtained. In Fig. 8, results for n-heptane show that a small change in the oxygen mass fraction from $Y_{O\infty}$ = 0.23 to $Y_{O\infty}$ = 0.25 results in a 60 percent increase in the maximum of the volume fraction profile at x = 10 cm. The volume fraction is less sensitive at higher oxygen mass fractions, since a change from $Y_{O\infty}$ = 0.35 to $Y_{O\infty}$ = 0.50 gives only a 50 percent increase in the maximum of the f_v profile. As $Y_{O\infty}$ increases, the outer edge of the soot layer moves with the flame toward the fuel surface, since temperature increases with $Y_{O\infty}$ and x = 10 cm corresponds to a smaller similarity variable η through ρ/ρ_∞ [10].

The increase in volume fraction of soot with $Y_{O\infty}$ occurs for two reasons. From the data in Table 2, the total pyrolysis rate at the fuel surface is doubled by increasing the oxygen mass fraction from $Y_{O\infty}$ = 0.23 to $Y_{O\infty}$ = 0.50. Thus, more fuel feeds the soot formation process at the higher oxygen concentrations. Also, an increase in the flame temperature increases the rate of soot formation as noted by Glassman and Yaccarino [18]. Profiles were also measured at u_∞ = 0.75 m/s and u_∞ = 2.25 m/s for n-heptane with $Y_{O\infty}$ = 0.35. The changes in f_v observed were consistent with the changes in the temperature and velocity fields predicted by similarity analyses as shown in Table 2 and Fig. 9.

For PMMA the width of the soot layer changes less with oxygen mass fraction than for the liquid fuels, as shown in Fig. 10. The distance from the fuel surface to soot onset is less for PMMA, and this distance is approximately unchanged with increasing oxygen mass fraction. Again, the increase in the local pyrolysis rate with $Y_{O\infty}$, as shown in Table 3, and the

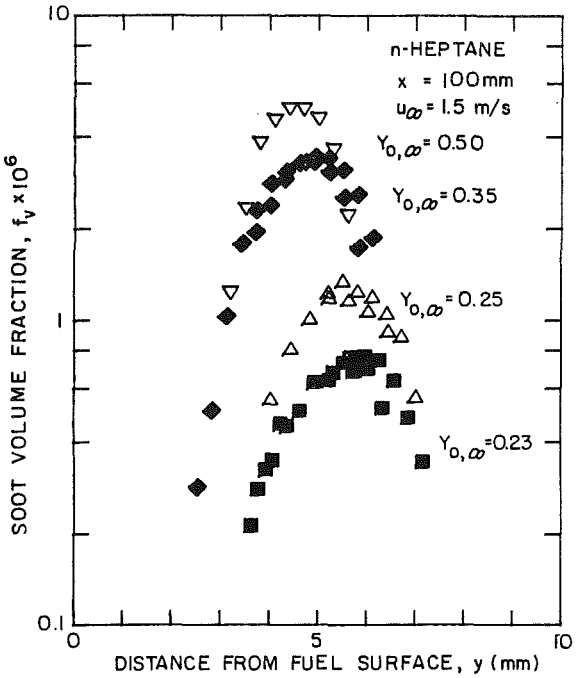

Fig. 8 Soot volume fraction, f_v, as a function of distance from the fuel surface at different oxygen mass fractions for n-heptane:

Symbol	$Y_{0\infty}$
■	0.23
△	0.25
◆	0.35
▽	0.50

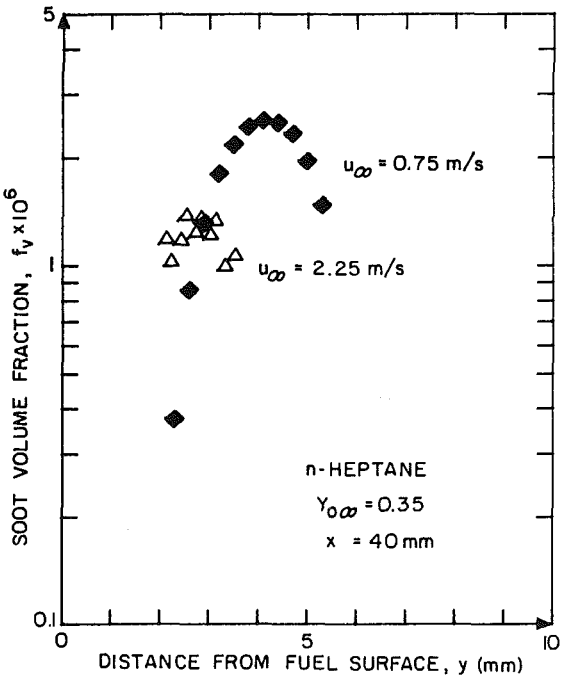

Fig. 9 Soot volume fraction, f_v, as a function of distance from the fuel surface at different free stream velocities for n-heptane at x = 4 cm, $Y_{0\infty}$ = 0.35

temperature increase lead to a large increase in the f_v maximum as $Y_{0\infty}$ increases. The particle radii do not change significantly with oxygen mass fraction as shown by the results in Table 1. For PMMA pool fires, the measurements of Santo and Tamanini [19] indicate the absorption coefficient increases with oxygen mass fraction, but the Schmidt

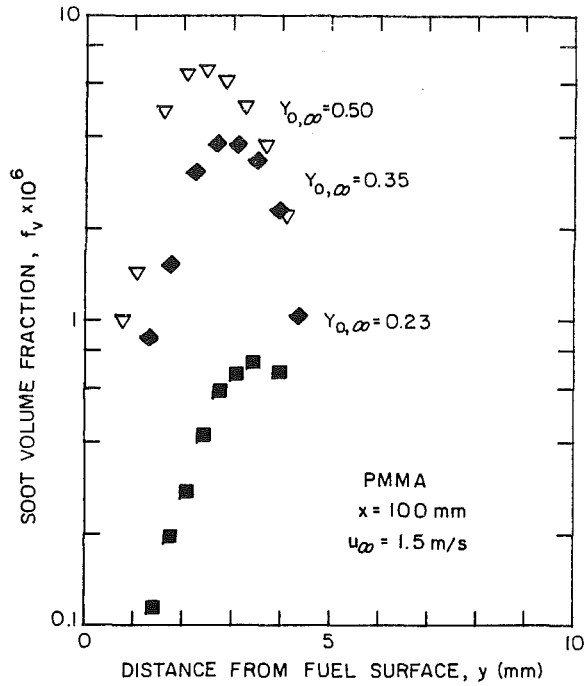

Fig. 10 Soot volume fraction, f_v, as a function of distance from the fuel surface at different oxygen mass fractions for PMMA. The symbol definitions are those given in the caption to Fig. 8.

Table 3 Local pyrolysis rates for PMMA with u_∞ = 150 cm/s

$Y_{0\infty}$	Streamwise position x(cm)	Local pyrolysis rate $\dot{m}_p$(g/m^2•s)
0.23	2	16
0.23	4	11
0.23	7	4.0
0.23	10	3.8
0.35	4	17
0.35	10	9.5
0.50	2	24
0.50	4	19
0.50	7	14
0.50	10	11

temperature is only weakly influenced. They concluded that soot volume fraction increases with an increase in oxygen mass fraction for $Y_{0\infty}$ between 0.18 and 0.21. By measuring sooting heights for ethene, Glassman and Yaccarino [18] found that increasing the oxygen mass fraction decreases the sooting tendency at lower oxygen mass fractions, but at higher $Y_{0\infty}$, in the range studied here, increasing the oxygen mass fraction increases the sooting tendency.

Conclusions

Soot volume fraction fields and particle size distributions have been determined in laminar, combusting, radiating forced flow boundary layers for several fuels and oxygen concentrations. The soot region is observed on the fuel side of the flame zone. The fuel ranking and soot volume fraction magnitude are preserved among small pool fires and boundary layer flames in free and forced flow. The forced flow system with a positive y-velocity field everywhere provides an interesting contrast to the free flow case where the y-velocity is positive only near the fuel surface. As a consequence of this distinction larger f_v are observed near the flame in forced flow than in free flow.

The soot volume fraction and the width of the soot layer increase with downstream distance primarily due to an in-

crease in particle concentration, since the particle size does not change significantly downstream, across the soot layer, or with oxygen mass fraction or fuel type. Soot volume fraction increases monotonically with mass fraction of oxygen, for $0.23 \leq Y_{0\infty} \leq 0.50$, but volume fraction is less sensitive to changes in $Y_{0\infty}$ at the higher oxygen mass fractions. It is also observed that the chemical structure of the fuel has a large effect on soot formation. Data such as these, when coupled with temperature, species and velocity fields from similarity analyses, make combusting boundary layers attractive systems for future work in soot formation, growth and destruction modeling.

Acknowledgment

This work was supported by the Center for Fire Research of the U.S.D.O.C. National Bureau of Standards under Grant No. NB 80-NAG-E6839 and administered through the Lawrence Berkeley Laboratory of the University of California under U.S.D.O.E. contract No. DE-AC03-76SF00098.

References

1 de Ris, J., "Fire Radiation — A Review," *Proceedings of the Seventeenth Symposium (International) on Combustion*, The Combustion Institute, 1979, pp. 1003–1016.

2 Pagni, P. J., and Bard, S., "Particulate Volume Fractions in Diffusion Flames," *Proceedings of the Seventeenth Symposium (International) on Combustion*, The Combusion Institute, 1978, pp. 1017–1028.

3 Bard, S., and Pagni, P. J., "Comparison of Laser Induced Fluorescence and Scattering in Pool Fire Diffusion Flames," *J. Quant. Spec. Rad. Trans.*, Vol. 25, 1981, pp. 453–461.

4 Bard, S., "Diffusion Flame Particulate Volume Fractions," Ph.D. dissertation, Mechanical Engineering Department, University of California, Berkeley, 1980.

5 Bard, S., and Pagni, P. J., "Carbon Particulate in Small Pool Fire Flames," ASME JOURNAL OF HEAT TRANSFER, Vol. 103, 1981, pp. 357–362.

6 Bard, S., and Pagni, P. J., "Spatial Variation of Soot Volume Fractions in Pool Fire Diffusion Flames," submitted to *Combustion and Flame.*

7 Beier, R. A., and Pagni, P. J., "Soot Volume Fraction Profiles in a Free Combusting Boundary Layer," Twentieth ASME/AIChE National Heat Transfer Conference, ASME Paper No. 81-HT-1.

8 Beier, R. A., "Soot and Radiation in Combusting Boundary Layers," Ph.D. dissertation, Mechanical Engineering Department, University of California, Berkeley, 1981.

9 Emmons, H. W., "The Film Combusion of Liquid Fuel," *Z. angew. Math. Mech.*, Vol. 36, 1956, pp. 60–71.

10 Pagni, P. J., "Diffusion Flame Analyses," *Fire Safety Journal*, Vol. 3, 1980/81, pp. 273–285.

11 Minchin, S. T., "Luminous Stationary Flames: The Quantitative Relationship between Flame Dimensions at the Sooting Point and Chemical Composition, with Special Reference to Petroleum Hydrocarbons," *Journal of the Institute of Petroleum Technologists*, Vol. 17, 1931, pp. 102–120.

12 Clarke, A. E., Hunter, T. G., and Garner, F. H., "The Tendency to Smoke of Organic Substances on Burning. Part I," *Journal of the Institute of Petroleum Technologists*, Vol. 32, May 1946, pp. 627–642.

13 Jagoda, I. J., Prado, G., and Lahaye, J., "An Experimental Investigation into Soot Formation and Distribution in Polymer Diffusion Flames," *Combustion and Flame*, Vol. 37, 1980, pp. 261–274.

14 Kent, J. H., Jander, H., and Wagner, H. Gg., "Soot Formation in Laminar Diffusion Flame," *Proceedings of the Eighteenth Symposium (International) on Combustion*, The Combusion Institute, 1980, pp. 1117–1126.

15 Haynes, B. S., and Wagner, H. Gg., "Sooting Structure in a Laminar Diffusion Flame," *Ber. Bunsenges. Phys. Chem.*, Vol. 84, 1980, pp. 499–506.

16 Haynes, B. S., Jander, H., Wagner, H. Gg., "Optical Studies of Soot-Formation Processes in Premixed Flames," *Ber. Bunsenges. Phys. Chem.*, Vol. 84, 1980, pp. 585–592.

17 Chang, P. H. P., and Penner, S. S., "Particle Size Measurements in Flames Using Light Scattering; Comparison with Diffusion-Broadening Spectroscopy," *J. Quant. Spectroc. Radiat. Transfer*, Vol. 25, 1981, pp. 105–110.

18 Glassman, I., and Yaccarino, P., "The Effect of Oxygen Concentration on Sooting Diffusion Flames," *Combustion Science and Technology*, Vol. 24, 1980, pp. 107–114.

19 Santo, G., and Tamanini, F., "Influence of Oxygen Depletion on the Radiative Properties of PMMA Flames," *Proceedings of the Eighteenth Symposium (International) on Combustion*, The Combustion Institute, 1980, pp. 619–631.

20 Kinoshita, C. M., and Pagni, P. J., "Stagnation-Point Combustion with Radiation," *Proceedings of the Eighteenth Symposium (International) on Combustion*, The Combustion Institute, 1980, pp. 1415–1426.

21 Beier, R. A., and Pagni, P. J., "Radiation in Combusting Boundary Layers." in preparation.

22 Sibulkin, M., Kulkarni, A. K., Annamalai, K., "Effects of Radiation on the Burning of Vertical Fuel Surfaces," *Proceedings of the Eighteenth Symposium (International) on Combustion*, The Combustion Institute, 1980, pp. 611–617.

23 Liu, C. N., and Shih, T. M., "Laminar, Mixed-Convection, Boundary-Layer, Nongray-Radiative, Diffusion Flames," ASME JOURNAL OF HEAT TRANSFER, Vol. 102, 1980, pp. 724–730.

24 Kerker, M., *The Scattering of Light and Other Electromagnetic Radiation*, Academic Press, 1969.

25 Wersborg, B. L., Howard, J. B., and Williams, G. C., "Physical Mechanisms in Carbon Formation in Flames," *Proceedings of the Fourteenth Symposium (International) on Combustion*, The Combustion Institute, 1973, pp. 929–940.

26 Hahn, G. H., and Shapiro, S. S., *Statistical Models in Engineering*, John Wiley and Sons, New York, 1968.

27 Lee, S. C., Yu, Q. Z., and Tien, C. L., "Radiation Properties of Soot from Diffusion Flames," *J. Quant. Spectrosc. Radiat. Transfer*, Vol. 27, 1982, pp. 387–396.

28 Lee, S. C., "Soot Radiation from Diffusion Flames," Ph.D. dissertation, Mechanical Engineering Department, University of California, Berkeley, 1981.

29 Lee, S. C., and Tien, C. L., "Optical Constants of Soot in Hydrocarbon Flames," *Proceedings of the Eighteenth Symposium (International) on Combustion*, The Combustion Institute, 1980, pp. 1159–1166.

30 Tien, C. L., and Lee, S. C., "Flame Radiation," *Prog. Energy Combust. Sci.*, Vol. 8, 1982, pp. 41–59.

31 Lee, S. C., and Tien, C. L., "Thermal Radiation of Spherical and Cylindrical Soot Particles," Paper No. 80-54, Western States Section of the Combustion Institute, Fall Meeting, 1980. Also submitted to *J. Quant. Spectrosc. Radiat. Transfer.*

32 Asano, S., and Yamamato, G., "Light Scattering by a Spheroidal Particle," *Applied Optics*, Vol. 14, 1975, p. 29–49.

33 Brown, G. L., and Roshko, A., "On Density Effects and Large Structures in Turbulent Mixing Layers," *Journal of Fluid Mechanics*, Vol. 64, 1974, pp. 775–816.

Low Reynolds Number Flow Between Interrupted Flat Plates

R. E. Roadman
Fabricating Technology Division,
Alcoa Laboratories,
Alcoa Center, Pa. 15069

R. I. Loehrke
Mechanical Engineering Department,
Colorado State University,
Fort Collins, Colo. 80523
Mem. ASME

The flow between pairs of flat plates was studied experimentally to gain insight into the operation of compact heat exchangers with interrupted surfaces. The plates were tested at low Reynolds number in both water and air streams. The investigation focused on the region of transition from steady to unsteady laminar flow between plates. A critical velocity was determined at which periodic oscillations were first observed. This velocity depends strongly on the thickness of the plates, t, plate length, L, and plate separation distance and weakly on flow disturbance level. Data for a range of geometries, $4 \leq L/t \leq 159$, are correlated using plate wake width as a single plate length scale. The downstream plate was found to have a pronounced upstream influence on the critical velocity. In a low-disturbance-level stream the critical velocity may be lower than that required to produce detectable oscillations at the same point in the upstream plate wake in absence of the second plate. This feedback effect may be responsible for the relative insensitivity of the results to the turbulence level in the free stream.

Introduction

Many compact heat exchanger surfaces consist, in part, of flat plate segments aligned with the flow direction. These devices typically operate at low Reynolds number. It is a common practice to interrupt these surfaces to inhibit the formation of thick laminar boundary layers. Sparrow et al. [1] have calculated that heat transfer improvement may be realized due to interruptions in a two-dimensional plate array even if the flow remains laminar and steady. Further improvement may be expected if the wakes which are formed when the boundary layers pass the end of a plate segment are unstable and undergo transition to an unsteady, vortical flow. In general, the flow in a compact heat exchanger may be quite complex. The flow and consequently the heat transfer may be sensitive to small changes in any of a large number of design and manufacturing variables. The philosophy adapted by the present authors, and by other workers in the field, is to try to gain insight into the complex fluid flow and heat transfer processes occurring in heat exchanger cores by studying related but simpler flows. This paper deals with the transition from steady laminar to unsteady flow in the wake region between two plates. The following paper [2] uses the results of this and a related study to interpret measurements of heat transfer from two aligned plates.

A considerable amount of information is available concerning flow over *isolated*, two-dimensional bluff bodies (particularly circular cylinders) [3, 4] and thin flat plates aligned with the flow direction [5, 6, 7]. The onset of instability is first detected in the far wake and the apparent origin moves toward the generating body as the Reynolds number increases. Theoretical and experimental determinations have been made of the critical conditions at the onset of wake instability. In contrast, little has been reported concerning the flow between closely coupled plates. Flow visualization studies [8, 9, 10] have documented that a similar transition process may exist but these explorations were not extensive enough to establish the critical conditions. The main objective of the experiments reported in this paper was to establish the conditions for the onset of unsteady flow between a pair of flat plates of finite thickness.

The Experiment

The flow over two plates aligned with the flow direction was studied using visualization techniques and hot-film anemometry in a water channel and hot-wire anemometry in a wind tunnel.

The water channel is an open flume 244-cm long with a 7.6-cm by 7.6-cm square cross section. The plates were mounted vertically in the channel, positioned and supported on the bottom by slots milled into the floor of the channel and on the top by slotted straps which span the test section. Water enters the flume through a bed of marbles and then passes through a series of screens and honeycomb prior to entering the test section.

Hydrogen bubbles were generated at a 0.02-cm platinum wire stretched across the channel at midheight. The d-c potential between this wire and a metal screen located downstream from the test section was pulsed at a known frequency to generate time lines in the flow. The spacing between successive time lines was measured from photographic records and used to determine the channel horizontal velocity profile. By this means it was determined that the velocity was essentially uniform over the central 85 percent of the channel. Similar vertical profiles obtained with the hydrogen bubble wire positioned vertically in the center of the channel showed a uniform mean velocity extending from the free surface down to about 95 percent of channel depth. With the plates in place, velocities were measured from horizontal time line separations midway between the plate surface and the sidewalls. Using this technique it is estimated that the uncertainty in velocity determination is about 5 percent.

Dye visualization was also used to study the flow patterns between plates. For the thickest plates dye was channeled through the center of the plates and fed directly into the boundary layers through 0.6-mm holes. Dyes of different color were precisely injected into the boundary layers on either side of the upstream plate to facilitate observations of mixing across the gap between plates. A comparison of the flow patterns revealed by these streakline with those indicated by the hydrogen bubbles showed no qualitative differences provided that the dye injection rate was slow and steady.

Measurements of wake oscillation frequency and amplitude were made using a cylindrical hot-film probe. These measurements were all taken near the leading edge of the second plate. The axis of the sensor was vertical. The probe support entered the water vertically downstream from and to the side of the second plate. The probe was connected to the probe support via a right-angle adaptor.

The general arrangement of the plates within the test section is shown in Fig. 1. Plates of different length and

Contributed by the Heat Transfer Division for publication in the JOURNAL OF HEAT TRANSFER. Manuscript received by the Heat Transfer Division November 9, 1981.

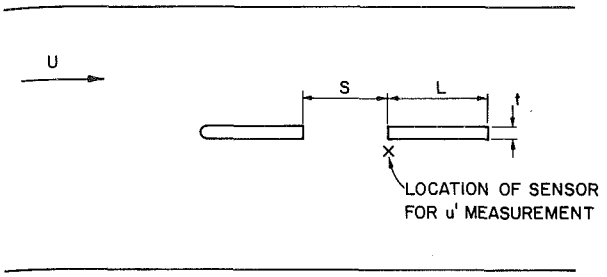

Fig. 1 Arrangement of plates in test section

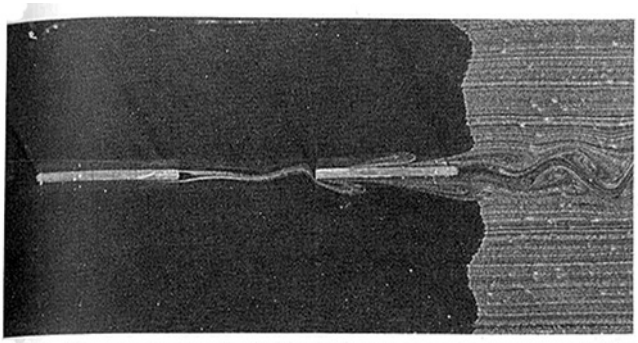

Fig. 2 The onset of unsteady flow between two plates as revealed by hydrogen bubbles. The direction of flow is from left to right: L = 2.54 cm, S = 2.54 cm, t = 0.16 cm.

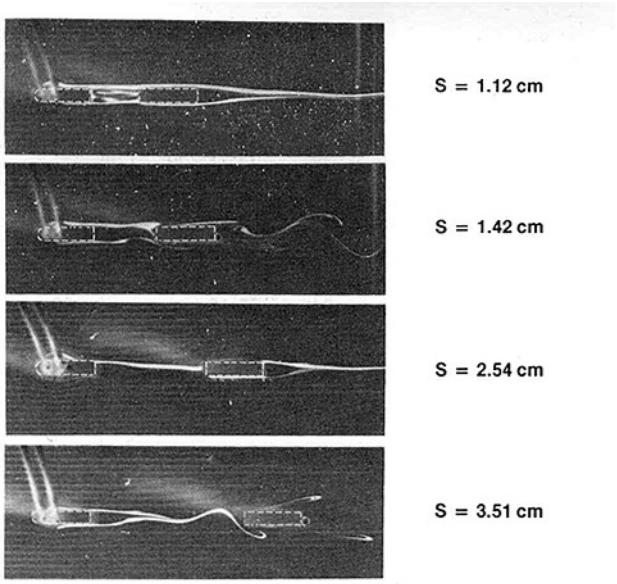

Fig. 3 The effect of plate spacing on the flow between plates at constant free-stream velocity. The direction of flow is from left to right: L = 1.27 cm, t = 0.32 cm, U = 2.9 cm/s.

thickness were used (see Table 1), but for most experiments the two plates in the channel were identical except that the leading edge of the upstream plate was rounded.

In order to extend the range of parametric variation and to assess the facility dependence of the results a series of experiments was run in a low-speed, open-return wind tunnel. In this facility the plates span the center of the 33-cm dia plexiglas test section, penetrate through the test section walls and are held in tension by clamps mounted outside the test section. The mean velocity is uniform over the central 90 percent of the tunnel but the free-stream turbulence intensity, which ranges from 1 to 2 percent depending on velocity, is about an order of magnitude higher than it is in the water channel just described. The hot-wire measurements made in this facility were comparable to the hot-film measurements made in the water channel.

The plates were made from a number of different materials depending on the plate size. The general criterion was to use the stiffest, straightest material possible consistent with the application. The plates used in the water channel were made from Plexiglas or aluminum, while those used in the wind tunnel were either aluminum or ground flat steel stock. The leading edge of the upstream plate was rounded to prevent separation and to provide a well-defined boundary layer at the trailing edge. The intent was to isolate leading and trailing edge effects. Both are considered in the following paper. In the course of developing the experimental techniques used in this work it was found that the principal influence of the plates on the results presented here, other than through the geometric variables explored, was due to plate vibration and plate misalignment. It is believed that the results presented here are those that would obtain for perfectly aligned, perfectly rigid plates. More details concerning the experimental facilities and techniques are presented in [11].

Results

Visual Observations. All of the plates tested produced the same basic flow patterns in the water channel. At low velocities the flow everywhere was laminar and steady. As the free-stream velocity was slowly increased from zero, with plate spacing held constant, a point was reached where sinusoidal oscillations appeared in upstream plate wake near the leading edge of the downstream plate. The appearance of these oscillations as revealed by hydrogen bubbles is shown in Fig. 2. The bubbles slowed down in the boundary layer of the first plate trail behind the main sheet of bubbles to mark the wake. The amplitude of these oscillations grew with further increases in velocity until discrete vortices were formed. These vortices, which were swept past the second plate, generally became stronger with increasing velocity but the flow remained laminar for a wide range of velocities in the sense that three-dimensional, random, fluctuating mixing motions were not visible either within the vortices or in the boundary layer of the second plate.

The critical velocity at which between-plate oscillations are first observed depends on the thickness of the plates, t, plate length, L, separation distance, S, and the disturbance level in the channel. In general, the critical velocity increases with decreasing plate thickness, plate length, plate separation, and disturbance level.

Nomenclature

b = wake width = $2\theta + t$
L = plate length
Re = Reynolds number
S = spacing between plates
t = plate thickness
u' = rms value of streamwise velocity fluctuation
U = free-stream mean velocity

Greek

β = frequency
θ = boundary layer momentum thickness at the trailing end of the upstream plate.

Superscript

$*$ = Condition at onset of oscillations between plates

Table 1

Plate geometry			Fluid	Conditions at the onset of oscillations S = 3 cm			
t (cm)	L (cm)	L/t	Air or water	U^* (cm/s)	θ^* (cm)	Re_L^*	Re_t^*
.32	1.27	4	W	3.5	.039	460	114
.32	1.27	4	A	50	.042	400	99
.16	2.54	16	W	4.6	.046	1370	85
.16	2.54	16	A	79	.047	1270	80
.16	5.08	32	W	5.6	.061	3020	95
.08	2.54	32	W	5.4	.042	1580	50
.04	3.18	80	A	176	.035	3540	44
.04	6.35 upstream / 5.08 downstream	159	A	138	.057	5540	35

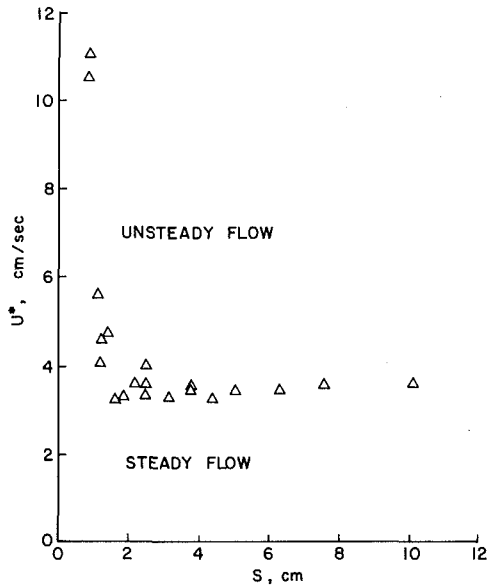

Fig. 4 Critical velocity for the onset of oscillations between two 0.32-cm thick plates in water

Observations were also made while holding the free-stream velocity constant and varying the spacing between plates. Two distinctly different flow regimes were identified as S was increased from zero. They are illustrated in the photographs in Fig. 3 which show the flow between two 0.32-cm thick plates (outlined by the dashed lines) at different spacings with the free-stream velocity kept constant. For these photographs dye was injected into the boundary layers through small holes on either side of the upstream plates. The meniscus formed where the dye feed tubes enter the water surface locally distorts the view of the dye streaklines.

For $S/t \lesssim 4$, the steady flow between the plates is fully separated, Fig. 3(*a*). Unsteady flow first appears in the form of asymetric periodic perturbations in the two separated shear layers similar to those shown in Fig. 3(*b*). For $S/t \gtrsim 4$, the separated region in steady flow closes upstream from the leading edge of the second plate. As S is increased beyond $4t$, the form of the initial unsteadiness changes from the two layer instability, Fig. 3(*b*), to the single wake instability, Fig. 3(*d*), with increasing cross flow evident at the leading edge of the second plate.

Transition Boundaries. A transition boundary was determined for each set of plates by fixing the plate spacing and slowly increasing the channel velocity until between-plate waves were observed. By repeating this procedure at a number of plate spacings, points, such as those plotted in Fig. 4, were generated. The general shape of the boundary for all plates is similar. For large plate separation ($S>2$ cm for the data shown in Fig. 4), the critical velocity depends only weakly on plate spacing. At small spacings the critical velocity rises sharply with decreasing spacing, the detailed form depending on plate geometry. A comparison of the critical velocities determined for the different plate pairs at a large spacing is shown in Table 1.

Also shown are corresponding values for the boundary layer momentum thickness at the trailing edge of the upstream plate, θ, calculated from laminar flat plate boundary layer theory (Blasius profile), and Reynolds numbers based on plate length and plate thickness. Sinusoidal oscillations in the hot-film output could be detected on an oscilloscope at about the same velocity as were undulations in the wake streaklines.

In contrast to the situation just decribed, the transition from a steady to an unsteady, periodic flow between plates in the wind tunnel could not always be precisely identified simply by observing the hot-wire output on an oscilloscope. With a free-stream turbulence intensity of approximately 2 percent in the wind tunnel, the hot-wire output always contained a strong unsteady component. In order to facilitate the identification of the point of onset of periodic flow in the wind tunnel velocity spectra were obtained at the leading edge of the downstream plate by passing the hot-wire signal through a spectrum analyzer. Spectra at this location are compared with free-stream spectra for one set of plates in Fig. 5. At a velocity of 0.77 m/s, which was just below the critical velocity for these plates, the two spectra are almost indistinguishable although the high-frequency content in the near plate spectrum is somewhat lower than in the free stream. At all of the velocities shown the boundary layers leaving the first plate must certainly have been laminar. The second set of spectra at U = 1.36 m/s show the emergence of periodic flow between plates as a spike at a frequency of about 90 Hz. The third set of spectra at U = 3.54 m/s show that the periodic fundamental has grown in amplitude and increased in frequency to about 320 Hz. Higher harmonics are also evident and the regions between harmonics also contain more energy than the free-stream presumably due to turbulent cascade processes. It appears that the same basic process which was observed in the low-disturbance water channel is taking place here in the presence of considerable background noise.

The Influence of the Downstream Plate. For a relatively quiet, disturbance-free channel, the critical velocity may be lower than that required to produce visible oscillations at the same point in the upstream plate wake in absence of the second plate. That is, the second plate provides an upstream influence which dominates the "natural" disturbances. This feedback manifests itself in another way. For a fixed channel

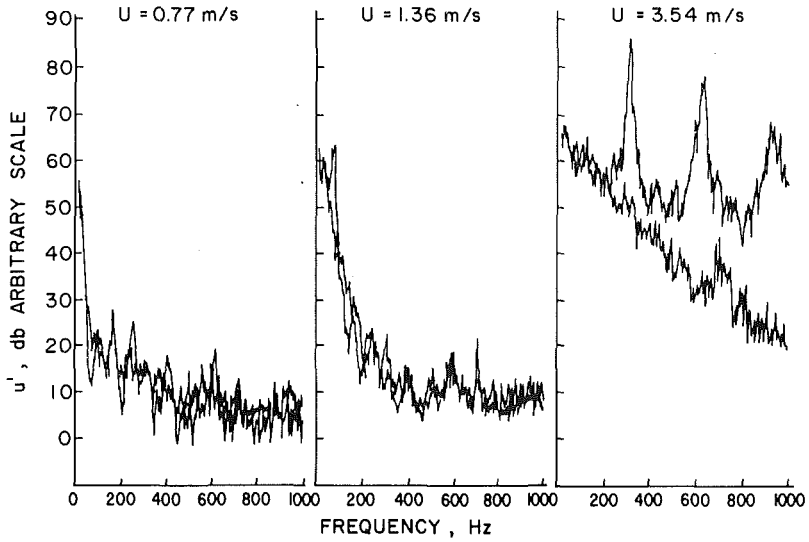

Fig. 5 Velocity spectra in the free stream (lower curves) and at the leading edge of the second plate in air: L = 2.54 cm, t = .16 cm, S = 6 cm, 10 Hz bandwidth

velocity the frequency of oscillations is essentially independent of S; however, the amplitude varies almost periodically with S. In fact, with the velocity set just above critical the wake between plates appears alternately steady and unsteady as the spacing is changed. This phenomenon is also illustrated by the sequence of photographs shown in Fig. 3. The flow between plates is steady for S = 2.54 cm while at smaller and larger spacings oscillations are apparent. This alternation between steady and unsteady flow may be repeated several times as the spacing is increased. This is shown in Fig. 6(a), where the rms value of the streamwise velocity fluctuation, u', measured by a hot-film probe stationed near the leading edge of the second plate is plotted versus plate spacing at a near critical value of mean velocity.

Evidence of upstream feedback from the second plate was also obtained in wind tunnel tests. In spite of the high background turbulence the modulation of the rms velocity signal at the leading edge of the downstream plate with changing spacing could still be detected. This is shown in Fig. 7, where rms level filtered around the 15 Hz fundamental is plotted versus plate spacing. As in the case of the water channel tests this effect was only measurable at velocities near critical and only for the periodic component.

Supercritical Velocities. The feedback process is less evident at supercritical velocities. The variation of u' with plate spacing shown in Fig. 6(a) for near critical flow over 0.32-cm thick plates is considerably changed in form at a velocity 20 percent higher than critical as seen in Fig. 6(b). Since the absolute u' level at a given plate spacing depends on the relative position of the probe with respect to the second plate, the probe and downstream plate were kept in the same position and the gap was changed by moving the upstream plate. The absolute rms levels for the curves shown in Figs. 6 and 7 cannot be compared, however, so u' is plotted on an arbitrary scale.

The frequency of the wake oscillations is an increasing function of velocity but essentially independent of plate spacing. The frequency change with velocity for tests run in air is shown in Fig. 8. The solid lines indicate the slopes, for different n, of the power law relation $\beta \sim U^n$. The value n = 3/2 has been found to describe the frequency variation in the wake of an isolated, thin flat plate [5]. The data for the thinnest (t = .04 cm) plate pair tested here follow this line

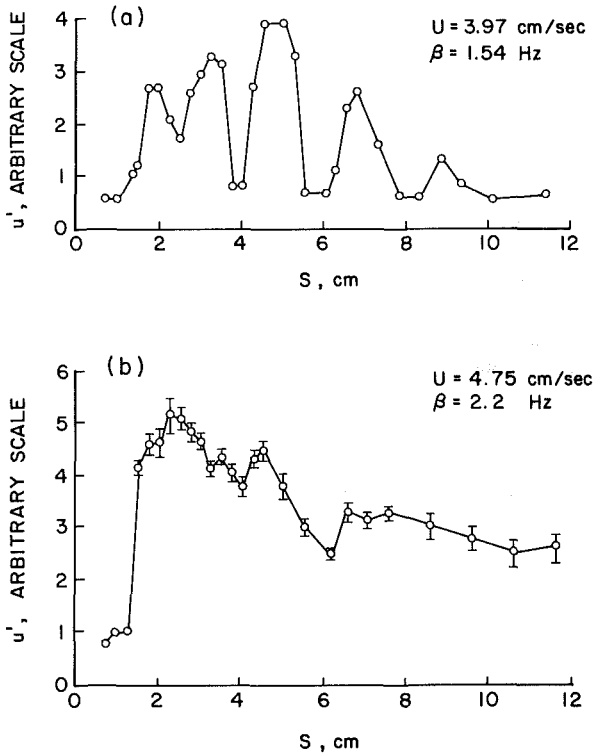

Fig. 6 RMS level of fluctuating velocity between two plates in water: L = 1.27 cm, t = 0.32 cm

fairly well. The frequency does not change as rapidly with velocity for the thicker plates. The exponent n = 4/3 more closely describes the rest of the plate-pair data over the limited Reynolds number range, just above critical, explored in both air and water. The n = 4/3 line forms an approximate, empirical lower bound on all the data with one exception. Localized velocity ranges were found in these tests in which the frequency was independent of velocity. In these ranges the wake oscillation frequency matched the frequency of the first transverse sloshing mode of the water channel and a resonant condition was observed.

Except for singular behavior under conditions of frequency

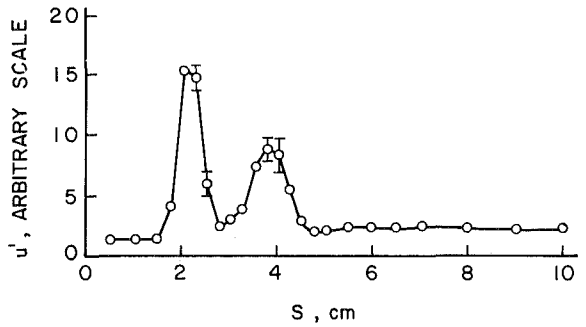

Fig. 7 RMS level of fluctuation velocity between two plates in air band-pass filtered between 10 and 20 Hz: L = 1.27 cm, t = 0.32 cm, U = 0.45 m/s

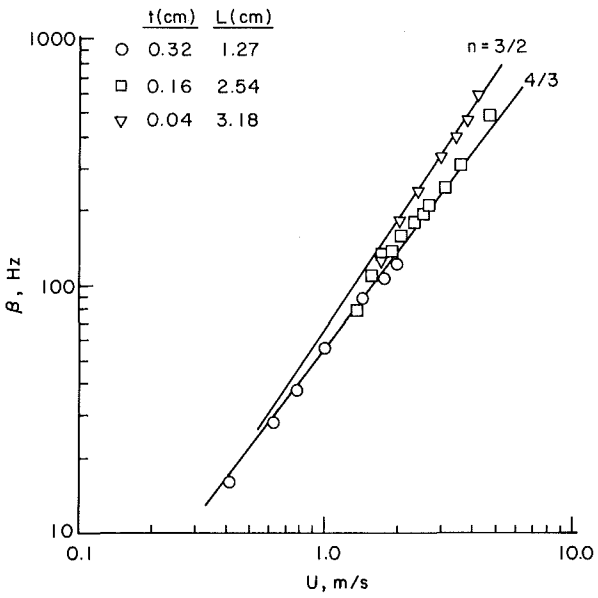

Fig. 8 Frequency of the fundamental, periodic velocity component between two plates in air

locking, the amplitude of the oscillations between plates increased with velocity until discrete vortices were formed. The vortices form closer to the upstream plate and sweep farther out in the transverse direction as the velocity is increased. Contrast the near critical flow shown in Fig. 3(*d*) with that shown in Fig. 9. At the higher velocities a local scouring of the boundary layer on the second plate could be observed as each vortex was swept by but, over the range of parameters investigated, transition to turbulence was never observed visually either in the second plate boundary layer or in the separated shear layers behind the first plate.

Discussion

The qualitative similarity in wake behind two-dimensional cylinders and plates has stimulated the search for a universal correlating parameter or parameters which would describe the characteristics of wakes produced by cylinders of arbitrary shapes. These efforts, which have focused on defining a single characteristic wake dimension, have not been entirely successful [12]. One might anticipate, however, based on the data for isolated flat plates and circular cylinders, that the conditions at the onset of instability at large plate spacing in the present experiments could be roughly correlated using a wake width, b, defined as the sum of the plate thickness plus twice the momentum thickness of the boundary layer at the end of the first plate. The Reynolds number formed using this length and the critical velocity, U^*, is plotted versus dimensionless spacing in Fig. 10 for all of the plates tested.

Although the range in $\mathrm{R\tilde{e}}^*_b$ at a given S/b is considerably

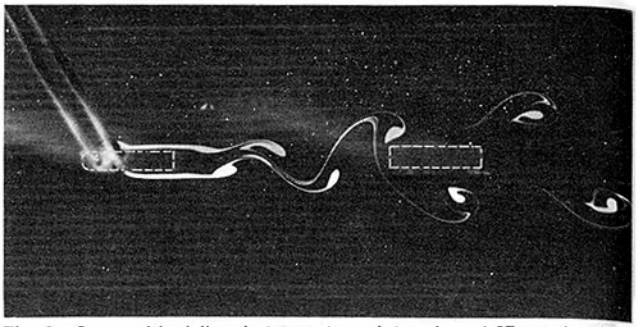

Fig. 9 Supercritical flow between two plates: L = 1.27 cm, t = 0.32 cm, S = 2.8 cm, U = 5.1 cm/s. The direction of flow is from left to right.

smaller than that for either $\mathrm{R\tilde{e}}^*_L$ or $\mathrm{R\tilde{e}}^*_t$ (see Table 1), the data do not collapse into a single curve. The scatter in the data is much greater than the uncertainty with which the critical Reynolds number and spacing were determined. One reason for this is certainly the variability of the disturbance level feeding into the unstable wake. In all the water channel experiments the flow was carefully controlled through the use of honeycomb and screens to minimize the mean flow distortion and turbulence upstream from the leading plate. The pump was isolated from the channel by flexible connections to minimize vibration input. It was found that the introduction of extraneous disturbances such as arise through channel or plate vibration could significantly reduce the critical Reynolds numbers from those shown in Fig. 10. When these extra disturbances were introduced into the flow with the velocity set just below the critical value as defined by Fig. 10, oscillations in the region between the two plates would grow. With the removal of the external disturbances, however, the flow would revert to a steady laminar state. Apparently, below the critical values shown in Fig. 10 the feedback mechanism from the second plate is not sufficiently strong to sustain the oscillatory flow even though the wake may be unstable. On the other hand, the contrast between the unsteady flow between two plates at just above the critical Reynolds numbers, shown in Fig. 10, with the steady flow at the same location in absence of the second plate indicate that these boundaries are associated with the feedback from the second plate and may be representative of the maximum Reynolds number at which the flow between plates may be steady. Disturbance feedback is a common feature of the shear-layer edgetone phenomenon [13]. It should be noted that the water data displaying the lowest critical Reynolds numbers are for the 0.08-cm thick plates which were locked in to the channel resonant frequency at the onset of unsteady flow.

The wind tunnel data show a smaller spread than the water channel data, presumably due to the absence of resonant coupling. Surprisingly, even with the high free-stream turbulence the conditions at the onset of periodic flow are not that much different than those for the low disturbance water channel.

The leading edges of all of the upstream plates tested here were rounded to prevent separation. Subsequent tests [14] have shown that the critical velocities for plates with blunt leading edges are not significantly different from those reported here, except possibly at small spacing ($S/t < 4$). The flow between plates at supercritical velocities was found to be much less two-dimensional when the upstream plate was blunt, however.

Conclusions

The critical velocity for the onset of oscillations in the flow between pairs of plates is a strong function of plate spacing at small values of plate spacing but is a very weak function for large spacings.

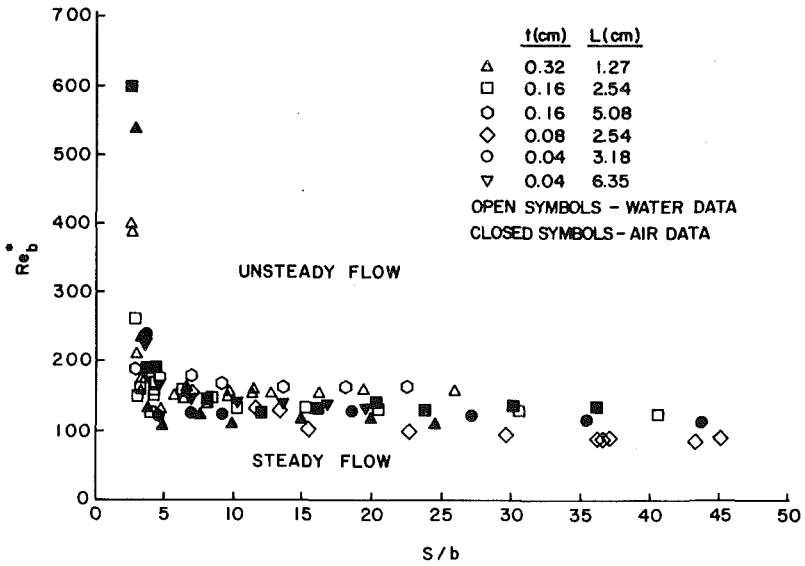

Fig. 10 Conditions at the onset of periodic flow between plates

A single characteristic length, the wake width, was found to correlate critical point data for the onset of oscillations in the flow between pairs of flat plates. The experiments on similar plates with $4 \leq L/t \leq 159$ covered conditions ranging from those in which the wake was formed chiefly by the thick boundary layers leaving the upstream plate to those in which the upstream plate resembled a bluff body with boundary layers thin compared to the body thickness. The critical velocity is a strong function of plate spacing for $S/b \leq 4$ and a weak function for $S/b > 5$.

The critical conditions are surprisingly insensitive to a free-stream turbulence level. A strong periodic component can be detected in the unsteady flow between two plates in highly turbulent streams. The velocity at which this periodic component first appears correlates well with the velocity at which sinusoidal undulations are first observed between plates in a low-turbulence-level channel.

A feedback process has been identified which can influence transition from steady to unsteady flow between plates. The flow between two plates may be unstable whereas the flow at the same location in the wake of an isolated plate may be stable at the same free-stream velocity. This feedback may account for the relative insensitivity of the stability boundary to free-stream turbulence level.

The frequency of the velocity fluctuations in supercritical flow is independent of plate spacing. The frequency was found to vary as $U^{4/3}$ with two exceptions. For the thinnest plates, $L/t \geq 80$, the velocity dependence was closer to $U^{3/2}$. A frequency locking was observed for certain water channel tests with frequency insensitive to velocity over a limited range of channel velocity. This lock-in was related to a channel-plate resonance condition.

Acknowledgments

The authors would like to acknowledge the photographic contribution of Gary Kirkpatrick. This research was supported by NSF through grant CME-8009046.

References

1 Sparrow, E. M., Baliga, B. R., and Patankar, S. V., "Heat Transfer and Fluid Flow Analysis of Interrupted Wall Channels, With Application to Heat Exchangers," ASME JOURNAL OF HEAT TRANSFER, Vol. 99, 1977, p. 4.

2 Zelenka, R. L., and Loehrke, R. I., "Heat Transfer From Interrupted Plates," ASME JOURNAL OF HEAT TRANSFER, Vol. 105, Feb. 83, pp. 172-177.

3 Morkovin, M. V., "Flow Around Circular Cylinder—A Kaleidoscope of Challenging Fluid Phenomena," *ASME Symposium on Fully Separated Flows*, 1964.

4 Berger, E., and Wille, R., "Periodic Flow Phenomena," *Annual Review of Fluid Mechanics*, Vol. 4, 1972, pp. 313-340.

5 Taneda, S., "Oscillation of the Wake Behind a Flat Plate Parallel to the Flow," *J. Phy. Soc. Japan*, Vol. 13, No. 4, 1958, pp. 418-425.

6 Taneda, S., "The Stability of Two-Dimensional Laminar Wakes at Low Reynolds Numbers," *J. Phy. Soc. Japan*, Vol. 18, No. 2, 1963, pp. 288-296.

7 Sato, H., and Kuriki, K., "The Mechanism of Transition in the Wake of a Thin Flat Plate Placed Parallel to a Uniform Stream," *Journal of Fluid Mechanics*, Vol. 11, 1961, pp. 321-352.

8 Adarkar, D. B., and Kays, W. M., "Heat Transfer in Wakes," Department of Mechanical Engineering Technical Report No. 55, Stanford University, Apr. 1963.

9 Shah, R. K., and Osborn, H. H., "Advanced Heat Exchanger Designs of Compact Heat Exchangers When Operating in a Marine Environment," Final Report on Navy Contract Nobs 92559, Air Preheater Co., May 11, 1967.

10 Liang, C. Y., "Heat Transfer, Flow Friction, Noise and Vibration Studies of Perforated Surfaces," Ph.D. thesis, University of Michigan, Ann Arbor, Mich., 1975.

11 Roadman, R. E., "The Flow in the Wake of Flat Plates at Low Reynolds Numbers," M.S. thesis, Mechanical Engineering Department, Colorado State University, 1975.

12 Gerrard, J. H., "The Mechanics of the Formation Region of Vortices Behind Bluff Bodies," *Journal of Fluid Mechanics*, Vol. 25, 1966, pp. 401-413.

13 Rockwell, D., and Naudascher, E., "Self-Sustained Oscillations of Impinging Free Shear Layers," *Annual Review of Fluid Mechanics*, Vol. 11, 1979, pp. 67-94.

14 Lane, J. C., "Characteristics of Interrupted-Plate Heat Exchanger Surfaces," M.S. thesis, Mechanical Engineering Department, Colorado State University, 1980.

Heat Transfer From Interrupted Plates

R. L. Zelenka
Mechanical Engineer,
Bureau of Reclamation,
Denver, Colo.

R. I. Loehrke
Mechanical Engineering Department,
Colorado State University,
Fort Collins, Colo. 80523
Mem. ASME

The forced convection heat transfer from two plates aligned with the flow direction in a wind tunnel was measured. The effects of leading edge bluntness, plate spacing distance, and Reynolds number on the leading and trailing plate average heat transfer rate were studied. The low Reynolds number, steady laminar and transitional flow regimes investigated are typical for compact heat exchangers. The measured heat transfer rate from the leading plate agrees well with laminar theory for thin plates when the leading edge is rounded. The heat transfer rate from the leading plate with a blunt nose ranges from slightly below theoretical at a Reynolds number which gives a long, steady separation bubble to well above theoretical under conditions of laminar separation and turbulent reattachment. The heat transfer rate from the second plate is influenced by the leading edge configuration of the first plate only at small plate spacing distances and high Reynolds number. At large spacings the mixing provided by the unsteady wake of the first plate dominates that due to the turbulence formed by leading edge separation on the first plate. The leading edge configuration of the second plate is important only at large values of plate spacing. The heat transfer rate from the second plate is generally higher than that predicted by theory for laminar, steady flow over thin plates and may be higher than that on the leading plate.

Introduction

One of the basic objectives in designing heat exchanger surfaces for enhanced heat transfer is to breakup or disrupt thick laminar boundary layers. Usually this is accomplished by introducing obstructions into the flow or by forming channels which cause local changes in the mean flow direction. The secondary flows which are induced by these means tend to improve cross-stream mixing and thus enhance the transfer of heat between fluid and surface. The operating price which is paid for this sort of enhancement is increased pressure drop. One measure of goodness which may be used to rate the effectiveness of different enhancement techniques is the ratio of heat transfer rate to pressure drop as expressed, for example, by the dimensionless ratio, j/f. Often, surface geometries which yield high j also yield low j/f.

A more subtle way to disrupt boundary layers is to interrupt sections of flat surface and allow the transverse motions arising from wake instabilities to mix the stream. This technique avoids some of the pressure losses associated with large separation regions and mean flow turning. Wake instability mixing has been identified as one of the mechanisms which may influence the performance of segmented fin and perforated plate heat exchangers [1, 2, 3].

The flow in a complete heat exchanger core may be very complex and subject to the influence of many variables. Shah [4] has enumerated twenty-one parameters which may affect the performance of perforated-plate heat exchangers. It is possible, although not necessarily efficient, to generate design data from core tests alone if they are performed with a sufficient variation of parameters. The process may be shortcut if flow modules [5] or major flow structures which strongly affect performance can be identified and if the dependence of these flow modules on the primary variables can be established. One approach to finding such flow structures is through the study of simple geometries which model some of the essential features of the heat exchanger surfaces. Although it may never be possible to predict with great accuracy the performance of a complete, complex heat exchanger core, it should be possible to identify the important variables and to formulate guidelines for the design of more efficient surfaces.

Pioneering work in this vein was reported by Adarkar and Kays [1], who studied, both theoretically and experimentally, the heat transfer from two in-line plates. They calculated, using steady-flow boundary-layer theory, the heat transfer rate on two identical plates of zero thickness for various spacings in the streamwise direction. Experimental results for serveral different plates showed areas of agreement and areas of disagreement with theory. Flow visualization studies helped to identify two causes for disagreement. One of these was the self-excited, unsteady flow between plates and the other was leading edge separation on plates with blunt noses. The domain of influence of these effects was, however, not completely established so this information could not be used to correlate the heat transfer data.

In a more recent work, Cur and Sparrow [6] performed extensive measurements on the two-plate geometry using mass transfer techniques. Effects attributed to the two mechanisms just described are pointed out but again no attempt is made to correlate the data in terms of these effects.

Two studies have recently been completed which focus on the fluid mechanic aspects of these important flow modules. Roadman and Loehrke [7] have expanded the base for their previous paper [2] concerning the flow between two plates. Several conclusions of this study are relevant to the present work. They find that:

1 Self-excited oscillations in the flow between plates begin at a Reynolds number based on wake width, b, of about 150 for $S/b > 4$.

2 Higher Reynolds numbers must be achieved before the instability starts for $S/b < 4$.

3 Increasing the Reynolds number above the critical values increases the amplitude of the wake oscillations. Discrete vortices are observed which sweep across the surface of the second plate.

The implication of these observations is that one should see an increase in the heat transfer rate on the second plate due to the mixing accompanying the finite amplitude oscillations and that this change should manifest itself as a transition in a heat transfer – Reynolds number plot when wake width is used as the characteristic length.

Contributed by the Heat Transfer Division and presented at the National Heat Transfer Conference, San Diego, California. Manuscript received by the Heat Transfer Division January 13, 1982.

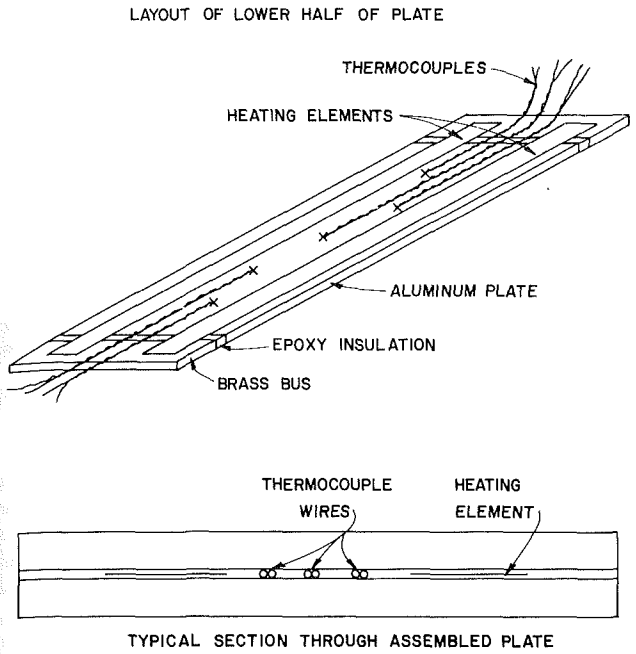

Fig. 1 Construction details of heated plate

Lane and Loehrke [8] have investigated the morphology of leading edge separation on blunt plates at low Reynolds number. They report that:

• A steady, laminar leading edge separation bubble forms on an isolated, long flat plate at a Reynolds number based on plate thickness of 100. The size of the bubble increases with increasing Reynolds number and reaches a maximum length of 6.5 times the plate thickness at $Re_t = 325$. The separated shear layer becomes unsteady at higher Reynolds number and so does the flow downstream from the reattachment point. The length of the bubble decreases and approaches four times the plate thickness at high Re_t.

For multiple in-line plates Lane [9] reports:

• No separation is detected at the leading edge of the second plate of a two-plate pair for plate spacings less than $4t$. Intermittent reverse flow occurs near the leading edge of the second plate for larger spacings, but the unsteady flow between the plates acts to prevent the formation of a steady separation bubble for spacings up to $S/t = 8$.

These results suggest that the heat transfer characteristics of the second plate should not be too sensitive to the shape of the leading edge of the second plate for moderate plate spacings. They also suggest that a transition in the heat transfer rate on a blunt first plate should be observed near $Re_t = 325$ due to the onset of unsteady flow in the separated shear layer.

The objectives of the work reported here were to identify the magnitude of the effect of each of these flow modules on heat transfer and to try to characterize heat transfer performance in terms of flow phenomena.

The Experiment

The average heat transfer coefficients for single and multiple plates placed in a low turbulence wind tunnel were determined from steady-state measurements. The test plates were formed by sandwiching two 0.025-mm thick, 0.5-cm wide, 30.5-cm long resistance heating strips between two 0.16-cm thick aluminum plates. The ends of the stainless steel heating strips were soldered to two brass bus plates and insulated from the aluminum plates with thin sheets of paper. A sketch showing the arrangement of the parts of a heated plate is presented in Fig. 1. Copper-constantan thermocouple junctions were soldered to one of the aluminum plates along the centerline at five spanwise locations and the leads were nested between the two heating strips. The 0.23-mm dia Teflon insulation around the 0.08-mm thermocouple wire established the separation distance between the aluminum plates. The entire assembly was then epoxied together to form a plate 0.33-cm thick and 2.44-cm long in the flow direction. The 30.5-cm long heated section of the plate spanned the wind tunnel test section. The brass buses extended through slots cut in the test section sides and supported the plate. The leading edges of the two plate assemblies constructed were initially blunt with sharp corners. The leading edge shape was changed during the course of the experimental program to alter the separation characteristics. These changes are detailed in the next section.

The experiments were performed in a low-speed, open-return wind tunnel. Air is drawn into a 30.5-cm square cross section test section through three turbulence reducing screens and a 9:1 contraction nozzle. The mean velocity is uniform over the center 90 percent of the test section and the turbulence intensity is less than 0.3 percent over the range of velocities used in these tests. Slots have been milled in the sidewalls of the Plexiglas test section to support the test plates. The slots are sealed, after the plates are positioned, to prevent leakage of air into the test section.

The mean air velocity was determined by measuring the eddy-shedding frequency of small diameter cylinders which spanned the test section and converting this frequency to velocity using the relationship obtained by Roshko [10]. This technique was supplemented by pitot tube readings at the higher velocities. A hot-wire anemometer probe was used to explore the flow around the plates to identify changes in flow regimes such as transition from steady to unsteady flow.

The plate geometry and wind tunnel velocity were set at the beginning of a test run and the electrical power to the test plates was adjusted so that the temperature of each plate was about 6°C above the air temperature. The measured spanwise plate temperature variation was always less than 1/4°C, and the calculated streamwise plate temperature variation was similarly small so that each plate surface approximated a constant temperature boundary. An average heat transfer coefficient was calculated for each plate from the measured data using the total power dissipation, the total plate surface area, and the difference between the plate center temperature and upstream air temperature.

Nomenclature

b = wake width
C_p = specific heat
f = friction factor
h = average heat transfer coefficient
j = Colburn factor $[h/\rho C_p U]\mathrm{Pr}^{2/3}$
$j^+ = j\sqrt{\dfrac{(t/L)\mathrm{ref}}{(t/L)}}$
L = plate length in streamwise direction
Pr = Prandtl number
Re_t = Reynolds number, $\dfrac{Ut}{\nu}$
S = spacing between plates in streamwise direction
t = plate thickness
$(t/L)\mathrm{ref}$ = 7.4
U = free stream velocity
ρ = density

Subscripts

I = upstream plate
II = downstream plate

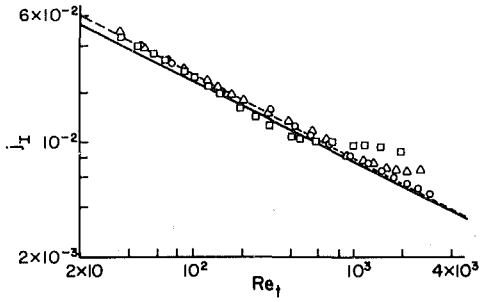

Fig. 2 Heat transfer from single plates, L/t = 7.4. Theory: ___ Pohlhausen (12), _ _ _ Dennis and Smith (13). Experiment: □ square leading edge, △ semicircular leading edge, ○ semi-elliptic leading edge.

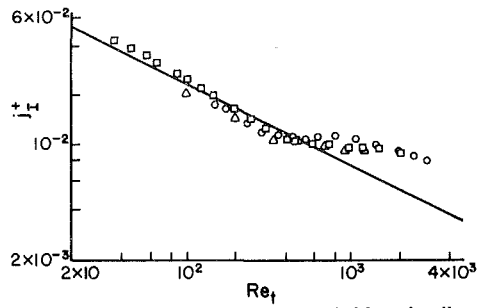

Fig. 4 Heat transfer from single plates with blunt leading edge. □ Present work t = .33 cm, L/t = 7.4; △ Cur and Sparrow [6] t = .20 cm, L/t = 12.5; ○ Adarkar and Kays [1] t = .30 cm, L/t = 16.7.

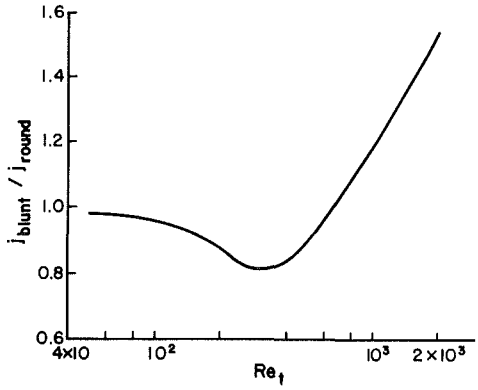

Fig. 3 Effect of leading edge shape on heat transfer rate for single plate, L/t = 7.4

Most of the data are correlated in terms of a Colburn j factor and a Reynolds number. Uncertainties in the primary measurements indicate that the Reynolds number uncertainty is ± 2 percent, the uncertainty in the Colburn factor for the first plate, j_I, is ±4 percent, and for the second plate, j_{II}, is ± 7 percent. The second plate is normally bathed in the heated wake of the first plate. As a consequence the heat transfer rate on the second plate depends on the temperature of the first plate. Part of the uncertainty in j_{II} reflects the influence of possible variations from the nominal condition of matched plate surface temperatures. Several tests at the lowest Reynolds number were duplicated with an 11°C temperature difference between plate and air. The results confirmed the predictions based on the work of Gilpin, Imura, and Cheng [11] that natural convection effects were insignificant. It is estimated that radiation may account for a maximum of 5 percent of the heat loss at the lowest Reynolds numbers.

Results and Discussion

Single Plates. An initial set of experiments was performed on a single isolated plate to explore the effects of leading edge separation. The plate geometry, L/t = 7.4, was chosen to reveal both the inhibiting and enhancing characteristics of leading edge separation and at the same time to be representative of heat exchanger geometries. The results of these experiments are summarized in Fig. 2. The solid line is the prediction of Pohlhausen [12] based on boundary layer theory, and the broken line is due to Dennis and Smith [13], who considered also the effects of streamwise temperature and velocity gradients. Both of these theories are for infinitely thin plates with one characteristic length, and they are plotted here mainly for reference purposes. They are presented with Re_t as the independent variable (obtained by multiplying Re_L by t/L for the test plate), because features which depend on leading edge separation should scale with plate thickness. In general, the experimental results closely follow the predictions of Dennis and Smith provided that leading edge separation is avoided. The data for the plate with a square leading edge fall below the broken line for $100 \leq Re_t \leq 650$. Lane and Loehrke found that a leading edge bubble first forms at Re_t = 100 and grows in size with increasing Reynolds number until the separated shear layer becomes unsteady. In these experiments the onset of unsteady flow along the side of the plate was first detected with a hot wire probe at Re_t = 300. At this point the separation bubble should cover much of the plate surface and indeed the measured heat transfer inhibition, relative to the broken line, is near a maximum. Further increases in Reynolds number increase the magnitude of the measured velocity oscillations and random, turbulent velocity spikes appear at about Re_t = 650. The apparent transition as indicated by the heat transfer data for this plate occurs near Re_t = 400.

The shape of the leading edge of this squared plate was subsequently changed and further heat transfer data obtained. These data indicate that the size of the separation bubble is greatly reduced with a semicircular leading edge but that "early" transition is still induced. The flow over a plate with a 2:1 semielliptic leading edge was steady over the entire Reynolds number range investigated. This latter configuration was employed in subsequent tests and will be referred to as a rounded leading edge. It will be contrasted with the square leading edge configuration which will be referred to as a blunt leading edge. The effect of leading edge separation on a single plate is summarized in Fig. 3, where the ratio of the average heat transfer coefficient for a plate with a blunt leading edge to that for a plate with a rounded leading edge is plotted versus Reynolds number. The ratio falls to 0.8 at Re_t = 300 for this plate and then rises dramatically at higher Reynolds numbers. The dip should be less pronounced for plates of larger L/t and the enhancement may be greater.

The results for the plate with a blunt leading edge are compared in Fig. 4 to those obtained by other investigators for plates with similar leading edges. The heat transfer data are compared relative to their position with respect to the Pohlhausen prediction through the use of the variable j^+. The work of Dennis and Smith [13] suggests that the boundary layer approximation will be noticeable at the lower Reynolds numbers and that the scaling used in j^+ should be altered accordingly. The simpler, analytic scaling was chosen, however, since the thin plate theory is only an approximation for these plates of finite thickness. The data in Fig. 4 were chosen to represent a range of plate thickness, plate length and L/t. They are typical of other data available in that they display a characteristic transition in heat transfer behavior at a Reynolds number based on plate thickness of about 400.

Multiple Plates. In these two-plate experiments the

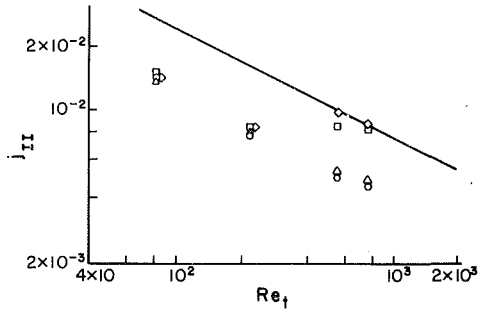

Fig. 5 Heat transfer from second plate, S/t = 0.3. Leading edge shape: ○ I round – II blunt, △ I round – II round, □ I blunt – II blunt, ◇ I blunt – II round. Solid line is the Pohlhausen prediction for the upstream plate.

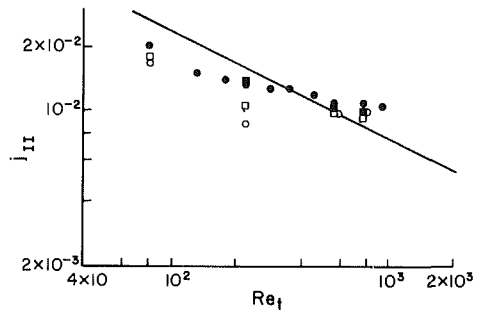

Fig. 6 Heat transfer from second plate. Open symbols – S/t = 3.0, closed symbols – S/t = 4.8. Leading edge shape: ○ I round – II blunt, □ I blunt – II blunt. Solid line is the Pohlhausen prediction for the upstream plate.

average heat transfer coefficients on the upstream and downstream plates were measured for various Reynolds numbers, plate spacings, and leading edge configurations. The heat transfer coefficient for the upstream plate at small plate spacings was somewhat lower than that for an isolated plate but aside from that no difference was detected so the focus of this presentation will be on the second plate. At the smallest spacing (S/t = 0.3) the geometric variable of primary importance is the leading edge shape of the upstream plate. This is illustrated in Fig. 5. The solid line is the Pohlhausen prediction for the upstream plate, which is included in this and the following three figures for reference. The flow around the plates is everywhere steady at the two lowest values of Reynolds number. It is also steady at the two highest values of Reynolds number if the leading edge of the upstream plate is round. If the leading edge of the upstream plate is blunt, however, the turbulence induced by leading edge separation at the higher two values of Reynolds number increases the heat transfer coefficient on the downstream plate.

As the spacing between the plates is increased the flow between the plates may become unsteady due to the instability of the first plate wake. The point at which this instability starts depends on the Reynolds number and plate spacing scaled using the wake width as a characteristic dimension [2,7]. For these relatively short plates, L/t = 7.4, the wake width is mainly determined by the plate thickness and to a lesser extent by the plate length and leading edge configuration. Evidence that the between-plate mixing dominates the enhancement of heat transfer on the second plate can be seen in Fig. 6. The heat transfer rate on the second plate at the higher Reynolds numbers for S/t = 3.0 is high regardless of the leading edge configuration. As the spacing is increased to S/t = 4.8 the amount of mixing which can be accomplished at a given Reynolds number before the wake hits the second plate increases and thus so does the heat transfer coefficient. The flow between the plates is always steady for Re_t = 80 so

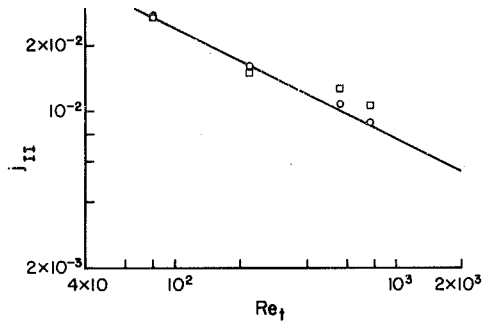

Fig. 7 Heat transfer from second plate, S/t = 24.2. Leading edge shape: ○ I blunt – II round, □ I blunt – II blunt. Solid line is the Pohlhausen prediction for the upstream plate.

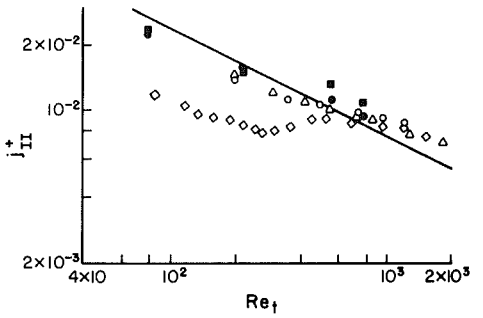

Fig. 8 Heat transfer from second plate. Present work t = .33 cm, S/t = 12.1. • I blunt – II round, ■ I blunt – II blunt; Adarkar and Kays [1] △ blunt plates, t = .51 cm, S/t = 10.0, ◇ thin plates, t_{max} = .15 cm, S/t_{max} = 16.7; Cur and Sparrow [6] ○ t = .20 cm S/t = 12.5. Solid line is the Pohlhausen prediction for the upstream plate.

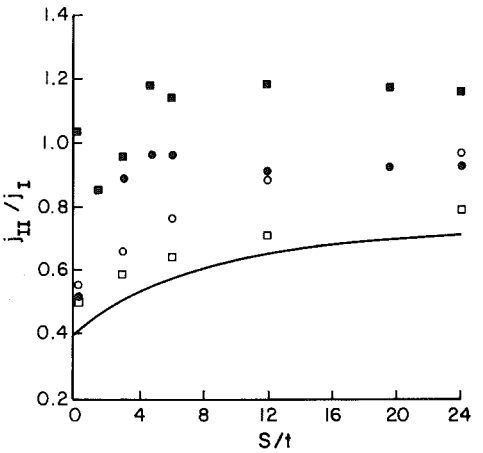

Fig. 9 Ratio of heat transfer rate from second plate to that from first plate. Open symbols – Re_t = 80, closed symbols – Re_t = 560. Leading edge shape: ○ I blunt – II round. □ I round – II blunt, • I round – II round, ■ I blunt – II blunt.

that the increase in j_{II} with increased spacing noted at this Reynolds number must be due to molecular diffusion.

A systematic effect of the leading edge configuration of the second plate was observed for $S/t \geq 12$. The heat transfer is enhanced at the higher Reynolds number if the leading edge is blunt as is shown in Fig. 7 for S/t = 24. The cause of this enhancement has not been identified but it may be due to the generation of new turbulence in an unsteady leading edge separation bubble on the second plate.

Experimental results of different investigators for second plate heat transfer are compared relative to the first plate Pohlhausen prediction in Fig. 8. The data for geometrically similar plates all show a modest transition from heat transfer coefficients slightly below those of the first plate at low

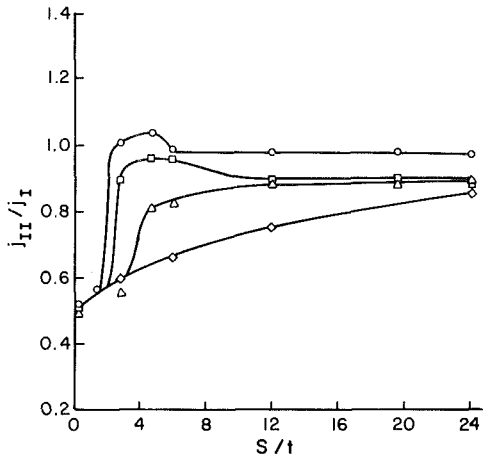

Fig. 10 Ratio of heat transfer rate from second plate to that from first plate. Both leading edges round. Re_t = ○ 770, □ 560, △ 220, ◇ 80.

Reynolds number to slightly above at high Reynolds number. A much more dramatic transition is evident in the results obtained by Adarkar and Kays for "thin plates." Two factors tend to accentuate the transition for these plates. First, they are closer together in terms of S/L than the other plates in this figure. This results in a lower level of heat transfer on the second plate in the steady, laminar, pretransition regime. Second, the plate section is not rectangular. Both the leading and trailing edges of these plates were tapered to minimize separation. The contribution of the wake instability mechanism to enhancement of second plate heat transfer is most evident when other mechanisms are suppressed.

The ratio of j_{II}/j_I as a function of plate spacing is presented in Fig. 9 along with the prediction of Adarkar and Kays based on thin-plate boundary-layer theory. The combinations of leading edge configurations shown represent the maximum spread in the data for each of the two Reynolds numbers chosen. At Re_t = 80 the heat transfer coefficient for the second plate is always less than that for the first plate. This is not the case at the higher Reynolds numbers. At Re_t = 560, for example, this ratio is greater than one at the smallest spacing for a blunt upstream plate because part of that plate is insulated by a separation bubble and part by the nose of the second plate while the second plate is bathed by "turbulent" flow generated in the separated shear layer. As the plate spacing is increased the first plate heat transfer rate increases and the ratio j_{II}/j_I drops below one. The flow instability which begins at about S/t = 3.0 at this Reynolds number causes the ratio to increase again to well above unity with further increases in spacing. When both the first and second plate leading edges are rounded the heat transfer coefficient ratio approaches, but does not exceed, unity as the plate spacing is increased for the two Reynolds numbers shown.

The action of the wake instability mechanism can be isolated by concentrating on the ratio of j_{II}/j_I for a pair of plates with round leading edges. The data plotted in Fig. 10 clearly show the effect of mixing between the two plates for $Re_t > 80$. The separation distance required to accomplish the bulk of this mixing decreases with increasing Reynolds number. Little additional increase in the ratio of heat transfer coefficients is realized for spacing larger than $S/t = 5$.

The measured heat transfer rate from the second plate deviated significantly from the predictions based on steady-flow boundary-layer theory over a wide Reynolds number range even at relatively small plate separation distances. The implication of this result to heat exchangers is twofold. First, it implies that augmentation may be achieved through a wake instability mechanism even at low Reynolds numbers with short plate interruptions. Second, the onset of unsteady flow would signal the end of the domain of applicability of the performance predictions based on steady flow theory. This limitation of the boundary layer approximation of Sparrow, Baliga, and Patankar [14] to the two-dimensional flow over an array of plates was pointed out by Shah [15] in his discussion of that paper. It also applies to the more recent calculations of Sparrow and Liu [16] and Patankar and Prakash [17]. Sparrow, Baliga and Patankar [18], in their closure following Shah's discussion, refer to the work of Loehrke, Roadman, and Read [2] as an example of what to expect with regard to unsteady flow in plate arrays. The present paper is a more comprehensive version of that earlier report. A logical next step for research applied to interrupted surface exchangers would be a combined analytical (numerical) and experimental attack on the transitional flow in two-dimensional arrays. Additional work is also required to assess the influence of three-dimensionality on the basic phenomena in certain offset-strip fin and perforated-plate heat exchangers.

Conclusions

The results of the experiments described here and the data from other referenced investigations support the following conclusions:

1 The average heat transfer coefficient for a single plate with a blunt leading edge depends on both the plate length and plate thickness. For a moderate range of variables around $L/t = 10$ the data can be fairly well correlated by plotting $j\sqrt{L/t}$ versus Re_t.

2 The heat transfer rate on a single blunt plate may be inhibited compared to that on a single rounded plate for $Re_t < 600$ due to the insulating effect of a leading edge separation bubble. At higher Reynolds number the heat transfer rate is enhanced due to turbulence generated in the separated, leading edge shear layer.

3 The influence of the turbulence generated in the separation bubble on the blunt upstream plate may be detected on the downstream plate, for small plate spacing, as an enhancement of the second plate heat transfer rate compared to that for a rounded upstream plate.

4 The enhancement of the second plate heat transfer rate due to the mixing associated with the unstable wake of the first plate overshadows the effect of the first plate leading edge shape for $S/t > 3$. The second plate heat transfer coefficient may approach or even exceed that of the first plate due to this mixing. Little additional improvement is realized for spacings greater than $S/t = 5$ and, in fact, for some configurations a shallow maximum in j_{II}/j_I is observed at this spacing. Although the wake flow cannot be completely described by the plate thickness alone, the domain of importance of this effect is roughly $S/t > 3$ and $Re_t > 200$.

5 The shape of the leading edge of the downstream plate is important only for $S/t \geq 12$ and high Reynolds number. The heat transfer rate is higher for a blunt second plate than for a round second plate for $Re_t \geq 560$.

Acknowledgment

This research was supported by NSF through Grant CME-8009046.

References

1 Adarkar, D. B., and Kays, W. M., "Heat Transfer in Wakes," Department of Mechanical Engineering Technical Report No. 55, Stanford University, Apr. 1963.

2 Loehrke, R. I., Roadman, R. E., and Read, G. W., "Low Reynolds Number Flow in Plates Wakes," ASME Paper 76-WA/HT-30, Nov. 1976.

3 Liang, C. Y., "Heat Transfer, Flow Friction, Noise, and Vibration Studies of Perforated Surfaces," Ph.D. thesis, University of Michigan, Ann Arbor, Mich., 1976.

4 Shah, R. K., "Perforated Heat Exchanger Surfaces, Part 2—Heat Transfer and Flow Friction Characteristics," ASME Paper 75-WA/HT-9, Nov. 1975.

5 Morkovin, M. V., "An Approach to Flow Engineering Via Functional Flow Modules," *Deutsche Luft-und Raumfahrt Forschungsbericht*, 72-27, May 1972.

6 Cur, N., and Sparrow, E. M., "Experiments on Heat Transfer and Pressure Drop for a Pair of Colinear, Interrupted Plates Aligned with the Flow," ASME *International Journal of Heat and Mass Transfer*, Vol. 21, 1978, pp. 1069-1080.

7 Roadman, R. E., and Loehrke, R. I., "Low-Reynolds-Number Flow Between Interrupted Flat Plates," ASME *Journal of Heat Transfer*, Vol. 105, Feb. 1983, pp. 166-171.

8 Lane, J. C., and Loehrke, R. I., "Leading Edge Separation From a Blunt Plate at Low Reynolds Number," ASME *Journal of Fluids Engineering*, Vol. 102, 1980, pp. 494-496.

9 Lane, J. C., "Characteristics of Interrupted-Plate Heat Exchanger Surfaces," M.S. thesis, Mechanical Engineering Department, Colorado State University, 1980.

10 Roshko, A., "On the Development of Turbulent Wakes from Vortex Streets," NACA Report 1191, 1954.

11 Gilpin, R. R., Imura, H., and Cheng, K. C., "Experiments on the Onset of Longitudinal Vortices in Horizontal Blasius Flow Heated From Below," ASME *Journal of Heat Transfer*, Vol. 100, Feb. 1978, pp. 71-77.

12 Jakob, M., *"Heat Transfer,"* John Wiley, Vol. 1, 1949, p. 469.

13 Dennis, S. C. R., and Smith, N., "Forced Convection From a Heated Flat Plate," *Journal of Fluid Mechanics*, Vol. 24, 1966, pp. 509-519.

14 Sparrow, E. M., Baliga, B. R., and Patankar, S. V., "Heat Transfer and Fluid Flow Analysis of Interrupted-Wall Channels, With Application to Heat Exchangers," ASME *Journal of Heat Transfer*, Vol. 99, Feb. 1977, pp. 4-11.

15 Shah, R. K., "Discussion—Heat Transfer and Fluid Flow Analysis of Interrupted-Wall Channels, With Application to Heat Exchangers," ASME *Journal of Heat Transfer*, Vol. 101, Feb. 1979, pp. 188-189.

16 Sparrow, E. M., and Liu, C. H., "Heat Transfer, Pressure Drop, and Performance Relationships for In-Line, Staggered, and Continuous Plate Heat Exchangers," *International Journal of Heat and Mass Transfer*, Vol. 22, 1979, pp. 1613-1625.

17 Patankar, S. V., and Prakash, C., "An Analysis of the Effect of Plate Thickness on Laminar Flow and Heat Transfer in Interrupted-Plate Passages," *International Journal of Heat and Mass Transfer*, Vol. 24, 1981, pp. 1801-1810.

18 Sparrow, E. M., Baliga, B. R., and Patankar, S. V., "Author's Closure on Heat Transfer and Fluid Flow Analysis of Interrupted-Wall Channels, With Application to Heat Exchangers," ASME *Journal of Heat Transfer*, Vol. 101, Feb. 1979, p. 189.

Particulate Fouling on the Gas-Side of Finned Tube Heat Exchangers

T. R. Bott

C. R. Bemrose

Department of Chemical Engineering,
University of Birmingham,
Birmingham B15 2TT, United Kingdom

A 0.3-m (12-in.) square vertical wind tunnel has been built to provide airflows in the range 2.4–5.8 m/s (490–1140 fpm) for fouling studies. Precipitated calcium carbonate dust can be fed into the airstream (which may be heated) prior to a heat exchanger model. The paper reports results on a four-row, four-pass spiral wound finned tube heat exchanger. Fouling tests have been carried out primarily near the extremes of surface heat flux available (1000 W/m^2 to -700 W/m^2). The results have been analyzed by the general method of Kays and London to give an effective nondimensional airside heat transfer parameter ($StPr^{2/3}$) and a friction factor. Tests have covered the Reynolds number range from 1350 to 3800. Normalization of fouling data to fixed Reynolds numbers has given friction factor curves which increase to an asymptotic level between 1.4 and 2.5 times the initial value, whilst $StPr^{2/3}$ values tend to fall by only 10–20 percent during the same time.

Introduction

Gas-side fouling of extended surface heat exchangers has received very little attention. One reason for this is the wide range of potential foulants on the gas-side, depending upon location and use. Other factors include the mainly uncontrolled nature of the air stream and the wide variety of different finned tube designs. In general, the design of the heat exchanger is unlikely to take into account the effect of a growing dirt layer in the thermal design or in the estimation of power consumption, either because it is assumed that the dirt layer is unimportant or, more likely, because there is no reliable information available. At best, a fouling factor (which is independent of time) may be used. The effects on thermal efficiency of dirt on the heat transfer surface are probably only of the same order of magnitude as the limits of the accuracy of the thermal design itself, so that in times of cheap energy, the increased power consumption required to move the gas through the heat exchanger could be tolerated. However, with severe increases in fuel costs, increased pressure drop across the finned tubes assumes much greater importance. Reductions in airflow brought about by the increased pressure drop, could, of course, lead to additional and unacceptable reductions in thermal efficiency. Rose [1] states that a dirt layer of only 1.27×10^{-4}m thickness over the fins of a typical bundle will increase the pressure drop by 20 percent for a given airflow rate.

Finned tube heat exchangers are used for both heating and cooling duties. The work described in this paper is applicable to both regimes. Extended surface heat exchangers are being used increasingly for cooling process streams. The arguments favouring air cooling compared with conventional water cooling of such streams are well known, and may be summarized:

1 The development of low cost finned tubes
2 Shortage of water, poor water quality, and increased water cost (including treatment costs)
3 Environmental problems with the use of water from natural sources, such as rivers and streams

However, the cost advantage of using air coolers depends upon an optimization of the design taking into account thermal duty, capital cost, and operating cost [2]. The annual operating costs are considerably influenced by the power consumption. For a given heat transfer requirement, the extremes of choice are a relatively cheap cooler with a high fan motor requirement or a more expensive, aerodynamically designed cooler with lower power consumption. Any one of a number of factors may result in the benefits of economic design not being realized, including air recirculation, the effects of manufacturing tolerances on finned tubes and fan motors, and the presence of dirt on the air side of the exchangers. The origin of the dirt may be either particulate matter carried forward in the air stream or as a result of corrosion. Dust particles in the atmosphere account for a large proportion of the difficulties due to fouling. The problem may be further aggravated by the presence of water liquid—say from rain—which can bind dust particles into a hard matrix. Air coolers on steel works where the atmosphere is very dusty are prone to this problem. Oil coolers on diesel train units tend to become blocked due to the presence of dust emanating from brake linings combined with the effects of temperature and the presence of moisture and oil mist. Units in coastal areas have been found to be fouled with salt from sea spray. Corrosion may be a direct result of corrosive agents contained in the airstream or may be due to leakage of the process stream into the air space. In some instances of poor performance, water containing dissolved solids is sprayed on to the finned tubes in order to remove additional heat as latent heat of vapourization. Under these evaporative conditions, solid residues appear on the fins and tubes.

Aluminum fins are popular but their use on chemical works has given rise to drastic reductions in air flow and consequent inefficiencies due to the combined effects of fouling and corrosion. The actual reduction in airflow depends not only on the length of time during which fouling and corrosion occur, but also on the shape of the fan curve and the normal operating point on that curve.

Conditions where heat exchangers are used for heating purposes are often more severe than those experienced in cooling. The gas stream is frequently more dirty than cooling air. The "dirt" may be the products of combustion (including the results of incomplete combustion) and as such, may contain hydrocarbons, ash, sulphurous compounds, etc. Often the gas is also corrosive as well as containing particulate matter. Other types of "dirt" arise when the gas stream is the exhaust from a manufacturing process, where the range of contaminants is almost unlimited. One of the hazards when

Contributed by the Heat Transfer Division and presented at the 20th ASME/AIChE National Heat Transfer Conference, Milwaukee, Wisconsin, August 2–5, 1981. Manuscript received by the Heat Transfer Division, October 9, 1981.

using heat exchangers in the heating mode is that the gas stream itself is being cooled, potentially giving rise to condensation.

Fouling of unfinned boiler tubes has been studied by several workers. Profos and Sharan [3] examined the effect of the geometrical arrangement of tubes on fouling using a model wind tunnel. Their foulant was gypsum and water. In Russia, Kuznetsov [4] sought to reduce the overall operating costs of steam boilers by selecting optimum gas velocities and tube arrangements, whilst Petrov [5] carried out fouling tests on air heaters using coal ash. Leont'ev and Tsalko [6] analyzed the thermal resistance of deposits and the heat flux under conditions of nonisothermal gas flow and obtained results consistent with their experimental data.

The previously mentioned increases in fuel costs are making heat recovery from exhaust gas streams more attractive financially. The limiting factor in deciding to install waste heat recovery equipment is frequently the problem of heat exchanger fouling. Extended surface heat exchangers are normally required for waste heat recovery, and there are various empirical criteria for the types of finning and tube geometries which are acceptable for use in different types of gas stream. Csathy [7] has given some recommendations for these criteria. The bonding of ash deposits on to boiler economizer tubes was studied by Rylands and Jenkinson in 1944 [8], and they offered practical suggestions for minimizing bonded scale formation. More recently, Silvestrini [9] has conducted tests on plain and serrated fin models in diesel exhaust next to an existing waste heat recovery unit. He concluded, from measuring the thickness of foulant at various positions, that there was no significant difference between plain and serrated fins, but that blockage and flow area reduction were worse with more closely spaced fins.

Despite the longstanding problems of gas-side fouling of extended surface heat exchangers, there has been remarkably little systematic study of the phenomenon.

Based on the survey carried out by Thackery [10], it is likely that gas-side fouling of extended surface heat exchangers costs, in the United Kingdom, in the region of 120 million dollars per annum. A major proportion of this cost will be associated with increased fan energy. For this reason alone, quite apart from considerations of improved design techniques, it is important that quantitative data on the effects of fouling on finned tube bundles is obtained and made widely available.

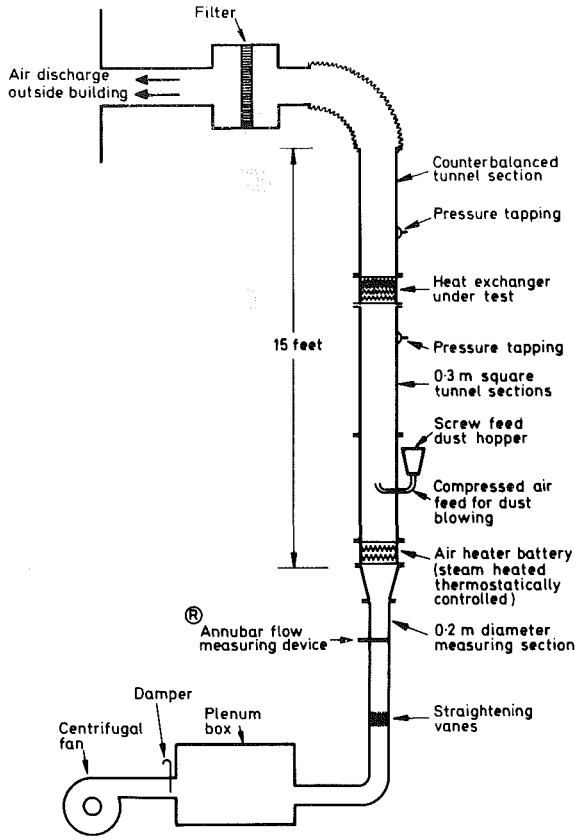

Fig. 1 Diagram of fouling wind tunnel

Experimental Procedure

A 0.3-m (12-in.) square vertical wind tunnel has been built to provide airflows in the range 2.4–5.8 m/s (490–1140 fpm). The temperature of the airstream can be thermostatically controlled between ambient and 50°C, and dust can be injected into the airstream by means of a screw-feed injector. In the present work, precipitated calcium carbonate nominally in

Nomenclature

A = total airside heat transfer area (including fins), m^2
A_c = test core free flow area, m^2
A_d = test core direct surface heat transfer area, m^2
c,c' = constants
c_p = air specific heat at constant pressure, J/kg K
f = friction factor, dimensionless
f_b = normalized friction factor at time $\theta = 0$, dimensionless
G = volume flow rate, m^3/hr
h = heat transfer coefficient, W/m^2 K
k = thermal conductivity, W/m K
L = length of test core in direction of air flow, m
l = fin length, m
m,m' = constants
NTU = number of heat transfer units, dimensionless
Nu = Nusselt number, dimensionless
p = constant
Pr = Prandtl number, dimensionless
Re = Reynolds number, dimensionless
r_h = flow passage hydraulic radius, m
St = Stanton number, dimensionless
T = temperature, °C
t = thickness, m
U = overall heat transfer coefficient, W/m^2 K
V = velocity, m/s
v = specific volume, m^3/kg

Greek Symbols

α,β = constants
Δp = pressure drop, Pa
η_f = fin efficiency, dimensionless
η_s = surface effectiveness, dimensionless
θ = time, min
ρ = density, kg/m^3
ϕ = constant

Subscripts

a = air
app = approximate
core = conditions within sample core
f = fin
i = inlet
o = outlet
m = mean
norm = normalized
t = tube
w = water

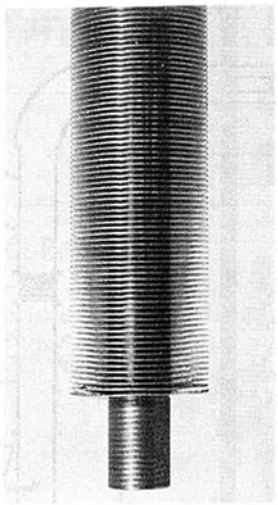

Fig. 2 Photograph of finned tube

the size range 3–30μm has been used. This material was chosen because of its ready availability and its basic safety. In particular, it poses neither health nor explosion hazards. Heat exchanger models 0.3-m (12-in.) square are fitted into the wind tunnel and may be fed with water on the primary side. The water stream may be either cold main's water, or hot water (up to 80°C) from a thermostatically controlled reservoir. The tunnel is shown diagramatically in Fig. 1.

One of the possibilities when running the rig with cold main's water is that condensation could occur if the surface temperature of the extended heat transfer surface is at a temperature below the dew point. This is unlikely to occur at the air flow rates involved unless the air passing through the heat exchanger is also cooled to a temperature near to the dew point. Even when inlet air temperatures up to 50°C have been used, no additional moisture has been added to the atmospheric humidity, so that condensation in the heat exchanger has not been likely. Future tests are planned to cover the condensation regime.

Instrumentation has been installed to measure airflows and associated temperatures and pressures, and also water flow and its associated temperatures. Fouling tests are carried out under predetermined conditions of surface heat flux (by setting air and water temperatures) and air velocity. Observations are made of the heat exchanger performance versus time. Periodically fouling (i.e., dust injection) is stopped whilst full performance data are obtained over the available range of air velocities. Because of concern that this procedure might affect the continuity of fouling, tests were carried out and have shown that there is no effect under the experimental conditions used.

The results reported in this paper have been obtained on a finned tube heat exchanger having the characteristics given in Table 1. The finned tubes have spiral wound (or plain helical circular) fins; Fig. 2 shows one of these tubes. The heat exchanger configuration used was four-row, four-pass, with 4½ tubes per row and with the tubes set on a staggered triangular pitch.

Apart from two tests, a constant dust injection rate of 21 g/min has been used. This gives dust concentrations of 0.65–1.5 g/m^3, which is equivalent to desert dust storm concentrations [11]. The justification for using tests accelerated to this degree was provided by two tests with a dust injection rate of 3.7 g/min. The rate of build-up of fouling (as measured by the friction factor—see later) was observed to be five times slower for this five-fold reduction of dust concentration whilst still approaching the same asymptotic level.

In order to simulate service conditions where the environmental dust is unlikely to be either clean or dry, a thin layer (averaging 0.017-mm thick) of a liquid normally used for coating air filters has been applied to the heat exchanger fins before fouling. The use of a bonding agent has been found by Cowell and Cross [12] to correlate with field experience. They found that alternately injecting dust and an oil spray provided a foulant layer very similar to that obtained on engine coolers. In the present work, an initial surface coating to provide a 100 percent capture probability for the impinging dry particles has produced a foulant build up which is very similar to that observed on process plant heat exchangers. The presence of the bonding agent has the added advantage of stabilizing the foulant layer for subsequent measurements under conditions of varying Reynolds number.

Tests have been carried out primarily near the extremes of surface heat flux available, namely a heated airstream (45°C) with cold water (5°C), and an ambient temperature airstream with hot water (75°C). The test details are given in Table 2.

Table 1 Characteristics of spiral wound finned tube

Tube outside diameter	0.0254m (1.0 in.)
Fin outside diameter	0.057m (2.25 in.)
Fin thickness	4.064×10^{-4}m (0.016 in.)
Fin density	410 fins per meter (10.5 fins/in.)
Tube material	steel
Fin material	aluminum
Fin bonding	mechanically peened into a spiral groove in the tube

Table 2 Test details

Test No	Air velocity m/s	Air Reynolds number	Dust injection rate g/min	Dust concentration g/m^3	Heat flux W/m^2
12	3.7	2150	21	1.02	−705
14	3.2	1900	21	1.18	−680
15	2.5	1500	21	1.50	−600
16	5.8	3500	21	0.65	−705
19	2.5	1500	3.7	0.26	−590
20	5.6	3300	3.7	0.12	−715
23	4.3	2800	21	0.87	980
24	4.8	3200	21	0.78	1010
25	3.4	2250	21	1.11	875
26	3.4	2400	21	1.11	940
27	2.6	1800	21	1.45	890
29	2.3	1350	21	1.64	−530
30	2.4	1650	21	1.57	−180
31	2.5	3800	21	0.68	−240

Results and Analysis

The results have been analyzed using the basic method of Kays and London [13, 14] to give values of $StPr^{2/3}$ and friction factor, f, versus time (for fouling tests), or Reynolds number (for performance tests). The airside Reynolds number for finned tube heat exchangers is based on a linear dimension (hydraulic diameter, $4r_h$) which is conventionally defined as

$$4r_h = \frac{4\,A_c L}{A}$$

For the four-row sample in question, $4r_h = 5.585 \times 10^{-3}$m in the clean condition. Pending the results of ongoing work to define the geometry of a growing layer of foulant, and recognizing from visual observation that the majority of the deposition occurs on the front and rear faces of the heat exchanger, a constant value of hydraulic diameter has been assumed throughout the tests.

Because of the known difficulty of accurately measuring the air temperature downstream of a heat exchanger, great care was taken with the waterside instrumentation for flows and temperatures, and particularly with $(T_{wo} - T_{wi})$ which was measured with a double differential thermocouple to ± 0.04°C.

Water flows and properties were calculated at the measured

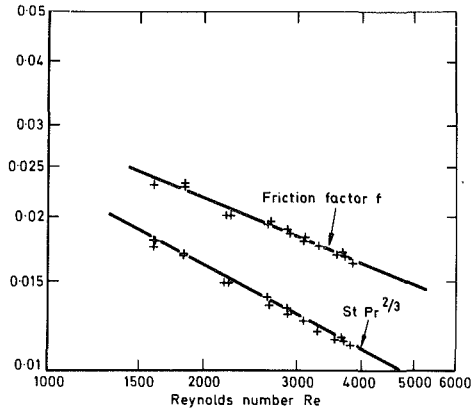

Fig. 3 Performance test—clean heat exchanger (Test No. 13)

temperatures. Airflow and properties were also calculated at the measured temperatures, taking account of moisture content but not the presence of dust (which constituted a maximum of 0.15 percent by weight of the throughput on the airside).

Using the waterside measurements, the actual quantity of heat transferred was calculated, and was used, together with the measured air inlet temperature, T_{ai}, to calculate the air outlet temperature, T_{ao}.

NTU and the overall heat transfer coefficient, U, are calculated from

$$\mathrm{NTU} = ln\left[\frac{\frac{T_{wi}+T_{wo}}{2}-T_{ai}}{\frac{T_{wi}+T_{wo}}{2}-T_{ao}}\right] \tag{1}$$

$$U = \frac{\mathrm{NTU}\times G\,\rho_a c_p}{A} \tag{2}$$

Using the hydraulic radius, r_h, an approximate Stanton number, $\mathrm{St_{app}}$ can be calculated:

$$\mathrm{St_{app}} = \frac{\mathrm{NTU}}{L}\times r_h \tag{3}$$

The turbulent water side heat transfer coefficient, h_w, has been calculated from the formula

$$\mathrm{Nu}_w = 0.027\,(\mathrm{Re}_w)^{0.8}(\mathrm{Pr}_w)^{0.33} \tag{4}$$

This formula is the Sieder and Tate [15] version of the Dittus-Boelter equation for viscous liquids, but neglecting the final term $(\mu/\mu_w)^{0.14}$ which is close to unity for water inside air cooled extended surface tubes. The coefficients used are those given by Wong [16] and by Coulson and Richardson [17]. No allowance has been made for the effects of tube surface roughness on the waterside since, for the type of heat exchanger considered, the waterside heat transfer coefficient is greater than 4000, whereas the corresponding coefficient on the air side is less than 80. As the total heat transfer resistance is calculated by adding reciprocal film coefficients even an error of 20 percent in the waterside coefficient results in less than 0.5 percent error in the airside coefficient.

An approximate airside heat transfer coefficient is obtained from

$$h_{\mathrm{app}} = \mathrm{St_{app}}\times\rho_a U_{\mathrm{core}} c_p \tag{5}$$

and used to compute fin efficiency

$$\eta_f = \frac{\tanh \phi l}{\phi l} \tag{6}$$

where

$$\phi = \left[\frac{2h_{\mathrm{app}}}{k_f t_f}\right]^{1/2}$$

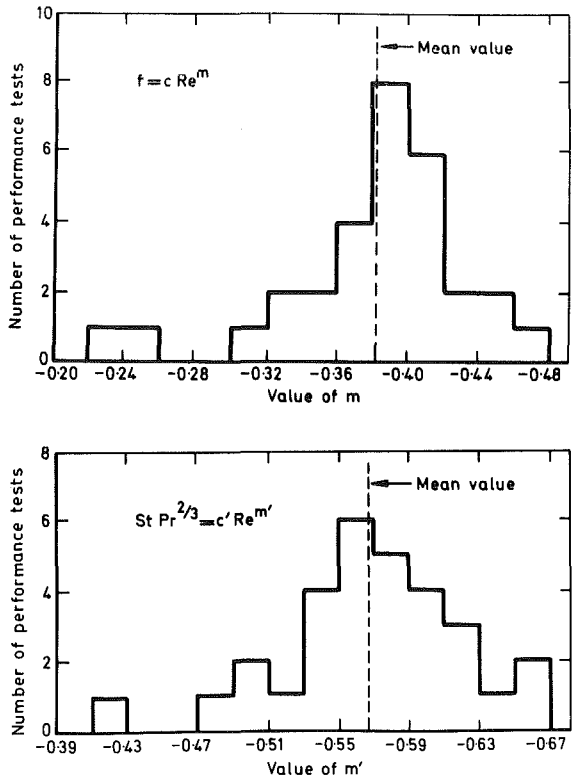

Fig. 4 Values of exponents m and m'

(Strictly, a more complex expression including Bessel functions should be applied for annular disk fins. However, with fin efficiencies in excess of 0.9, as in this case, the differences are not significant).

Surface effectiveness, η_s, is deduced from

$$\eta_s = \frac{A_d + A_f\eta_f}{A}$$

The effect of a thin uniform fouling deposit over the entire secondary surface has been considered by Epstein and Sandhu [18]. Their analysis is not directly applicable to the present study, where fouling deposits are neither thin nor uniform, but provides a valuable pointer for future consideration. At present, in order to simplify the initial analysis, it has been assumed that the fouling layer modifies the airside heat transfer coefficient, which is obtained from

$$h_a = \frac{1}{\eta_s\left[\frac{1}{U}-\frac{A}{A_w h_w}-\frac{A}{A_d}\left(\frac{t}{k_t}\right)\right]}$$

This value of h_a is used to recalculate the fin efficiency in an iterative loop. In general, only two iterations have been required to calculate h_a to within 1 percent.

From the value of h_a, the standard nondimensional heat transfer grouping ($\mathrm{StPr}^{2/3}$) is obtained for plotting against the airside Reynolds number, Re_a.

The friction factor, f, is likewise calculated according to Kays and London [14].

$$f = \frac{r_h v_i}{v_m L}\left[\frac{\Delta p_{\mathrm{core}}\times 2}{G^2\times v_{\mathrm{core}}} - 2\left(\frac{v_o}{v_i}-1\right)\right] \tag{7}$$

where

$$v_m = \frac{2}{(T_{ai}\rho_{ai}+T_{ao}\rho_{ao})}\left[\frac{T_{wi}+T_{wo}}{2}-\left(\frac{T_{ao}-T_{ai}}{\mathrm{NTU}}\right)\right] \tag{8}$$

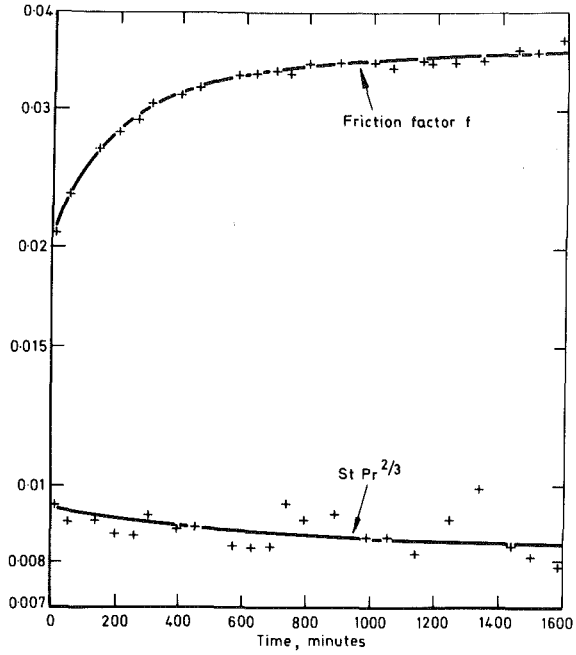

Fig. 5 Fouling Test No. 24

For the heat exchanger in its clean condition the performance and friction factor variation with Reynolds number is shown in Fig. 3 on a log-log plot. The straight line relationship conforms to the results of Kays and London [13].

A total of thirty such performance tests have been carried out before, during and after the fouling tests. Surprisingly, all of these performance tests have produced straight line log-log plots of similar slope, but vertically displaced from each other. These straight lines imply that the proportionate change in either $StPr^{2/3}$ or friction factor due to fouling, is independent of the Reynolds number. The relationships are thus in the form

$$f = c\mathrm{Re}^{m} \text{ and } \mathrm{StPr}^{2/3} = c'\mathrm{Re}^{m'}$$

Values of m, c, m', and c' have been computed for each performance test, to give the best straight line fit. The values of c and c' depend on sample history, but the values of m and m' are history independent. Figure 4 shows the range of variation of m and m'. The mean values are:

$$m = -0.381 \text{ (standard deviation } 0.052)$$

and

$$m' = -0.569 \text{ (standard deviation } 0.052)$$

Fouling tests have lasted for up to 120 hrs although they have more typically been of the order of 30 hrs. It is impractical to maintain the air velocity and Reynolds number completely constant throughout this length of time, and variations of up to 10 percent have occurred. Fortunately, the constant slope of both the friction factor and the heat transfer versus Reynolds number curves permits a ready standardizing procedure for each point. For this purpose each experimental point has been normalized to a Reynolds number ($\mathrm{Re}_{\mathrm{norm}}$) chosen by inspection of the data. The normalizing has used the relationships:

$$f_{\mathrm{norm}} = f\left[\frac{\mathrm{Re}_{\mathrm{norm}}}{\mathrm{Re}}\right]^{-0.38}$$

and

$$[\mathrm{StPr}^{2/3}]_{\mathrm{norm}} = \mathrm{StPr}^{2/3}\left[\frac{\mathrm{Re}_{\mathrm{norm}}}{\mathrm{Re}}\right]^{-0.57}$$

Figure 5 shows the variation of f_{norm} and $(\mathrm{StPr}^{2/3})_{\mathrm{norm}}$ with time for test number 24. The friction factor shows a steady increase with time, and there is little scatter on these points.

Table 3 Calculated constants for friction factor curve

Test No	α (asymptotic value)	$\beta \times 10^3$	p mins	Initial fouling rate % increase/min
12	2.30	1.45	273	0.13
14	2.48	1.95	212	0.25
15	1.91	3.35	137	0.14
16	1.66	1.90	425	0.16
19	2.05	0.91	550	0.044
20	2.13	0.14	3780	0.012
23	2.44	3.63	117	0.26
24	1.72	1.92	567	0.24
25	2.11	1.89	212	0.16
26	1.43	6.41	106	0.16
27	1.66	6.85	68	0.19
29	1.47	2.05	730	0.20
30	2.36	0.39	1290	0.064
31	1.39	1.02	575	0.036

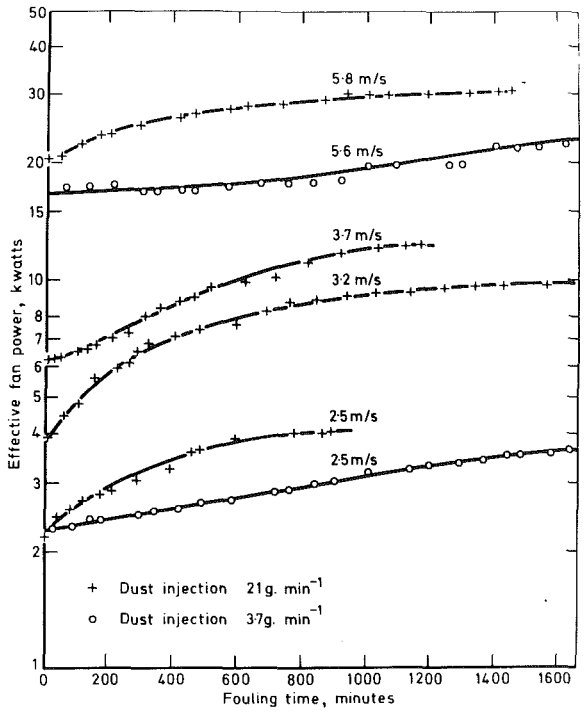

Fig. 6 Effective fan power for 10 ft × 10 ft heat exchanger

Heat transfer measurements on the other hand are notoriously prone to scatter, particularly where they are made over periods of days or weeks (as in this case). The observation of many thousands of points has led to the conclusion that $StPr^{2/3}$ tends to fall by 10–20 percent during the course of a test, as shown by the line in Fig. 5.

The increase in friction factor with time has been fitted to an exponential form of curve. For this purpose, in order to make all the tests comparable, the friction factors have all been normalized to constant Reynolds number (as above) and then expressed in terms of f_b, the normalized value at time $\theta = 0$. A relationship of the form

$$\frac{f}{f_b} = \alpha[1 - e^{-\beta(\theta+p)}]$$

has been assumed and the growth parts of the curves have been fitted to this equation to generate the values of the constants α, β, and p.

The values of these constants are given in Table 3. It might be expected that the shape of the friction factor curve (represented by β) and the asymptotic friction factor (represented by α) would exhibit a monotonic correlation with air velocity; this does not seem to be the case based on present

evidence. A similar dependence on heat flux might also be expected but this, too, is not apparent from the data.

Initial fouling rates (measured as a percentage increase in f_b per minute) have been measured for each test. These values are also given in Table 3, but again do not give simple correlations with the independent variables used.

The rate of deposit buildup is usually described as a combination of deposition and removal rates. Due to changing flow area and pattern as the foulant layer grows, these rates will vary with time.

The development and effect of gas-side fouling is clearly complex, and probably involves interactions among several variables. Work on other heat exchanger geometries and on further variables is in hand with a view to establishing the various relationships.

When the results are translated into process plant terms, they mean that the fan power consumed increases substantially (in line with the increase in friction factor) as fouling proceeds. The impact of this is clearly seen in Fig. 6 where the data presented in this paper have been extrapolated to a 10-ft square heat exchanger. At an air velocity of 3.7 m/s, the fan power increases by 6 kW (from 6 kW to 12 kW) before reaching an asymptotic level. For such a heat exchanger in continuous service this represents an increased electricity charge of about 3600 dollars per annum based on a unit charge of 7.2 cents/kWh (3p/kWh). In this assessment, no account has been taken of reduced thermal efficiency. The capital cost of the heat exchanger and its fan would be of the order of 25,000 dollars, so that the potential increase in running cost due to fouling is of the same order as the expected return on the capital investment. This indicates the importance of understanding and taking account of airside fouling when providing the financial justification for new plant.

Conclusion

A method and apparatus have been established for studying particulate fouling of air/water heat exchangers using air at temperatures up to 50°C and water from 5–80°C.

Analysis of the first results has shown that graphs of friction factor versus Reynolds number always give straight lines on a log-log plot, before, during and after completion of fouling tests. These straight lines have similar slopes and conform to

$$f = c\,\mathrm{Re}^{-0.38}$$

Similar straight lines have been observed for plots of $\mathrm{StPr}^{2/3}$ versus Reynolds number, conforming to the equation

$$\mathrm{StPr}^{2/3} = c'\,\mathrm{Re}^{-0.57}$$

During fouling, the friction factor increases to an asymptotic level between 1.4 and 2.5 times the starting value.

The present work provides a firm experimental foundation on which further studies of the effects of variables can be based. The existence of consistent, straight-line relationships between friction factor, $\mathrm{StPr}^{2/3}$ and Reynolds numbers shows that particulate fouling on the gas-side of heat exchangers, which has previously received little attention, can in fact be studied and analyzed systematically.

Acknowledgments

This work has been funded by the United Kingdom Department of Energy as part of the United Kingdom contribution to an International Energy Agency project on extended surface heat transfer. The financial and technical assistance of the Department, and also of the United Kingdom Atomic Energy Authority (as operating agents for the total project) are gratefully acknowledged. In partiuclar, the help given by Dr. David Vincent of the Department of Energy and Dr. G. F. Hewitt of UKAEA is similarly acknowledged. The authors are also greatly indebted to Mr. Eric Oxley, who has undertaken most of the experimental work on the test rig.

References

1 Rose, J. C., "Some Problems Associated with the Operation and Testing of Air-Cooled Heat Exchangers," *Proceeding of the Conference on Air Coolers*, Institution of Mechanical Engineers, London, Sept. 1970, pp. 77–87.

2 Russell, C. M. B., and Bos, W. H., "The Economic Design of Air Coolers," *Proceeding of the Conference on Air Coolers*, Institution of Mechanical Engineers, London, 24th September 1970, pp. 14–40.

3 Profos, P., and Sharan, H. N., "Effect of Tube Spacing and Arrangement Upon the Fouling Characteristics of Banks of Tubes," *Sulzer Technical Review*, Vol. 4, 1960, pp. 31–43.

4 Kuznetsov, V. A., "Selecting Gas Velocities and Optimum Profiles for the Convective Surfaces in Steam Boilers Taking Fouling into Account," *Thermal Engineering*, Vol. 16, No. 8, Aug. 1969, pp. 68–72.

5 Petrov, V. A., "Fouling of Air Heater Tubes on the Air Side," *Thermal Engineering*, Vol. 15, No. 3, 1968, pp. 21–23.

6 Leont'ev, A. I., and Tsalko, E. A., "Heat and Mass Transfer During the Formation of Deposits on a Heating Surface," *High Temperature*, Vol. 9, No. 2, Mar./Apr. 1971, pp. 289–296.

7 Csathy, D., "Heat Recovery from Dirty Gas," presented at Sixth National Conference on Energy and the Environment, Pittsburgh, Pa., May 1979.

8 Rylands, J. R., and Jenkinson, J. R., "Bonded Deposits on Economizer Heating Surfaces," *J.I. Elec. E.*, Vol. 91, Pt. 2, No. 20, Apr. 1944, pp. 77–88.

9 Silvestrini, R., "Heat Exchanger Fouling and Corrosion," *Chem. Eng. Prog.*, Vol. 75, No. 12, 1979, pp. 29–34.

10 Thackery, P. A., "The Cost of Fouling in Heat Exchange Plant," *Conference on Fouling: Science or Art?*, University of Surrey, Guildford, Mar. 1979, pp. 1–9.

11 British Standard BS 1701:1970. "Air Filters for Air Supply to Internal Combustion Engines and Compressors, other than for Aircraft," British Standards Institution, 1970.

12 Cowell, T., and Cross, D. A., "Airside Fouling of Internal Combustion Engine Radiators," presented at International Off-Highway Meeting and Exposition, Sept. 1980. S.A.E. Paper No. 801012, Society of Automotive Engineers, 1980.

13 Kays, W. M., and London, A. L., *Compact Heat Exchangers*, 2d ed., McGraw-Hill, New York, 1964.

14 Kays, W. M., and London, A. L., "Heat Transfer and Flow Friction Characteristics of some Compact Heat Exchanger Surfaces: Part 1—Test System and Procedure," ASME *Trans.*, Vol. 72, 1950, pp. 1075–1085.

15 Sieder, E. N., and Tate, G. E., "Heat Transfer and Pressure Drop of Liquids in Tubes," *Ind. Eng. Chem.*, Vol. 28, No. 12, Dec. 1936, pp. 1429–1434.

16 Wong, H. Y., *Handbook of Essential Formulae and Data on Heat Transfer for Engineers*, Longman, London, 1977.

17 Coulson, J. M., and Richardson, J. F., *Chemical Engineering*, Vol. 1, 3d ed., Pergamon Press, Oxford, 1977.

18 Epstein, N., and Sandhu, K., "Effect of Uniform Fouling Deposit on Total Efficiency of Extended Heat Transfer Surfaces," *Proceedings of the 6th International Heat Transfer Conference*, Toronto, Vol. 6, Aug. 1978, pp. 397–402.

Evaluation of a Method for Heat Transfer Measurements and Thermal Visualization Using a Composite of a Heater Element and Liquid Crystals

S. A. Hippensteele

L. M. Russell

F. S. Stepka

NASA Lewis Research Center,
Cleveland, Ohio 44135

Commercially available elements of a composite consisting of a plastic sheet coated with liquid crystal, another sheet with a thin layer of a conducting material (gold or carbon), and copper bus bar strips were evaluated and found to provide a simple, convenient, accurate, and low-cost measuring device for use in heat transfer research. The particular feature of the composite is its ability to obtain local heat transfer coefficients and isotherm patterns that provide visual evaluation of the thermal performances of turbine blade cooling configurations. Examples of the use of the composite are presented.

Introduction

As turbine inlet gas temperature and pressure increase, the heat loads to the turbine also increase and more complex turbine blade cooling configurations are needed to provide the desired metal temperatures and component life. The attainment of accurate metal temperature predictions and effectively cooled and durable parts requires accurate knowledge of local thermal loading in terms of the local heat transfer coefficients. The most common method used to determine these coefficients consists of finite heater strips with thermocouples [1–5]. This method, however, only provides average heat transfer coefficients over a relatively large area and is generally used in one-dimensional idealizations of the problem. As a consequence methods for measuring *local* heat transfer are needed, particularly at near-room-temperature conditions, where the investigation can be conducted at relatively low cost and both turbine flow and heat transfer dimensionless parameters can be preserved.

This paper, which summarizes the information contained in reference [6], describes and illustrates the use of a method that can determine *local* heat transfer coefficients by making use of a composite of a conductive heating element and a liquid-crystal-coated sheet. Liquid crystals have been used for indicating temperature change for many years [7] and have recently been used in heat transfer research by formulating and spraying liquid crystals on a test surface [8] or on a carbon-impregnated paper heater attached to a test surface [9, 10]. However, these methods of applying the liquid crystals are not particularly convenient. The unique feature of the layered composite described in this paper is its simplicity, convenience of application and use, and the commercial availability of elements for fabricating the composite. The composite was tested in a variety of applications.

Description of Composite Elements

Liquid-Crystal Sheet. There are three types of liquid crystals: smectic, nematic, and cholesteric. The molecular structure of the liquid crystal determines the particular type. The cholesteric type was used in this study. The unique property of cholesteric liquid crystals is their ability to reflect definite colors at specific temperatures for a given material. Cholesteric substances mixed in various proportions can produce many different temperature-color combinations. The color change for the liquid crystal that was used in this study ranges from clear at ambient temperature (before melting starts) through red as the temperature increases and then to yellow, green, blue, and finally clear again at the highest temperature (after melting completely). These color changes are repeatable and reversible as long as the liquid crystals are not physically damaged by excessive temperature. More information about the theory of liquid crystals can be obtained from reference [7].

The liquid-crystal material used in this study was purchased commercially as sheets that consisted of the liquid crystals laid on a black plastic sealing material and covered by a transparent Mylar layer. This liquid-crystal sheet produces a single band of temperature related colors that are brighter than the sprayed-on method where several different temperature ranges of colors are produced. The overall thickness of the sheet was 0.203 mm (0.008 in.), and it was available in 0.305-m (1-ft) widths of any length. The two liquid-crystal sheets used herein had calibrated yellow color temperatures of about 38 and 32°C (100 and 89°F). Other temperature ranges are available up to 55°C (131°F) or higher if specially fabricated.

Heater Element. The heater element consisted of either a thin, vapor-deposited coating of gold on a polyester film or a carbon-impregnated coating on a plastic sheet. Both were purchased commercially. The overall thickness of the sheets with their coating were 0.127 mm (0.005 in.) and 0.178 mm (0.007 in.), respectively. The sheets with the gold deposit were

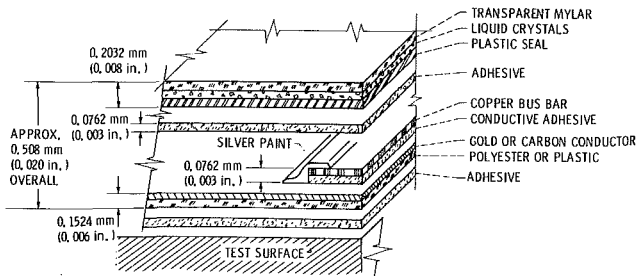

Fig. 1 Liquid-crystal sheet electric heater composite (not to scale)

Contributed by the Heat Transfer Division and presented at the International Gas Turbine Conference, Houston, Texas, March 8–12, 1981. Manuscript received by the Heat Transfer Division December 14, 1981. Paper No. 81-GT-93.

0.914-m (3-ft) wide, could be purchased in any length, and had an electrical resistance of 3.3 ohms/sq. The carbon-coated sheets were 43.2-cm (17-in.) wide, could be purchased in lengths of 55.9 cm (22 in.), and had an electrical resistance of 50 ohms/sq. A third type of heater element (not included in this evaluation) consisted of carbon impregnated cardboard having a resistance of 50 ohms/sq.

Composite. The composite of the liquid crystal and the heater sheet, made up of commercially available materials, is shown in cross section in Fig. 1. The lower layer of the composite was the heater sheet. The copper bus bars were attached to the conductive side (top) along two opposing outer edges of the sheet. Although the copper strips had conductive adhesive backing, this adhesive alone did not produce adequate or consistent electrical contact. A silver-impregnated paint was therefore used to bridge a portion of the copper strip and conductive material, as shown in the figure. The upper layer of the composite was the liquid-crystal sheet. The liquid-crystal sheet was attached to the lower layer (heater sheet) by an adhesive, with the bus bars sandwiched between. Electric wires were connected to the bus bars by standard soldering methods. The overall thickness of the composite was approximately 0.508 mm (0.020 in.).

The composite sheet can be attached to the test surface by any adhesive that would give smooth, uniform contact over the surface. In this study, a thin, paperlike material with double adhesive backing was used both for attaching the composite to the test surface and for attaching the liquid-crystal sheet and the heater sheet together.

Evaluation

Apparatus and Procedure.

Liquid-Crystal Sheet. The liquid-crystal sheets were calibrated for color versus temperature by immersing the sheet in a hot water bath and observing and photographing (with strobe lights) the color changes as the water gradually cooled to room temperature. The water bath was stirred before temperature mesurements and photographs were taken. The sheet had been enclosed in a watertight plastic bag before immersion to protect it from any possible detrimental effects of the water. The water temperature was measured by a copper-constantan thermocouple and a precision digital voltmeter.

Heater Element. Two types of heater elements were examined: vapor-deposited gold on a polyester film and a conductive, carbon coating on a plastic sheet. The accuracy of the heat transfer coefficient depends on the uniformity of heating in the heater element portion of the composite. Heating uniformity was therefore measured. To determine heating uniformity in the vapor-deposited gold sheets, two methods were used: measuring the uniformity of light transmission, and measuring the voltage at regular intervals over the surface. Only the voltage-measuring method, using a digital multimeter, was used for the carbon-coated sheets. It was reasoned that the uniformity of the gold sheet for heating was related to the uniformity of the gold thickness and in turn to the uniformity of the light transmission through the gold, or the light density. The light density was measured by using a video image processor and a scanning microdensitometer.

Composite. After separate evaluations were made of the liquid-crystal sheet and the two types of heater element sheets, selected liquid-crystal sheets laminated to the heater sheets were evaluated as composites. Copper bus bars were attached to opposite edges of the heater sheets as described previously (Fig. 1). A conventional power supply and digital multimeters were used to measure the amounts of electric power passing into the heater sheets. The composite sheets were suspended horizontally in a cardboard frame surrounded by plastic walls to provide a dead air space that would minimize the free-convection heat transfer. Knowing the uniformity of the liquid-crystal sheets and that of the heater sheets evaluated earlier, we could now assess the uniformity of the composite by passing electric power into it. The resulting liquid-crystal temperature pattern was recorded with a 35-mm camera by using color film and strobe lights as in the water calibration discussed previously.

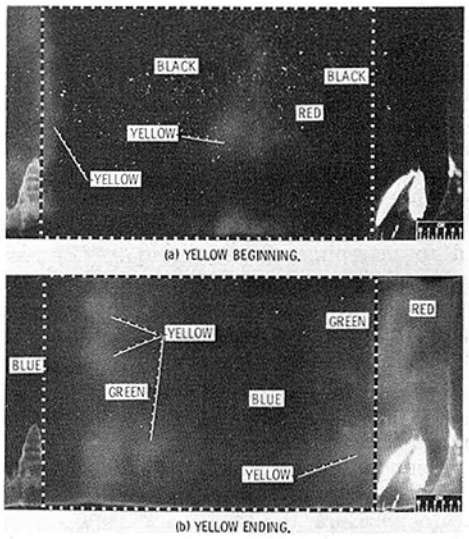

Fig. 2 Uniformity test of the gold heater sheet and a liquid-crystal sheet with electrical power supplied

Although the effects of free convection [11] on creating nonuniform heat transfer were initially of concern, simple tests were run to allay this concern.

Determination of the heating uniformity of the composites requires the use of an air energy balance for the surface-convection heat transfer

$$q_e - q_l = hA\,(t_c - t_a) \tag{1}$$

Specifically, to determine the heating uniformity of any area in a composite sheet requires two measurements: the $q_{e,1}$, required to produce the first sign of the calibrated color being used, and the $q_{e,2}$, required to produce the last sign of this same calibrated color. The first measurement shows the localized hottest spot and the second shows the coldest spot. The maximum percentage error in a given composite of the localized heat flux was obtained from the expression

$$\left[\frac{q_{e,2} - q_{e,1}}{(q_{e,2} + q_{e,1})/2}\right] \times 100 \tag{2}$$

More results are given in reference [6].

Results and Discussion.

Liquid-Crystal Sheet. The results of a typical temperature

Nomenclature

A = area
h = heat transfer coefficient
q = heat flux (or electric power input)
t = temperature
1,2 = conditions

Subscripts

a = air
c = liquid crystal at calibrated color
e = electric power input
l = losses

color calibration covered a range of temperatures from 52.1°C (125.8°F) to 36.1°C (96.9°F). The colors that corresponded to the hottest to coldest temperatures included blue, green, yellow, and red. At 38.1°C (100.5°F), or green, the sheet had only a slight amount of yellow. At 37.6°C (99.7°F), or yellow, it had only a slight amount of red. Therefore the yellow color occurred very uniformly over the entire liquid-crystal sheet and represented an extremely narrow temperature band. For this reason the yellow color was used to determine the 37.6°C (99.7°F) temperature isotherm in this particular liquid-crystal sheet. The yellow color appears between the dominant red and green colors and is estimated to define an isotherm temperature to within 0.2°C (0.4°F). Others [12, 13] claim that by special selection of the types of liquid crystals an accuracy of 0.1°C (0.2°F) can be achieved. The ANSI type T (copper-constantan) thermocouple material used here has a maximum error in absolute temperature indication of 0.42°C (0.75°F). However, when the same thermocouple and microvoltmeter are used to measure the difference between the water calibration temperature and the air temperature during testing, only a negligible error exists. This sheet was used in the first three tests made to illustrate the uses of the composite. Water bath calibrations were done for other liquid-crystal sheets, and each specific color resulting from a particular water bath temperature was very uniform throughout the sheet. However, the specific colors did vary for given temperatures from sheet to sheet. It is therefore necessary to calibrate each particular sheet when using it to obtain quantitative heat transfer data. Also, the viewing angle for the liquid crystal in research use should not be much different than that when calibrating the material. The reason for this is that a shift in the color band positions (temperature indication) occurs with changes in the viewing angle to the liquid-crystal sheet surface. This shift, however, was only significant when the viewing angle changed from the surface-normal by more than about 30 deg.

In summary, the liquid-crystal sheets evaluated herein responded very uniformly to temperature over their entire area. Using the calibrated, highly temperature-sensitive yellow color provides an accurate means of determining a detailed temperature isotherm to within 0.2°C (0.4°F).

Heater Element. The light transmission and the surface voltage measurements provided information on the relative uniformity of the conductive materials and are not discussed herein, but can be obtained from [6]. A more appropriate method of evaluating the heater element is described next. In this method the combination of the heater element and the liquid-crystal sheet is tested. Because the liquid-crystal sheet is very uniform and accurate, any nonuniformity shown in the liquid-crystal sheet while it is in the composite is a direct result of the nonuniformity of the heat flux in the heater sheet.

Composite. Two composites containing liquid-crystal sheets that had a yellow color calibration temperature of 31.7°C (89.0°F) were made and evaluated. The first composite also contained a 30.5- by 61.0-cm (12- by 24-in.) portion of a gold sheet randomly chosen from the 91.4-cm (36-in.) wide roll material. The second composite also contained a randomly chosen 21.6- by 27.9-cm (8.5- by 11.0-in.) carbon-coated heater sheet.

The first composite (Fig. 2) was used to show, quantitatively, the nonuniformity in the heat flux (or heat transfer coefficient) due to the nonuniformity of the gold film in the heater sheet. The bus bars were located along the top and bottom edges. The nonuniformities in this composite are located inside the dashed lines. This area, which is 41.7 = cm (16.4 = in.) long by 28.2 = cm (11.1 = in.) wide, excludes the extreme nonuniformities along each end of the composite. Note that the light spots in the lower right corner are strobe light reflections. The first measurement, showing the localized hot spots, is shown in Fig. 2(*a*). The second measurement, showing the localized cold spots, is shown in Fig. 2(*b*). The respective heat transfer rates are 39.2 and 46.0 W. From these data and equation (2) the maximum percentage error in the localized heat flux within this specified area was determined to be ±8 percent. This is the same error that could be expected in the heat transfer coefficient within this specified area. By making more measurements in between these two, localized spots can be calibrated, and therefore localized heat fluxes or heat transfer coefficients can be corrected. Also, the areas of these large sheets that have more uniform heat fluxes and thereby more accurate heat transfer coefficient can be selected. Because the vapor deposited gold layer is very sensitive to abrasion, care must be taken to avoid producing kinks which cause cracks and therefore electrical discontinuities.

To show that the nonuniform effects of free convection had a negligible effect on the heat transfer, the suspended composite sheet was rotated and oriented in several different positions (horizontally as well as slightly tilted) in the dead air space. The nonuniformity in the color (temperature) pattern of the composite was found to be consistant within the sheet, that is, the pattern was not related to the particular orientation of the sheet. This indicates that any nonuniformity in the free convection heat transfer caused only a negligible effect in the resulting nonuniform color (temperature) pattern in the heated composite.

The second composite, containing the carbon-coated heater element, was briefly evaluated, but no photographs were taken. The uniformity of its heat flux, as revealed by the resulting liquid-crystal isotherm colors, was as good as that of the gold-coated heater sheet material. Handling problems (producing kinks or cracks) were not observed. Even purposely made surface scratches did not produce any noticeable localized temperature nonuniformities. Based on the preliminary findings the carbon-coated material appears to be as good as, or maybe better than, the gold coated material for use as the heater element.

In summary, the tests of the composites indicate that localized heat flux or measurement of heat transfer coefficients can be determined to about ±8 percent or even less if careful selection is made of the heater sheet.

Recommended Procedure for Use

The following procedure must be followed when quantitative heat transfer data are desired. The specific liquid-crystal sheet used must be water calibrated to determine the temperature of the yellow color isotherm. The most uniform heater sheet area must be chosen by making up different composites and observing the heat flux nonuniformities (isotherms). This should be done while electric power is applied to the heater sheet and the composite is suspended horizontally in a dead air space. Once a sheet is selected, additional measurements of the nonuniform heat flux may be needed in order to calibrate the localized areas of the sheet, as discussed earlier in this paper. These additional measurements will allow the correction of the localized heat transfer coefficient because the yellow pattern, being an isotherm, does not necessarily represent an iso-heat transfer coefficient.

As shown in equation (1) the heat losses must be accounted for. When the selected composite sheet is installed in the test facility, preliminary calibration measurements must be made just before testing if quantitative heat transfer data are to be obtained. The sum of the heat losses can be determined by measuring the electric power input to the heater element that is required to bring the liquid-crystal temperature up to the calibrated yellow color. At the yellow isotherms these heat losses will be the same as during the tests because the tem-

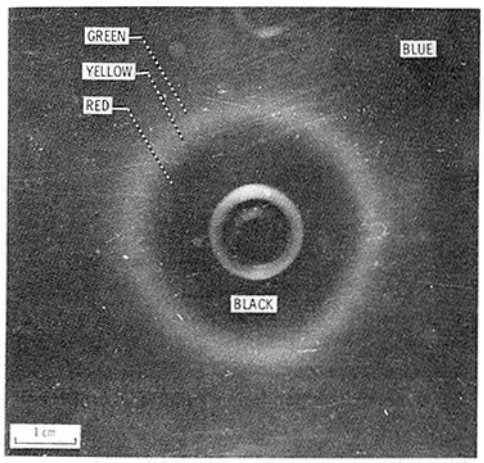

Fig. 3 Single-hole jet impinging on a flat plate

peratures will be the same. This is to be done before any airflow (e.g., impingement, film cooling, passage, etc.) is provided to the test model. Of course, as with any quantitative heat transfer study the use of guard heaters and insulation and the establishment of equilibrium conditions are necessary. Because of the variation in thermocouple material, it is best to use the same thermocouple in the test as was used in the water calibration of the liquid-crystal sheet. In this way the error in the thermocouple will be cancelled out when the temperature difference is taken between the water calibration temperature of the yellow isotherm and the air temperature during the test. From the measured sum of the heat flux losses, the heated area of the sheet, and the additional electric power input to obtain the yellow color for the research flow environment, the local heat transfer coefficient is determined by using equation (1). It is this additional electric power input (heat flux) that is being transferred from the sheet to the environment to compensate for the heat transfer coefficient present during the test.

Illustrations of Use

Apparatus and Procedure. The apparatus for illustrating the use of the liquid-crystal and heater element composite for several heat transfer applications where knowledge of local heat transfer coefficients is needed is described below.

The general procedure for conducting the tests was to first flow current through the heater sheet until color change started to occur in the liquid-crystal sheet. The composite and the test apparatus were allowed to reach thermal equilibrium with occasional slight changes in the current flow. Next, the tunnel gas flows and coolant flows were set to the desired values. Then the electric current through the heater sheet was changed to provide the desired temperature patterns. After equilibrium conditions were reached, the input electrical heat flux was measured and still photographs of the thermal patterns were taken with a 35-mm camera. The illumination was provided by two conventional strobe lights.

The use of the composite sheet was demonstrated in a variety of applications that included (*a*) a single jet of air impinging on a flat plate; (*b*) a large array of jets impinging on a flat plate, showing the effects of two different hole patterns; (*c*) the endwall of a planar turbine vane cascade with airflow through the cascade; and (*d*) flow out of a row of cooling air holes in a cylinder in crossflow, which simulates a film-cooled turbine vane leading edge. Apparatus for these applications consisted of various transparent plastic (acrylic) test sections that permitted visual observations and photographs of color patterns in the liquid crystal sheet. The composite of the sheets was attached to the wall on which the local heat transfer coefficients or thermal patterns were to be

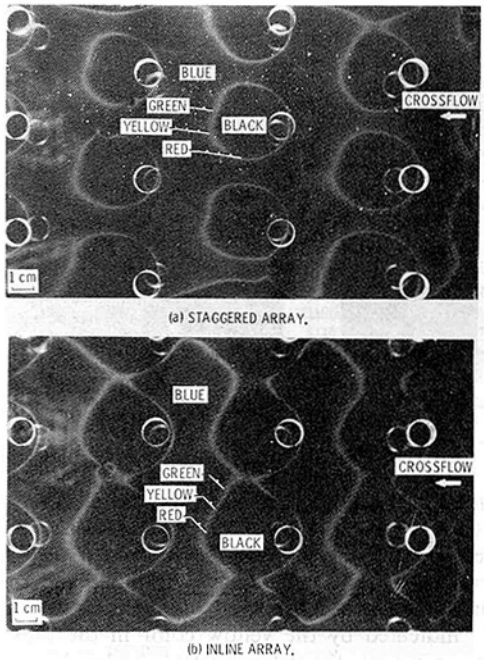

Fig. 4 Impingement cooling, downstream rows 5 to 8

determined. Only information on the configuration of the apparatus is presented herein. More details are presented in reference [6].

The impingement plates tested had (*a*) a single hole, (*b*) an array of eight rows of holes with an in-line hole pattern, an (*c*) an array of eight rows of holes with a staggered hole pattern. All holes were 1.27 cm (0.50 in.) in diameter. For Test (*a*) just mentioned the conditions were set to be within the applicable range of the heat transfer coefficient correlation of reference [14] so that an approximate comparison of results could be made. For Tests (*b*) and (*c*) the geometry and flow conditions were within the experimental range of the data in [4].

The endwall of the cascade had an axial chord of 11.4 cm (4.5 in.), a ratio of pitch to axial chord of 1.08, and an aspect ratio (span to axial chord) of 1.34. Airflow Reynolds number (based on actual chord) was in the range of experimental results from flow visualization experiments at the endwall of this cascade reported in [15].

The cylinder for film air injection was 11.4 cm (4.5 in.) in diameter, 15.2 = cm (6.0 = in.) high, and with 1.09 = cm (0.43 = in.) holes at an angle of 30 deg to the vertical for supplying the injection air. For this test the vertical centerline through the two holes was located at an angular distance of 30 deg from the stagnation point. This apparatus was the same as that used for flow visualization reported in [16].

Results and Discussion.

Impingment Cooling. The thermal pattern on the liquid-crystal sheet at a typical test condition of the impingement of a single jet onto a flat plate is shown in Fig. 3. The figure shows the concentric patterns representing isotherms or regions of constant heat transfer coefficients generated by the impacting jet (assuming uniform heat flux from the heater element). Although the contrast between the different colors is not as apparent on the black-and-white photograph as on the colored data photograph (see [6] in color), the color changes starting at the center are black, dark red, red, yellow, green, blue, and black. The yellow color, representing a temperature of 37.6°C (99.7°F), gave the most distinctive change and was considered as the one that could best be used for quantitatively determining the local heat transfer coefficient, as described in the section, Evaluation.

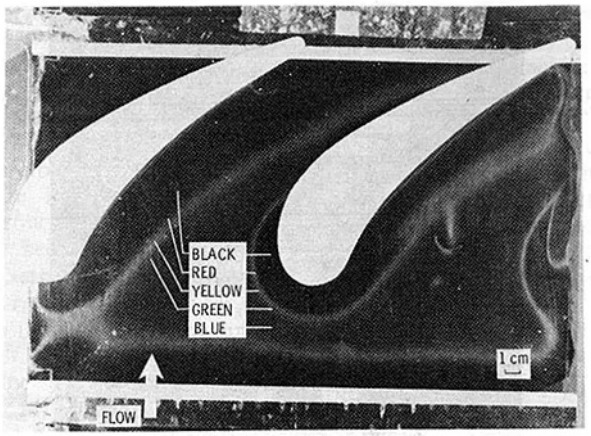

Fig. 5 Vane endwall of a cascade

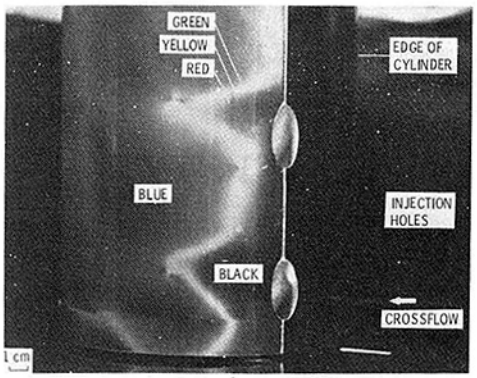

Fig. 6 Film injection from a cylinder in crossflow

By increasing the electric power input into the composite at a constant-airflow condition, the convective heat pickup was increased. Equation (1) shows that this heat pick-up is the difference between the electric power input and the losses. Since the air temperature and the reference temperature of the wall (as indicated by the yellow color in the liquid-crystal sheet) are constant, the magnitude of the local heat transfer coefficient, h, (as indicated by yellow) also increases with electric power input. Although the measurements made with the single jet were not intended to provide absolute values of the local h pattern, approximate values showed a trend of decreasing h with increasing radii similar to that obtained in reference [14].

The resulting isotherm and constant heat transfer coefficient patterns for the in-line and staggered impingement hole arrays are shown in Fig. 4. The photographs, which were taken of the fifth to eighth rows downstream, show how the accumulation of upstream flow progressively influences the deflection of the thermal pattern in the downstream direction. The results for both arrays show the distinct influence of the impingement from each hole. As a result the local heat transfer coefficient varies across the wall. In an application of impingement cooling this variation of heat input could cause variations in local temperature and induce thermal gradients that could affect the life of the part.

The relative cooling effectiveness of the two arrays is indicated by the relative extent of the dark areas (indicated) inside the yellow isotherm. These are areas of high heat transfer coefficients. Comparison of the two arrays shows that for the same condition of flow the in-line hole array has larger areas of higher coefficients and therefore is more effectively cooled than the staggered array configuration. The photograph also shows that the relative cooling effectiveness for both configurations increased with downstream distance. The results agree with those of [4], which are obtained from one-dimensional measurements of the heat transfer coefficients in the streamwise direction by means of copper heater strips.

Endwall of a Cascade. The isotherm and local heat transfer coefficient patterns for the endwall of a cascade are shown in Fig. 5. The photograph shows that the region of high heat transfer at the endwall surrounds the airfoil. This is the region bounded by the yellow color. The heat transfer coefficient was higher nearer the airfoil, as indicated by the color change from red to black. The photograph also shows that the region of high heat transfer at the wall is larger in extent near the pressure surface than near the suction surface. These results support the flow visualization that was conducted with this cascade [15], which showed that a leading-edge-generated vortex near the endwall moved away from the leading-edge pressure surface as it traveled downstream. This vortex apparently reduced the boundary layer on the wall near the pressure side as it progressed downstream, resulting in the higher heat transfer coefficient indicated in [17].

Film Injection Form a Cylinder. The isotherm and heat transfer coefficient pattern obtained by the injection of air from a row of two holes in a cylinder in crossflow are shown in Fig. 6. The holes were located at an angle of 30 deg from the stagnation point. This test simulated the flow of cooling air from film cooling holes at the leading edge of a turbine vane. Although the holes in the cylinder were inclined at an angle of 30 deg from the vertical, the main stream dominated the flow direction of the injected flow. This is shown in Fig. 6 by the isotherms downstream of the hole, which show only a slight deviation from the mainstream direction. The figure also shows that the influence of the injected air on cooling is also constrained to a narrow region downstream of the hole with only little spreading. These results support those in [16] obtained by visualization of the flow out of this cylinder.

Concluding Remarks

The composite of liquid crystal and heater element investigated herein, when used in a test installation in which proper accounting is made for conduction and radiation losses, provides a relatively convenient, simple, inexpensive, and accurate device for the high-resolution measurement of heat transfer and for determining local heat transfer coefficients at near-room-temperature conditions for a variety of applications. This investigation, which evaluated the accuracy and feasibility of commercially available elements of the composite, provided the basis for using the composite for quantitative heat transfer experiments. The liquid-crystal sheet of the composite was found to indicate a temperature to within 0.2°C (0.4°F) at the calibrated yellow color of 37.6°C (99.7°F). Other sheets have color change temperatures up to 250°C (482°F) but with limited sensitivities. The electrically generated heat flux out of the heater element was found to vary within 8 percent for a specified area of large heater sheets. Consideration of these accuracies indicated that if the composite elements can be selected within a specified area, and if conduction and radiation losses to other parts of test installation are properly accounted for, the local heat transfer coefficient error can be held to values even smaller than 8 percent.

Although the method was used herein primarily to illustrate qualitatively the results expected from application of the composite, the results confirmed inferences from flow visualization and heat transfer results of others in addition to providing information on local heat transfer that was not available in those experiments.

In conclusion, the method can be used for both comparisons of relative heat transfer performance of geometric configurations and quantitative local heat transfer deter-

mination. Some of the applications for the method in addition to the four examined qualitatively herein include various configurations of airfoils, coolant passages in multipass blade designs, curved ducts of different aspect ratios, and other three-dimensional geometries.

References

1 Eriksen, V. L., "Summary Report on Film Cooling Effectiveness and Heat Transfer with Injection Through Holes," NASA CR-72991, Aug. 1971.

2 Choe, H., Kays, W. M., and Moffat, R. J., "Turbulent Boundary Layer on a Full-Coverage Film-Cooled Surface—An Experimental Heat Transfer Study with Normal Injection," NASA CR-2642, Jan. 1976.

3 Luckey, D. W., and L'Ecuyer, M. R., "Stagnation Region Gas Film Cooling—Spanwise Angled Cooled Injection," TSPC-TR-76-2, Purdue University, Lafayette, Ind. (AD-A035716) Dec. 1976.

4 Florschuetz, L. W., Metzger, D. E., Takeuchi, D. I., and Berry, R. A., "Multiple Jet Impingement Heat Transfer Characteristic—Experimental Investigation of Inline and Staggered Arrays with Crossflow," ERC-R-79034, Arizona State University, Tempe, Ariz. (NASA CR-3217.) Jan. 1980.

5 VanFossen, Jr., G. J., "Heat Transfer Coefficients for Staggered Arrays of Short Pin Fins," ASME Paper No. 81-GT-75, Mar. 1981.

6 Hippensteele, S. A., Russell, L. M., Stepka, F. S., "Evaluation of a Method for Heat Transfer Measurements and Thermal Visualization Using a Composite of a Heater Element and Liquid Crystals," NASA TM 81639, Apr. 1981.

7 Fergason, J. L., "Liquid Crystals," *Scientific American*, Vol. 211, No. 2, Aug. 1964, pp. 76–85.

8 den Ouden, C., and Hoogendoorn, C. J., "Local Convective-Heat-Transfer Coefficients for Jets Impinging on a Plate—Experiments Using a Liquid-Crystal Technique," *Proceedings of the Fifth International Heat Transfer Conference*, Vol. V, AIChE, New York, 1974, pp. 293–297.

9 Cooper, T. E., Field, R. J., and Meyer, J. F., "Liquid Crystal Thermography and Its Application to the Study of Convective Heat Transfer," ASME JOURNAL OF HEAT TRANSFER, Vol. 97, Aug. 1975, pp. 442–450.

10 do Carmo Durao, M., "Investigation of Heat Transfer in Straight and Curved Rectangular Ducts Using Liquid Crystals Thermography," M.S. thesis (AD-A045131), Naval Postgraduate School, Monterey, Calif., June 1977.

11 Velarde, M. G., and Normand, C., "Convection," *Scientific American*, Vol. 243, No. 1, July 1980, pp. 92–108.

12 Butefisch, K. A., "The Liquid Crystal Method for the Visualization and Measurement of Heat Transfer Distributions," *Methods for Heat Transfer Measurement*, DLR-Mitt 75-11, European Space Agency, Paris, Feb. 1976, pp. 48–68.

13 McComas, J. P., "Experimental Investigation of Ground Effects on a Heated Cylinder in Cross-Flow," M.S. thesis, (AD/A-004240), Naval Postgraduate School, Monterey, Calif., Dec. 1974.

14 Walz, D. R., "Spot Cooling and Heating of Surfaces With High Velocity Impinging Air Jets, Part 2—Circular Jets on Plane and Curved Surfaces," TR 61 (AD-607727), July 1964, Stanford University, Calif.

15 Gaugler, R. E., and Russell, L. M., Streakline Flow Visualization Study of a Horseshoe Vortex in a Large-Scale, Two-Dimensional Turbine Stator Cascade," ASME Paper No. 80-GT-4, Mar. 1980.

16 Russell, L. M., "Flow Visualization of Discrete Hole Film Cooling with Spanwise Injection over a Cylinder," NASA TP-1491, July 1979.

17 Graziani, R. A., Blair, M. F., Taylor, J. R., and Mayle, R. E., "An Experimental Study of Endwall and Airfoil Surface Heat Transfer in a Large Scale Turbine Blade Cascade," ASME *Journal of Engineering for Power*, Vol. 102, No. 2, 1980, pp. 257–267.

Journal of Heat Transfer

Technical Notes

This section contains shorter technical papers. These shorter papers will be subjected to the same review process as that for full papers.

Pool Boiling of Dilute Surfactant Solutions

Yu Min Yang[1] and Jer Ru Maa[1]

Introduction

The goals of research workers in the field of boiling heat transfer are to transmit the largest heat flux by applying the smallest temperature difference between the heating surface and the boiling liquid and to bring the critical heat flux to the highest possible value. Various means have been developed with this aim in mind, including the use of additives to modify the fluid flow properties [1-5].

A small amount of surfactant makes the vapor-liquid interfacial properties very different from that of pure water. This difference may influence significantly the inception, growth, coalescence, and detachment characteristics of the vapor bubbles in the boiling process. This work is an experimental study of pool boiling of a dilute aqueous solution of surfactants with the expectation of some improvement in heat transfer coefficient and critical heat flux values.

The Additives

The surfactants used in this study are sodium lauryl benzene sulfonante (SLBS) and sodium lauryl sulfate (SLS). Because all experiments were carried out under very low concentrations, these additives had no noticeable influence over the physical properties of the boiling water, except surface tension, which was significantly reduced.

The Apparatus

Two sets of apparatuses were used. Figure 1 shows the one designed for the study of pool boiling from a horizontal heating surface facing upward. Boiling occurs at the center portion of the top surface of a copper block, which is heated by three cartridge heaters inserted into holes at its lower ends. Heat loss in the radial direction is reduced to a minimum by proper insulation. The junctions of three Cole Parmer IT 18, 0.009-in. dia, Teflon coated copper/constantan thermocouples are placed on the center line of the copper block by inserting through holes drilled in the radial direction. The temperature of the center portion of the heating surface is determined by extrapolating of these thermocouple readings. The copper block is enlarged at the boiling surface. Distortion of the isotherms occurs in the outer regions of the enlarged area and leads to nonuniformity of the boiling surface temperature. However, in this work, we are interested only in the boiling surface temperature at the center point of the heating surface. The linearity of the thermocouple reading close to the top heating surface indicates that the extrapolated value of this temperature is satisfactory. Boiling on the polished top surface of the copper block can be illuminated, observed, and photographed through view windows on the sides of this apparatus. A reflux condenser, 7, is used to minimize the loss of pool liquid and a supplementary heater, 6, is provided for bringing up and maintaining the pool temperature at the desired level.

A second apparatus, as shown in Fig. 2, is designed for the studies of the critical heat flux. The construction of this apparatus is similar to the one described above except that the heating element is made of a nickel wire (0.116-mm, dia, 12-cm length). The electric current is supplied to this heating element through two nickel plated copper bars. The heat flux released from the wire heater to the surrounding liquid is controlled by the applied current and voltage. Because apparatus was used only for the determination of the critical

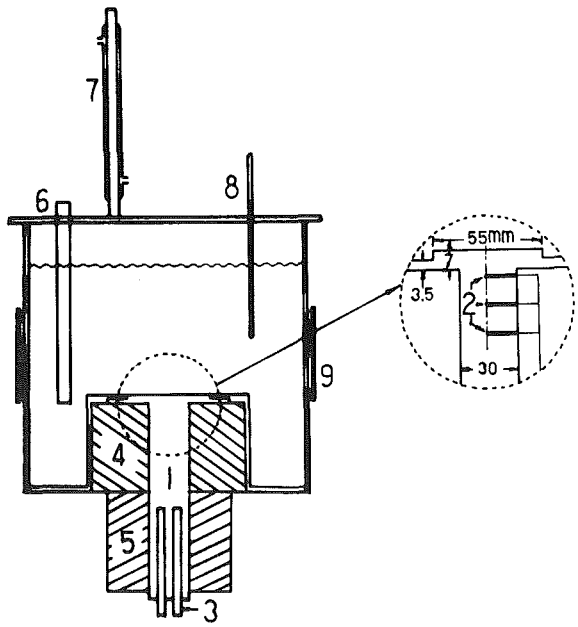

Fig. 1 Apparatus for pool boiling on a horizontal heating surface facing upward: 1, copper block; 2, thermocouple junctions; 3, cartridge heaters; 4, glass fiber insulation; 5, asbestos tube; 6, supplementary heater; 7, reflux condenser; 8, thermometer; 9, view window

[1]Chemical Engineering Department, Cheng Kung University, Tainan, Taiwan, Republic of China.

Contributed by the Heat Transfer Division for publication in the JOURNAL OF HEAT TRANSFER. Manuscript received by the Heat Transfer Division May 4, 1982.

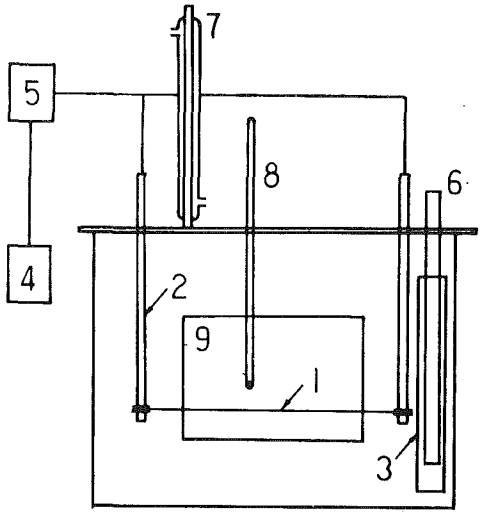

Fig. 2 Apparatus for pool boiling on a horizontal wire heater: 1, heater wire; 2, nickel-coated copper bar; 3, glass tube; 4, voltage stablizer; 5, d-c power supply; 6, supplementary heater; 7, reflux condenser; 8, mercury thermometer; 9, view window

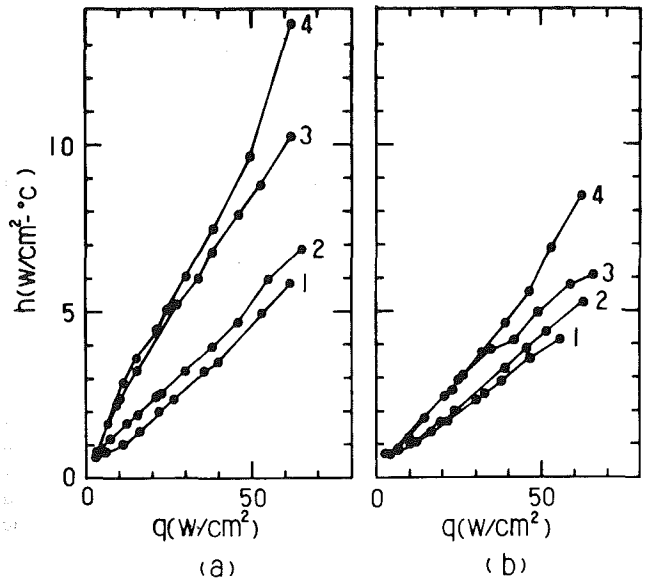

Fig. 3 Effect of surfactants on the heat transfer coefficient: (a) SLS; (b) SLBS (1, pure water; 2, 20 ppm; 3, 50 ppm; 4, 100 ppm)

heat fluxes, no attempt was made to measure the wire temperature.

Experimental Results

Boiling experiment without subcooling were carried out under atmospheric pressure. The boiling behavior of the dilute surfactant solutions is very different from that of pure water. It was observed that these additives have the effect of reducing the tendency of coalescence between vapor bubbles generated on the surface of the heating element. Thus for the same heat flux the vapor bubbles become significantly smaller in size but larger in number than the case of pure water, and boiling can be carried out at a heat flux far beyond the critical heat flux for the case of pure water.

Experimental data in Fig. 3 for the pool boiling on a horizontal heating surface facing upward show that in the nucleate boiling regime the addition of small amounts of surfactants makes the heat transfer coefficient considerably higher. If we write

$$h \propto \sigma^n,$$

the plots of h versus σ on log-log papers for various q values, as shown in Fig. 4, yield that n equals approximately -3.3 and -1.5 for the solutions of SLS and SLBS, respectively. There is some disagreement among the n values reported in the literature. They range from -2.5 to $+1.28$ [5, 6].

Hysteresis effect was observed among the pool boiling data of dilute surfactant solutions. The descending and the ascending portions of the boiling curves separate from each other significantly. This effect is not observed in the boiling of pure water on the same heating surface. Data on the descending portion of the boiling curve were adopted in the construction of the curves in Fig. 3.

The critical burn-out heat flux, q_c, was studied using the second apparatus illustrated in Fig. 2. Figure 5 shows that q_c also increased considerably by the addition of small amounts of surfactants. It is also interesting to note that SLS, which has stronger effect on the heat transfer coefficient than SLBS, has relatively weaker effect on the critical heat flux. If we write

$$q_c \propto \sigma^m$$

The plots of q_c versus σ on log-log papers, as shown in Fig. 6, yield m equal approximately to -0.60 and -1.22 for the solutions of SLS and SLBS, respectively. The m value reported in the literature by several authors is 0.25 [7].

Discussions

It is well known that surface tension of the boiling liquid

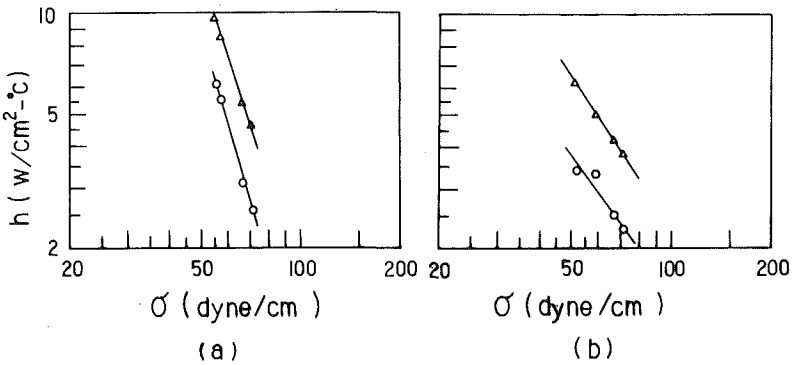

Fig. 4 The effect of surface tension of the surfactant solutions on the heat transfer coefficient: (a) SLS, (b) SLBS (△, $q = 50$ w/cm^2; ○, $q = 30$ w/cm^2

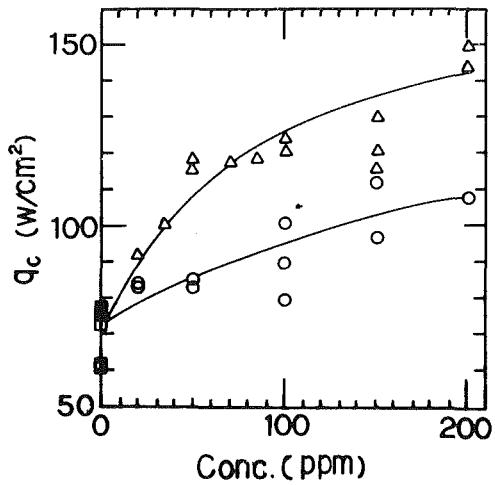

Fig. 5 Effect of surfactants on the critical heat flux: △, SLBS; ○ SLS; □, pure water

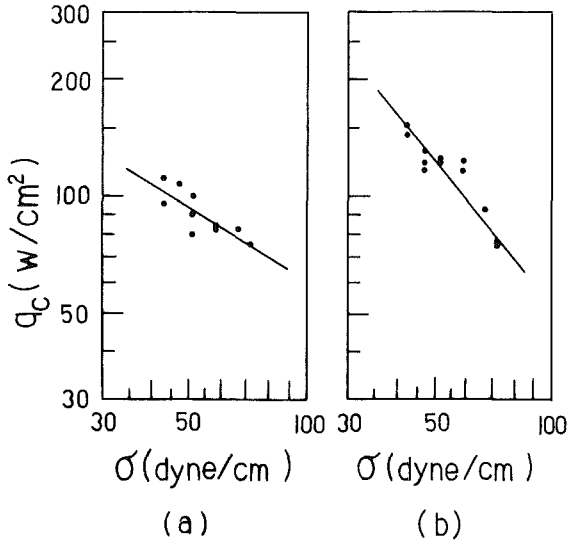

Fig. 6 The effect of surface tension of the surfactant solutions on the critical heat flux: (*a*) SLB, (*b*) SLBS

plays an important role in the inception, growth, coalescence, and detachment processes of the vapor bubbles and has significant influence over the boiling heat transfer coefficient and critical heat flux. When an additive is used to modify the vapor-liquid interfacial properties, it alters also the boiling mechanism. Depletion of the adsorbed additive molecules at the vapor-liquid interface due to the expansion of the vapor bubbles may cause the surface tension to increase or decrease locally. The vapor bubbles are thus stabilized or destablized and the bubble-bubble and bubble-heating surface interactions become quite different from that of pure liquid.

In the case of this work, the depletion of surfactant at the expanding portion of the bubble surface causes the surface tension to increase locally. Further expansion is thus retarded and the bubbles become more stable and difficult to coalesce. This phenomenon can be called the "Marangini effect" in the broader sense. It is also interesting to note that a given concentration of SLS and SLBS results in about the same reduction in surface tension but yields different critical heat fluxes and heat transfer coefficients. This can perhaps be explained because the strength of the "Marangoni effect" is not only related to the change in surface tension, but also to the difference in other physical properties of the solute, most importantly the diffusivity.

Experimental results of this work demonstrate that the heat transfer coefficient and critical heat flux of the boiling process can be improved considerably by the addition of small amount of surfactants. If this method becomes applicable under industrial conditions it may lead to a significant increase in power level of boilers and boiling water nuclear reactors without increase in their size and operating temperature. Foaming in the vapor space accompanied with the using of surfactant is an expected problem to be solved.

References

1 Lowery, A. J., Jr., and Westwater, J. W., "Heat Transfer to Boiling Methanol-Effect of Added Agents," *Industrial and Engineering Chemistry*, Vol. 49, No. 9, 1957, pp. 1445-1448.

2 Jontz, J. E., and Myers, J. E., "The Effect of Dynamic Surface Tension on Nucleate Boiling Coefficients," *AIChE Journal*, Vol. 6, No. 1, 1960, pp. 34-38.

3 Kotchaphakdee, P., and Williams, M. C., "Enhancement of Nucleate Pool Boiling with Polymeric Additives," *International Journal of Heat and Mass Transfer*, Vol. 13, 1970, pp. 835-848.

4 Gannett, H. J., Jr., and Williams, M. C., "Pool Boiling in Dilute Non-Aqueous Polymer Solutions," *International Journal of Heat and Mass Transfer*, Vol. 14, 1971, pp. 1001-1005.

5 Shibayama, S., Katsuta, M., Suzuki, K., Kurose, T., and Hatano, Y., "A Study of Boiling Heat Transfer in a Thin Liquid Film," *Heat Transfer (Japan Research)*, Vol. 9, No. 4, 1980, pp. 12-40.

6 Westwater, J. W., "Boiling of Liquids," in *Advances in Chemical Engineering*, edited by T. B. Drew, and J. W. Hoopes, Vol. 1, Academic Press Inc., New York, 1958, pp. 1-76.

7 Rohsenow, W. M., "Boiling," in *Handbook of Heat Transfer*, edited by W. M. Rohsenow, and J. P. Hartnett, McGraw-Hill, 1973, Sec. 13, pp. 1-75.

Critical Heat Flux of Narrow Vertical Annuli With Closed Bottoms[1]

Yung Chang[2] and Shi-Chune Yao[3]

Introduction

Narrow annuli may exist in various heat transfer equipment. When a heated narrow vertical annulus is closed at the bottom and filled with liquid, boiling may occur and critical heat flux may be exceeded. A practical example is the narrow annuli between the heated tubes and the tube sheet in vertical steam generators. The gaps of the annuli are usually in the order of 0.25 mm; the bottom ends of the annuli are closed by welding.

Serious corrosion has been observed on the heated tubes near the bottom tube sheet. It is believed that confinement in the narrow annuli with closed bottoms results in a low critical heat flux and operation in the transition boiling regime. At these locations corrosion may proceed at rates [1] several orders of magnitude higher than elsewhere in the steam generator. The study of the fundamental nature of critical heat flux in the vertical closed-bottom narrow annulus will be important to the understanding of the thermal-hydraulic related corrosion.

Katto and Yokoya et al. [2] investigated the boiling and dryout of saturated water between a heated horizontal flat plate and a movable optical assembly placed above the plate

[1] This work was performed when the first author was studying at Carnegie-Mellon University, Pittsburgh, Pa.

[2] Bell Laboratories, Indianapolis, Ind. 46206

[3] Associate Professor, Department of Mechanical Engineering, Carnegie-Mellon University, Pittsburgh, Pa. 15213. Mem. ASME

Contributed by the Heat Transfer Division for publication in the JOURNAL OF HEAT TRANSFER. Manuscript received by the Heat Transfer Division November 30, 1981.

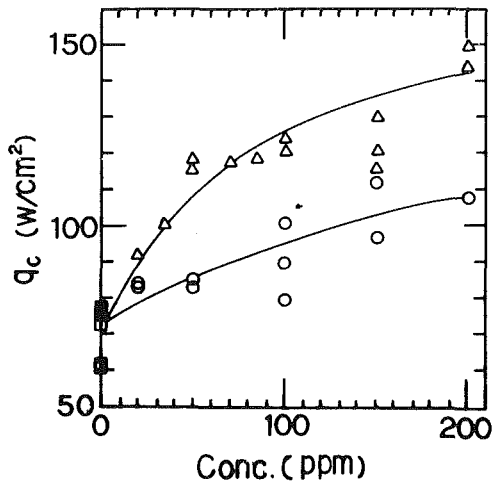

Fig. 5 Effect of surfactants on the critical heat flux: △, SLBS; ○ SLS; □, pure water

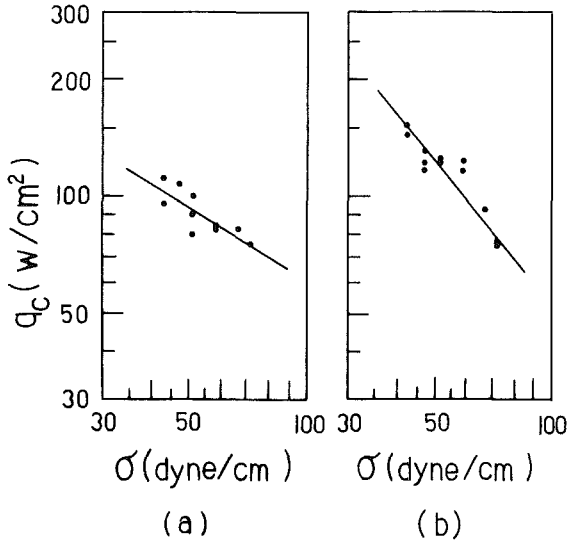

Fig. 6 The effect of surface tension of the surfactant solutions on the critical heat flux: (*a*) SLB, (*b*) SLBS

plays an important role in the inception, growth, coalescence, and detachment processes of the vapor bubbles and has significant influence over the boiling heat transfer coefficient and critical heat flux. When an additive is used to modify the vapor-liquid interfacial properties, it alters also the boiling mechanism. Depletion of the adsorbed additive molecules at the vapor-liquid interface due to the expansion of the vapor bubbles may cause the surface tension to increase or decrease locally. The vapor bubbles are thus stabilized or destablized and the bubble-bubble and bubble-heating surface interactions become quite different from that of pure liquid.

In the case of this work, the depletion of surfactant at the expanding portion of the bubble surface causes the surface tension to increase locally. Further expansion is thus retarded and the bubbles become more stable and difficult to coalesce. This phenomenon can be called the "Marangini effect" in the broader sense. It is also interesting to note that a given concentration of SLS and SLBS results in about the same reduction in surface tension but yields different critical heat fluxes and heat transfer coefficients. This can perhaps be explained because the strength of the "Marangoni effect" is not only related to the change in surface tension, but also to the difference in other physical properties of the solute, most importantly the diffusivity.

Experimental results of this work demonstrate that the heat transfer coefficient and critical heat flux of the boiling process can be improved considerably by the addition of small amount of surfactants. If this method becomes applicable under industrial conditions it may lead to a significant increase in power level of boilers and boiling water nuclear reactors without increase in their size and operating temperature. Foaming in the vapor space accompanied with the using of surfactant is an expected problem to be solved.

References

1 Lowery, A. J., Jr., and Westwater, J. W., "Heat Transfer to Boiling Methanol-Effect of Added Agents," *Industrial and Engineering Chemistry*, Vol. 49, No. 9, 1957, pp. 1445-1448.

2 Jontz, J. E., and Myers, J. E., "The Effect of Dynamic Surface Tension on Nucleate Boiling Coefficients," *AIChE Journal*, Vol. 6, No. 1, 1960, pp. 34-38.

3 Kotchaphakdee, P., and Williams, M. C., "Enhancement of Nucleate Pool Boiling with Polymeric Additives," *International Journal of Heat and Mass Transfer*, Vol. 13, 1970, pp. 835-848.

4 Gannett, H. J., Jr., and Williams, M. C., "Pool Boiling in Dilute Non-Aqueous Polymer Solutions," *International Journal of Heat and Mass Transfer*, Vol. 14, 1971, pp. 1001-1005.

5 Shibayama, S., Katsuta, M., Suzuki, K., Kurose, T., and Hatano, Y., "A Study of Boiling Heat Transfer in a Thin Liquid Film," *Heat Transfer (Japan Research)*, Vol. 9, No. 4, 1980, pp. 12-40.

6 Westwater, J. W., "Boiling of Liquids," in *Advances in Chemical Engineering*, edited by T. B. Drew, and J. W. Hoopes, Vol. 1, Academic Press Inc., New York, 1958, pp. 1-76.

7 Rohsenow, W. M., "Boiling," in *Handbook of Heat Transfer*, edited by W. M. Rohsenow, and J. P. Hartnett, McGraw-Hill, 1973, Sec. 13, pp. 1-75.

Critical Heat Flux of Narrow Vertical Annuli With Closed Bottoms[1]

Yung Chang[2] and Shi-Chune Yao[3]

Introduction

Narrow annuli may exist in various heat transfer equipment. When a heated narrow vertical annulus is closed at the bottom and filled with liquid, boiling may occur and critical heat flux may be exceeded. A practical example is the narrow annuli between the heated tubes and the tube sheet in vertical steam generators. The gaps of the annuli are usually in the order of 0.25 mm; the bottom ends of the annuli are closed by welding.

Serious corrosion has been observed on the heated tubes near the bottom tube sheet. It is believed that confinement in the narrow annuli with closed bottoms results in a low critical heat flux and operation in the transition boiling regime. At these locations corrosion may proceed at rates [1] several orders of magnitude higher than elsewhere in the steam generator. The study of the fundamental nature of critical heat flux in the vertical closed-bottom narrow annulus will be important to the understanding of the thermal-hydraulic related corrosion.

Katto and Yokoya et al. [2] investigated the boiling and dryout of saturated water between a heated horizontal flat plate and a movable optical assembly placed above the plate

[1] This work was performed when the first author was studying at Carnegie-Mellon University, Pittsburgh, Pa.

[2] Bell Laboratories, Indianapolis, Ind. 46206

[3] Associate Professor, Department of Mechanical Engineering, Carnegie-Mellon University, Pittsburgh, Pa. 15213. Mem. ASME

Contributed by the Heat Transfer Division for publication in the JOURNAL OF HEAT TRANSFER. Manuscript received by the Heat Transfer Division November 30, 1981.

and separated by a small gap. They suggested that the dryout condition in this confined space is controlled by the balance between the consumption of the liquid on the heat surface and the supply of the liquid between the intermittent jetting of vapor.

Boiling on a horizontal tube with an annular type of confinement was studied experimentally by Jensen, Cooper, and Bergles [3]. The dryout heat flux was found to be directly proportional to the clearance and inversely proportional to the length of the annulus. Compared to an open tube, the dryout heat flux was reduced by a factor of 10.

Kusuda and Imura [4, 5] performed critical heat flux experiments with subcooled and saturated liquids in vertical closed-bottom tubes and annuli. The annuli consisted of a heated outside shroud and an unheated core. The correlation established from their flooding analysis did not agree satisfactorily with their data. Similar types of experiments for tubes have also been performed by Griffith et al. [6]. The physical nature of countercurrent flooding at the critical heat flux condition has been pointed out.

The critical heat flux for tubes of different diameters has been correlated by Nejat [7, 8] using flooding considerations. In the derivation, he used the Kutateladze number and a limiting correlation for large tubes. The correlation was based upon data having Bond numbers in the range of 18 to 100. He suggested that the dryout heat flux for tubes with smaller diameters is also a function of Bond number.

In the present study the critical heat flux of narrow vertical annuli with closed bottoms is investigated for various fluids at different pressures. Different dimensions of the annuli were studied giving Bond numbers (based on gap) in the range from 0.127 to 2.44. Analysis is also performed to establish a semiempirical correlation for this problem.

Experimental

Apparatus and Procedure. The overall test assembly is shown in Fig. 1. The electrically heated tube was placed inside a hollow quartz cylinder with a small gap in between. The annulus was closed at the bottom and opened to the pool at the top. Experiments were performed in the pools of Freon-113, acetone, and distilled demineralized water.

The heated section was made of a stainless steel 304 seamless tube with 0.71-mm wall thickness, 25.4-mm o.d. and 101.6-mm heated length. The top of the heated tube was thermally shrink-fitted to a copper tube which had the same o.d. but 1.42-mm wall thickness. The bottom end of the heated tube was shrink fitted to a copper block. The stainless steel tube was heated with direct current.

The hollow quartz cylinders were milled to the dimensions of 63.5-mm o.d. with the i.d. 26.04, 27.00, and 30.56-mm to form different gap sizes with respect to the heated tube. Both the inside and the outside surfaces of the quartz were polished to 50–80 finish and were clear enough to see through. Three of the annuli tested were 76.2-mm long with the gap sizes 0.32, 0.80, and 2.58-mm, respectively. There was another short one having 25.4-mm length and 0.32-mm gap. The bottom of the annuli were sealed with a Teflon ring. Two positioners at the top and bottom of the quartz were used to maintain the concentric position of the quartz cylinder with respect to the heated tube.

The liquid pool was constructed from a Pyrex glass pipe with 101.6-mm i.d. and 457.5-mm length. The vapor generated during boiling experiments was released to a separate condenser. The liquid level was maintained at 100-mm above the top of the annulus by periodically adding the make-up liquid to the pool. The saturation temperature of the pool was maintained by an immersion heater. For pressurized tests, compressed nitrogen was connected to the system; for low pressure tests, a diffusion pump was used.

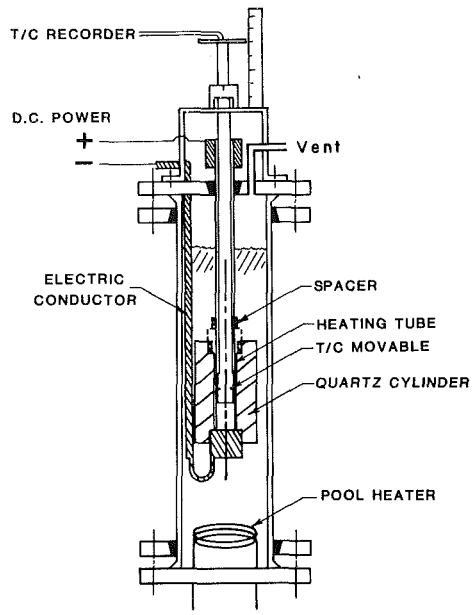

Fig. 1 The set-up of the experiment

The inner-wall temperature of the heated tube was measured by a movable sensor. Two type-K, stainless-steel-sheathed ungrounded thermocouples with 0.81-mm dia. were pressed against the inner wall by springs with a force of 0.48 Newtons. The thermocouples were calibrated and the temperature recorded with an accuracy of ± 0.28°C. The outside surface temperature was calculated from the steady-state heat conduction equation.

The same heating tube was used for all the tests. The tube surface was polished before each test with a #320 sandpaper. Nucleation sites at the bottom of annulus were formed naturally between the Teflon seal and the copper block. The steady state was achieved within 3 min after a change of heat flux and data were then recorded. The thermocouples were located 12-mm below the top opening of the narrow annulus to detect early critical heat flux. Before the experiment, the fluid in the pool was degassed by boiling for a half hour using the pool heater. Before reaching the critical heat flux, the boiling was performed on the heated tube such that the surface of the tube was also degassed. The details of the experimental set-up and procedure have been described in [9].

Critical Heat Flux Data. Critical heat flux was detected by the thermocouples as a continuous excursion. Although the CHF may start at some other location, during the 3 min of waiting time the thermocouple will sense the increase of temperature. Usually the CHF does not start at the bottom of the tube because at that moment there is always a small liquid pool at the bottom of the annulus. In general, the critical heat flux in a narrow annulus with a closed bottom is considerably lower than the critical heat flux for open-pool boiling. For example, the critical heat flux for open-pool boiling of Freon-113 at 1 atm is about 200 KW/m^2; however, the measured critical heat flux for the 0.32-mm gap annulus with 76.2-mm height is only 6.3 KW/m^2. The reduction is by a factor of about 1/32.

The critical heat flux data of the present study are listed in Table 1 for water, acetone, and Freon-113 with three gap sizes and two lengths of the annuli. The system pressure is in the range of 0.60 to 4.04 atm. Generally, the smaller the gap size the lower the critical heat flux. The wall superheat at critical heat flux is also found to decrease with reduction in gap size. The critical heat flux decreases when the length of the annulus increases.

Analysis

The significant difference between the pool boiling critical heat flux and the critical heat flux of narrow vertical annulus with closed bottom may be attributed to the different limiting mechanisms for the liquid to come into contact with the heated surface. As shown schematically in Fig. 2, when the critical heat flux is approached the outward vapor flow prohibits sufficient flow of liquid down into the narrow annulus. This local phenomenon is similar to that of hydrodynamic countercurrent flooding in tubes.

The countercurrent flooding of two phase flow in round tubes is a well-studied problem. For tubes with very small diameters (for example, when Bond number is less than 50) the correlation proposed by Wallis [10] based on the superficial velocities gives the best fit of data. The hydrodynamic flooding in annular geometry with a Bond number of about 4.40 has been studied by Shire et al. [11]. Their results for 2.54 cm o.d. and 1.58 cm i.d. annulus can also be correlated satisfactorily by the Wallis correlation but with a different empirical constant.

As shown in Table 2, the Bond number range in the present experiments is from 0.127 to 2.44. Since the Bond number is generally small, the Wallis correlation may be used to describe the local hydrodynamic countercurrent flooding. For an annulus with a closed bottom the flooding and the dryout will start near the top opening where the vapor velocity is the highest. It is also important to notice that the critical heat flux occurs when the supply of liquid is "insufficient" to remove all the heat applied to the annulus. Once this condition is reached, the liquid inventory in the annulus begins to be depleted and dryout is initiated.

Following the above concept, the critical heat flux may be found from analysis. The Wallis correlation is in the form of

$$j_g^{*1/2} + j_l^{*1/2} = C \qquad \text{for Bo} < 50 \tag{1}$$

where

$$\text{Bo} = S/(\sigma/g(\rho_l - \rho_g))^{1/2} \tag{2}$$

$$j_g^* = j_g \rho_g^{1/2}/(g D(\rho_l - \rho_g))^{1/2} \tag{3}$$

$$j_l^* = j_l \rho_l^{1/2}/(g D(\rho_l - \rho_g))^{1/2} \tag{4}$$

and

$$j_g = \dot{M}_g/\rho_g A \tag{5}$$

$$j_l = \dot{M}_l/\rho_l A \tag{6}$$

where A is the cross-sectional area of the annulus, Bo is the Bond number for the gap, D is a characteristic dimension, C is a constant depending upon geometry of the opening where liquid enters the channel, g is the acceleration of the gravity, j is the superficial velocity over the flow cross-section, j^* is the nondimensional superficial velocity, $\dot{M}$ is the total mass flow rate, S is the gap size of the annulus, ρ is the density of fluid, and σ is the surface tension of liquid to vapor.

Since the annulus has a closed bottom, the steady-state mass flow rate of liquid coming into the annulus at the top opening should equal to the mass flow rate of vapor going out of the top opening. Furthermore, if all the heat supplied to the annulus goes into vaporization, the mass flow rates can be related to the wall heat flux, q_w, by

$$\dot{M}_g = \dot{M}_l = q_w A_w / h_{fg} \tag{7}$$

where A_w is the area of the heated surface in the annulus, and h_{fg} is the latent heat of evaporation. Substituting the equations (3-7) into equation (1), and assuming that the gap size is much smaller than the diameter of the heated tube, the critical heat flux corresponding to the onset of countercurrent flooding becomes

$$B_l\left[\left(\frac{\rho_g}{\rho_l}\right)\left(1+\left(\frac{\rho_l}{\rho_g}\right)\right)^2\right] = C^2 \tag{8}$$

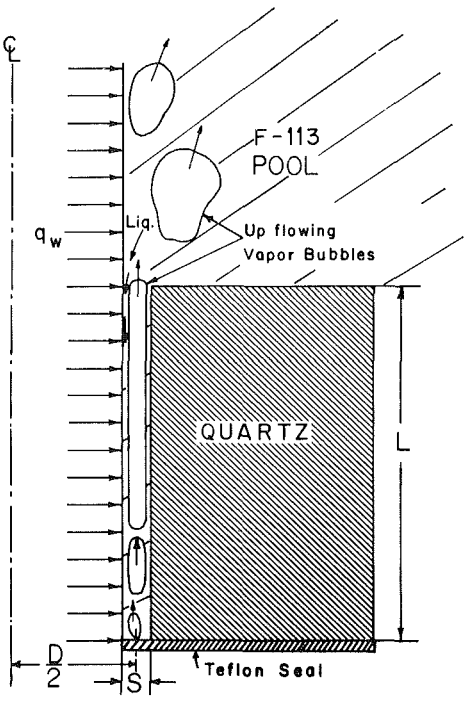

Fig. 2 The fluid behavior near critical heat flux

Table 1 Summary of critical heat flux data

	S(mm)	L(mm)	P(atm)	q(kw/m^2)	$T_w - T_s$(°C)
Water	2.58	76.2	1	210.1	16.11
	0.80	76.2	1	82.0	9.72
	0.32	76.2	1	25.2	3.06
Acetone	2.58	76.2	1	109.5	18.33
	0.80	76.2	1	37.2	7.78
	0.32	25.4	1	35.0	7.78
	0.32	76.2	1	10.8	3.05
F-113	2.58	76.2	1	69.4	18.06
	0.80	76.2	1	21.1	15.83
	0.32	25.4	1	17.4	4.72
	0.32	76.2	1	6.29	0.83
	0.32	76.2	0.60	5.54	1.11
	0.32	76.2	2.02	7.55	0.83
	0.32	76.2	3.04	8.53	1.39
	0.32	76.2	4.04	8.78	1.67

Table 2 Summary of bond numbers in present study (1 atm)

Gap (mm)	F-113	Acetone	Water
0.32	0.300	0.197	0.127
0.80	0.757	0.495	0.319
2.58	2.44	1.60	1.03

where the boiling number, B_l, is defined by

$$B_l \equiv \frac{q_w L}{h_{fg}\rho_g S V} \tag{9}$$

where L is the length of the annulus, and the characteristic vapor slug velocity, V, is

$$V \equiv \left[\frac{g D(\rho_l - \rho_g)}{\rho_l}\right]^{1/2} \tag{10}$$

The boiling number, B_l, is defined as the ratio of outgoing vapor velocity ($q_w L/h_{fg}\rho_g S$) to the inertia dominant bubble rising velocity, V, for slug flow in the annulus [10]. The characteristic dimension, D, was chosen as the average diameter of the annulus, i.e., the inner diameter plus the dimension of one gap size.

As stated before, the critical heat flux occurs when liquid supply is insufficient" to cool the heated annulus. The

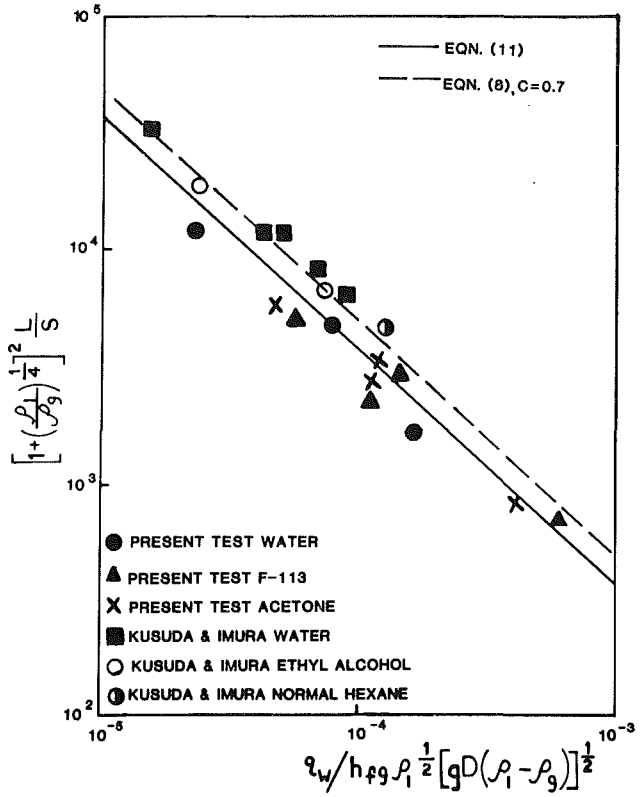

Fig. 3 The comparison of the correlation and the data

constant, C, in equation (8) has to be determined from experimental data.

Discussion

The critical heat flux data listed in Table 1 for Freon-113, acetone, and distilled demineralized water with different dimensions of annuli and system pressures can be correlated by the equation (8). In Table 1, $(Tw - Ts)$ is the wall superheat. From the best fit of the data the value of C is determined. In addition, the experimental data of Kusuda and Imura [5] for water, ethyl alcohol, and normal hexane are also correlated using the same constant. The resulting correlation is

$$B_1\left[\left(\frac{\rho_g}{\rho_1}\right)\left(1+\left(\frac{\rho_1}{\rho_g}\right)\right)^2\right]=0.38 \qquad (11)$$

As shown in Fig. 3, the comparison of the correlation and the data is satisfactory. In the same figure, equation (8), with the C value taken from Wallis's flooding correlation for a sharp edge annulus ($C=0.7$) [12], is also shown for comparison. This value is close to the present data, but is not the best, even though it gives a slightly better fit to the data of Kusuda and Imura [5]. A similar but different formulation has been derived by Nejat [8] for vertical tubes with a closed lower end. The constant value is also different. This is because the geometry concerned in [8] is different from the present study.

It is interesting to point out that the data of [5] are based upon the experiments with the annulus heated from the outer surface. The present experiment is performed with the inner wall of the annulus heated.

Since the present correlation is limited to small Bond numbers, the Wallis correlation for countercurrent flooding was used. The Wallis correlation is independent of liquid surface tension. Therefore, the present correlation is also independent of surface tension or the Bond number. Although the water has about three times higher surface tension than that of Freon-113 or acetone, all the data has been correlated satisfactorily by equation (11).

Conclusion

The critical heat flux in a narrow vertical annulus with a closed bottom is generally much lower than that in the open pool boiling due to the different controlling mechanisms. The critical heat flux for the present problem is initiated by countercurrent flooding at the top of the annulus where the vapor velocity is the highest rather than the local hydrodynamics at the heated surface, as in pool boiling. The correlation of critical heat flux, derived from the Wallis countercurrent flooding conditions, fits the experimental data satisfactorily for the gap Bond number in the range of 0.127 to 3.17. The correlation is independent of the liquid surface tension.

Acknowledgment

The authors are grateful for the support of the Office of Naval Research under Agreement No. N00014-79-C-0623 in performing this study.

References

1 Mann, G. M. W., "Distribution of Sodium Chloride and Sodium Hydroxide Between Steam and Water at Dryout in an Experimental Once-Through Boiling," *Chem. Eng. Science*, Vol. 30, 1975, pp. 249-260.

2 Katto, Y., Yokoya, S., and Teraoka, K., "Nucleate and Transition Boiling in a Narrow Space Between Two Horizontal, Parallel Disk Surfaces," *Bulletin of JSME*, Vol. 20, (143), 1977.

3 Jensen, M. K., Cooper, P. E., and Bergles, A. E., "Boiling Heat Transfer and Dryout in Restricted Annular Geometries," *AIChE Symposium*, Vol. 16th National Heat Transfer Conference, Paper No. 14, 1976, pp. 205-214.

4 Kusuda, H., and Imura, H., "Boiling Heat Transfer in an Open Thermosyphon," *Bulletin of JSME*, Vol. 16 (101), 1973, pp. 1723-1740.

5 Kusuda, H., and Imura, H., "Stability of a Liquid Film in a Countercurrent Annular Two Phase Flow," *Bulletin of JSME*, Vol. 17 (114), 1974, pp. 1613-1618.

6 Griffith, P., Schumann, N. A., and Neustal, A. D., "Flooding and Burn-Out in Closed-end Vertical Tubes," *Symposium on Two Phase Flow*, Institute of Mechanical Engineering, London, Paper No. 5, 1962.

7 Nejat, Z., "Maximum Heat Flux for Countercurrent Two Phase Flow in A Closed End Vertical Tube," *Proceedings of the 6th Int. Heat Transfer Conference*, Vol. 1, 1978, pp. 441-444.

8 Nejat, Z., "Effect of Density Ratio on Critical Heat Flux in Closed End Vertical Tubes," *Int. J. Multiphase Flow*, Vol. 7, 1981, pp. 321-327.

9 Chang, Y., "The Effect of Confinement and Transient to Pool Boiling on Vertical Tubes," Ph.D. thesis, Carnegie-Mellon University, 1981, pp. 10-16.

10 Wallis, G. B., *One Dimensional Two-Phase Flow*, McGraw-Hill, 1969, pp. 285-286.

11 Shire, G. L., Pickering, A. R., and Blacker, P. T., "Film Cooling of Vertical Fuel Rods," Technical Report AEEW-R343, UKAEA, 1964.

12 Wallis, G. B., *One Dimensional Two-Phase Flow*, McGraw-Hill, 1969, p. 339.

Numerical Solution to Axisymmetric Thawing and Heating of Frozen Logs

H. P. Steinhagen[1] and G. E. Myers[2]

Nomenclature

A = area through which heat flows (m^2)
c = specific heat (J/kgK)
C^* = conductance per unit capacitance (1/s)

[1] Department of Forest Products, University of Idaho, Moscow, Idaho 83843
[2] Department of Mechanical Engineering, University of Wisconsin-Madison, Madison, Wis. 53706, Mem. ASME

Contributed by the Heat Transfer Division for publication in the JOURNAL OF HEAT TRANSFER. Manuscript received by the Heat Transfer Division February 13, 1981.

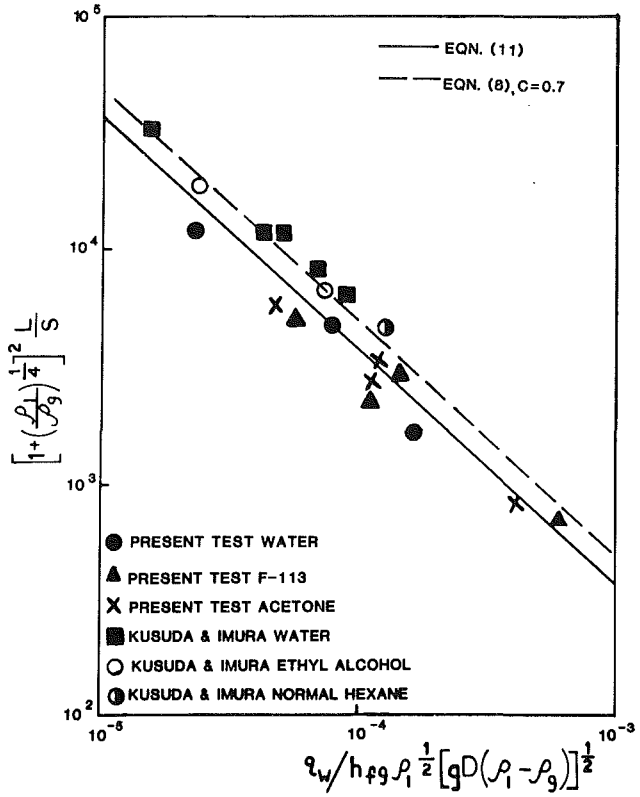

Fig. 3 The comparison of the correlation and the data

constant, C, in equation (8) has to be determined from experimental data.

Discussion

The critical heat flux data listed in Table 1 for Freon-113, acetone, and distilled demineralized water with different dimensions of annuli and system pressures can be correlated by the equation (8). In Table 1, $(Tw - Ts)$ is the wall superheat. From the best fit of the data the value of C is determined. In addition, the experimental data of Kusuda and Imura [5] for water, ethyl alcohol, and normal hexane are also correlated using the same constant. The resulting correlation is

$$B_1\left[\left(\frac{\rho_g}{\rho_1}\right)\left(1+\left(\frac{\rho_1}{\rho_g}\right)\right)^2\right]=0.38 \qquad (11)$$

As shown in Fig. 3, the comparison of the correlation and the data is satisfactory. In the same figure, equation (8), with the C value taken from Wallis's flooding correlation for a sharp edge annulus ($C=0.7$) [12], is also shown for comparison. This value is close to the present data, but is not the best, even though it gives a slightly better fit to the data of Kusuda and Imura [5]. A similar but different formulation has been derived by Nejat [8] for vertical tubes with a closed lower end. The constant value is also different. This is because the geometry concerned in [8] is different from the present study.

It is interesting to point out that the data of [5] are based upon the experiments with the annulus heated from the outer surface. The present experiment is performed with the inner wall of the annulus heated.

Since the present correlation is limited to small Bond numbers, the Wallis correlation for countercurrent flooding was used. The Wallis correlation is independent of liquid surface tension. Therefore, the present correlation is also independent of surface tension or the Bond number. Although the water has about three times higher surface tension than that of Freon-113 or acetone, all the data has been correlated satisfactorily by equation (11).

Conclusion

The critical heat flux in a narrow vertical annulus with a closed bottom is generally much lower than that in the open pool boiling due to the different controlling mechanisms. The critical heat flux for the present problem is initiated by countercurrent flooding at the top of the annulus where the vapor velocity is the highest rather than the local hydrodynamics at the heated surface, as in pool boiling. The correlation of critical heat flux, derived from the Wallis countercurrent flooding conditions, fits the experimental data satisfactorily for the gap Bond number in the range of 0.127 to 3.17. The correlation is independent of the liquid surface tension.

Acknowledgment

The authors are grateful for the support of the Office of Naval Research under Agreement No. N00014-79-C-0623 in performing this study.

References

1 Mann, G. M. W., "Distribution of Sodium Chloride and Sodium Hydroxide Between Steam and Water at Dryout in an Experimental Once-Through Boiling," *Chem. Eng. Science*, Vol. 30, 1975, pp. 249–260.

2 Katto, Y., Yokoya, S., and Teraoka, K., "Nucleate and Transition Boiling in a Narrow Space Between Two Horizontal, Parallel Disk Surfaces," *Bulletin of JSME*, Vol. 20, (143), 1977.

3 Jensen, M. K., Cooper, P. E., and Bergles, A. E., "Boiling Heat Transfer and Dryout in Restricted Annular Geometries," *AIChE Symposium*, Vol. 16th National Heat Transfer Conference, Paper No. 14, 1976, pp. 205–214.

4 Kusuda, H., and Imura, H., "Boiling Heat Transfer in an Open Thermosyphon," *Bulletin of JSME*, Vol. 16 (101), 1973, pp. 1723–1740.

5 Kusuda, H., and Imura, H., "Stability of a Liquid Film in a Countercurrent Annular Two Phase Flow," *Bulletin of JSME*, Vol. 17 (114), 1974, pp. 1613–1618.

6 Griffith, P., Schumann, N. A., and Neustal, A. D., "Flooding and Burn-Out in Closed-end Vertical Tubes," *Symposium on Two Phase Flow*, Institute of Mechanical Engineering, London, Paper No. 5, 1962.

7 Nejat, Z., "Maximum Heat Flux for Countercurrent Two Phase Flow in A Closed End Vertical Tube," *Proceedings of the 6th Int. Heat Transfer Conference*, Vol. 1, 1978, pp. 441–444.

8 Nejat, Z., "Effect of Density Ratio on Critical Heat Flux in Closed End Vertical Tubes," *Int. J. Multiphase Flow*, Vol. 7, 1981, pp. 321–327.

9 Chang, Y., "The Effect of Confinement and Transient to Pool Boiling on Vertical Tubes," Ph.D. thesis, Carnegie-Mellon University, 1981, pp. 10–16.

10 Wallis, G. B., *One Dimensional Two-Phase Flow*, McGraw-Hill, 1969, pp. 285–286.

11 Shire, G. L., Pickering, A. R., and Blacker, P. T., "Film Cooling of Vertical Fuel Rods," Technical Report AEEW-R343, UKAEA, 1964.

12 Wallis, G. B., *One Dimensional Two-Phase Flow*, McGraw-Hill, 1969, p. 339.

Numerical Solution to Axisymmetric Thawing and Heating of Frozen Logs

H. P. Steinhagen[1] and G. E. Myers[2]

Nomenclature

A = area through which heat flows (m^2)
c = specific heat (J/kgK)
C^* = conductance per unit capacitance (1/s)

[1] Department of Forest Products, University of Idaho, Moscow, Idaho 83843
[2] Department of Mechanical Engineering, University of Wisconsin-Madison, Madison, Wis. 53706, Mem. ASME

Contributed by the Heat Transfer Division for publication in the JOURNAL OF HEAT TRANSFER. Manuscript received by the Heat Transfer Division February 13, 1981.

d = distance between adjacent nodes (m)
H = latent heat of fusion (J/kg)
k = thermal conductivity (W/mK)
M = moisture content (percent of dry mass)
n = number of nodes immediately surrounding focal node i (−)
r = radial coordinate (m)
T = temperature (K)
t = time (s)
V = volume (m^3)
ΔT = temperature interval (K)
ρ = density (kg/m^3)

Subscripts

e = surface
i, j = position nodes, i being the focal node and j any adjacent node
0 = initial
s = phase change
w = water
∞ = ambient

Introduction

This study examines the suitability of the computerized finite-difference scheme HEAT [1] to calculate transient temperatures during axisymmetric thawing and heating of frozen wood logs. Logs to be cut into veneers must be thawed during the winter months and heat-conditioned for improved cutting performance. Estimates of log heating times required to reach target temperatures are important. The calculations have been compared with data from earlier experiments [2] in which logs were thawed in agitated water; one of these comparisons is discussed in some detail in the present article. A more explicit description of the thawing problem is given in [3] from which this paper was abstracted.

Approach

Applying the nonlinear heat conduction formulation to axisymmetric thawing, we have the following

$$\frac{1}{r}\left\{\frac{\partial}{\partial r}\left[k(r,T)r\frac{\partial T}{\partial r}\right]\right\}=\rho(r,T)c(r,T)\frac{\partial T}{\partial t};$$

$$0<r<r_e; \quad t>0 \tag{1a}$$

$$\frac{\partial T}{\partial r}=0; \quad r=0; \quad t>0 \tag{1b}$$

$$T_e=T_\infty; \quad r=r_e; \quad t>0 \tag{1c}$$

$$T=T_0; \quad 0<r<r_e; \quad t=0 \tag{1d}$$

The concept of two phases simultaneously existing during thawing is handled through only one equation by assuming position- and temperature-dependent thermal properties that discontinuously change with the phase. Latent heat effects are thought to be incorporated in the specific heat over a finite thawing-temperature interval [4].

HEAT [1] provides an approximate solution by way of solving simultaneous equations of the form

$$\frac{dT_i}{dt}=\sum_{j=1}^{n} C_{ji}^{*}(T_j-T_i) \tag{2a}$$

where

$$C_{ji}^{*}=\left(\frac{k_{ji}A_{ji}}{d_{ji}}\right)\left(\frac{1}{\rho_i V_i c_i}\right) \tag{2b}$$

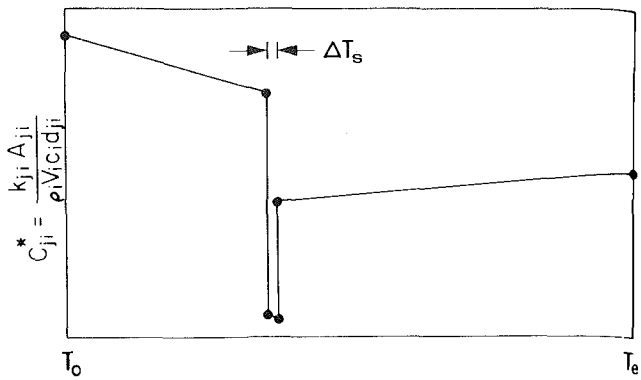

Fig. 1 Typical profile of C_{ji}^{*} over temperature

The quantity C_{ji}^{*}, in addition to the constants T_e and T_0, is computer input data and must be evaluated for some temperature points, as shown in Fig. 1, by the dots.[3] The fictitious thawing interval, ΔT_s, (Fig. 1) is a computational parameter, adjusted to obtain agreement with experimental results. Within the thawing interval the effective specific heat is

$$c_i=c_{i,s}+\frac{H_i}{\Delta T_s} \tag{3a}$$

where the latent heat of frozen wood is

$$H_i=H_w\left(\frac{M_i-30\text{ percent}}{M_i+100\text{ percent}}\right) \tag{3b}$$

This concept considers only the free water (M > 30 percent) as frozen, the bound water phase change being negligible [5].

Computations were carried out for the logs identified in experimental paper [2] as numbers 1, 4, 7, 10. In accordance with the known log specifications, thermal conductive properties were determined using [6]. The thermal property values of log No. 1 are given in Table 1. These values were used to prepare the computer input data of C_{ji}^{*}.

Results and Discussion

Temperature profiles of log No. 1 during thawing and heating are given in Fig. 2. The solid lines refer to data established in the earlier experiments [2]. Symbols represent the comparable computational results. For a given position and temperature, the discrepancy between measured and computed time was usually within the 10 percent target. This was also observed for the other three logs studied in the project. The computational error seemed to increase when the latent heat effect entered the calculations. This appears to be due to the discontinuity and the use of a fictitious thawing interval by which HEAT accommodates the latent heat effect. From a practical point of view, however, it appears that HEAT has provided acceptable solutions to the problem of axisymmetric thawing and heating of frozen wood logs with position- and temperature-dependent thermal properties.

Calculations with constant, though distinct, thermal properties in each phase were considerably less cumbersome to prepare than with variable properties. The resulting error was usually again within target.

Solutions have been generalized into charts [7], covering a large range of values that the nondimensionalized parameters can assume. This was done to assist heating vat operators at veneer mills in estimating log thawing times without their having to resort to finite-difference techniques.

[3] We define C_{ji}^{*} as the conductance per unit capacitance. In this way, we circumvent the shortcoming of HEAT which allows only the conductance but not the capacitance to be temperature-dependent.

Table 1 Thermal properties of log No. 1

Node	r (m)	ρ (kg/m^3)	$c \times 10^{-3}$ (J/kgK)						k (W/mK)			
			−23°C	−.5(−)°C	−.5(+)°C[a]	.5(−)°C[a]	.5(+)°C	27°C	−23°C	−.5°C	.5°C	27°C
1[b]	.1524	840	2.0	2.3	120	120	3.0	3.1				
2	.1397	840	2.0	2.3	130	130	3.0	3.2	.41	.40	.31	.34
3	.1270	860	2.0	2.3	130	130	3.0	3.2	.43	.41	.32	.35
4	.1143	860	2.0	2.3	140	140	3.1	3.2	.44	.43	.33	.36
5	.1016	860	2.0	2.3	140	140	3.1	3.2	.45	.44	.33	.37
6	.0889	850	2.1	2.3	150	150	3.2	3.3	.46	.45	.33	.37
7	.0762	860	2.1	2.3	160	160	3.2	3.4	.47	.46	.34	.38
8	.0635	850	2.1	2.3	160	160	3.2	3.4	.47	.45	.33	.37
9	.0508	800	2.1	2.3	160	160	3.2	3.4	.46	.45	.32	.35
10	.0381	750	2.1	2.3	160	160	3.2	3.4	.44	.43	.31	.34
11	.0254	810	2.1	2.4	180	180	3.4	3.5	.46	.45	.32	.36
12	.0127	840	2.1	2.4	200	200	3.5	3.7	.50	.49	.34	.38
13	.0000	880	2.2	2.4	210	210	3.6	3.8	.56	.55	.37	.41

[a]includes latent heat
[b]surface node with specified temperature $T_e = 27°C$

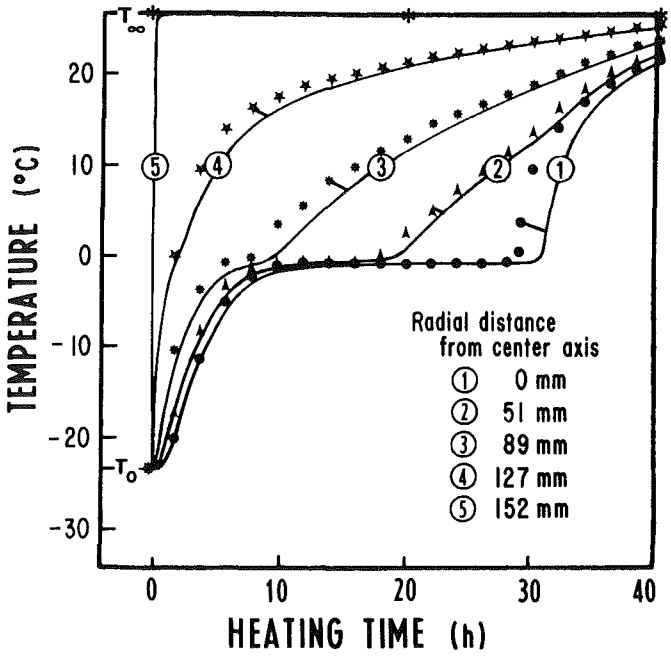

Fig. 2 Transient temperature distribution in log No. 1

Acknowledgments

The study was supported by the School of Natural Resources, College of Agriculture and Life Sciences, University of Wisconsin-Madison, and by funds provided under McIntire-Stennis Public Law No. 87-788. Special thanks go to John F. Lutz, U.S. Forest Products Laboratory, Madison, Wisconsin, and Professor Hans Kubler, University of Wisconsin-Madison Department of Forestry, for instigating and supporting this research.

References

1 Beckman, W. A., "HEAT (Heat Transfer Computer Program in FORTRAN V Language)," EES Report No. 37, Engineering Experiment Station, University of Wisconsin, Madison, 1972.

2 Steinhagen, H. P., "Heating Times for Frozen Veneer Logs—New Experimental Data," *Forest Products Journal*, Vol. 27, No. 6, 1977, pp. 24–28.

3 Steinhagen, H. P., "Heating Times for Frozen and Nonfrozen Veneer Logs," Ph.D. thesis, University of Wisconsin, Madison, 1978, University Microfilms, Ann Arbor, MJN78-04884.

4 Bonacina, C., Comini, G., Fasano, A., and Primicerio, M., "Numerical Solution of Phase-Change Problems," *International Journal of Heat and Mass Transfer*, Vol. 16, 1973, pp. 1825–1832.

5 Kubler, H., "Shrinkage and Swelling of Wood by Coldness," (in German) Holz als Roh- und Werkstoff, Vol. 20, No. 9, 1962, pp. 364–368.

6 Steinhagen, H. P., "Thermal Conductive Properties of Wood, Green or Dry, from −40° to +100°C—A Literature Review," USDA Forest Service General Technical Report FPL-9, Forest Products Laboratory, Madison, 1977.

7 Steinhagen, H. P., Myers, G. E., and Kubler, H., "Heating Time Charts for Frozen and Nonfrozen Veneer Logs," *Forest Products Journal*, Vol. 30, No. 4, 1980, pp. 27–37.

A Numerical Study of the Thawing Process of a Frozen Coal Particle

J. F. Raymond[1] and B. Rubinsky[1]

Introduction

The following work is relevant to problems inherent to the transport of coal by rail during the winter months. Mined coal contains significant quantities of water due to its porosity. Consequently, it freezes as it is transported by boxcar to the processing plant [1]. The frozen coal particles adhere to themselves and to the boxcar, requiring the use of various heating devices to thaw the coal prior to unloading or the use of mechanical techniques to free the coal from the boxcars [1]. Production costs have been significantly increased due to the time lost to heating the boxcars and thawing the coal. An analysis of the thawing process could provide meaningful insight into minimizing the economic disadvantages incurred as coal is transported under harsh winter conditions.

A recent study [2] has recognized that the thawing process in a conglomerate of frozen coal particles is influenced by the natural and forced convection heat transfer mechanisms. This paper concentrates on the thawing process of a single coal particle in the presence of natural convection. As a simplification, the coal particle is modeled as a radially symmetric sphere. A numerical analysis, using the finite element method, provides the radial movement of the phase front with time and the radial temperature distribution. Interesting results have been obtained regarding the thawing time, as parameters such as ambient air temperature and humidity ration have been varied. The numerical model accounts for water condensation or evaporation from the coal particle surface.

[1]Department of Mechanical Engineering, University of California, Berkeley, Calif. 94720

Contributed by the Heat Transfer Division for publication in the JOURNAL OF HEAT TRANSFER. Manuscript received by the Heat Transfer Division, February 19, 1982.

Table 1 Thermal properties of log No. 1

Node	r (m)	ρ (kg/m^3)	$c \times 10^{-3}$ (J/kgK)						k (W/mK)			
			−23°C	−.5(−)°C	−.5(+)°C[a]	.5(−)°C[a]	.5(+)°C	27°C	−23°C	−.5°C	.5°C	27°C
1[b]	.1524	840	2.0	2.3	120	120	3.0	3.1				
2	.1397	840	2.0	2.3	130	130	3.0	3.2	.41	.40	.31	.34
3	.1270	860	2.0	2.3	130	130	3.0	3.2	.43	.41	.32	.35
4	.1143	860	2.0	2.3	140	140	3.1	3.2	.44	.43	.33	.36
5	.1016	860	2.0	2.3	140	140	3.1	3.2	.45	.44	.33	.37
6	.0889	850	2.1	2.3	150	150	3.2	3.3	.46	.45	.33	.37
7	.0762	860	2.1	2.3	160	160	3.2	3.4	.47	.46	.34	.38
8	.0635	850	2.1	2.3	160	160	3.2	3.4	.47	.45	.33	.37
9	.0508	800	2.1	2.3	160	160	3.2	3.4	.46	.45	.32	.35
10	.0381	750	2.1	2.3	160	160	3.2	3.4	.44	.43	.31	.34
11	.0254	810	2.1	2.4	180	180	3.4	3.5	.46	.45	.32	.36
12	.0127	840	2.1	2.4	200	200	3.5	3.7	.50	.49	.34	.38
13	.0000	880	2.2	2.4	210	210	3.6	3.8	.56	.55	.37	.41

[a]includes latent heat
[b]surface node with specified temperature $T_e = 27°C$

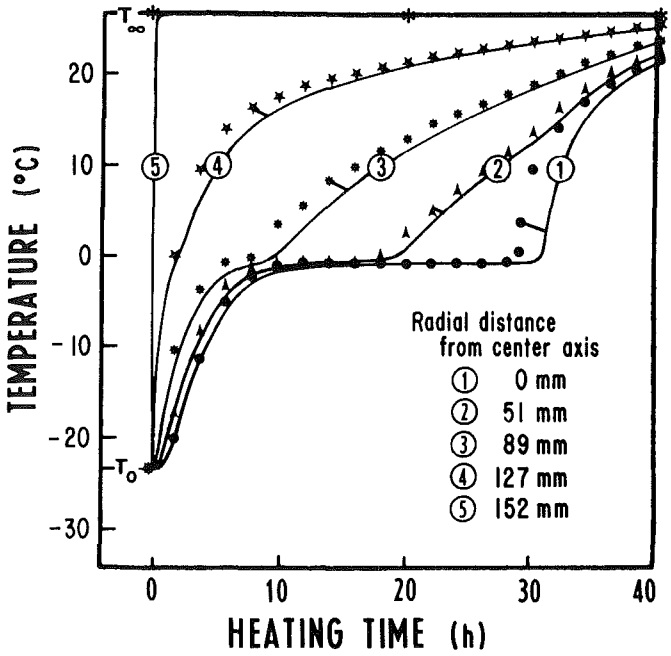

Fig. 2 Transient temperature distribution in log No. 1

Acknowledgments

The study was supported by the School of Natural Resources, College of Agriculture and Life Sciences, University of Wisconsin-Madison, and by funds provided under McIntire-Stennis Public Law No. 87-788. Special thanks go to John F. Lutz, U.S. Forest Products Laboratory, Madison, Wisconsin, and Professor Hans Kubler, University of Wisconsin-Madison Department of Forestry, for instigating and supporting this research.

References

1 Beckman, W. A., "HEAT (Heat Transfer Computer Program in FORTRAN V Language)," EES Report No. 37, Engineering Experiment Station, University of Wisconsin, Madison, 1972.

2 Steinhagen, H. P., "Heating Times for Frozen Veneer Logs—New Experimental Data," *Forest Products Journal*, Vol. 27, No. 6, 1977, pp. 24–28.

3 Steinhagen, H. P., "Heating Times for Frozen and Nonfrozen Veneer Logs," Ph.D. thesis, University of Wisconsin, Madison, 1978, University Microfilms, Ann Arbor, MJN78-04884.

4 Bonacina, C., Comini, G., Fasano, A., and Primicerio, M., "Numerical Solution of Phase-Change Problems," *International Journal of Heat and Mass Transfer*, Vol. 16, 1973, pp. 1825–1832.

5 Kubler, H., "Shrinkage and Swelling of Wood by Coldness," (in German) Holz als Roh- und Werkstoff, Vol. 20, No. 9, 1962, pp. 364–368.

6 Steinhagen, H. P., "Thermal Conductive Properties of Wood, Green or Dry, from −40° to +100°C—A Literature Review," USDA Forest Service General Technical Report FPL-9, Forest Products Laboratory, Madison, 1977.

7 Steinhagen, H. P., Myers, G. E., and Kubler, H., "Heating Time Charts for Frozen and Nonfrozen Veneer Logs," *Forest Products Journal*, Vol. 30, No. 4, 1980, pp. 27–37.

A Numerical Study of the Thawing Process of a Frozen Coal Particle

J. F. Raymond[1] and B. Rubinsky[1]

Introduction

The following work is relevant to problems inherent to the transport of coal by rail during the winter months. Mined coal contains significant quantities of water due to its porosity. Consequently, it freezes as it is transported by boxcar to the processing plant [1]. The frozen coal particles adhere to themselves and to the boxcar, requiring the use of various heating devices to thaw the coal prior to unloading or the use of mechanical techniques to free the coal from the boxcars [1]. Production costs have been significantly increased due to the time lost to heating the boxcars and thawing the coal. An analysis of the thawing process could provide meaningful insight into minimizing the economic disadvantages incurred as coal is transported under harsh winter conditions.

A recent study [2] has recognized that the thawing process in a conglomerate of frozen coal particles is influenced by the natural and forced convection heat transfer mechanisms. This paper concentrates on the thawing process of a single coal particle in the presence of natural convection. As a simplification, the coal particle is modeled as a radially symmetric sphere. A numerical analysis, using the finite element method, provides the radial movement of the phase front with time and the radial temperature distribution. Interesting results have been obtained regarding the thawing time, as parameters such as ambient air temperature and humidity ration have been varied. The numerical model accounts for water condensation or evaporation from the coal particle surface.

[1]Department of Mechanical Engineering, University of California, Berkeley, Calif. 94720

Contributed by the Heat Transfer Division for publication in the JOURNAL OF HEAT TRANSFER. Manuscript received by the Heat Transfer Division, February 19, 1982.

Previous work regarding phase transformation in a fluid which permeates a porous solid matrix has been performed in connection with the artificial freezing of soil [3], the thawing of permafrost [4], and condensation in fibrous insulation [5]. Several numerical methods using finite elements for the solutions of phase transformation problems have been reported in the technical literature. They include the use of the enthalpy model [6] and the phase front tracking methods [7, 8, 9]. Recent studies on solidification processes in a one-dimensional spherical geometry employ perturbation methods [10] and the finite difference method [11]. The significance of this study is that it presents a numerical solution by means of finite elements and that it includes the effects of condensation or evaporation on the outer surface.

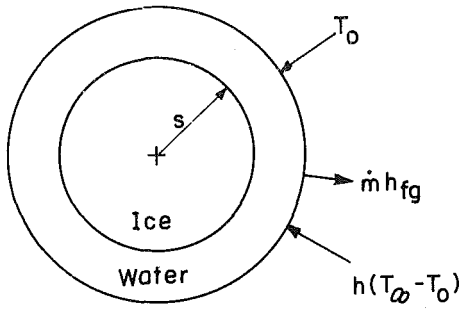

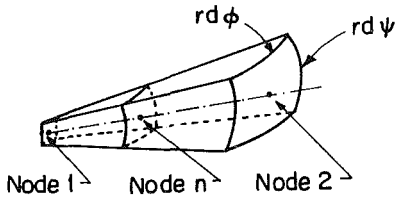

Fig. 1 Schematic of coal particle and typical finite element section

Analysis

The porous coal sphere is initially saturated with water, and uniform composition is assumed. The particle is assumed to be suspended in an isothermal field governed by natural convection, and the water in the porous matrix is completely frozen at the initial time. A step change in the ambient air temperature will initiate the melting of the ice in the coal particle. Depending on the temperature of the outer surface of the particle and the moisture content in the ambient air, water will either condense on the coal particle surface or evaporate from the surface. It is assumed that film condensation occurs on the outer surface and that the condensate layer is negligibly thin. Ignoring the water shell around the particle will tend to optimize the thawing rate for most cases considered. During evaporation it is assumed that the melting ice provides an infinite reservoir of moisture transported to the surface due to the capillary action of the pores. The air on the surface of the coal particle is saturated and the moisture content will depend on the surface temperature of the coal particle. A simplified one-dimensional analysis will be performed for the problem, and the discussed geometry is shown schematically in Fig. 1.

As a result of the physical assumption, the governing equations reduce to

$$(\rho c_p)_{\text{eff},m} \frac{\partial \theta_m}{\partial t} = \frac{k_{\text{eff},m}}{r^2} \frac{\partial}{\partial r}\left(r^2 \frac{\partial \theta_m}{\partial r}\right); 0 \le r \le R,\ t > 0 \qquad (1)$$

where $m = s, f$ for the solid or liquid regions, respectively, $\theta_m = T_m - T_{ph}$; T is temperature; t, time; r, radius; and R, the outer radius of the coal particle. The effective properties are a combination of the thermal properties of coal and the thermal properties of the solid or liquid phase of water

$$k_{\text{eff},m} = (1-\epsilon)k_c + \epsilon k_m,\ (\rho c)_{\text{eff},m} = [(1-\epsilon)(\rho c)_c + \epsilon(\rho c)_m] \qquad (2)$$

where ρ is density; c, heat capacity; k, thermal conductivity; ϵ = volumetric water fraction; and the subscript c stands for coal. The formulation of the efffective properties given above assumes that parallel heat flow occurs in coal and water. This model will give a maximal value for the thermal conductivity in a porous media, [12].

Note that during thawing with evaporation the water content in the thawed region will change with time. This model allows for the consequent variation of the effective properties in the thawed region by changing the values for the volumetric water fraction, ϵ, in equation (2) as a function of time to satisfy conservation of mass in the coal particle. The model assumes that the effective properties are independent on the space variable, i.e., a uniform water distribution is assumed in the thawed region. The possibility of a dry-out front, providing a second phase interface moving in from the surface, is also neglected. This is consistent with the absence of a water distribution in the thawed region and is reasonable for small geometries due to the capillary action of the pores. The thermal properties in this analysis were taken to be independent of temperature although the numerical method used here does not preclude the variation of thermal properties with temperature.

The initial condition and the boundary conditions in the solid and liquid regions are given by equation (3)

$$\theta_s(r,0) = \theta_i;\ \frac{\partial \theta_s(0,t)}{\partial r} = 0;\ -k_{\text{eff},f}\frac{\partial \theta(R,t)}{\partial r}$$

$$= h(\theta(\infty,t) - \theta(R,t)) - \dot{m} h_{fg} \qquad (3)$$

where h is an average heat transfer coefficient, $\dot{m}$ the water mass flux, and h_{fg} the latent heat of vaporization. The water mass flux, $\dot{m}$, for an air-water vapor system is given by [13]

$$\dot{m} = g\frac{m(\infty,t) - m(R,t)}{m(R,t) - 1} \qquad (4)$$

where m is the mass fraction of water vapor in air (kg water/kg air), while g is the mass transfer conductance, which for water vapor in air is equal to h/c [13]. The mass fraction, m, can be defined in terms of P, the total pressure of the water air mixture, and P_w, the partial pressure of water vapor [13]

$$m = \frac{P_w}{1.61\mathrm{P} - 0.61\,P_w} \qquad (5)$$

The conditions on the phase change interface are

$$k_{\text{eff},s} \cdot \frac{\partial \theta_s(s,t)}{\partial r} - k_{\text{eff},f} \cdot \frac{\partial \theta_f(s,t)}{\partial r} = \rho_f \cdot \epsilon \cdot L \cdot \frac{ds}{dt},$$

$$\theta_s(s,t) = \theta_f(s,t) = 0 \qquad (6)$$

The radially symmetric sphere has been divided into spherical sectors of parametric elements. Such an element is shown in Fig. 1. The temperature is taken to be uniform across the surface area defined by each node location. The standard finite element formulation used in the solution of this problem is [14]

$$\underline{C} \cdot \dot{\underline{\theta}} + \underline{K} \cdot \underline{\theta} = \underline{Q} \qquad (7)$$

The specific matrices for the problem discussed in this work are given below.

$$\underline{K} = \underline{K}_C + \underline{K}_{NC};\ \underline{Q} = \underline{Q}_{NC} + \underline{Q}_H \qquad (8)$$

where

$$C = 4\pi \cdot \sum_m \int_{r(m)} H^{(m)T} \cdot (\rho c)_{\text{eff}} \cdot H^{(m)} \cdot r^2 dr$$

Table 1 Thermophysical properties

	Coal	Ice	Water	
Density	0.135×10^{4}	0.897×10^{3}	0.100×10^{4}	kg/m^3
Heat capacity	0.170×10^{4}	0.123×10^{4}	0.423×10^{4}	J/kg−K
Conductivity	0.025×10^{-3}	0.225×10^{-2}	0.552×10^{-3}	KW/m−K
Latent heat vaporization	–	–	0.250×10^{4}	kJ/kg
Latent heat melting	–	0.325×10^{3}	–	KJ/kg

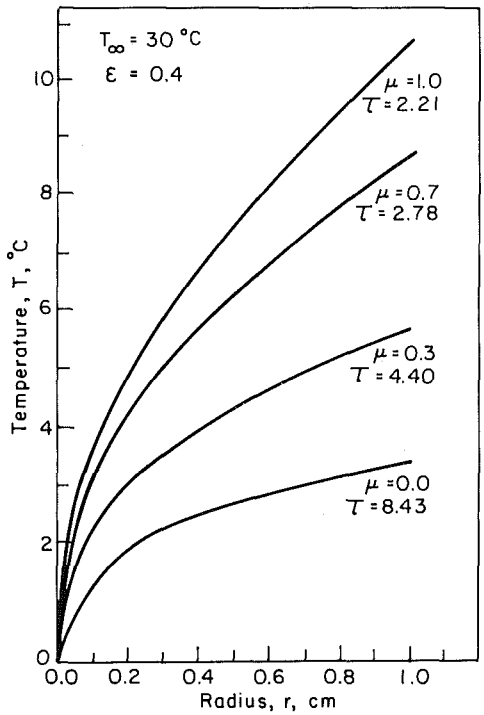

Fig. 2 Final temperature distribution with variation in degree of saturation

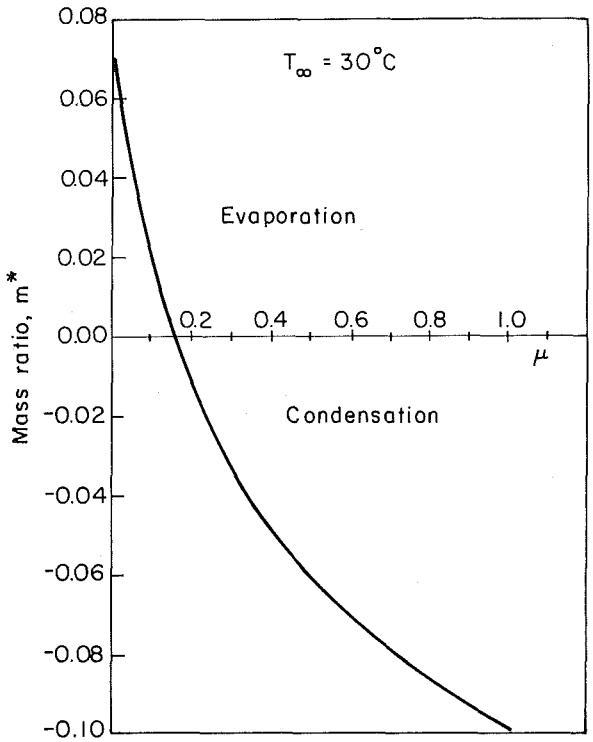

Fig. 3 Mass of water leaving surface versus degree of saturation

$$K_C = 4\pi \cdot \sum_m \int_{r^{(m)}} B^{(m)^T} \cdot k_{\text{eff}} \cdot B^{(m)} \cdot r^2 \cdot dr$$

$$K_{NC} = 4\pi \cdot (H^{ST} \cdot h \cdot H^S) R^2$$

$$Q_{NC} = 4\pi \cdot (H^{ST} \cdot h \cdot H^S) R^2 \cdot \theta(\infty, t)$$

$$Q_H = 4\pi \cdot (H^{ST} \cdot h \cdot H^S) R^2 \cdot \frac{(m(\infty,t) - m(R,T))}{c \cdot (m(R,t) - 1)}$$

where the superscript (m) indicates element (m); superscript s indicates the surface, and T transpose of matrix.

It should be noted in the solution of equation (6) that Q_H is dependent upon θ through the values for $m(R,t)$, the humidity ratio of the air at the outer surface of the coal particle. The energy released due to the change of phase is regarded in this work as an additional heat source of intensity

$$Q_s = 4\pi\rho\epsilon L \cdot s^2 \frac{ds}{dt} \tag{10}$$

The front tracking finite element method utilizes an additional node, n, to define the phase front location. The location of this node is tracked continuously in time. The node is regarded as an external node of any element. Since a linear interpolation function is used to this solution, a two-node element is divided into two new elements when the phase front is located within the element. The global heat capacity and conductivity matrices are updated at each time step for the new position of the phase front location. The energy released on the phase change interface is considered a local heat source at the node corresponding to the change of phase interface. Equation (6) is solved at time, t, using an Euler-forward integration scheme, for the temperature at time $t+\Delta t$ at all the stationary nodes and for the position of the phase change interface at time $t+\Delta t$ at the node corresponding to the phase change location. A detailed description of this numerical method has been presented by Rubinsky and Cravalho in [9].

Discussion

Parametric studies were made using the finite element program described in the previous section. Ambient air temperature, and humidity ratio were varied to determine their effect on the melting rate and the temperature distribution of the frozen coal sphere. The tests were run for a sphere of 1-cm radius. An initial temperature of 0°C was assumed for the coal particle, and a uniform time step of one second was used throughout the analysis. The initial temperature of 0°C was used to reduce the number of variable parameters. The thermal properties used in this analysis are listed in Table 1. The heat transfer coefficient for natural convection around a sphere was calculated from [15], while the expression for the partial pressure of water in the air as a function of temperature was taken from [16]. The results of these tests are depicted in the attached graphs.

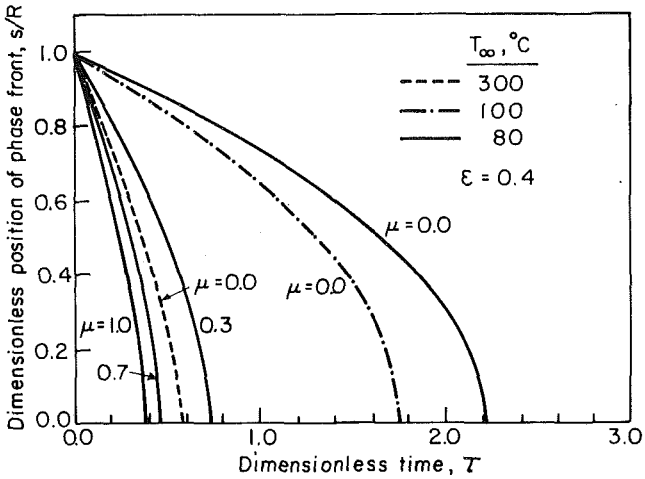

Fig. 4 Dimensionless phase front location versus time with varying degrees of saturation and ambient temperature

Figure 2 shows the temperature profile at the instance the phase change interface will reach the center of the sphere and it indicates the time at which the center will be reached as a function of the humidity ratio in the air. The conditions for which the results have been obtained are given in the figure. The degree of saturation μ in the ambient air is the ratio of the humidity ratio at specified conditions to that at full saturation [16]. An increase in the degree of saturation from 0 to 30 percent at 30°C reduces the dimensionless thawing time, $\tau = \alpha_f \cdot t/R^2$, by one half. The effect is significant and is due to the additional heat generated on the coal surface during condensation. Figure 2 shows that the temperature profile in the coal particle at the time of total melting increases as the degree of saturation μ is increased. This suggests that condensation is a predominant heat transfer mechanism which could considerably affect the thawing time in a load of frozen coal.

The amount of water evaporated or condensed on the coal particle surface is shown in Fig. 3 for various ambient conditions.

Figure 4 shows the position of the phase front as a function of time for moist air at 80°C and for dry air at 100 and 300°C. When compared, the time required to thaw a coal particle in the presence of 300°C is comparable to that required to thaw the particle in the presence of 80°C saturated air.

Conclusions

A finite element method using a front tracking technique was applied for the solution of the problem of thawing a coal particle in the presence of condensation or evaporation from the outer surface.

The conclusions to be drawn from the tests completed strongly indicate that the thawing time is most significantly reduced by means of an increased humidity ratio in the ambient air. The effect of condensation is to be highly regarded as a most expeditious means of increasing the rate of melting. Merely controlling the degree of moisture in the ambient air provides an alternative for enhancing the thawing process by simple, economic means. Such a method would eliminate the hazard of spontaneous ignition when air at a high temperature is used to thaw the coal.

Acknowledgment

We would like to thank Professor D. W. Fuerstenau for the interest he expressed in this study and the continuing support through the Office of Surface Mining with the U.S. Department of the Interior, and the Mining and Mineral Resources and Research Institute at the University of California, Berkeley.

References

1 *Keystone Coal Industry Manual*, McGraw-Hill Publication, 1979.

2 Rubinsky, B., "Natural Convection on a Vertical Flat Plate in a Solidifying Porous Medium," University of California, Berkeley, Report FM-82-2.

3 Hashemi, H. T., and Sliepcevich, C. M., "Effect of Seepage Stream on Artificial Soil Freezing," *Journal of Solid Mech. and Found Div., Proceedings of the ASCE*, 1973, pp. 267-289.

4 Wheeler, J. A., "Simulation of Heat Transfer from a Warm Pipeline Buried in Dermafrost," AIChE Symposium Series, 130, Vol. 69, 1973, pp. 206-207.

5 Ogniewicz, Y., and Tien, C. L., "Analysis of Condensation in Porous Insulation," *International Journal of Heat and Mass Transfer*, Vol. 24, 1981, pp. 421-425.

6 Comini, G., and Del Guidice, S., "Finite Element Solutions of Nonlinear Heat Conduction Problems With Special Reference to Phase Change," *Int. Journal Meth. Eng.*, Vol. 8 1976, pp. 613-624.

7 Bonnerot, R., and Janet, P., "Numerical Computation of the Free Boundary for the Two-Dimensional Stefan Problem by Space-Time Finite Elements," *J. of Comp. Phys.*, Vol. 25, 1977, pp. 163-181.

8 Miller, K., and Miller, R. N., "Moving Finite Elements. I," *Siam J. Numer. Anal.*, Vol. 18, pp. 1019-1033.

9 Rubinsky, B., and Cravalho, E. G., "A Finite Element Method for the Solution of One-Dimensional Phase Change Problems," *International Journal of Heat and Mass Transfer*, Vol. 24, 1981, pp. 1987-1989.

10 Redroso, R. I., and Domoto, G. A., "Inward Spherical Solidification-Solution by the Method of Strained Coordinates," *International Journal of Heat and Mass Transfer*, Vol. 16, 1973, pp. 1037-1043.

11 Tao, L. C., "Generalized Numerical Solutions of Freezing a Saturated Liquid in Cylinders and Spheres," *AIChE Journal*, Vol. 13, 1967, p. 165.

12 Lunardini, V. J., *Heat Transfer in Cold Climates*, Van Nostrand Reinhold Co., 1981, pp. 147-159.

13 Kays, W. M., and Crawford, M. E., *Convection Heat and Mass Transfer*, McGraw-Hill, 1980.

14 Bathe, K., and Wilson, E. L., *Numerical Methods in Finite Element Analysis*, Prentice Hall, Inc., 1976.

15 *ASHRAE Handbook and Product Directory, 1977 Fundamentals*, 4th ed., New York, 1980, p. 5.2

16 Chiang, T., Ossin, A., and Tien, C. L., "Laminar Free Convection from a Sphere," ASME *Transactions*, Series C, Vol. 86, No. 4, 1969, pp. 537-542.

Heat Transfer With Ablation in a Half-Space Subjected to Time-Variant Heat Fluxes

B. T. F. Chung[1], T. Y. Chang[2], J. S. Hsiao[3], and C. I. Chang[4]

Heat transfer in solids involving ablation is of great importance in numerous military and space applications. To date, the only available exact solution is restricted to the case of semi-infinite solids subject to a uniform heat flux [1]. Analytical approximate solutions of the same problem were presented by Goodman [2, 3] and Altman [4] using a heat balance integral method.

To simulate the ablation phenomena in the atmosphere entry environment, Vallerani [5] applied the heat balance integral technique to a class of ablation problems of a semi-infinite solid subjected to heat flux of the form $q_0 \sim t^m$, where m is a constant; Zien [6, 7] employed the θ-moment integral method to treat one-dimensional transient ablation problem with two specific time-dependent boundary heat fluxes, namely, $q_0 \sim t^m$ and $q_0 \sim e^t$. A large discrepancy was detected in the predicted ablation speed and ablation thickness based on these two approximate analyses.

The purpose of this study is to present an exact solution for

[1, 2]The University of Akron, Akron, Ohio 44325. Mem. ASME

[3]The University of Akron, Akron, Ohio 44325. Student Mem. ASME

[4]Naval Research Laboratory, Washington, D.C. 20375. Assoc. Mem. ASME

Contributed by the Heat Transfer Division for publication in the JOURNAL OF HEAT TRANSFER. Manuscript received by the Heat Transfer Division March 17, 1982.

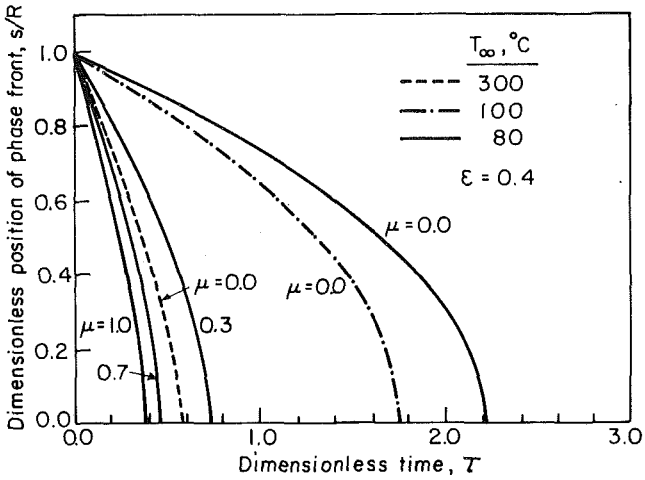

Fig. 4 Dimensionless phase front location versus time with varying degrees of saturation and ambient temperature

Figure 2 shows the temperature profile at the instance the phase change interface will reach the center of the sphere and it indicates the time at which the center will be reached as a function of the humidity ratio in the air. The conditions for which the results have been obtained are given in the figure. The degree of saturation μ in the ambient air is the ratio of the humidity ratio at specified conditions to that at full saturation [16]. An increase in the degree of saturation from 0 to 30 percent at 30°C reduces the dimensionless thawing time, $\tau = \alpha_f \cdot t/R^2$, by one half. The effect is significant and is due to the additional heat generated on the coal surface during condensation. Figure 2 shows that the temperature profile in the coal particle at the time of total melting increases as the degree of saturation μ is increased. This suggests that condensation is a predominant heat transfer mechanism which could considerably affect the thawing time in a load of frozen coal.

The amount of water evaporated or condensed on the coal particle surface is shown in Fig. 3 for various ambient conditions.

Figure 4 shows the position of the phase front as a function of time for moist air at 80°C and for dry air at 100 and 300°C. When compared, the time required to thaw a coal particle in the presence of 300°C is comparable to that required to thaw the particle in the presence of 80°C saturated air.

Conclusions

A finite element method using a front tracking technique was applied for the solution of the problem of thawing a coal particle in the presence of condensation or evaporation from the outer surface.

The conclusions to be drawn from the tests completed strongly indicate that the thawing time is most significantly reduced by means of an increased humidity ratio in the ambient air. The effect of condensation is to be highly regarded as a most expeditious means of increasing the rate of melting. Merely controlling the degree of moisture in the ambient air provides an alternative for enhancing the thawing process by simple, economic means. Such a method would eliminate the hazard of spontaneous ignition when air at a high temperature is used to thaw the coal.

Acknowledgment

We would like to thank Professor D. W. Fuerstenau for the interest he expressed in this study and the continuing support through the Office of Surface Mining with the U.S. Department of the Interior, and the Mining and Mineral Resources and Research Institute at the University of California, Berkeley.

References

1 *Keystone Coal Industry Manual*, McGraw-Hill Publication, 1979.

2 Rubinsky, B., "Natural Convection on a Vertical Flat Plate in a Solidifying Porous Medium," University of California, Berkeley, Report FM-82-2.

3 Hashemi, H. T., and Sliepcevich, C. M., "Effect of Seepage Stream on Artificial Soil Freezing," *Journal of Solid Mech. and Found Div., Proceedings of the ASCE*, 1973, pp. 267-289.

4 Wheeler, J. A., "Simulation of Heat Transfer from a Warm Pipeline Buried in Dermafrost," AIChE Symposium Series, 130, Vol. 69, 1973, pp. 206-207.

5 Ogniewicz, Y., and Tien, C. L., "Analysis of Condensation in Porous Insulation," *International Journal of Heat and Mass Transfer*, Vol. 24, 1981, pp. 421-425.

6 Comini, G., and Del Guidice, S., "Finite Element Solutions of Nonlinear Heat Conduction Problems With Special Reference to Phase Change," *Int. Journal Meth. Eng.*, Vol. 8 1976, pp. 613-624.

7 Bonnerot, R., and Janet, P., "Numerical Computation of the Free Boundary for the Two-Dimensional Stefan Problem by Space-Time Finite Elements," *J. of Comp. Phys.*, Vol. 25, 1977, pp. 163-181.

8 Miller, K., and Miller, R. N., "Moving Finite Elements. I," *Siam J. Numer. Anal.*, Vol. 18, pp. 1019-1033.

9 Rubinsky, B., and Cravalho, E. G., "A Finite Element Method for the Solution of One-Dimensional Phase Change Problems," *International Journal of Heat and Mass Transfer*, Vol. 24, 1981, pp. 1987-1989.

10 Redroso, R. I., and Domoto, G. A., "Inward Spherical Solidification-Solution by the Method of Strained Coordinates," *International Journal of Heat and Mass Transfer*, Vol. 16, 1973, pp. 1037-1043.

11 Tao, L. C., "Generalized Numerical Solutions of Freezing a Saturated Liquid in Cylinders and Spheres," *AIChE Journal*, Vol. 13, 1967, p. 165.

12 Lunardini, V. J., *Heat Transfer in Cold Climates*, Van Nostrand Reinhold Co., 1981, pp. 147-159.

13 Kays, W. M., and Crawford, M. E., *Convection Heat and Mass Transfer*, McGraw-Hill, 1980.

14 Bathe, K., and Wilson, E. L., *Numerical Methods in Finite Element Analysis*, Prentice Hall, Inc., 1976.

15 *ASHRAE Handbook and Product Directory, 1977 Fundamentals*, 4th ed., New York, 1980, p. 5.2

16 Chiang, T., Ossin, A., and Tien, C. L., "Laminar Free Convection from a Sphere," ASME *Transactions*, Series C, Vol. 86, No. 4, 1969, pp. 537-542.

Heat Transfer With Ablation in a Half-Space Subjected to Time-Variant Heat Fluxes

B. T. F. Chung[1], T. Y. Chang[2], J. S. Hsiao[3], and C. I. Chang[4]

Heat transfer in solids involving ablation is of great importance in numerous military and space applications. To date, the only available exact solution is restricted to the case of semi-infinite solids subject to a uniform heat flux [1]. Analytical approximate solutions of the same problem were presented by Goodman [2, 3] and Altman [4] using a heat balance integral method.

To simulate the ablation phenomena in the atmosphere entry environment, Vallerani [5] applied the heat balance integral technique to a class of ablation problems of a semi-infinite solid subjected to heat flux of the form $q_0 \sim t^m$, where m is a constant; Zien [6, 7] employed the θ-moment integral method to treat one-dimensional transient ablation problem with two specific time-dependent boundary heat fluxes, namely, $q_0 \sim t^m$ and $q_0 \sim e^t$. A large discrepancy was detected in the predicted ablation speed and ablation thickness based on these two approximate analyses.

The purpose of this study is to present an exact solution for

[1, 2]The University of Akron, Akron, Ohio 44325. Mem. ASME

[3]The University of Akron, Akron, Ohio 44325. Student Mem. ASME

[4]Naval Research Laboratory, Washington, D.C. 20375. Assoc. Mem. ASME

Contributed by the Heat Transfer Division for publication in the JOURNAL OF HEAT TRANSFER. Manuscript received by the Heat Transfer Division March 17, 1982.

one-dimensional ablation in a solid subject to time-varying heat fluxes using a coordinate transformation coupling a finite difference scheme. The results are then used to compare with the corresponding analytical approximate solutions. Three different heat flux boundary conditions are considered. They are in terms of linear, exponential, and "power-law" functions of time.

Mathematical Analyses

Consideration is given to the case of one-dimensional heat conduction in a semi-infinite solid which is initially at a uniform temperature, T_0. The solid is subjected to a time variant heat flux at the front surface ($x=0$). The surface temperature starts to increase until it reaches the melting temperature, T_m. As a result, ablation takes place. The problem can be best analyzed by subdividing it into two time domains, namely, preablation and ablation periods. Assuming constant thermal properties of the material and further assuming that the melt is completely removed upon formation, we can write the governing equations for each time period as follows:

Preablation period:

$$\frac{\partial\theta}{\partial t}=\alpha\frac{\partial^2\theta}{\partial x^2} \quad 0\le t\le t_m, \quad 0<x<\infty \tag{1}$$

$$\theta=0 \quad \text{at} \quad t=0, \quad 0<x<\infty \tag{2}$$

$$-k\frac{\partial\theta}{\partial x}=\frac{q_0(t)}{T_m-T_0} \quad \text{at} \quad x=0, \quad t>0 \tag{3}$$

$$\theta=0 \quad \text{as} \quad x\to\infty, \quad t>0 \tag{4}$$

Ablation period:

$$\frac{\partial\theta}{\partial t}=\alpha\frac{\partial^2\theta}{\partial x^2} \quad t_m<t<\infty, \quad s\le x<\infty \tag{5}$$

$$\theta=\theta_i \quad \text{at} \quad t=t_m, \quad s<x<\infty \tag{6}$$

$$\theta=0 \quad \text{as} \quad x\to\infty; \quad t\ge t_m \tag{7}$$

$$\theta=1 \quad \text{at} \quad x=s(t), \quad t\ge t_m \tag{8}$$

$$-k(T_m-T_0)\frac{\partial\theta}{\partial x}+\rho H\frac{ds}{dt}=q_0(t) \quad \text{at} \quad x=s(t), \quad t\ge t_m \tag{9}$$

where $\theta=(T-T_0)/(T_m-T_0)$, s is ablation thickness, q_0 is the heat flux at the boundary, H the heat of ablation, t_m is the time when the ablation just starts, and θ_i is the temperature distribution at the onset of the ablation. Both θ_i and t_m are obtained from the solution of preablation period. Equations (1-9) will be solved using the heat balance integral, θ-moment integral, and finite difference methods.

Heat Balance Integral Method.

Preablation Period. Integrating equation (1) from 0 to ∞, and introducing an exponential temperature profile of the form [5]

$\theta=[q_0\,\delta/(T_m-T_0)k]\exp[-x/\delta]$ gives $\delta=[\alpha/q_0\int_0^t q_0\,dt]^{1/2}$

Closed form solutions for δ can be obtained for each of specified heat fluxes mentioned above and were given in reference [8].

Ablation Period. Integrating equation (5) from the recession surface position, $s(t)$ to infinity, making use of equations (7-9) and assuming a temperature profile of the form, $\theta=\exp[-(x-s)/\delta]$, we obtain the following expressions

$$\frac{d\delta}{dt}+\frac{ds}{dt}=\frac{\alpha}{\delta} \tag{10}$$

$$k(T_m-T_0)/\delta+\rho H\frac{ds}{dt}=q_0 \tag{11}$$

δ and s can be solved from equations (10) and (11) by using Runge-Kutta method with the aid of initial condition, $s=0$, $\delta=\delta_m$ at $t=t_m$. For the case of constant heat flux at wall, equations (10) and (11) can be solved exactly.

Θ- Moment Integral Method.

Preablation Period. A second integral equation is established by multiplying θ on both sides of equation (1), integrating the resulting expression from 0 to infinity, and employing the following temperature distribution suggested by Zien [6, 7]

$$\theta=\frac{q_0\delta}{(T_m-T_0)k}\phi\exp\left(-\frac{x}{\delta}\right) \tag{12}$$

there is obtained

$$\delta^2\phi=\frac{\alpha}{q_0}\int_0^t q_0(t)\,dt \tag{13}$$

$$\delta^3\phi^2=\frac{2\alpha}{q_0^2}\int_0^t q_0\phi\,\delta(2-\phi)\,dt \tag{14}$$

Both ϕ and δ can be solved in closed forms for the aforementioned three types of heat flux (see reference [8] for details)

Ablation Period. For the ablation period, the following integral equation is employed in addition to the conventional heat balance integral equation

$$\frac{d}{dt}\int_s^\infty\theta^2dx+\frac{ds}{dt}=-2\alpha\left(\frac{\partial\theta}{\partial x}\right)_{x=s}-2\alpha\int_s^\infty\left(\frac{\partial\theta}{\partial x}\right)^2dx \tag{15}$$

Using $\theta=\exp[-(x-s)/\delta]$ along with the heat balance integral equation and equations (8-9) we arrive at

$$(1+3\nu)\frac{d\delta}{dt}-2\alpha(1+\nu)/\delta=-2\gamma q_0(t) \tag{16}$$

$$s=\frac{1}{1+\nu}\left[\gamma\int_{t_m}^t q_0(t)\,dt+\delta_m-\delta\right] \tag{17}$$

where $\gamma=1/[\rho C_p(T_m-T_0)]$. Both t_m and δ_m are obtained from the preablation period. Note that equation (17) is more general as compared to Zien's formula [7], since the former is applicable to any time-dependent boundary heat flux.

Numerical Solution.

Preablation Period. Taking Laplace transform of equations (1-4) with the aid of convolution theorem gives

$$\theta=\beta\int_0^t\frac{q_0(t-v)}{\sqrt{\pi v}}\exp\left(-\frac{x^2}{4\alpha v}\right)dv \tag{18}$$

where $\beta=\sqrt{\alpha}/(T_m-T_0)k$. With $q_0(v)$ specified above, the closed-form solutions for commencing melting time, t_m, can be obtained [8][5].

Ablation Period. Employing the coordinate transformations, $z=(x-s)/\sqrt{\alpha t_m}$ and $y=(t-t_m)/t_m$, equations (5-9) are reduced to

$$\frac{\partial\theta}{\partial y}=\frac{\partial^2\theta}{\partial z^2}+\sqrt{\frac{t_m}{\alpha}}\frac{ds}{dt}\left(\frac{\partial\theta}{\partial z}\right) y>0, \quad 0\le z<\infty \tag{19}$$

$$\theta=\theta_i \quad \text{at} \quad y=0 \quad z\ge0 \tag{20}$$

$$\theta=0 \quad \text{as} \quad z\to\infty, \quad y>0 \tag{21}$$

$$\theta=1 \quad \text{at} \quad z=0, \quad y>0 \tag{22}$$

$$\frac{-k(T_m-T_0)}{\sqrt{\alpha t_m}}\frac{\partial\theta}{\partial z}+\rho H\frac{ds}{dt}=q_0(t) \quad \text{at} \quad z=0, \quad y>0 \tag{23}$$

[5] Equation (34) of reference [8] is in error. It should read: t_m is the root of equation: $\text{erf}(t_m/t_c)\exp(t_m/t_c)=1/(A\beta t_c^{1/2})$.

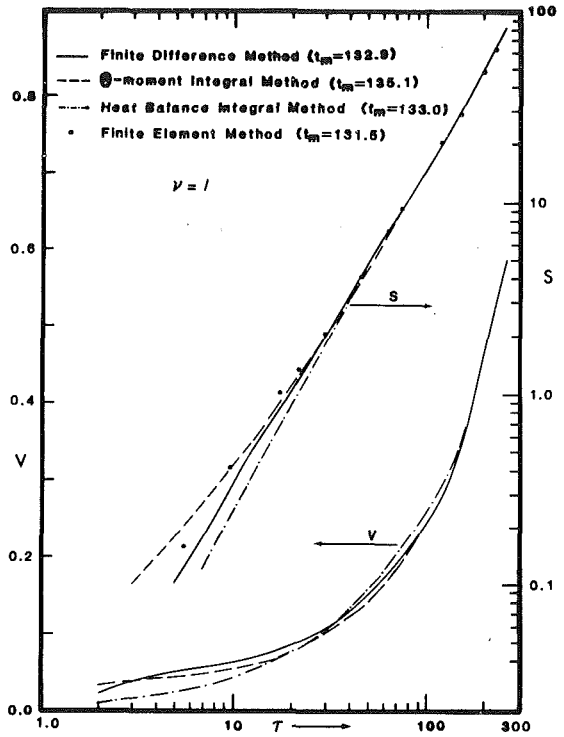

Fig. 1 Comparisons of ablation thickness and speed of various methods for $q_0 = t^2$

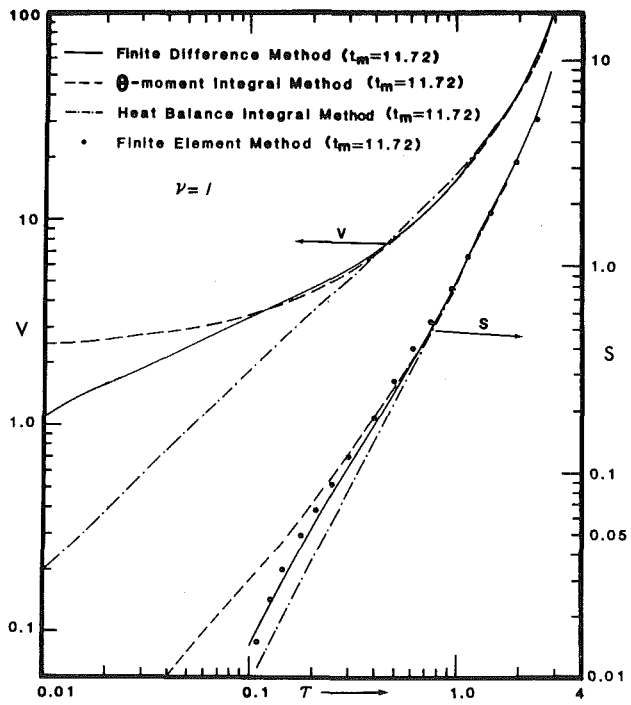

Fig. 2 Comparisons of ablation thickness and speed of various methods for $q_0 = \exp(t/t_c)$

It is seen that the moving boundary is converted to a stationary one through the transformation. An explicit finite difference scheme is now chosen for solving equation (19). With a choice of $\Delta y/\Delta z^2 = 1/2$, the finite difference representation of equation (19) reads

$$\theta_{i,j+1} = \frac{1}{2}\left[1+\sqrt{\frac{t_m}{\alpha}}\frac{ds}{dt}\frac{\Delta z}{2}\right]\theta_{i+1,j}$$

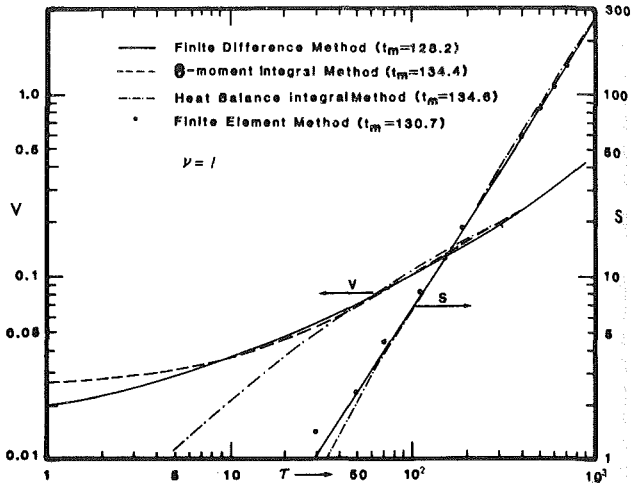

Fig. 3 Comparisons of ablation thickness and speed of various methods for $q_0 = 100(10 + t)$

$$+\frac{1}{2}\left[1-\sqrt{\frac{t_m}{\alpha}}\frac{ds}{dt}\frac{\Delta z}{2}\right]\theta_{i-1,j} \tag{24}$$

where $\theta(z,y) = \theta(i\Delta z, j\Delta y)$. The ablation speed is evaluated from equation (23)

$$\frac{ds}{dt} = \frac{1}{\rho H}\left\{q_0(t) + \frac{k(T_m - T_0)}{2\sqrt{\alpha t_m}\Delta z}\left[-\frac{11}{3}\theta_{1,j} + 6\theta_{2,j} - 3\theta_{3,j} + \frac{2}{3}\theta_{4,j}\right]\right\} \tag{25}$$

Substituting equation (25) into equation (24), the temperature distribution at the next time increment is computed explicitly. The current temperature distribution is then substituted into equation (25) to evaluate the ablation speed.

Results and Discussion

Typical numerical results based on the aforementioned three different analyses are illustrated in Figs. 1-3. Three specific heat flux boundary conditions are chosen in the present computations, namely, $q_0 = t^2$, $q_0 = e^{t/t_c}$ and $q_0 = 1000 + 100\ t$. The reference time, characteristic length and characteristic speed, employed in the plots are $t_c = 1$ s, $l_c = \sqrt{\alpha t_c}$, and $V_c = \sqrt{\alpha/t_c}$, respectively. $[\tau = (t - t_m)/t_c]$. The values of thermal diffusivity, heat of ablation, conductivity, and temperature difference, $(T_m - T_0)$ are taken to be 1.30×10^{-7} m^2/s, 3.38×10^8 W-s/Kg, 2.22 W/m − °K and 20°K, respectively. Stefan number, ν, is set equal to unity.

As can be seen, the agreement in the predicted ablation thickness based on the above methods is reasonably good, especially for the case of linear heat flux shown in Fig. 3 in which the solid and dash lines for s are practically coincident. Overall, the classical heat balance integral method tends to underpredict the ablation thickness and the ablation speed at the smaller time. This is especially true for the case of exponential surface heat flux.

For further comparison, the corresponding finite element solutions for ablation thickness are also included. Details of the finite element heat transfer analysis involving ablation are documented elsewhere [9]. This finite element solution could be improved with more refined grids.

The values of t_m based on various methods for the above three different surface conditions are also included in the figures. The predicted ablation speed based on both approximate analyses deviate somewhat from the finite difference solutions. In general, the θ-moment integral method shows a good improvement over the heat balance integral

method. The drawback of Zien's method is that it fails to predict a zero speed at the onset of ablation as it should be. Nevertheless, the method has its merits in view of its simplicity and general accuracy.

Acknowledgments

This work was partially supported by U.S. Naval Research Laboratory under the contract ONR N00014-80-C-0888.

References

1 Landau, H. G., "Heat Conduction in A Melting Solid," *Quarterly Applied Math.*, Vol. 8, 1950, pp. 312–319.

2 Goodman, T. R., "The Heat Balance Integral and Its Application to Problems Involving a Change of Phase," *Trans ASME*, Vol. 80, 1958, pp. 335–342.

3 Goodman, T. R., "Integral Methods for Nonlinear Heat Transfer," *Advances in Heat Transfer*, Vol. 1, 1964, pp. 51–122.

4 Altman, M., "Some Aspect of the Melting Solution for A Semi-Infinite Slab," *Chem. Eng'g. Progress Symposium Series*, Vol. 57, 1961, pp. 16–23.

5 Vallerani, E., "Integral Technique Solution to a Class of Simple Ablation Problems," *Meccanica*, Vol. 9, 1964, pp. 94–101.

6 Zien, T. F., "Study of Heat Conduction with Phase Transition Using an Integral Method," *AIAA Progress Astronautics and Aeronautic Thermophysics of Spacecraft and Outer Planet Entry Probes*, Vol. 56, 1977, pp. 87–111.

7 Zien, T. F., "Integral Solutions of Ablation Problems with Time-Dependent Heat Flux," *AIAA J.*, Vol. 16, No. 12, 1978, pp. 1287–1295.

8 Chung, B. T. F., Chang, T. Y., Hsiao, J. S., and Chang, C. I., "Heat Transfer with Ablation in A Half-Space Subjected to Time Variant Heat Fluxes," presented at ASME Winter Annual Meeting, Washington, D.C., 1981, Paper No. 81-WA/HT-34.

9 Chung, B. T. F., Chang, T. Y., Hsiao, J. S., and Chang, C. I., "A Finite Element Analysis of Heat Transfer in Solid with Radiation and Ablation," *Proceedings 7th International Heat Transfer Conference*, Munich, Germany, 1982 (in press).

Optimal Heat Transfer Assemblies With Thin Straight Fins

M. Kovarik[1]

A simple criterion of optimality of finned duct assemblies for heat transfer is defined. A necessary condition of optimality in the defined sense is found for assemblies with straight thin fins. A reduction of design effort resulting from the application of this condition is demonstrated.

Nomenclature

a = scaling parameter, see equation (6)
A = fin cross-sectional area, m^2
B = function expressing boundary condition
c = cost of assembly per unit length of duct, dollar/m
c_0 = cost per unit length of duct, dollar/m
c_1 = cost per unit volume of fin, dollar/m^3
$D_{1,2}$ = constants of integration
h = heat transfer coefficient, W/m^2K
I = integral defined by equation (16)
J = performance index, W/dollar
k = thermal conductivity, W/mK
m = fin parameter, see equation (26), dimensionless
n = number of fins
q = rate of heat loss per unit projected area of fin, W/m^2
Q = heat flux at the root of the fin, per unit length, W/m
s = function prescribing the values of the (ky) product
t = temperature, °C
T_0 = temperature of the tip, °C
T_1 = temperature of the root, °C
v = fin thickness, m
x = width coordinate, dimensionless
X = fin width, m
y = thickness coordinate, dimensionless
Y = fin thickness at root, m
z = fin width coordinate, m

1 Introduction

The design of extended heat transfer surfaces in the shape of fins has been analysed with a view to obtaining the lowest possible mass of heat conducting material for a given heat flux to be transferred from the surface to the environment. The earliest work by Schmidt [1] is concerned with linear heat transfer and uniform coefficient of heat transfer over the entire fin surface, with a constant thermal conductivity of material. Schmidt's results are supported by a more rigorous treatment of the same problem by Le Foll et al. [2]. Duffin [3] recasts the problem into a variational form and confirms that, under the conditions summarised above, the fin of minimum mass is so shaped that its temperature is a linear function of the distance from the tip of the fin.

The more complex problem of optimal fin with a more general temperature dependent heat rejection mode is discussed by Wilkins [4] and a set of solutions for fourth-power radiation heat transfer is given by the same author [5]. References [1–5] restrict attention to the mass of the fin itself, rather than to the broader problem involving the entire finned duct assembly.

Optimal arrangement of heat collecting finned pipes has been studied by the present author [6], the consideration including the cost of both the pipes and the fins, subject to linear uniform heat transfer.

Recent numerical work by Sparrow et al. [7] shows that in fin arrays in a forced convection system the heat transfer coefficient varies along the fin. Their results "demonstrate that the conventional uniform heat transfer coefficient model is inapplicable to shrouded fin arrays". More recently a nonuniform heat transfer coefficient has been reported by Sparrow and Acharya [8] in fins cooled by natural convection.

The recent findings [7, 8] indicate the inapplicability of optimal design results based on uniform heat transfer coefficient to some arrangements of finned ducts, and cast doubt on many others.

The consideration of position-dependent and nonlinear heat transfer processes leads to differential equations for which no general analytical method of solution is available. Numerical methods of evaluation must be resorted to and approximate solutions are obtained. However, any general property of optimal solutions can serve as an accuracy check on approximate solutions, and more usefully, as a necessary condition suitable for the elimination of variables. If a necessary condition can be applied in the analysis, the search for an optimum is reduced in scope by one dimension. In the following two sections, a general necessary condition of optimal solutions to a problem of finned duct assemblies is derived.

[1]Principal Research Scientist, Division of Energy Technology, Commonwealth Scientific and Industrial Research Organization, Highett, Victoria, Australia 3190

Contributed by the Heat Transfer Division for publication in the JOURNAL OF HEAT TRANSFER. Manuscript received by the Heat Transfer Division February 25, 1982.

method. The drawback of Zien's method is that it fails to predict a zero speed at the onset of ablation as it should be. Nevertheless, the method has its merits in view of its simplicity and general accuracy.

Acknowledgments

This work was partially supported by U.S. Naval Research Laboratory under the contract ONR N00014-80-C-0888.

References

1 Landau, H. G., "Heat Conduction in A Melting Solid," *Quarterly Applied Math.*, Vol. 8, 1950, pp. 312–319.

2 Goodman, T. R., "The Heat Balance Integral and Its Application to Problems Involving a Change of Phase," *Trans ASME*, Vol. 80, 1958, pp. 335–342.

3 Goodman, T. R., "Integral Methods for Nonlinear Heat Transfer," *Advances in Heat Transfer*, Vol. 1, 1964, pp. 51–122.

4 Altman, M., "Some Aspect of the Melting Solution for A Semi-Infinite Slab," *Chem. Eng'g. Progress Symposium Series*, Vol. 57, 1961, pp. 16–23.

5 Vallerani, E., "Integral Technique Solution to a Class of Simple Ablation Problems," *Meccanica*, Vol. 9, 1964, pp. 94–101.

6 Zien, T. F., "Study of Heat Conduction with Phase Transition Using an Integral Method," *AIAA Progress Astronautics and Aeronautic Thermophysics of Spacecraft and Outer Planet Entry Probes*, Vol. 56, 1977, pp. 87–111.

7 Zien, T. F., "Integral Solutions of Ablation Problems with Time-Dependent Heat Flux," *AIAA J.*, Vol. 16, No. 12, 1978, pp. 1287–1295.

8 Chung, B. T. F., Chang, T. Y., Hsiao, J. S., and Chang, C. I., "Heat Transfer with Ablation in A Half-Space Subjected to Time Variant Heat Fluxes," presented at ASME Winter Annual Meeting, Washington, D.C., 1981, Paper No. 81-WA/HT-34.

9 Chung, B. T. F., Chang, T. Y., Hsiao, J. S., and Chang, C. I., "A Finite Element Analysis of Heat Transfer in Solid with Radiation and Ablation," *Proceedings 7th International Heat Transfer Conference*, Munich, Germany, 1982 (in press).

Optimal Heat Transfer Assemblies With Thin Straight Fins

M. Kovarik[1]

A simple criterion of optimality of finned duct assemblies for heat transfer is defined. A necessary condition of optimality in the defined sense is found for assemblies with straight thin fins. A reduction of design effort resulting from the application of this condition is demonstrated.

Nomenclature

a = scaling parameter, see equation (6)
A = fin cross-sectional area, m^2
B = function expressing boundary condition
c = cost of assembly per unit length of duct, dollar/m
c_0 = cost per unit length of duct, dollar/m
c_1 = cost per unit volume of fin, dollar/m^3
$D_{1,2}$ = constants of integration
h = heat transfer coefficient, W/m^2K
I = integral defined by equation (16)
J = performance index, W/dollar
k = thermal conductivity, W/mK
m = fin parameter, see equation (26), dimensionless
n = number of fins
q = rate of heat loss per unit projected area of fin, W/m^2
Q = heat flux at the root of the fin, per unit length, W/m
s = function prescribing the values of the (ky) product
t = temperature, °C
T_0 = temperature of the tip, °C
T_1 = temperature of the root, °C
v = fin thickness, m
x = width coordinate, dimensionless
X = fin width, m
y = thickness coordinate, dimensionless
Y = fin thickness at root, m
z = fin width coordinate, m

1 Introduction

The design of extended heat transfer surfaces in the shape of fins has been analysed with a view to obtaining the lowest possible mass of heat conducting material for a given heat flux to be transferred from the surface to the environment. The earliest work by Schmidt [1] is concerned with linear heat transfer and uniform coefficient of heat transfer over the entire fin surface, with a constant thermal conductivity of material. Schmidt's results are supported by a more rigorous treatment of the same problem by Le Foll et al. [2]. Duffin [3] recasts the problem into a variational form and confirms that, under the conditions summarised above, the fin of minimum mass is so shaped that its temperature is a linear function of the distance from the tip of the fin.

The more complex problem of optimal fin with a more general temperature dependent heat rejection mode is discussed by Wilkins [4] and a set of solutions for fourth-power radiation heat transfer is given by the same author [5]. References [1–5] restrict attention to the mass of the fin itself, rather than to the broader problem involving the entire finned duct assembly.

Optimal arrangement of heat collecting finned pipes has been studied by the present author [6], the consideration including the cost of both the pipes and the fins, subject to linear uniform heat transfer.

Recent numerical work by Sparrow et al. [7] shows that in fin arrays in a forced convection system the heat transfer coefficient varies along the fin. Their results "demonstrate that the conventional uniform heat transfer coefficient model is inapplicable to shrouded fin arrays". More recently a nonuniform heat transfer coefficient has been reported by Sparrow and Acharya [8] in fins cooled by natural convection.

The recent findings [7, 8] indicate the inapplicability of optimal design results based on uniform heat transfer coefficient to some arrangements of finned ducts, and cast doubt on many others.

The consideration of position-dependent and nonlinear heat transfer processes leads to differential equations for which no general analytical method of solution is available. Numerical methods of evaluation must be resorted to and approximate solutions are obtained. However, any general property of optimal solutions can serve as an accuracy check on approximate solutions, and more usefully, as a necessary condition suitable for the elimination of variables. If a necessary condition can be applied in the analysis, the search for an optimum is reduced in scope by one dimension. In the following two sections, a general necessary condition of optimal solutions to a problem of finned duct assemblies is derived.

[1]Principal Research Scientist, Division of Energy Technology, Commonwealth Scientific and Industrial Research Organization, Highett, Victoria, Australia 3190

Contributed by the Heat Transfer Division for publication in the JOURNAL OF HEAT TRANSFER. Manuscript received by the Heat Transfer Division February 25, 1982.

2 The Problem Formulation

Consider a fin of given profile. Let the fin be straight, i.e., such that its surface is formed by translation of the cross section, as in Fig. 1, along a straight line normal to its plane, and thin so that the heat flow in the fin is in one direction.

With reference to Fig. 1, the dimensionless quantities x and y are defined as

$$x = z/X \tag{1}$$

$$y = v/Y \tag{2}$$

y being the dimensionless thickness of the fin.

The heat is assumed to flow in the x-direction within the fin and leave the surface of the fin with flux density, q; this is assumed to depend in an arbitrary manner on the position, x, and the local temperature, t.

An energy balance on the differential element, dx, of the fin yields

$$\frac{d}{dx}\left(ky\frac{dt}{dx}\right) = X^2 Y^{-1} q(t,x) \tag{3}$$

where k is the thermal conductivity.

The heat transfer process is postulated to be independent of the scale factors X and Y.

With boundary conditions in the form

$$B_0(t, dt/dx) = 0 \tag{4a}$$

$$B_1(t, dt/dx) = 0 \tag{4b}$$

for both ends, equations (3) and (4) represent a second-order boundary value problem.

For any prescribed product $(ky) = s(x)$ and heat flux density $q(t,x)$, the particular integral, if it exists, has the form

$$t = t(a, x, D_1, D_2) \tag{5}$$

where

$$a = X^2 Y^{-1} \tag{6}$$

and the constants D_1 and D_2 correspond to the boundary conditions expressed in equation (4).

The heat flux at the root per unit length of duct is

$$Q = X\int_0^1 q(t,x)\,dx \tag{7}$$

The cross-sectional area of the fin in the x,y-plane

$$A = XY\int_0^1 y\,dx \tag{8}$$

3 Optimization

If the cost of a fin is proportional to its cross-sectional area with the cost per unit volume of material being c_1 and the cost per unit length of the attached duct or pipe c_0, then the cost of unit length of a duct with n identical fins is

$$c = c_0 + c_1 nA \tag{9}$$

A simple performance index which can be defined in the above terms is the quantity of heat flux dissipated by the fins per unit cost of the finned duct assembly for a given temperature at the root of the fin

$$J = nQ/c \tag{10}$$

where Q and c are defined by equations (7) and (9).

An optimal finned duct must have the characteristic dimensions X, Y selected so that J attains its maximum. Necessary conditions for that are

$$\frac{\partial J}{\partial X} = 0 \tag{11}$$

$$\frac{\partial J}{\partial Y} = 0 \tag{12}$$

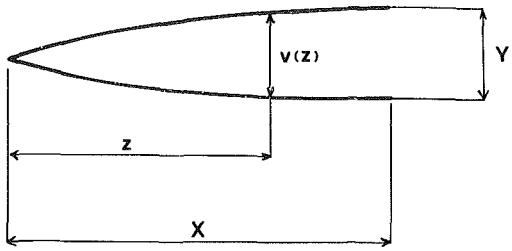

Fig. 1 Coordinate system on a fin

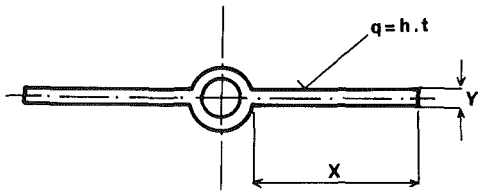

Fig. 2 Rectangular fin

Performing the differentiations on equation (10) after substitutions from equations (7) and (9) yields

$$c^{-2}\left(c\frac{\partial Q}{\partial W} - c_1 nQ\frac{\partial A}{\partial W}\right) = 0 \tag{13}$$

where W stands for either X or Y.

The partial derivatives in equation (13), from equations (7) and (8), are

$$\frac{\partial Q}{\partial X} = QX^{-1} + IX\frac{\partial a}{\partial X} \tag{14}$$

$$\frac{\partial Q}{\partial Y} = IX\frac{\partial a}{\partial Y} \tag{15}$$

where

$$I = \int_0^1 \frac{\partial q}{\partial t}\frac{\partial t}{\partial a}\,dx \tag{16}$$

and

$$\frac{\partial A}{\partial X} = A/X \tag{17}$$

$$\frac{\partial A}{\partial Y} = A/Y \tag{18}$$

From equation (6)

$$\frac{\partial a}{\partial X} = 2aX^{-1} \tag{19}$$

and

$$\frac{\partial a}{\partial Y} = -aY^{-1} \tag{20}$$

so that equation (13) can be written, for the two interpretations of W, as

$$(c_1 nA + c_0)(Q + 2aIX) - c_1 nAQ = 0 \tag{21}$$

$$(c_1 nA + c_0)aIX + c_1 nAQ = 0 \tag{22}$$

From equations (21) and (22) the quantities I and Q can be eliminated leaving an equation for the optimal cross-sectional area

$$A = c_0/(2c_1 n) \tag{23}$$

which may be interpreted as

$$c_0/2 = c_1 nA \tag{24}$$

or the cost of optimal fins is half the cost of the duct. This

result confirms and extends a similar conclusion of previous work [6], where equation (24) was found to apply to two different cases of linear heat transfer on a heat collecting fin of a solar energy absorber.

4 Applications

It is intended to show how the results of sections 2 and 3 extend the existing theory of optimal fins. While the present work is not limited to uniform linear heat transfer, the advance achieved will be seen most clearly on a simple example.

Consider a pipe with two fins of rectangular profile as on Fig. 2, transferring heat uniformly on both sides to an environment of temperature 0. Let the root temperature of the fin be T_1, with other parameters being identified below

$$n=2, \qquad A=XY, \qquad q(x,t)=2ht$$

Total heat flux at the root per unit length is then, from equation (7) and as given in reference [9]

$$Q=2hT_1X\,m^{-1}\tanh m \tag{25}$$

where

$$m=X(2h/kY)^{1/2} \tag{26}$$

By equation (23), the optimal cross-sectional area, A, is a constant, given by the cost parameters c_0, c_1; therefore, the differentiation indicated by equation (11) applies only to the numerator of J and the outcome is, as in reference [9], a necessary condition of optimality

$$\tanh \quad m=3m\cosh^{-2}m \tag{27}$$

which can be written as

$$\sinh(2m)=6m \tag{28}$$

The root of this equation is 1.419, so that the thickness of the optimal fin is, from equation (26)

$$Y=0.977\,(A^2h/k)^{1/3} \tag{29}$$

where A is given by equation (23).

Earlier results [9] enable the determination of optimal Y for a given X. By contrast, equations (23) and (29) determine Y from the cost factors; the width X follows from $A = XY$.

Earlier results permit the verification of optimal *proportions* (X/Y) of a rectangular fin by measurement of tip and root temperature excess over the ambient. These are, according to [9], related by

$$T_0=0.457\,T_1$$

As there are two independent *dimensions* (X, Y), an additional condition is required for the verification of optimality in the sense of the present problem. This condition is provided by equation (24).

5 Conclusion

An optimal finned duct assembly, maximizing the performance index of equation (10) and utilizing thin straight fins, can be designed on the basis of analysis presented in sections 2 and 3. Whereas earlier work sought the optimal proportion X/Y of a fin, the present findings relate to the two discrete dimensions, X and Y, which satisfy the optimality conditions, equations (11) and (12), of the finned duct assembly. Where the temperature distribution in the fin is known, the additional necessary condition of optimality is sufficient for the complete verification of optimality of existing assemblies. This was shown in section 4.

If the cost factors, c_1 and c_0, are interpreted as density of the fin material and weight per unit length of duct, respectively, the resulting optimal design is one of minimum mass of the assembly.

The theory applies to systems with locally nonuniform heat transfer with arbitrary dependence on surface temperature.

The assumption that the heat flux density, q, depends only on the local temperature, t, and relative position, x, restricts the validity of the present result to situations where the similarity of the heat flux field remains preserved while the dimensions, X and Y, vary in the neighborhood of the optimal configuration. Where this similarity holds only approximately, the conclusions apply to a degree of approximation which is, at this stage, still unknown. The same restriction applies to earlier theories of optimal fins.

Acknowledgment

The author is indebted to his colleagues P. F. Lesse and P. J. Banks for helpful discussions and to N. Stokes for a suggestion which simplified the presentation.

References

1 Schmidt, E., "Die Waermeuebertragung durch Rippen," *Zeitschrift des Vereines Deutscher Ingenieure*, Vol. 70, 1926, pp. 885–889.

2 Le Foll, J., Gellin, P., and de Robert, E., "Heat Transfer from Longitudinally Finned Cartridges," *Proceedings of the Second United Nations International Conference on the Peaceful Uses of Atomic Energy*, United Nations, Geneva, Vol. 7, 1958, pp. 701–716.

3 Duffin, R. J., "A Variational Problem Relating to Cooling Fins," *Journal of Mathematics and Mechanics*, Vol. 8, 1959, pp. 47–56.

4 Wilkins, J. E., Jr., "Minimum-Mass Thin Fins and Constant Temperature Gradients," *Journal of Society for Industrial and Applied Mathematics*, Vol. 10, No. 1, 1962, pp. 62–73.

5 Wilkins, J. E., Jr., "Minimum Mass Thin Fins for Space Radiators," *Proceedings of the 1960 Heat Transfer and Fluid Mechanics Institute*, Stanford University, 1960, pp. 229–243.

6 Kovarik, M., "Optimal Distribution of Heat Conducting Material in the Finned Pipe Solar Energy Collector," *Solar Energy*, Vol. 2, 1978, pp. 477–484.

7 Sparrow, E. M., Baliga, B. R., and Patankar, S. V., "Forced Convection Heat Transfer from a Shrouded Fin Array with and without Tip Clearance," ASME JOURNAL OF HEAT TRANSFER, Vol. 100, 1978, pp. 572–579.

8 Sparrow, E. M., and Acharya, S., "A Natural Convection Fin with a Solution Determined Non-Monotonically Varying Heat Transfer Coefficient," ASME JOURNAL OF HEAT TRANSFER, Vol. 103, 1981, pp. 218–225.

9 Eckert, E. R. G., and Drake, R. M., Jr., *Analysis of Heat and Mass Transfer*, McGraw-Hill, 1972.

Transient Response of Circular Pins

H. S. Chu,[1] C. K. Chen,[1] and C. I. Weng[1]

Nomenclature

- a = radius of the pin
- Bi = Biot number = ha/κ
- L = length of the pin
- q_0^* = heat flux at base of the pin
- $\dot{q}_0$ = dimensionless base heat flux = $q_0^* L/(T_b - T_\infty)$
- q^* = heat flux transferred to the surroundings
- $\dot{q}_f$ = dimensionless heat flux transferred to the surroundings = $q^*L/\kappa(T_b - T_\infty)$
- r^*, z^* = coordinate system
- r, z = dimensionless coordinates = r^*/L, z^*/L
- T_b = base temperature
- T_∞ = ambient temperature
- β = hL/κ

[1] Department of Mechanical Engineering, National Cheng Kung University, Tainan, Taiwan

Contributed by the Heat Transfer Division for publication in the JOURNAL OF HEAT TRANSFER. Manuscript received by the Heat Transfer Division September 29, 1981.

result confirms and extends a similar conclusion of previous work [6], where equation (24) was found to apply to two different cases of linear heat transfer on a heat collecting fin of a solar energy absorber.

4 Applications

It is intended to show how the results of sections 2 and 3 extend the existing theory of optimal fins. While the present work is not limited to uniform linear heat transfer, the advance achieved will be seen most clearly on a simple example.

Consider a pipe with two fins of rectangular profile as on Fig. 2, transferring heat uniformly on both sides to an environment of temperature 0. Let the root temperature of the fin be T_1, with other parameters being identified below

$$n=2, \qquad A=XY, \qquad q(x,t)=2ht$$

Total heat flux at the root per unit length is then, from equation (7) and as given in reference [9]

$$Q=2hT_1X\,m^{-1}\tanh m \tag{25}$$

where

$$m=X(2h/kY)^{1/2} \tag{26}$$

By equation (23), the optimal cross-sectional area, A, is a constant, given by the cost parameters c_0, c_1; therefore, the differentiation indicated by equation (11) applies only to the numerator of J and the outcome is, as in reference [9], a necessary condition of optimality

$$\tanh \quad m=3m\cosh^{-2}m \tag{27}$$

which can be written as

$$\sinh(2m)=6m \tag{28}$$

The root of this equation is 1.419, so that the thickness of the optimal fin is, from equation (26)

$$Y=0.977\,(A^2h/k)^{1/3} \tag{29}$$

where A is given by equation (23).

Earlier results [9] enable the determination of optimal Y for a given X. By contrast, equations (23) and (29) determine Y from the cost factors; the width X follows from $A = XY$.

Earlier results permit the verification of optimal *proportions* (X/Y) of a rectangular fin by measurement of tip and root temperature excess over the ambient. These are, according to [9], related by

$$T_0=0.457\,T_1$$

As there are two independent *dimensions* (X, Y), an additional condition is required for the verification of optimality in the sense of the present problem. This condition is provided by equation (24).

5 Conclusion

An optimal finned duct assembly, maximizing the performance index of equation (10) and utilizing thin straight fins, can be designed on the basis of analysis presented in sections 2 and 3. Whereas earlier work sought the optimal proportion X/Y of a fin, the present findings relate to the two discrete dimensions, X and Y, which satisfy the optimality conditions, equations (11) and (12), of the finned duct assembly. Where the temperature distribution in the fin is known, the additional necessary condition of optimality is sufficient for the complete verification of optimality of existing assemblies. This was shown in section 4.

If the cost factors, c_1 and c_0, are interpreted as density of the fin material and weight per unit length of duct, respectively, the resulting optimal design is one of minimum mass of the assembly.

The theory applies to systems with locally nonuniform heat transfer with arbitrary dependence on surface temperature.

The assumption that the heat flux density, q, depends only on the local temperature, t, and relative position, x, restricts the validity of the present result to situations where the similarity of the heat flux field remains preserved while the dimensions, X and Y, vary in the neighborhood of the optimal configuration. Where this similarity holds only approximately, the conclusions apply to a degree of approximation which is, at this stage, still unknown. The same restriction applies to earlier theories of optimal fins.

Acknowledgment

The author is indebted to his colleagues P. F. Lesse and P. J. Banks for helpful discussions and to N. Stokes for a suggestion which simplified the presentation.

References

1 Schmidt, E., "Die Waermeuebertragung durch Rippen," *Zeitschrift des Vereines Deutscher Ingenieure*, Vol. 70, 1926, pp. 885–889.

2 Le Foll, J., Gellin, P., and de Robert, E., "Heat Transfer from Longitudinally Finned Cartridges," *Proceedings of the Second United Nations International Conference on the Peaceful Uses of Atomic Energy*, United Nations, Geneva, Vol. 7, 1958, pp. 701–716.

3 Duffin, R. J., "A Variational Problem Relating to Cooling Fins," *Journal of Mathematics and Mechanics*, Vol. 8, 1959, pp. 47–56.

4 Wilkins, J. E., Jr., "Minimum-Mass Thin Fins and Constant Temperature Gradients," *Journal of Society for Industrial and Applied Mathematics*, Vol. 10, No. 1, 1962, pp. 62–73.

5 Wilkins, J. E., Jr., "Minimum Mass Thin Fins for Space Radiators," *Proceedings of the 1960 Heat Transfer and Fluid Mechanics Institute*, Stanford University, 1960, pp. 229–243.

6 Kovarik, M., "Optimal Distribution of Heat Conducting Material in the Finned Pipe Solar Energy Collector," *Solar Energy*, Vol. 2, 1978, pp. 477–484.

7 Sparrow, E. M., Baliga, B. R., and Patankar, S. V., "Forced Convection Heat Transfer from a Shrouded Fin Array with and without Tip Clearance," ASME JOURNAL OF HEAT TRANSFER, Vol. 100, 1978, pp. 572–579.

8 Sparrow, E. M., and Acharya, S., "A Natural Convection Fin with a Solution Determined Non-Monotonically Varying Heat Transfer Coefficient," ASME JOURNAL OF HEAT TRANSFER, Vol. 103, 1981, pp. 218–225.

9 Eckert, E. R. G., and Drake, R. M., Jr., *Analysis of Heat and Mass Transfer*, McGraw-Hill, 1972.

Transient Response of Circular Pins

H. S. Chu,[1] C. K. Chen,[1] and C. I. Weng[1]

Nomenclature

- a = radius of the pin
- Bi = Biot number = ha/κ
- L = length of the pin
- q_0^* = heat flux at base of the pin
- $\dot{q}_0$ = dimensionless base heat flux = $q_0^* L/(T_b - T_\infty)$
- q^* = heat flux transferred to the surroundings
- $\dot{q}_f$ = dimensionless heat flux transferred to the surroundings = $q^*L/\kappa(T_b - T_\infty)$
- r^*, z^* = coordinate system
- r, z = dimensionless coordinates = r^*/L, z^*/L
- T_b = base temperature
- T_∞ = ambient temperature
- β = hL/κ

[1] Department of Mechanical Engineering, National Cheng Kung University, Tainan, Taiwan

Contributed by the Heat Transfer Division for publication in the JOURNAL OF HEAT TRANSFER. Manuscript received by the Heat Transfer Division September 29, 1981.

γ = L/a
θ = dimensionless temperature = $(T - T_\infty)/(T_b - T_\infty)$
$\tilde{\theta}$ = Laplace transform of $\theta = \int_0^\infty \theta e^{-st} dt$
τ = dimensionless time = $\alpha t/L^2$
η = dimensionless temperature = $\kappa(T - T_\infty)/q_0^* L$
ν_n = $\sqrt{\xi_n^2\gamma^2 + s}$

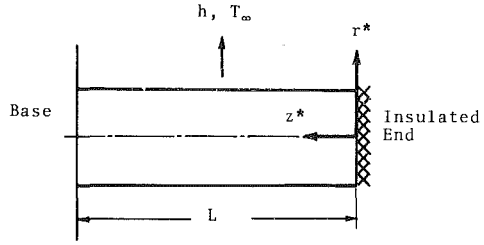

Fig. 1 Configuration of pin

Introduction

The performance of the various forms of fin under steady-state condition has been studied in great detail as shown in [1] and [2]. Chapman [3] first investigated the transient response of an annular fin with uniform thickness subjected to a step change of base temperature, and Suryanarayana [4] applied the method of Laplace transformation to examine the transient behavior of straight fins with the various base boundary conditions. However, both of their methods were confined to one-dimensional analysis. In fact, Irey [5] had shown that the error resulting from the one-dimensional approximation is significant and should not be ignored for the case of large Biot number. The purpose of this paper is to study the transient response of the pin with constant cross section, which is subjected to a constant base temperature or constant heat flux based on a two-dimensional analysis. The solution in a double series form is obtained by utilizing the Laplace transformation technique and the method of separation variables.

Analysis

The configuration of the pin is shown in Fig. 1. The analysis is based on the following assumptions: (*a*) the heat transfer coefficient of the ambient fluid, h, is constant, (*b*) all the physical properties are considered as constant, (*c*) the pin is initially at the ambient temperature, T_∞, (*d*) there is no heat source or sink in the pin, (*e*) the pin is insulated at one end ($z^* = 0$), and (*f*) the temperature distribution in the pin is axisymmetric.

Constant Base Temperature. The governing differential equation for the temperature distribution in the pin and its associated initial and boundary conditions in dimensionless form are

$$\frac{\partial^2\theta}{\partial r^2} + \frac{1}{r}\frac{\partial\theta}{\partial r} + \frac{\partial^2\theta}{\partial z^2} = \frac{\partial\theta}{\partial\tau} \tag{1}$$

$\tau = 0 \quad \theta = 0$

$\tau > 0 \quad r = 0 \quad \theta =$ a finite value

$$r = \frac{1}{\gamma} \quad \frac{\partial\theta}{\partial r} = -\beta\theta \tag{2}$$

$$z = 0 \quad \frac{\partial\theta}{\partial z} = 0, \; z = 1 \; \theta = 1$$

After taking Laplace transform with respect to time, the solution in the transformed plane is given by

$$\tilde{\theta} = \sum_{n=1}^{\infty} \frac{2\mathrm{Bi}\, J_0(\xi_n\gamma r)}{(\xi_n^2 + \mathrm{Bi}^2)J_0(\xi_n)} \cdot \frac{\cosh(\sqrt{\xi_n^2\gamma^2 + s}\cdot z)}{s\cdot\cosh(\sqrt{\xi_n^2\gamma^2 + s})} \tag{3}$$

where ξ_n is the nth root of the equation

$$\xi J_1(\xi) - \mathrm{Bi} J_0(\xi) = 0 \tag{4}$$

The inverse transform of equation (3) is

$$\theta = \sum_{n=1}^{\infty} \frac{2\mathrm{Bi}\, J_0(\xi_n\gamma r)}{(\xi_n^2 + \mathrm{Bi}^2)J_0(\xi_n)} \cdot \left\{ \frac{\cosh(\xi_n\gamma z)}{\cosh(\xi_n\gamma)} + \sum_{k=1}^{\infty} \frac{(-1)^k(2k-1)\pi \quad e^{-\left[\xi_n^2\gamma^2 + \frac{(2k-1)^2\pi^2}{4}\right]\tau} \cdot \cos\frac{(2k-1)}{2}\pi z}{\xi_n^2\gamma^2 + (2k-1)^2\pi^2/4} \right\} \tag{5}$$

The convergence of this series is quite slow for small τ. In order to get a better estimation of temperature distribution for small τ, it is desirable to find a more rapidly convergent solution. From equation (3), for large values of s, we have

$$\tilde{\theta} = \sum_{n=1}^{\infty} \frac{2\mathrm{Bi} J_0(\xi_n\gamma r)}{(\xi_n^2 + \mathrm{Bi}^2)J_0(\xi_n)} \cdot \frac{1}{s}\{e^{-\nu_n(1-z)} + e^{-\nu_n(1+z)} - e^{-\nu_n(3-z)} - e^{-\nu_n(3+z)}\} \tag{6}$$

From the Duhamel formula, one obtains

$$L^{-1}\left\{\frac{e^{-f(z)\cdot\sqrt{\xi_n^2\gamma^2+s}}}{s}\right\} = \int_0^\tau e^{-\xi_n^2\gamma^2 t} \cdot L^{-1}\{e^{-f(z)\cdot\sqrt{s}}\}dt \tag{7}$$

The term $e^{-\xi_n^2\gamma^2 t}$ in the integral of equation (7) can be replaced by its integrated mean value $1/\tau\int_0^\tau e^{-\xi_n^2\gamma^2 t}dt$. For the applicable range of τ, it can be determined by the following criterion

$$\left| \frac{\left(\frac{1 - e^{\xi_n^2\gamma^2\tau}}{\xi_n^2\gamma^2\tau}\right) - e^{-\xi_n^2\gamma^2\tau}}{e^{-\xi_n^2\gamma^2\tau}} \right| < 1 \text{ percent}$$

The inverse transform of equation (6) for small time is then given by

$$\theta = \sum_{n=1}^{\infty} \frac{2\mathrm{Bi}\, J_0(\xi_n\gamma r)}{(\xi_n^2 + \mathrm{Bi}^2)J_0(\xi_n)} \cdot \frac{1 - e^{-\xi_n^2\gamma^2\tau}}{\xi_n^2\gamma^2\tau} \cdot \left\{\mathrm{erfc}\left(\frac{1-z}{2\sqrt{\tau}}\right) + \mathrm{erfc}\left(\frac{1+z}{2\sqrt{\tau}}\right) - \mathrm{erfc}\left(\frac{3-z}{2\sqrt{\tau}}\right) - \mathrm{erfc}\left(\frac{3+z}{2\sqrt{\tau}}\right)\right\} \tag{8}$$

For a set of given values of Bi, γ, τ, the ratio of first term ($n = 1$) to the second term ($n = 2$), R_{12}, is usually larger than 10, and the ratio of the first term to the third and the fourth are $R_{13} > 30$ and $R_{14} > 100$, respectively. Hence, we can conclude that the first term ($n = 1$) in equation (8) will govern the temperature distribution for the case of small τ. Same argument is also valid for equation (5). Therefore, the first term is the dominant term.

The pin has reached the steady state if the first term in equation (5) reaches 99 percent or over of its steady-state value. By this definition, the time for the pin to reach steady-state τ_{st} can be obtained from equation (5); that is,

$$\tau_{st} = \frac{4}{4\xi_1^2\gamma^2 + \pi^2} \cdot \ln\left\{\frac{400\pi\cosh(\xi_1\gamma)}{4\xi_1^2\gamma^2 + \pi^2}\right\} \tag{9}$$

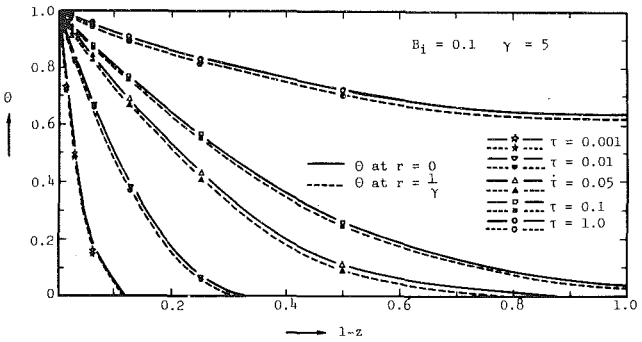

Fig. 2 Step change in temperature for the case of $B_i = 0.1$ and $\gamma = 5$

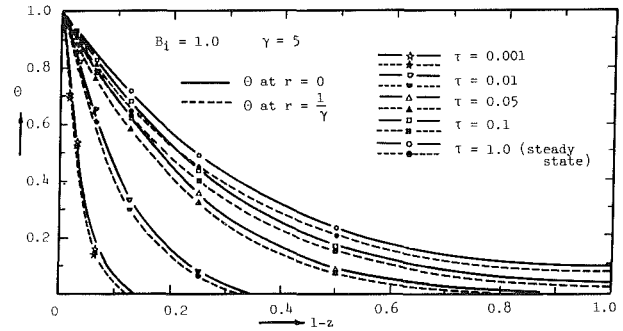

Fig. 3 Step change in temperature for the case of $B_i = 1.0$ and $\gamma = 5$

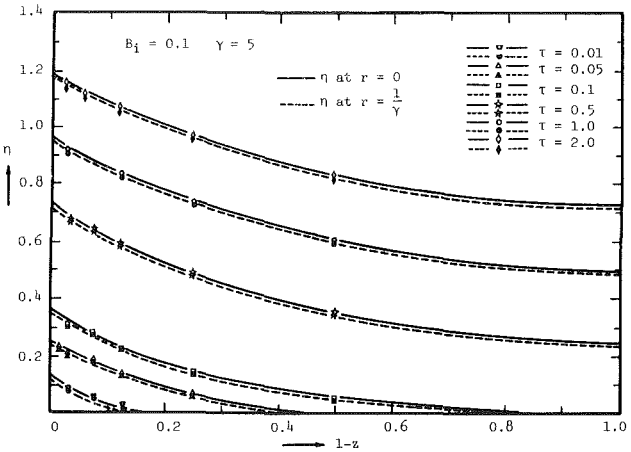

Fig. 4 Step change in heat flux for the case of $B_i = 0.1$ and $\gamma = 5$

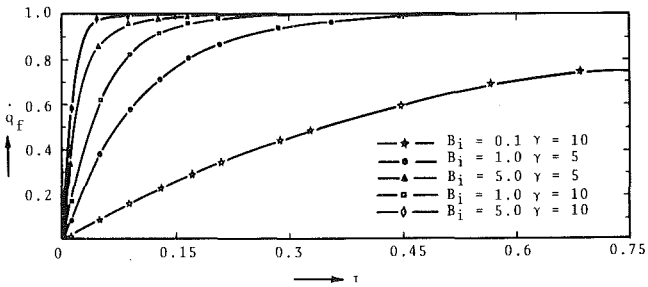

Fig. 5 Heat fluxes for the case of step change in base heat flux

The nondimensional base flux can be obtained as

$$\dot{q}_0 = \sum_{n=1}^{\infty} \frac{2\mathrm{Bi}^2}{\xi_n^2\gamma^2(\xi_n^2+\mathrm{Bi}^2)}\left\{\frac{\xi_n\gamma\sinh(\xi_n\gamma)}{\cosh(\xi_n\gamma)} + \sum_{k=1}^{\infty}\frac{(2k-1)^2\pi^2 e^{-[\xi_n^2\gamma^2+(2k-1)^2\pi^2/4]\tau}}{2\,\xi_n^2\gamma^2+(2k-1)^2\pi^2/4}\right\} \tag{10}$$

The actual heat flux transferred from the pin to the surroundings is

$$\dot{q}_f = \sum_{n=1}^{\infty}\frac{2\mathrm{Bi}^2}{(\xi_n^2+\mathrm{Bi}^2)}\left\{\frac{\sinh(\xi_n\gamma)}{\xi_n\gamma\cosh(\xi_n\gamma)} + \sum_{k=1}^{\infty}\frac{2\,e^{-(\xi_n^2\gamma^2+(2k-1)^2\pi^2/4)\tau}}{\xi_n^2\gamma^2+(2k-1)^2\pi^2/4}\right\}. \tag{11}$$

In equations (10) and (11), it is seen that the value of $\dot{q}_0$ will be exactly equal to that of $\dot{q}_f$ as the value of τ approaches infinity. In fact, this result is a very reasonable one, and is readily understandable.

As before, to find other equations which converge more rapidly for the case of small τ, we can obtain

$$\dot{q}_0 = \sum_{n=1}^{\infty}\frac{2\mathrm{Bi}(1-e^{-\xi_n^2\gamma^2\tau})}{(\xi_n^2+\mathrm{Bi}^2)\xi_n^4\gamma^4\tau^{3/2}\sqrt{\pi}}\cdot\left\{1-2e^{-\frac{1}{\tau}}+e^{-\frac{4}{\tau}}\right\} \tag{12}$$

$$\dot{q}_f = \sum_{n=1}^{\infty}\frac{4\,\mathrm{Bi}^2\sqrt{\tau}}{(\xi_n^2+\mathrm{Bi}^2)}\cdot\frac{1-e^{-\xi_n^2\gamma^2\tau}}{\xi_n^2\gamma^2\tau}\cdot\left\{\frac{1}{\sqrt{\pi}}-\frac{2}{\sqrt{\pi}}e^{-\frac{1}{\tau}} + \frac{1}{\sqrt{\pi}}e^{-\frac{4}{\tau}}-\frac{2}{\sqrt{\pi}}\mathrm{erf}\left(\frac{1}{\sqrt{\tau}}\right)+\frac{2}{\sqrt{\tau}}\mathrm{erf}\left(\frac{2}{\sqrt{\tau}}\right)\right\} \tag{13}$$

Constant Base Heat Flux. The nondimensional equation and the corresponding initial and boundary conditions are the same as equation (1), except the last boundary condition is replaced by

$$z = 1 \qquad \frac{\partial\eta}{\partial z} = 1$$

By the same procedures as shown in equations (1-13) we get the solution

$$\eta = \sum_{n=1}^{\infty}\frac{2\mathrm{Bi}\,J_0(\xi_n\gamma r)}{(\xi_n^2+\mathrm{Bi}^2)J_0(\xi_n)}\cdot\left\{\frac{\cosh(\xi_n\gamma z)}{\xi_n\gamma\sinh(\xi_n\gamma)}-\frac{e^{-\xi_n^2\gamma^2\tau}}{\xi_n^2\gamma^2} + \sum_{k=1}^{\infty}\frac{2(-1)^{k+1}e^{-(\xi_n^2\gamma^2+k^2\pi^2)\tau}\cdot\cos(k\pi z)}{\xi_n^2\gamma^2+k^2\pi^2}\right\} \tag{14}$$

As before, we can find a more rapidly converging solution for small value of τ.

$$\eta = \sum_{n=1}^{\infty}\frac{2\mathrm{Bi}\,J_0(\xi_n\gamma r)}{(\xi_n^2+\mathrm{Bi}^2)J_0(\xi_n)}\cdot\frac{1-e^{-\xi_n^2\gamma^2\tau}}{\xi_n^2\gamma^2\tau}\cdot\left\{2\sqrt{\frac{\tau}{\pi}}\cdot(e^{-(1-z)^2/4\tau} + e^{-(1+z)^2/4\tau}+e^{-(3-z)^2/4\tau}+e^{-(3+z)^2/4\tau} - (1+z)\,\mathrm{erfc}\left(\frac{1+z}{2\sqrt{\tau}}\right)-(1-z)\,\mathrm{erfc}\left(\frac{1-z}{2\sqrt{\tau}}\right) - (3-z)\,\mathrm{erfc}\left(\frac{3-z}{2\sqrt{\tau}}\right)-(3+z)\,\mathrm{erfc}\left(\frac{3+z}{2\sqrt{\tau}}\right)\right\} \tag{15}$$

The criterion for the pin to attain steady state is

$$\tau_{st} = \frac{1}{\xi_1^2\gamma^2}\,ln\left\{\frac{100\sinh(\xi_1\gamma)}{\xi_1\gamma}\right\} \tag{16}$$

From equation (14), we can calculate the rate of heat transferred to the surroundings

$$\dot{q}_f = \dot{q}_0\sum_{n=1}^{\infty}\frac{4\mathrm{Bi}^2}{(\xi_n^2+\mathrm{Bi}^2)\xi_n^2}(1-e^{-\xi_n^2\gamma^2\tau}) \tag{17}$$

As τ approaches ∞, $\dot{q}_f$ and $\dot{q}_0$ will have exactly the same value.

From equation (15)

$$\dot{q}_f = \dot{q}_0 \sum_{n=1}^{\infty} \left\{ \frac{8\mathrm{Bi}^2}{(\xi_n^2 + \mathrm{Bi}^2)} \frac{1 - e^{-\xi_n^2 \gamma^2 \tau}}{\xi_n^2 \gamma^2 \tau} \left(\mathrm{erf}\left(\frac{2}{\sqrt{\tau}}\right) - 2\mathrm{ECI}\left(\frac{2}{\sqrt{\tau}}\right)\right)\right\} \tag{18}$$

where $\mathrm{ECI}(x) = \int_0^x t \cdot \mathrm{erfc}(t) \cdot dt$

Conclusions

We have performed a series of calculations for different values of Biot number. Typical results are presented in Figs. 2, 3, and 4. It is shown that the greater the value of the Biot number, the larger the net difference of temperature between center line and surface is. For the case of Bi = 5, γ = 5, the temperature difference will increase 25–35 percent, a fact which certainly cannot be neglected. Therefore, we can conclude that when the Biot number is not small, the approximate results obtained from one-dimensional analysis are no longer satisfactory. Quantitatively, the threshold value of the Biot number in a two-dimensional analysis is around 1.0, correspondingly to an error of less than 10 percent. The above conclusions are similar for both the cases of step change in base temperature and in base heat flux.

The time needed for the actual heat flux, $\dot{q}_f$, to become equal to the base flux, $\dot{q}_0$, is shown in the Fig. 5. It is apparent that the transient to steady state is shorter as Bi becomes larger.

References

1 Harper, W. B., and Brown, D. R., "Mathematical Equations for Heat Conduction in the Fins of Air Cooled Engines," NACA Report No. 158, 1922, pp. 679–708.

2 Gardner, K. A., "Efficiency of Extended Surface," ASME JOURNAL OF HEAT TRANSFER, Series C, Vol. 67, 1945, pp. 621–631.

3 Chapman, A. J., "Transient Heat Conduction in Annular Fins of Uniform Thickness," *Chemical Engineering Symposium Series*, Vol. 55, No. 29, 1959, pp. 195–201.

4 Suryanarayana, N. Y., "Transient Response of Straight Fins," ASME JOURNAL OF HEAT TRANSFER, Series C, Vol. 97, 1975, pp. 417–423.

5 Irey, R. K., "Errors in the One-Dimensional Fin Solution," ASME JOURNAL OF HEAT TRANSFER, Series C, Vol. 90, 1968, pp. 175–176.

The Thermal Resistance of an Insulating Slab Penetrated by Metal Rods[1]

L. W. Hunter[2] and S. Favin[2]

Introduction

In many practical situations, a slab of an insulating material heated from one side is penetrated by metal rods (see Fig. 1). Water pipes, reinforcing rods, conduits, and electric cables, for example, frequently pass through walls of buildings. Then it is often desired to understand the metal's effect on the heat flow through the wall. The heat flow is an important factor in the cost of heating and cooling the building. The metal also lessens the fire resistance of the wall. Figure 1 may also be considered as a "fin" problem where the rods (fins) create an "extended surface" that increases the heat transfer.

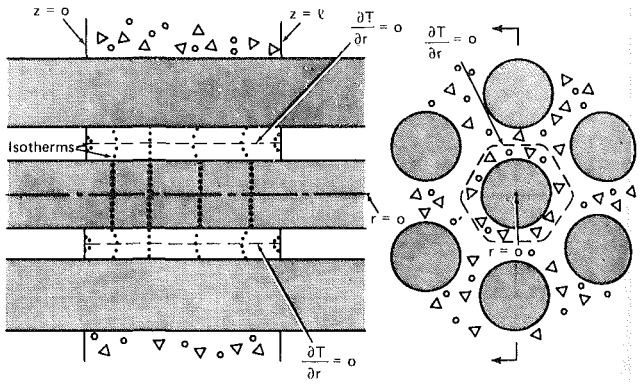

Fig. 1 Metal rods penetrating a slab

Our representative model is an array of equally sized, equally spaced metal rods through a slab heated from one side. We assume a steady state has been reached.

Two features of the model simplify the physical picture. First, the temperature in each rod is radially constant, due to the high thermal conductivity of the rod. Secondly, between each rod and its nearest neighbors is a surface where the radial heat flux is zero ($\partial T/\partial r = 0$) as shown qualitatively in Fig. 1. Since the rods are equivalent and uniformly spaced, a useful starting approximation is that the no-flux surface is a cylinder of radius equal to one-half the distance between nearest neighbor rods ($r = b$). These simplifications allow us to focus on one rod enclosed by an annulus of slab whose curved surface is insulated. For an irregular array of unequal rods, the surface $\partial T/\partial r = 0$ would not resemble the surface of a cylinder but our model could still provide conservative estimates.

Results of representative numerical calculations show how the backface temperature of the slab is affected by the geometry and thermal properties of the penetration and the heating intensity. A simple formula is found to be accurate over a wide range of practical conditions.

The Governing Equations

The slab and rod temperatures are governed by equations which describe radial (r) and axial (z) heat conduction in the slab coupled to axial conduction in the rod. The boundary conditions describe convective heat exchanges with the rooms and perfect thermal contact between the rod and the slab. To distinguish among the four regions of the problem, the hot room is labeled, 1, the cold room, 2, the rod, 3, and the slab has no label. The differential equations are

$$\frac{d^2 T_3}{dz^2} = \begin{cases} -\dfrac{2H_1}{ak_3}(T_1 - T_3), & \text{for } z<0, \quad (1) \\ -\dfrac{2k}{ak_3}\dfrac{\partial T}{\partial r}, & \text{for } 0<z<l, \quad r=a, \quad (2) \\ \dfrac{2H_2}{ak_3}(T_3 - T_2), & \text{for } l<z \quad (3) \end{cases}$$

and

$$\frac{\partial^2 T}{\partial z^2} + \frac{1}{r}\frac{\partial}{\partial r}\left(r\frac{\partial T}{\partial r}\right) = 0, \qquad \text{for } 0<z<l, \quad a<r<b \quad (4)$$

Here, a is the rod radius, l is the slab thickness, H is a heat

[1] Supported by the U.S. Nuclear Regulatory Commission

[2] The Johns Hopkins University, Applied Physics Laboratory, Laurel, Md. 20707

Contributed by the Heat Transfer Division for publication in the JOURNAL OF HEAT TRANSFER. Manuscript received by the Heat Transfer Division January 13, 1982.

As τ approaches ∞, $\dot{q}_f$ and $\dot{q}_0$ will have exactly the same value.

From equation (15)

$$\dot{q}_f = \dot{q}_0 \sum_{n=1}^{\infty} \left\{ \frac{8\mathrm{Bi}^2}{(\xi_n^2 + \mathrm{Bi}^2)} \frac{1 - e^{-\xi_n^2 \gamma^2 \tau}}{\xi_n^2 \gamma^2 \tau} \left(\mathrm{erf}\left(\frac{2}{\sqrt{\tau}}\right) - 2\mathrm{ECI}\left(\frac{2}{\sqrt{\tau}}\right)\right)\right\} \tag{18}$$

where $\mathrm{ECI}(x) = \int_0^x t \cdot \mathrm{erfc}(t) \cdot dt$

Conclusions

We have performed a series of calculations for different values of Biot number. Typical results are presented in Figs. 2, 3, and 4. It is shown that the greater the value of the Biot number, the larger the net difference of temperature between center line and surface is. For the case of Bi = 5, γ = 5, the temperature difference will increase 25–35 percent, a fact which certainly cannot be neglected. Therefore, we can conclude that when the Biot number is not small, the approximate results obtained from one-dimensional analysis are no longer satisfactory. Quantitatively, the threshold value of the Biot number in a two-dimensional analysis is around 1.0, correspondingly to an error of less than 10 percent. The above conclusions are similar for both the cases of step change in base temperature and in base heat flux.

The time needed for the actual heat flux, $\dot{q}_f$, to become equal to the base flux, $\dot{q}_0$, is shown in the Fig. 5. It is apparent that the transient to steady state is shorter as Bi becomes larger.

References

1 Harper, W. B., and Brown, D. R., "Mathematical Equations for Heat Conduction in the Fins of Air Cooled Engines," NACA Report No. 158, 1922, pp. 679–708.

2 Gardner, K. A., "Efficiency of Extended Surface," ASME JOURNAL OF HEAT TRANSFER, Series C, Vol. 67, 1945, pp. 621–631.

3 Chapman, A. J., "Transient Heat Conduction in Annular Fins of Uniform Thickness," *Chemical Engineering Symposium Series*, Vol. 55, No. 29, 1959, pp. 195–201.

4 Suryanarayana, N. Y., "Transient Response of Straight Fins," ASME JOURNAL OF HEAT TRANSFER, Series C, Vol. 97, 1975, pp. 417–423.

5 Irey, R. K., "Errors in the One-Dimensional Fin Solution," ASME JOURNAL OF HEAT TRANSFER, Series C, Vol. 90, 1968, pp. 175–176.

The Thermal Resistance of an Insulating Slab Penetrated by Metal Rods[1]

L. W. Hunter[2] and S. Favin[2]

Introduction

In many practical situations, a slab of an insulating material heated from one side is penetrated by metal rods (see Fig. 1). Water pipes, reinforcing rods, conduits, and electric cables, for example, frequently pass through walls of buildings. Then it is often desired to understand the metal's effect on the heat flow through the wall. The heat flow is an important factor in the cost of heating and cooling the building. The metal also lessens the fire resistance of the wall. Figure 1 may also be considered as a "fin" problem where the rods (fins) create an "extended surface" that increases the heat transfer.

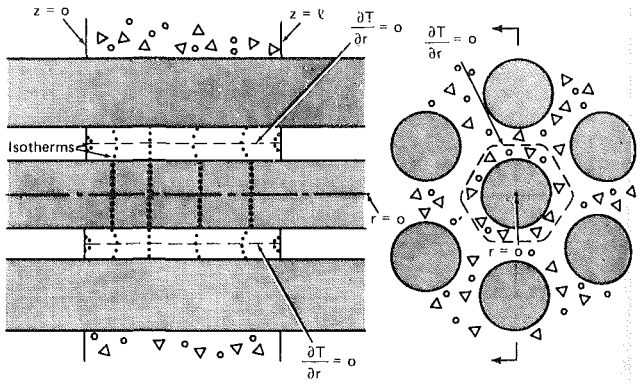

Fig. 1 Metal rods penetrating a slab

Our representative model is an array of equally sized, equally spaced metal rods through a slab heated from one side. We assume a steady state has been reached.

Two features of the model simplify the physical picture. First, the temperature in each rod is radially constant, due to the high thermal conductivity of the rod. Secondly, between each rod and its nearest neighbors is a surface where the radial heat flux is zero ($\partial T/\partial r = 0$) as shown qualitatively in Fig. 1. Since the rods are equivalent and uniformly spaced, a useful starting approximation is that the no-flux surface is a cylinder of radius equal to one-half the distance between nearest neighbor rods ($r = b$). These simplifications allow us to focus on one rod enclosed by an annulus of slab whose curved surface is insulated. For an irregular array of unequal rods, the surface $\partial T/\partial r = 0$ would not resemble the surface of a cylinder but our model could still provide conservative estimates.

Results of representative numerical calculations show how the backface temperature of the slab is affected by the geometry and thermal properties of the penetration and the heating intensity. A simple formula is found to be accurate over a wide range of practical conditions.

The Governing Equations

The slab and rod temperatures are governed by equations which describe radial (r) and axial (z) heat conduction in the slab coupled to axial conduction in the rod. The boundary conditions describe convective heat exchanges with the rooms and perfect thermal contact between the rod and the slab. To distinguish among the four regions of the problem, the hot room is labeled, 1, the cold room, 2, the rod, 3, and the slab has no label. The differential equations are

$$\frac{d^2 T_3}{dz^2} = \begin{cases} -\dfrac{2H_1}{ak_3}(T_1 - T_3), & \text{for } z<0, \quad (1) \\ -\dfrac{2k}{ak_3}\dfrac{\partial T}{\partial r}, & \text{for } 0<z<l, \quad r=a, \quad (2) \\ \dfrac{2H_2}{ak_3}(T_3 - T_2), & \text{for } l<z \quad (3) \end{cases}$$

and

$$\frac{\partial^2 T}{\partial z^2} + \frac{1}{r}\frac{\partial}{\partial r}\left(r\frac{\partial T}{\partial r}\right) = 0, \qquad \text{for } 0<z<l, \quad a<r<b \quad (4)$$

Here, a is the rod radius, l is the slab thickness, H is a heat

[1] Supported by the U.S. Nuclear Regulatory Commission

[2] The Johns Hopkins University, Applied Physics Laboratory, Laurel, Md. 20707

Contributed by the Heat Transfer Division for publication in the JOURNAL OF HEAT TRANSFER. Manuscript received by the Heat Transfer Division January 13, 1982.

transfer coefficient, and k is a thermal conductivity. The boundary conditions on T_3 require that $T_3 \to T_1$ as $z \to -\infty$, $T_3 \to T_2$ as $z \to +\infty$, and that T_3 and dT_3/dz are continuous at $z = 0$ and $z = l$. The boundary conditions on T are

$$-k\frac{\partial T}{\partial z} = H_1(T_1 - T) \qquad \text{at } z=0 \tag{5}$$

$$-k\frac{\partial T}{\partial z} = H_2(T - T_2) \qquad \text{at } z=l \tag{6}$$

$$\frac{\partial T}{\partial r} = 0 \qquad \text{at } r=b \tag{7}$$

and

$$T = T_3 \qquad \text{at } r=a \tag{8}$$

Note that T and T_3 are coupled through equations (2) and (8).

Physical Pictures

Two limits of the solution have very simple mathematical forms:

$$\frac{T_1 - T}{T_1 - T_2} = \frac{z^* + (H_1^*)^{-1}}{1 + (H_1^*)^{-1} + (H_2^*)^{-1}} \qquad \text{for } a << b \tag{9}$$

and

$$\frac{T_1 - T}{T_1 - T_2} = \frac{z^* + \eta_1^{-1}}{1 + \eta_1^{-1} + \eta_2^{-1}} \qquad \text{for } a \to b \tag{10}$$

The definitions of the nondimensional variables here are

$$z^* = z/l \tag{11}$$

$$H_1^* = lH_1/k, \qquad H_2^* = lH_2/k \tag{12}$$

$$\eta_1 = \left(\frac{2aH_1}{k_3}\right)^{1/2}\frac{l}{a}, \qquad \eta_2 = \left(\frac{2aH_2}{k_3}\right)^{1/2}\frac{l}{a} \tag{13}$$

The first limit is the temperature the slab would have in the absence of any penetrating rod. In the second limit, the slab is as hot as the rod, and the rod is effectively insulated from $z = 0$ to $z = l$. The temperature is then independent of the slab conductivity.

Figure 2 compares the two limits. The heat transfer coefficients have only a slight effect here. The true rod temperature lies between the two limits, namely, in the shaded zones shown. Thus, given the parameter values, it is easy to determine the qualitative effect of the rod on the slab. When the rod radius is large enough, the rod heats the back face and cools the exposed face. This situation is common. However, it is apparent that a metal rod can also cool the back face and even warm the front face if the radius is small enough.

As a numerical example, a nominal 1 in. (1.315 in.-o.d.) stainless steel pipe through a 6 in. concrete wall gives $ak_3/lk = 0.82$ so the back face is heated. A 1/4 in. rod of the same material gives 0.16 and the back face is cooled.

In both equations (9) and (10), there is no radial heat flux. A third important limit is obtained at large b and represents an isolated rod through the wall. In this case, heat does flow radially so the temperature distribution does not have a simple form.

Numerical Results

In our calculations, we emphasize the kinds of trends that arise and how they merge into the asymptotic limits. We concentrate on the back face temperatue at the rod.

In each chart, the parameters not varied are assigned nominal values as follows: $a = 1.8 \times 10^{-3}$ m; $b = 2.7 \times 10^{-3}$ m; $H_1 = 200\ \mathrm{Wm^{-2}K^{-1}}$; $H_2 = 20\ \mathrm{Wm^{-2}K^{-1}}$; $k = 0.40\ \mathrm{Wm^{-1}K^{-1}}$; $k_3 = 350\ \mathrm{Wm^{-1}K^{-1}}$; $l = 0.15$ m. The nominal rod radius was chosen partly to best show the qualitative nature of the trends but also to represent the conductor in a #12 American wire gauge wire. The rod

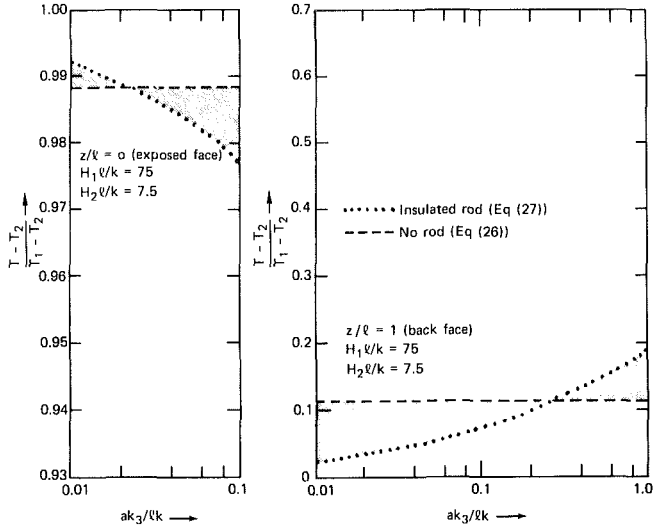

Fig. 2 Two limiting cases

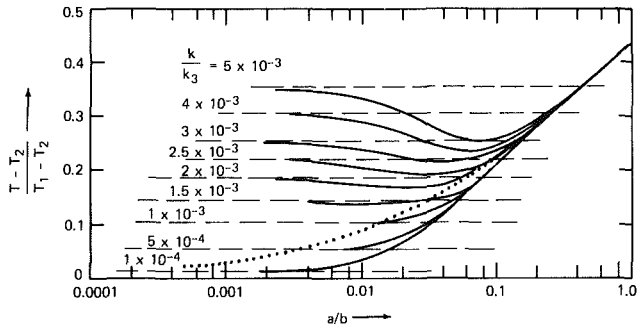

Fig. 3 The influence of a and k

conductivity is for copper. The "slab" conductivity is an approximate value for sealants. The nominal heat transfer coefficient, H_1, makes the initial heat flux to the slab equal to

$$H_1(T_1 - T_2) = 14\ \mathrm{Wcm^{-2}} \text{ when } T_1 = 900\ \mathrm{K} \text{ and } T_2 = 300\ \mathrm{K}$$

Calculations were also made with H_1 seven times less but the same kind of trends were found and, in fact, the curves were not displaced radically. We note that T_1 and T_2 can have any values in the charts.

Figure 3 has the same format as Fig. 2. The dashed lines are again calculated from equation (9), the "no-rod" limit, and the dotted line from equation (10), the "insulated-rod" limit. We vary the rod radius, a, along the horizontal axis and the rod conductivity, k, from curve to curve. The radius varies from about 0.001 to 2.0 mm and the conductivity from about 0.04 to 2 $\mathrm{Wm^{-1}K^{-1}}$, the latter value being typical for concrete. Nominal conditions are at $a/b = 0.67$ and $k/k_3 = 1.1 \times 10^{-3}$. Under these conditions, with $T_1 = 900$ K and $T_2 = 300$ K, the back face temperature is 540 K.

We see first that each calculated curve threads between its two asymptotes, as discussed for Fig. 2, and passes through the cross-over point. Second, each curve approaches its no-rod limit as $a \to 0$, and its insulated rod limit as $a \to b$. The insulated rod limit is quite accurate when a exceeds 20 percent of b, in which case the temperature is independent of k, the only thermal property of the slab needed in steady state. Third, each curve rises monotonically to the right of its cross-over point. In other words, given that the back face is being heated (Fig. 2), a rod with a larger radius will produce a hotter face temperature.

A large b, the slab temperature approaches the third limit,

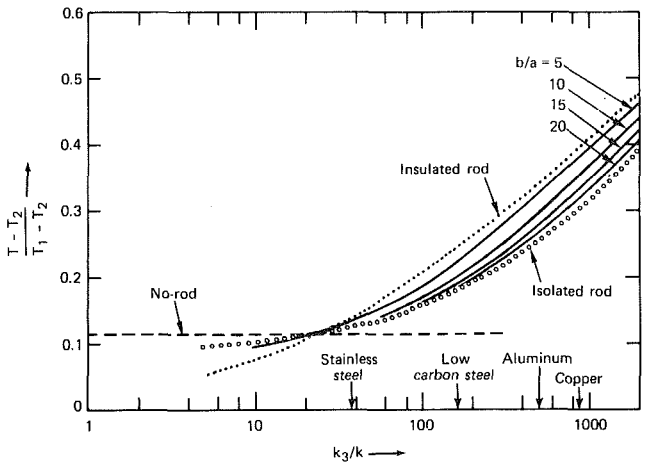

Fig. 4 The influence of k_3 and b

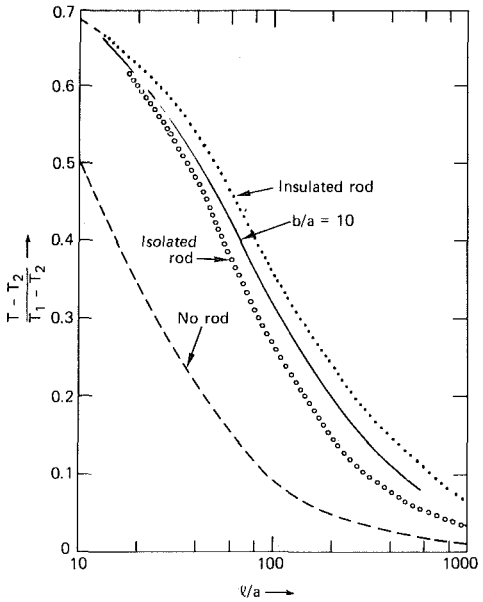

Fig. 5 The influence of l

namely, the isolated rod limit. This is demonstrated in Figs. 4 and 5, where the limit is plotted with circles.

In Fig. 4, the rod conductivity k_3 is varied along the horizontal axis and the spacing b varied from curve to curve. The conductivity varies from about 4 to 800 $Wcm^{-1}K^{-1}$ and the spacing from 0.3 mm to infinity. Nominal conditions are at $k_3/k = 875$ (copper rods) and $b/a = 1.5$.

In Fig. 4, the isolated rod limit is effectively reached at $b/a > 30$. At smaller b/a, the calculations thread between the isolated rod limit and the insulated rod limit. These two limits provide tighter bounds on the calculations. The accuracy of the insulated rod limit is not strongly affected by the rod conductivity for a wide range of practical metals. The figure also shows that the temperature increases as k_3 increases, and decreases as b increases, in both cases provided the back face is being heated by the rod.

Figure 5 shows that the best defense against heat flow through the slab is to increase the slab thickness, l. The thickness varies from about 2 cm to 1 m. Nominal conditions are at $l/a = 83$. Note that the temperature decreases markedly as l increases.

Summary

The back face temperature of a slab penetrated by equally sized, equally spaced rods is shown to be predicted with reasonable accuracy over a wide range of practical conditions by the simple formula, equation (10). Then the slab and rod temperatures are equal functions of z. The heat flux across the plane $z = 0$ is

$$\frac{k_3}{l}\frac{1}{(1+\eta_1^{-1}+\eta_2^{-1})}(T_1-T_2)$$

in each rod and k/k_3 times this value in the slab.

Temperature Distribution in an Electrically Heated Wide Metallic Foil

J. D. Tarasuk[1] and G. S. P. Castle[2]

It is commonly assumed that a current passing through a wide rectangular metallic foil is evenly distributed and that heat generated per unit surface area in such a foil is uniform.

A simple test [1] in which a metallic foil, equipped with thermocouples, was supported by a Perspex frame indicated that large temperature variations were possible in the plane of the foil. Tests showed that under a broad range of conditions this temperature distribution was not significantly influenced by the mode of heat transfer, 60 Hz, a-c or d-c current, foil orientation, foil material (resistance was maintained constant by varying foil thickness), foil aspect ratio, or the use of compensating bus bars. It was found that the temperature, and hence the electrical power dissipation, could be in the order of 30 percent higher near the center of the foil as compared to the temperature near the foil edge.

In view of these unexpected results, further quantitative tests were carried out. In one series of tests, 36 gauge copper-constantan thermocouples were spot welded to the foil. The foil used in all these tests was 302 precision Stainless Steel, 0.025-mm thick, 15-cm high and of various widths (3.5, 4.6, 5.1, and 6.5 cm). Copper bus bars were attached to the width dimension and were thermally insulated from the supporting frame. Both a-c and d-c stabilized currents were used. The foil was heated in a draught-free Perspex enclosure and was mounted in a vertical plane. Tests were carried out in which the same model was rotated so that the 15 cm dimension was either vertical or horizontal. Similarity of the results excluded the possibility of a natural convective effect.

Thickness of the foil and weight samples were measured to ensure uniformity. The direction in which the foil was rolled in the forming process did not affect the temperature distribution. In a second series of tests, an infrared radiometric microscope (Barnes Engineering Co., optical pyrometer, model #RM-2B) was used to scan the foil surface from a distance of 46 cm. This instrument averaged the surface temperature over a 2-mm dia region and provided a direct readout on a meter scale to within ± 0.5 deg centigrade. To ensure that natural convective effects were minimized, the foil was placed in an evacuated chamber. The temperature scans were obtained through a window transparent to the infrared wavelengths emitted by the foil. Figure 1 illustrates the arrangement of the apparatus. It should be noted that similar results occurred even when the foil was not in an evacuated environment. The irradiation within the isothermal 1-cm thick walled steel vacuum chamber was assumed to be constant and did not effect the foil temperature

[1] Associate Professor, Faculty of Engineering Science, University of Western Ontario, London, Ontario, Canada N6A 5B9.

[2] Professor, Faculty of Engineering Science, University of Western Ontario.

Contributed by the Heat Transfer Division for publication in the JOURNAL OF HEAT TRANSFER. Manuscript received by the Heat Transfer Division July 9, 1981.

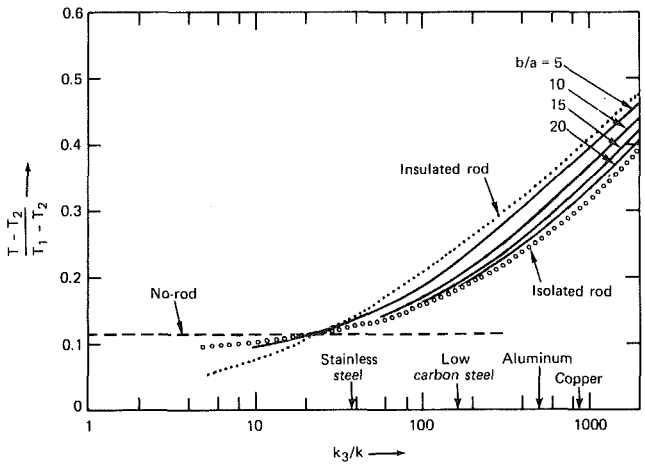

Fig. 4 The influence of k_3 and b

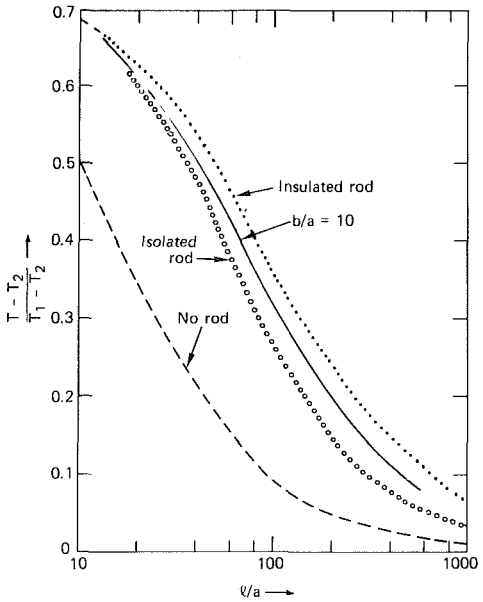

Fig. 5 The influence of l

namely, the isolated rod limit. This is demonstrated in Figs. 4 and 5, where the limit is plotted with circles.

In Fig. 4, the rod conductivity k_3 is varied along the horizontal axis and the spacing b varied from curve to curve. The conductivity varies from about 4 to 800 $Wcm^{-1}K^{-1}$ and the spacing from 0.3 mm to infinity. Nominal conditions are at $k_3/k = 875$ (copper rods) and $b/a = 1.5$.

In Fig. 4, the isolated rod limit is effectively reached at $b/a > 30$. At smaller b/a, the calculations thread between the isolated rod limit and the insulated rod limit. These two limits provide tighter bounds on the calculations. The accuracy of the insulated rod limit is not strongly affected by the rod conductivity for a wide range of practical metals. The figure also shows that the temperature increases as k_3 increases, and decreases as b increases, in both cases provided the back face is being heated by the rod.

Figure 5 shows that the best defense against heat flow through the slab is to increase the slab thickness, l. The thickness varies from about 2 cm to 1 m. Nominal conditions are at $l/a = 83$. Note that the temperature decreases markedly as l increases.

Summary

The back face temperature of a slab penetrated by equally sized, equally spaced rods is shown to be predicted with reasonable accuracy over a wide range of practical conditions by the simple formula, equation (10). Then the slab and rod temperatures are equal functions of z. The heat flux across the plane $z = 0$ is

$$\frac{k_3}{l}\frac{1}{(1+\eta_1^{-1}+\eta_2^{-1})}(T_1-T_2)$$

in each rod and k/k_3 times this value in the slab.

Temperature Distribution in an Electrically Heated Wide Metallic Foil

J. D. Tarasuk[1] and G. S. P. Castle[2]

It is commonly assumed that a current passing through a wide rectangular metallic foil is evenly distributed and that heat generated per unit surface area in such a foil is uniform.

A simple test [1] in which a metallic foil, equipped with thermocouples, was supported by a Perspex frame indicated that large temperature variations were possible in the plane of the foil. Tests showed that under a broad range of conditions this temperature distribution was not significantly influenced by the mode of heat transfer, 60 Hz, a-c or d-c current, foil orientation, foil material (resistance was maintained constant by varying foil thickness), foil aspect ratio, or the use of compensating bus bars. It was found that the temperature, and hence the electrical power dissipation, could be in the order of 30 percent higher near the center of the foil as compared to the temperature near the foil edge.

In view of these unexpected results, further quantitative tests were carried out. In one series of tests, 36 gauge copper-constantan thermocouples were spot welded to the foil. The foil used in all these tests was 302 precision Stainless Steel, 0.025-mm thick, 15-cm high and of various widths (3.5, 4.6, 5.1, and 6.5 cm). Copper bus bars were attached to the width dimension and were thermally insulated from the supporting frame. Both a-c and d-c stabilized currents were used. The foil was heated in a draught-free Perspex enclosure and was mounted in a vertical plane. Tests were carried out in which the same model was rotated so that the 15 cm dimension was either vertical or horizontal. Similarity of the results excluded the possibility of a natural convective effect.

Thickness of the foil and weight samples were measured to ensure uniformity. The direction in which the foil was rolled in the forming process did not affect the temperature distribution. In a second series of tests, an infrared radiometric microscope (Barnes Engineering Co., optical pyrometer, model #RM-2B) was used to scan the foil surface from a distance of 46 cm. This instrument averaged the surface temperature over a 2-mm dia region and provided a direct readout on a meter scale to within ± 0.5 deg centigrade. To ensure that natural convective effects were minimized, the foil was placed in an evacuated chamber. The temperature scans were obtained through a window transparent to the infrared wavelengths emitted by the foil. Figure 1 illustrates the arrangement of the apparatus. It should be noted that similar results occurred even when the foil was not in an evacuated environment. The irradiation within the isothermal 1-cm thick walled steel vacuum chamber was assumed to be constant and did not effect the foil temperature

[1] Associate Professor, Faculty of Engineering Science, University of Western Ontario, London, Ontario, Canada N6A 5B9.

[2] Professor, Faculty of Engineering Science, University of Western Ontario.

Contributed by the Heat Transfer Division for publication in the JOURNAL OF HEAT TRANSFER. Manuscript received by the Heat Transfer Division July 9, 1981.

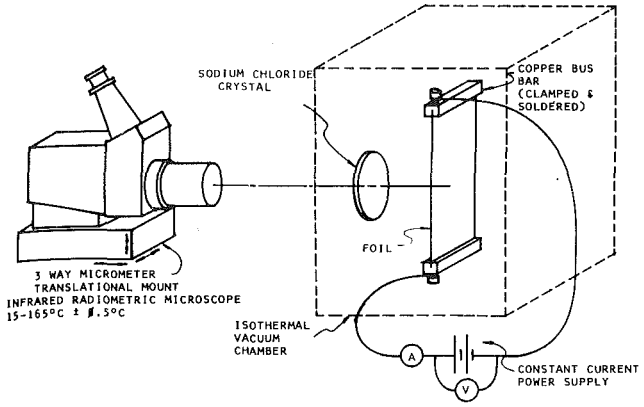

Fig. 1 Experimental arrangement

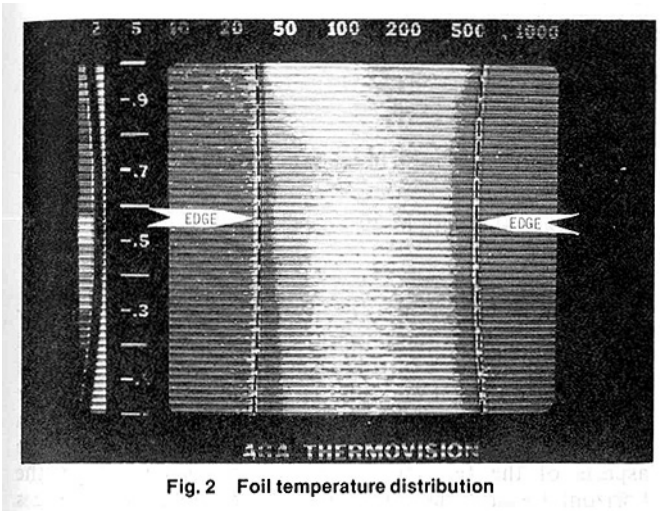

Fig. 2 Foil temperature distribution

distribution. The vacuum was maintained at 0.001-mm Hg during the tests.

A qualitative study was also made using temperature-sensitive liquid crystals and an AGA Thermovision camera. Both methods showed that the temperatures in the center of the foil were significantly higher than those at the foil edges. A typical thermogram is shown in Fig. 2. High temperature regions are indicated by the light regions on the thermogram.

Typical results of the temperature variation as obtained by the radiometer are shown in Fig. 3. The chamber was at room temperature (21°C) and the foil center temperature (T_{max}) are noted on Fig. 3. These results agreed closely with the results obtained by thermocouples and were found to be similar to the results found in reference [1].

The reason for this nonuniformity in surface temperature is believed to be a redistribution of the current due to the Longitudinal Hall Effect. In this uncommon phenomenon [2], the current-carrying electrons undergo a lateral inward force due to the self magnetic field produced by the current flow. The magnitude of this force is negligibly small in good conductors of normal aspect ratios and low current density. However, in the case considered here, the material (302 Stainless Steel) is a relatively poor conductor, the ratio of conductor width to thickness is large and the current densities are high. According to Smythe [2] these are all conditions in which the Longitudinal Hall Effect may be significant. This large aspect ratio results in large variations in the relative magnetic field strengths across the width of the foil. As an example, consider the idealized situation of an infinitely thin foil having current uniformly distributed across the width. This situation can be solved exactly using classical

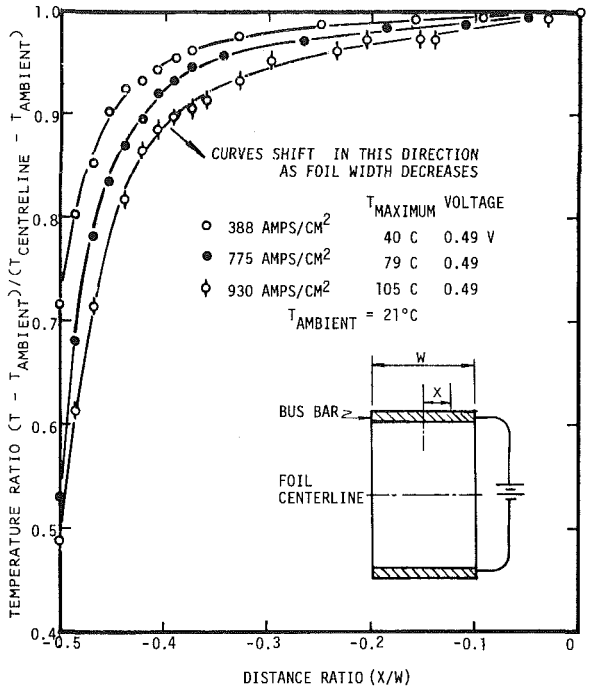

Fig. 3 Temperature variation along the centerline of an electrically heated 5.08 cm foil

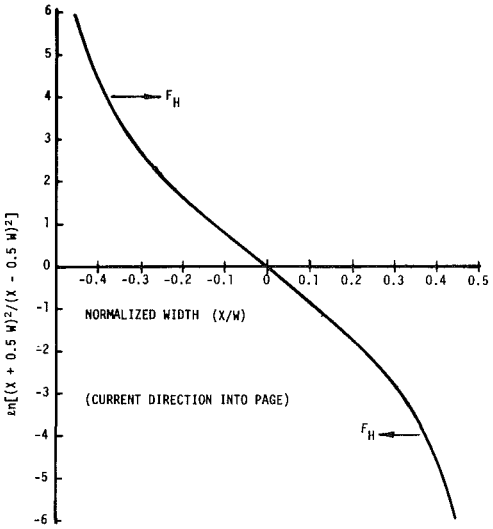

Fig. 4 The vertical component of normalized magnetic flux density as a function of position across the width of an infinitely thin foil with a uniform current distribution

magnetostatic theory. The expression for the vertical component of the magnetic field density in Wb/m^2 is given by [3]

$$B_y = -\frac{\mu_0 K}{4\pi} ln \frac{(X+.5\ W)^2}{(X-.5\ W)^2}$$

where μ_0 is the permeability of free space (H/m), K is the current per unit width (A/m), X is the position across the foil (m), with the center of the foil taken as the origin, and W is the width of the foil (m).

The resulting relative distribution in the magnetic flux density is shown in Fig. 4.

The force on any charge carrier is given by the Lorentz equation as

$$\bar{F}_H = q\bar{v} \times \bar{B}$$

where q is the charge on one electron (C), v is the velocity of

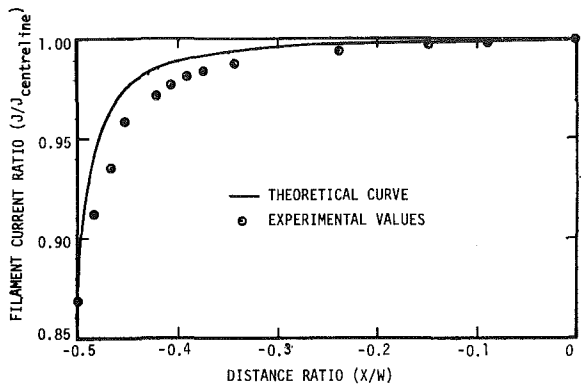

Fig. 5 Comparison of theoretical and experimental current ratios in the 5.08 cm foil for a current density of 388 amps/cm^2

the electrons (m/s), and B is the magnetic flux density (Wb/m^2).

Referring to Fig. 4, it can be seen that for a current flow moving into the page, the charge carriers will experience a lateral force tending to deflect them towards the centerline of the foil. The magnitude of this force is maximum at the edges of the foil, decreasing towards the centerline. This deflection of the charge carriers produces a lateral component of electric field, the amplitude of which varies with position across the foil. Under equilibrium conditions this field can be expressed as

$$\bar{E}_H = R_H \bar{J} \times \bar{B}$$

where E_H is the electric field induced by the Longitudinal Hall Effect (V/m), J is the local value of current density (A/m^2), B is the magnetic flux density (Wb/m^2), and R_H is the Hall Coefficient of the material (V.m^3/A.Wb). The Hall Coefficient can be shown to be inversely proportional to the number of charge carriers per unit volume and thus increases as resistance increases.

The net result of this lateral deflection of the charge carriers is to increase the current density towards the centerline of the foil leading to higher resistance heating and thus higher surface temperatures.

From this qualitative description, it can be seen that an analytical solution is nonlinear since the magnetic field depends upon the current distribution and this in turn is modified by the field. In addition, the electrical resistance and Hall Coefficient for the material is a function of temperature.

The effect was analyzed using a filament model to represent the metallic foil. In this model the foil was represented by N separate current carrying filaments running parallel to the length of the foil. An iterative procedure was used to calculate the relative current densities in each of the filaments by initially assuming a uniform current distribution, calculating the resulting Hall electric field between adjacent filaments, and then imposing the constraint that the current density must redistribute laterally to counteract this induced electric field. Current densities were calculated using $N = 101$ filaments, and the resulting values were then assumed at the appropriate positions across the width of the foil and compared to the experimental measurements by calculating the necessary current densities required to produce the power dissipation to give rise to the measured values of surface temperature. In making these calculations, several assumed values of the material constants were required, since they were not available for the material used. The most uncertain parameter was the value of Hall Coefficient, which was taken to be 5.2×10^{-7} V.m^3/A.Wb. Although this value is two orders of magnitude larger than tabulated values for mild steel at room temperature, it seems not an unreasonable value when it is considered that the stainless steel used had a resistance fifteen times larger than mild steel and the resistance would be even larger at the higher temperatures used in this study.

Figure 5 shows some typical experimental results along with values arrived at from the numerical solution. The general agreement between the two led to the conclusion that this effect was, in fact, a result of the Longitudinal Hall Effect.

These results show that the heat flux from an electrically heated wide metallic foil may be nonuniform and that serious errors may exist in heat transfer studies if this is not taken into account.

References

1 Tarasuk, J. D., "An Interferometric Study of Natural Convection During the Interaction of Surfaces for a Long Rectangular Block," Ph.D. thesis, University of Saskatchewan, 1969.

2 Smythe, W. R., *Static and Dynamic Electricity*, McGraw-Hill, 2d ed., 1950, p. 232.

3 Zahn, M., *Electromagnetic Field Theory*, John Wiley, 1979, p. 342.

Some Aspects of Natural Convection in a Corner

C. Rodighiero[1] and L. M. de Socio[2]

1 Introduction

In this note some aspects of the free convection in a corner are investigated for the physical condition of an isothermal and vertical flat plate of finite height, L, perpendicular to an infinite adiabatic flat wall (Fig. 1). To the authors' knowledge this problem has not yet been dealt with in the literature, in spite of its practical relevance. Figure 1 sketches the intricate aspects of the flow field, where a shear layer over the horizontal wall deviates upward near the corner and merges with the new thermal boundary layer whose origin is at the leading edge (LE) of the isothermal plate. In stable conditions, interferometric observation did not reveal any recirculating region. Finally, a plume leaves from the trailing edge (TE) of the vertical wall. Of this intriguing general picture two main points were explored: namely, the heat transfer characteristics of the isothermal plate, and the occurrence of instability phenomena.

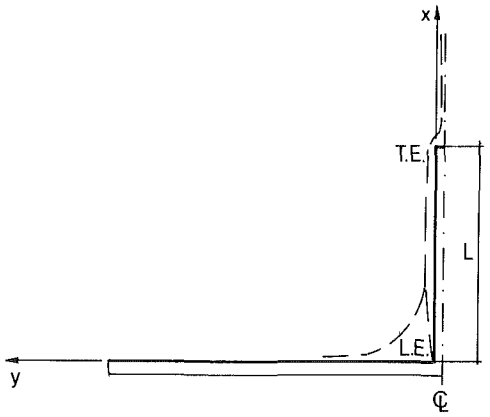

Fig. 1 A sketch of the flow in the corner

[1] Graduate student.

[2] Professor, Institute of Applied M echanics, Politecnico di Torino, Torino 10129, Italy. Mem. ASME

Contributed by the Heat Transfer Division for publication in the JOURNAL OF HEAT TRANSFER. Manuscript received by the Heat Transfer Division November 13, 1981.

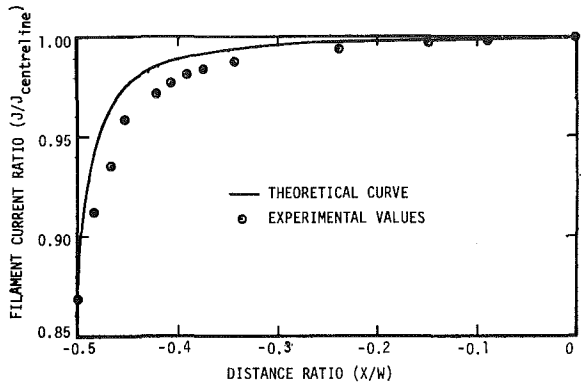

Fig. 5 Comparison of theoretical and experimental current ratios in the 5.08 cm foil for a current density of 388 amps/cm^2

the electrons (m/s), and B is the magnetic flux density (Wb/m^2).

Referring to Fig. 4, it can be seen that for a current flow moving into the page, the charge carriers will experience a lateral force tending to deflect them towards the centerline of the foil. The magnitude of this force is maximum at the edges of the foil, decreasing towards the centerline. This deflection of the charge carriers produces a lateral component of electric field, the amplitude of which varies with position across the foil. Under equilibrium conditions this field can be expressed as

$$\bar{E}_H = R_H \bar{J} \times \bar{B}$$

where E_H is the electric field induced by the Longitudinal Hall Effect (V/m), J is the local value of current density (A/m^2), B is the magnetic flux density (Wb/m^2), and R_H is the Hall Coefficient of the material (V.m^3/A.Wb). The Hall Coefficient can be shown to be inversely proportional to the number of charge carriers per unit volume and thus increases as resistance increases.

The net result of this lateral deflection of the charge carriers is to increase the current density towards the centerline of the foil leading to higher resistance heating and thus higher surface temperatures.

From this qualitative description, it can be seen that an analytical solution is nonlinear since the magnetic field depends upon the current distribution and this in turn is modified by the field. In addition, the electrical resistance and Hall Coefficient for the material is a function of temperature.

The effect was analyzed using a filament model to represent the metallic foil. In this model the foil was represented by N separate current carrying filaments running parallel to the length of the foil. An iterative procedure was used to calculate the relative current densities in each of the filaments by initially assuming a uniform current distribution, calculating the resulting Hall electric field between adjacent filaments, and then imposing the constraint that the current density must redistribute laterally to counteract this induced electric field. Current densities were calculated using $N = 101$ filaments, and the resulting values were then assumed at the appropriate positions across the width of the foil and compared to the experimental measurements by calculating the necessary current densities required to produce the power dissipation to give rise to the measured values of surface temperature. In making these calculations, several assumed values of the material constants were required, since they were not available for the material used. The most uncertain parameter was the value of Hall Coefficient, which was taken to be 5.2×10^{-7} V.m^3/A.Wb. Although this value is two orders of magnitude larger than tabulated values for mild steel at room temperature, it seems not an unreasonable value when it is considered that the stainless steel used had a resistance fifteen times larger than mild steel and the resistance would be even larger at the higher temperatures used in this study.

Figure 5 shows some typical experimental results along with values arrived at from the numerical solution. The general agreement between the two led to the conclusion that this effect was, in fact, a result of the Longitudinal Hall Effect.

These results show that the heat flux from an electrically heated wide metallic foil may be nonuniform and that serious errors may exist in heat transfer studies if this is not taken into account.

References

1 Tarasuk, J. D., "An Interferometric Study of Natural Convection During the Interaction of Surfaces for a Long Rectangular Block," Ph.D. thesis, University of Saskatchewan, 1969.

2 Smythe, W. R., *Static and Dynamic Electricity*, McGraw-Hill, 2d ed., 1950, p. 232.

3 Zahn, M., *Electromagnetic Field Theory*, John Wiley, 1979, p. 342.

Some Aspects of Natural Convection in a Corner

C. Rodighiero[1] and L. M. de Socio[2]

1 Introduction

In this note some aspects of the free convection in a corner are investigated for the physical condition of an isothermal and vertical flat plate of finite height, L, perpendicular to an infinite adiabatic flat wall (Fig. 1). To the authors' knowledge this problem has not yet been dealt with in the literature, in spite of its practical relevance. Figure 1 sketches the intricate aspects of the flow field, where a shear layer over the horizontal wall deviates upward near the corner and merges with the new thermal boundary layer whose origin is at the leading edge (LE) of the isothermal plate. In stable conditions, interferometric observation did not reveal any recirculating region. Finally, a plume leaves from the trailing edge (TE) of the vertical wall. Of this intriguing general picture two main points were explored: namely, the heat transfer characteristics of the isothermal plate, and the occurrence of instability phenomena.

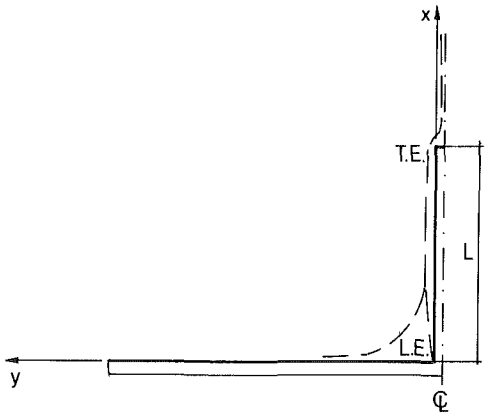

Fig. 1 A sketch of the flow in the corner

[1] Graduate student.

[2] Professor, Institute of Applied M echanics, Politecnico di Torino, Torino 10129, Italy. Mem. ASME

Contributed by the Heat Transfer Division for publication in the JOURNAL OF HEAT TRANSFER. Manuscript received by the Heat Transfer Division November 13, 1981.

2 Experimental Apparatus

In the experimental apparatus the horizontal plate was made of a wooden board, 0.05-m thick, and 6-m long, at the middle of which the isothermal vertical plate was fixed. The width of the adiabatic wall was 0.80 m. The two plates were placed between vertical plexiglass sidewalls, 1.5-m high, in which optical glass windows were installed. A distance of 3.5 m was left between the horizontal wall and the ceiling of a 5 m $\times$ 5 m room.

Three different vertical plates were tested, each of them corresponding to a sandwich of two external copper plates 0.005-m thick, two 0.5-mm intermediate mica sheets, and an internal heating element made of NiCr 0.8 mm $\times$ 1 mm ribbon. The entire length of the ribbon was divided into sections suitably connected to the voltage source in order to assure isothermal conditions for the plate. All the external surfaces were painted dull black.

The heights of the three panels were 0.127 m, 0.21 m, and 0.3 m, respectively, so that three different aspect ratios of the vertical plate were tested for their influence on the heat transfer results and on the plume. The entire apparatus was symmetrical with respect to the middle vertical plane.

In each metal plate, five 0.25-mm J thermocouples were located, one at the center and four at the corners, 20 mm from the sides. Two more thermocouples were installed at each end of the wooden board in order to provide the readings of the ambient temperature, T_o. Two other thermocouples, symmetric to the heated plate and 1 cm apart from its LE confirmed the adiabaticity of the horizontal plate. A Solartron Multimeter was adopted for the thermocouple signals, with a maximum error of 0.1 percent in the entire range of readings of the temperatures, whereas the electrical input to the heating system was measured within an accuracy of 1 percent. In the laminar regime, the magnitude of $T_w - T_o$ varied between 10 and 80 K, where T_w is the vertical wall temperature.

A Wollaston interferometer, which could be used also as a Schlieren and shadowgraph system, provided the means for local heat flux measurements and for visualization. A HeNe Laser source of 8 mW was adopted together with two spherical mirrors of 28 cm of diameter and 3 m of focal length. A 5 cm $\times$ 5 cm Wollaston quartz biprism of 5 deg divergence angle was used, and the fringe shifts were measured on pictures taken on a semitransparent glass screen.

The isothermal conditions of the metal plates were checked by means of the thermocouples and by means of an AGA thermograph with a maximum deviation of 0.2° K over the entire surface at T_w = 97 K. Steady conditions were verified on the continuous recording of the thermocouples, when temperature fluctuations in a hour were less than the accuracy of the measuring device. Maximum time for reaching steadiness was of about 8 hrs.

The interferometric data provided the local Nusselt number values, $Nu_x = hx/k$, where h is the local heat transfer coefficient and k is the thermal conductivity, and, by integration over the vertical abscissa, the mean Nusselt number, Nu, for the plate.

For comparison purposes, the values of Nu were also calculated from the electrical power input, taking into account, approximately, the radiation and heat conduction losses at the sidewalls. The electrically measured Nu differ in excess by a maximum of 12 percent from the interferometric data, which were reduced according to the procedure of [1, 2].

3 Results

The usual Grashof number definition is adopted, $Gr = g\beta(T_w - T_o)L^3/\nu^2$, where g is the acceleration of gravity, and β and ν are the thermal expansion coefficient and the kinematical viscosity of the fluid, respectively. The Rayleigh number is given by Ra = Pr Gr, where Pr is the Prandtl number, ν/α, and α is the thermal diffusivity. The local Rayleigh number, Ra_x, corresponds to the reference length, x.

The laminar range of explored Rayleigh numbers varied between 10^6 and 1.8×10^8, before flow instability was first observed. Figure 2 shows, from the left, two shadographs of the region close to the LE and one shadowgraph of the zone near the TE at Pr = 0.7. The width of each photographic strip corresponds to 1.8 cm. Whereas the boundary layer thickness increases with x, the heat transfer coefficient decreases, as

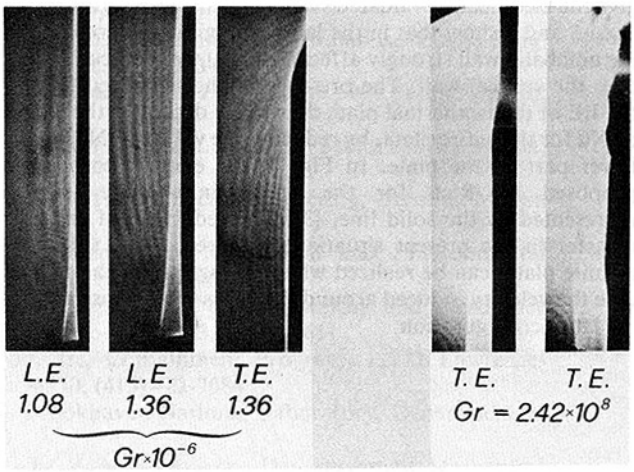

Fig. 2 Shadowgraphs of the flow at different Grashof numbers

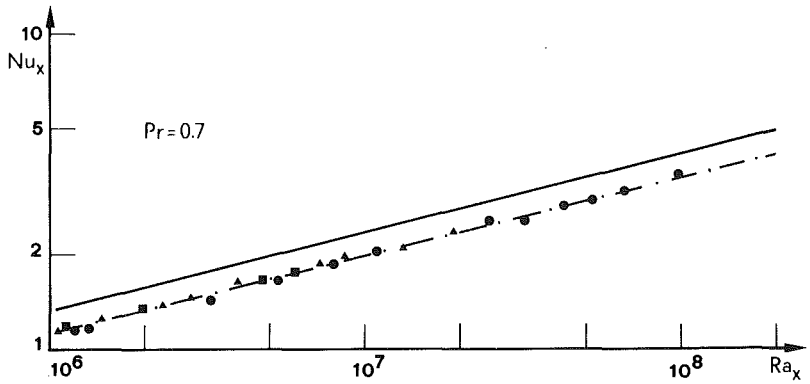

Fig. 3 Local Nusselt number distribution versus local Rayleigh number: squares, L = 0.127 m; triangles, L = 0.21 m; circles, L = 0.3 m

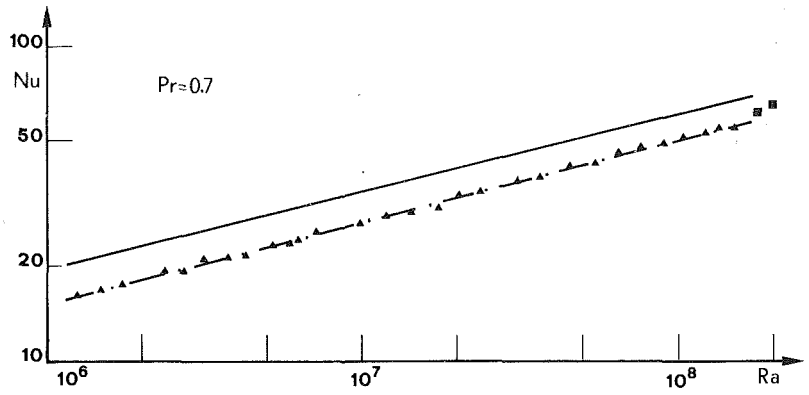

Fig. 4 Average Nusselt number distribution versus Rayleigh number

shown by the luminous external line. This is confirmed by the results in Fig. 3.

The experimental Nu_x distribution versus Ra_x is shown in Fig. 3 for the three tested plates. As shown, the influence of the aspect ratio of the plate and the effects of the thickness of the sandwich were almost negligible. The experimental results fit well the line $Nu_x = 0.412\ Ra_x^{0.243}$. The solid line corresponds to the data for the isothermal semi-infinite vertical plate [3]. Figure 4 shows the average Nusselt number versus the Rayleigh number. In this case the experimental data are well fitted by the law $Nu = 0.465\ Ra^{0.253}$. Whereas the triangles correspond to the interferometric data, the squares give the electrically evaluated Nu in the unstable region. Both Figs. 3 and 4 show that in the laminar regime the presence of the adiabatic wall strongly affects the heat transfer coefficient over the vertical wall. The presence of the separated flow at the LE of the isothermal plate drastically decreases the values of Nu for the entire plate, by reducing the values of Nu_x in the lower part of the plate. In Fig. 4, the empiric correlation proposed by Rich for the semi-infinite plate is also represented by the solid line, [3]. The reduction of the heat transfer in the present situation, with respect to the semi-infinite plate, can be realized when noting that in the former case the velocity induced around the LE is less intense than in the latter configuration.

As previously stated, at $Ra \simeq 1.8 \times 10^8$ instability phenomena first occurred in the form of long air bubbles which developed in the corner region and rapidly moved upward along the vertical wall. A new bubble is formed near the LE only shortly after the previous one dissappears in the plume. This situation is illustrated in the last two pictures at the r.h.s. of Fig. 2. There, two shadowgraphs, both taken at the same Grashof number, are given: in the left one a laminar boundary layer develops on the surface up to the TE, whereas in the right one the shear layer is strongly perturbed by the bubble and the departing plume is turbulent.

Acknowledgment

This work was partially supported by CNR Grant No. CT 80.01131.07.

References

1 Sernas, V., Fletcher, L. S., and Jones, J. A., "An Interferometric Heat Flux Measuring Device," ISA Transactions, Vol. 11, 1972, pp. 346-357.

2 Sernas, V., "The Wollaston Prism Schlieren Interferometer, in *Advanced Measurement Techniques in Fluid Mechanics*, von Kàrmàn Institute for Fluid Dynamics Lecture Series 96, 1977, pp. 1-31.

3 Rich, B. R., "An Investigation of Heat Transfer from an Inclined Flat Plate in Free Convection," ASME *Transactions*, Vol. 75, 1953, pp. 489-499.

ERRATA

Corrections to "Nonlinear Stability of Film Condensation," by M. Unsal and W. C. Thomas, published in the August 1980 issue of the ASME JOURNAL OF HEAT TRANSFER, pp. 483–488:

An algebraic error has been noted in the analysis of the referenced article. To correct this error, the integer 53 in equations (35), (39), and (44) should be replaced by 11. The integer 131 in equation (43) should be replaced by 47. These corrections result in larger equilibrium wave amplitudes and smaller nonlinear wavespeeds than those reported in Figs. 5–8. The amplitude and wavespeed predictions corresponding to Kapitza's experiments are corrected as follows:

For waves on an alcohol film: $\epsilon a = 0.282,\ c_r = 1.90$

For waves on a water film: $\epsilon a = 0.283,\ c_r = 1.90$